CHAPTER 1

Figures

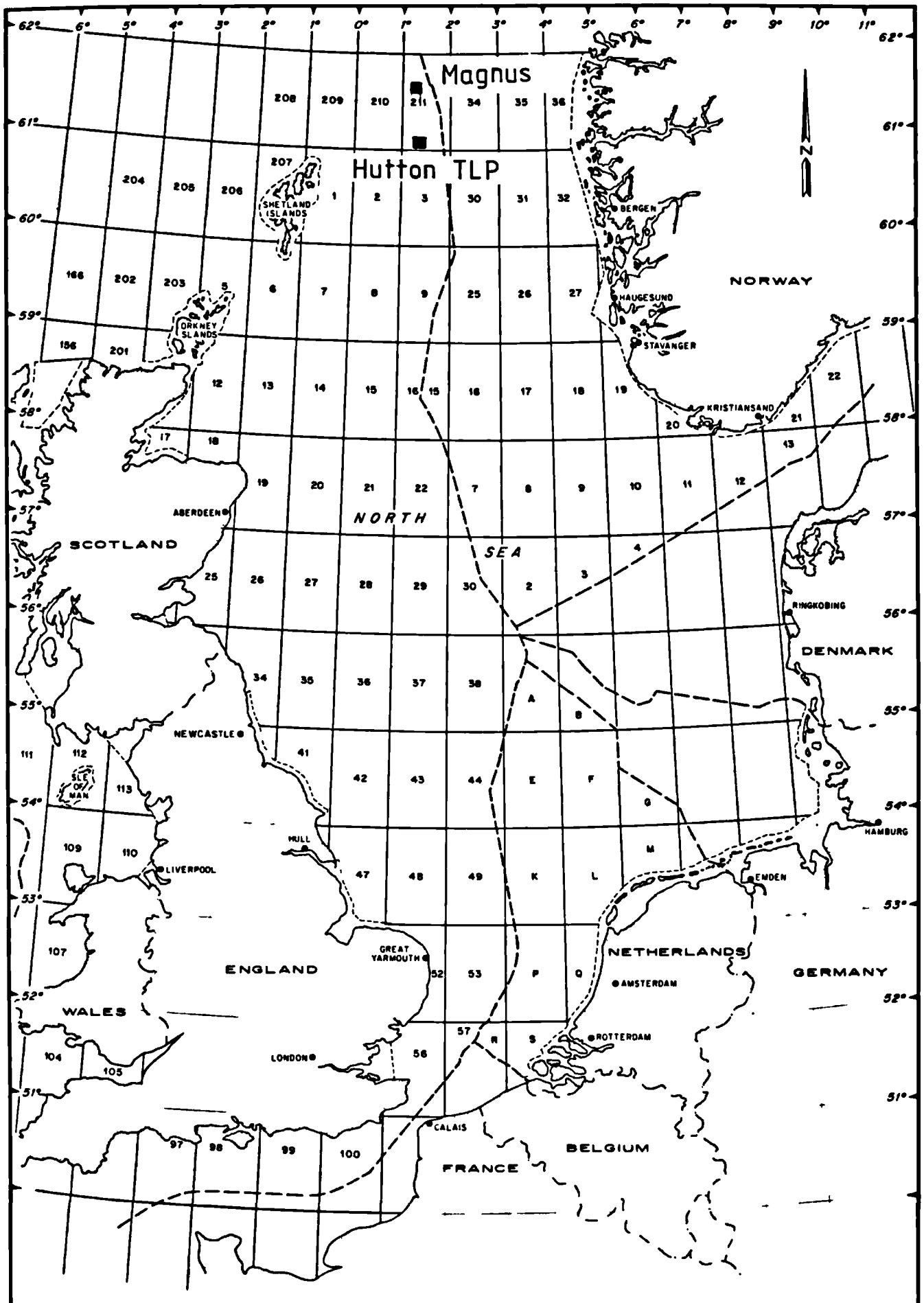


Figure 1.1 VICINITY MAP

CHAPTER 2

Tables and Figures

ndex No	Reference	Penetration Metres	Diameter MM	L/D	Mean Cu kpa	Mean Cu/σ'_v	Overall α	Atterberg Limits LL	PL	PI%	Set up weeks	Comments
1	Housel (1950)	20.4	406	29	13	0.21	0.97	?	?	?	4 to 6	Conical pile tips
2	Mansur and Focht (1956)	17.7	610	45	30	0.21	1.01	60-100		30-70	"	"
3	"	20.4	457	34	30	0.21	0.76	"		"	"	"
4	"	20.4	610	27	30	0.21	0.96	"		"	"	"
5	"	20.4	762	32	30	0.21	0.92	"		"	"	"
6	"	19.5	610	50	32	0.24	1.00	"		"	"	"
7	"	22.9	457	95	32	0.21	1.10	"		"	"	"
8	Peck (1958)	38.1/25.9	273	117	155	0.61	0.63	?		12-15	2 to 4	Closed end piles
9	"	33.5/22.3	273	102	145	0.66	0.64	?		"	"	(Samples from 2"
10	"	38.4/27.1	273	120	155	0.61	0.59	?		"	"	Shelby tubes)
11	"	35.9/24.7	273	111	151	0.63	0.58	?		"	"	"
12	"	52.0	273	190	107	0.39	0.49	?		"	"	"
13	"	48.8/39.6	273	162	165-48	0.56	0.49	?		"	"	"
14	Peck (1961)	22.9	324	71	52-48	0.57	0.52	?		"	1 to 1.5	Open pipe piles
15	"	45.7	324	142	52-62	0.35	0.42	?		"	"	driven in
16	"	22.9	324	71	52-48	0.57	0.45	?		"	"	Lacustrine clay,
17	"	66.5	324	205	60-81	0.27	0.52	?		"	"	(Samples from 2" Shelby tubes)

Table 2.1 (a)

Index No	Reference	Penetration Metres	Diameter MM	L/D	Mean Cu kpa	Mean Cu/σ'_v	Overall α	Atterberg Limits% LL	PL	PI	Set up weeks	Comments
18C	Fox et al (1970)	6.1	762	8	260	6.9	0.53	30-35	15-17	15-20	0.1	Open pipe pile in
18T	"	6.1	762	8	260	6.9	"	"	"	"	"	sequence of Boulder
19T	"	9.1	762	12	309	5.5	0.43	"	"	"	"	clay to 12 metres,
20C	"	12.2	762	16	366	4.9	0.43	"	"	"	"	then sand and Lias cla
20T	"	12.2	762	16	366	4.9	"	"	"	"	"	Redriving between
21C	"	15.2	762	20	383	4.1	0.36	30-60	15-28	15-35	"	tests, set up after
21T	"	15.2	762	20	383	4.1	"	"	"	15-35	"	120 hours equivalent t
22C	"	18.3	762	24	393	3.5	0.40	"	"	15-35	"	16.5%. Samples from
22T	"	18.3	762	24	393	3.5	0.36	"	"	15-35	"	2" Shelby Tubes.
23	Woodward et al (1961)	13.7	324	42	45-53	0.4	0.94			10-20	?	Closed pile
24T	"	13.7	324	42	137	1.2	0.47			"	?	"
25	Tomlinson (1970)	2.4	168	14	109	4.7	0.92			40-50	4	Conical Pile tips,
26	"	2.9	168	17	110	4.0	0.82			40-50	"	1½" UU tests from
27	"	4.6	168	27	121	2.8	0.63			40-50	"	U100 driven samples,
28	"	4.6	168	27	121	2.8	0.68			40-50	"	London clay
29	"	5.5	168	33	130	2.5	0.59			40-50	"	"
30	"	5.5	168	33	130	2.5	0.57			40-50	"	"

Table 2.1 (b)

Index No	Reference	Penetration Metres	Diameter MM	L/D	Mean Cu kpa	Mean Cu/σ'_v	Overall α	Atterberg Limits% LL	PL	PI	Set up weeks	Comments
1	McClelland and	30.5	610	50	52-86	0.54	0.59	50		25-35	0.1 to 1.5	Pipe pile (open)
2	Golder (1970)	48.2	610	79	64-86	0.32	0.59	"		"	"	"
3	McClelland Eng.	43.9	305	144	28-62[2]	0.18-0.41	0.46-1.1	?		40-70	7	"
3*	"	"	"	"	38-43	0.23	0.79	?		40-70	"	Field Vane Cu Values
4	"	33.5	324	103	35	0.29	0.86	?		40-70	1 to 2	Pipe pile (open)
5	"	33.5	324	103	49	0.45	0.56	?		40-70	"	"
6	Darragh and Bell (1969)	30.5	324	94	45-81[2]	0.38-0.48	0.49-0.65	50.100		20-50	3	closed end pile
7[T]	McClelland Eng.	20.3	324	63	113	0.71	0.47	?		"high"	1	open pipe pile
8	Seed and Reese (1957)	7.0	156	45	12	0.24	0.80	42	24	18	4	closed end pile
9	Blessey (1970)	30.4	508	60	24	0.24	0.96	?		750	?	" " "
0	Peck (1958)	24.4	324	75	61	0.62	0.56	?		730	1	" " "
1	"	27.4	324	85	61	0.55	0.55	?		"	1	" " "
2	McClelland and Lipscombe (1956)	101.5	356	285	10	0.18	0.92	?		40-70	3	open pipe pile

Notes: (Pile tests are in compression except where the symbol T by the Index No. indicates a tension test)
1 Penetrations have been adjusted for any superficial sand layers, with appropriate reductions in total shaft capacity.
2 Ranges of Cu, Cu/σ'_v and α have been extended by the use of confined triaxial tests in addition to unconfined compression tests.

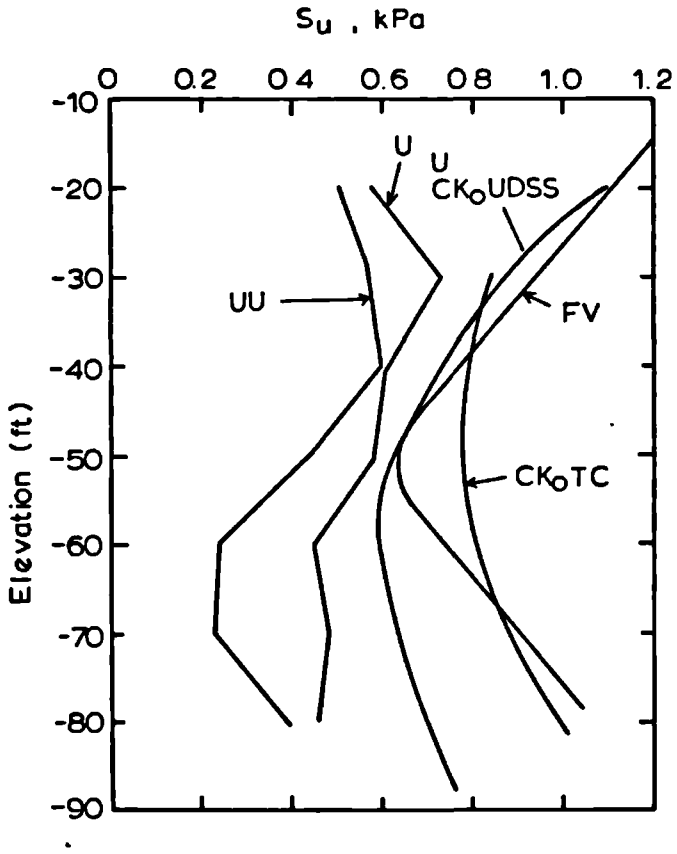
Table 2.1 (c)

Range of Plasticity Index	< 20%	20-50%	> 50%
% of Pile Tests	44	27	29
Mean α values	0.52	0.64	0.78
% of tests with $Cu/\sigma'_v < 0.5$[1]	17	0	42
Mean set up time (weeks)	1.77	4.50	4.64

Division of Pile Tests by Soil Plasticity Index.

Table 2.2

[1] A value of Cu/σ'_v below 0.5 indicates an overconsolidation ratio below 2.0 for most K_o consolidated clays, Ladd et al (1977)



U	Unconfined Compression
UU	Unconsolidated undrained compressio
CIU	Isotropically consolidated undrained compression
CK_OTC	K_o consolidated undrained compressi
CK_O UDSS	K_o consolidated undrained direct sim shear

Figure 2.1. Average undrained shear strengths in the Boston Blue clay at MIT campus, showing the sensitivity of C_u to the method of measurement, after Morrison (1984

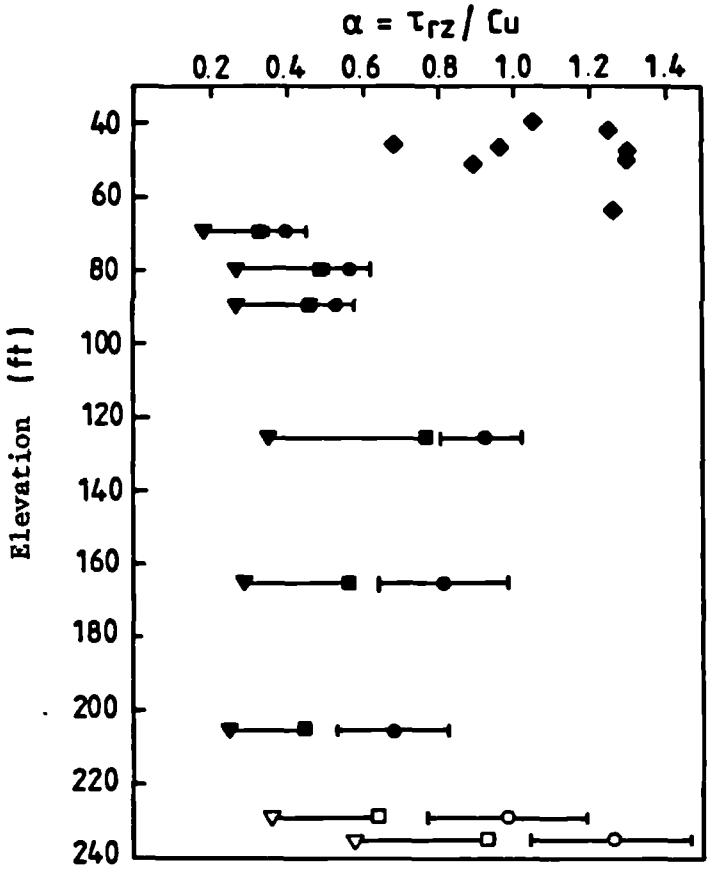


Figure 2.2.
Sensitivity of α to C_u test method; Boston Blue clay, after Morrison (1984).

Strength Profile	Type of shear with PLS cell	
	compression	tension
UU	o	o
Field strength	□	□
Shansep k_0 plane strain compression	▽	▽
Pile load tests in BBC (after Trow 1984)	◆	

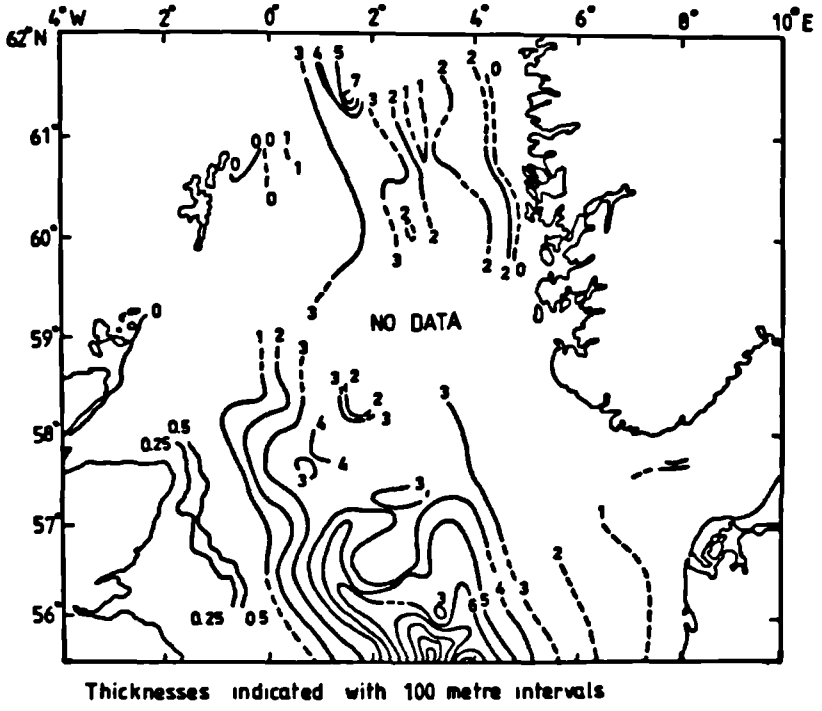
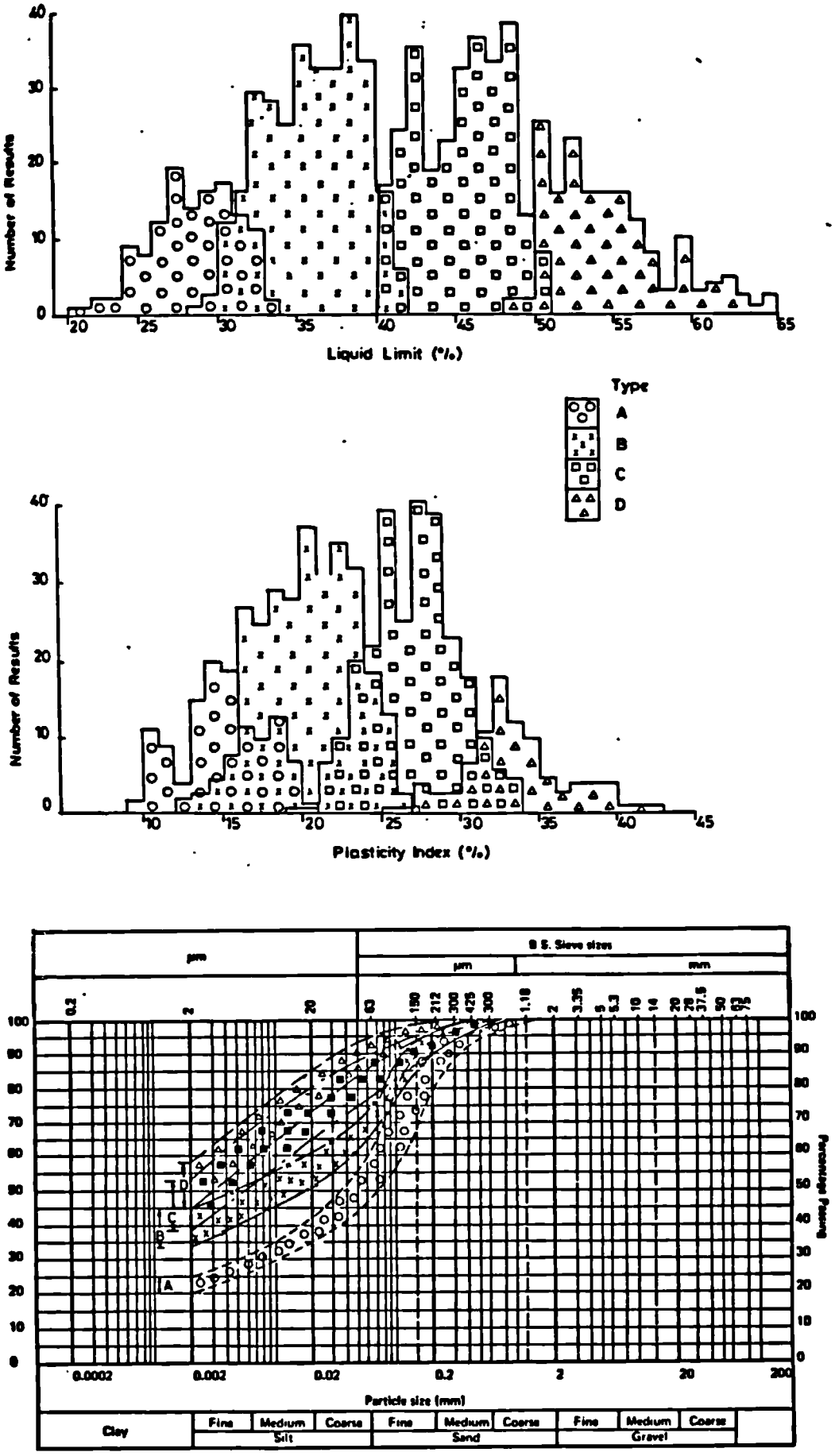
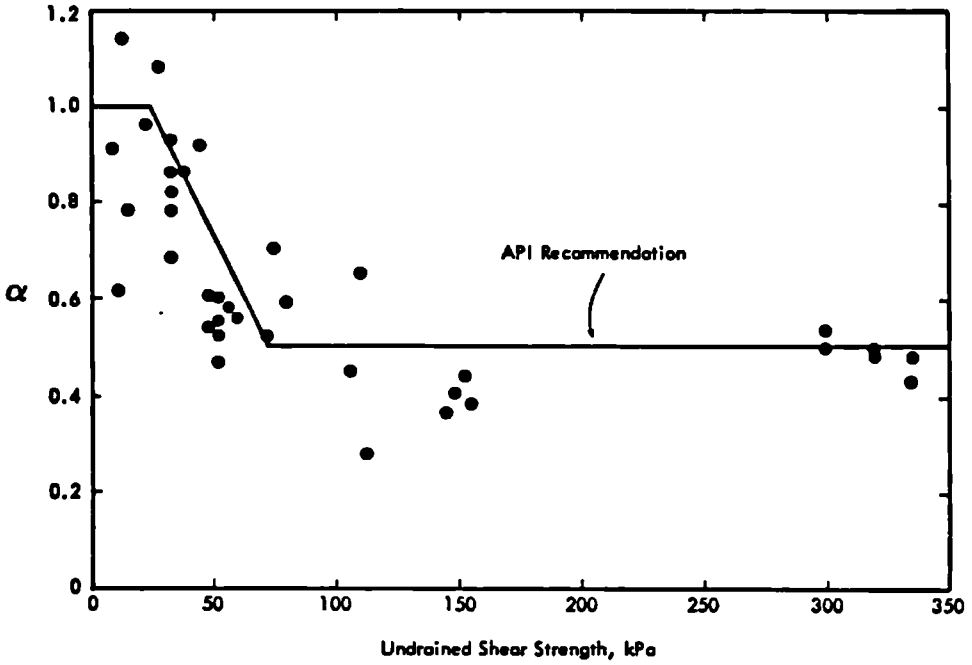
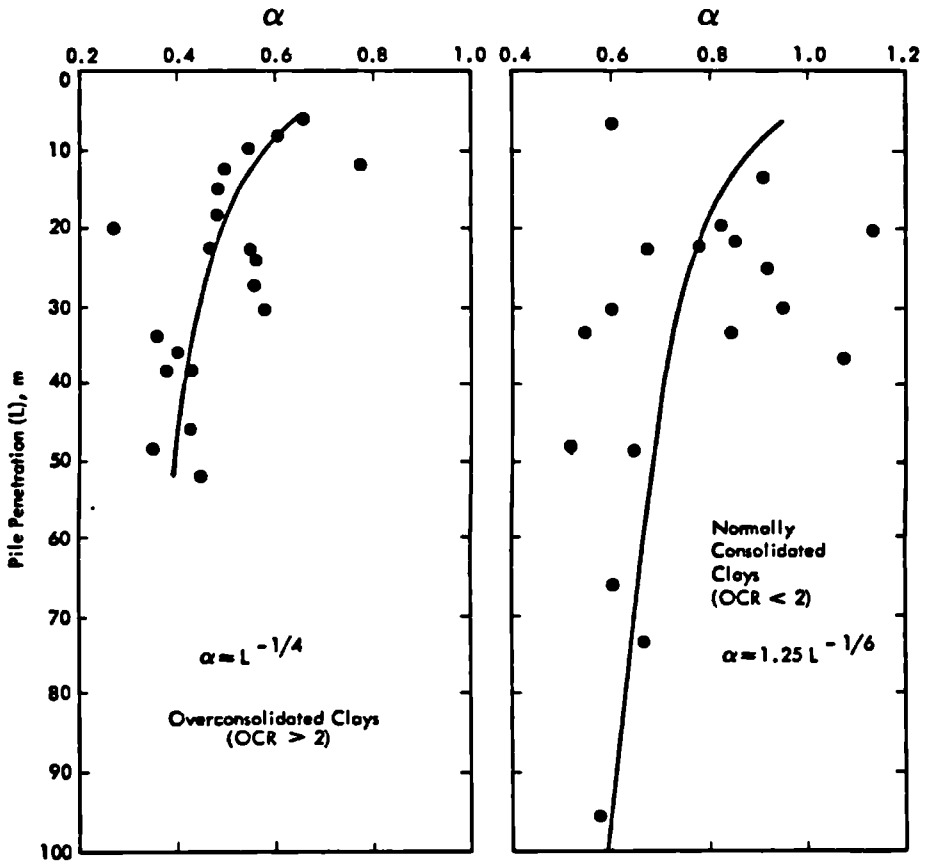


Figure 2.3. Isopachyte map of total quaternary thickness in North Sea, after Caston (1977).



Figures 2.4 and 2.5. Histograms of Atterberg limits and grading curves prepared by Hight (1983) from a survey of several Northern North Sea platform sites.





Evaluation of Trend Lines

	OCR > 2	OCR < 2
L = 10 m	0.58	0 88
L = 50 m	0.40	0.70
L = 100 m	0.32	0.58

Figures 2.6 and 2.7. Summary of API data base points after Semple (1984).

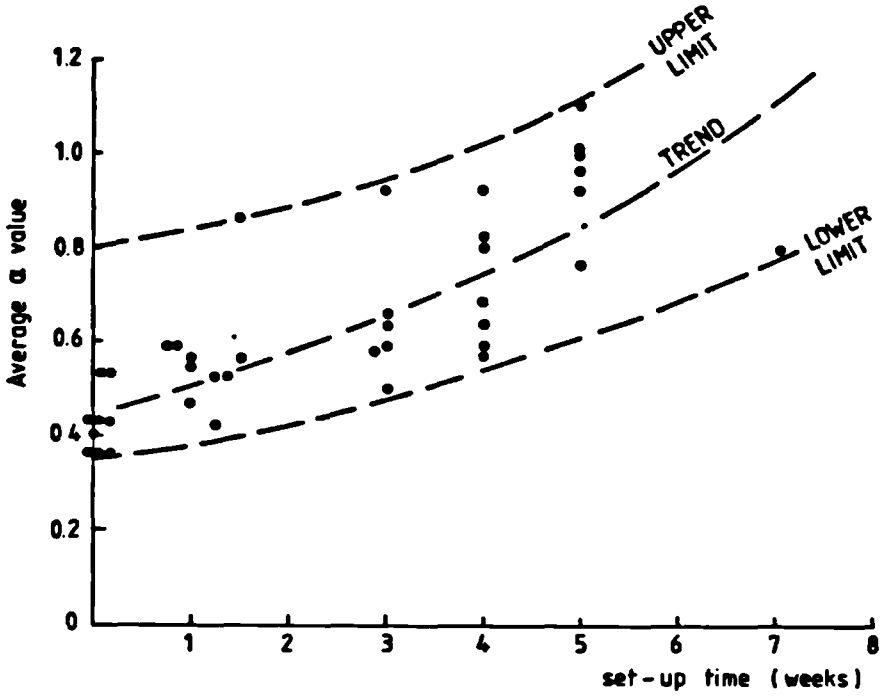


Figure 2.8. Apparent trend of α with set up time for API data base.

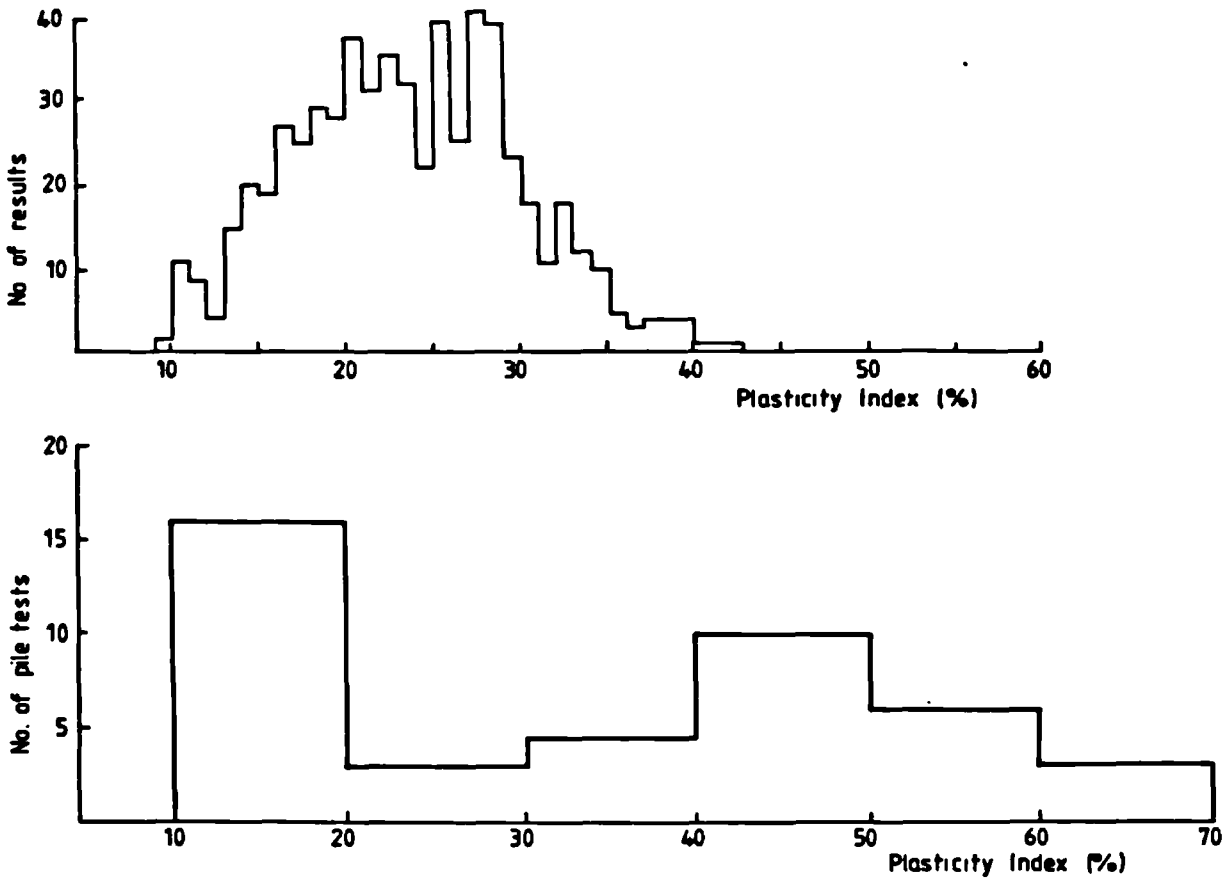


Figure 2.9. Plasticity index histograms; a) For North Sea sites, after Hight (1983), b) For API data base sites.

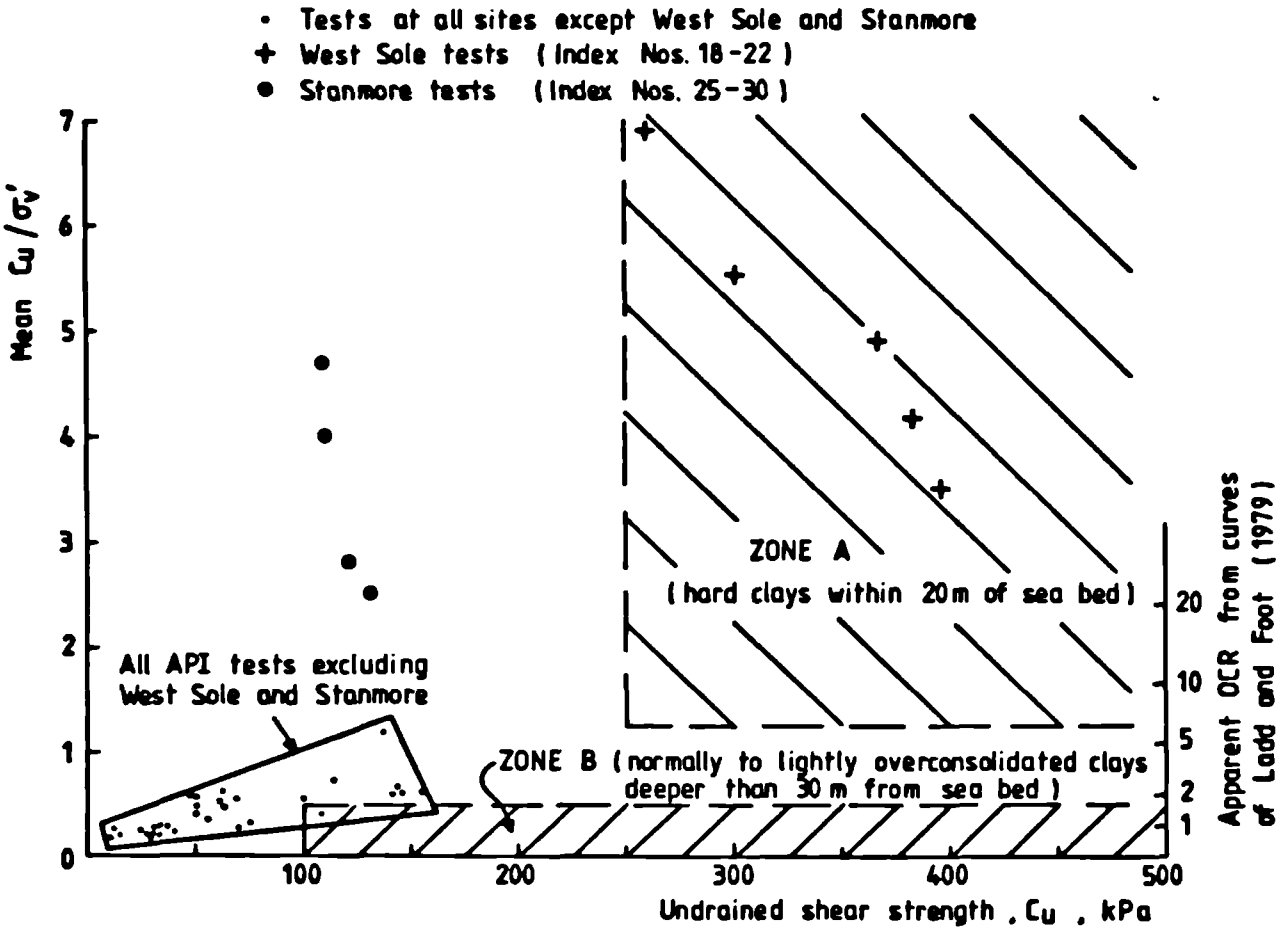


Figure 2.10. Comparison of strength – OCR scatter from API data base sites and North Sea zones A and B.

CHAPTER 3

Tables and Figures

AFTER GENS (1982)

TABLE 3.1

GENERAL STUDIES OF CLAY BEHAVIOUR

	Clay	LL	PI	Type	TRIAXIAL						PLANE STRAIN				SS	Reference
					IC		AC		KC		IC		AC		AC	
					U	D	U	D	U	D	U	D	U	D	UD	
					CE	CE	CE	CE	CE	CE	CE	CE	CE	CE		
1	LC⁻	25	12	R												Gens (1982)
2	Drammen	57	27	I												Andersen et al (1980)
3	Bath Kaolinite	48	15	P												Broms and Ratnam (1963)
4	Buckshot	57	36	R												Donaghe and Townsend (1975, 1978)
5	EAPBL	79	53	R												
6	San Francisco Bay Mud	88	45	I												Duncan and Seed (1966b)
7	Holywood	51	28	I												Crooks and Graham (1976)
8	Kinnegar	83.5	52.5	I												
9	Spestone Kaolin	74	32	R												Balasubramaniam (1969)
		72	33	R												Hamoly (1972) Hambly and Roscoe (1969)
		72	32	R												Parry and Nadarajah (1974)
		76	37	R												Sketchley and Bransby (1973)
		72	33	R												Thurairajah (1962)
		N/A	N/A	R												Wroth and Loudon (1967)
10	Soft Bangkok	118	75	I												Balasubramaniam and Chaudry (1976, 1978 et al 1975)
11	Weathered Bangkok	123	82	I												Balasubramaniam and Zue Ming (1980)
		123	82	I												Balasubramaniam and Uddin (1977)
12	Weald	43	25	R												Henkel (1956, 1959, 1960)
		46	22	R												Henkel and Sowa (1963)
		46	25	R												Henkel and Wade (1966)
		43	25	R												Parry (1960)

TABLE 3.1 (contd)

	Clay	LL	PI	Type	TRIAXIAL IC U C	TRIAXIAL IC U E	TRIAXIAL IC D C	TRIAXIAL IC D E	TRIAXIAL AC U C	TRIAXIAL AC U E	TRIAXIAL AC D C	TRIAXIAL AC D E	TRIAXIAL KC U C	TRIAXIAL KC U E	TRIAXIAL KC D C	TRIAXIAL KC D E	PLANE STRAIN IC U C	PLANE STRAIN IC U E	PLANE STRAIN IC D C	PLANE STRAIN IC D E	PLANE STRAIN AC U C	PLANE STRAIN AC U E	PLANE STRAIN AC D C	PLANE STRAIN AC D E	SS UD	Reference
13	London	78	52	R	●		●																			Henkel (1956, 1959, 1960)
		78	52	R	●		●																		●	Parry (1960)
14	Grundite	54.5	28.5	R	◢		◢		◢		◢		◢		◢											Khera and Krizek (1967)
		54.5	28.5	R	◢		◢		◢		◢		◢		◢											Khera and Krizek (1968)
		54.5	28.5	R	●																					Perloff and Osterberg (1964)
15	Marine	25-45	18	I			●		●																●	Koutsoftas (1981)
16	Kawasaki		38	I	◢		◢		◢		◢		◢		◢											Ladd (1965)
17	Buckshot		39	I	◢		◢		◢		◢		◢		◢											
18	Portsmouth	35	15	I	◢		◢		◢		◢		◢		◢						◢		◢		●	Ladd and Edgers (1972)
19	Portland	44	20	I	◢		◢		◢		◢		◢		◢										◢	
20	Bangkok	65	41	I	◢		◢		◢		◢		◢		◢										●	
21	Maine Organic	65	34	I	◢		◢		◢		◢		◢		◢										●	
22	Atchafalaya	95	75	I	◢		◢		◢		◢		◢		◢						◢		◢		●	
23	Connecticut Valley	65 35	39 12	I	◢		◢		◢		◢		◢		◢						◢		◢		●	
24	Boston Blue	41	21	R	◢		◢		◢		◢		◢		◢											Ladd and Varallyay (1965)
		41	21	R	◢		◢		◢		◢		◢		◢						◢		◢			Ladd et al (1971)
		41	21	R	●																				●	Ladd and Edgers (1972)
25	Kaolinite	NA	NA	R	◢		◢		◢		◢		◢		◢											Lee and Morrison (1970)
26	Higgins	38	17	R	◢		◢		◢		◢		◢		◢											
27	Valley of Mexico	366	85	I	◢		◢		◢		◢		◢		◢											Leon and Alberro (1977)
28	Hokkaido S.A	52	21	R	●				●																	Mitachi and Kitago (1976)
29	Hokkaido S.B.	51	21	R	●				●																	
30	Hokkaido	72	32	R	●				●																	

TABLE 3.1 (contd.)

	Clay	LL	PI	Type	TRIAXIAL												PLANE STRAIN						SS		Reference
					IC				AC				KC				IC				AC				AC		
					U		D		U		D		U		D		U		D		U		D		U	D	
					C	E	C	E	C	E	C	E	C	E	C	E	C	E	C	E	C	E	C	E	C	E	
31	Sapporo	86	49	R																							Mitachi and Kitago (1979)
		86	49	R																							Mitachi and Kitago (1980)
32	Kaolinite	44	9	R																							Murthy et al (1981)
33	Silty	82	22	R																							
34	Calcium illite	85	48	P																							Olson (1962)
35	Sodium illite	85	50	R																							Olson (1963)
		85	50	R																							Olson and Hardin (1963)
36	Calcium Montmor.	200	167	R																							Mesri and Olson (1970)
37	Sodium Montmor.	1050	NA	R																							
38	Sianey Kaolin	50	16	P																							Poulos (1978)
39	Drammen	33	15	I																							Simons (1960 a)
40	Oslo	39	18	I																							Simons (1960 b)
41	Haney	44	18	I																							Vaid and Campanella (1974)
42	Glacial	54	27	R																							Wu et al (1963)
43	Rann of Kutch	91	49	R																							Yudhbir and Varadajan (1974)
44	Kanpur	38	18	R																							
45	Haga	42	16	I																							Lacasse (1979 b)

TABLE 3.1 (contd.)

 Tests carried out on samples at several OCR's

 Tests carried out at OCR = 1

 Tests carried out at one OCR value (OCR $\neq$ 1)

IC	Isotropically Consolidated Samples
AC	Anisotropically Consolidated Samples
KC	K-conselidated samples
U	Undrained tests
D	Drained tests
C	Compression tests
E	Extension tests
SS	Simple shear tests
LL	Liquid limit
PI	Plasticity index
R	Samples reconstituted in the laboratory
I	Undisturbed samples

Soil	ϕ'	M_{TXL}	M_{PS}	$\sigma'_z/Cu(o)$	σ'_θ (Cu (o)	σ'_r(Cu(o)	OCR = 1.0 $\sigma'_r/\sigma'_{initial}$	OCR = 8.0
Boston Blue Clay	30^{o} [1]	1.2		2.08	1.08	3.08	1.90	4.67
			0.87	1.50	0.50	2.51	1.55	3.80
London Clay	25^{o} [2]	0.98		1.69	0.69	2.69	1.18	2.40
			0.73	1.25	0.25	2.25	0.99	2.01
Kaolin	23^{o} [3]	0.898		1.56	0.56	2.56	0.81	1.60
			0.677	1.17	0.17	2.17	0.68	1.36

Table 3.2 Predictions of stresses at pile face immediately after cavity expansion, cam-clay model.

1. Calculated from $M_{TXL} = 1.2$ Randolph et al. (1979)
2. Calculated from $M_{PS} = 0.732$ Wroth et al (1979)
3. From Francescon (1983), $\phi' = 23^{o}$.

Test Type	Laboratory Result	Total Stress MIT model Prediction	% error	Mod.Cam Clay Prediction	% error
(all ko consolidated)	Cu/σ'_{vo}	Cu/σ'_{vo}		Cu/σ'_{vo}	
Plane Strain Active	0.325	0.365	12% +	0.340	5% +
Plane Strain Passive	0.250	0.150	40% -	0.340	36% +
Triaxial Compression	0.325	0.325	0	0.295	10% -
Triaxial Extension	0.125	0.125	0	0.295	230% +
Direct Simple Shear (DSS)	0.200	0.260	30% +	0.340	70% +

Notes

(i) Measured ϕ' values fell between 40^{o} and 33^{o} for all tests.

(ii) Parameters for mod. Cam-Clay predictions taken from Randolph et al. (1979). include the assumption that $(\phi')_{TXL} = 30^{o}$.

(iii) Non uniformities in DSS test considered to reduce peak strength by 10%.

Table 3.3 Undrained strength predictions for Boston Blue Clay. (After Levadoux and Baligh (1980)).

Radial Distance from centre	σ'_r/Cu	σ'_θ/Cu	σ'_z/Cu	$\Delta u/Cu$
$r=r_o$	1.5	0.5	1.0	4.5
$r=5r_o$	2.0	0.5	-	2.4
$r=10r_o$	2.2	0.8	-	0.9
initial values	1.6	1.6	3.0	-

Notes

(i) Cu is taken as 3 x σ'_{vo} (see Table 2.4)

(ii) No values are given for σ'_z by the authors for $r>r_o$

Table 3.4 Predictions of streses after expansion of a cylindrical cavity in Boston Blue Clay using MIT model, OCR = 1.0 (After Levadoux and Baligh (1980))

Radial Distance from centre	σ'_r/Cu	σ'_θ/Cu	σ'_z/Cu	$\Delta u/Cu$	Vertical Distance from Tip.
$r=r_o$	1.1	0.7	0.9	6.5	0
$r=5r_o$	1.3	1.1	-	2.9	0
$r=10r_o$	2.3	1.4	-	0.9	0
$r=r_o$	0.5	1.0	1.5	3.3	12.5 r_o
$r=5r_o$	1.1	1.0	-	2.7	12.5 r_o
$r=10r_o$	2.0	1.3	-	1.7	12.5 r_o
initial values	1.6	1.6	3.0	-	at all points

Table 3.5 Predictions of stresses around a cone or pile penetrating a deep layer of Boston Blue Clay. MIT strain path solution for OCR = 1.0, with the total stress Model 1. (After Levadoux and Baligh (1980))

Notes:

(i) Results near tip are taken from solution for 60^o cone.

Feature	Model Tests	Field Tests
Ability to obtain representative boundary conditions for test.	v. difficult	Not difficult
Severity of cell action effects for transducers installed in soil	Considerable	Generally less
Uniformity of clay layer	Good	Generally poor
Ability to control Cu, OCR	Good	Generally none
Knowledge of initial stresses, pore pressures, soil properties	Satisfactory	Less satisfactory
Time scale, costs	Generally less	Considerable
Method of Installation	Usually Jacked	Usually driven

Table 3.6 Comparison of Field and Laboratory studies.

Reference	Comments
1. Lo and Stermac (1965)	3 case histories of measurements in Ontario. (i) 2 Model piles, 14m long, 0.09m diameter installed in soft clay (ii) Test H piles, 14m long installed in silt and varved clay. (iii) H pile group, 14m(?) long installed in varved and laminated clay.
2. Apendino et al (1979)	Case history in normally consolidated clay layer, Po Delta. Closed end tubular piles, 0.508m diameter, 42 to 48m long,driven individually and in large groups.
3. Blanchet et al (1980)	Case histories for steel and timber piles driven into soft sensitive clays, St Lawrence Valley. 3 sites are considered; pile diameters from 0.37 to 0.2m and lengths from 15 to 38 metres.
5. Roy et al (1981)	Case history for 6 steel piles jacked into soft sensitive clay at St. Alban test site, Quebec. Pile diameter 0.219 metres, lengths 7.7 metres.
6. Steenfelt et al (1981)	Model piles installed into consolidated kaolin. Pile diameter 0.019m, length 0.450mm.
4. Levadoux and Baligh (1980)	Model piles, or penetrometers, installed in Boston Blue Clay with multi-point pore pressure measurements. Diameter 0.038m, length 0.5 metres.

Table 3.7 Case histories of pore water pressure measurements near piles.

Reference, Site	Pile Dimensions (M) Length[a]	Diam.	Embed[b]	Inst. Depth[c]	Stress on pile Face Δu/Cu	σ'r/Cu	Soil OCR	Details, Cu,Kpa	Notes PIZ
Reese and Seed (1955) S.Francisco 1	4.26 (driven)	0.15	7.1	0.56 0.70 0.95	3.1 6.4 13.2	2.0 1.8 2.0	≈1.0 ≈1.0 ≈1.0	14 14 14	18 18 18
Koizumi and Ito (1967) Tokyo 2	5.55 (driven)	0.30	7.55	0.5[A] 0.5[B] 0.8[A] 0.8[B]	3.2 4.6 2.7 4.7	<0 <0 1.2 1.2	≈1.8 ≈1.8 ≈1.5 ≈1.5	25 25 35 35	50 50 60 60
Bakholdin and Bolshakov (1973) 3	4.5 (driven)	0.20	4.5	0.47 0.67 0.88	2.3 3.3 4.0	0 0 0	≈1.5 ≈1.0 ≈1.0	10 10 10	3-9 3-9 3-9
Butterfield and Johnson (1973) London clay, Hampshire Basin 4	3.7 (jacked)	0.10	5.7	0.47 0.61 0.79 0.96	? ? ? ?	3.0-? 3.3-? 4.7-? 6.0-?	≈15 ≈12 ≈10 ≈8	50 75 75 75	38 38 38 38
Sutton et al (1979) Forties, FD North Sea 5	73 (driven)	1.37	73	0.56 0.75 0.96	7.0 6.8 9.9	1.0 1.6 1.6	≈1.0 ≈1.3 ≈1.0	100 200 200	? ? ?
Fathallah (1978) Model tests, Kaolin 6	0.685 (jacked)	0.063	0.685	0.25 0.55 0.85	2.8 - 3.5	3.2 3.5? 3.7	1.0 1.0 1.0	28 28 28	31 31 31
O'Neil et al. (1982) Field tests Beaumont clay 7	13 (driven,closed end steel pipes,single and group)	0.273	9.9	0.2 0.7	neg. to 3.5	not given	6.3 5.2	86 158	45-55 12-17
Francescon (1984) Model Tests with Kaolin	0.410 (jacked)	0.019	0.410/ 0.300	0.5 "	4.9-5.5 3.7-4.9 2.9-4.1 2.3-3.6 3.6 2.6	0-0.2 0-0.75 0.2-0.3 0.1-0.9 0.4 0.1	1 2 4 8 17 25	A B 46 11-55 46 46 42 38.5 38 31.5 - 25 - 19	31 31 31 31 31 31
		(i) Saugus site			(6 holes)				
Morrison (1984) Field tests with Model pile and 'PLS' cell	1.72 " " " "	0.038 " " " "	15 20 25 30 35	1.0 " " " "	4.4-5.7 7.9-10.1 8-9.2 8.4-9.0 8.7-9.9	0-0.7 0-0.7 0-1.0 0-1.0 0-0.9	3.0 2.0 1.35 1.35 1.35	50 50 50 55 60	12-20 " 18-25 " "
		(ii) MIT site			(1 hole)				
	" " "	" " "	20 25 30	" " "	7.0 6.2 6.5	0.3-1.3 1.4 1.1	2.2 1.5 1.5	70 80 95	12-25 " "

Table 3.8

a effective shaft length
b depth to tip.
c Inst depth / b

Notes for Table 3.8.

1. Only an average Cu and PI value are given by the authors, the top 9ft of the pile was inserted through a cased hole.

2. Two piles, A and B were used. The top of each pile was formed in a two metre deep excavation.

3. There is very limited soils data for this case. Cu was estimated to be 10 kpa, from Cu 0.3 σ'_v. Banerjee (1979) gives a different interpretation assuming $Cu/\sigma'_v = 0.11 + 0.37$ P.I. Pre cast concrete piles were used in this study.

4. No pore pressures were measured here. The authors assume drained behaviour but, as the data were recorded overa 3 hour long installation period, excess pore pressures probably remained.

5. The installation was lost after 10 days due to cable failure

6. Fathallah consolidated his kaolin in one increment of load, and then relaxed the vertical stresses in order to install the pile. Between unloading the clay bed and installing the pile considerable swelling took place. The initial conditions in the soil therefore varied with distance from the boundaries, with negative initial values of u, σ_θ and σ_r developing before installation.

7. The tests described by O Neil et al showed considerable scatter. This was considered to result from the use of flat load cell plates on the circular pile section ,and a pronouced temperature sensitivity in the instruments. During installation the pile face piezometers desaturated , probably as a result of negative pwps , and no data were available for 48 hours.The pwp data show the effects of installation to have been incompletely equilibrated at the time of the first load test.The tabulated data do not therefore correspond to ultimate conditions.Both single piles and a group were used for the study, with instruments located at three levels below the 3 metre deep starter holes.

8. Francescon reports two tests series, A and B,performed with different boundary conditions and consolidation patterns. In series A the vertical dimensions of the clay cylinder were kept constant and a fixed radial stress maintained furing pile installation. In series B an annulus of soil near the pile was exposed to the atmosphere during installation and was free to heave. The soil for series A was consolidated separately, sampled, then reconsolidated before testing. In each case the shear strength was around 45 kpa. In series B the soil was consolidated insitu and tests were carried out in a rigid walled tank. The shear strengths varied with OCR, giving $11<Cu<55$ kpa. These variations in procedure resulted in consistent differences between the results of the two test series.

9. Morrison reports two test series with a piezo-lateral stress (PLS) cell in Boston Blue Clay. Profiles of penetration and dissipation data were recorded at the Saugus and MIT campus sites. The PLS cell was located 27 diameters from the pile tip. In his thesis, Morrison prefers the use of σ'_{vo} to Cu for normalising stress measurements. For this table Cu has been evaluated from the field vane strengths reported for the two sites.

Reference	Constitutive Law	Definition of Time factor T	Predictions for dissipation of Pile Face		
			Initial pwp. distn.	T for 50% dissipation	
				$\Delta u/Cu$	T_{50}
Soderberg (1962)	Elastic	$C_v.t/r_o^2$, C_v assumed	- -	-	0.6-1.5
Hagerty and Garlanger (1972)	Elastic	C_vt/r_o^2, C_v assumed	$U_r/U_o=r_o/r$	-	≈ 1.0
Butterfield and Bannerjee (1970)	Elastic during consolid-ation	C_vt/r_o^2, C_v found from $C_v=\frac{k}{\gamma_N}.(K'+\frac{4}{3}G)$	Elastic - plastic cavity expansion	5.0	3.0
Randolph et al (1979)	Elastic	C_vt/r_o^2, C_v found from $C_v=\frac{k.2G(1-v')}{(1-2v')}$	Elastic-plastic cavity expansion	4.0 3.0	2.0 1.0
as above	Elastic-plastic	C_vt/r_o^2, C_v as above	as above	3.9	1.5
as above	Mod.CAM clay	$K.Cu(o)t/\gamma_w r_o^2$ (λ, k and G values input to soil model)	as above (Mod. CAM. clay).	3.9 3.0	1.5×10^{-2} 1.4×10^{-2}

Table 3.9

Soil, Notes		$\sigma'_\theta/Cu_{(o)}$	$\sigma'_z/Cu_{(o)}$	$\sigma'_r/Cu_{(o)}$	$\sigma'_{r\infty}/\sigma'_{r\ initial}$ OCR= 1.0	OCR= 8.0	$\frac{Cu_\infty}{Cu_o}$ [5]
Boston Blue Clay	[1]	3.0	3.0	4.9	3.0	7.4	1.6
London Clay	[2]	4.2	4.2	5.8	2.5	5.2	1.5
Kaolin	[3]	4.5	4.5	6.5	2.0	4.1	1.3
	[4]	3.8	3.8	5.5	1.7	3.4	1.4

Table 3.10 Effective stresses at pile-soil boundary after full consolidation. Predicted by Cam-clay cavity expansion theory. See Section 3.6 for initial conditions and assumptions.

Notes
1. A value of $C_\infty/Cu_o = 1.3$ was computed for OCR = 8.
2. From Wroth et al (1979).
3. From Wroth et al (1979) assuming 'plane strain' $M = 0.68$ $\lambda = 0.25$, $(K_o)_{nc} = 0.69$.
4. As above $M = 0.90$, the 'triaxial' value.
5. Strength gains varied with radius and were not significant for r>R.

	Reference	Pile radius,m	Soil	% Dissipation	C_v, m^2/yr.
1	Reese and Seed (1955)	0.075	Bay Mud, approx. OCR ≈1.0	50%	2.5 to 15
2	Koizumi and Ito (1967)	0.150	Sensitive high PI clay, 1.87 OCR > 1.5	50%	6.0 to 8.2
3	Roy et al. (1981)	0.1095	Sensitive clay, OCR ≈ 1.0	50%	9.3 to 16.8
4	Sutton et al (1979)	0.685	North Sea Clay OCR ∿ 1.0	15 to 30%	3.8 to 28.5
					OCR C_v
5	Francescon (1983)	0.0095 (Model pile, Series A)	Kaolin various OCR's.	50%	1 38
				"	4 5.7
				"	8 3.6
6	Morrison (1984)	0.019 (PLS tests, Sauguss site)	Boston Blue clay, profile of OCR's.	50%	OCR C_v
					3.8 29
					3.2 29
					2.0 29
					1.3 46

Table 3.11 Values of C_v calculated from pore pressure dissipation at the pile face, using an approximate, linear theory.

Notes:

(i) Coefficients found from cavity expansion solution of Randolph et al. (1979), using linear theory with T_v as a function of initial $\Delta u/Cu$.

(ii) Oedometer C_v values are given in three of the above references;

Reference	C_v Normally consolidated	C_v swelling
Roy, et al (1981)	0.3 m^2/yr	32 m^2/yr
Francescan (1983)	15.8 m^2/yr	79 m^2/yr
Morrison (1984)	0.9 - 5.4 m^2/yr	9-54 m^2/yr

eference	Installed Depth Z/E	Final σ'_r/Cu(o)	Z Dissipation of excess pwp.	Initial σ'_r/Cu(o) (Estimated)	Final/Initial $\sigma'_{r\infty}/\sigma'_{r\ initial}$
eese and Seed 1955)	Mean of all points on shaft	1.3 (Mean)	100	1.7 (Mean)	0.75 (Mean)
oizomi and Ito 1967)	0.5(B) 0.8(B)	1.30 1.43	100 100	1.3 1.0	1.00 1.43
akholdin and olshakov 1973)	0.47 0.67 0.88	0.5+ 1.0+ 1.5+	90 70 90	1.5 1.7 2.0	0.33+ 0.59+ 0.75+
utton et al 1979)	0.56 0.75 0.96	1.2+ 1.3+ 3.0+	15 30 43	2.0 2.0 2.0	0.62+ 0.67+ 1.5+
Neil et al (1982)	OCR Depth 6.3 5m 5.2 10m	Single Group 0.4 2.1 1.1 1.9	incomplete, neg.in places	0.86 0.79	Single Group 0.5 2.5 1.4 2.4
rancescon (1983) z/E = 0.5	OCR=1 2 4 8 17 50	Series A Series B 4.0 3.0 (Mean) 3.5 3.0 3.0 2.6 2.9 2.3 2.0 1.8	100 100 100 100 100 100	3.2 2.4 1.9 1.6 1.3 1.0	Series A Series B 1.25 0.94 1.45 1.25 1.58 1.37 1.81 1.43 1.54 1.80
lorrison (1984) PLS cell, 27Diam. from tip on deeply penet-rating model pile (i) Saugus Site	OCR Depth 3.0 15M 2.0 20M 1.35 25M 1.35 30M 1.35 35M	1.8 3.2 2.5 2.5 2.5	100 100 100 100 100	1.8 2.1 2.4 2.5 2.5	1.0 1.5 1.1 1.0 1.0
(ii) MIT site	2.5 20m 1.5 25M 1.5 30M	2.0 2.0 1.9	100 100 100	2.2 1.8 1.7	0.9 1.1 1.1

Table 3.12

lotes: (i) + indicates incomplete consolidation
(ii) σ'_{rI} values estimated from Brooker and Ireland (1965), where not stated in source reference.
Measurements of effective radial stresses at the pile face after consolidation.

OCR	Cu_∞/Cu_o
1	1.43 - 1.50
2	1.26 - 1.18
4	1.07 - 1.12
8	1.02 - 1.07

Table 3.13 Gains in strength near pile shaft after full equilibration, Series A tests, Francescon (1983)

OCR	δ' at peak	δ' past peak
1	14.4^o	12.8^o
2	14.9^o	15.3^o
4	13.1^o	11.9^o
8	16.8^o	14.2^o

Table 3.1 4 Pile-soil friction angles deduced from test Series A data, after Francescon (1983)

Reference	Pile diameter/type	Soil type	Pore-pressure/Cu	Comments
Lo and Stermac (1964)	368 mm/timber 610 mm/Franki	O.C. Silty-Clay	0.2 - 0.25	Piezometers located about one pile radius from pile face
Airhart et al. (1969)	406 mm/steel pipe pile	O.C. Beaumont Clay	0-0.13	Measurements at pile face
Clark and Meyerhof (1972(a))	75 mm/steel pipe pile	Midium plasticity clay (PI = 20.4)	0.2 - 0.6	Measurements at a distance of one pile radius from pile face
Massarsch, Broms and Sundquist (1975)	75-125 mm/steel	Norwegian Quick Clay	0.15 - 1.25	Measurements along the shaft
Puech and Jezequel (1980)	273 mm/closed-ended steel pile	Silty clay (PI = 28)	0.6 [1]	Measurements at pile face
Roy, Blanchet and Tavernas (1981)	219 mm/steel	Soft, sensitive, Champlain Clay 10% < PI < 27%	0.6 - 1.5	At pile face
			0	At a distance of two pile radii from the shaft

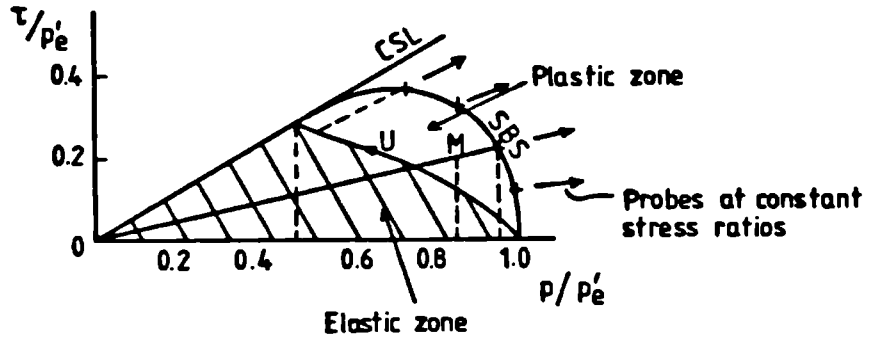
Table 3.1 5 Measurements of pore presssures generated along the shafts of displacement piles during loading, (after Martins (1983)).

[1] differs from Martins' interpretation.

Layer considered	Range of OCR	Mean reduction in σ'_r on loading to peak capacity	Mean value of δ' at peak capacity
Upper and Middle BBC	2.0 to 4.8	52% in compression	30^o
Lower BBC	1.35	50% in compression 25% in tension	21^o

Table 3.16 Effects of pile loading measured in preliminary tests at Saugus site, using PLS cell. Morrison (1984)

(a) From isotropic consolidation



SBS State Boundary Surface
U Undrained stress path
+ Yield points from stress probes

(b) From k_o consolidation

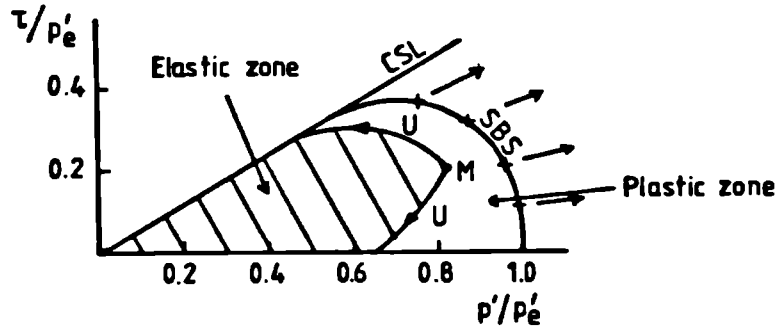


Figure 3.1 The differences between the state boundary surface and undrained stress paths for isotropically and Ko consolidated Lower Cromer Till (LCT), after Gens (1982).

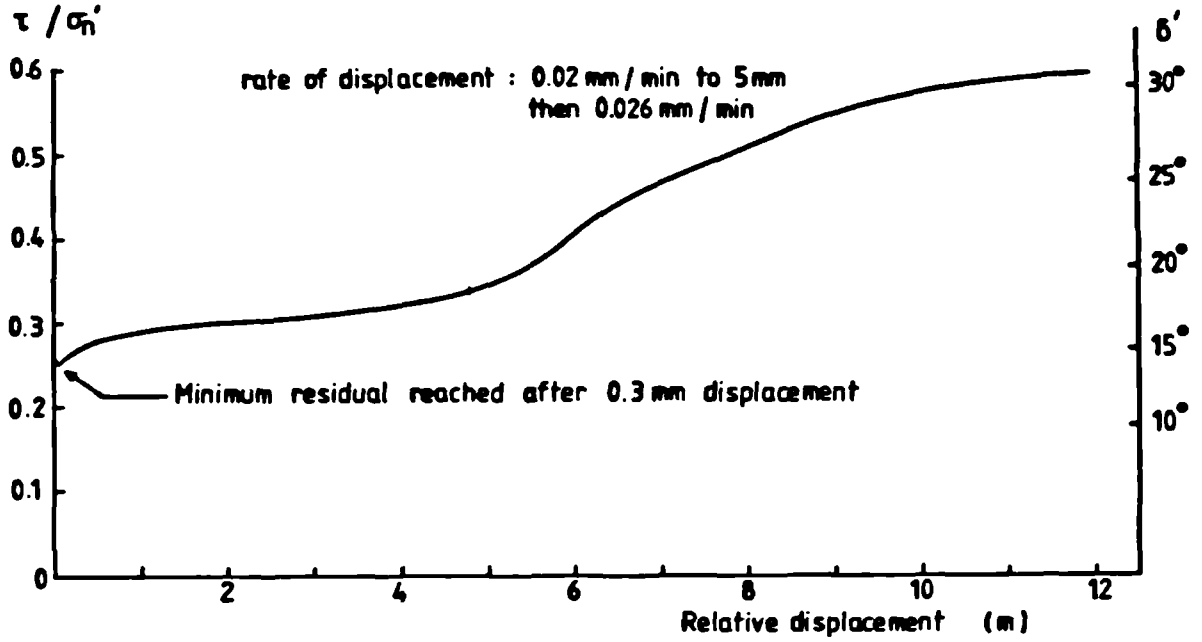


Figure 3.2. Strength – displacement plot for ring shear test; LCT against steel, after Lemos (1985).

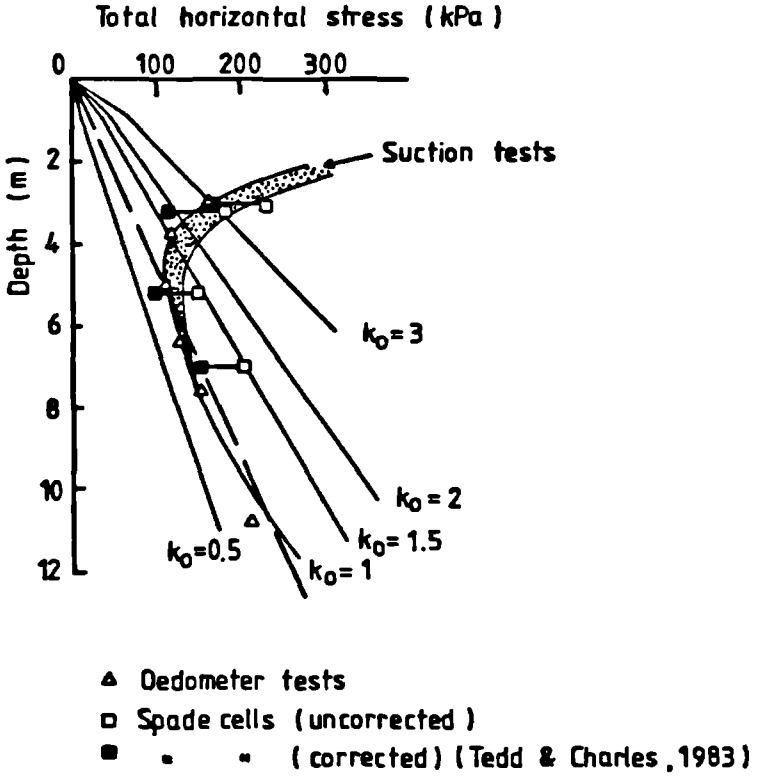


Figure 3.3. Measurements of horizontal total stress at Cowden, after Powell et al. (1983).

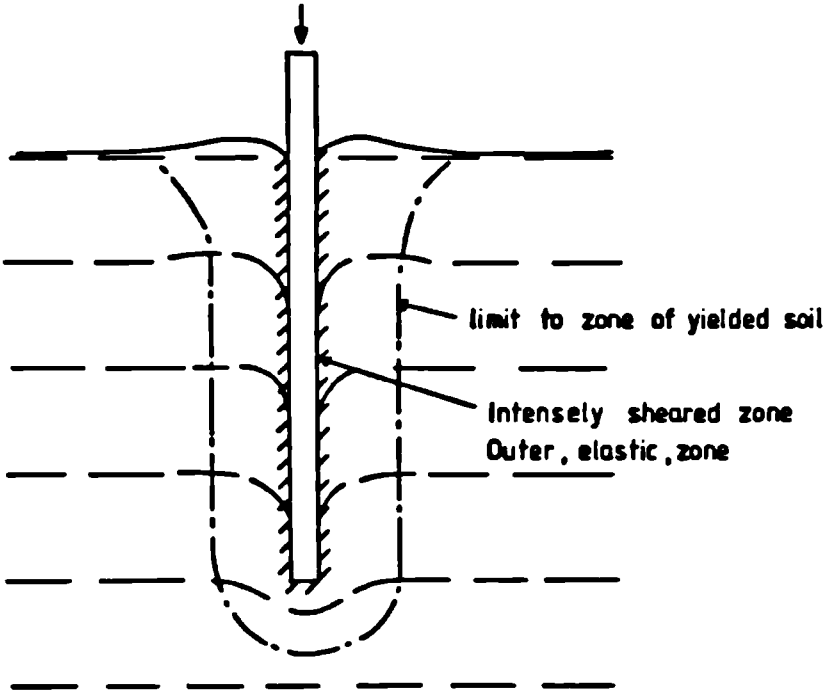


Figure 3.4. Schematic diagram of pile installation effects.

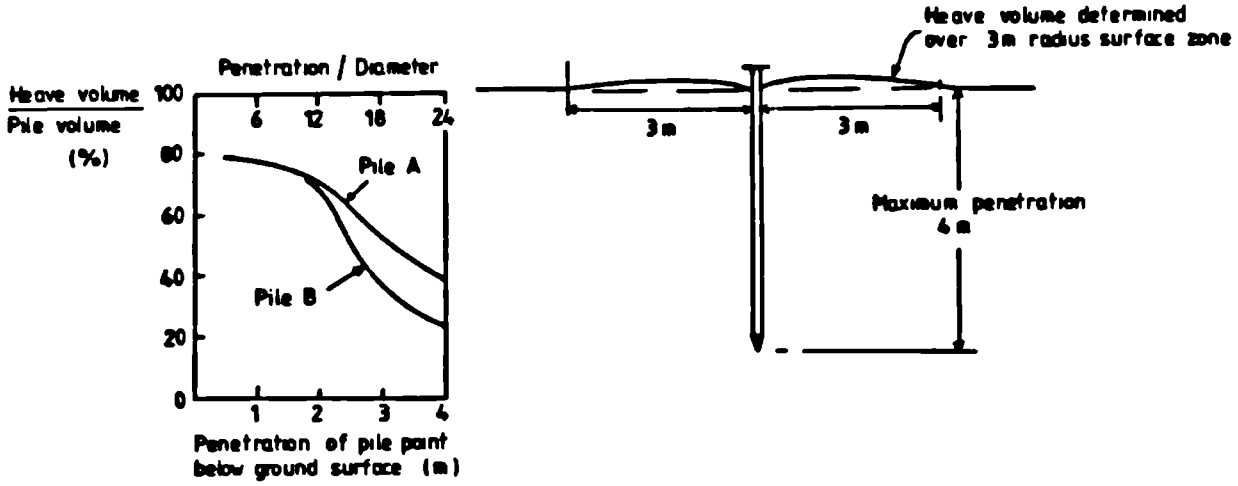


Figure 3.5. Ground Heave during installation, after Cooke et al. (1979).

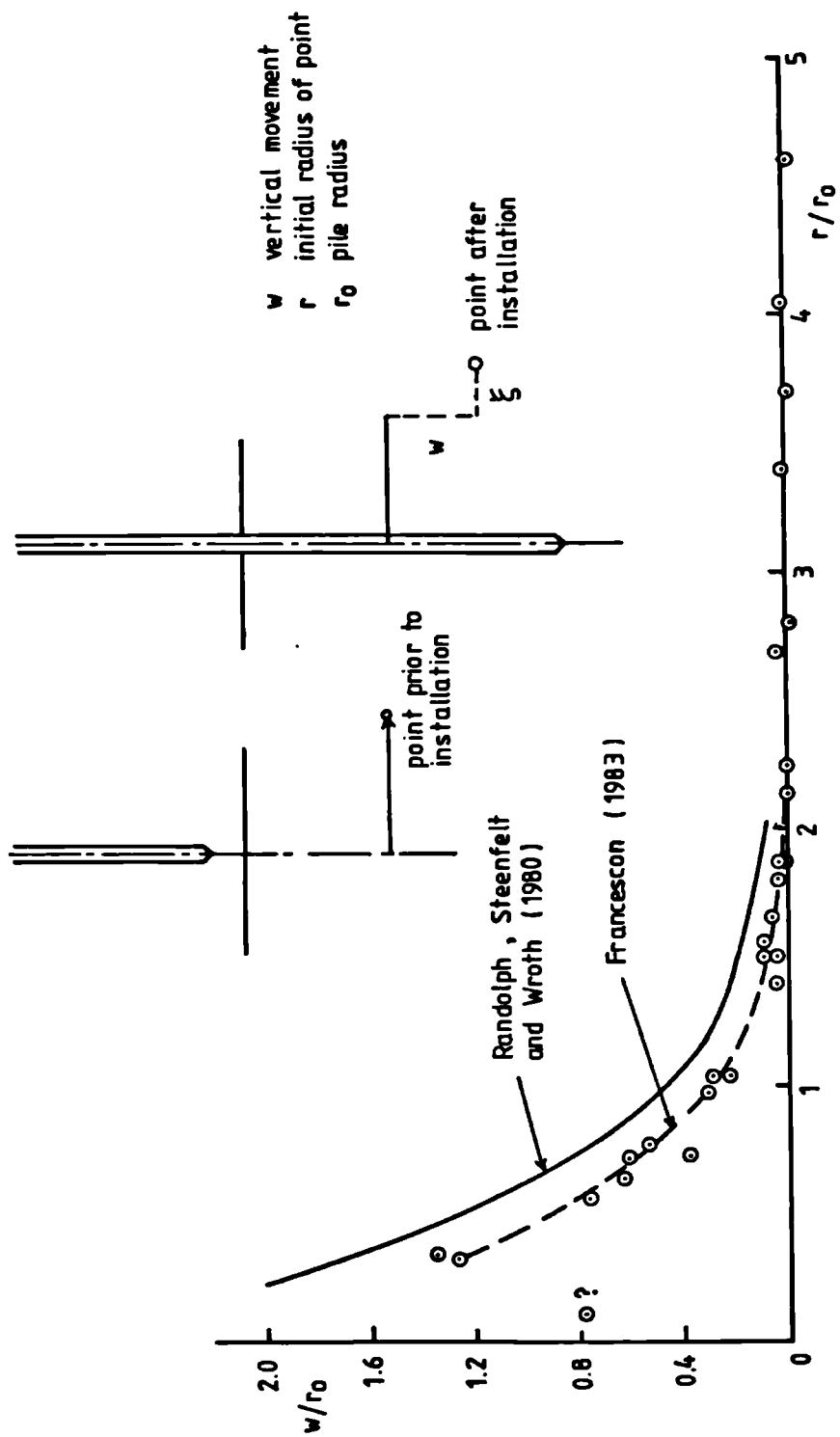


Figure 3.6. Vertical soil movements at depth after installation, after Francescan (1983)

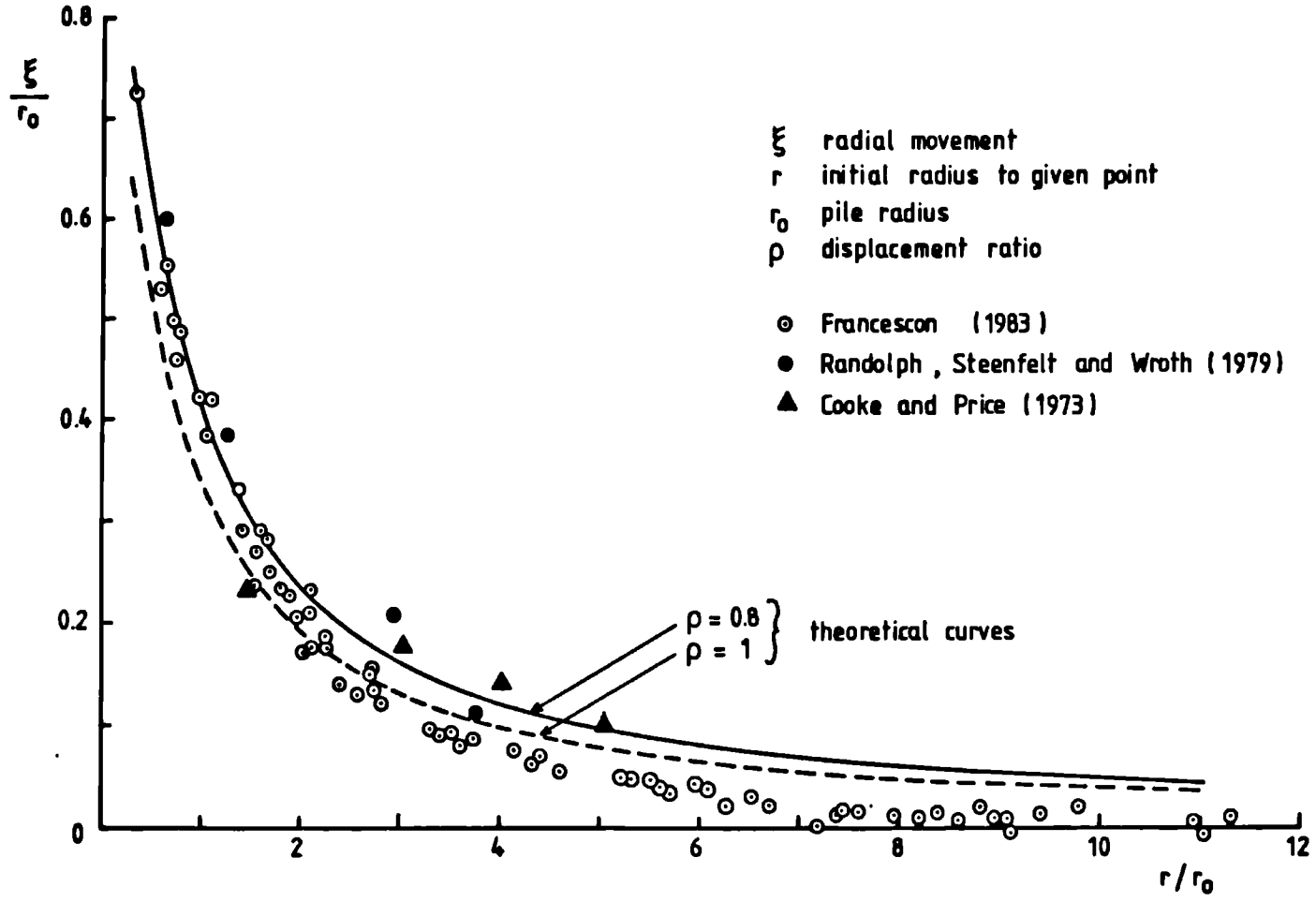


Figure 3.7. Radial soil movements at depth after installation, after Francescan (1983).

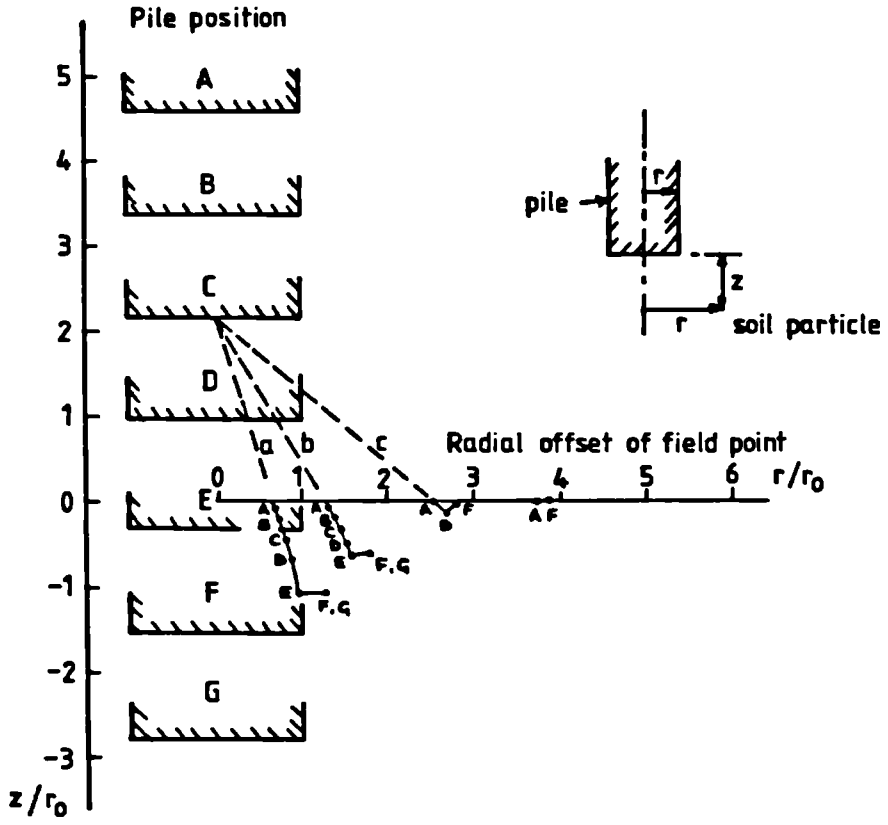


Figure 3.8. Soil trajectories at depth during pile installation, after Wroth et al. (1979).

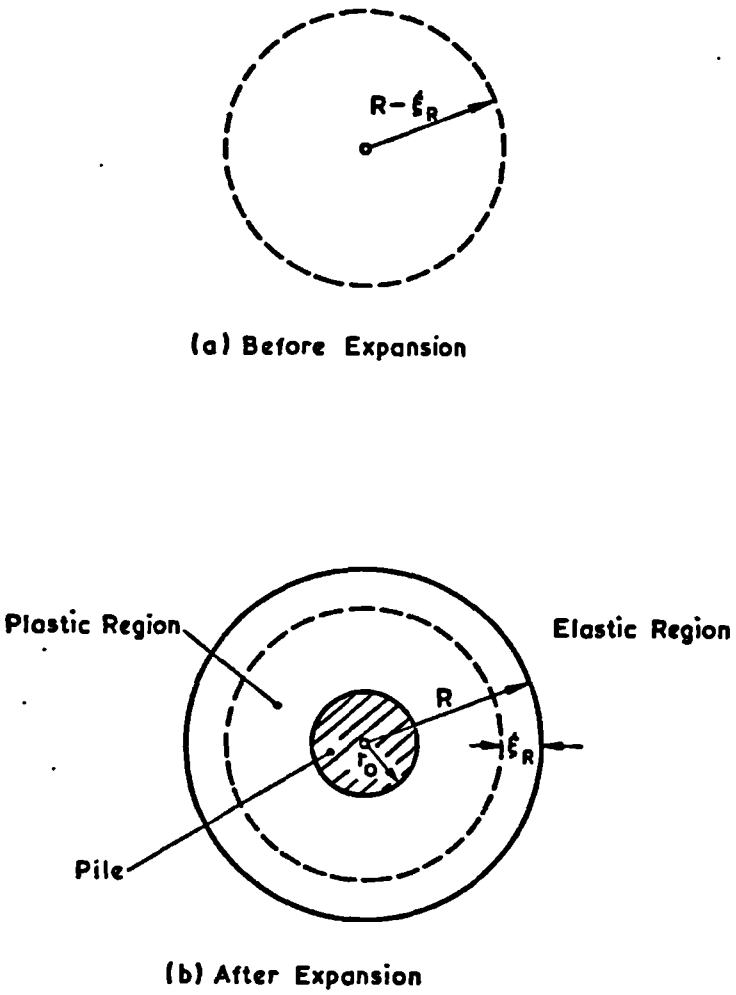


Figure 3.9. Schematic diagram of cylindrical cavity expansion.

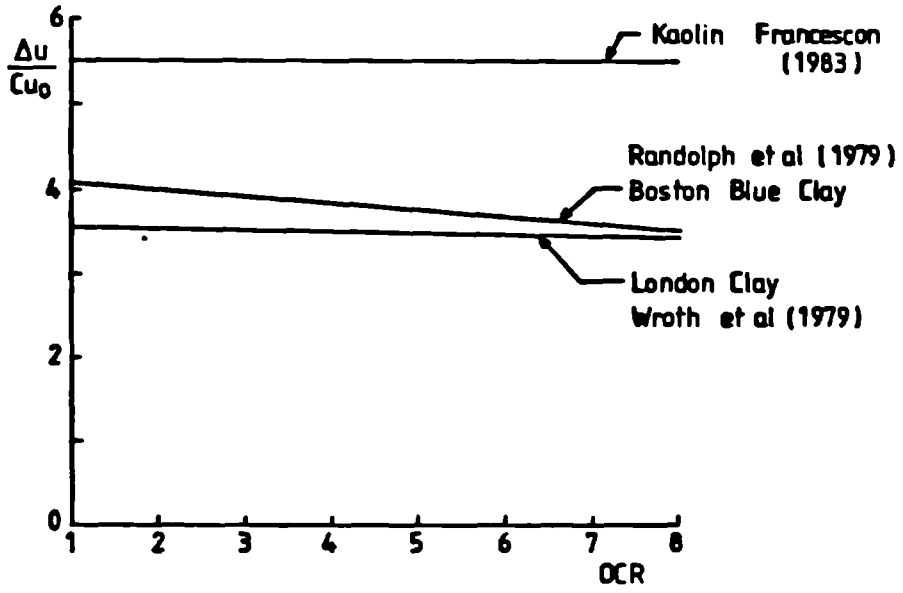


Figure 3.10. Predictions of cavity expansion theory for pore water pressure increases at pile face during installation.

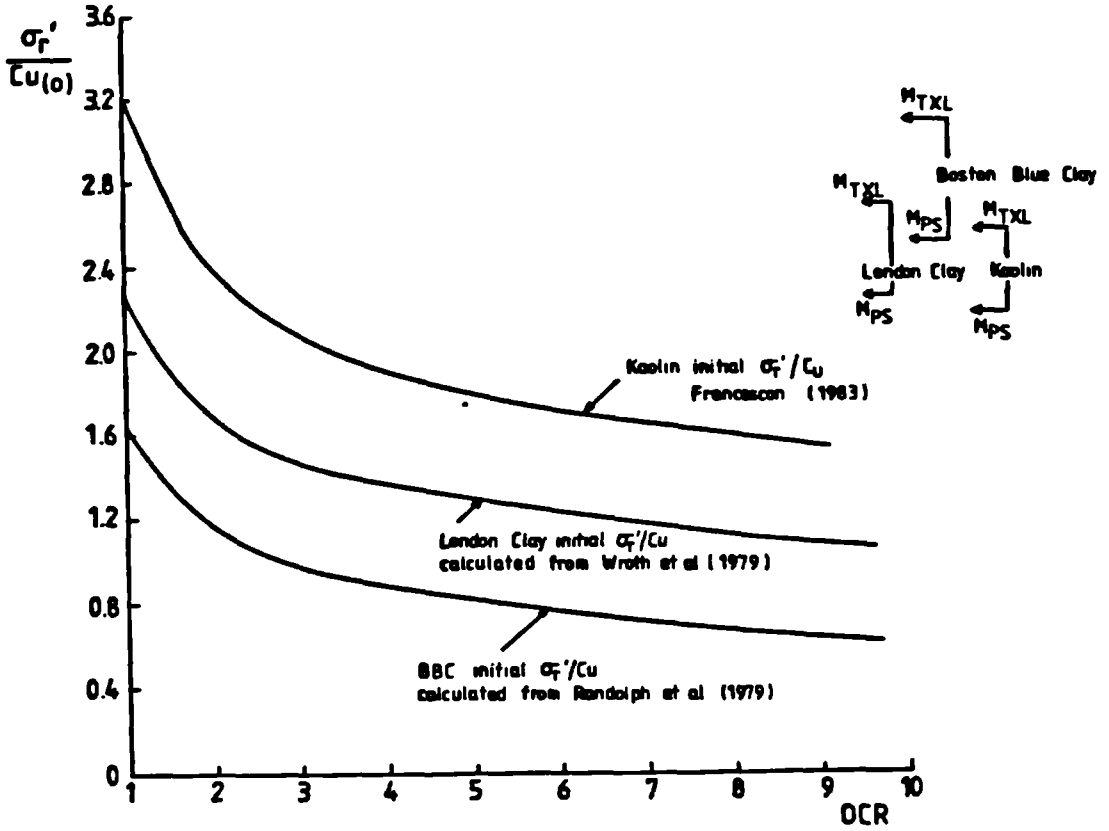


Figure 3.11. Predictions of cavity expansion theory for σ'_r at pile face after installation.

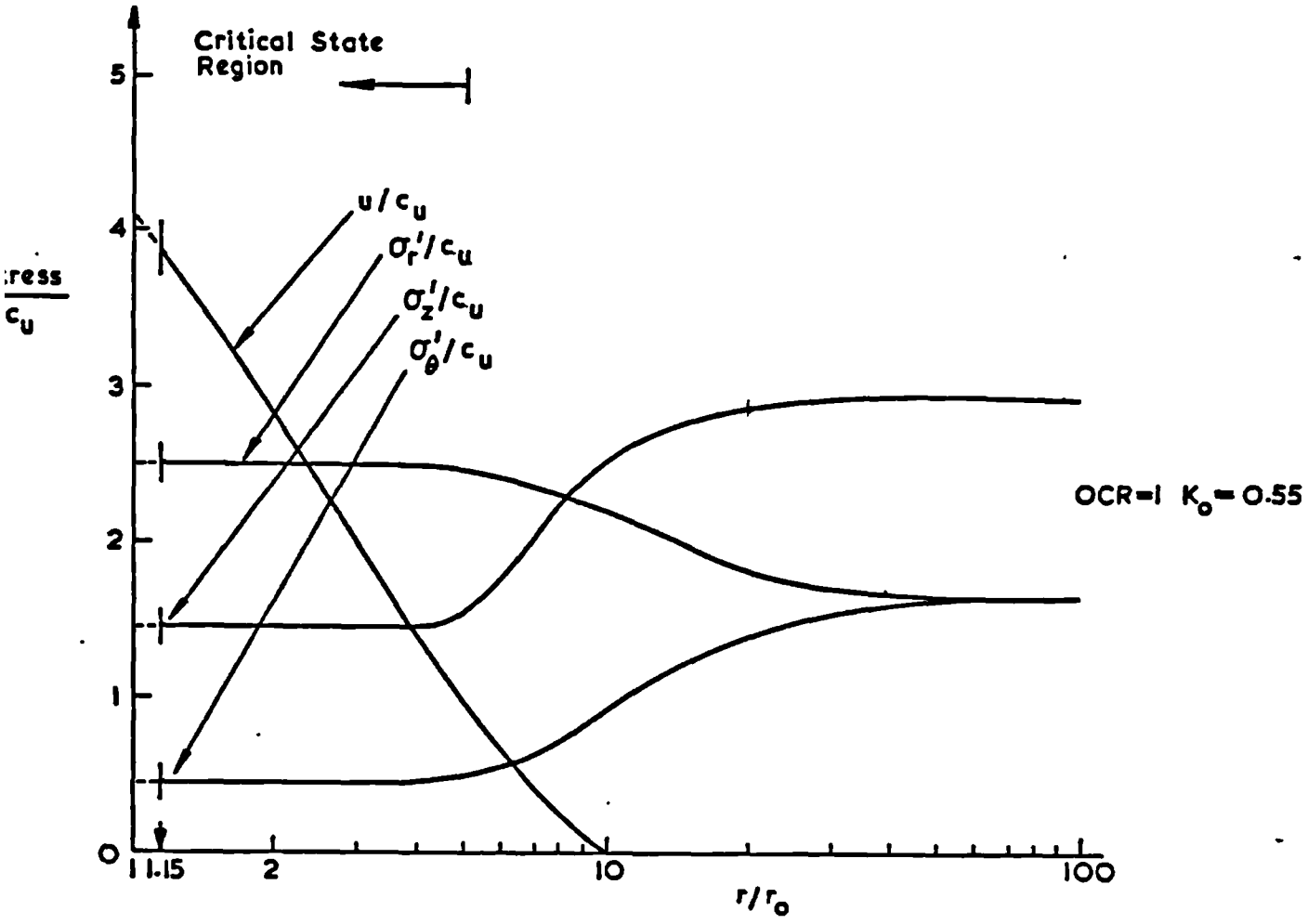


Figure 3.12. Predictions of cavity expansion theory for radial distributions of stresses.

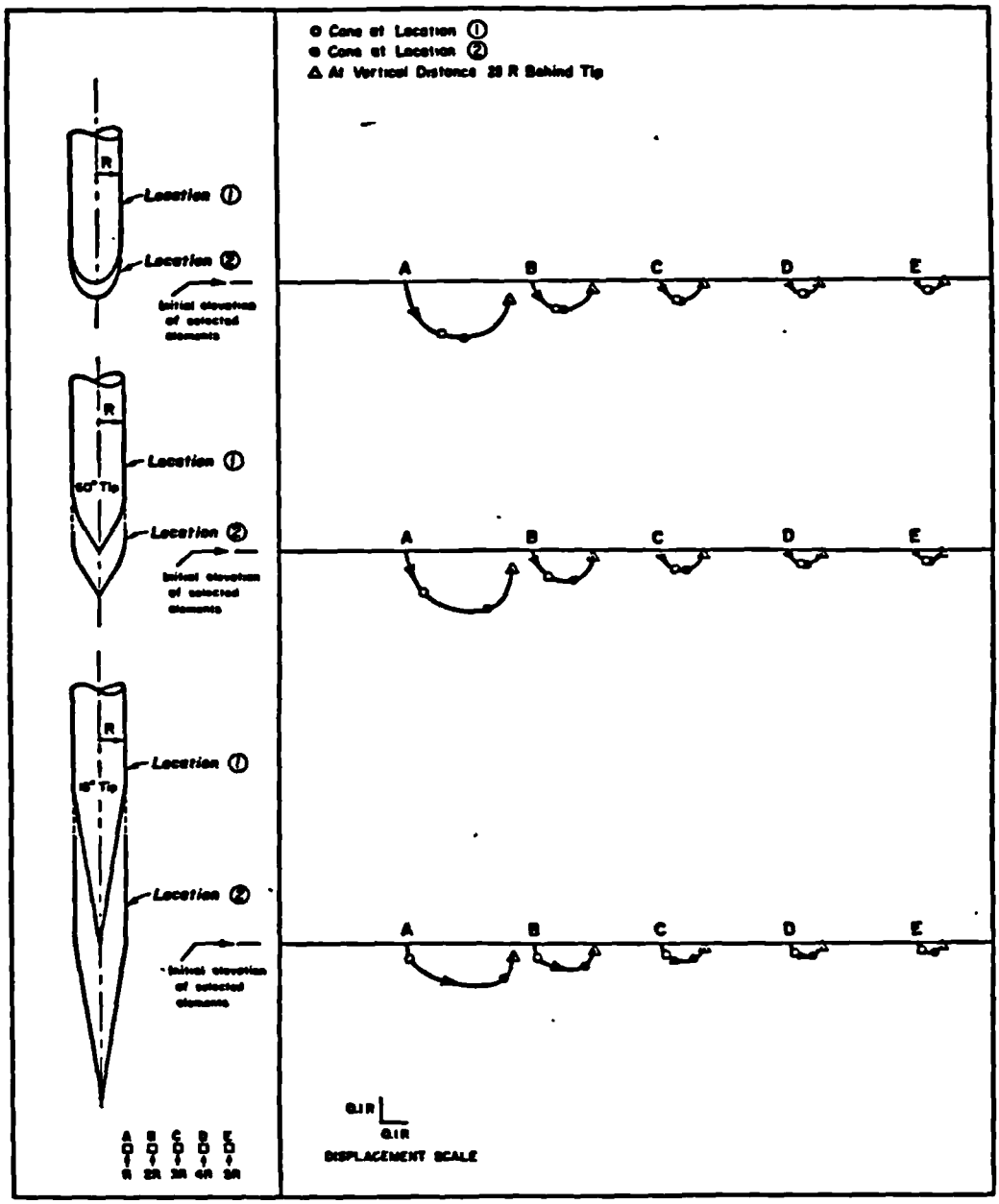


Figure 3.13. Soil trajectories at depth during pile installation, predicted by strain path method, after Baligh and Levadoux (1982).

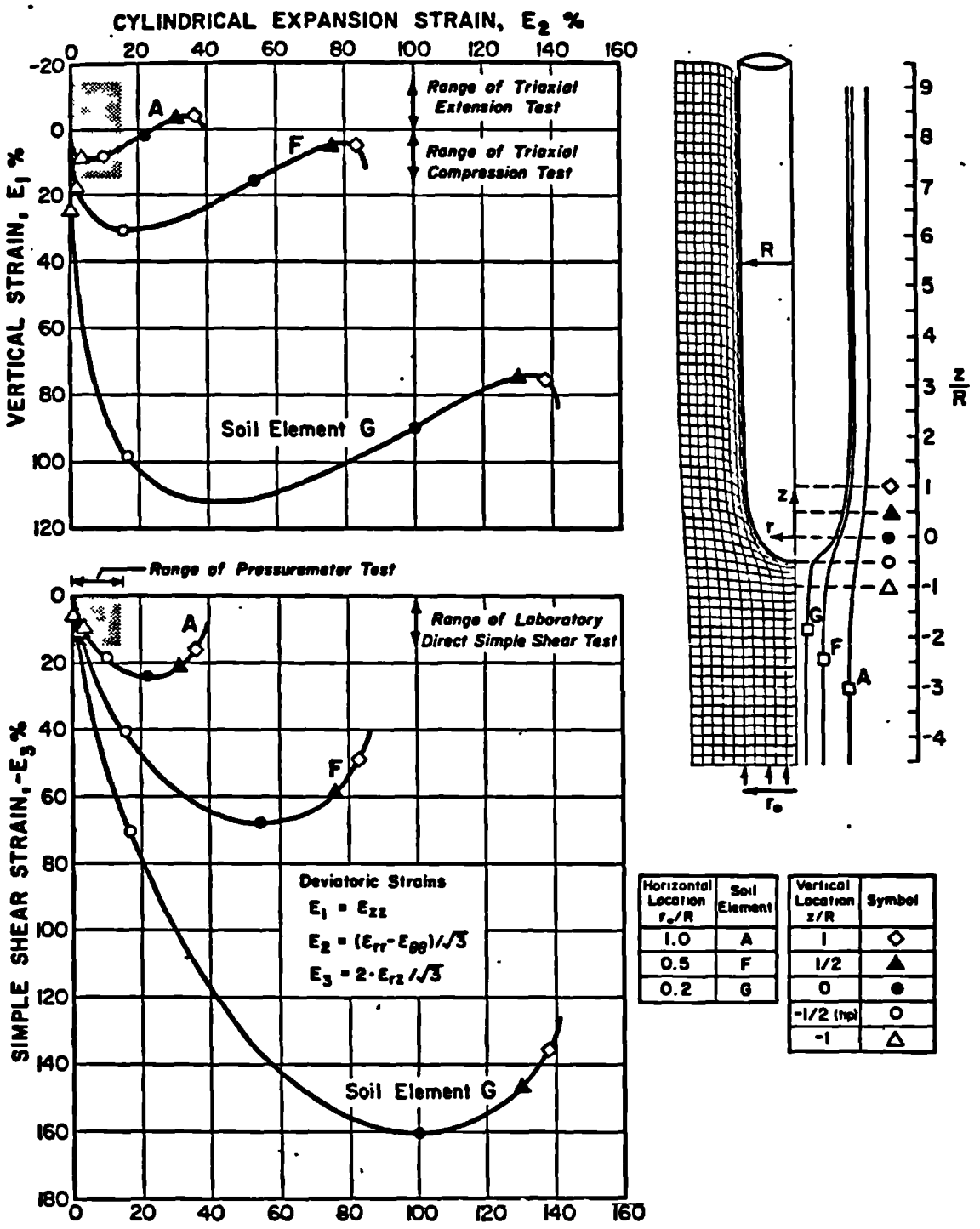
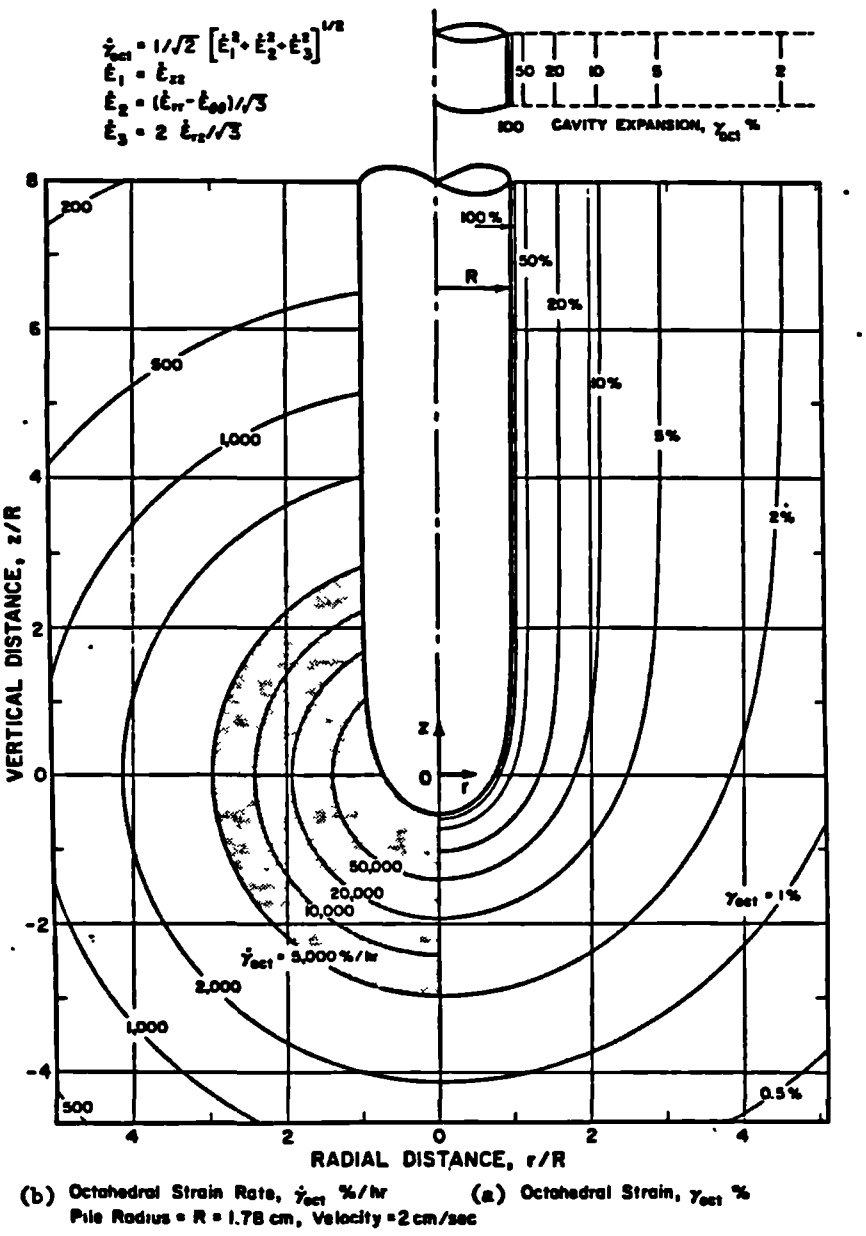


Figure 3.14. Components of strain developed during the penetration of a simple pile, after Baligh and Levadoux (1982).



(b) Octahedral Strain Rate, $\dot{\gamma}_{oct}$ %/hr (a) Octahedral Strain, γ_{oct} %
Pile Radius = R = 1.78 cm, Velocity = 2 cm/sec

Figure 3.15. Contours of octahedral shear strain developed during simple pile penetration, after Baligh and Levadoux (1982).

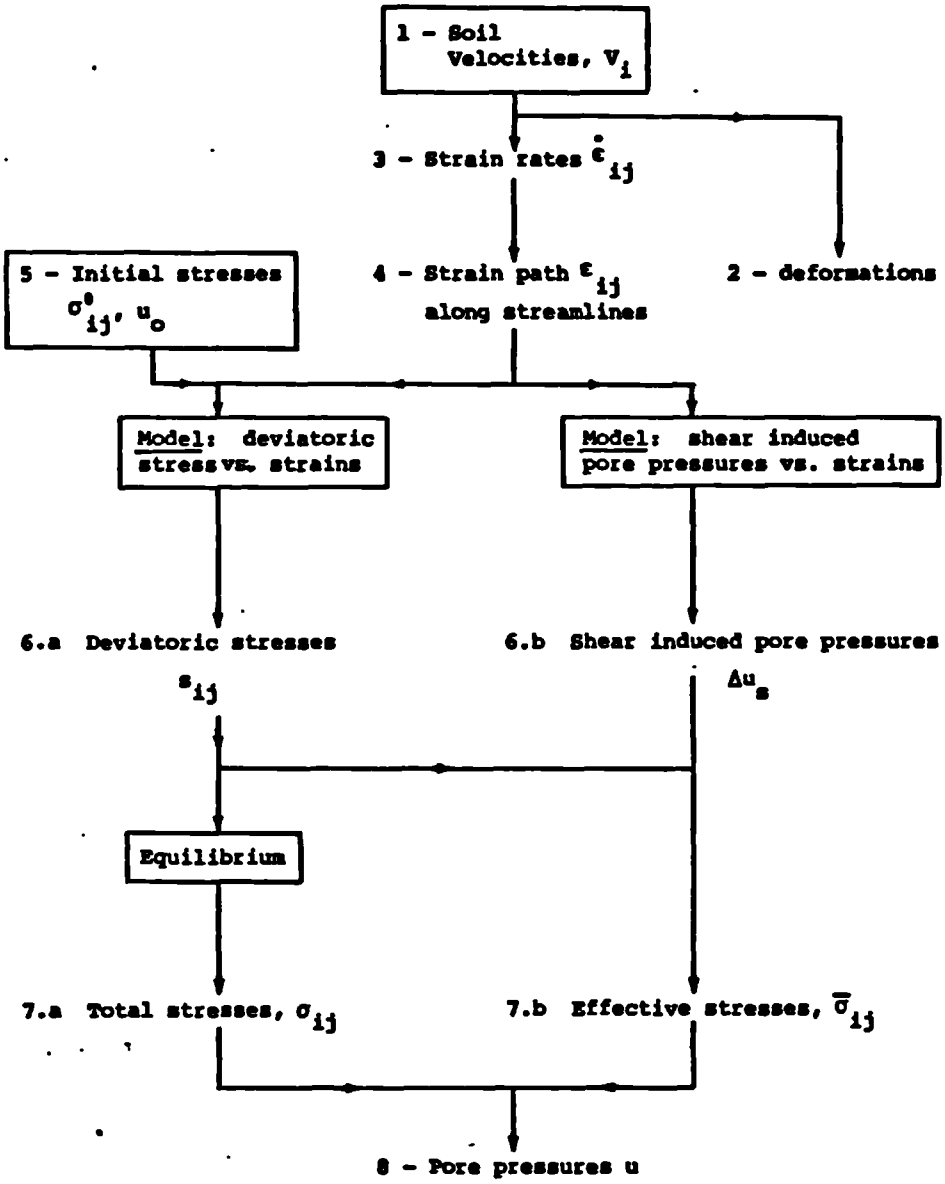


Figure 3.16. Schematic of strain path analysis; total stress models. After Baligh and Levadoux (1982).

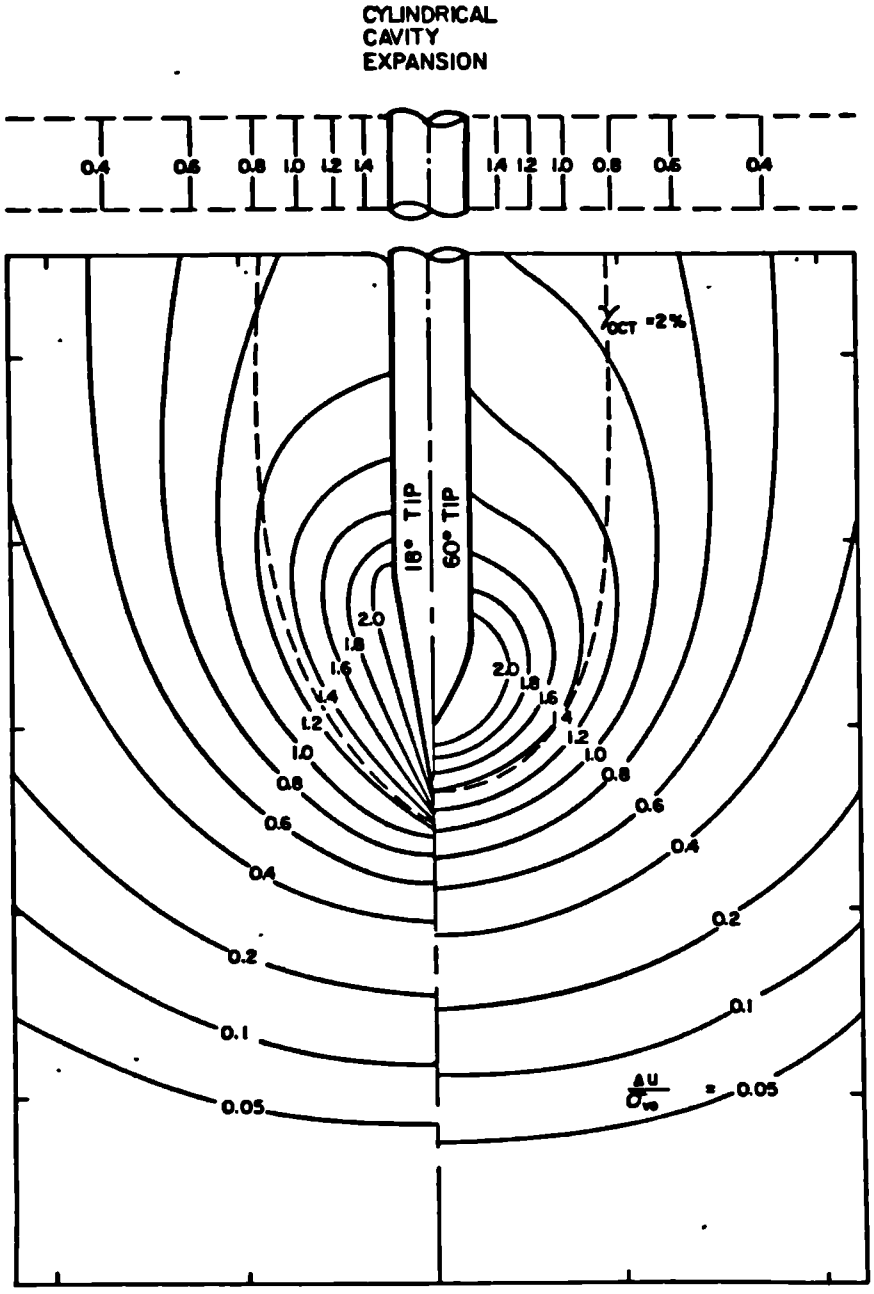


Figure 3.17. Contours of pore pressures generated by conically tipped displacement piles, after Baligh and Levadoux (1982).

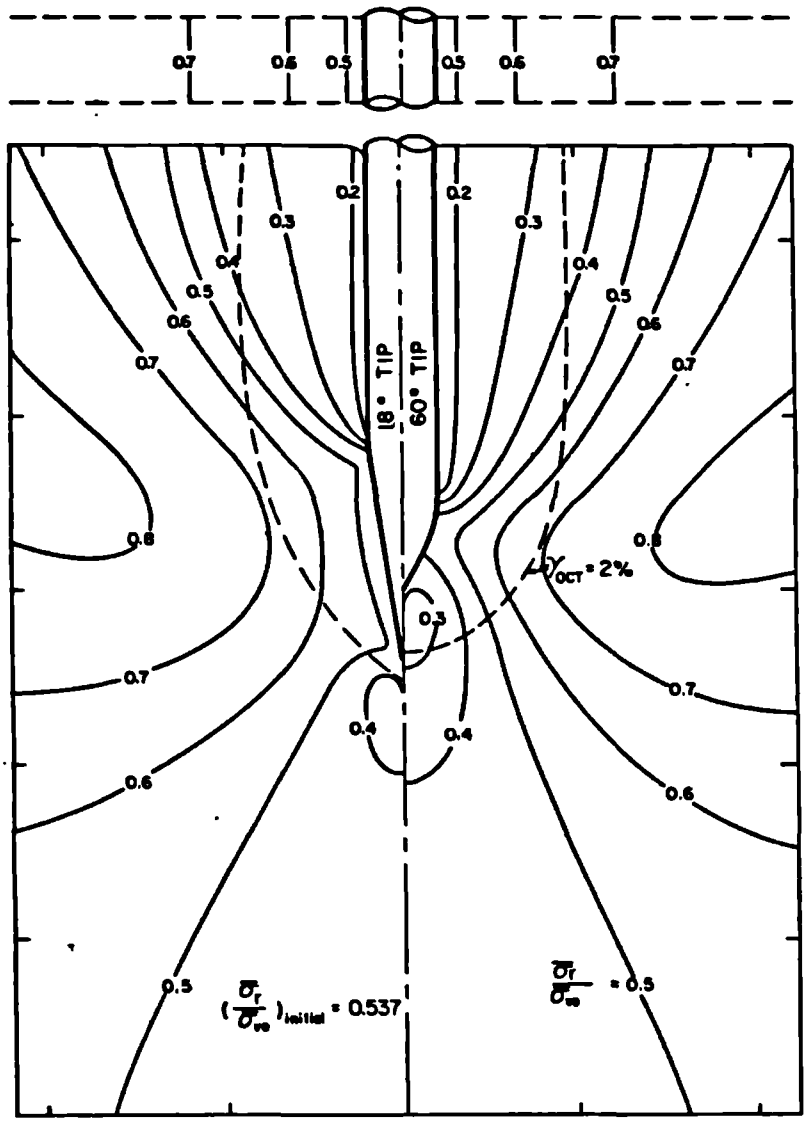


Figure 3.18. Contours of σ_r during steady penetration of conically tipped piles, after Baligh and Levadoux (1982).

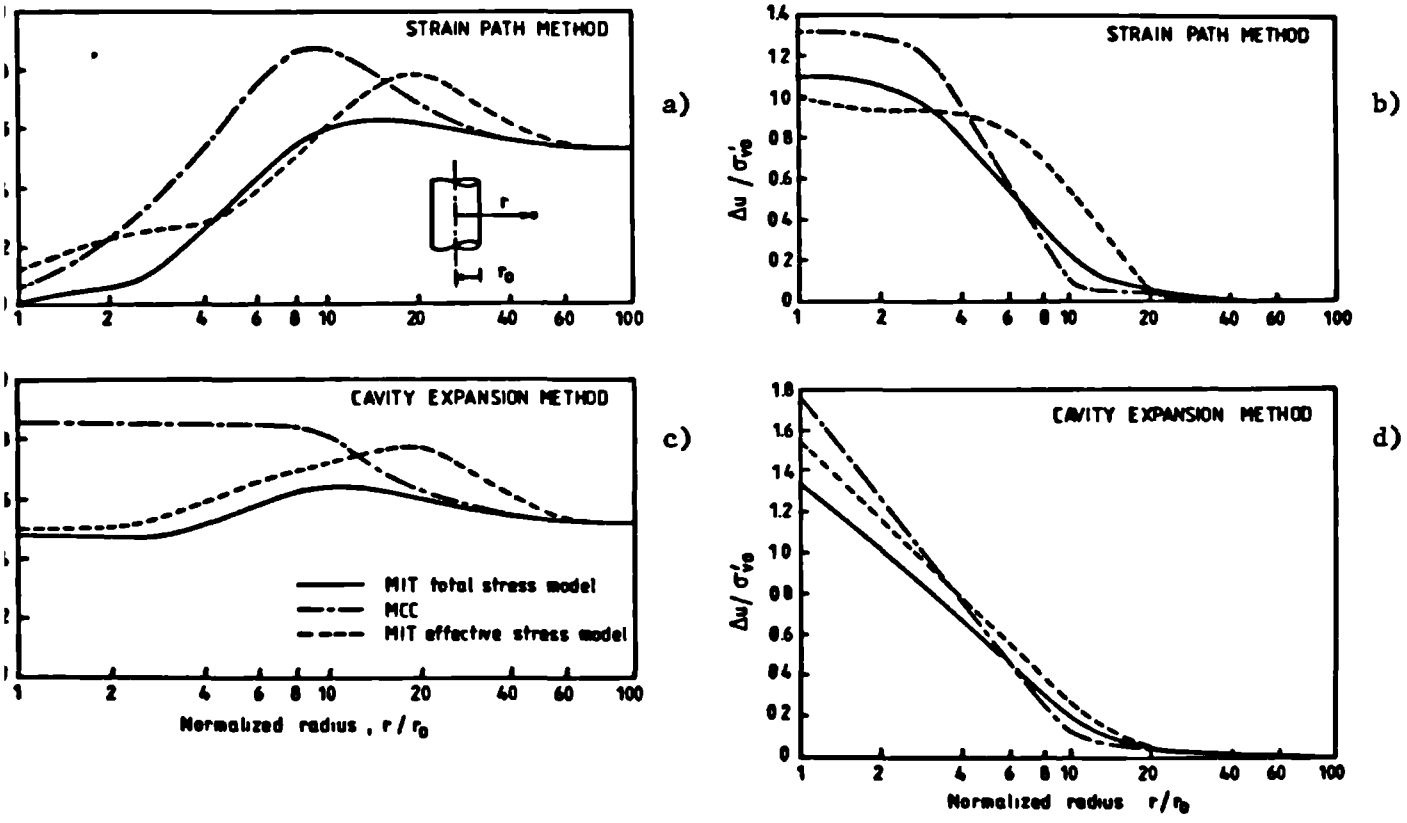


Figure 3.19 a), b), c) and d). Predictions of σ'_r and Δu for simple pile penetration and cavity expansion strain fields, various soil

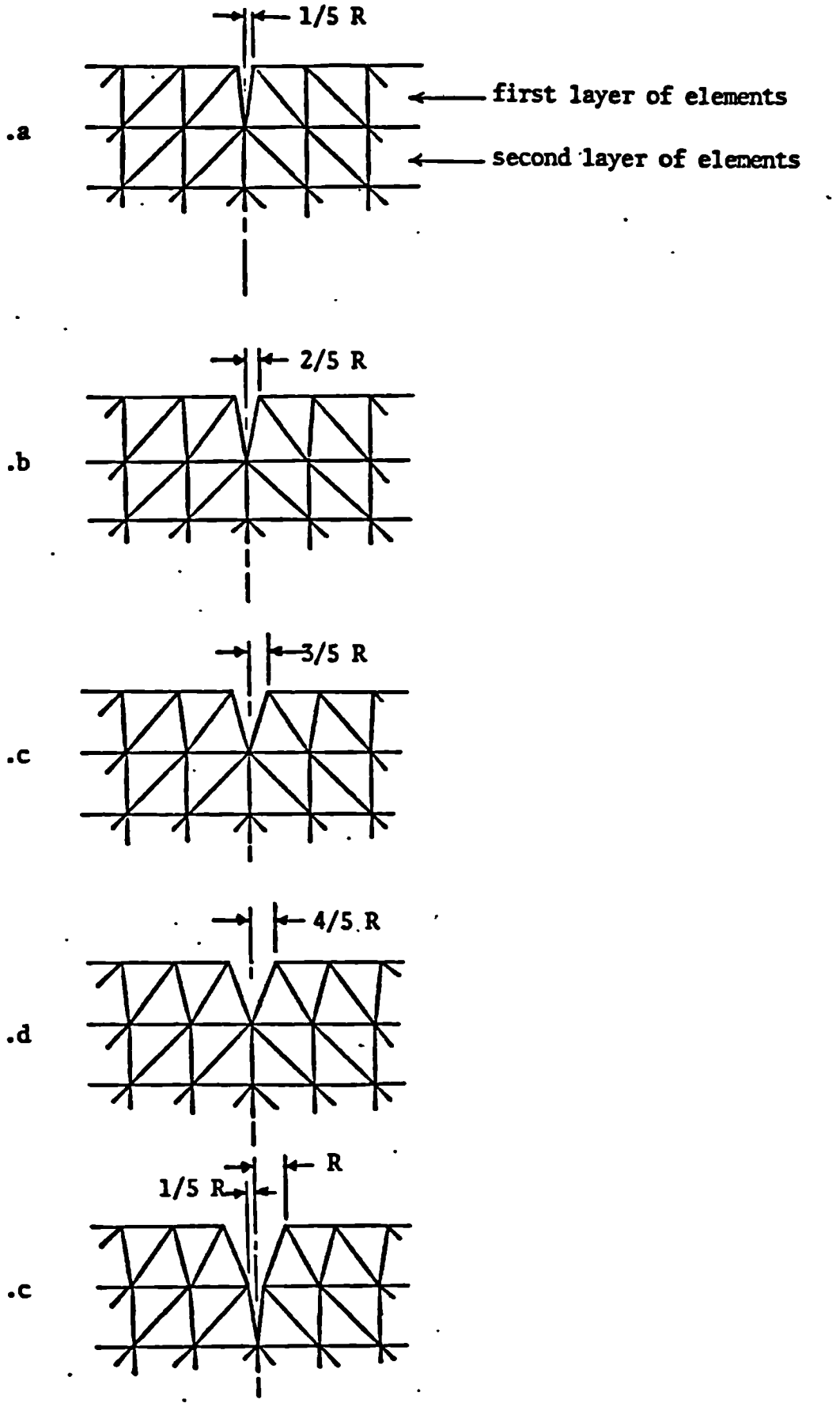


Figure 3.20. Finite element simulation of pile installation, after Fathalah (1978).

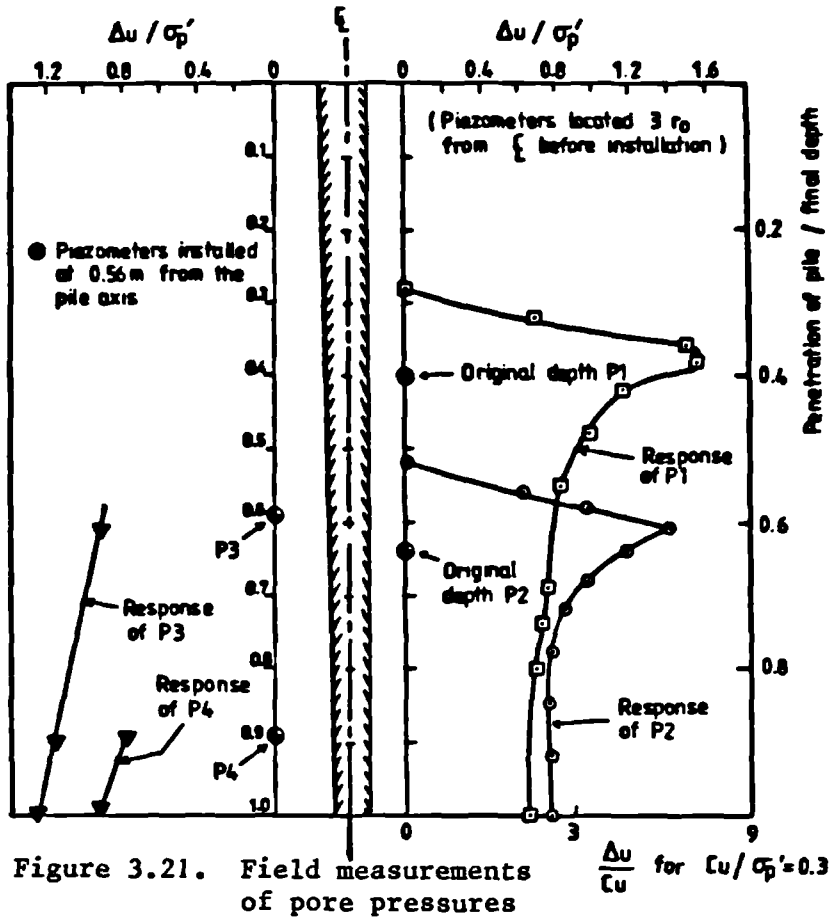


Figure 3.21. Field measurements of pore pressures generated by installation, after Blanchet et al. (1980).

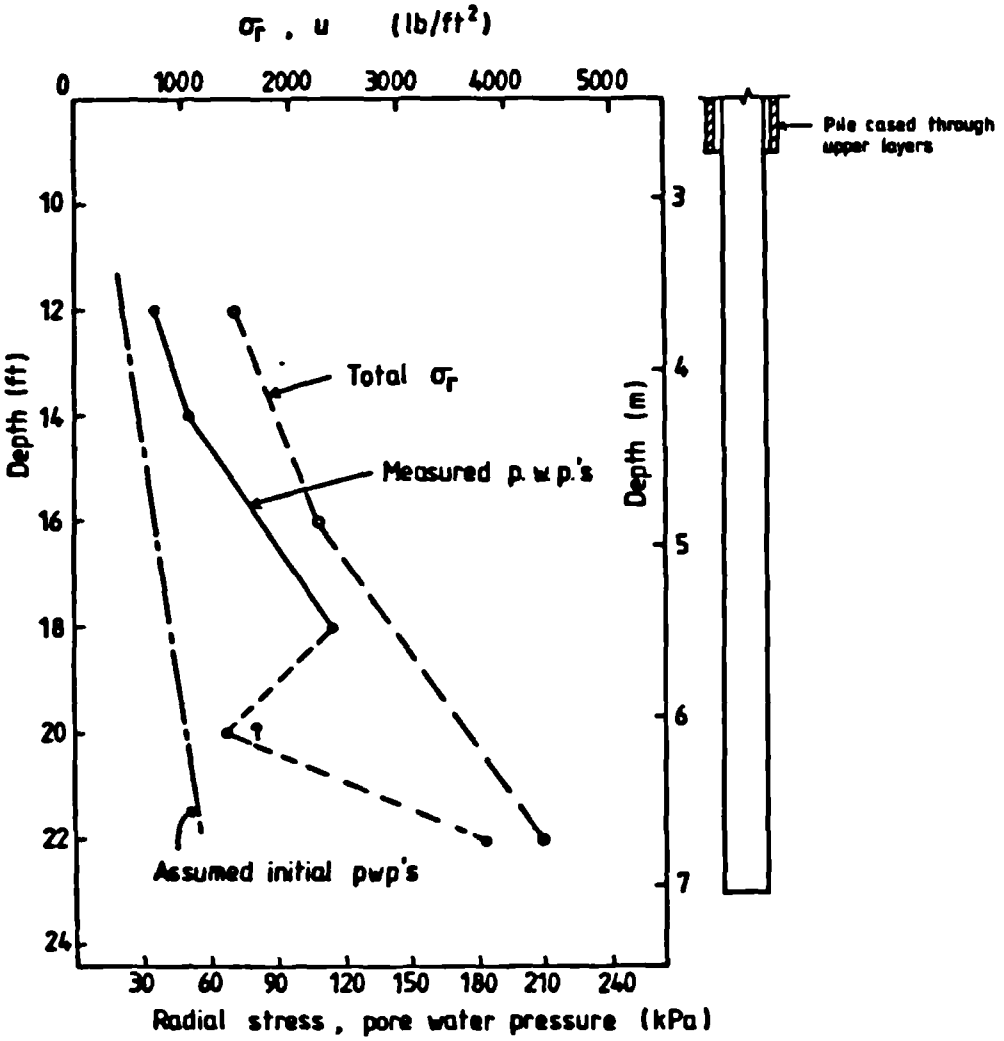


Figure 3.22. Field measurements of radial stresses and pore pressures

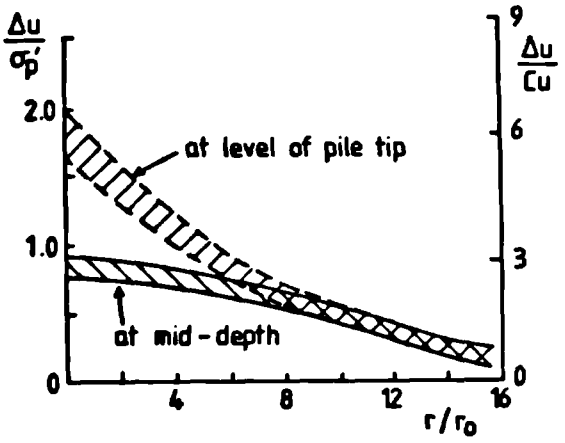


Figure 3.23. Radial distributions of pore water pressure increases due to pile installation, after Blanchet et al. (1980).

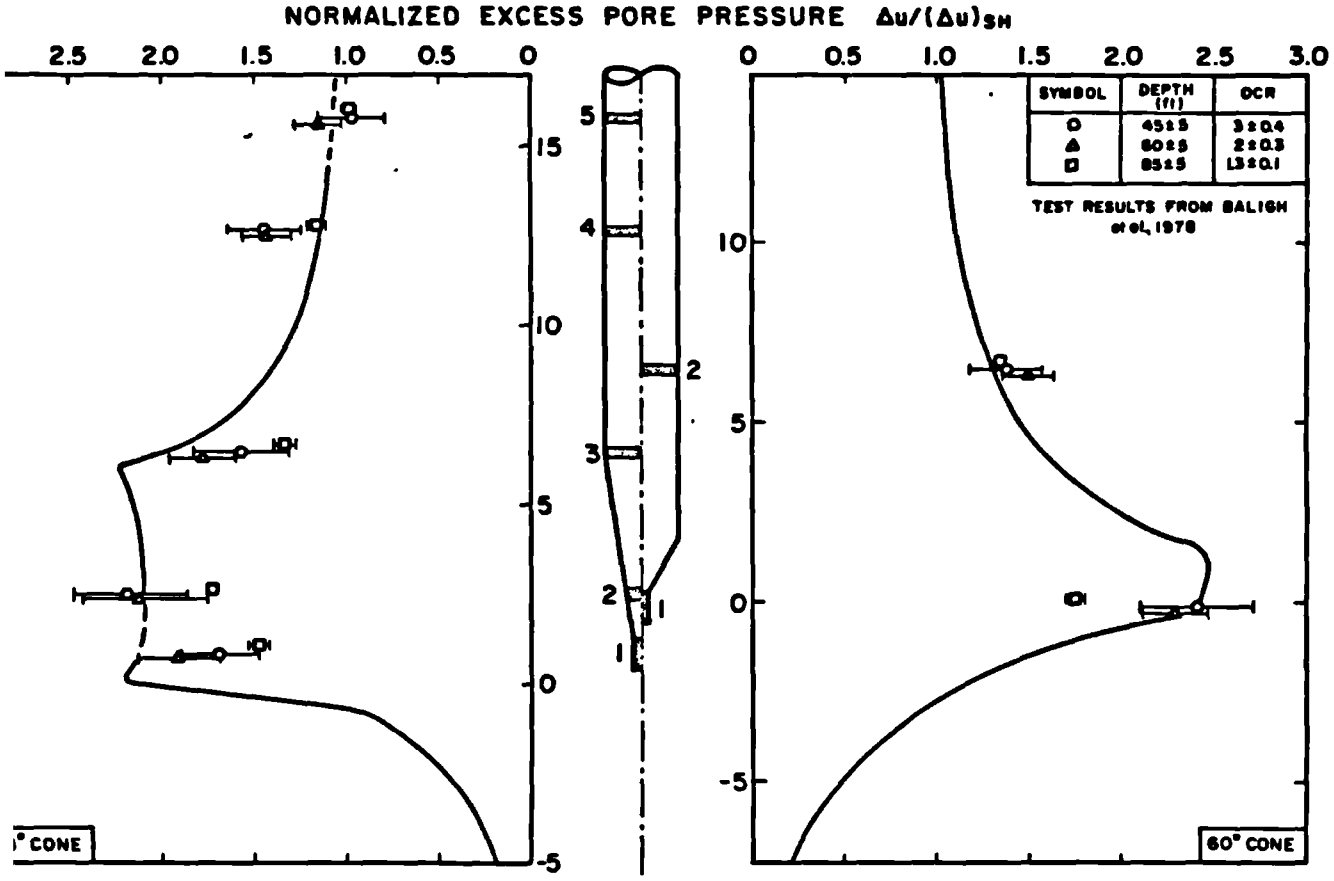


Figure 3.24. Strain path method predictions and field measurements of pore pressure increases for long penetrometers in Boston Blue clay. After Baligh and Levadoux (1982).

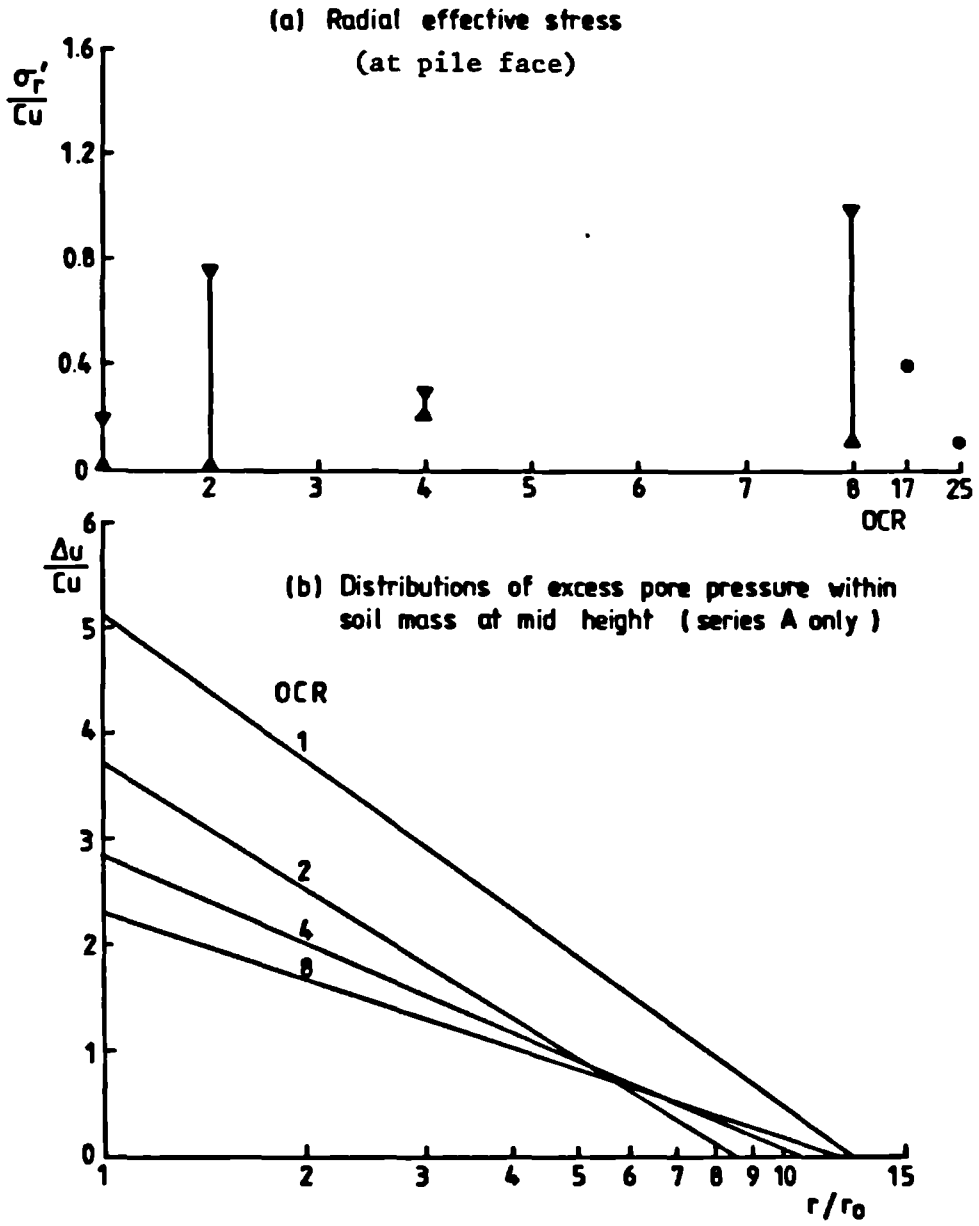


Figure 3.25 a) and b). Measurements of installation effects for model piles in Kaolin, after Francescan (1983).

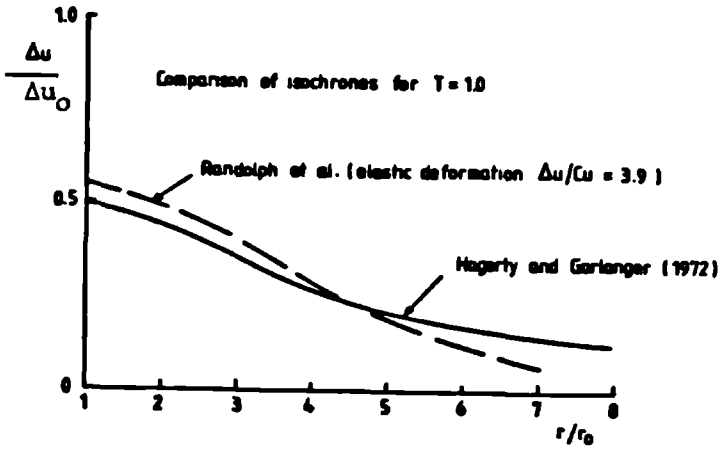
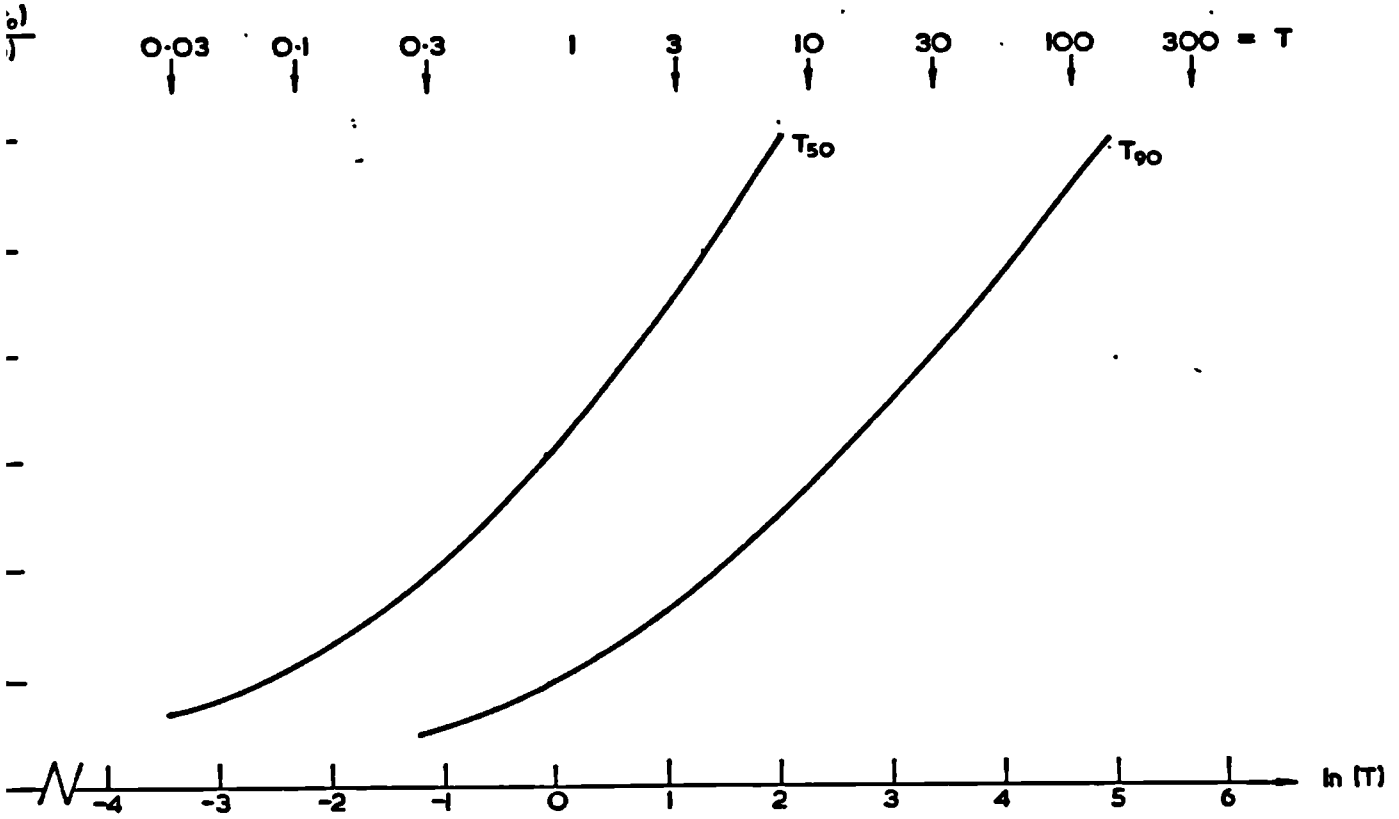


Figure 3.26. Linear consolidation solutions for dissipation after pile installation.



Variation of times for 50% and 90% consolidation with the ratio $u_{max}^{\wedge}(r_o)/c_u$

Figure 3.27. Linear consolidation solutions for dissipation after pile installation, after Randolph et al. (1979).

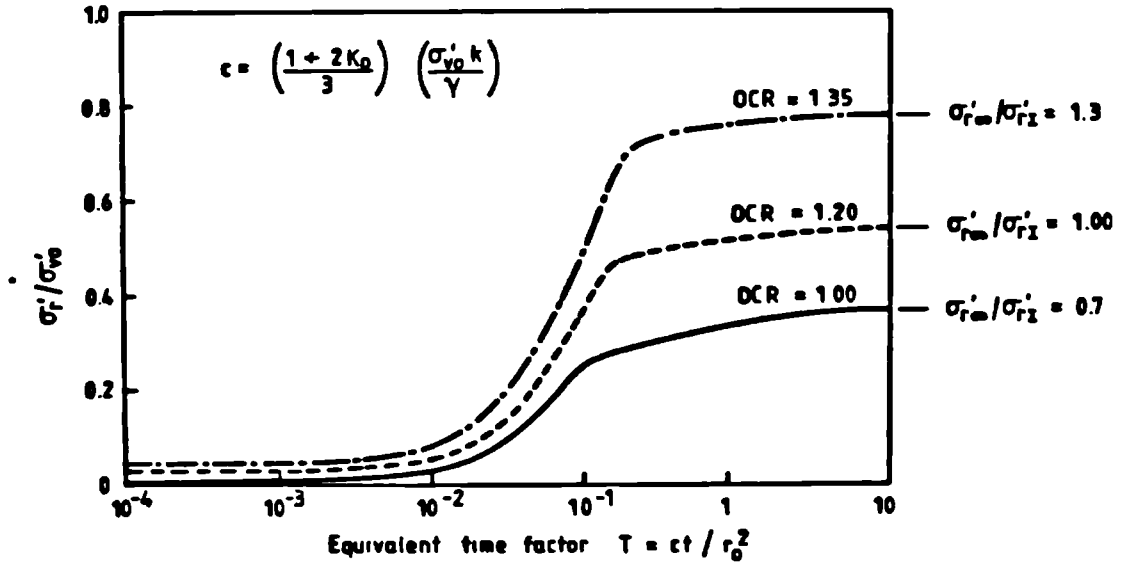
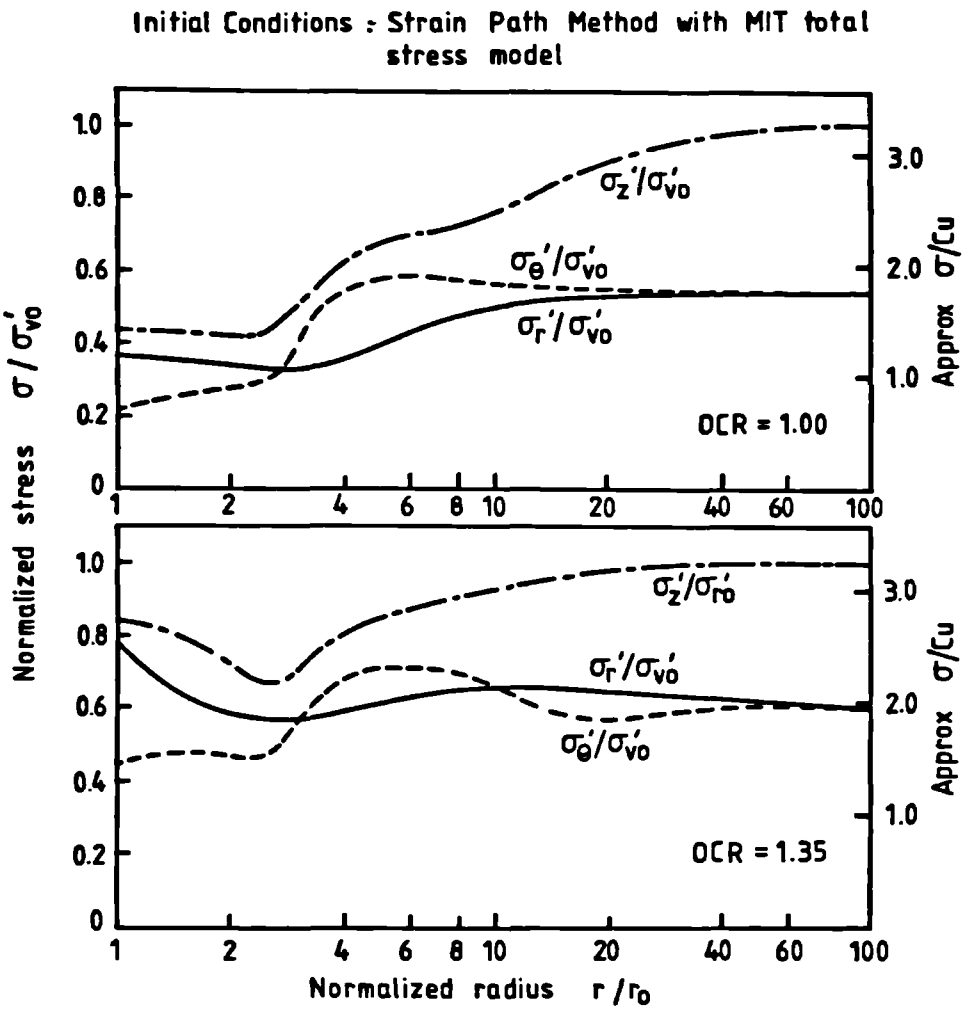


Figure 3.28. Non-linear coupled consolidation analysis for dissipation after pile installation, after Kavvadas (1982).



OCR	P'_I/σ'_{vo}	P'_∞/σ'_{vo}
1.00	0.70	0.34
1.35	0.73	0.69

Predicted mean effective stress at the pile face

Figure 3.29. Predictions of final stress distributions around middle section of a pile installed in Boston Blue clay; non-linear analysis from strain path method, after Kavvadas (1982).

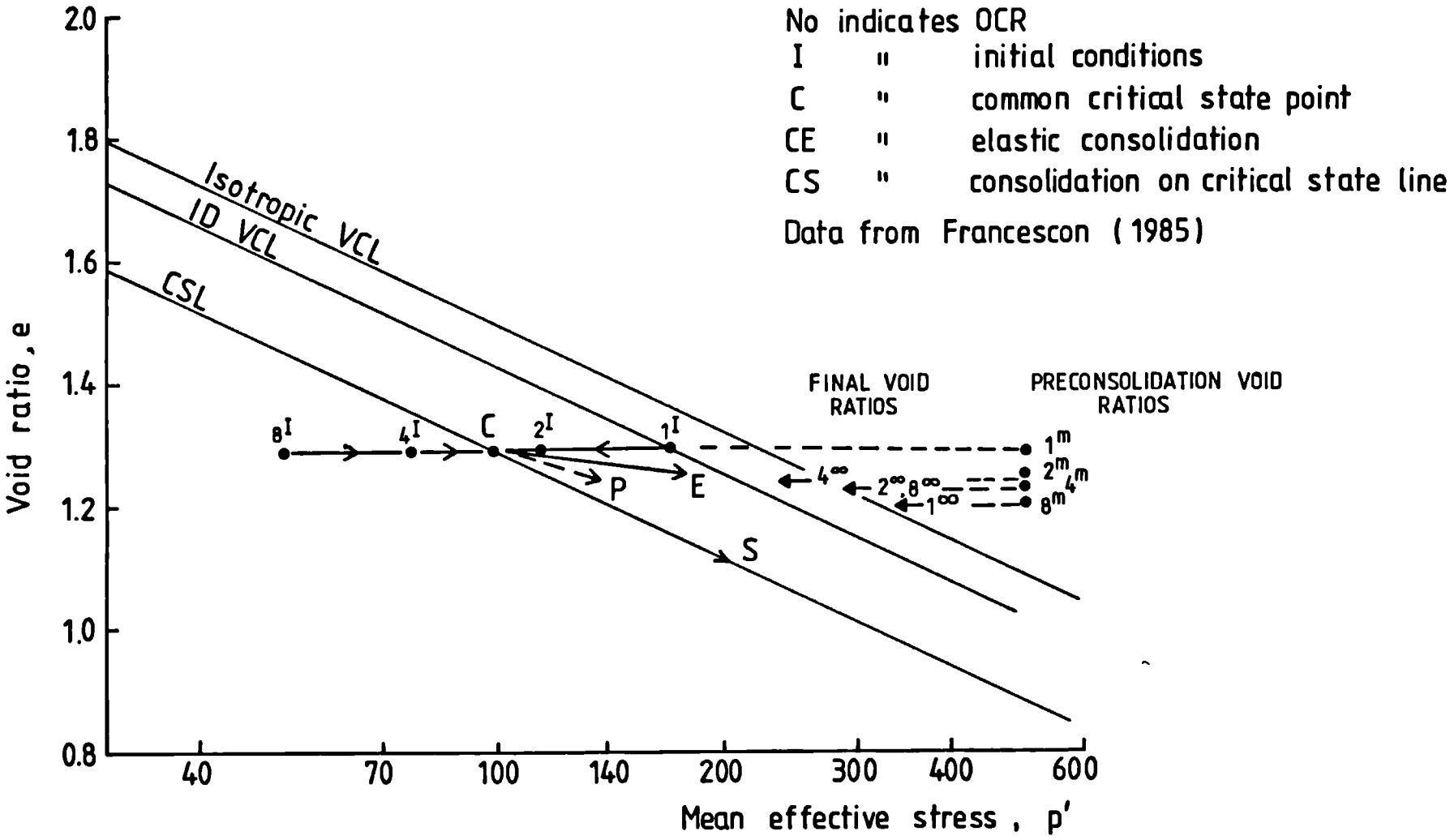


Figure 3.30.Relationships between initial and final e - p' states for clay near to the pile face in model pile tests conducted by Francescan (1983).

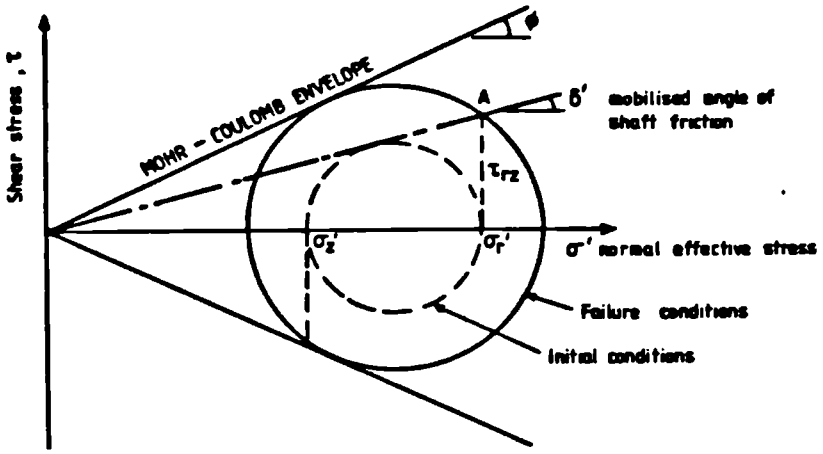


Figure 3.31. Relationship between δ' and ϕ' for a soil which is elastic before failure, after Martins (1983).

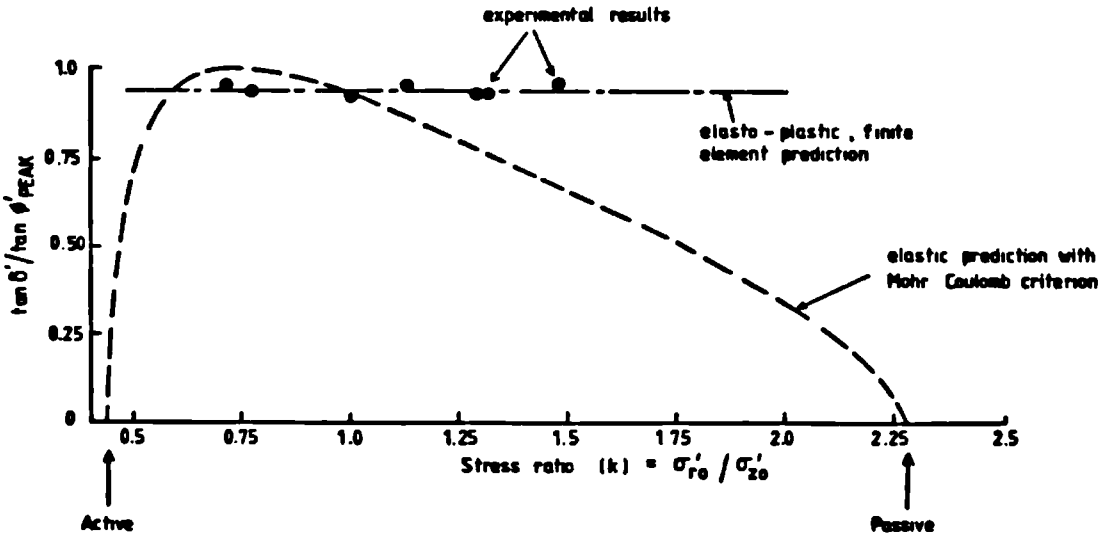
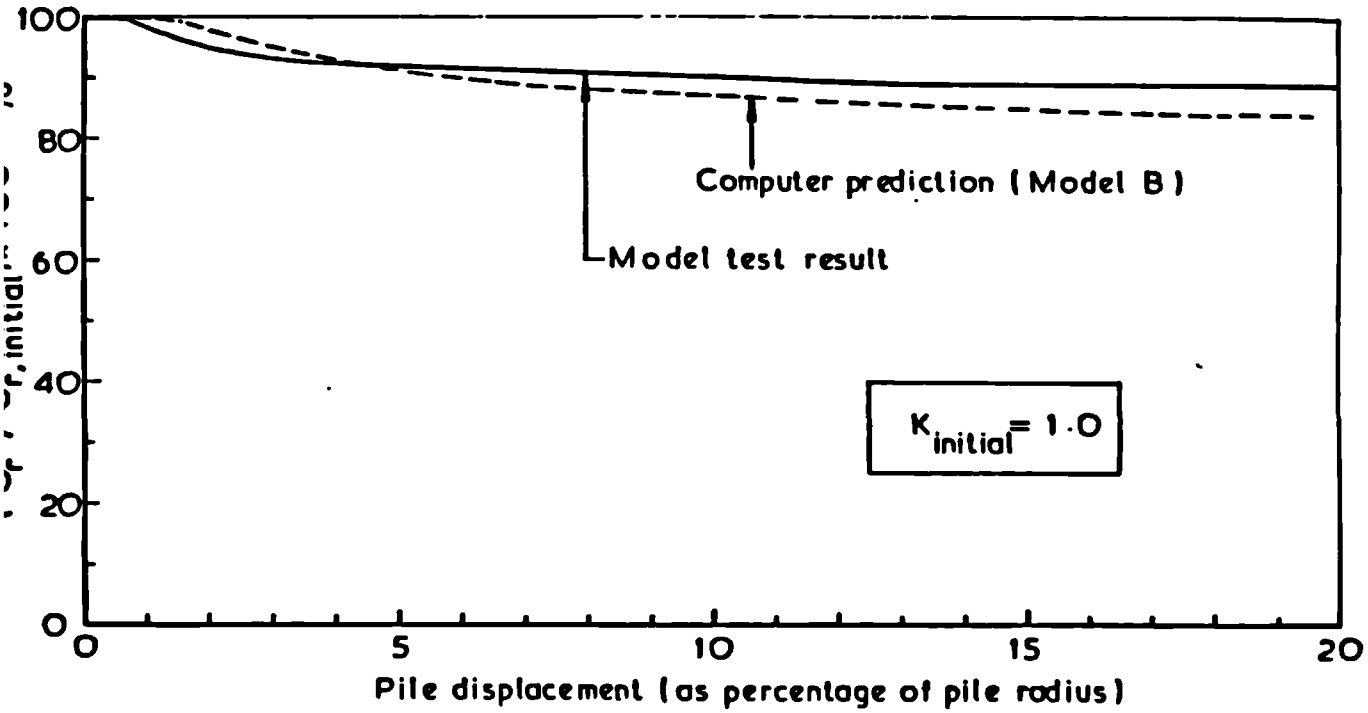
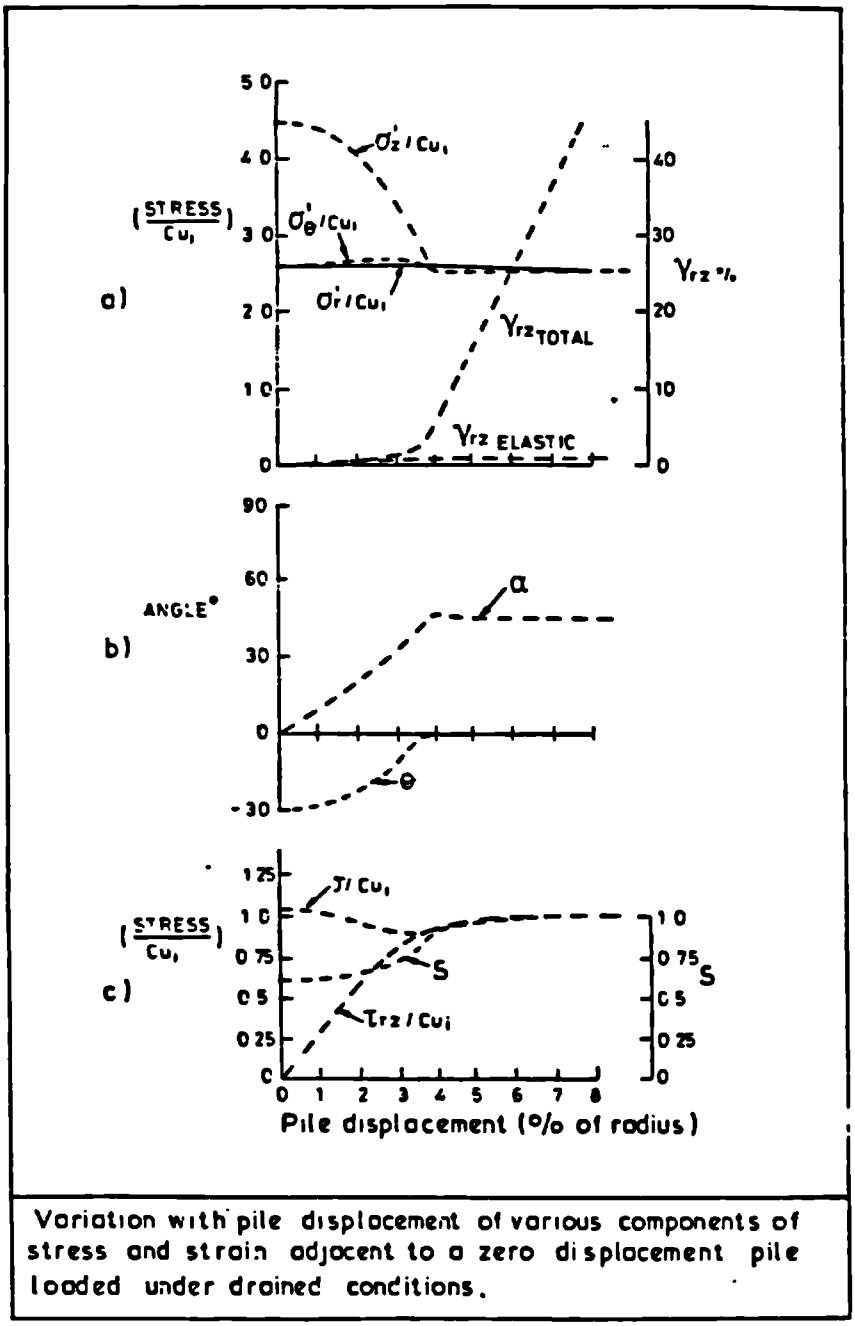


Figure 3.32. Comparison between theoretical and experimental values for tan δ'/tan ϕ', after Martins (1983).



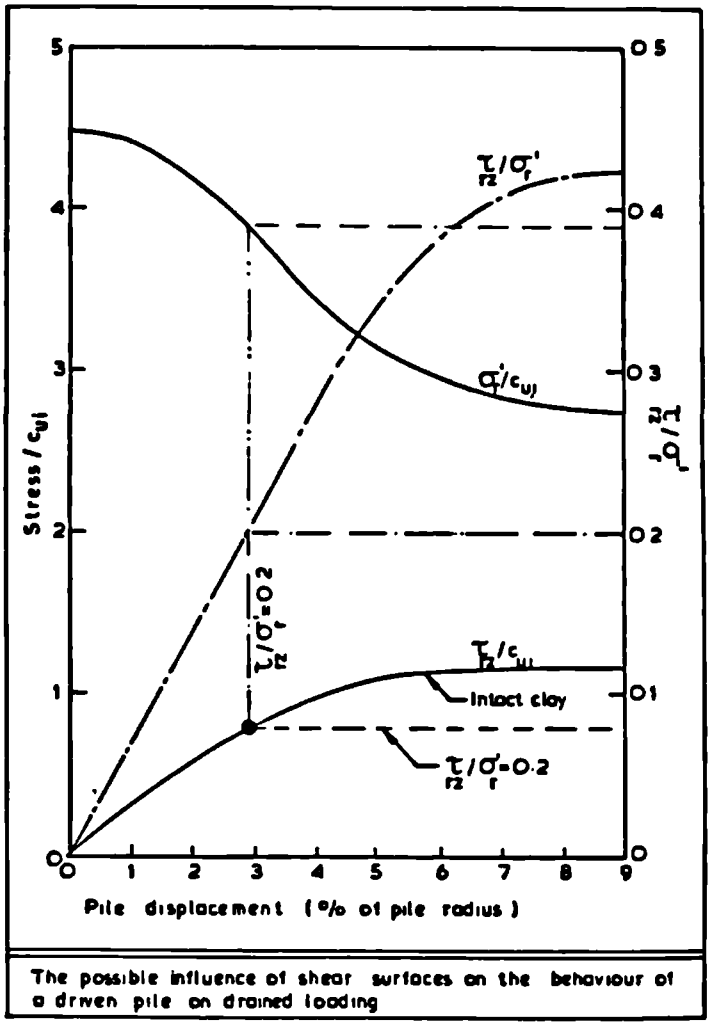


Variation with pile displacement of various components of stress and strain adjacent to a zero displacement pile loaded under drained conditions.

Figure 3.33 (above) Comparison between experiment and predicti for drained pile loadin after Martins (1983).

Figure 3.34. Predicted stress changes for a zero-displacement pile in

Figure 3.35. The effect of a residual shear surface, with tan $\phi'_r = 0.2$, on the stress displacement curves of a displacement pile, after Martins (1983).



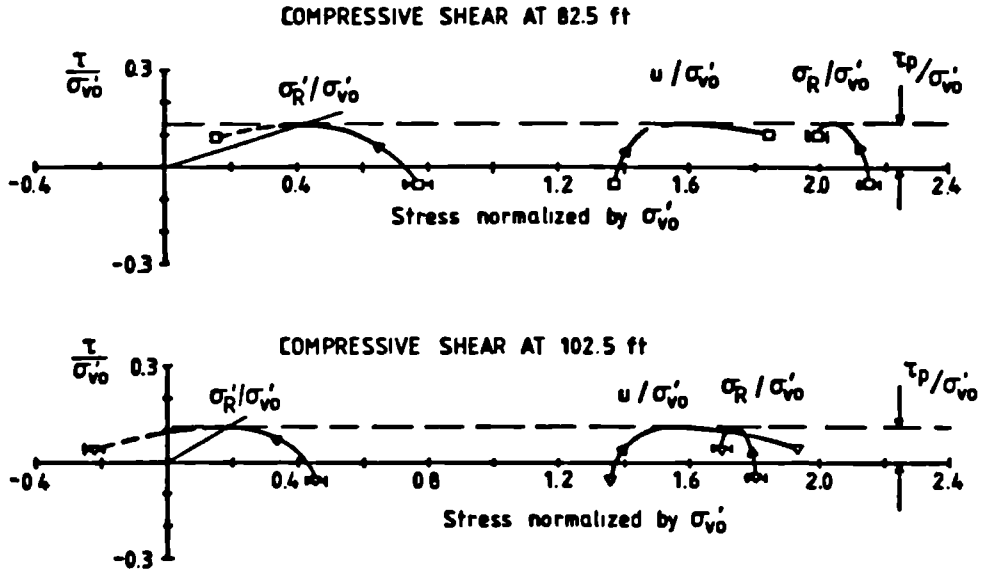


Figure 3.36. Field measurements of stress changes induced by pile loading, after Morrison (1984).

CHAPTER 4

Tables and Figures

Identification	Soil Models (Yield criterion)[1]	Initial stresses	Soil parameters
A	Sand-Mohr Coulomb Clay-Tresca	Assumed insitu K_o distribution[2]	As shown on Fig.4.7 α=0.5 at interface
B	as above	as above	As shown on Fig.4.7 α=1.0, softening as B, Fig. 4.12
C	as above	as above	As above, but softening as C, Fig. 4.12
D	as above	as above	As A but with Young's modulus increased by 500%.
F	Sand-Mohr Coulomb,Clay-modified Cam Clay	'Cavity expansion' values[3]	As shown on Fig.4.8 (Parameters from Drammen clay)
G	as above	as above	As shown on Fig.4.9 (Parameters for Hutton site)
H	as above	Assumed insitu K_o distribution[2]	As shown on Fig.4.10 (Parameters for Hutton site)

Table 4.1 Summary of parameters for Analyses A to H.

Notes. 1. All three models are elasto-plastic, the yield criterion is used as a convenient label.

2. This distribution was derived by Fugro.

3. The initial stresses for F and G were assumed to be those recommended by Randolph et al (1979) as a lower bound for full consolidation after installation. The vertical effective stresses were assumed equal to the overburden values with $\sigma'_\theta = \sigma'_v = K_o \sigma'_r$ and k_o value taken as $(1-\sin\phi')$.

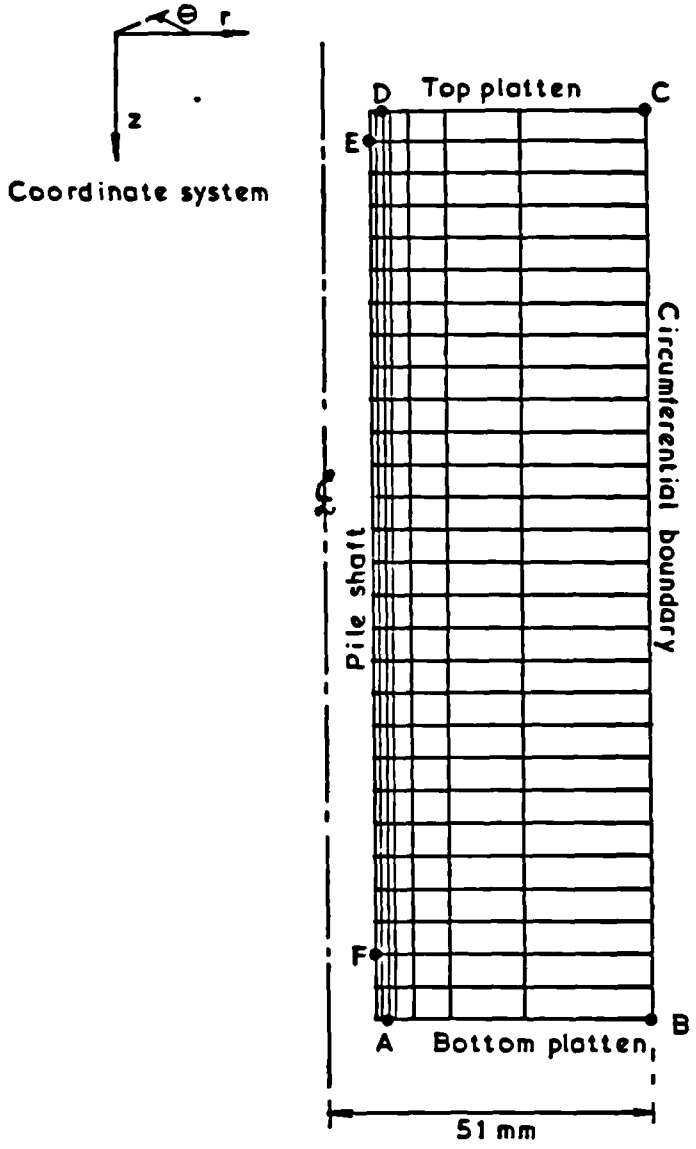


Figure 4.1. Finite element simulation of Model pile system, after Martins (1983)

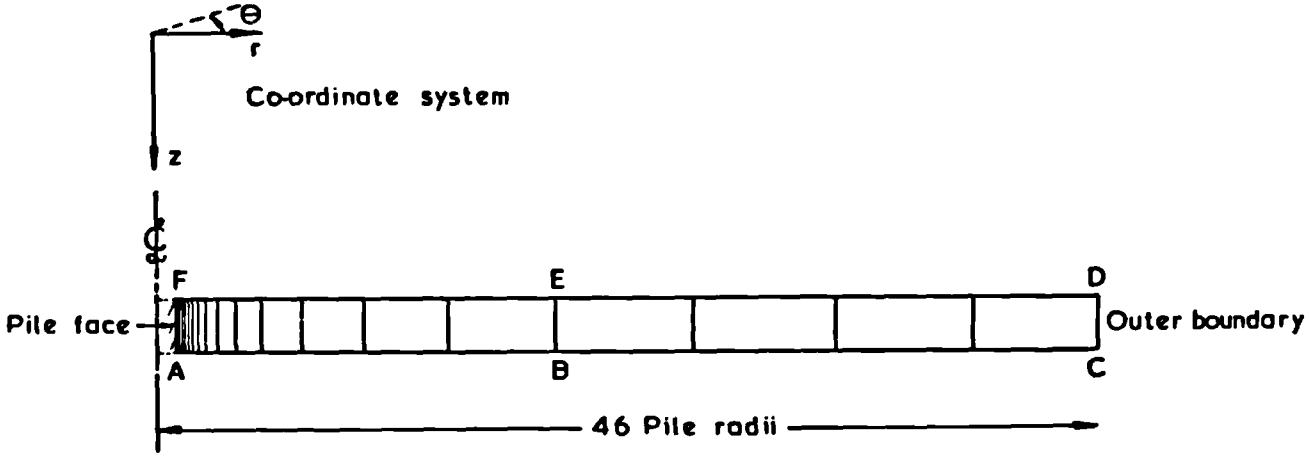


Figure 4.2. Finite element simulation of a segment from a long pile, after Martins (1983).

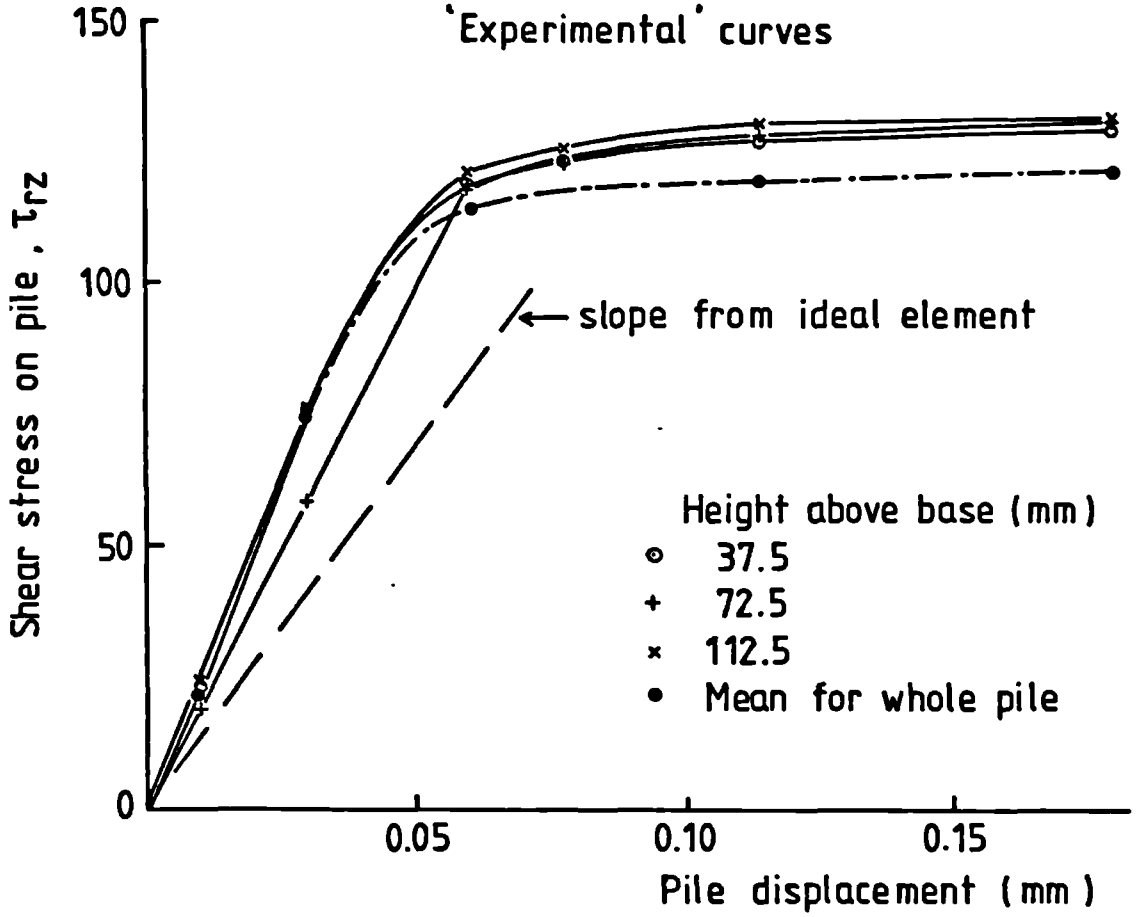


Figure 4.3. Predictions for Model pile shear stress-displacement relationships.

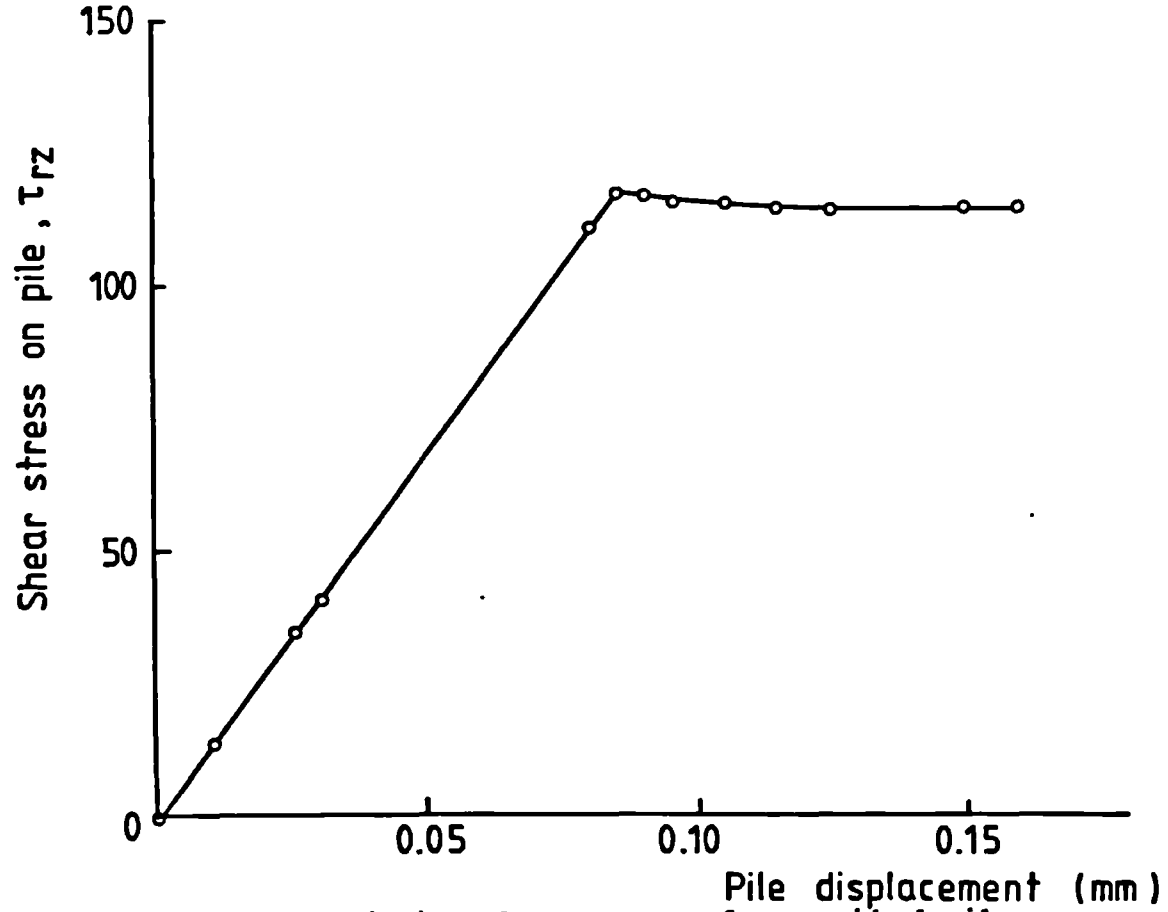
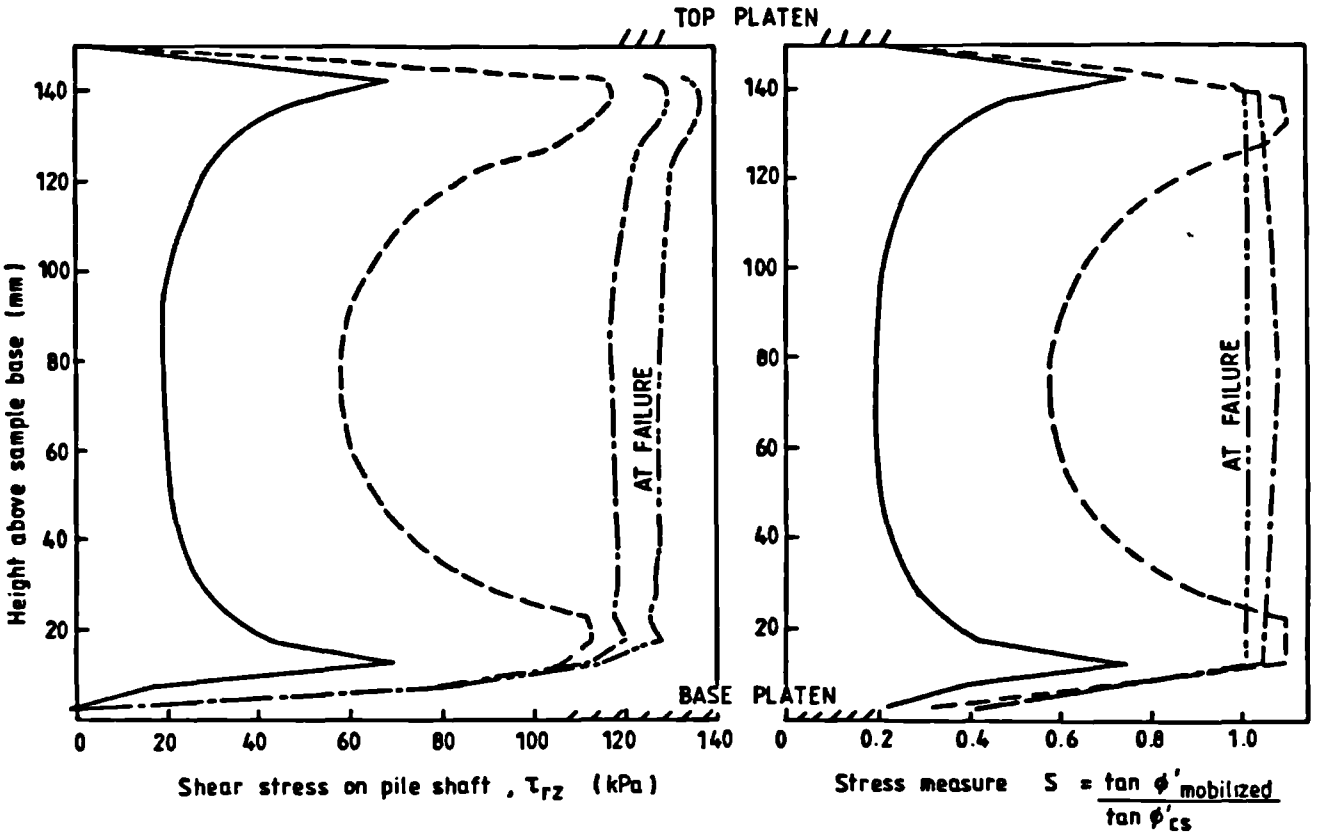


Figure 4.4. Predictions for a segment from an ideal pile.

Figure 4.5. Predictions of τ_{rz} and S distributions over the shaft of the model pile.



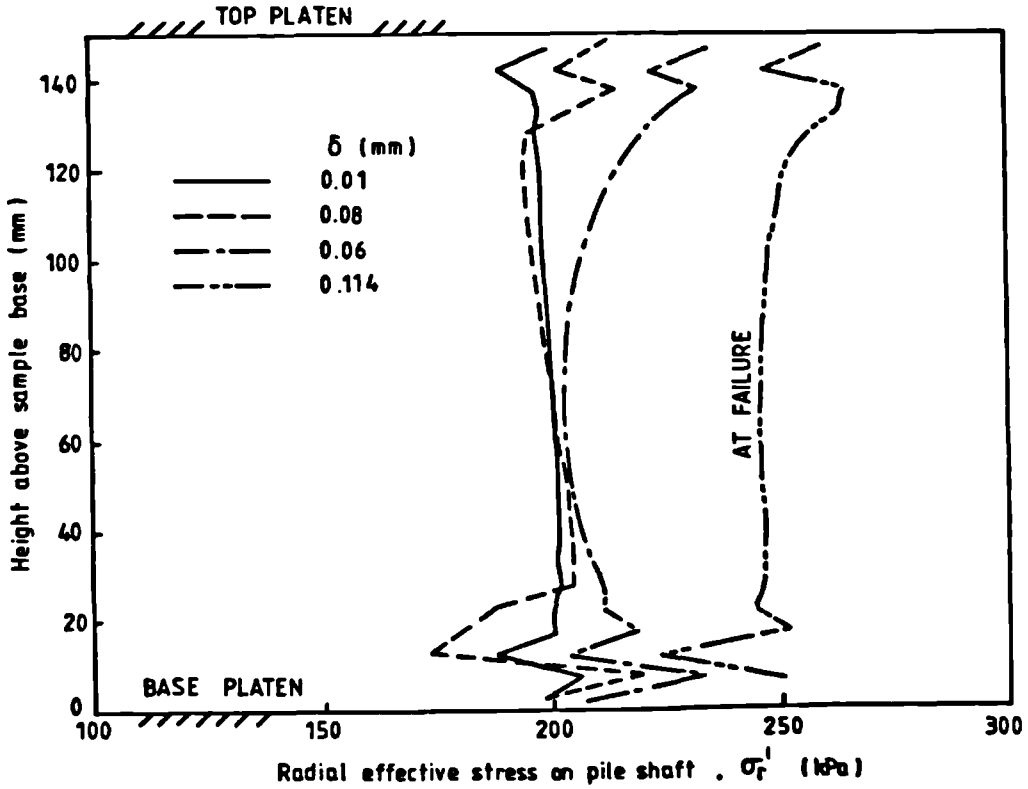
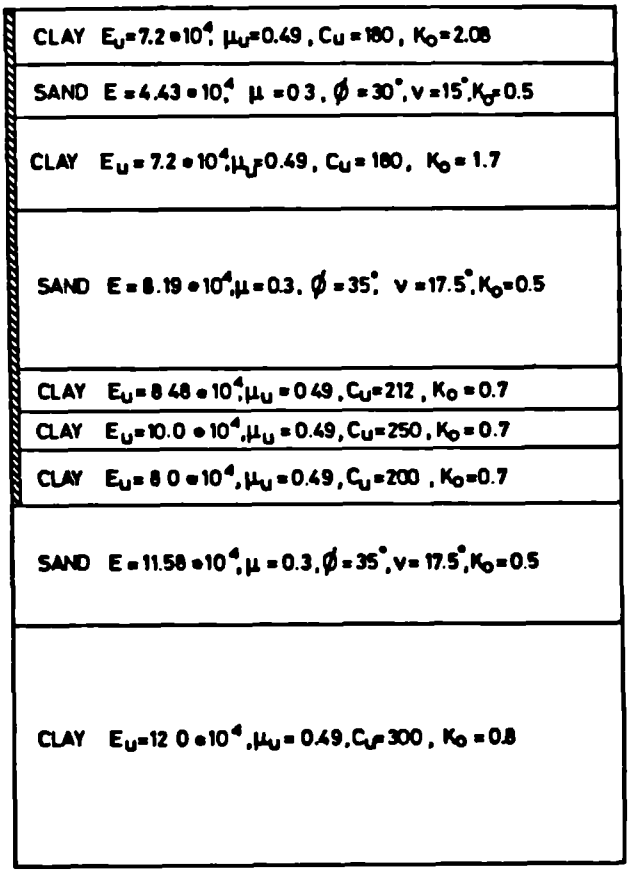


Figure 4.6. Predictions of σ_r' over the shaft of the model pile.



E, E_u and C_u values in kN/m^2

Figure 4.7. Assumed soi properties and initial stresses fo runs A to C

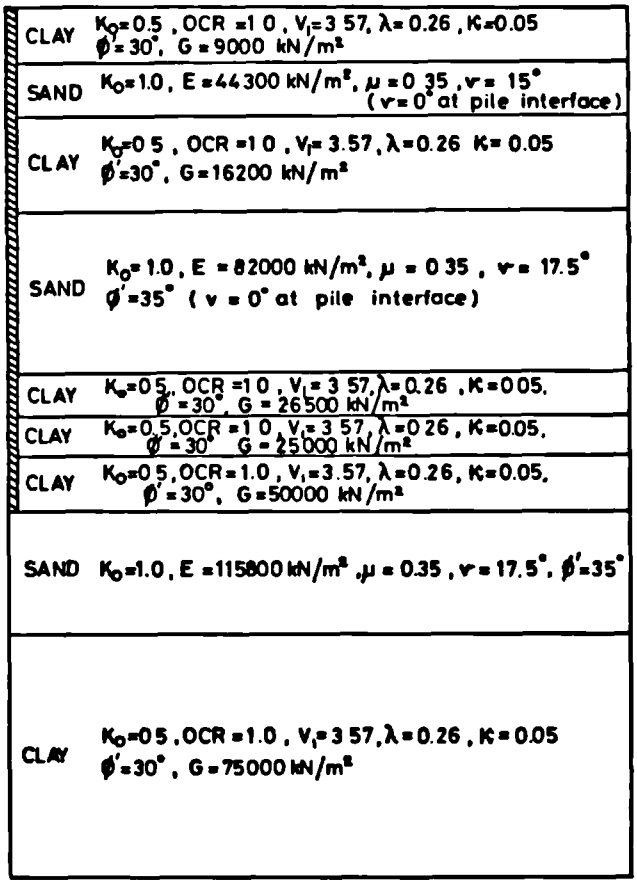


Figure 4.8. Assumed soi properties and initial stresses fo run F.

In all cases $\sigma'_{\theta i} = \sigma'_{zi} = K_o \sigma'_{ri}$

λ = slope of virgin consolidation line in v–$\ln(p')$ space

K = slope of swelling line v–$\ln(p')$ space

V_i = specific volume at unit pressure on virgin consolidation line

v = angle of dilation, E = Young's modulus

G = shear modulus, μ = Poisson's ratio

CLAY	K_o = 2.08, OCR = 49, V_i = 2.54, λ = 0.12, K = 0.02, ϕ' = 30°, G = 9000 kN/m²
SAND	K_o = 0.5, E = 44300 kN/m², μ = 0.35, ν = 15°, ϕ' = 30°, (ν = 0° at pile interface)
CLAY	K_o = 1.7, OCR = 8, V_i = 2.54, λ = 0.12, K = 0.02, ϕ' = 30°, G = 16200 kN/m²
SAND	K_o = 0.5, E = 82000 kN/m², μ = 0.35, ν = 17.5°, ϕ' = 35° (ν = 0° at pile interface)
CLAY	K_o = 0.7, OCR = 1.5, V_i = 2.54, λ = 0.12, K = 0.02, ϕ' = 30°, G = 26500 kN/m²
CLAY	K_o = 0.7, OCR = 1.5, V_i = 2.54, λ = 0.12, K = 0.02, ϕ' = 30°, G = 25000 kN/m²
CLAY	K_o = 0.7, OCR = 1.5, V_i = 2.54, λ = 0.12, K = 0.02, ϕ' = 30°, G = 50000 kN/m²
SAND	K_o = 0.5, E = 115800 kN/m², μ = 0.35, ν = 17.5°, ϕ' = 35°
CLAY	K_o = 0.8, OCR = 1.0, V_i = 2.54, λ = 0.12, K = 0.02, ϕ' = 30°, G = 75000 kN/m²

In all cases $\sigma'_{ri} = \sigma'_{\theta i} = K_o \sigma'_{zi}$

Hvorslev surface employed on dry side

Figure 4.9. Assumed soil properties and initial stresses for run G.

CLAY	K_o = 0.5, OCR = 1.0, V_i = 2.54, λ = 0.12, K = 0.02, ϕ' = 30°, G = 9000 kN/m²
SAND	K_o = 1.0 E = 44300 kN/m², μ = 0.35, ν = 15° (ν = 0° at pile interface) ϕ' = 30°
CLAY	K_o = 0.5, OCR = 1.0, V_i = 2.54, λ = 0.12, K = 0.02, ϕ' = 30°, G = 16200 kN/m²
SAND	K_o = 1.0, E = 82000 kN/m², μ = 0.35, ν = 17.5° ϕ' = 35° (ν = 0° at pile interface)
CLAY	K_o = 0.5, OCR = 1.0, V_i = 2.54, λ = 0.12, K = 0.02 ϕ' = 30°, G = 26500 kN/m²
CLAY	K_o = 0.5, OCR = 1.0, V_i = 2.54, λ = 0.12, K = 0.02 ϕ' = 30°, G = 25000 kN/m²
CLAY	K_o = 0.5, OCR = 1.0, V_i = 2.54, λ = 0.12, K = 0.02 ϕ' = 30°, G = 50000 kN/m
SAND	K_o = 1.0, E = 115800 kN/m², μ = 0.35, λ = 17.5°, ϕ' = 35°
CLAY	K_o = 0.5, OCR = 1.0, V_i = 2.54, λ = 0.12, K = 0.02 ϕ' = 30°, G = 75000 kN/m²

In all cases $\sigma'_{\theta i} = \sigma'_{zi} = K_o . \sigma'_{ri}$

λ = slope of virgin consolidation line in v - ln (p) space

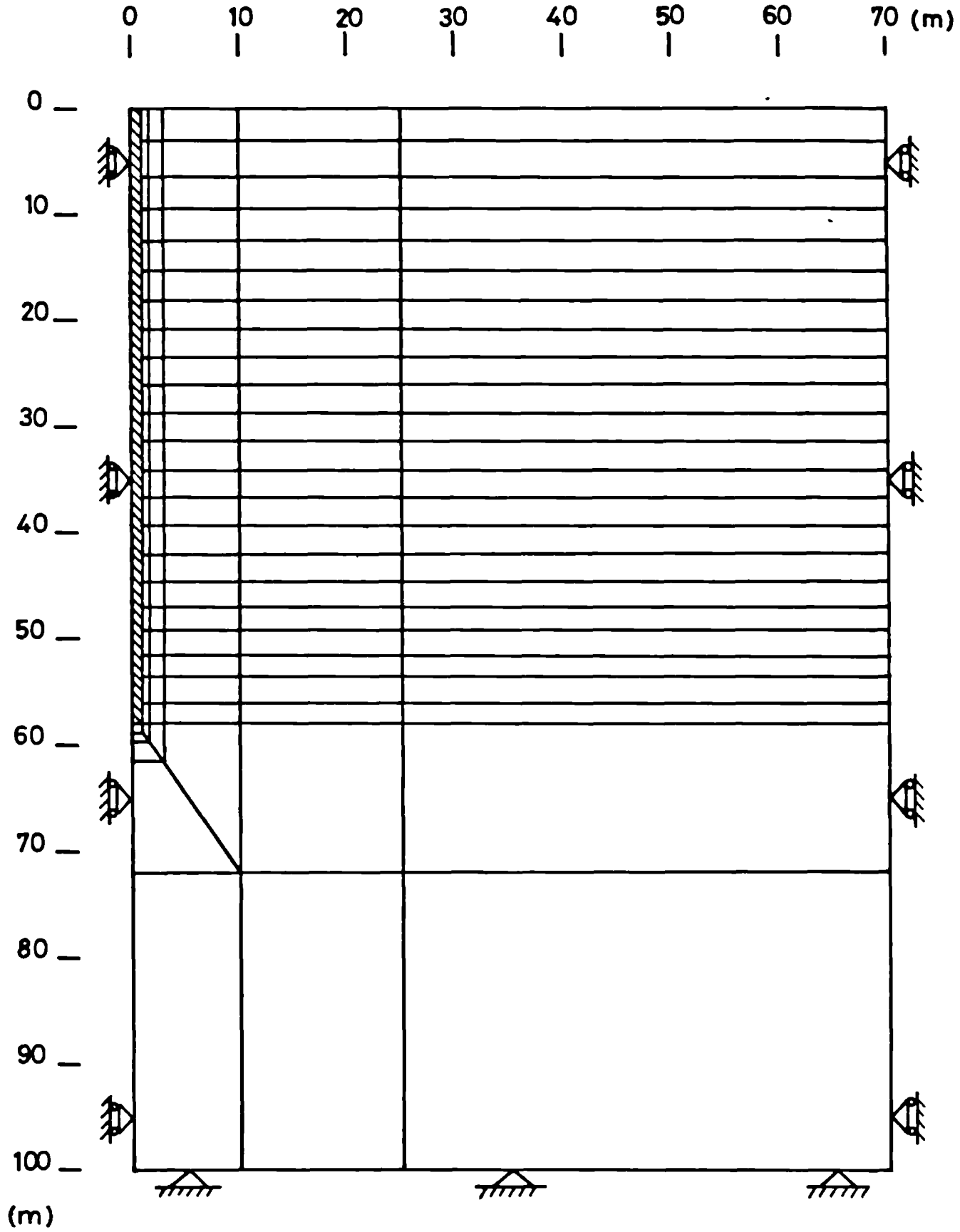
K = slope of swelling line in v - ln (p) space

V_i = specific volume at unit pressure on virgin consolidation line

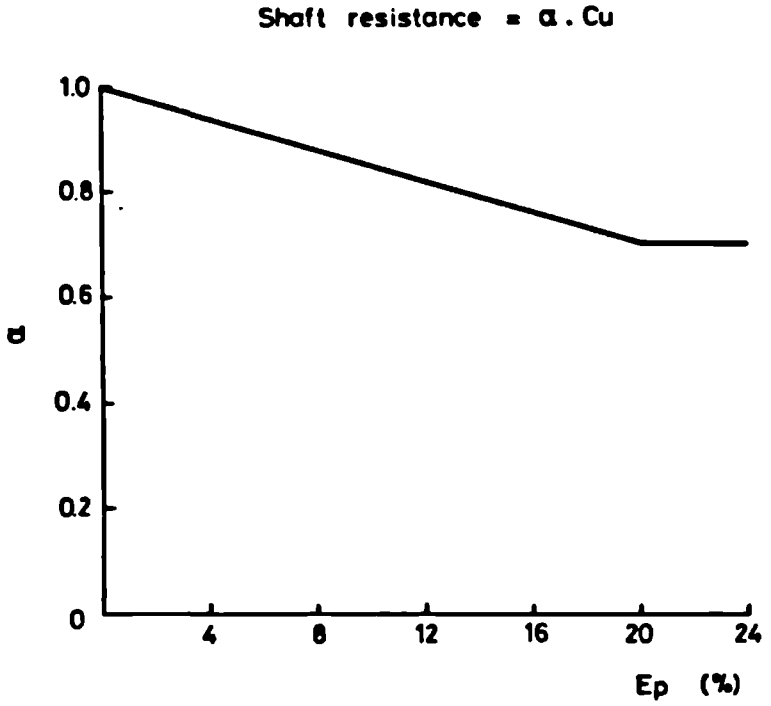
ν = angle of dilation E = Young's Modulus

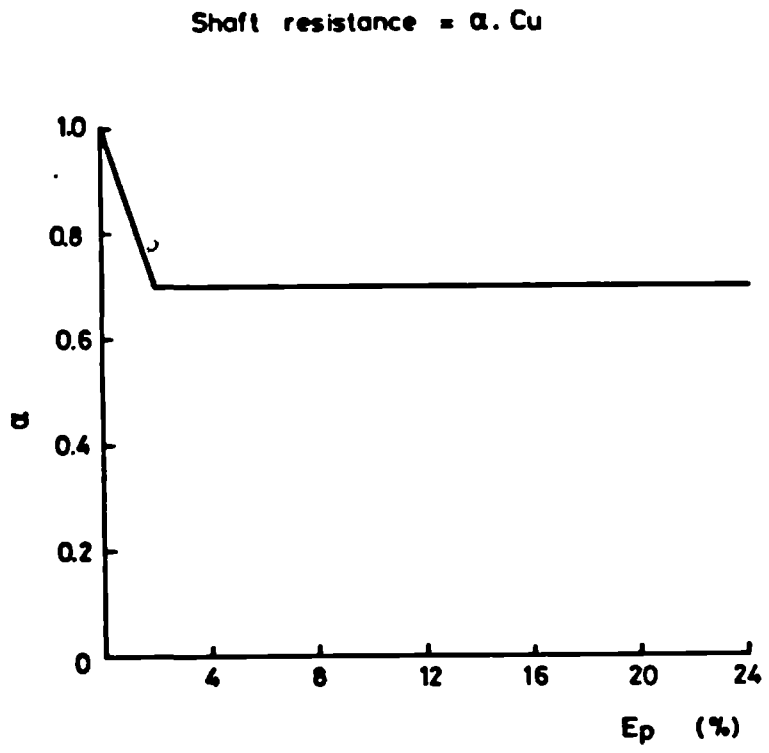
G = Shear modulus μ = Poisson's ratio

Figure 4.10. Assumed soil properties and initial stresses for run H.



igure 4.11. Finite Element mesh for Hutton TLP piles.

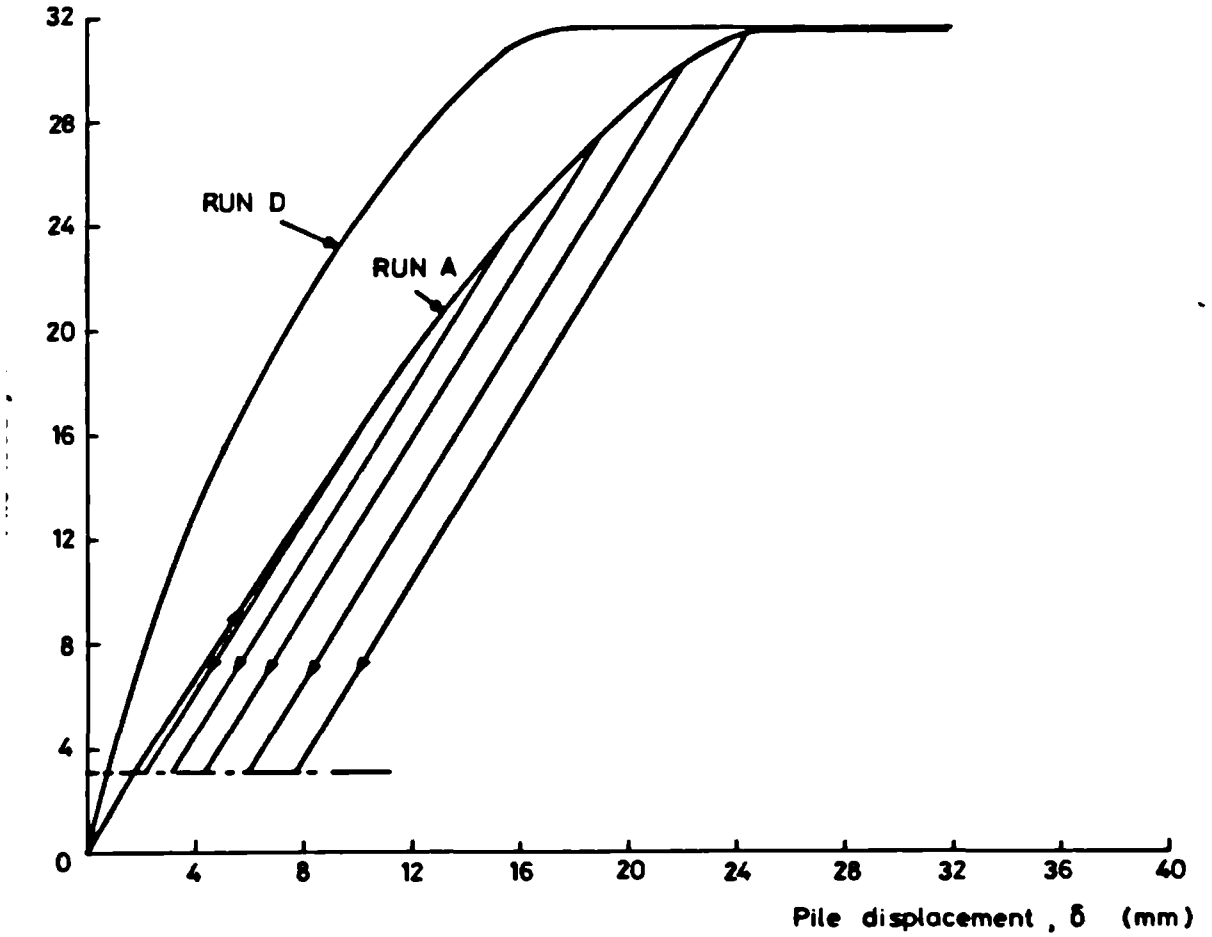




$$E_p^2 = \tfrac{2}{3}\left[(\varepsilon_1^p-\varepsilon_2^p)^2+(\varepsilon_1^p-\varepsilon_3^p)^2+(\varepsilon_2^p-\varepsilon_3^p)^2\right]$$

ε_1^p, ε_2^p and ε_3^p = the principal plastic strains

Figure 4.12. Strain softening at pile face for run B above, and run C below.



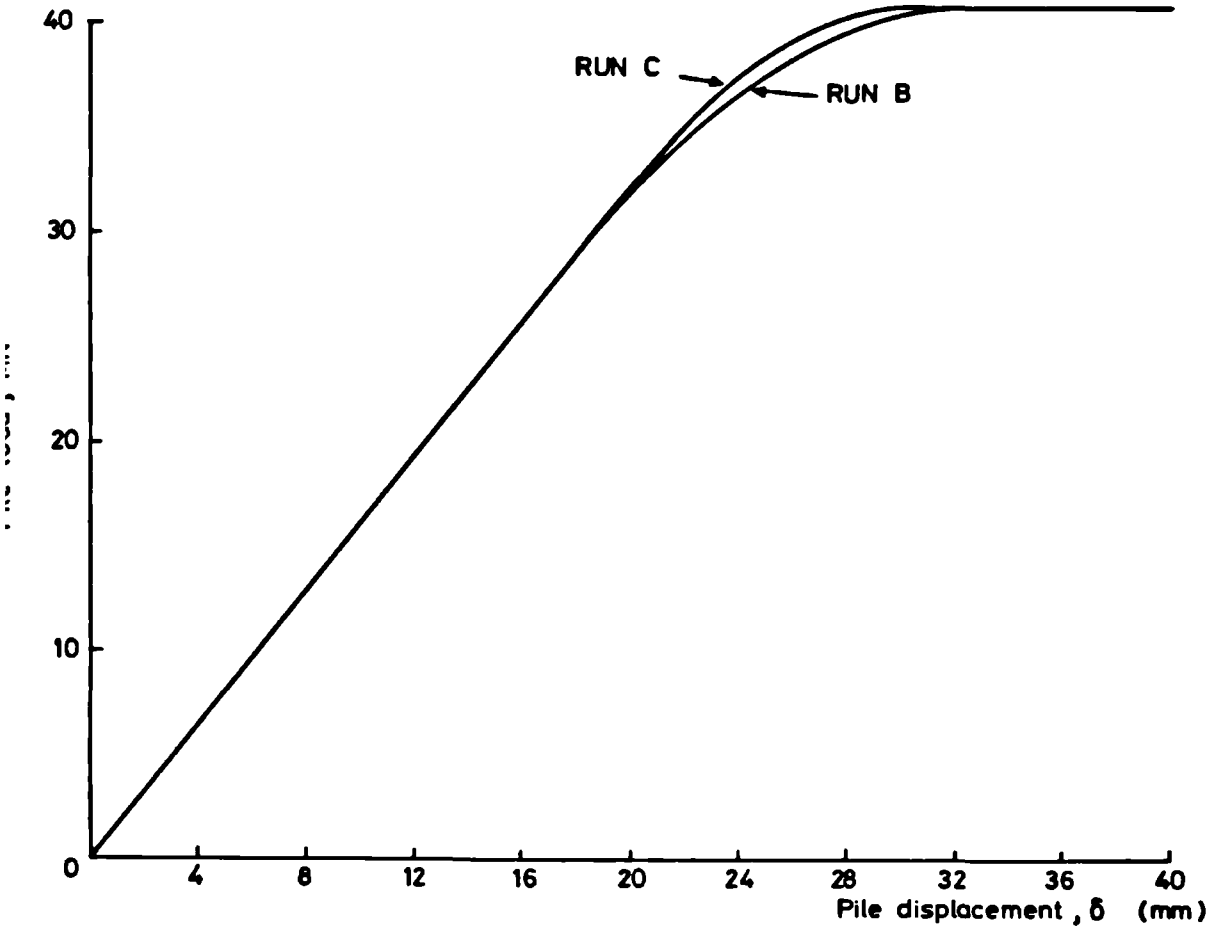
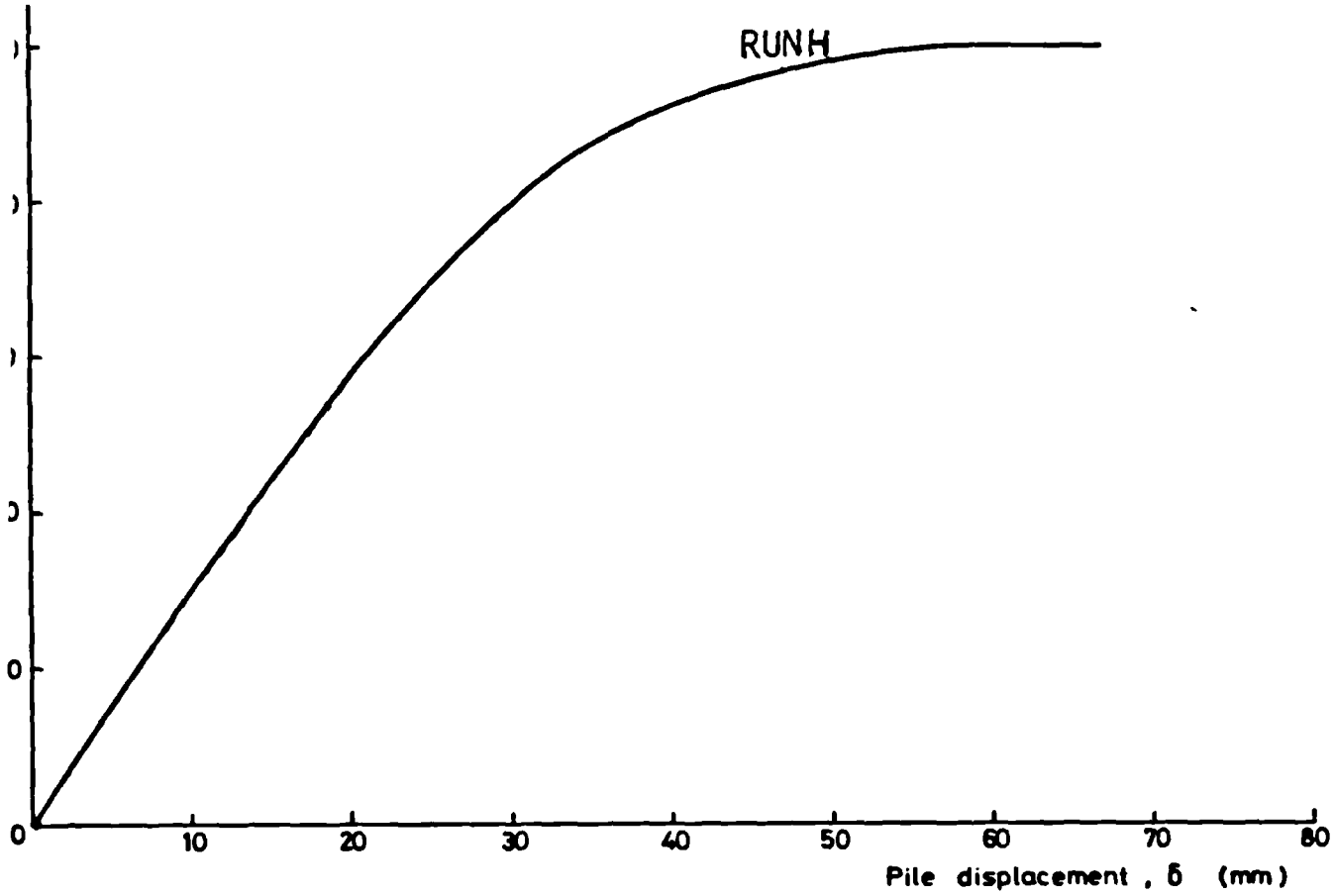


Figure 4.13. Load settlement curves.



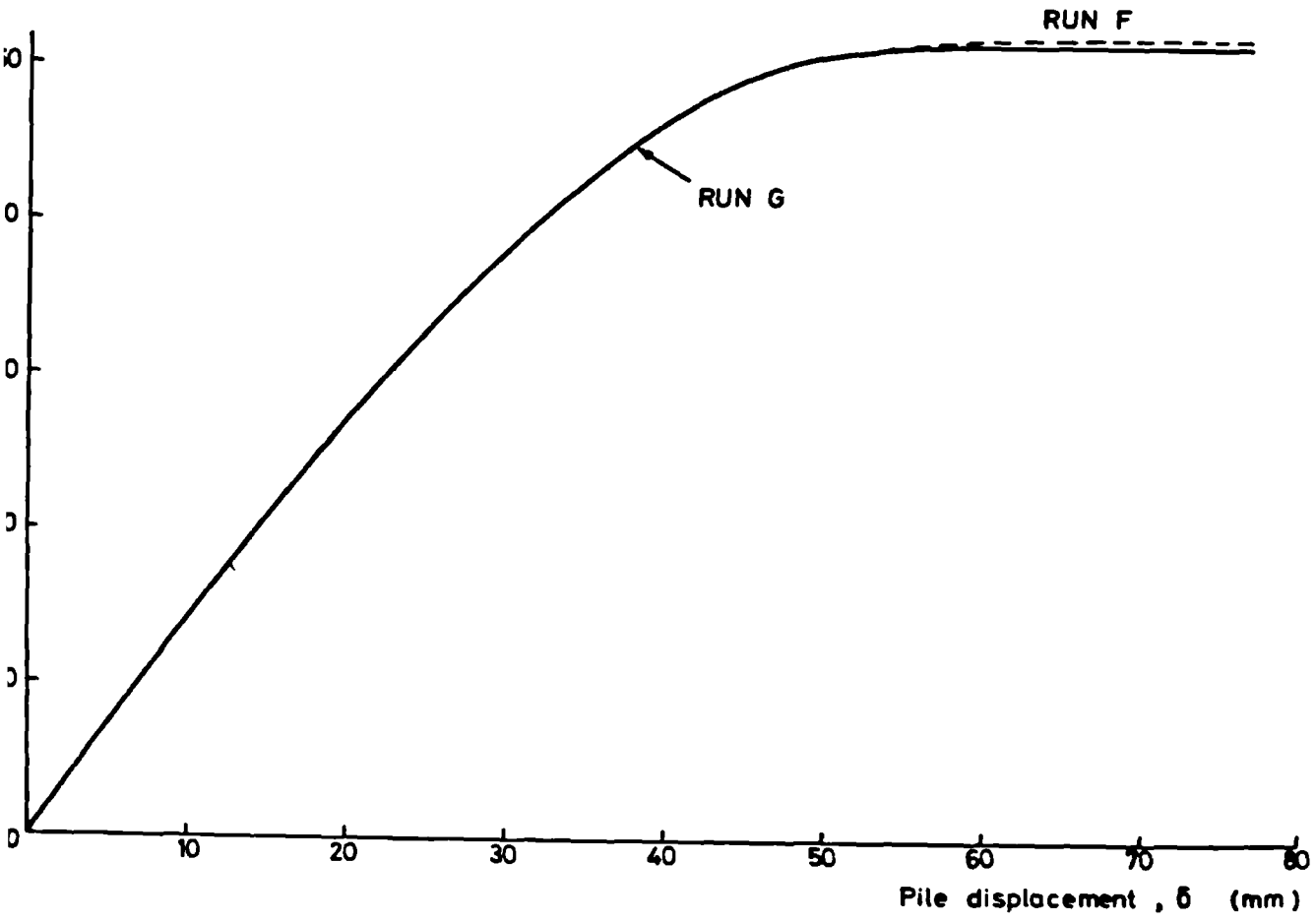


Figure 4.14. Load settlement curves.

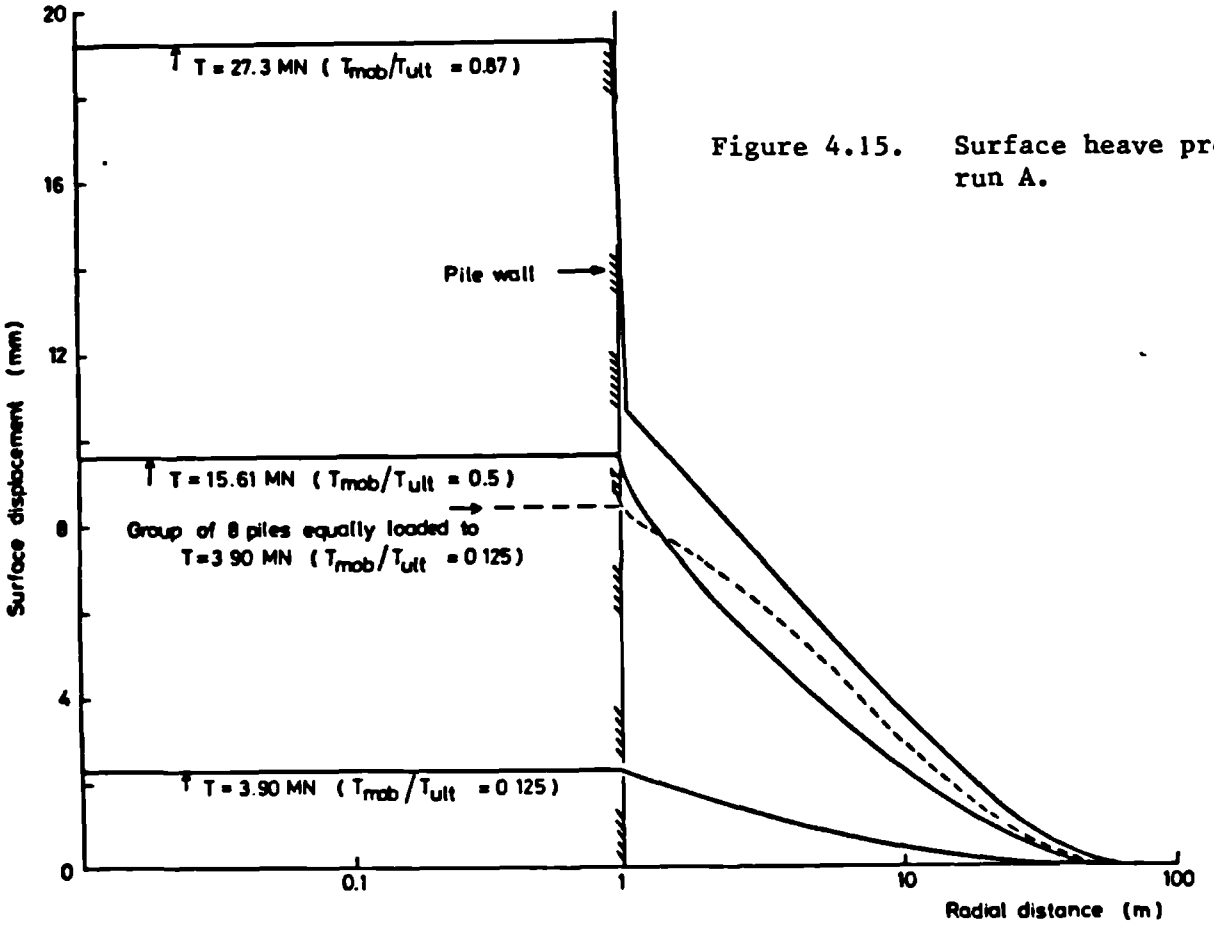


Figure 4.15. Surface heave profiles, run A.

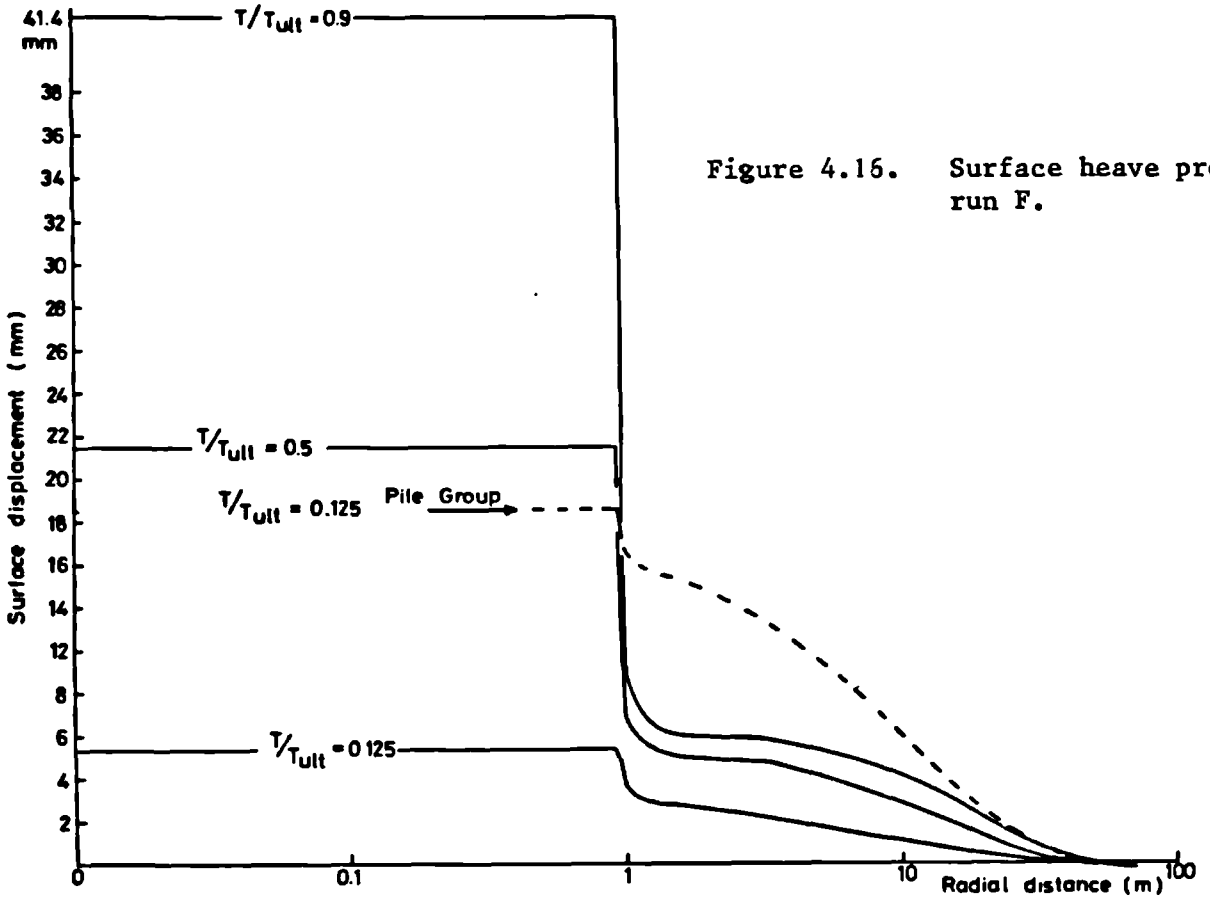


Figure 4.16. Surface heave profiles, run F.

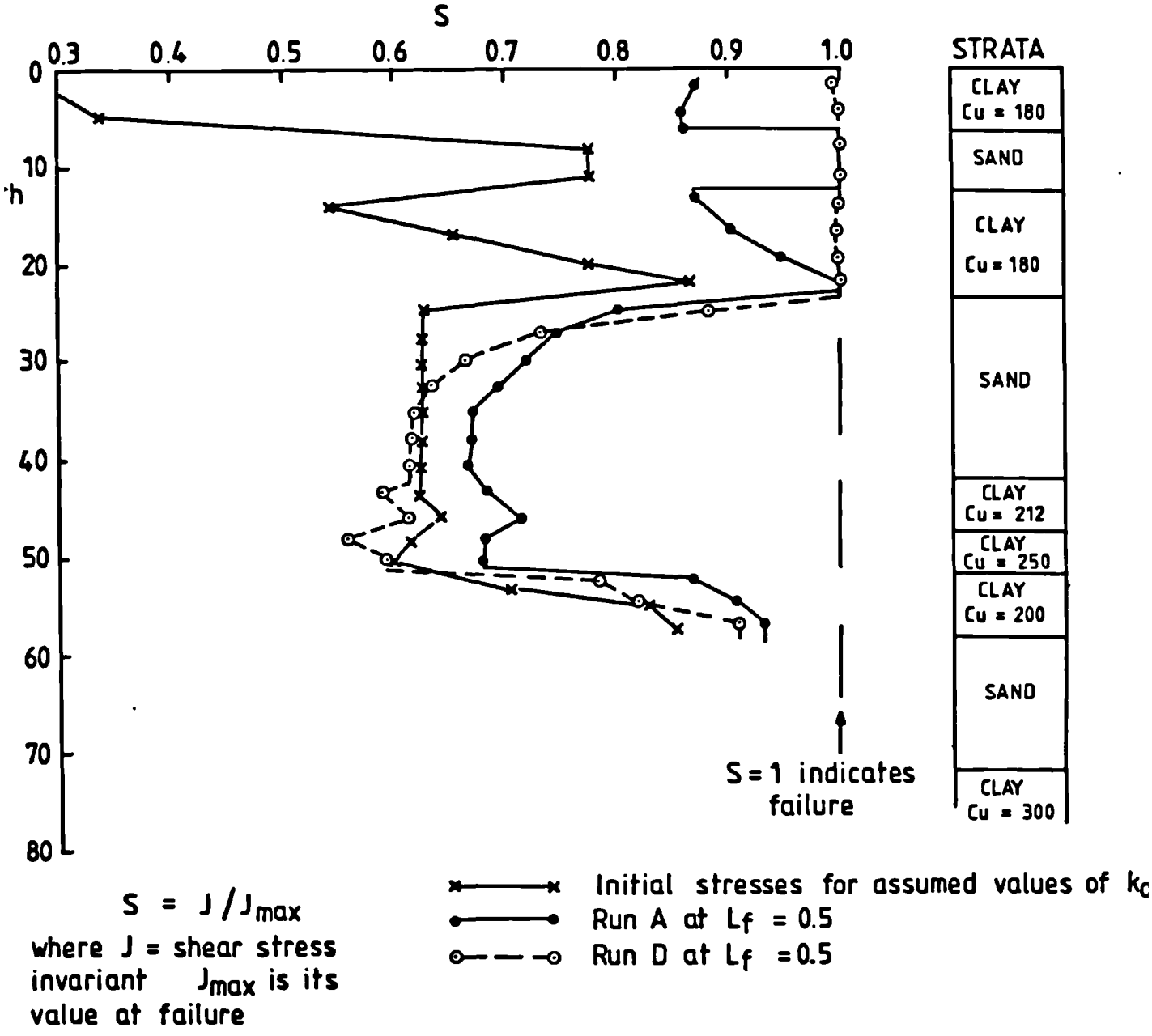
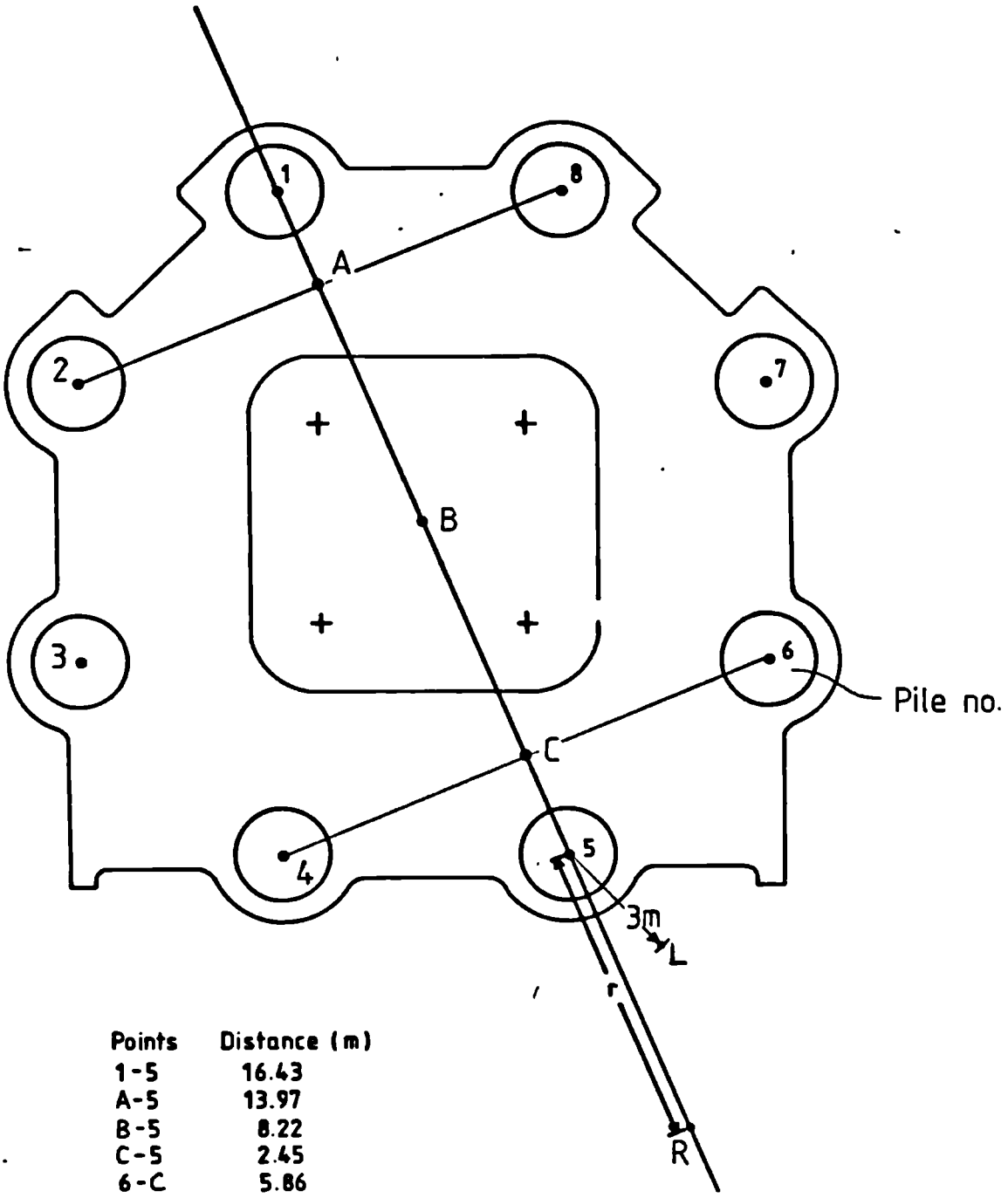


Figure 4.17. Distribution of stress measures, over pile shaft, runs A and D at $L_f = 0.5$.



Points	Distance (m)
1-5	16.43
A-5	13.97
B-5	8.22
C-5	2.45
6-C	5.86
7-B	8.26
8-A	5.86

(For a remote datum r is 50 m)

Figure 4.18. Plan view of Hutton TLP pile template, showing distances between piles, and definitions of points L and R.

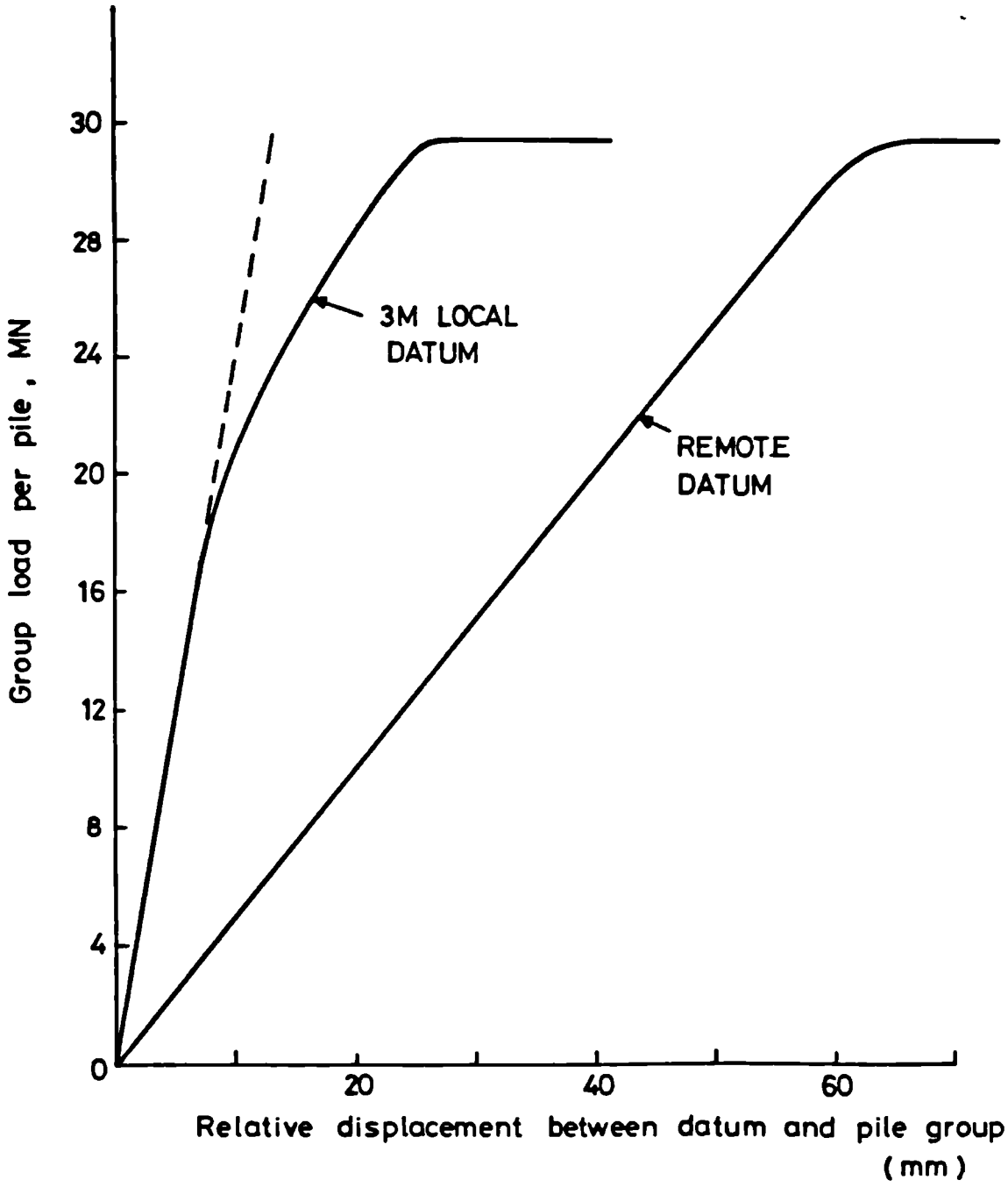


Figure 4.19. Load-displacement behaviour for a pile group Run A.

CHAPTER 5

Tables and Figures

DEPTH (METRES)	TOTAL NO OF 'GOOD' SAMPLES	AVERAGE LENGTH (MM)	TOTAL NO OF 'POOR' SAMPLES	AVERAGE LENGTH (MM)
0 to 10	5	268	5	234
10 to 20	1	290	3	117
20 to 30	2	325	5	184
30 to 40	1	330	4	104
40 to 50	1	230	4	190
50 to 60	1	310	2	140
60 to 70	3	285	5	192
70 to 80	2	585	1	300
80 to 90	2	435	4	178
90 to 100	2	420	-	-

Table 5.1 Sample stock from Magnus site, Fugro investigation

('poor condition' implies sealing broken and sample exposed)

$\bar{\sigma}_v'$	Day No
4.5	2.5
16	5
40	7
95	9
200	11.5
100	14.5

Table 5.2 Consolidation programme for Anisotropically consolidated Blocks prepared in the 229 mm odeometer

Transducer	Model	Range	No Employed[1]	Sensitivity	Resolution[2]	Mean error from[3] best straight line
Pressure	Bell and Howell	1000 kpa	10	71.4 to 79.8 kpa/mv	0.07 kpa	± 1.0 kpa (typical)
Pressure	Senso-metric (SP.91 KES)	2000 kpa	4	10.1 to 11.4 kpa/mv	0.01 kpa	± 0.5 kpa (typical)
Pore-water Pressure	Druck (PDCR 81)	1600 kpa	2	11.4 to 12.1 kpa/mv	0.01 kpa	± 0.3 kpa
Load Cell	Imperial College	4500 N	5	116.1 to 123.0 N/mv	0.12 N	± 1.5N
Displacement	Minister Precision Engineering	25 mm	4	4.18 to 4.27 mm/mv	0.004 mm	± 0.01 mm

Table 5.3 Typical calibration results for electrical transducers

Notes
1 On apparatus operated by the author
2 With the Solartron, DTU system
3 Mean result from Dead Weight micrometer calibration cycle

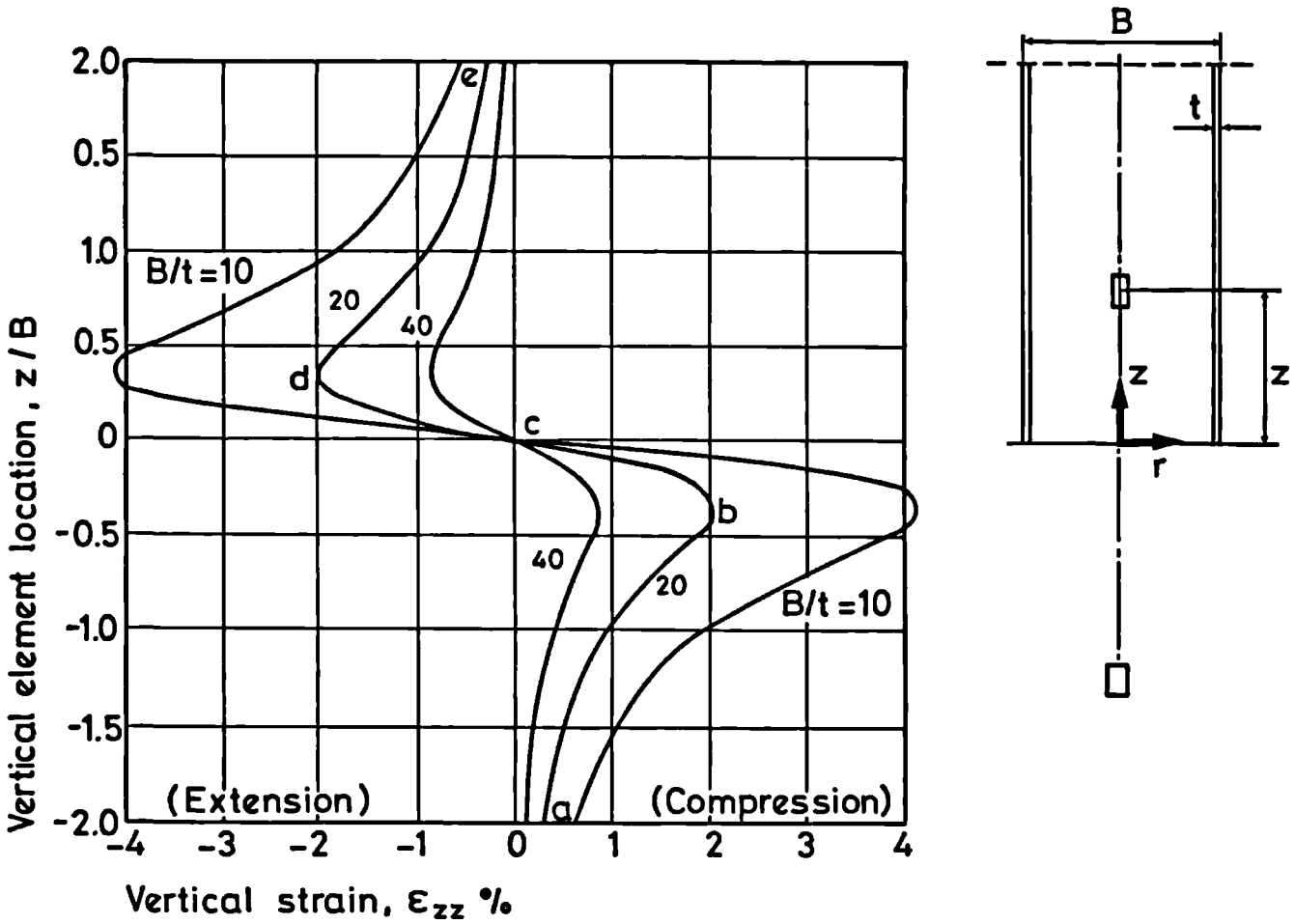


Figure 5.1. Strains developed on the centre line of a tube sampler, after Baligh (1984).

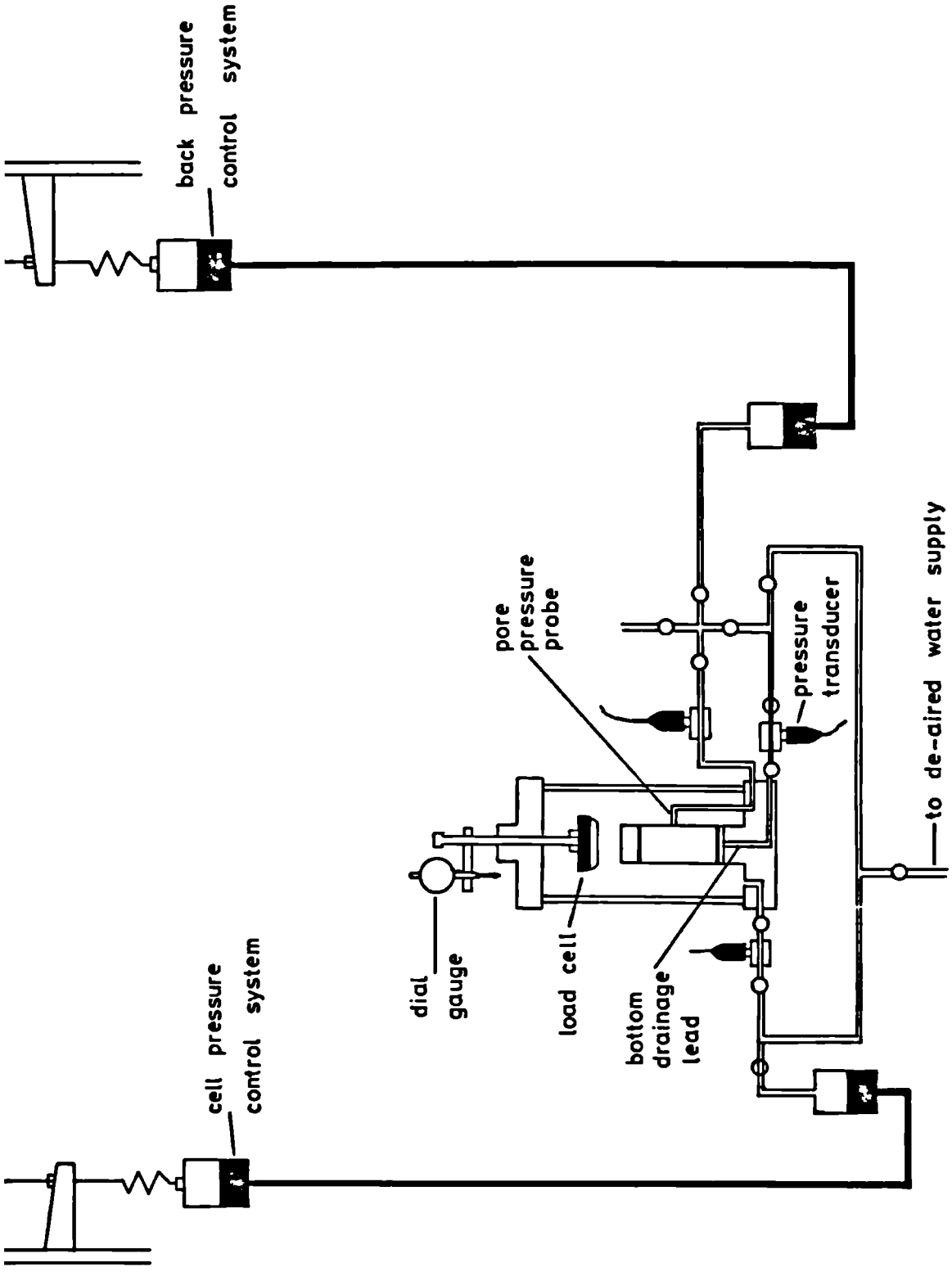


Figure 5.2. General arrangement for 102 mm diameter triaxial tests.

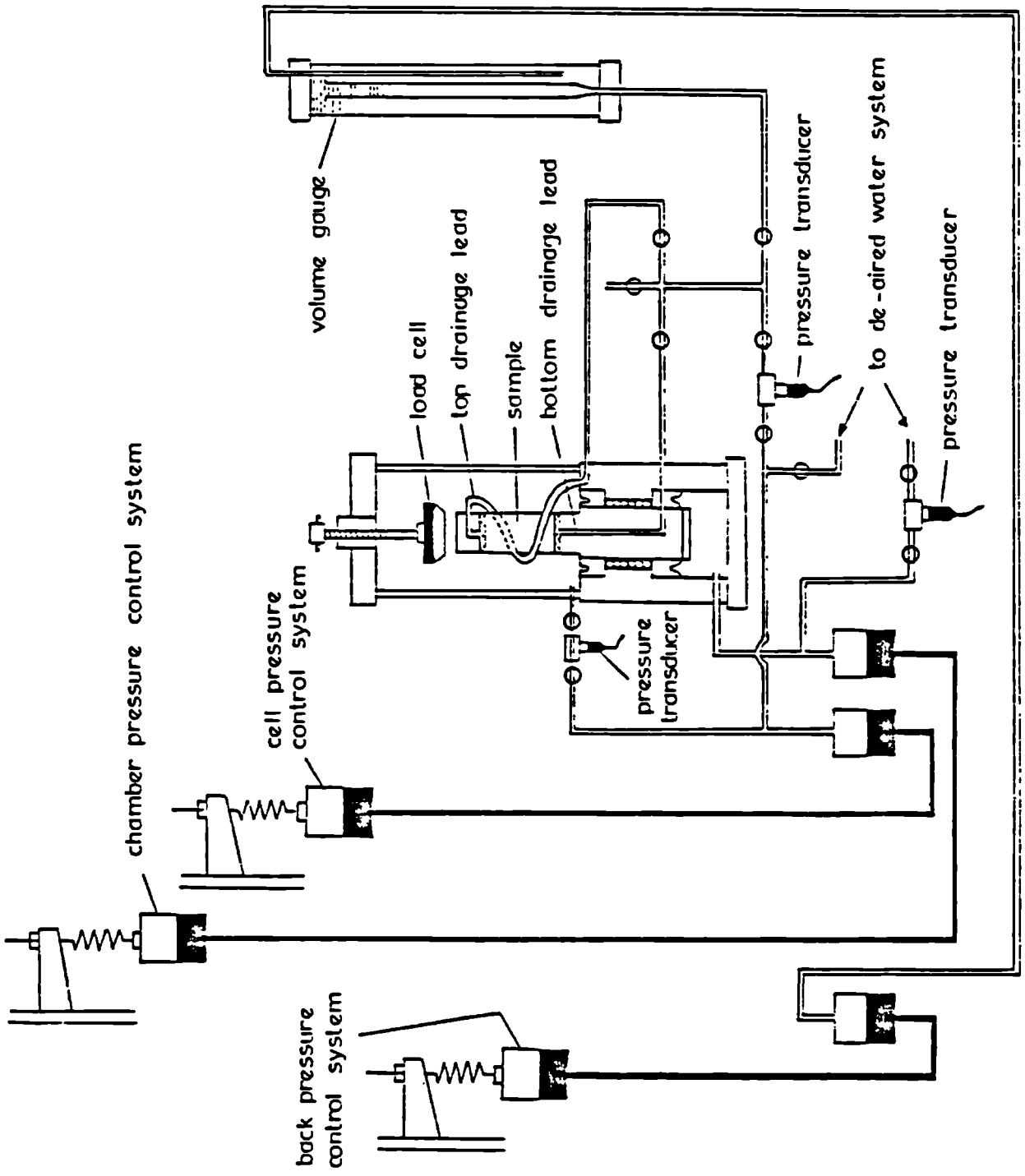


Figure 5.3. General arrangement for stress path cells.

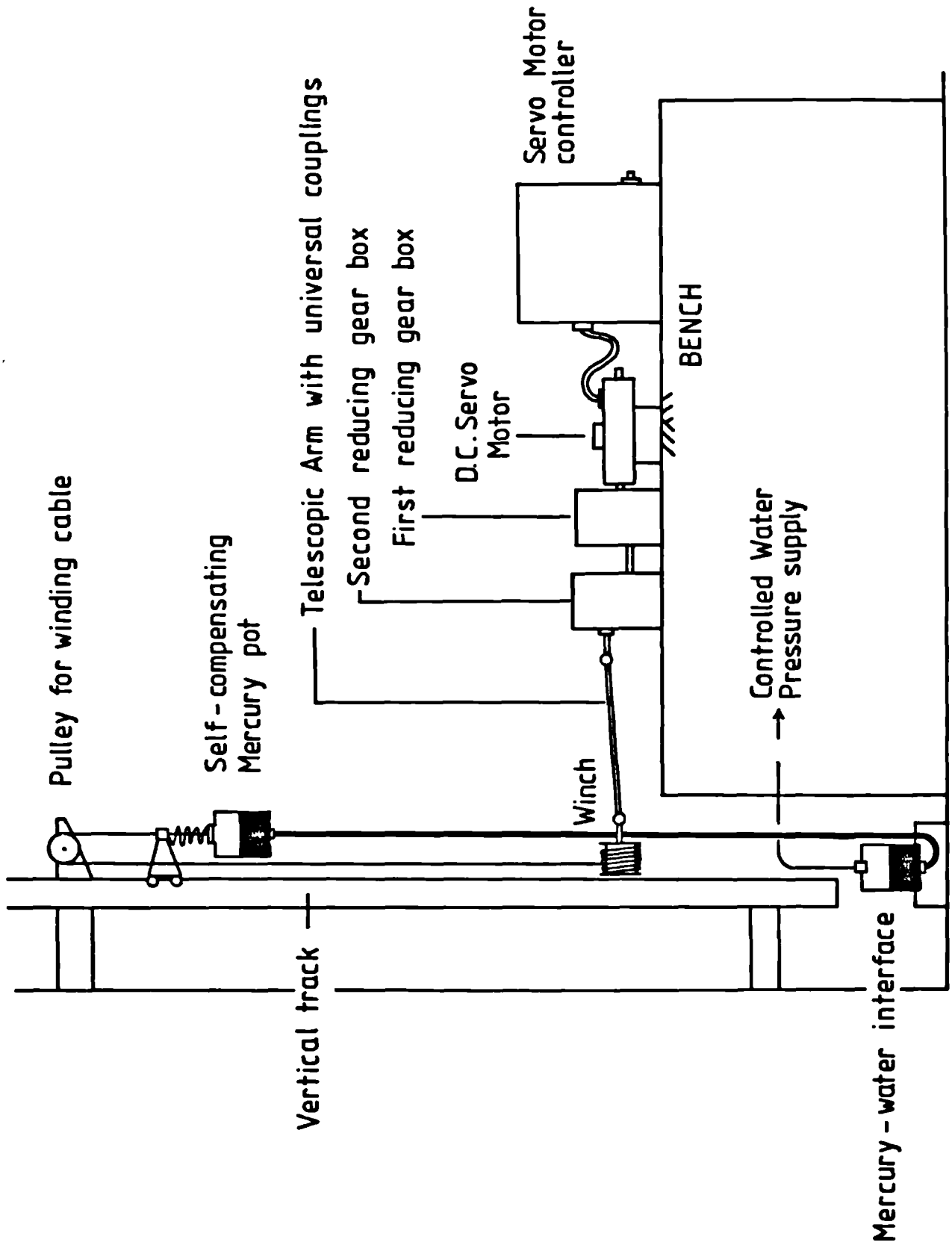


Figure 5.4. Stress control system for stress-path cells.

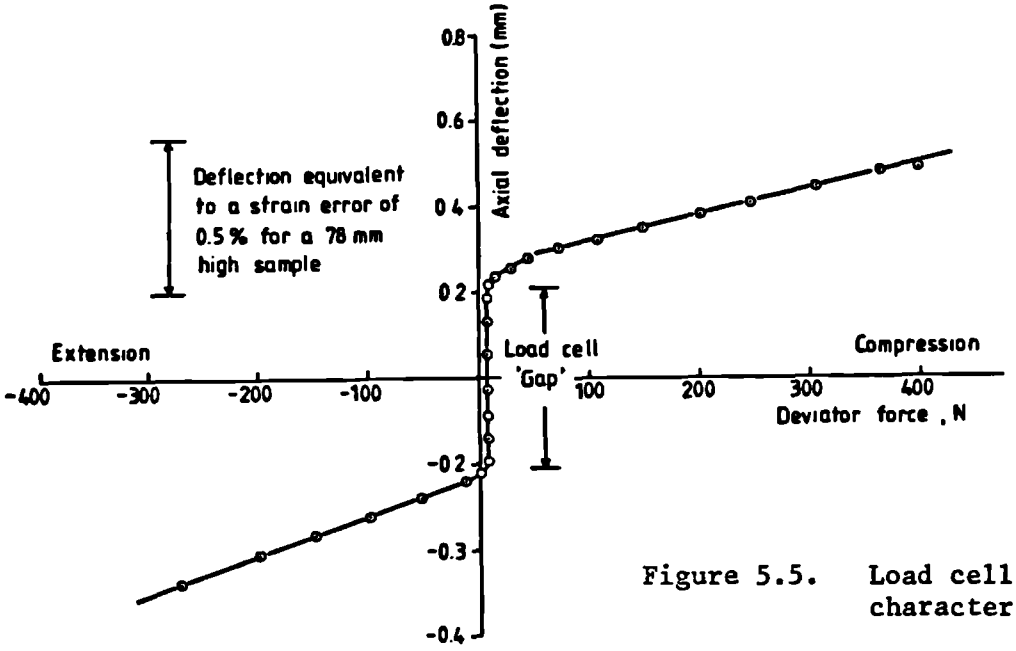


Figure 5.5. Load cell compliance characteristics.

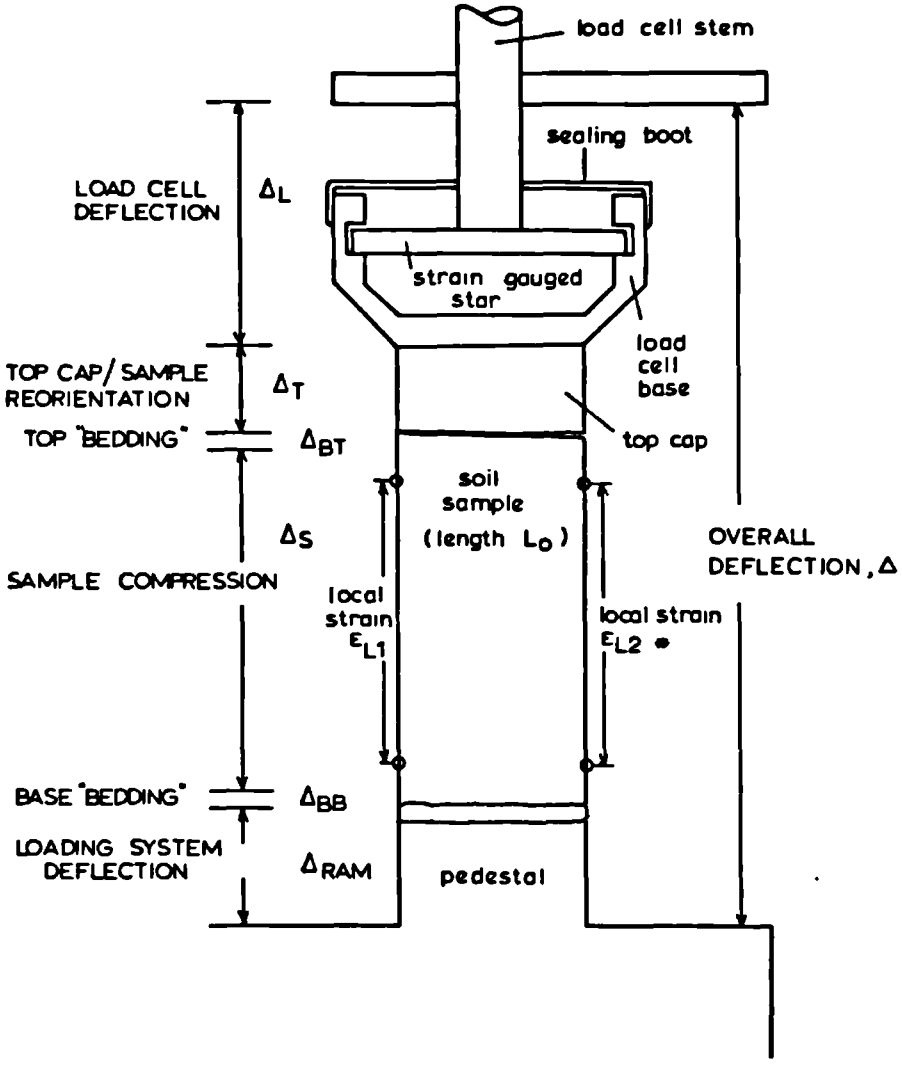
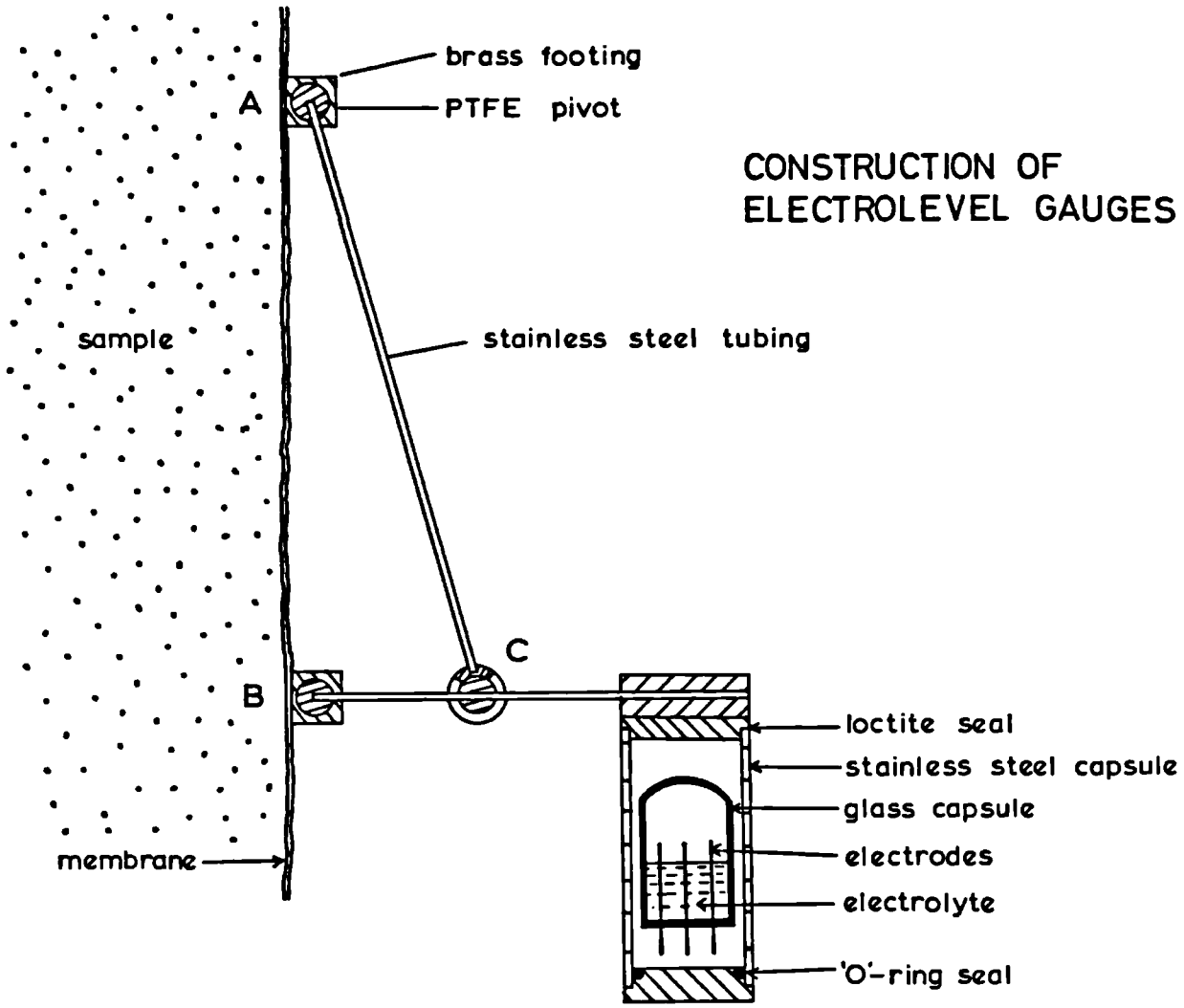


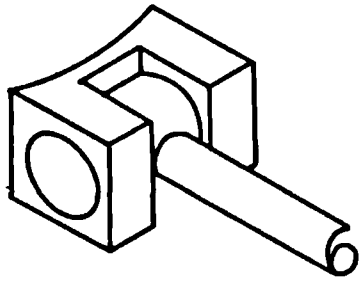
Figure 5.6. SOURCES OF ERROR IN EXTERNAL STRAIN MEASUREMENTS

* Note : ε_{L1} is the larger of the two strains

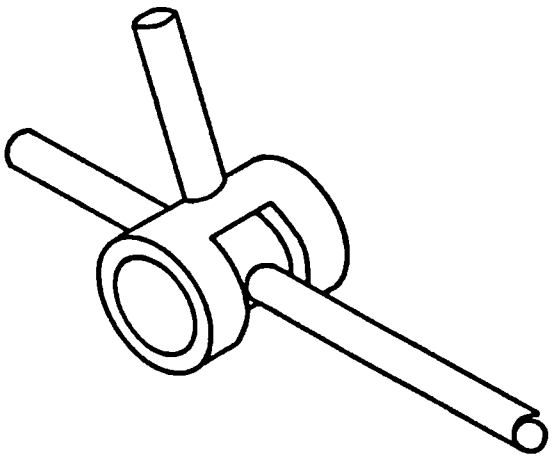
$$\varepsilon_L = (\varepsilon_{L1} + \varepsilon_{L2}) / 2$$

Figure 5.7.

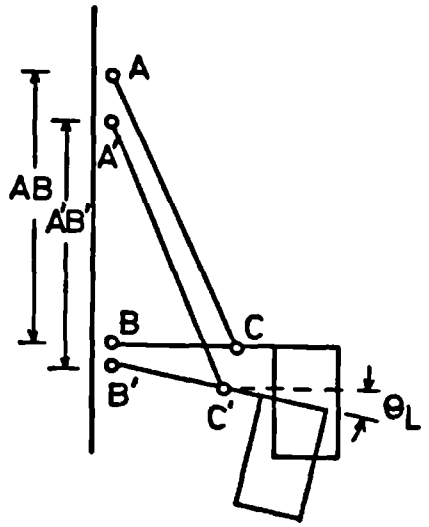




HINGES A and B



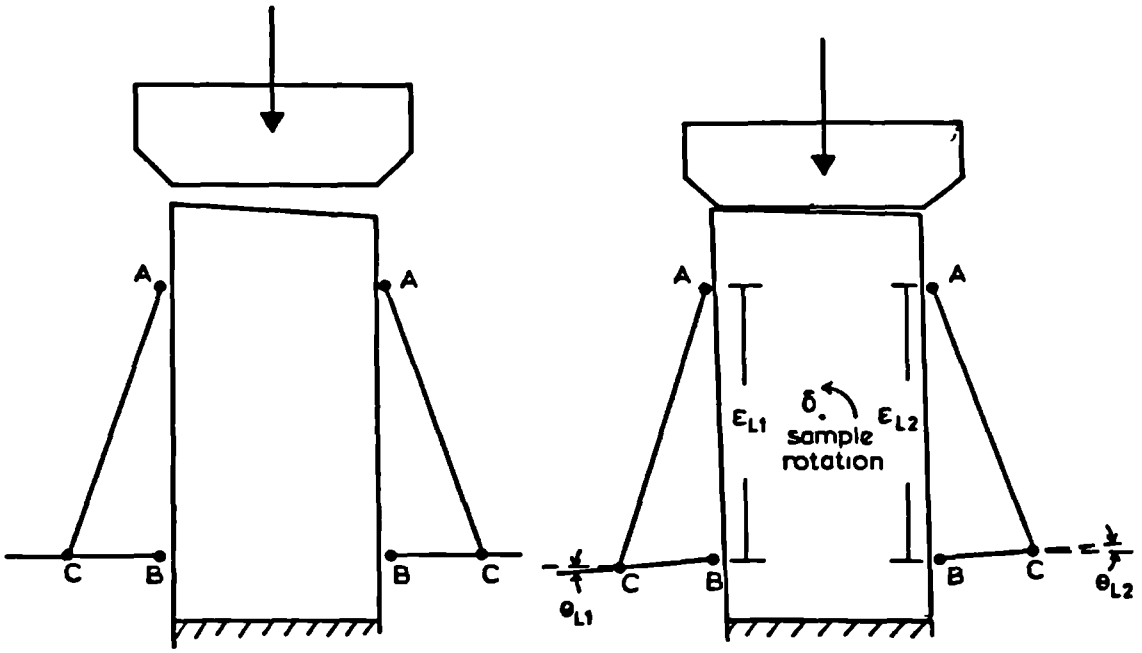
HINGE C



$$\varepsilon_L = \left(\frac{BC}{AB}\right)\theta_L$$

for small θ and AB remaining vertical

Figure 5.8. Strain-tilt relationship for electrolevel gauges.



(i) non parallel end before test, electrolevel axes horizontal

(ii) tilting caused in early stage of test θ_{L1} positive, θ_{L2} negative

for similar triangles experiencing small rotations, with angles in radians

$$\theta_{L1} = \delta + \varepsilon_{L1}\left(\frac{AB}{BC}\right)$$

$$\theta_{L2} = -\delta + \varepsilon_{L2}\left(\frac{AB}{BC}\right)$$

$$\varepsilon_L = \frac{\varepsilon_{L1} + \varepsilon_{L2}}{2} = \frac{\theta_{L1} + \theta_{L2}}{2}\left(\frac{BC}{AB}\right)$$

Figure 5.9. The effect of sample rotation.

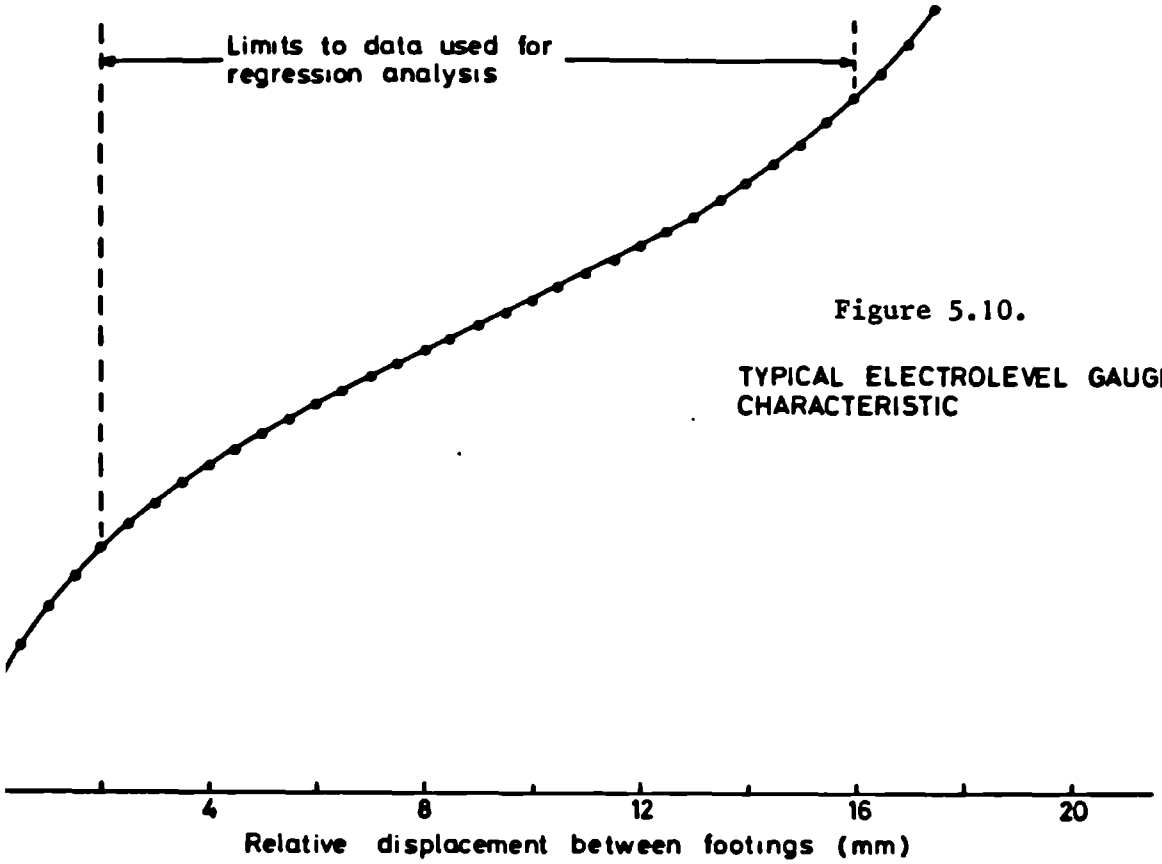
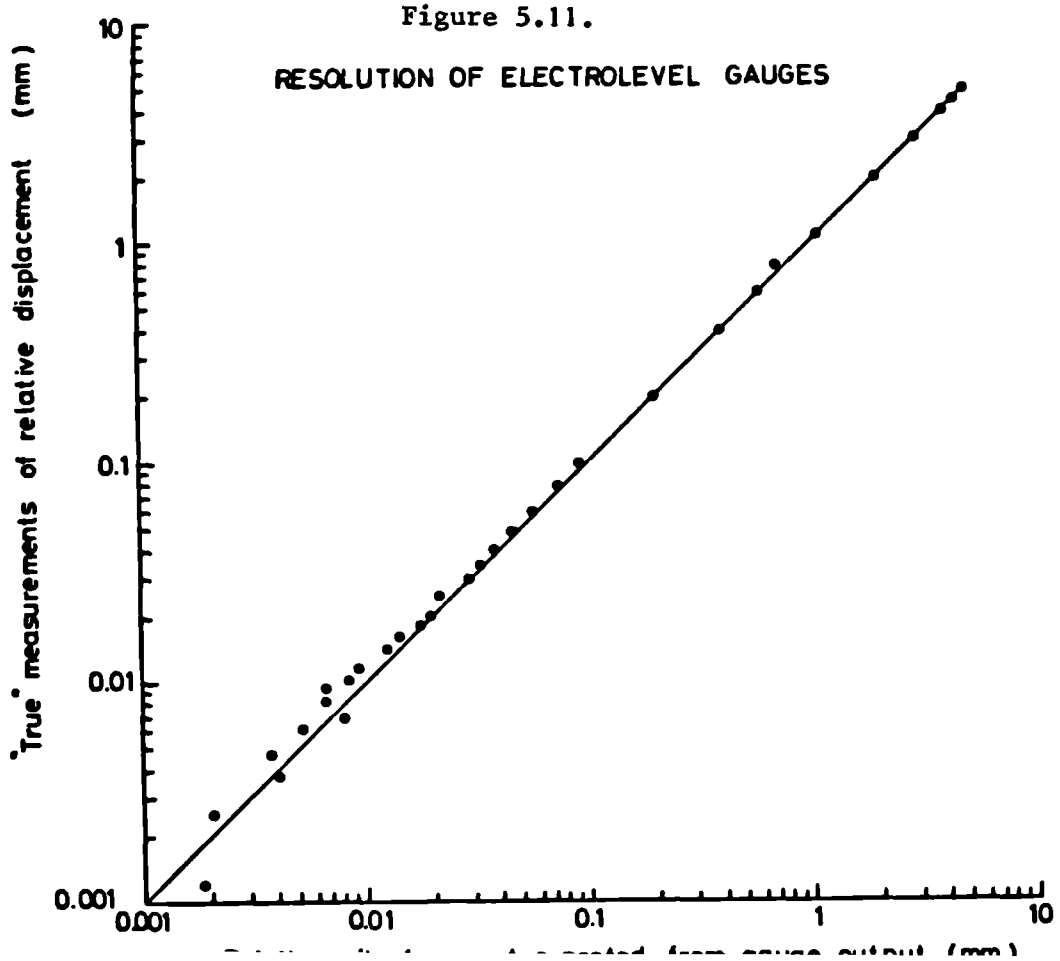


Figure 5.10.

TYPICAL ELECTROLEVEL GAUGE CHARACTERISTIC

Figure 5.11.

RESOLUTION OF ELECTROLEVEL GAUGES



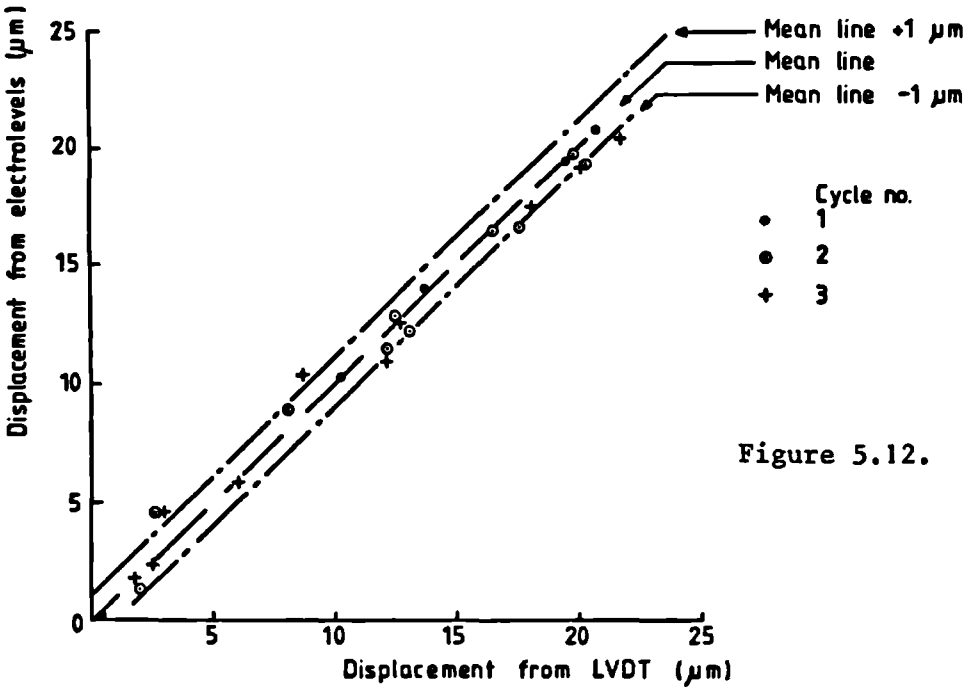
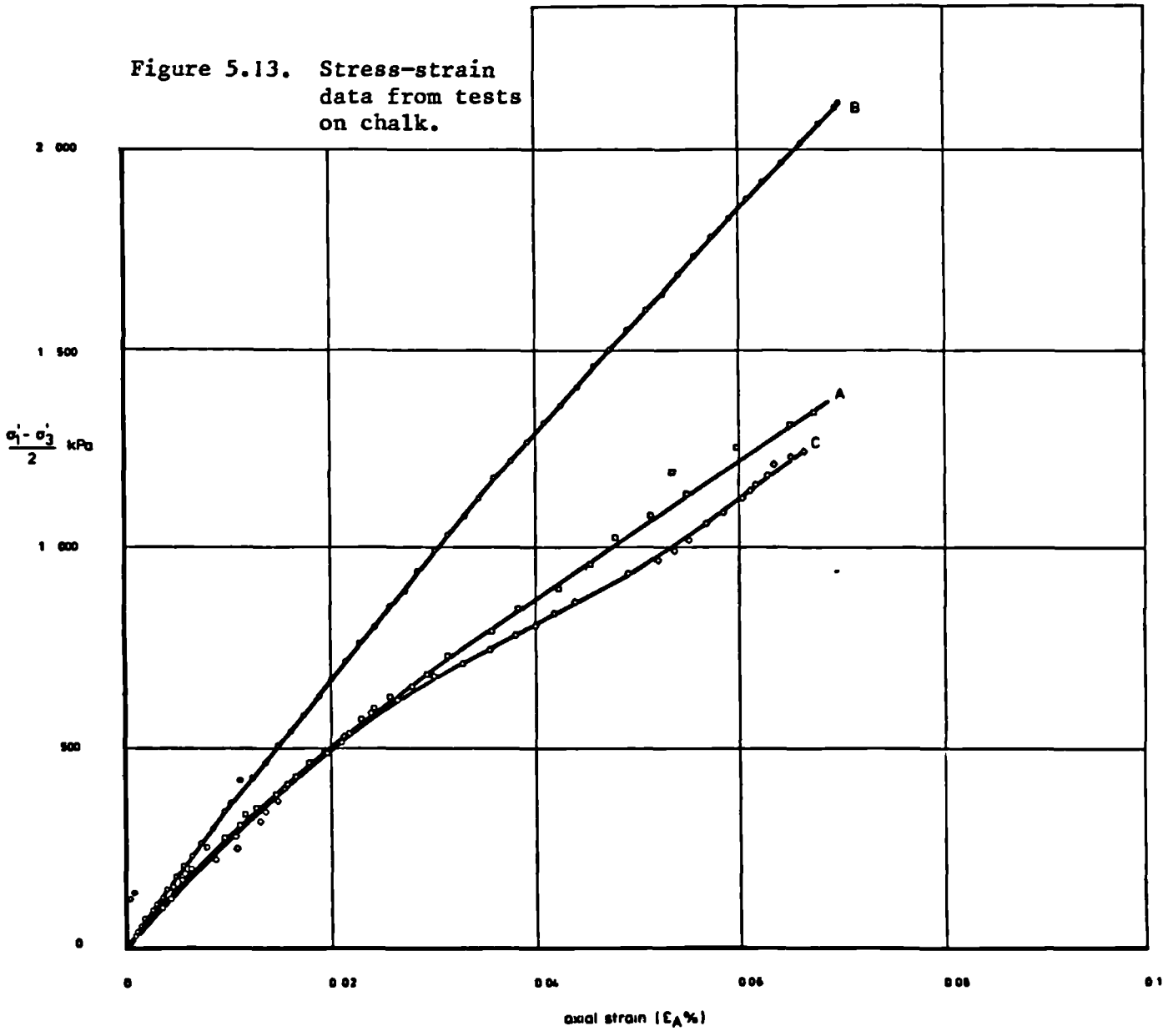


Figure 5.12. Cyclic repeatability tests.

Figure 5.13. Stress-strain data from tests on chalk.



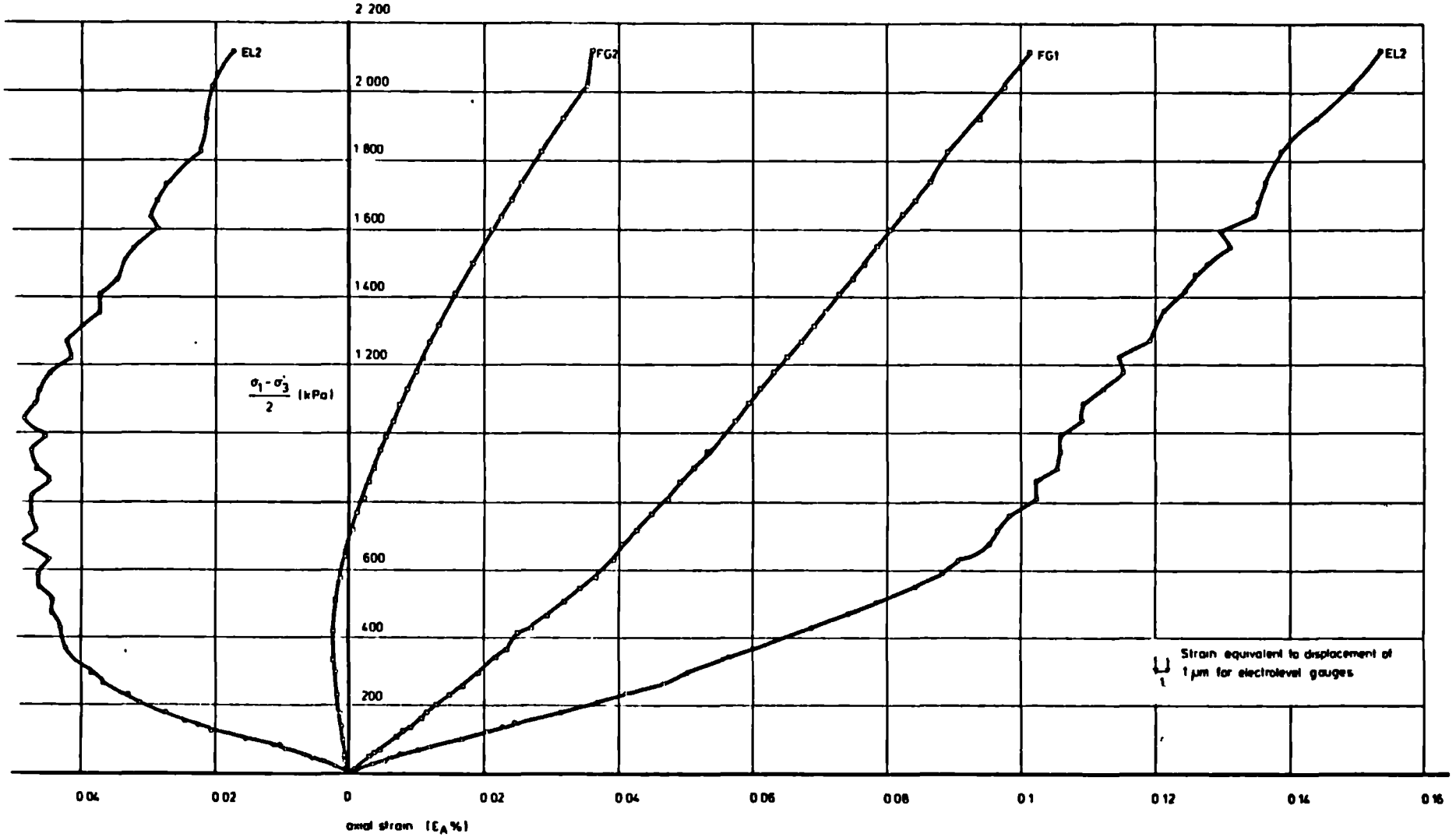


Figure 5.14. Individual stress-strain-measurements for test B.

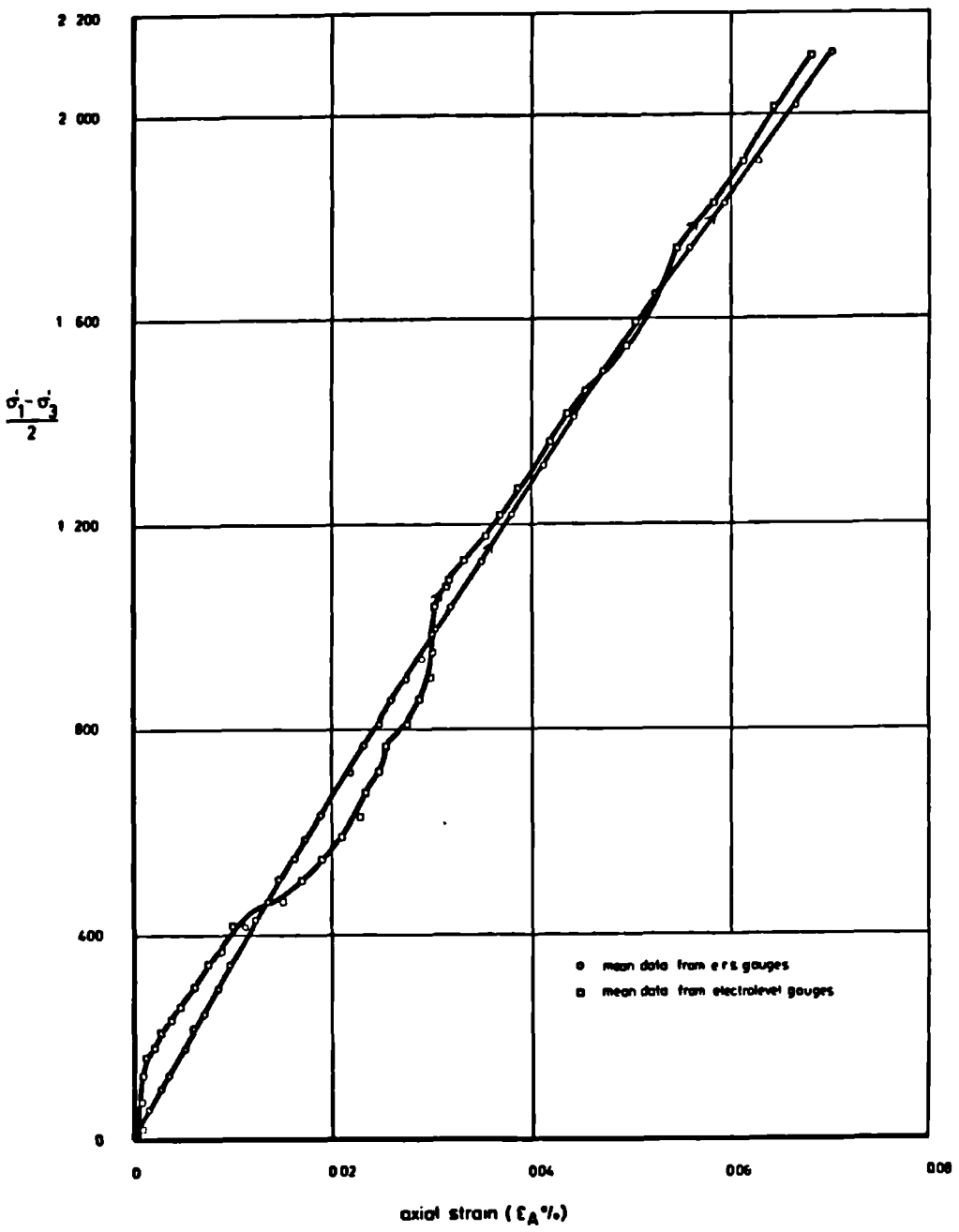


Figure 5.15. Mean stress-strain curves, test B, loading.

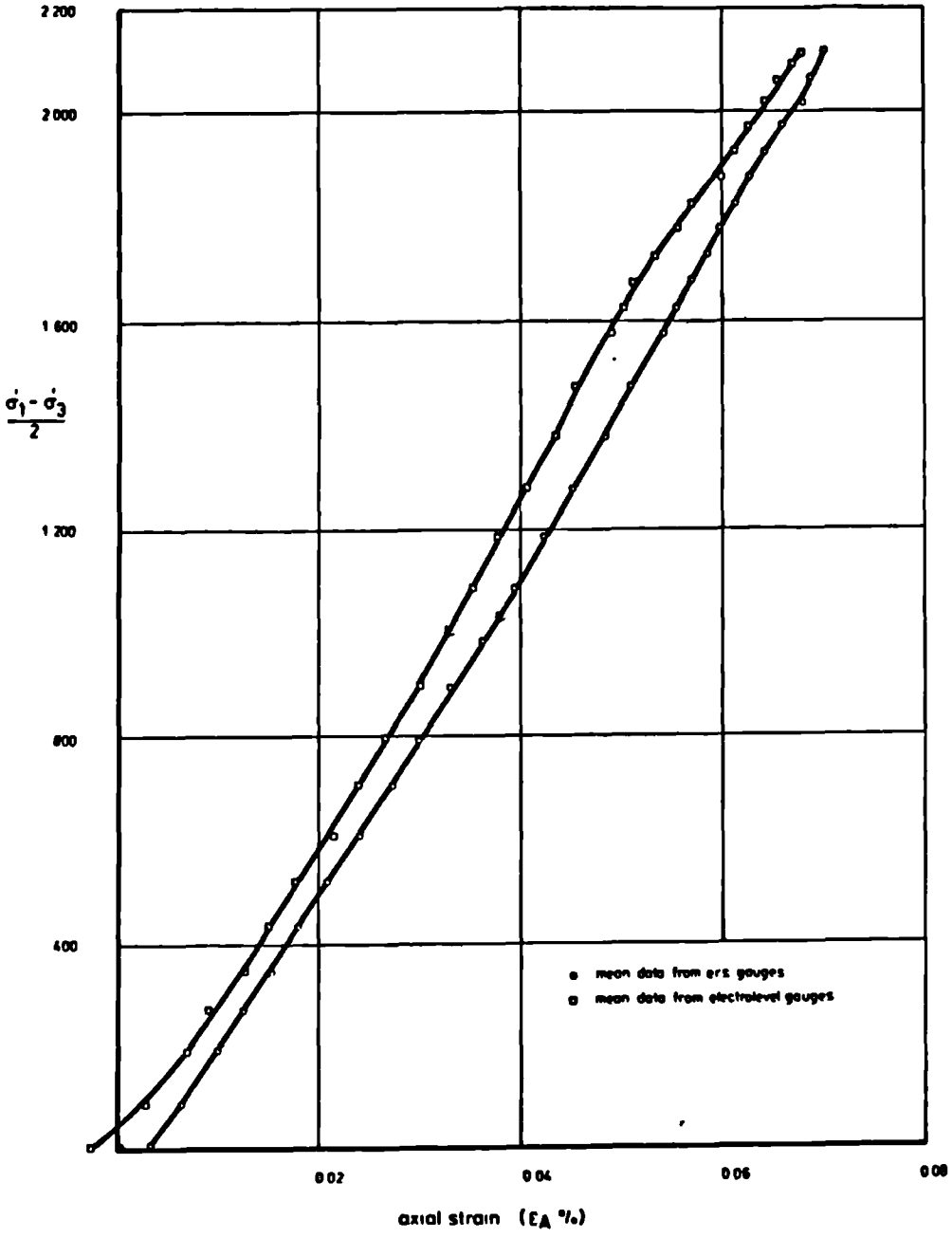


Figure 5.16. Mean stress-strain curves, test B, unloading.

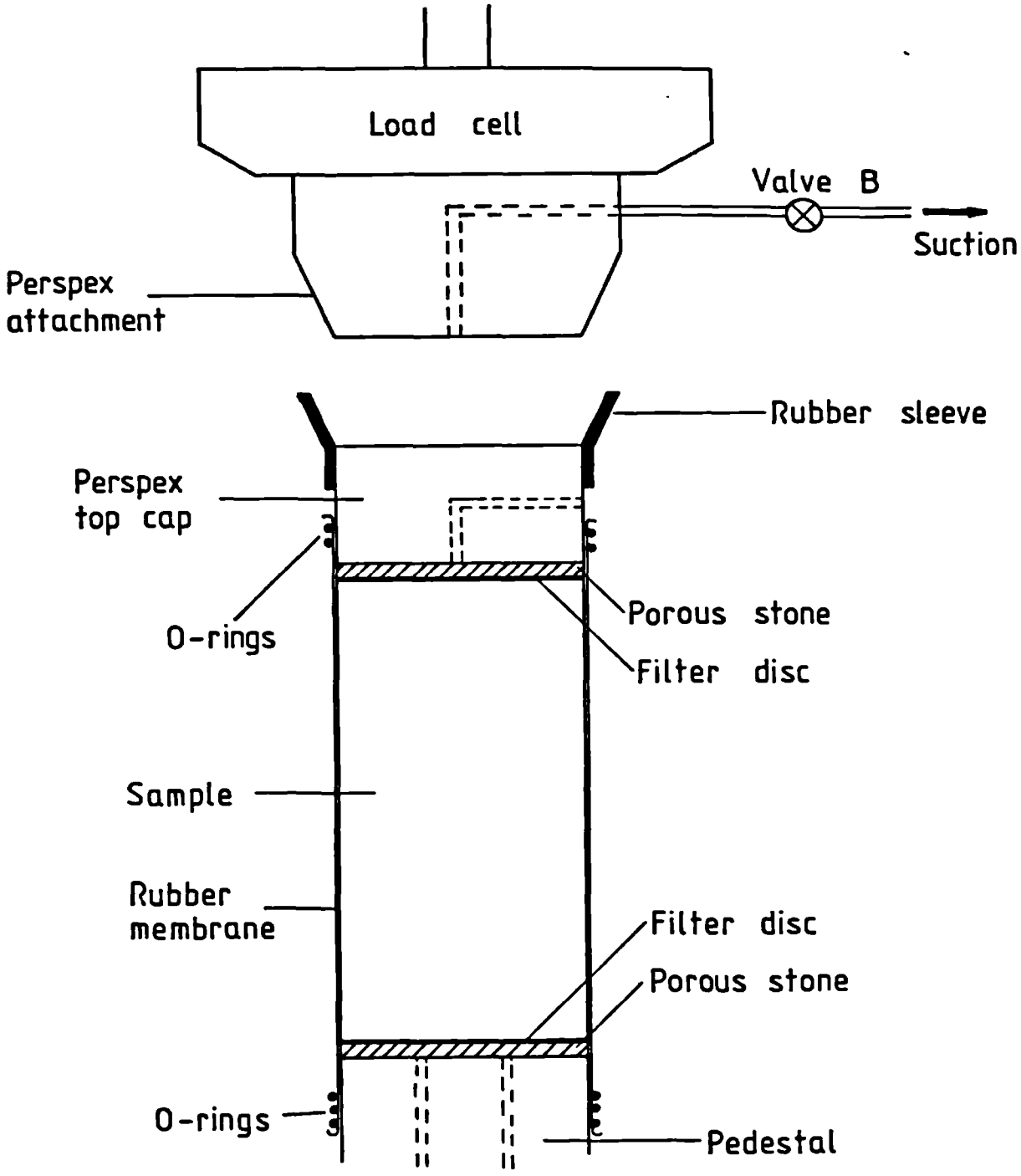
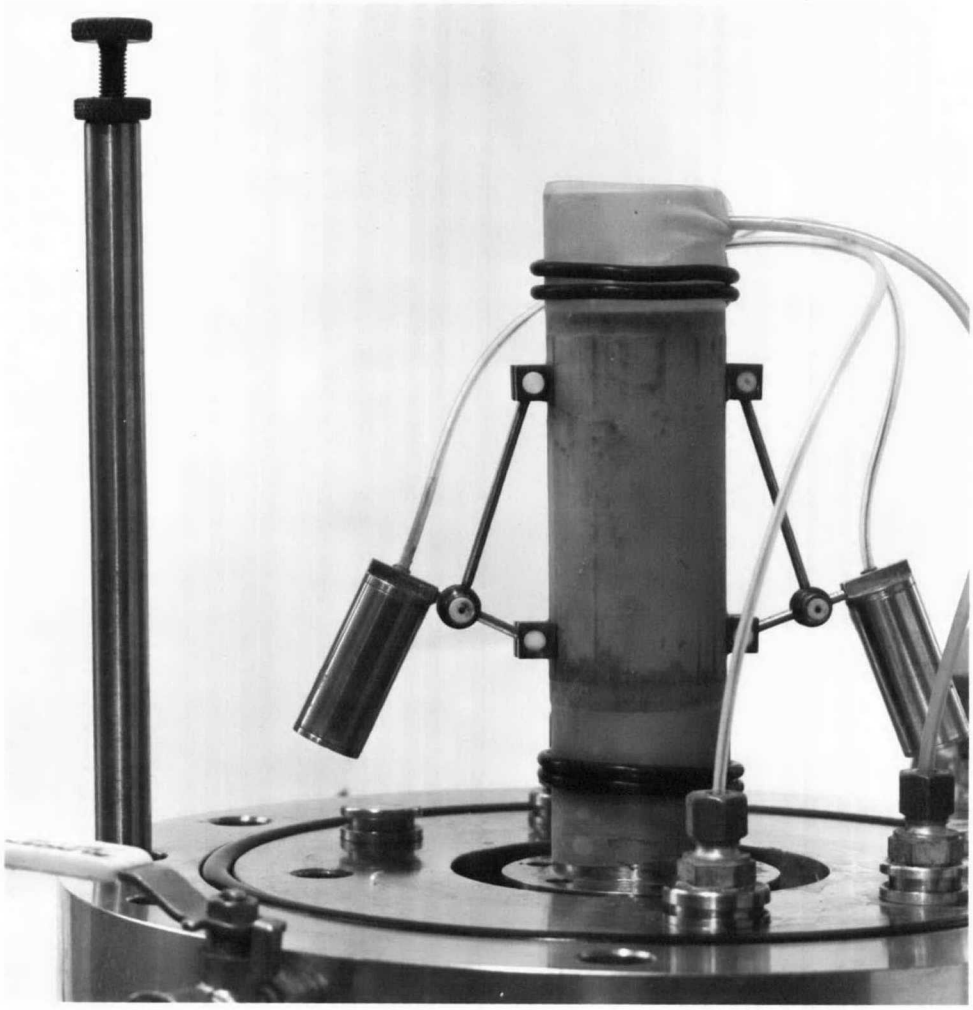


Figure 5.17. Suction cap arrangement for tests where $\sigma_r > \sigma_A$.

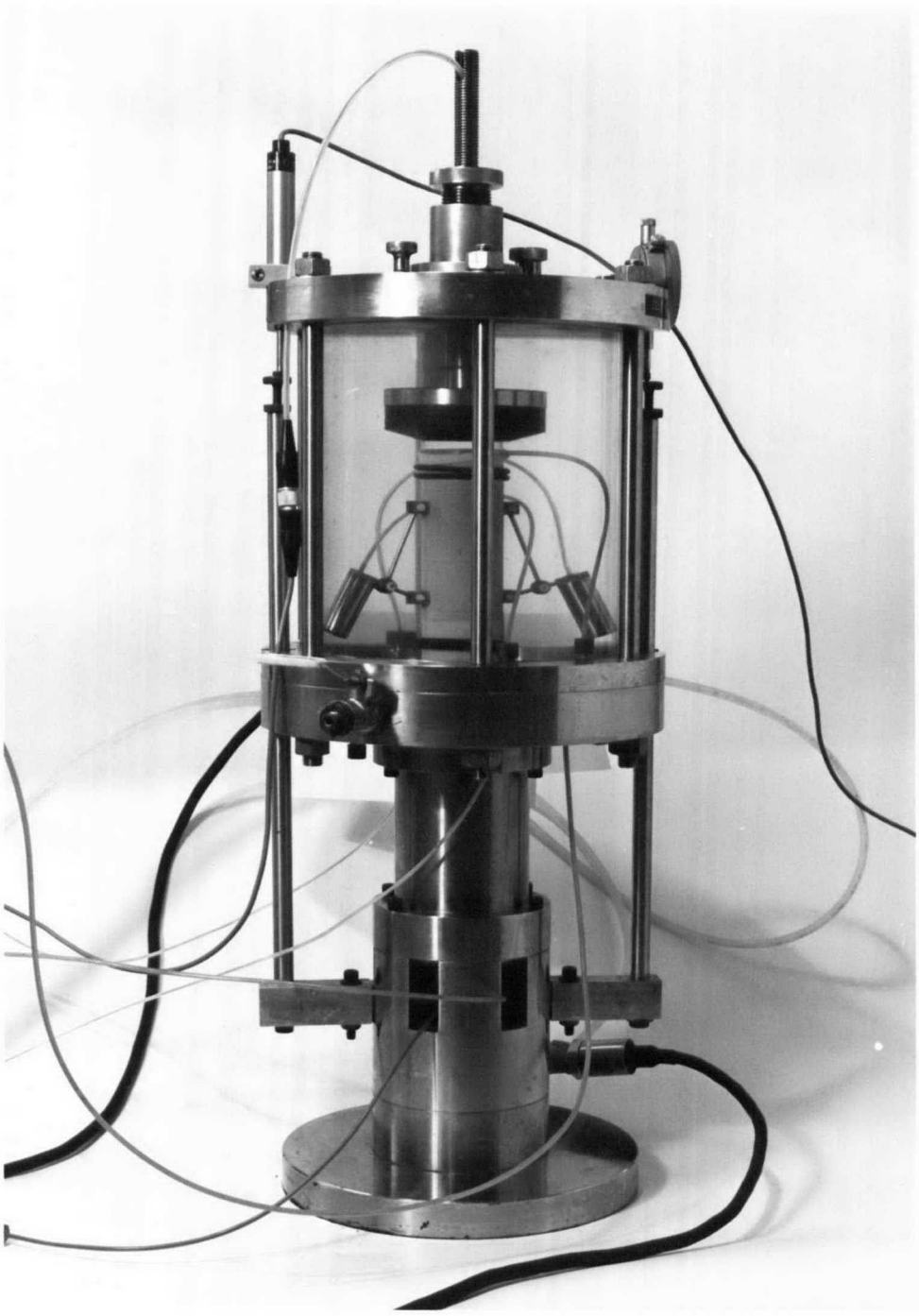
OPPOSITE

Figure 5.18. Electro-level gauges set on sample.



OPPOSITE

Figure 5.19. Sample and instrumentation assembled in stress path cell.



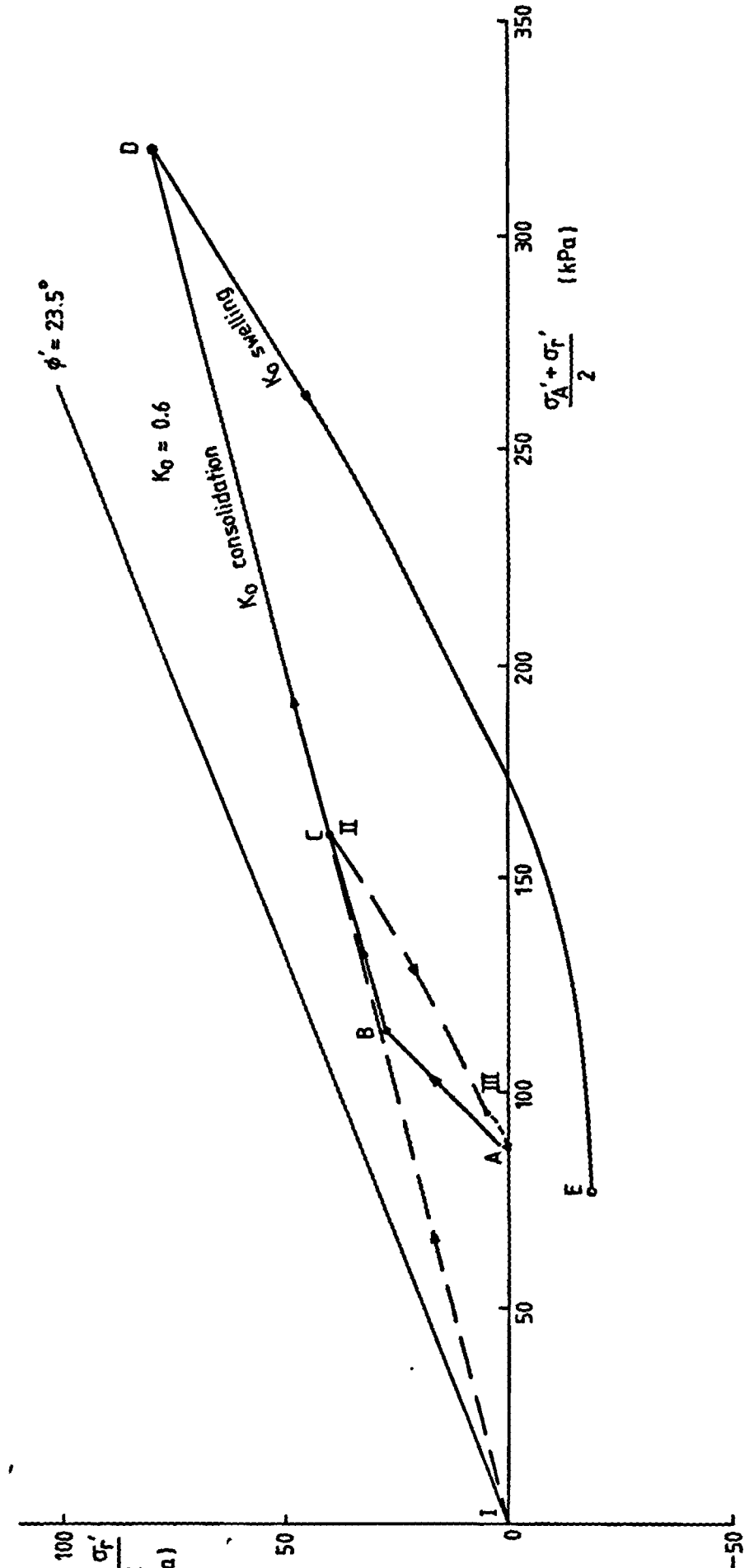


Figure 5.20. Consolidation and swelling stress paths for K_o consolidated London clay tests.

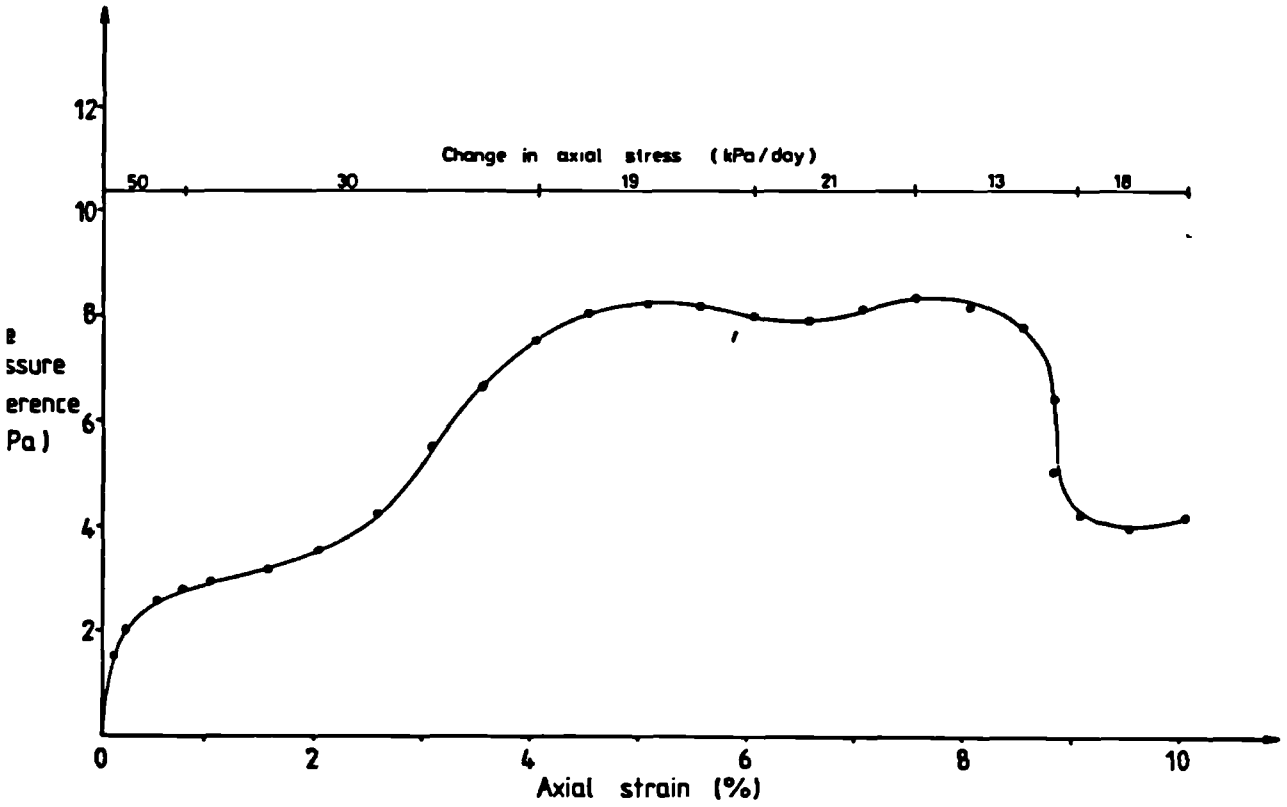


Figure 5.21. Excess pore pressures at sample mid-height for various rates of K_o consolidation, London clay.

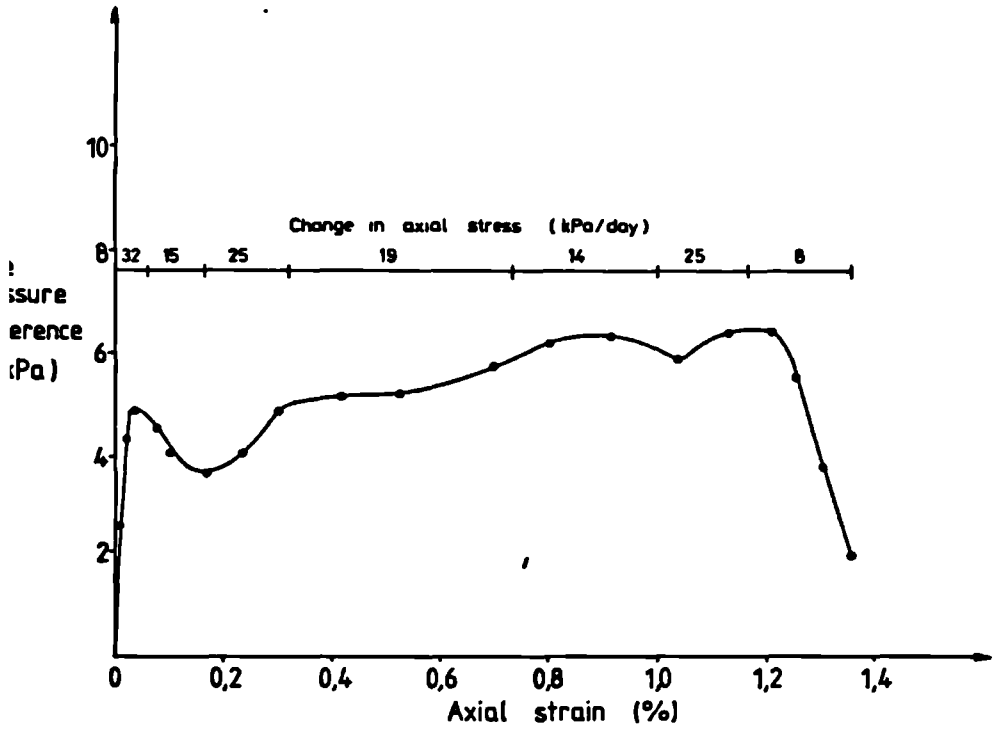


Figure 5.22. Excess pore pressure at sample mid-height for various rates of K_o swelling, London clay.

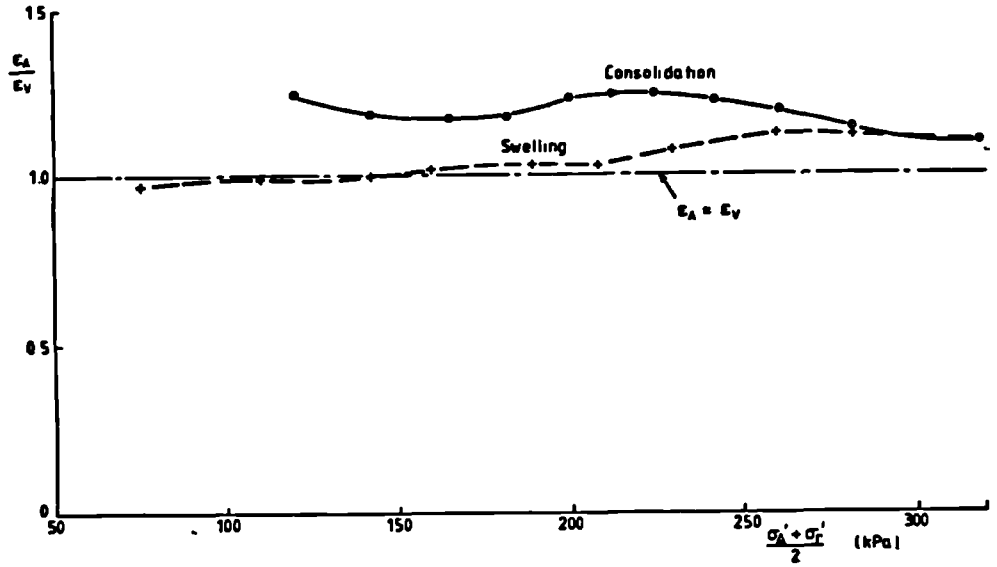


Figure 5.23. Ratio of axial strain to volume strain for London clay following stress paths given in Figure 5.20.

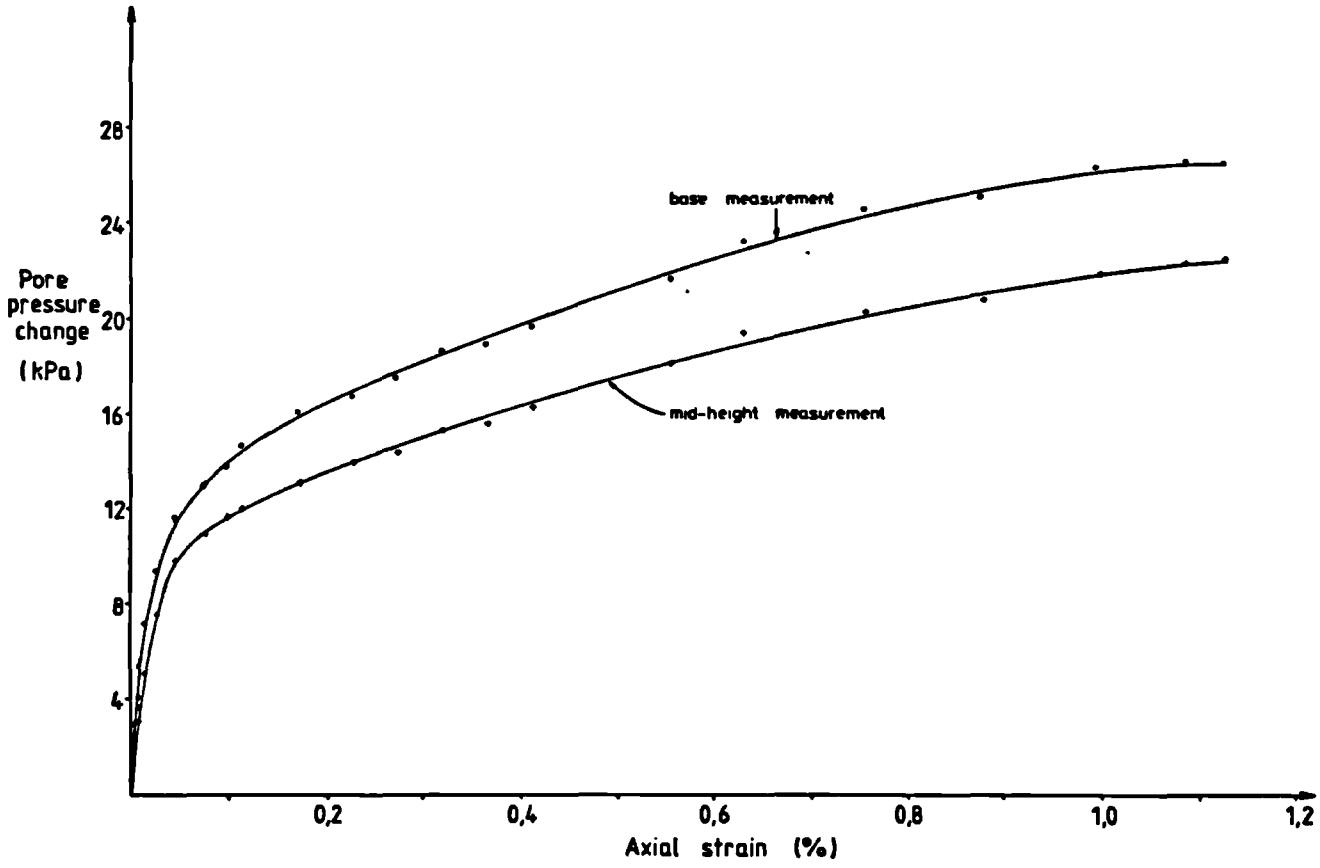


Figure 5.24. Base and mid-height pore pressures for London clay shearing at 45% axial strain per day.

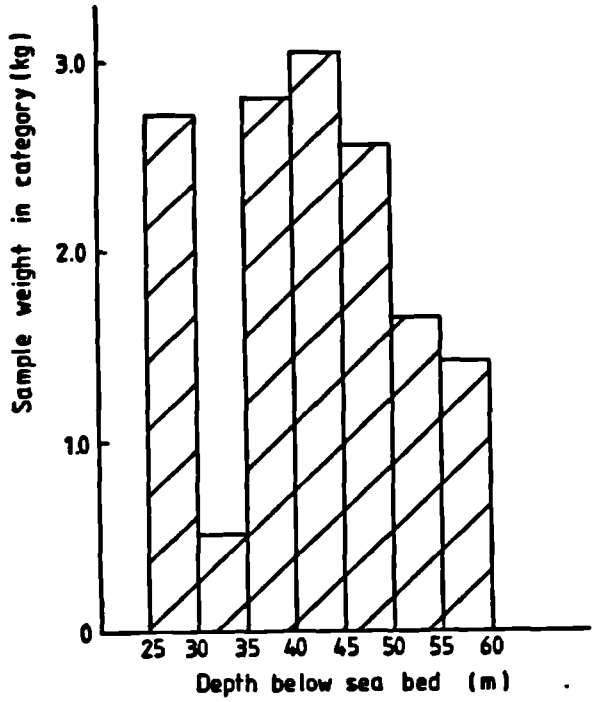


Figure 5.25. Histogram of samples incorporated into the Magnus reconstituted mix.

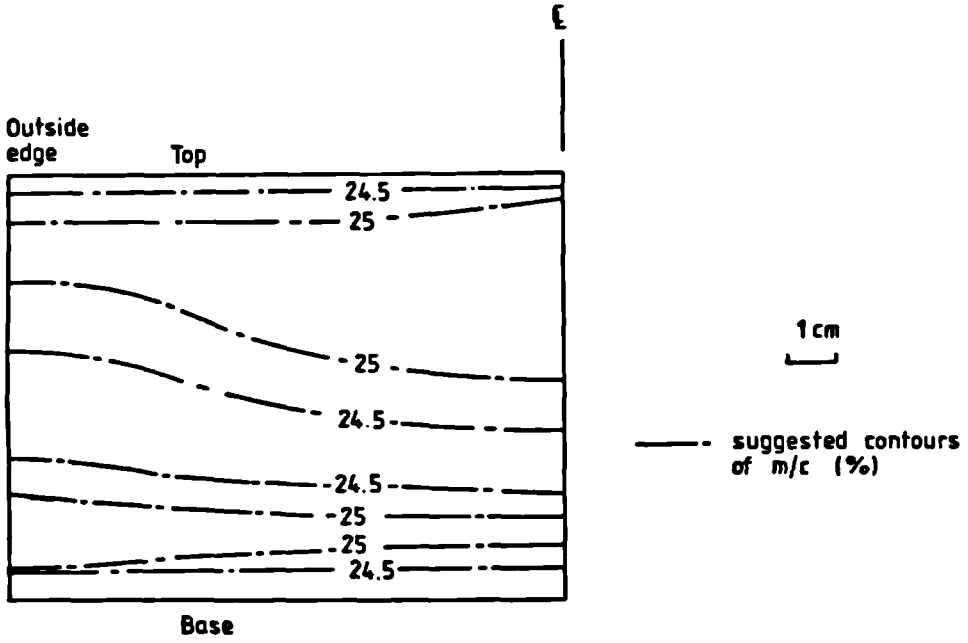


Figure 5.26. Distribution of water content within a block of reconstituted Magnus clay.

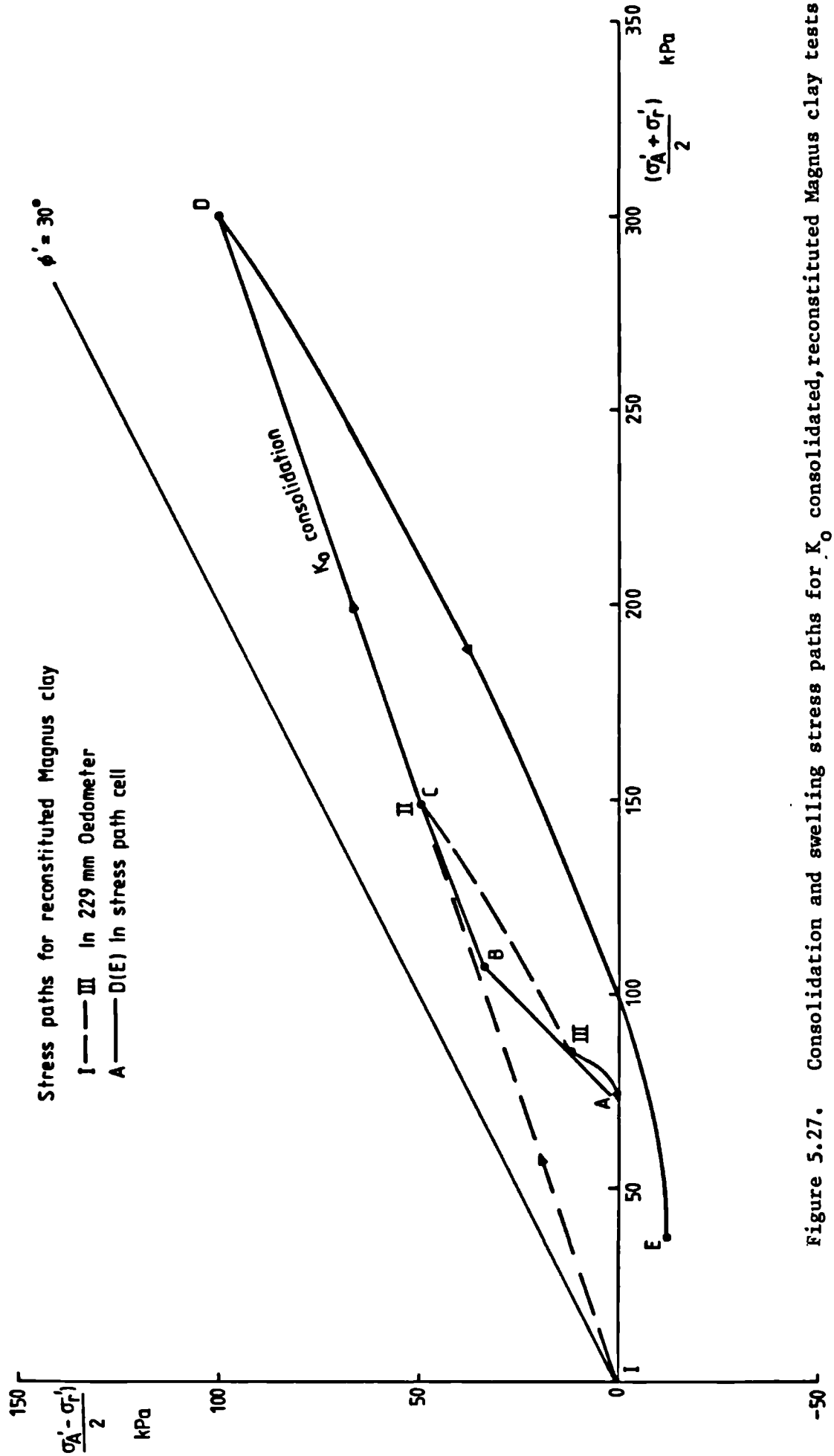


Figure 5.27. Consolidation and swelling stress paths for K_o consolidated, reconstituted Magnus clay tests.

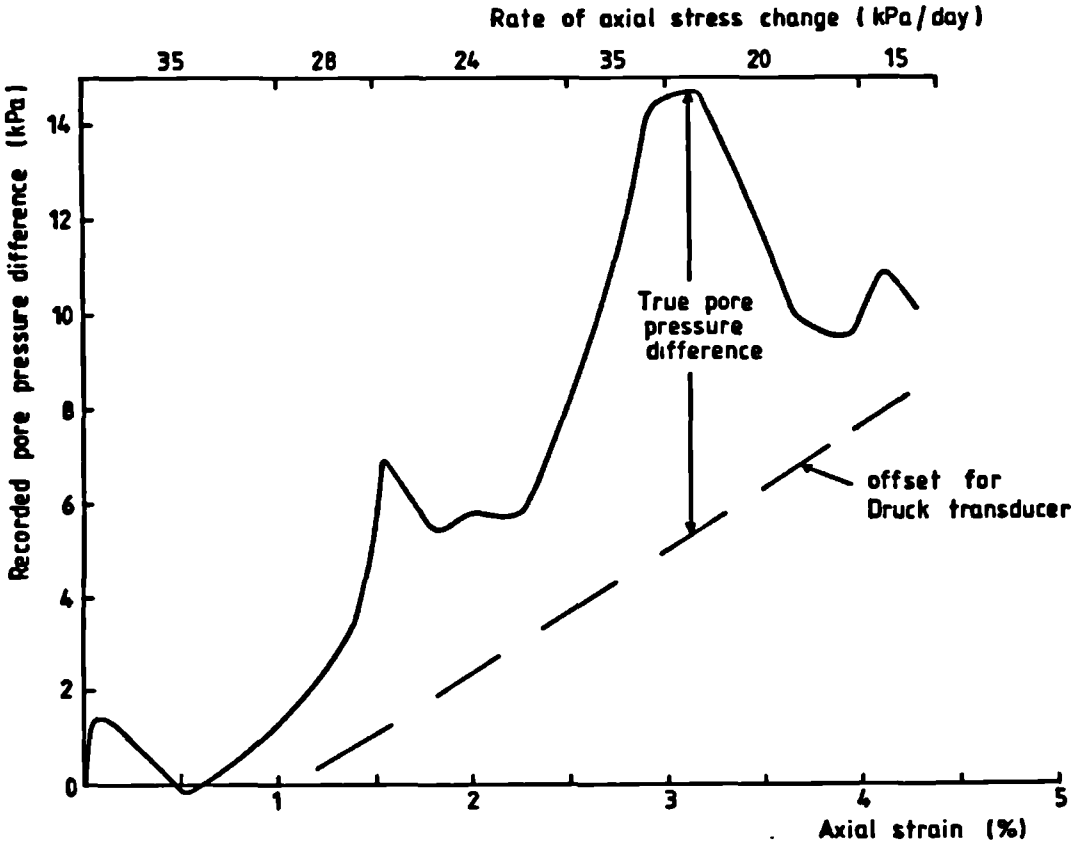


Figure 5.28. Excess pore pressures at sample mid-height for various rates of K_o consolidation, reconstituted Magnus clay.

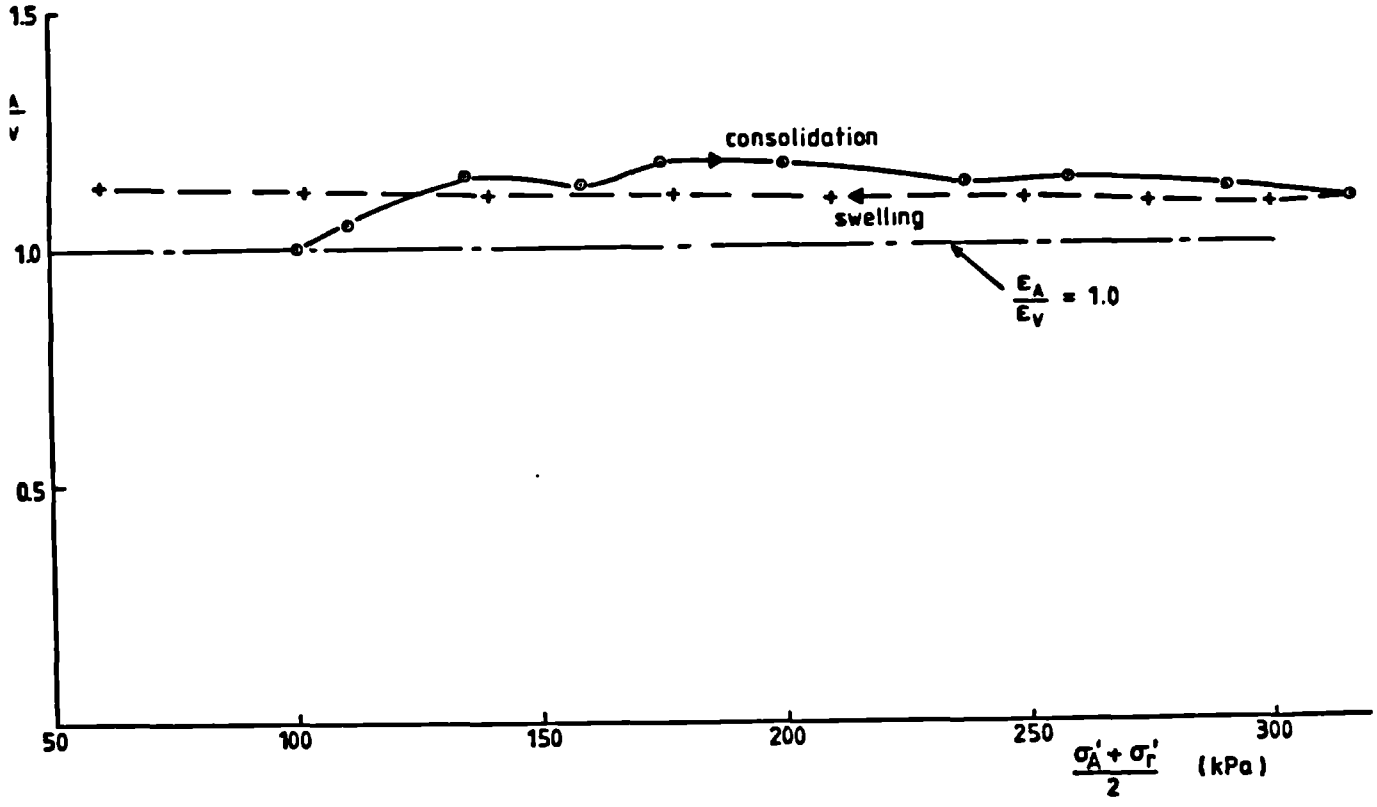


Figure 5.29. Ratio of axial strain to volume strain for Magnus clay following stress paths given in Figure 5.27.

OPPOSITE

Figure 5.30. Photographs of thin sections of intact Magnus hard clay, with and without, 45 degree rotation of polarising lens. Gas filled void spaces are shown circled.

0
5
10
mm

CHAPTER 6

Tables and Figures

Series	Test	σ'_{vc}, Kpa	OCR	Shearing Conditions
R	MR1	400	1.0	Undrained compression
"	MR1A	400	1.0	" " (see 1)
"	MR1.4	400	1.4	" "
"	MR2	400	2.0	" "
"	MR4	400	3.7	" "
"	MR8	400	7.4	" "
"	MR21	400	21.0	" "
RE	MRE1	400	1.0	Undrained extension
"	MRE1s	400	1.0	" " (see 2)
"	MRE2s	400	2.1	" " "
"	MRE4	400	4.0	" "
"	MRE4d	400	4.0	Drained extension (see 3)
"	MRE17	440	17.2	Undrained extension
RS	MRS1	400	1.0	Undrained compression after perfect sampling
"	MRS2	400	2.1	" " " " "
RR	MRR1	400	1.0	Undrained compression after extension
"	MRR4	400	4.0	" " " "
"	MRR17	440	17.2	" " " "

Table 6.1 a). Tests on samples K_o consolidated in the triaxial cells

Notes

1. MR1A was allowed to consolidate for 20 days at σ'_{vc} = 400 Kpa, σ'_H = 200 Kpa, before shearing.
2. MRE1s and MRE2 were carried out under stress control at a relatively slow rate.
3. MRDE4 was a drained extension test, inadvertently performed after a motor malfunction.

Series	Test	σ'_{vc}, Kpa	OCR	Shearing Conditions
RI	MRI1	382	1.0	Undrained compression
"	MRI2	398	2.0	" "
"	MRI2C	200	1.9	" " , lubricated ends, (see note 4)
"	MRI4	398	4.2	" "

Table 6.1 b). Tests on samples isotropically consolidated in the triaxial cells.

Notes

4. MRI2 the shearing phase of MTI2C included a number of load-unload cycles.

Series	Test	σ'_{vc}, Kpa	OCR	Shearing Conditions
RU	MRU(i)	200	2.0	Undrained compression, fixed ends, standard rate
"	MRU(ii)	200	2.0	" " , lubricated ends, standard rate
"	MRU(iii)	200	2.0	" " , " " , fast rate
"	MRU(iv)	200	2.0	" " , " " , slow rate
RUD	MRUD(i)	200	2.0	Drained compression, fixed ends, slow rate
"	MRUD(ii)	200	2.0	" " , " " , fast rate
"	MRUD(iii)	200	2.0	" " , " " , " "
"	MRUD(iv)	200	2.0	" " , lubricated ends, fast rate

Table 6.1 c). Tests on samples taken from reconstituted blocks without consolidation

Test	Pre-shear Conditions		Peak Strength	Stiffness			Strain rate
	p'_o Kpa	K_o Kpa	C_{up} Kpa	$E_{u(0.01)}$ Kpa	L	$E_u/p'_o)_{0.01}$	$t_{0.1}$ Mins.
MR1	267	0.50	122	2.22×10^5	0.185	831	38
MR1A	267	0.50	139	2.89×10^5	0.238	1118	43
MR1.4	206	0.59	122	4.50×10^5	0.270	2184	50
MR2	158	0.72	108	3.59×10^5	0.353	2272	52
MR4	106	0.96	94	2.26×10^5	0.386	2132	65
MR8	65	1.34	67	1.13×10^5	0.407	1738	105
MR21	43.1	2.00	55	8.20×10^4	0.359	1902	67
MRE1	265	0.50	60 @ 5%	3.16×10^5	0.439	1190	65
MRE1s	266	0.50	N/A	2.56×10^5	0.434	975	780
MRE2s	157	0.71	N/A	1.44×10^5	0.336	761	780
MRE4	101	0.97	52 @ 6%	9.60×10^4	0.331	953	41
MRE4d	101	0.97	N/A	$4.96 \times 10^{4*}$	0.368^*	498^*	380
MRE17	43	1.90	30 @ 2%	3.74×10^4	0.321	860	37
MRS1	192	1.00	108	2.63×10^5	0.404	1371	60
MRS2	156	1.00	102	3.25×10^5	0.336	2083	57
MRR.1	126	3.15	86	1.88×10^5	0.355	1489	52
MRR4	107	3.10	70	1.14×10^5	0.453	1062	39
MRR.17	66	3.28	N/A	9.00×10^4	0.387	1360	45
MRI1	381	1.00	131	2.60×10^5	0.407	682	80
MRI2	200	1.00	109	2.43×10^5	0.400	1214	70
MRI2C	103	1.00	N/A	1.37×10^5	0.401	1377	37
MRI4	97	1.00	96	2.14×10^5	0.294	2195	68
MRU(i)	59	1.00	45	9.80×10^4	0.435	1661	47
MRU(ii)	72	1.00	48	1.03×10^5	0.421	1437	50
MRU(iii)	72	1.00	N/A	9.8×10^4	0.456	1207	11
MRU(iv)	67	1.00	45	8.40×10^4	0.387	1244	540
MRUD(i)	70	1.00	N/A	$5.20 \times 10^{4*}$	0.465^*	743^*	1820^*
MRUD(ii)	59	1.00	N/A	$6.18 \times 10^{4*}$	0.432^*	1047^*	420^*
MRUD(iii)	56	1.00	N/A	$\simeq 4 \times 10^{4*}$	$\simeq 0.5^*$	$\simeq 700^*$	600^*
MRUD(iv)	68	1.00	N/A	$6.20 \times 10^{4*}$	0.46^*	911^*	24^*

Table 6.2. Summary of Reconstituted Triaxial Tests

* Denotes drained tests, parameters are $E'_{(0.01)}$, $(E'/p'_o)_{0.01}$ etc.

OCR	1	2	4	8	18
Series					
R	0.303	0.554	0.878	1.22	3.05
RE	0.155+	-	0.52+	-	1.18+
RS	0.273	0.510	-------- as R ----------		
RR	0.212	-	0.720	-	-
RI	0.344	0.540	1.021	-	-
RU	-	0.448	-	-	-

Table 6.3. Comparisons for Cu/σ'_{vo} from different test series, reconstituted Magnus clay.

(+ indicates tests where peak strengths were not necessarily obtained).

				Pre-shear Conditions			Strength	Stiffness			Strain
Group	Test	Test Type	Depth m	p'_o Kpa	σ'_{vo} Kpa	K_o	Cu_p Kpa	$E_{u(0.01)}$ Kpa	L	$(E_u/p'_o)_{0.01}$	rate, $t_{0.1}$ Mins
I	MI1	CIU[1]	3.9	43	43	-	173	9.4×10^4	0.340	2,190	120
I	MI2	CAU[2]	9.8	180	125	1.63	308	3.46×10^5	0.302	1,920	299
I	MI3	CIU[3]	17.0	220	220	-	470	3.84×10^5	0.320	1,748	66
II	MI4	UU	21.7	251	251	-	254	4.44×10^5	0.365	1,769	96
II	MI5	CAU[4]	25.9	270	286	0.92	262	4.76×10^5	0.384	1,760	115
II	MI6	UU	37.2	443	443	-	309	5.9×10^5	0.334	1,331	92
II	MI7	CAU	37.2	336	414	0.72	272	5.9×10^5	0.363	1,754	72
III	MI8	CAU	59.2	458	684	0.51	270	4.36×10^5	0.237	951	53
III	MI9	UU	67.2	474	474	-	255	5.1×10^5	0.333	1,076	150
III	MI10	CAU	67.2	507	744	0.52	275	7.44×10^5	0.194	1,469	60
IV	MI11	UU	83.5	753	753	-	513	1.01×10^6	0.308	1,525	75
IV	MI12	CAU	83.5	655	926	0.56	528	1.07×10^6	0.279	1,634	85
III	MP1	UU	62.6	530	530	-	279	-	-	-	-
III	MP2	UU	67.2	590	590	-	270	-	-	-	-
IV	MP3	UU	93.3	850	850	-	604	-	-	-	-

Table 6.4. Summary for triaxial tests on intact samples.

Notes

1 Initial p' value was 530 Kpa

2 " " " 414 "

3 " " " 473 "

4 " " " 370 "

CIU Isotropically consolidated, undrained compression

CAU Anisotropically " , " "

UU Unconsolidated, but stabilised, undrained compression

Rate of Displacement mm/minute	ϕ'_r
131	31.4°
0.086	26.8°
0.058	27.5°
0.017	26.3°

Table 6.5. Dependence of ϕ'_r on rate of displacement, Magnus soil-soil shear, $\sigma'_n \simeq$ 500 Kpa.

MRC1	Consolidation Conditions	OCR	p'_o Kpa	Max. G	Equiv. Max. Eu/p'_o	L^2	Equiv. $(Eu/p'_o)_{0.01}$
MRC1	Isotropic	1.0	400	5.8×10^4	435	0.28	337
MRC2	"	4.0	100	5.0×10^4	1,500	0.50	1310
MRC3	Isotrop. Adjusted[1]	2.0	70	1.6×10^4	686	0.28	454

Table 6.6. Resonant column test data for reconstituted Magnus soil.

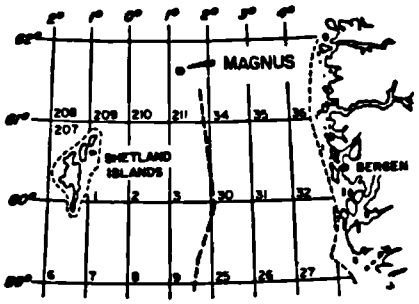
Notes

1 'Consolidated' at estimated initial stress

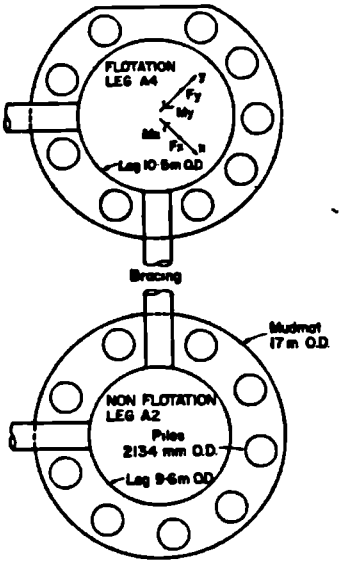
2 Defined here as G at 0.05%/G at 0.005%.

Test	$(Eu/p'_o)_{0.01}$
MRI1	682
MRI4	1,291
MRUU(iii)	1,361

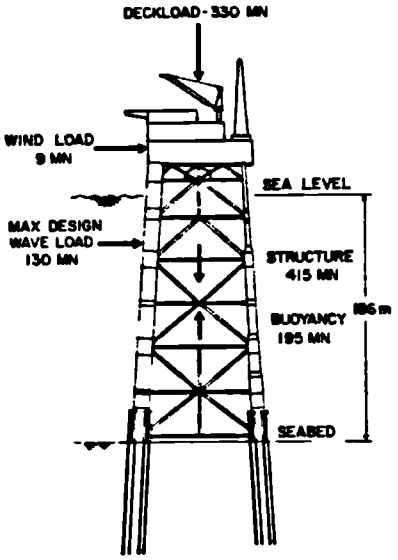
Table 6.7. Comparative triaxial test data.



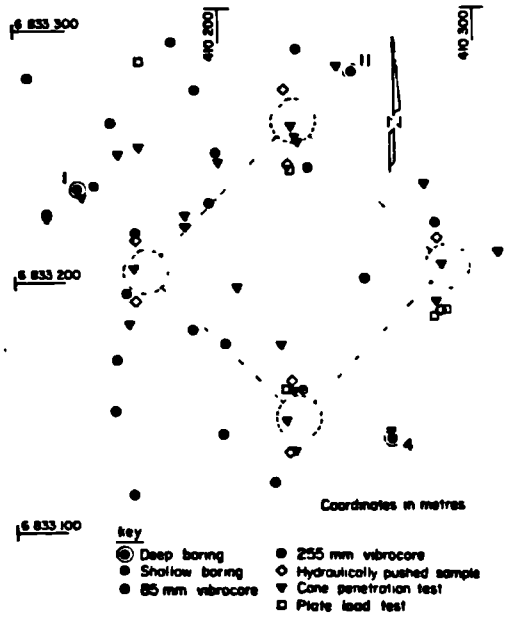
Vicinity map



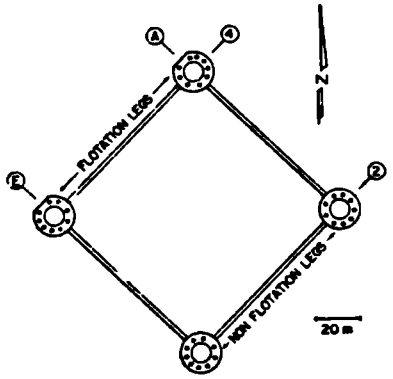
Pile group details



Magnus structure



Plan of investigations



Base of structure

Figure 6.1. Details of Magnus Platform, foundations and site investigation plan, after Rigden and Semple (1983).

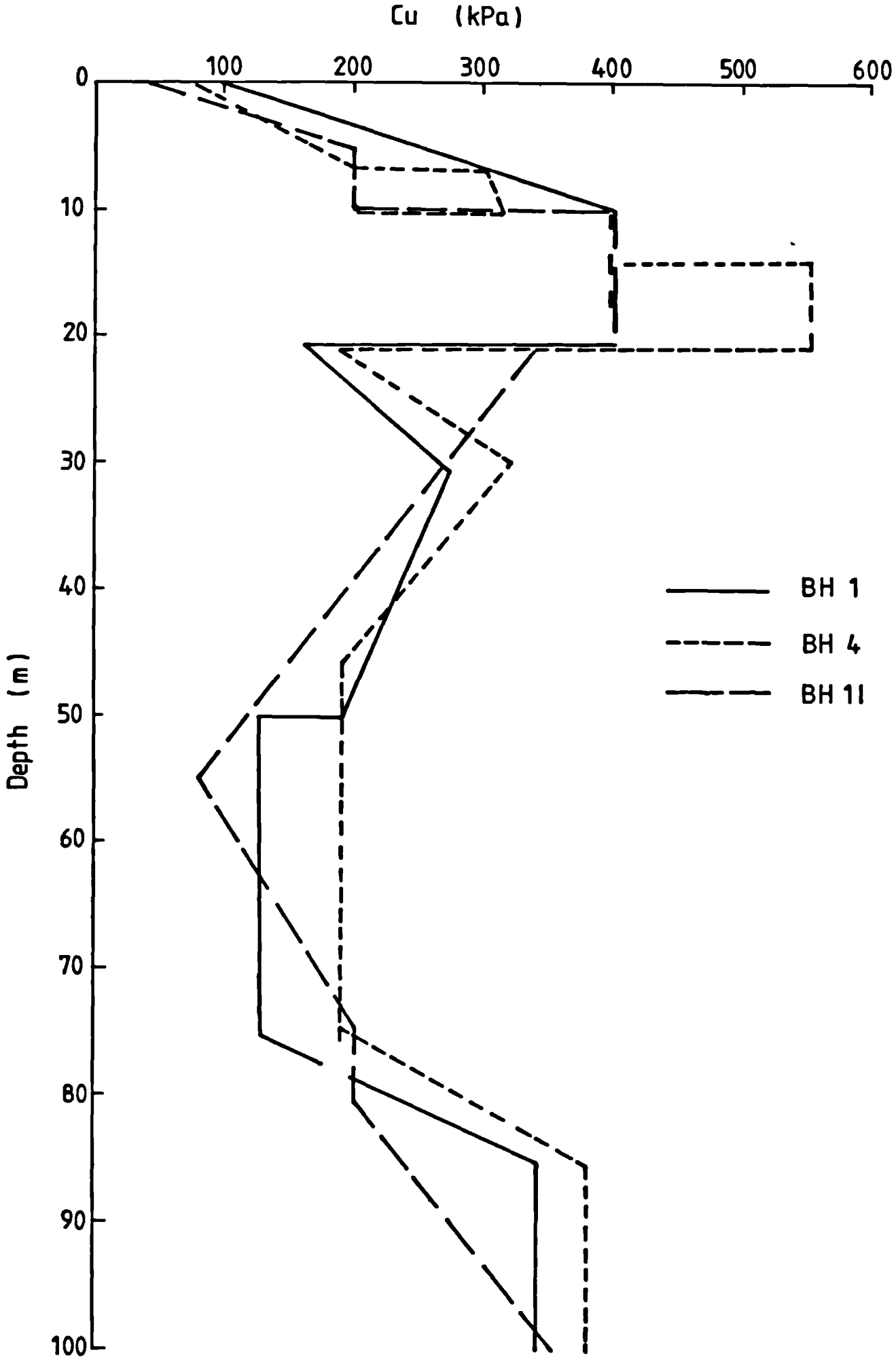
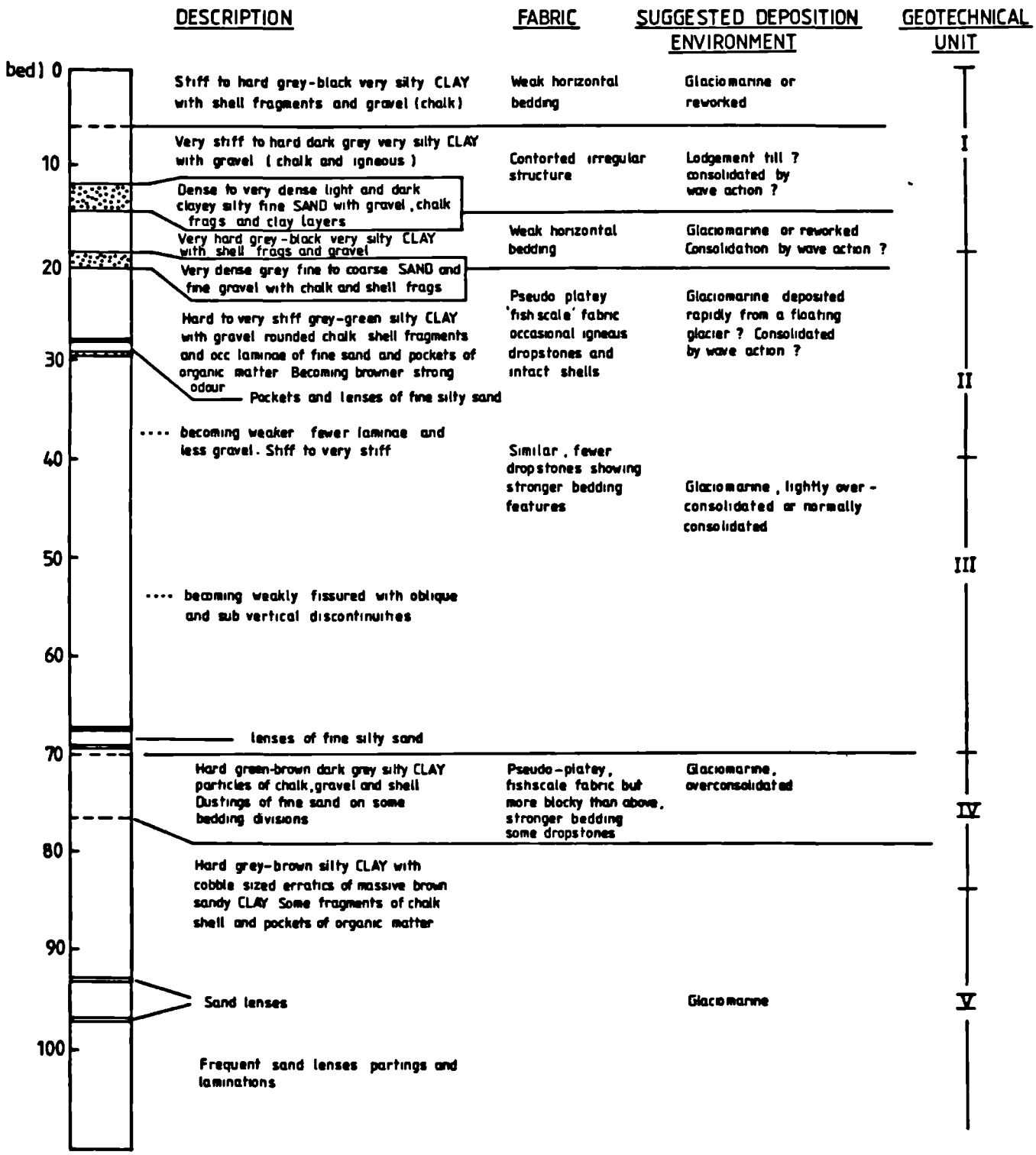


Figure 6.2. Profiles of undrained shear strength, after Rigden and Semple (1983).



I.C. LOG FOR BOREHOLE 11 , MAGNUS SITE

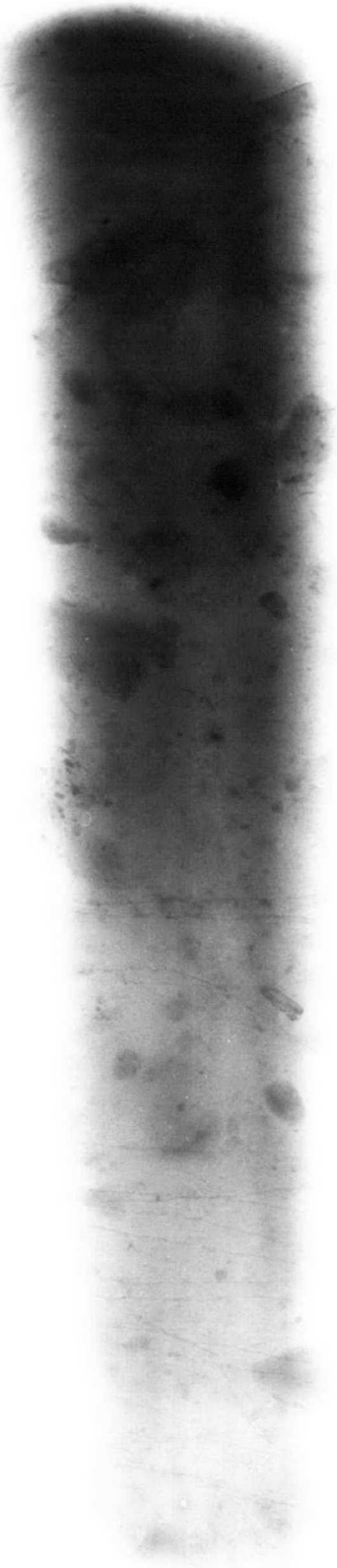
Figure 6.3.

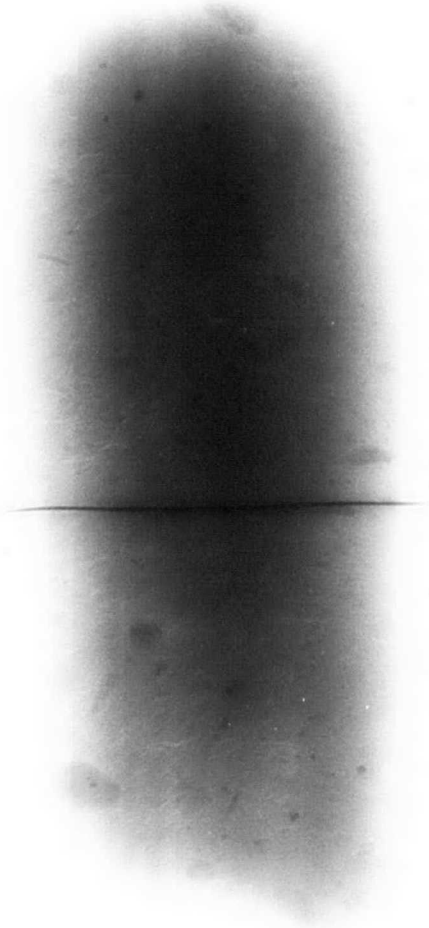
OPPOSITE

Figure 6.4. X-ray images of Magnus samples (actual size).

LEFT RIGHT

a) 0.5 m depth b) 44.8 m depth





OPPOSITE

Figure 6.4. X-ray images of Magnus samples (actual size).

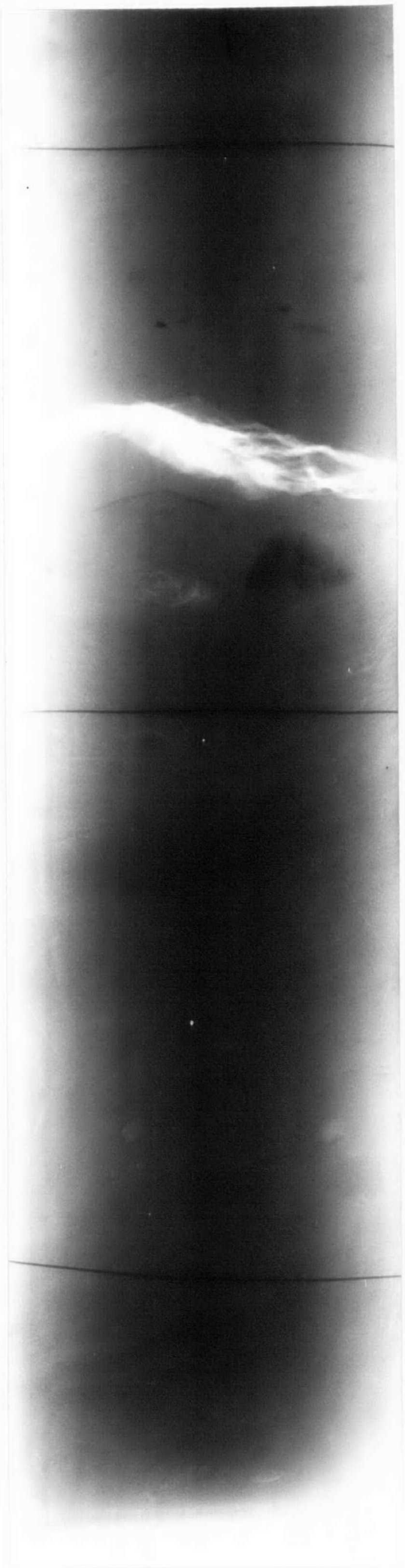
LEFT

c) 63.1 m depth

RIGHT

d) 67.7 m depth



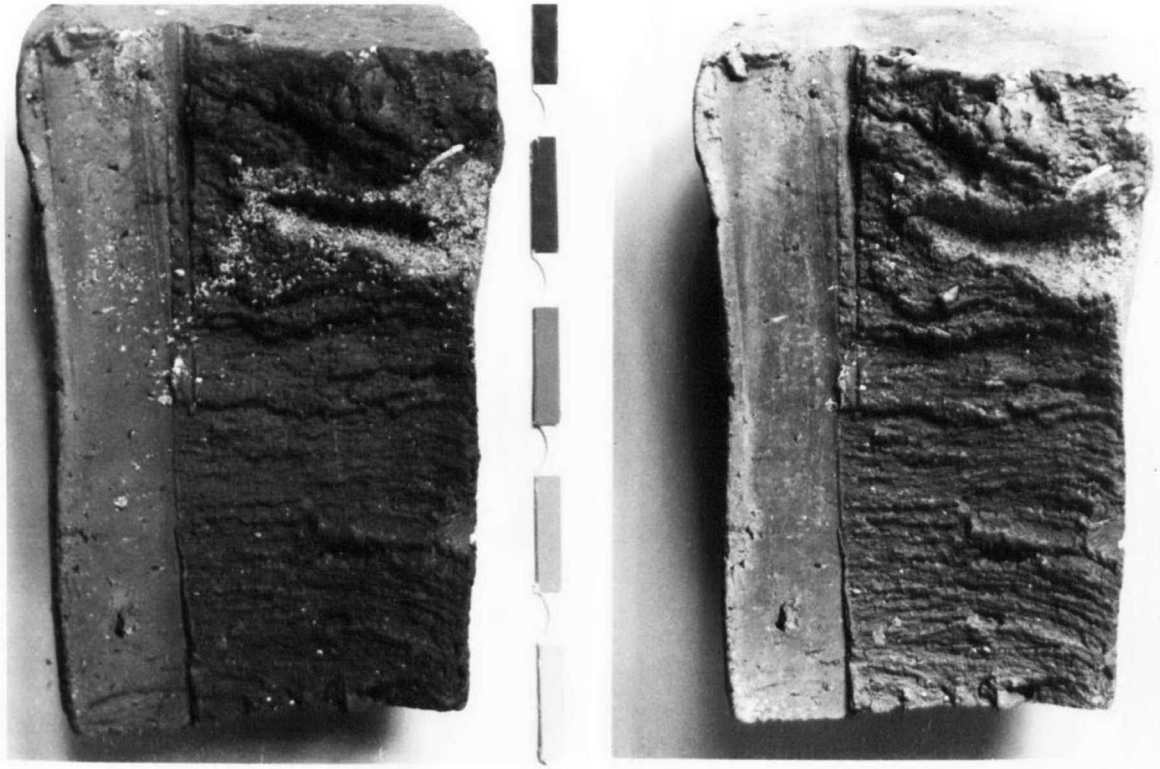


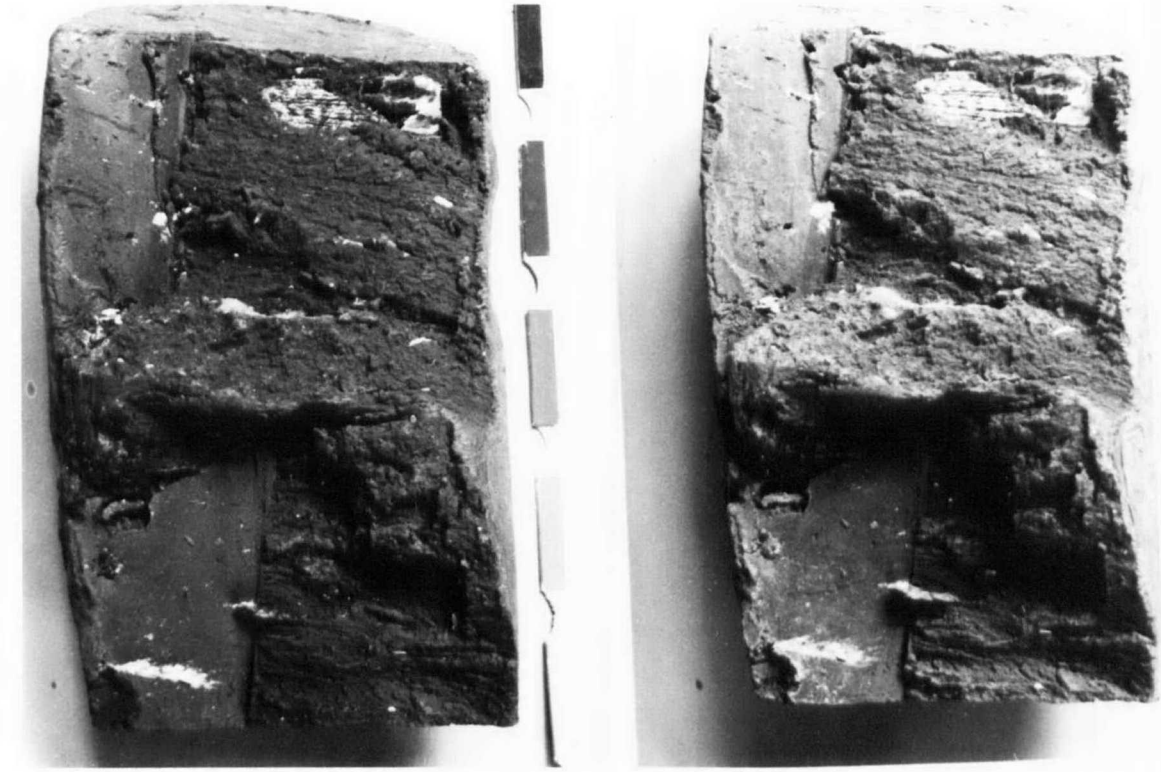
OPPOSITE

Figure 6.5. Photographs of Magnus samples.
(left natural m/c, right part air dried)

a) TOP - 4.1 metres depth

b) BOTTOM - 6.7 metres depth





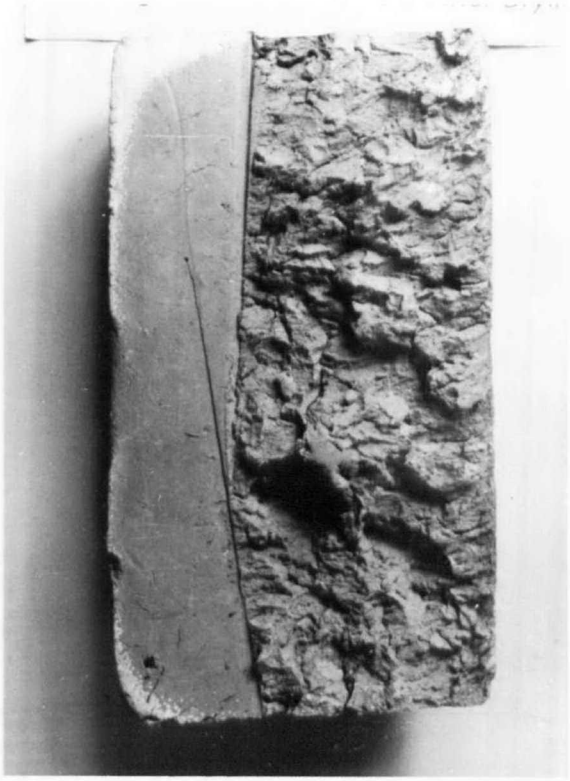
OPPOSITE

Figure 6.5 (cont'd). Photographs of Magnus samples.
(left natural m/c, right part air dried)

c) TOP - 19.3 metres depth

d) BOTTOM - 35.2 metres depth







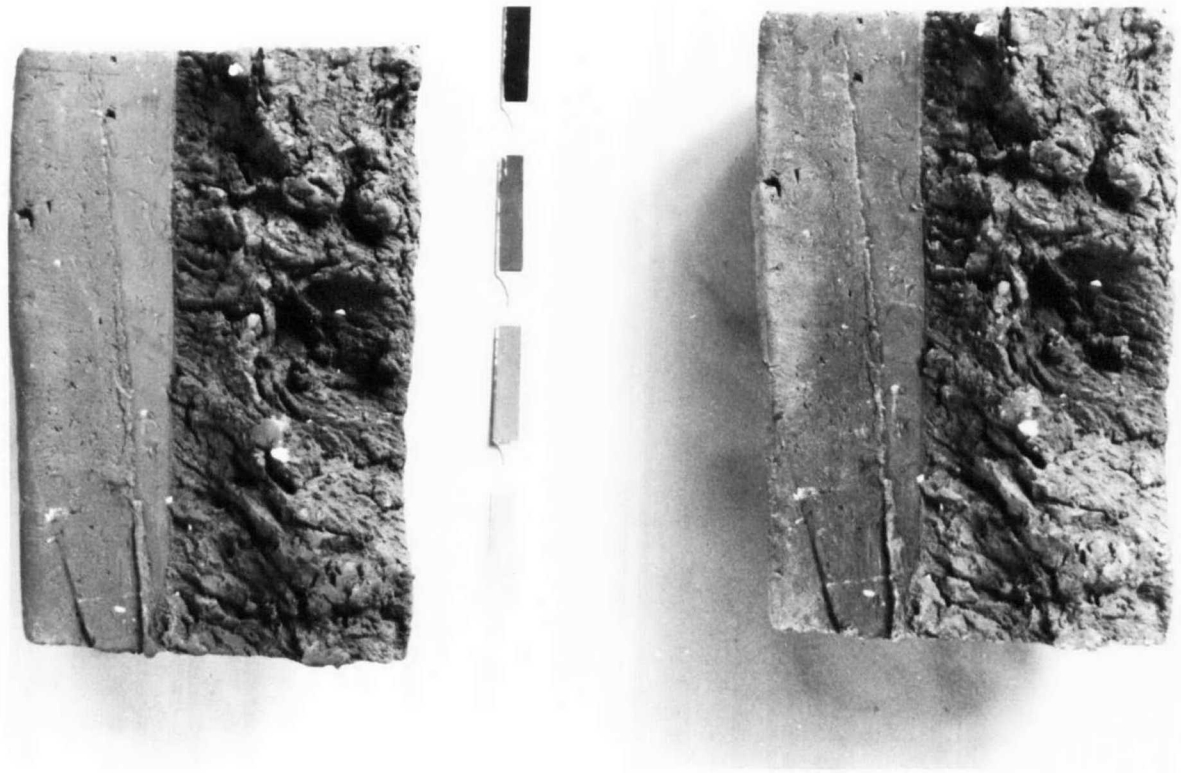


OPPOSITE

Figure 6.5 (cont'd). Photographs of Magnus samples.
(left natural m/c, right part air dried)

e) TOP - 46.2 metres depth

f) BOTTOM - 55.3 metres depth

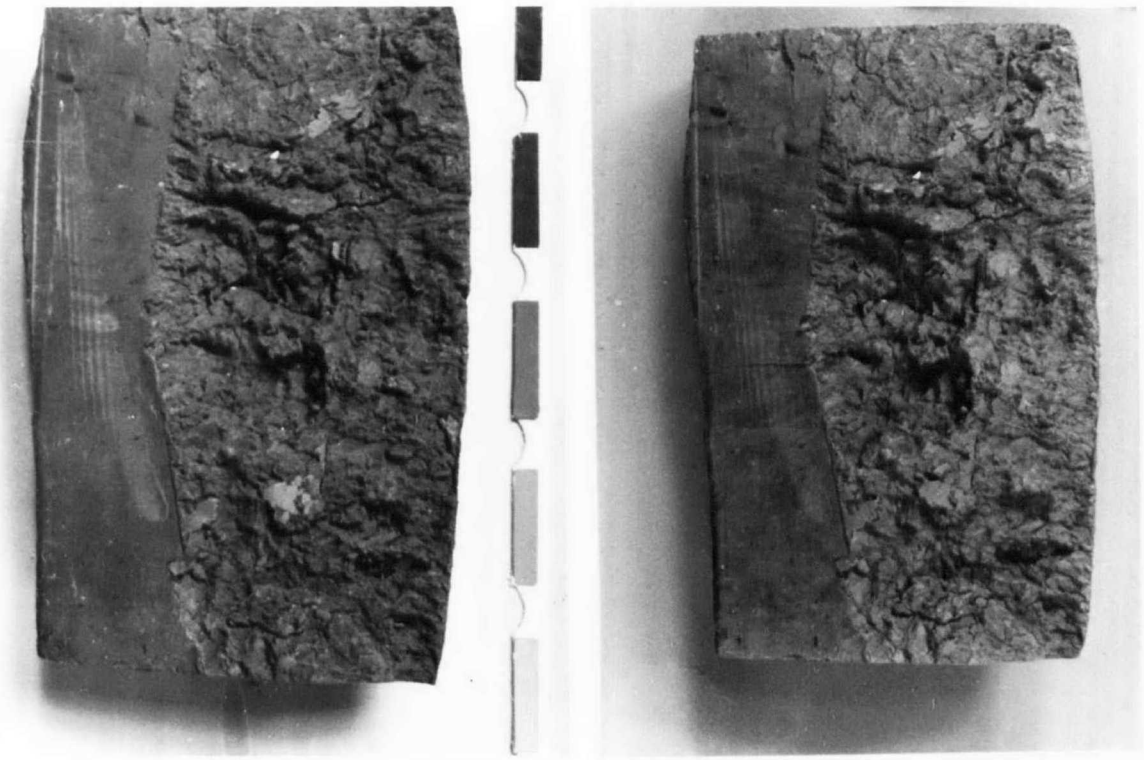


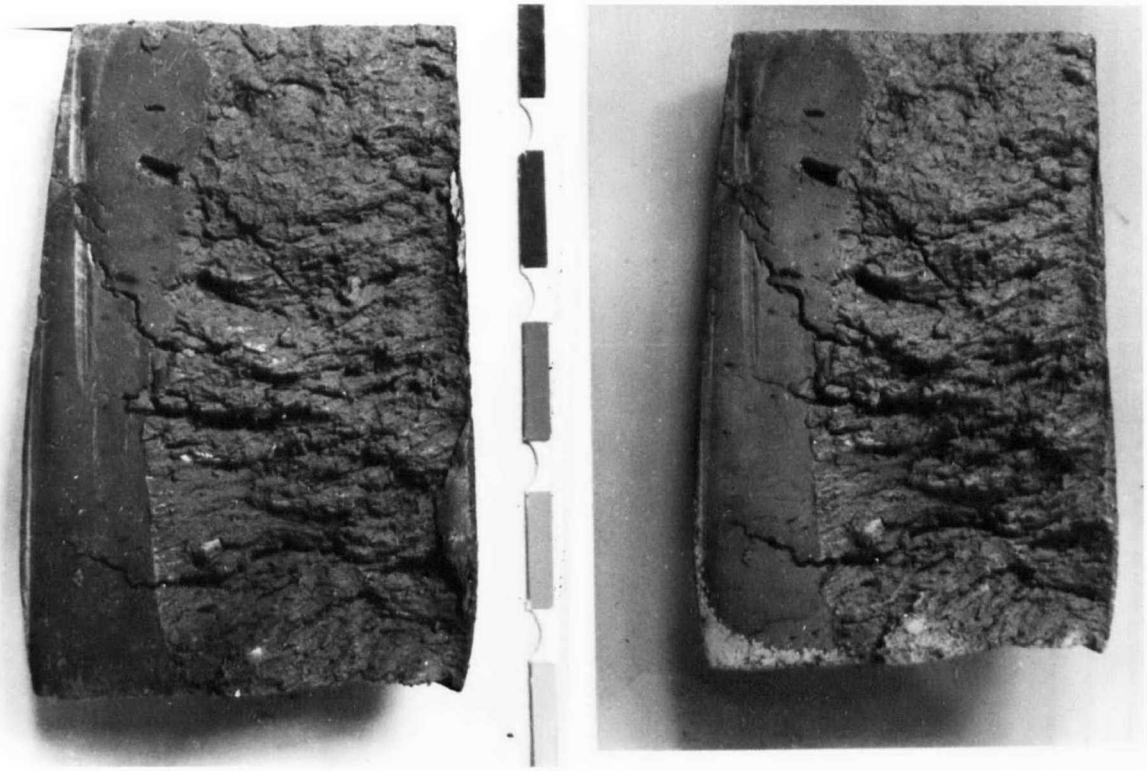
OPPOSITE

Figure 6.5 (cont'd). Photographs of Magnus samples.
(left natural m/c, right part air dried)

g) TOP - 85.4 metres depth

h) BOTTOM - 95.2 metres depth





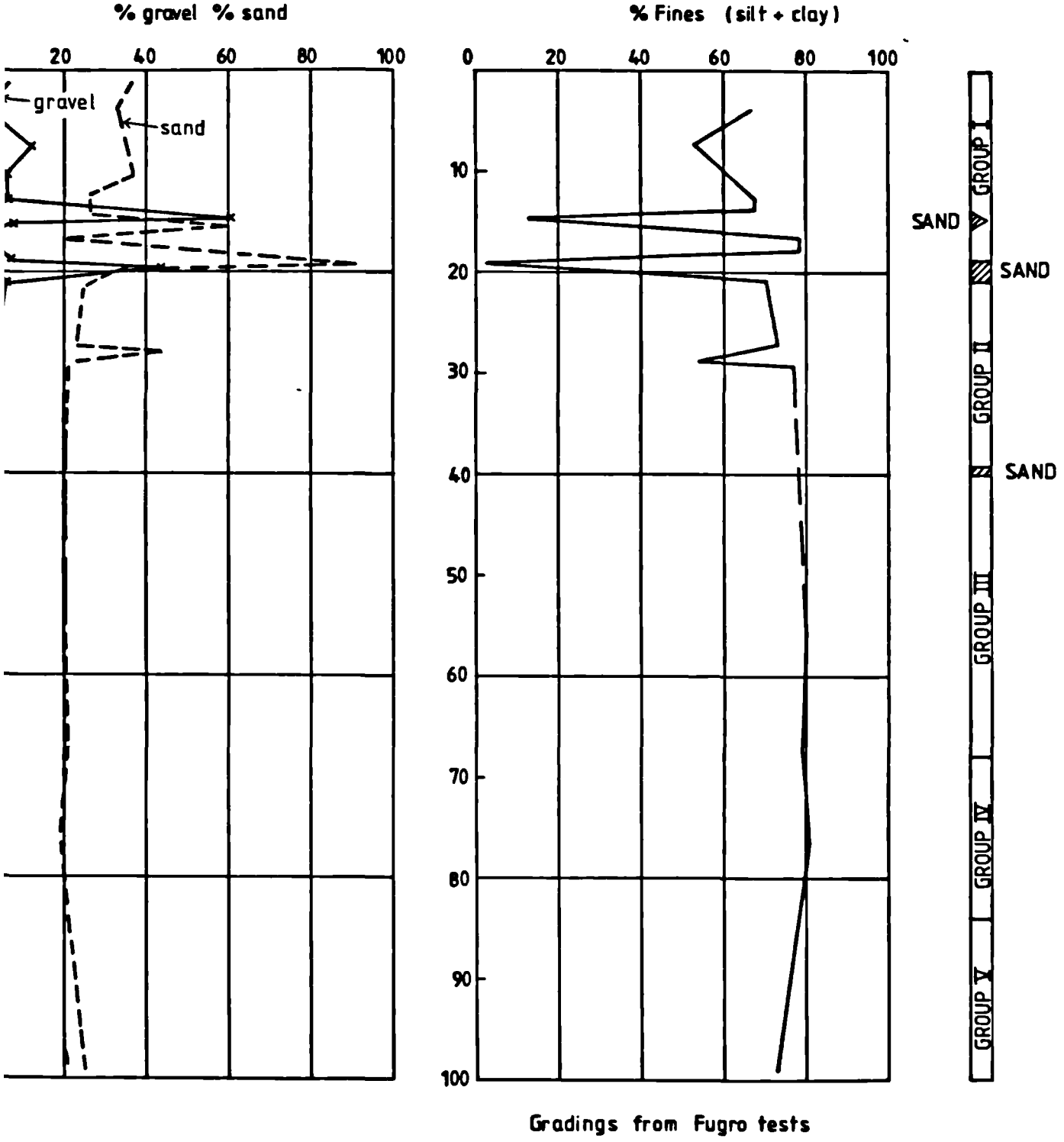
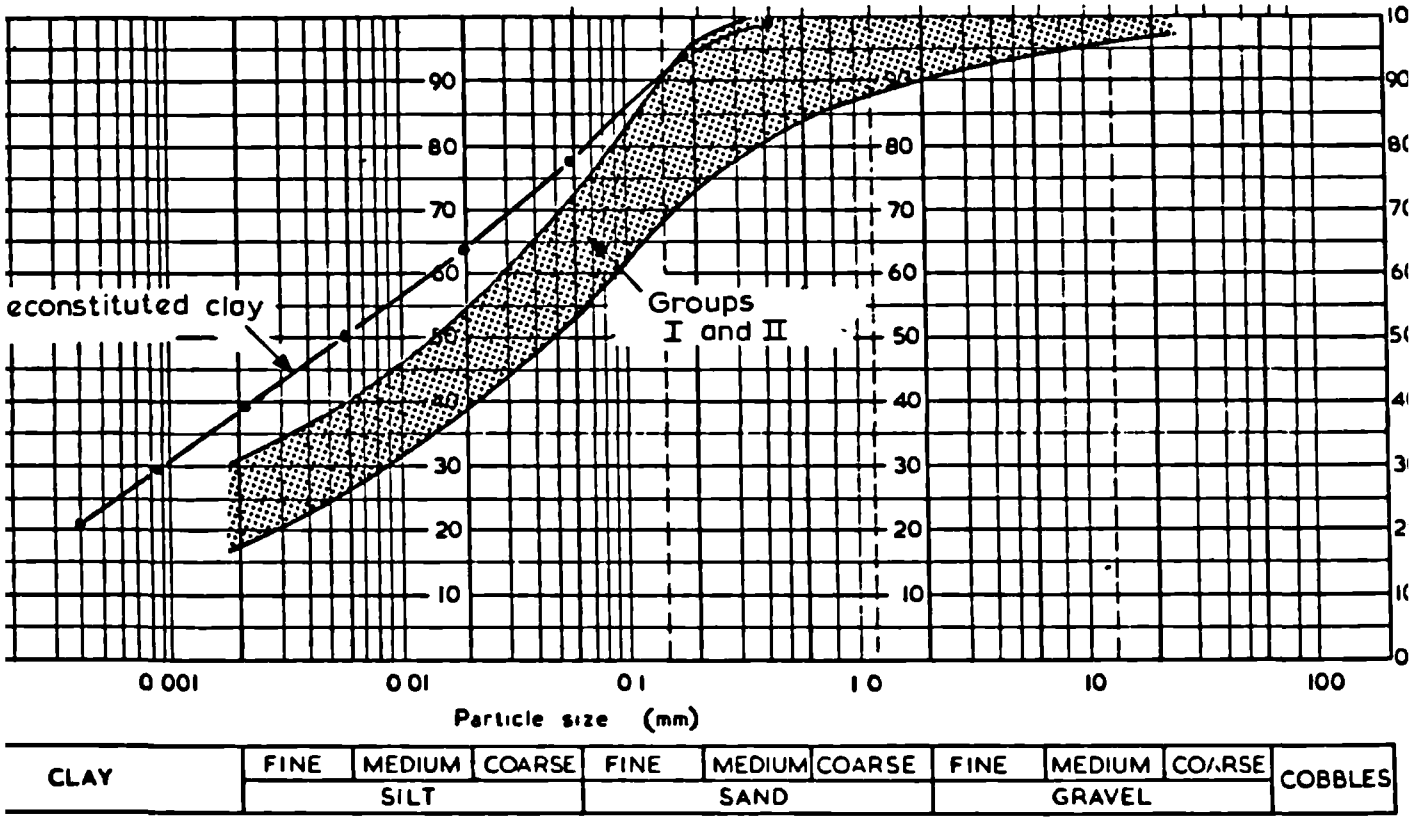


Figure 6.6. Variations in gradings with depth.



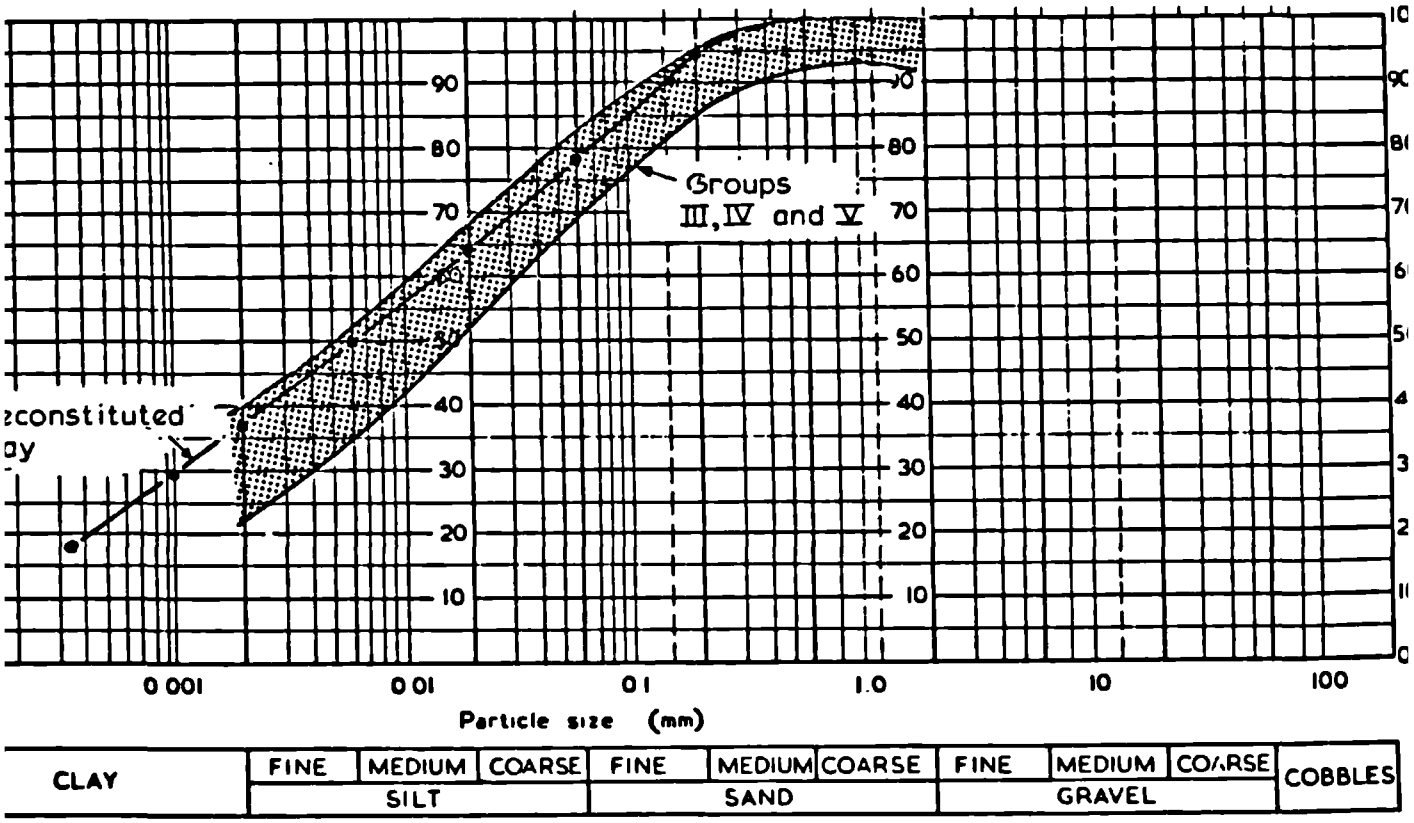


Figure 6.7. Summary of Magnus gradings.

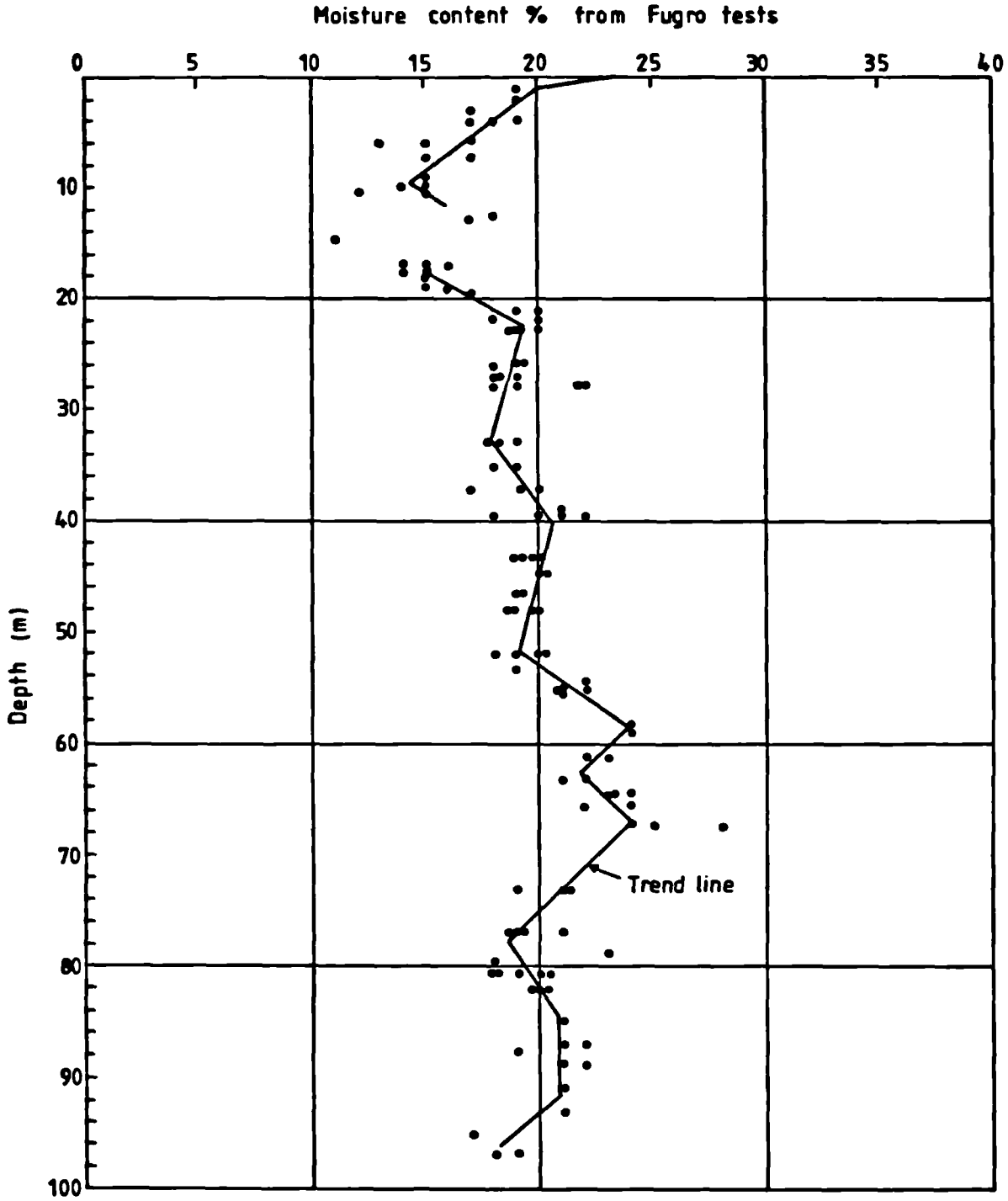


Figure 6.8 a). Water content variations with depth.

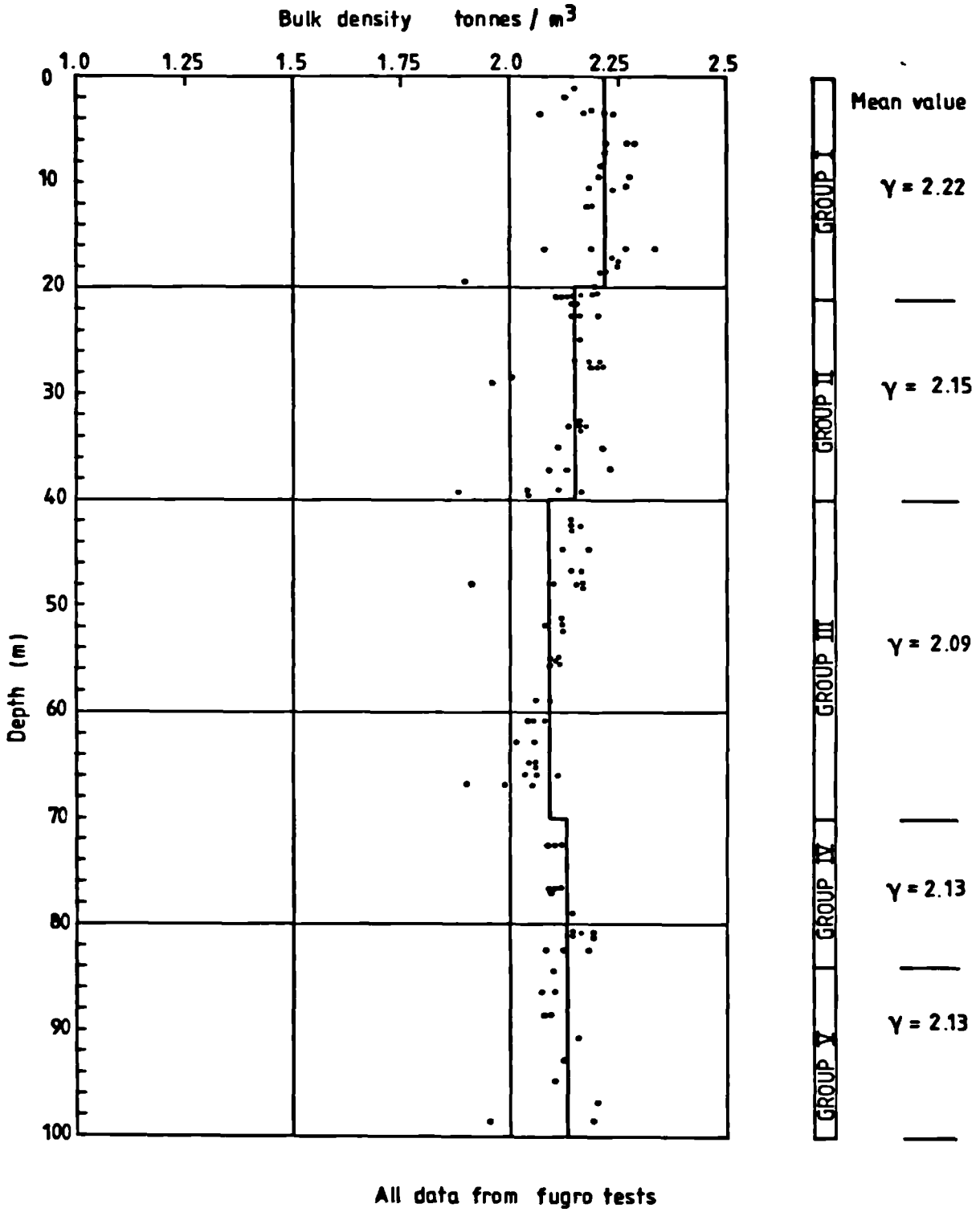
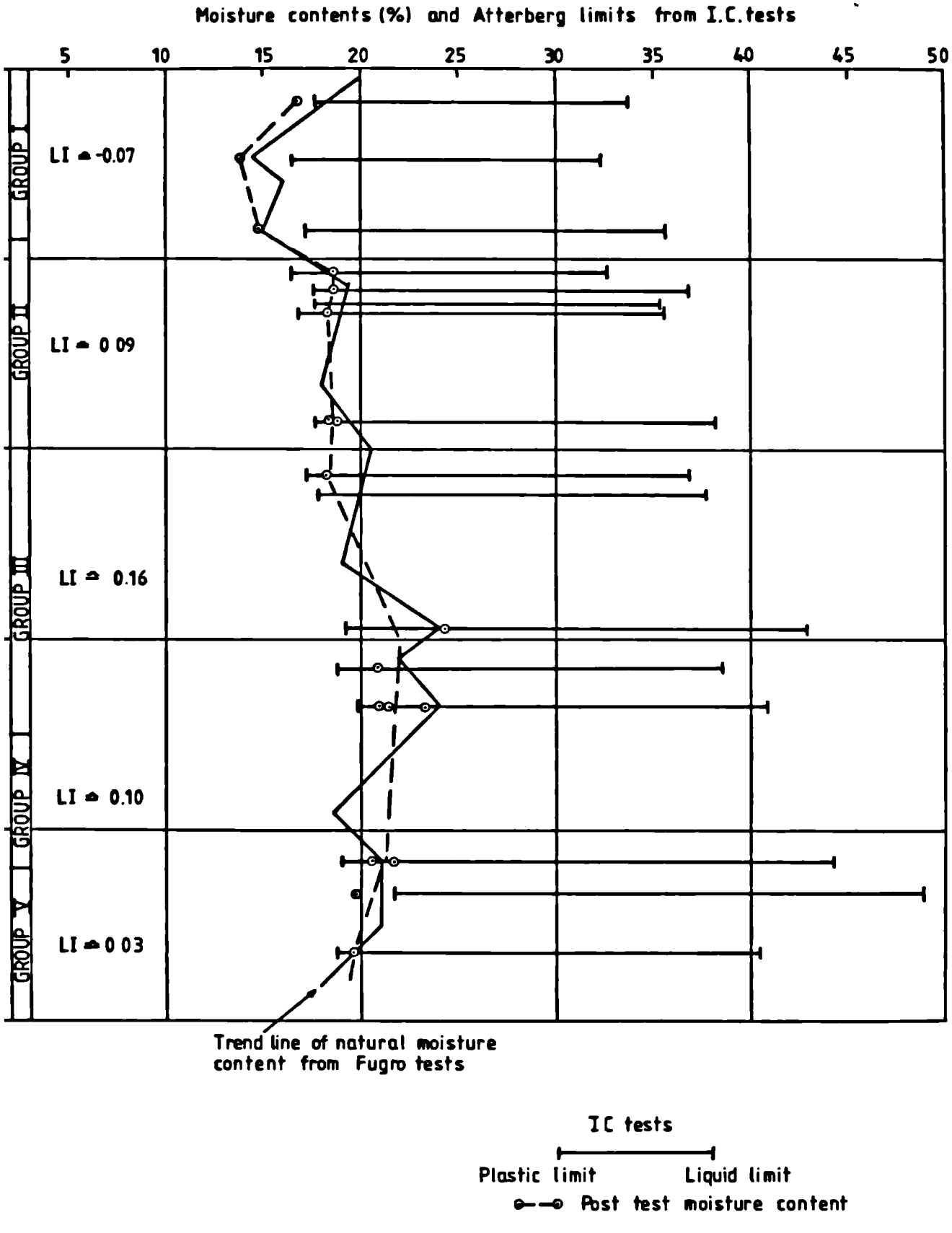


Figure 6.8 b). Bulk density variations with depth.

Figure 6.8 c). Atterberg limits and water contents.



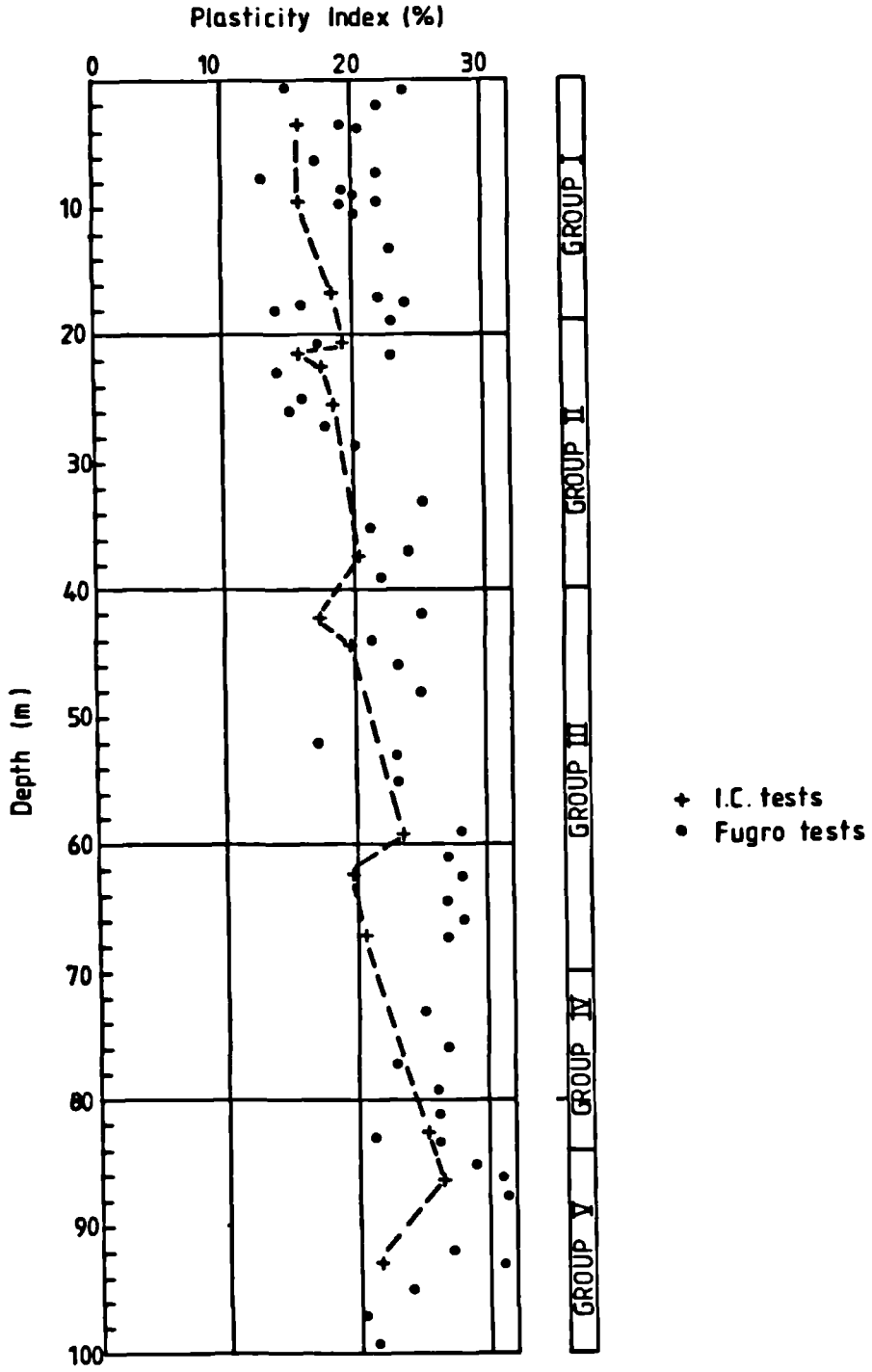


Figure 6.9. Plasticity index - depth relationship.

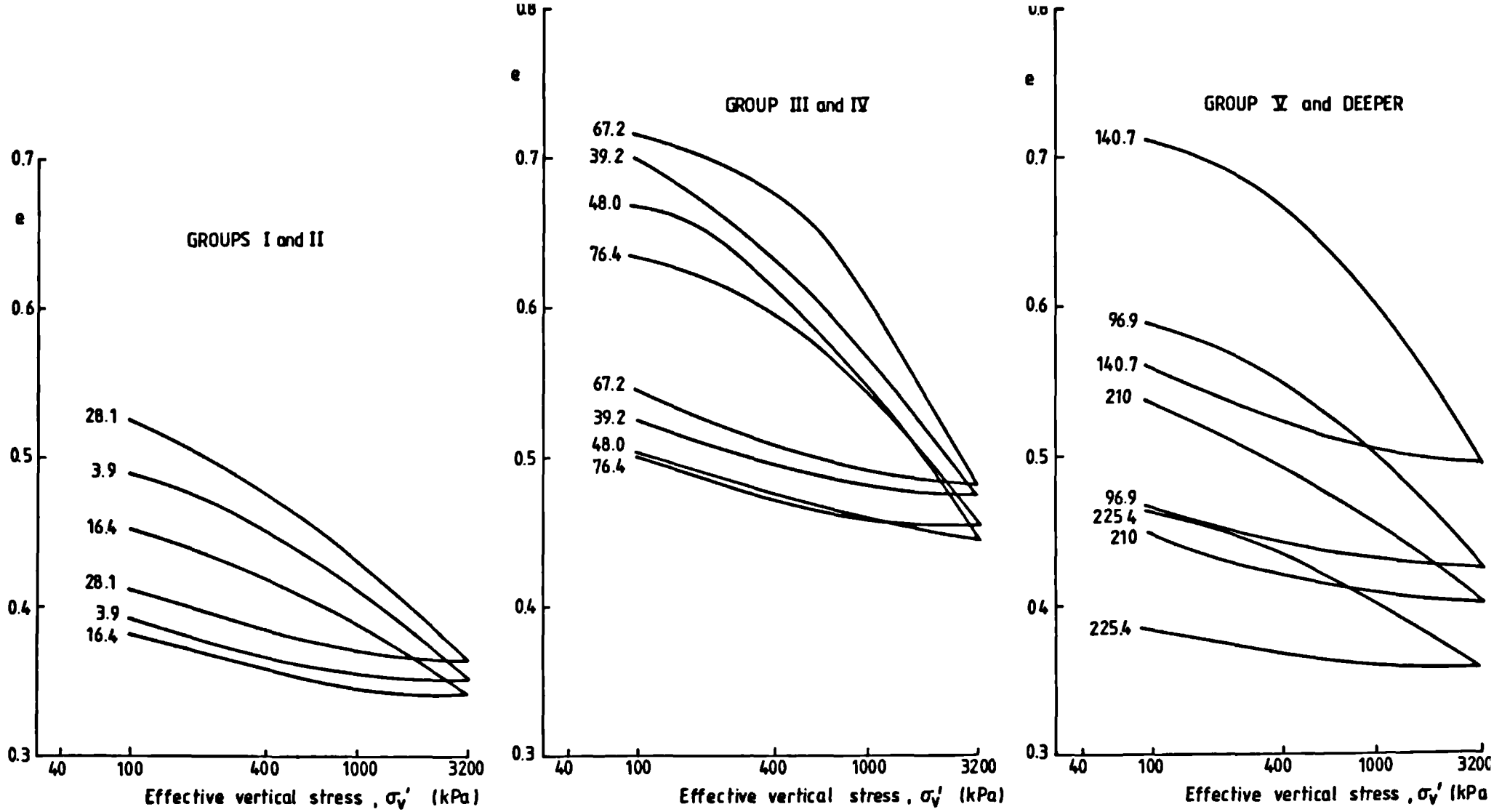


Figure 6.10. Voids ratio - log σ'_v curves for intact Magnus samples.

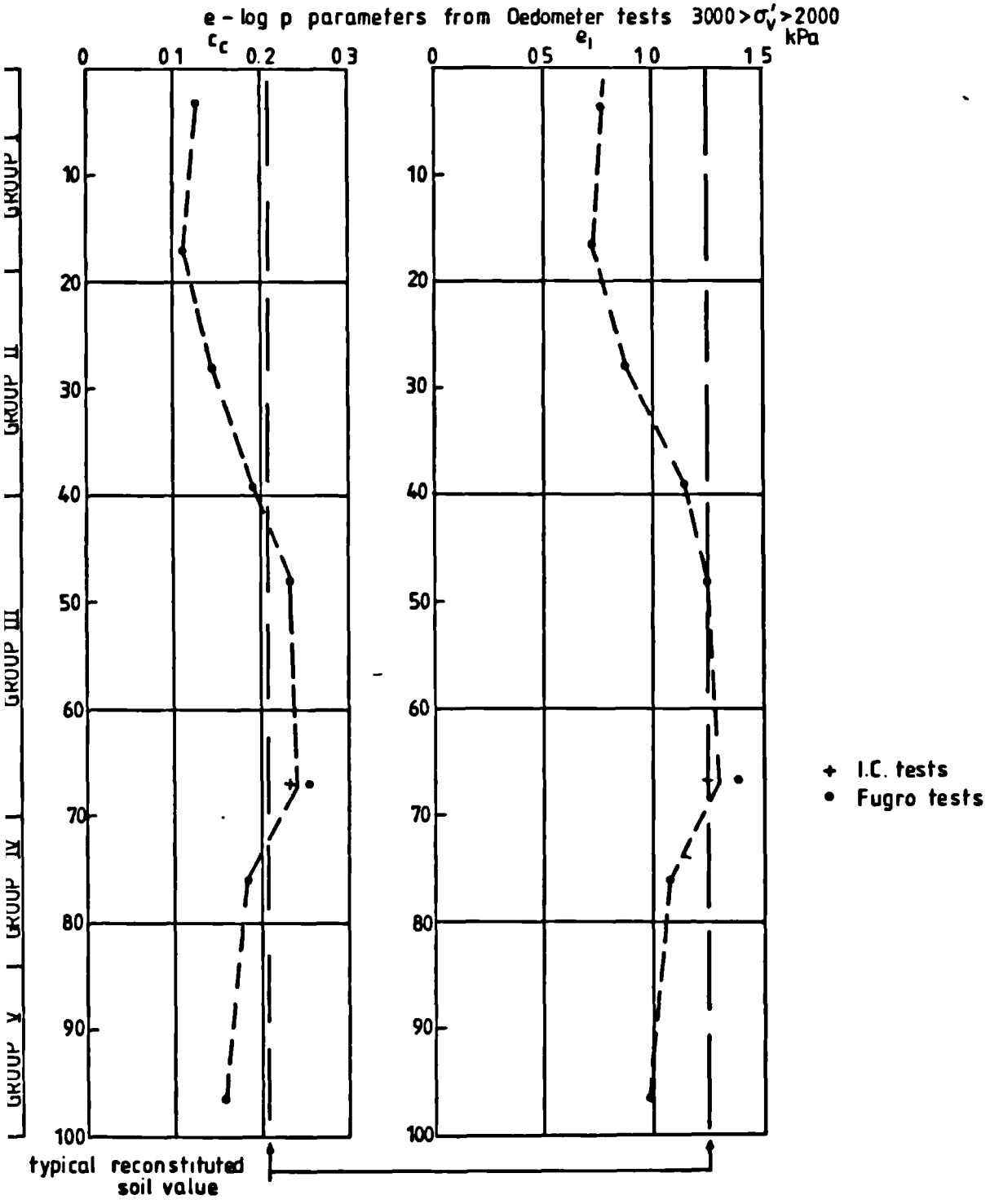


Figure 6.11. Summary of VCL parameters for intact Magnus samples.

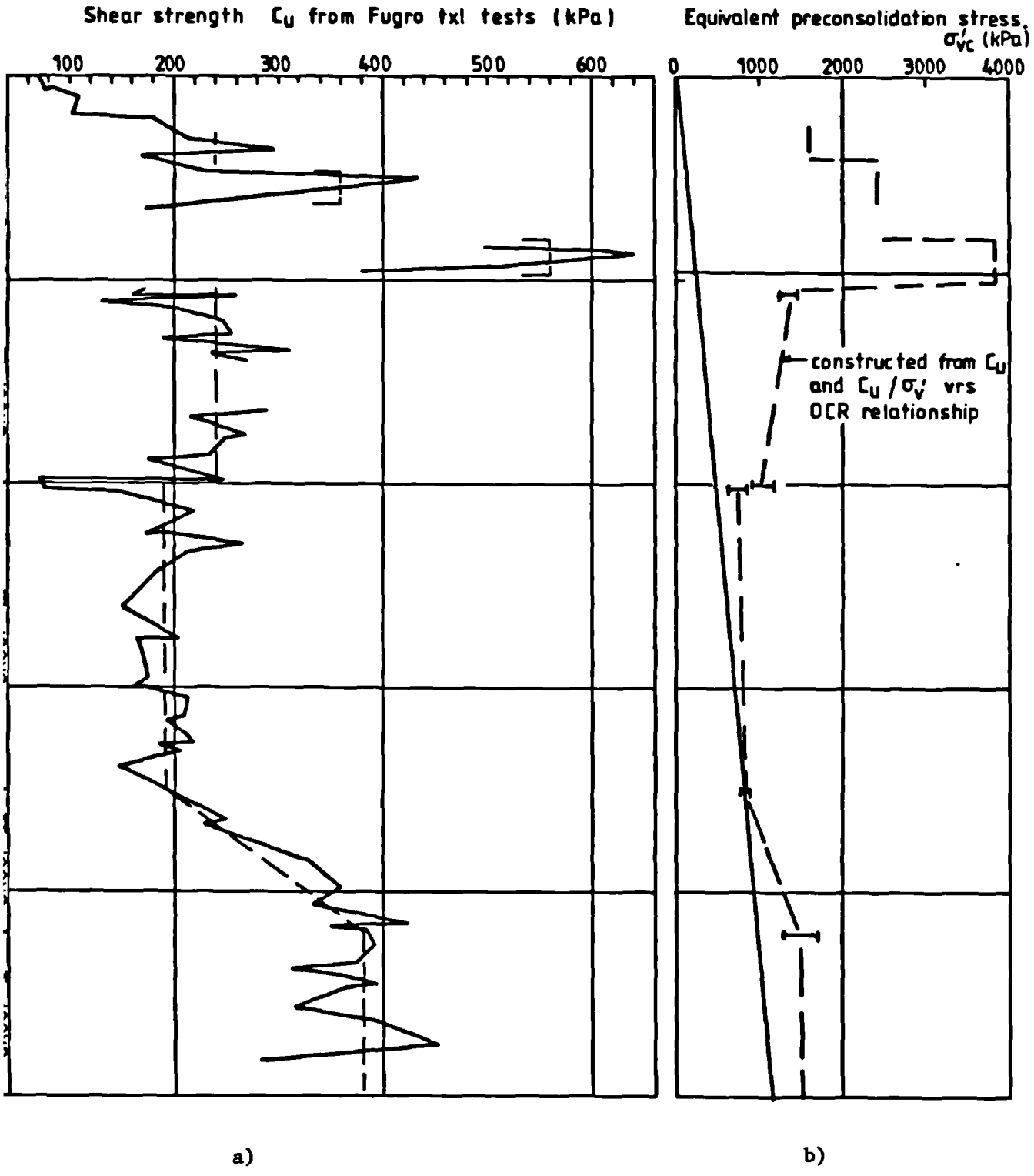


Figure 6.12. Undrained shear strength profile, Borehole 11.

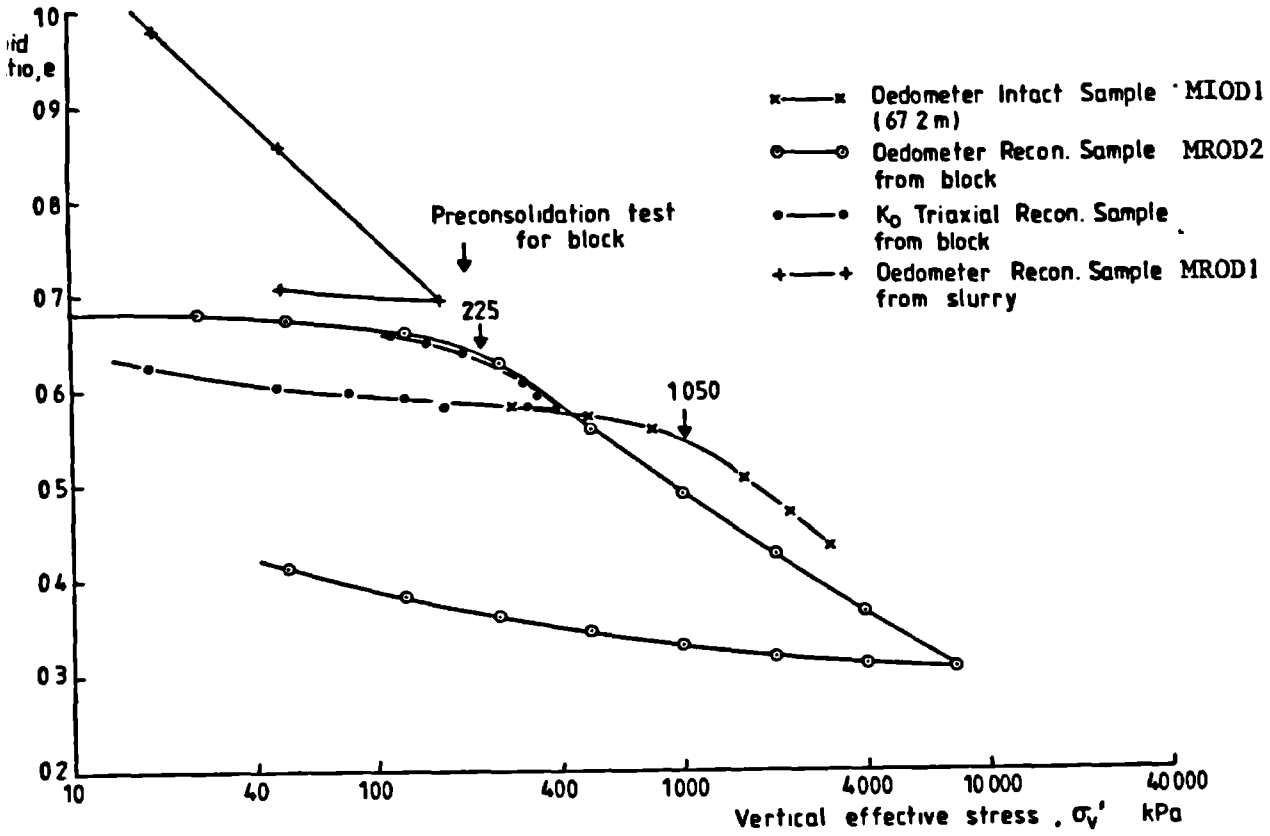


Figure 6.13. Voids ratio - log σ'_v curves for reconstituted Magnus clay and an intact sample from 67.2 metres depth.

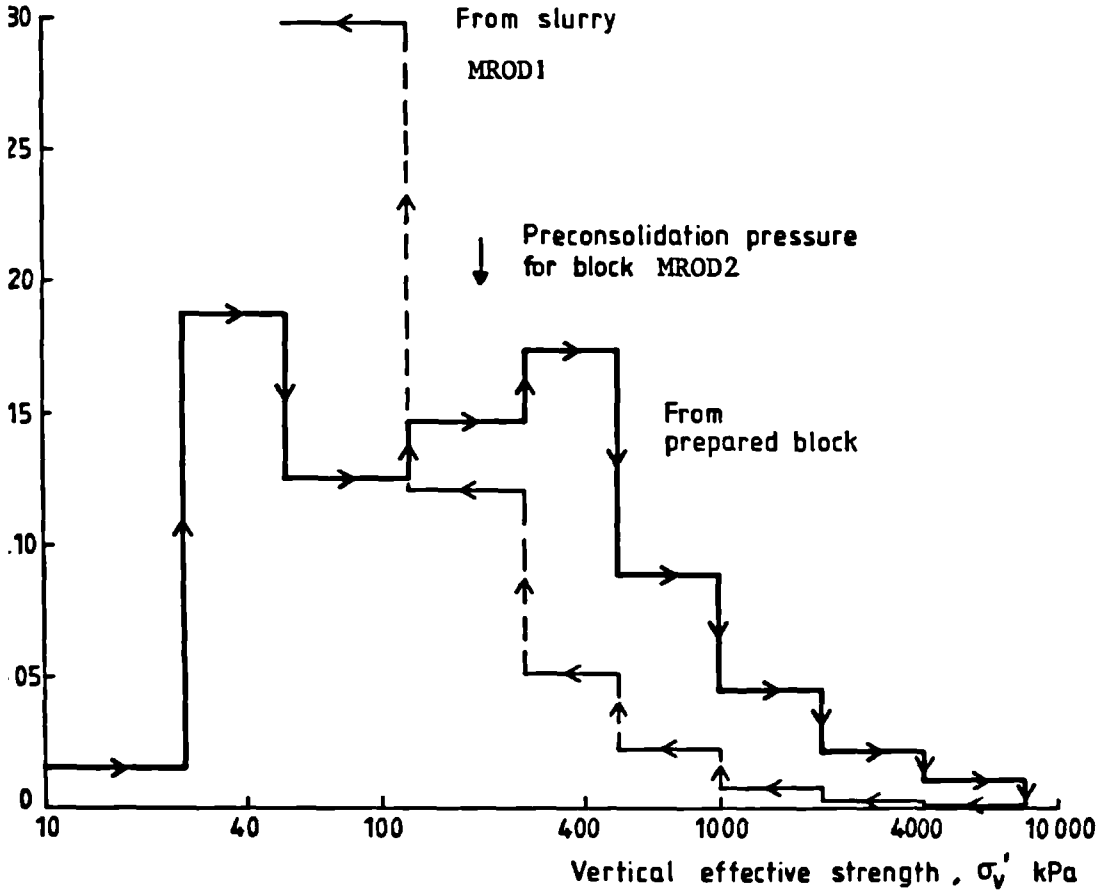


Figure 6.14 a). Compressibility - log σ'_v relationships, reconstituted

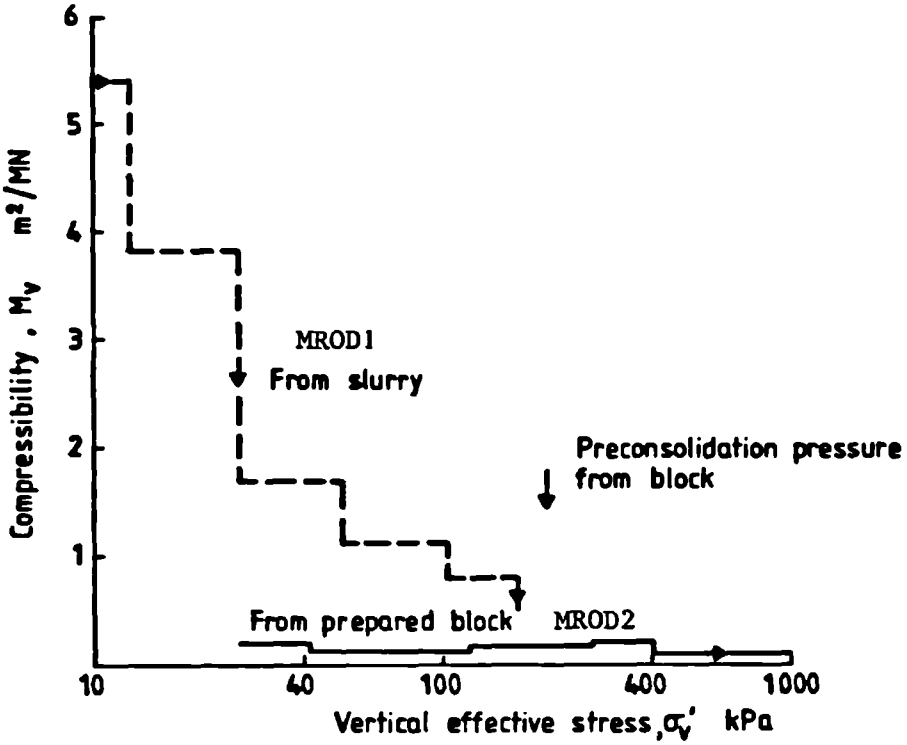


Figure 6.14 b). As 6.14 a) compressed scale showing slurry data at low pressures.

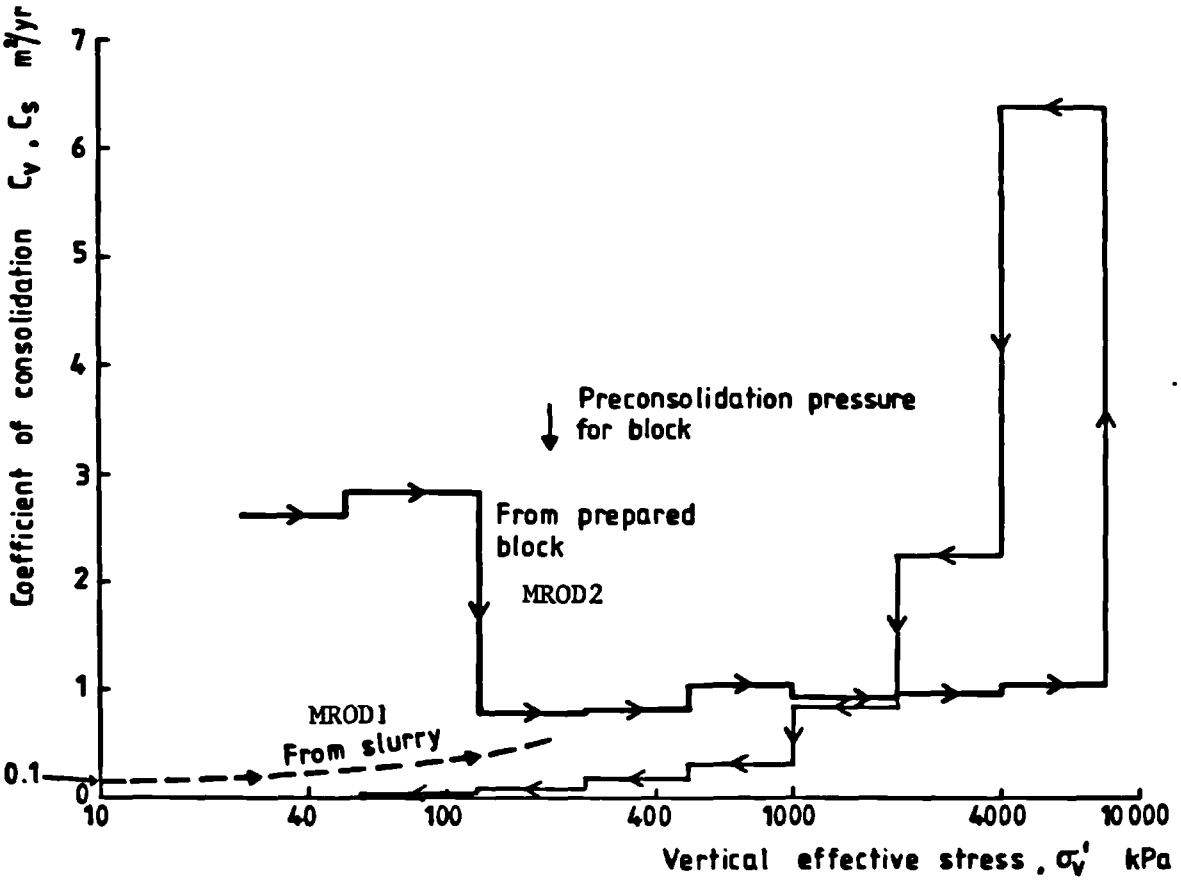


Figure 6.14 c). Consolidation coefficients varying with stress state, reconstituted Magnus clay.

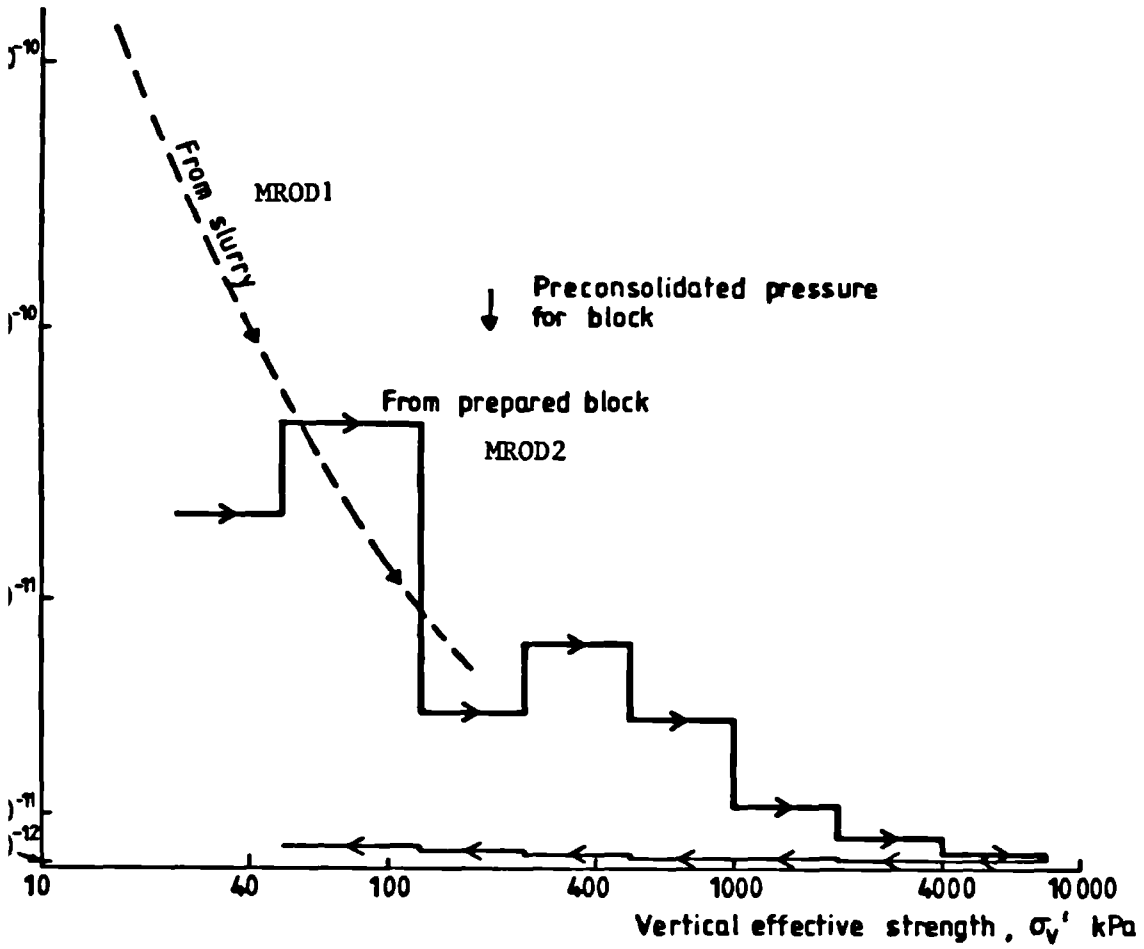


Figure 6.14 d). Permeability - log σ'_v relationships, reconstituted Magnus clay.

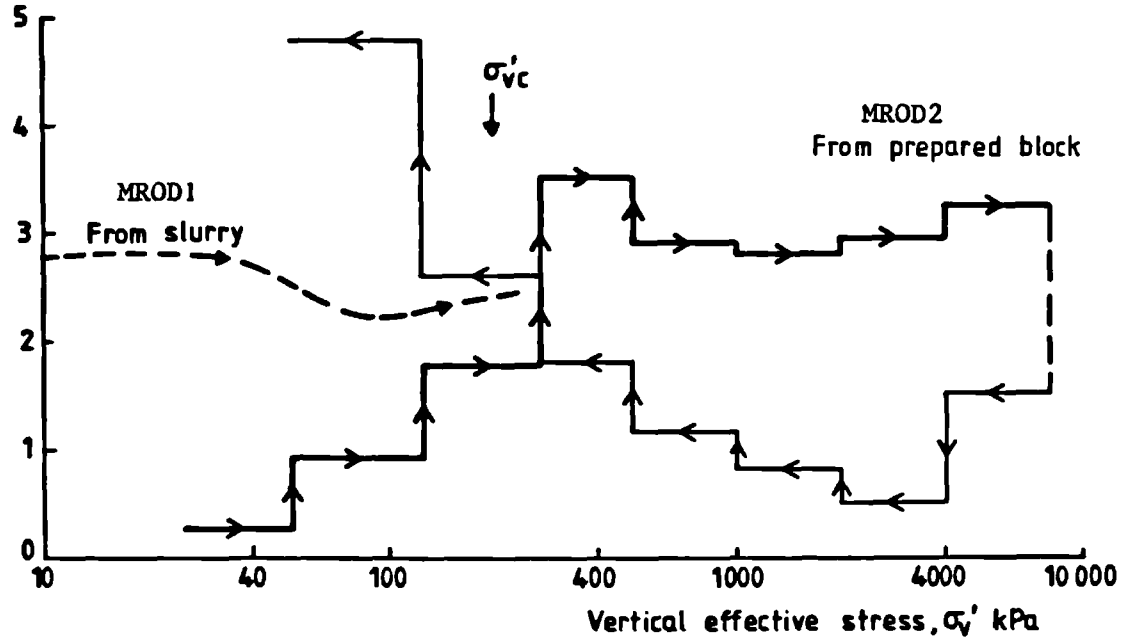


Figure 6.14 e). Secondary consolidation - log σ' relationships.

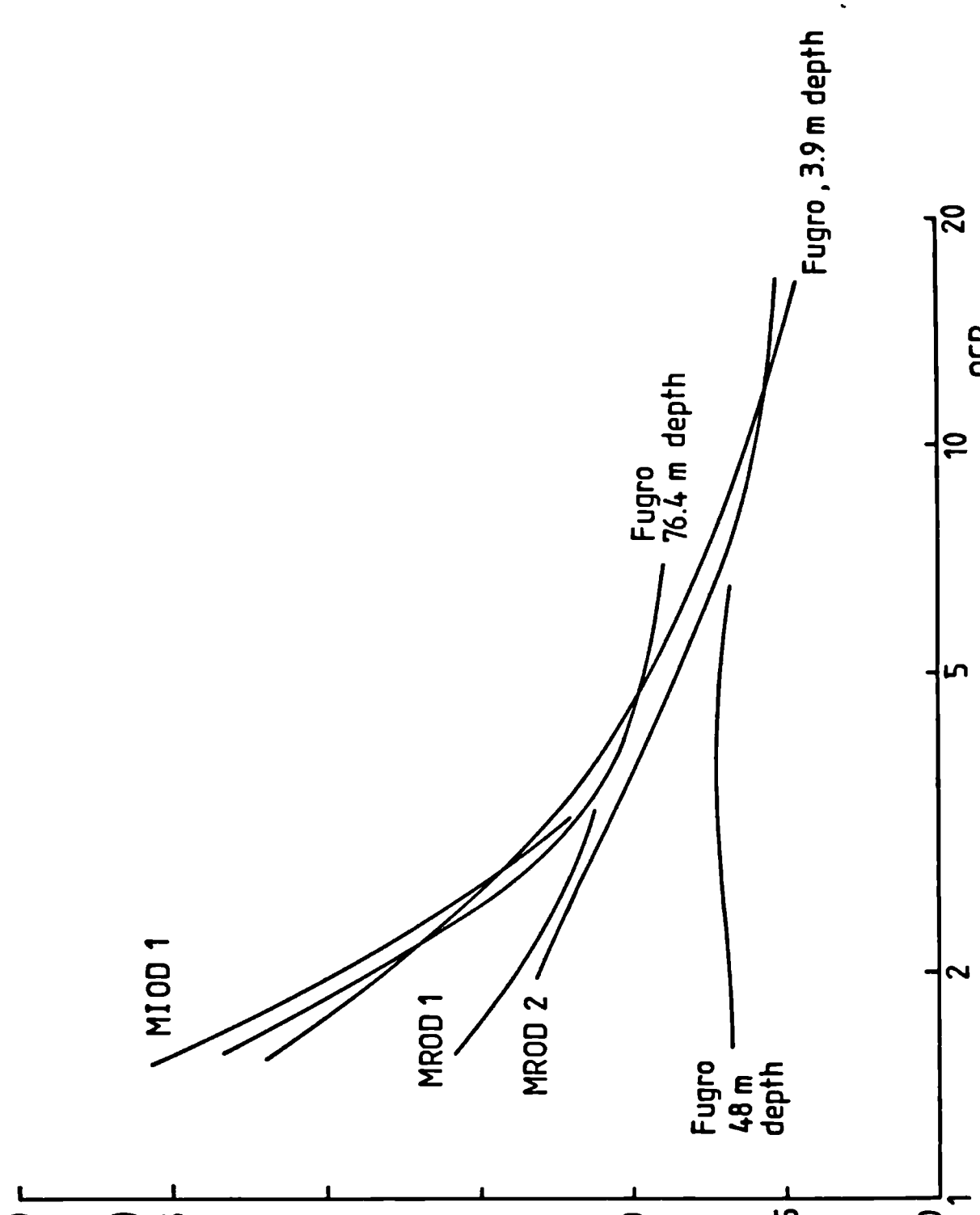
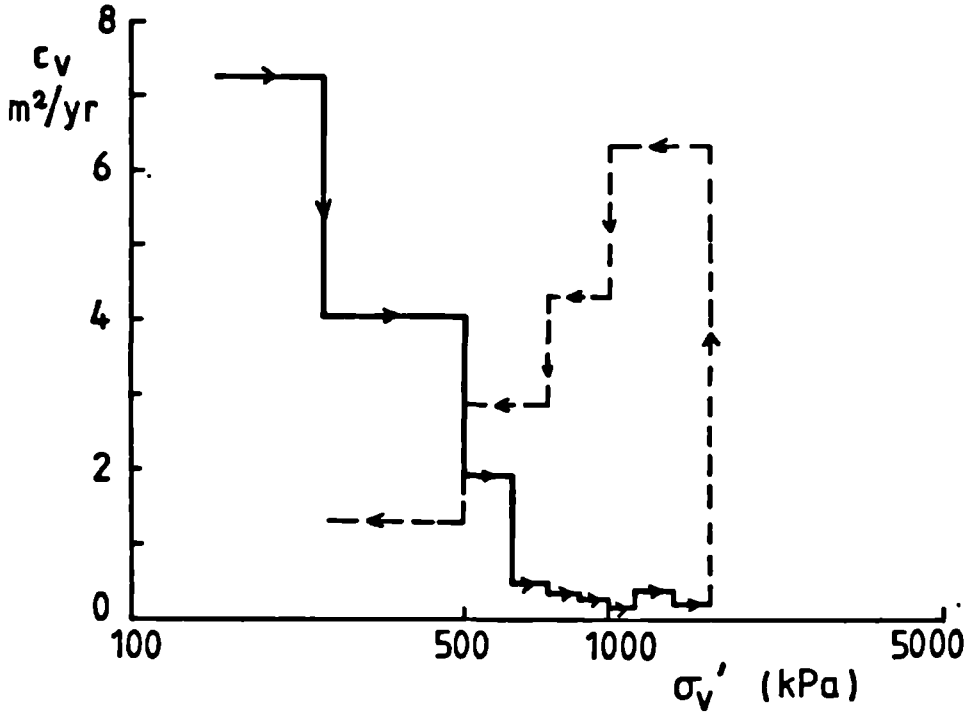


Figure 6.15 Ratio of compression to swelling index as a function of OCR.



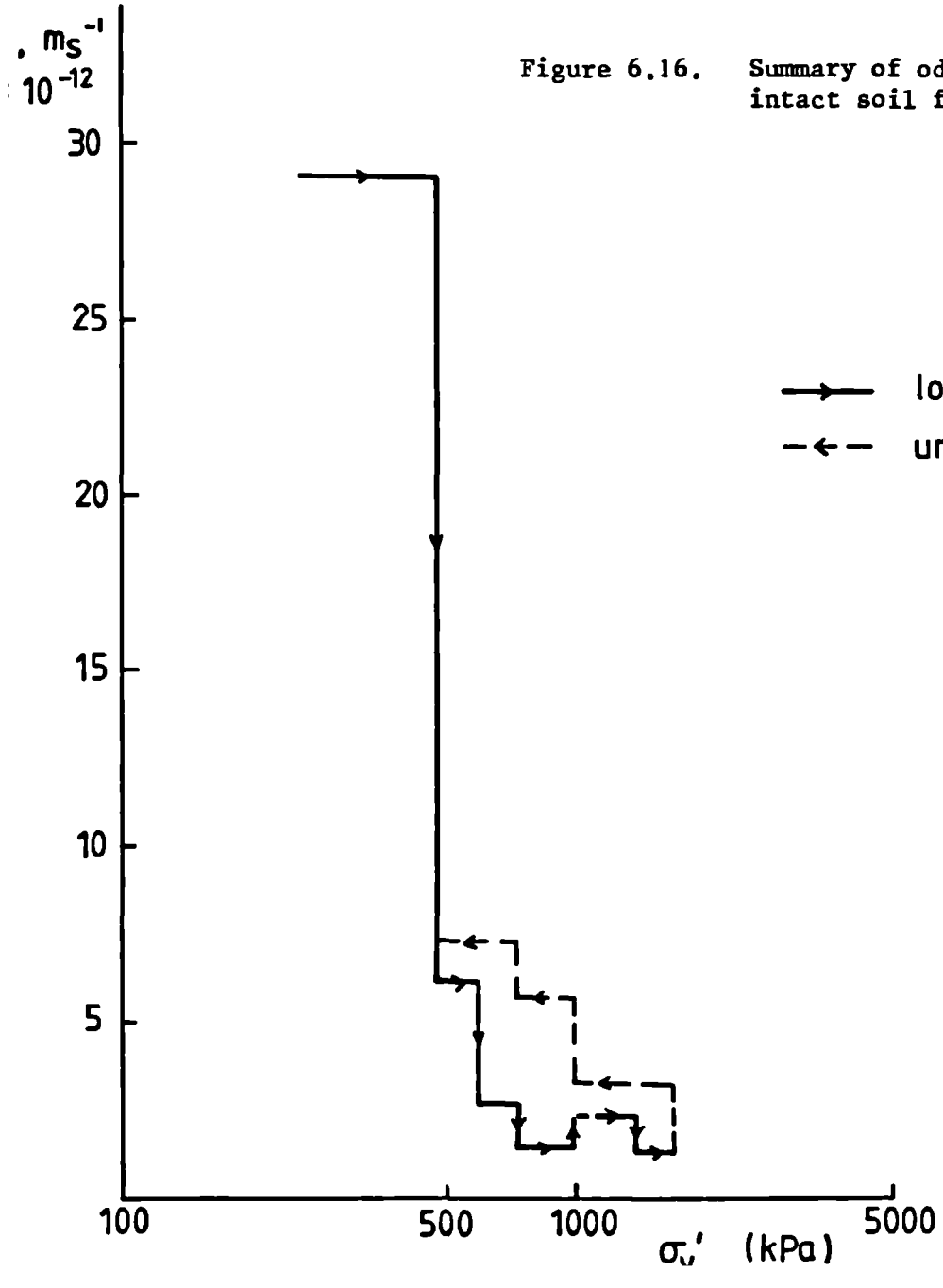


Figure 6.16. Summary of odometer test MIOD1, intact soil from 67.2 metres depth.

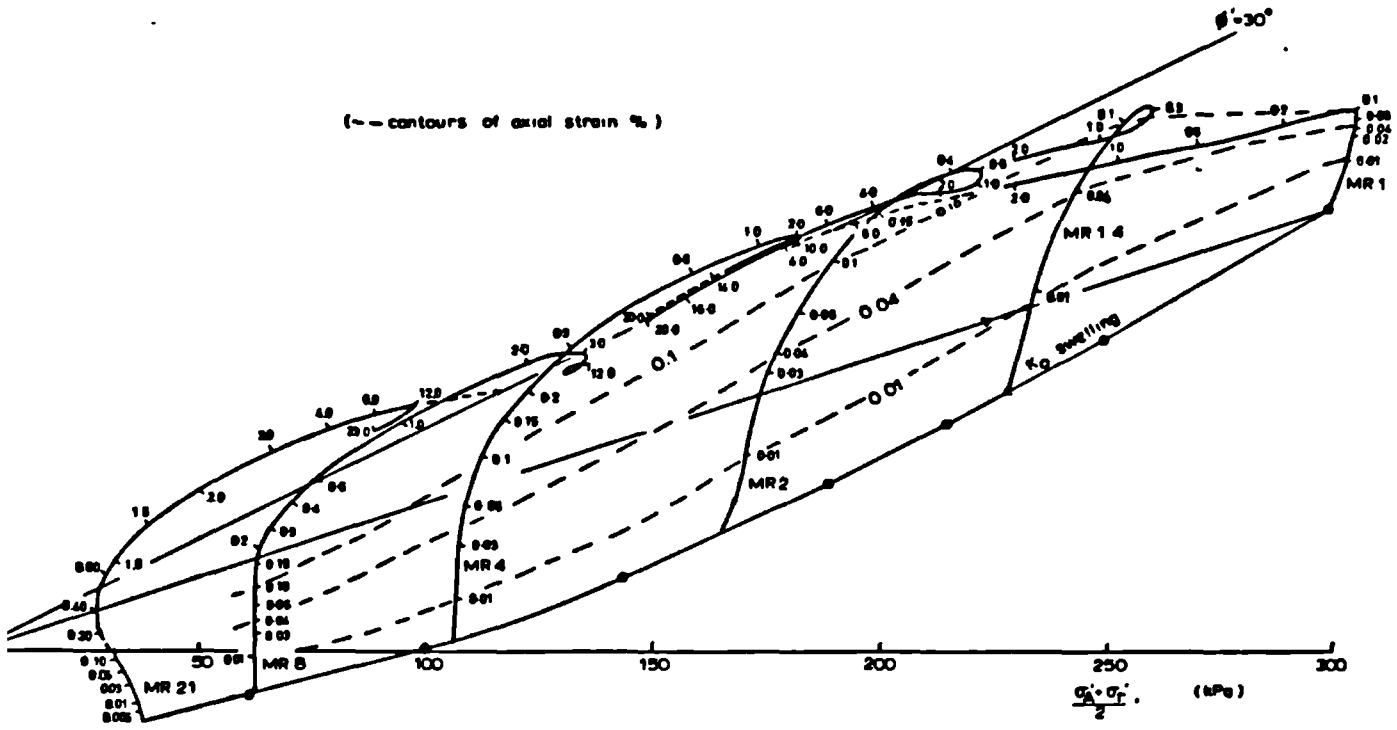


Figure 6.17 a). Effective stress paths during undrained shear, series MR.

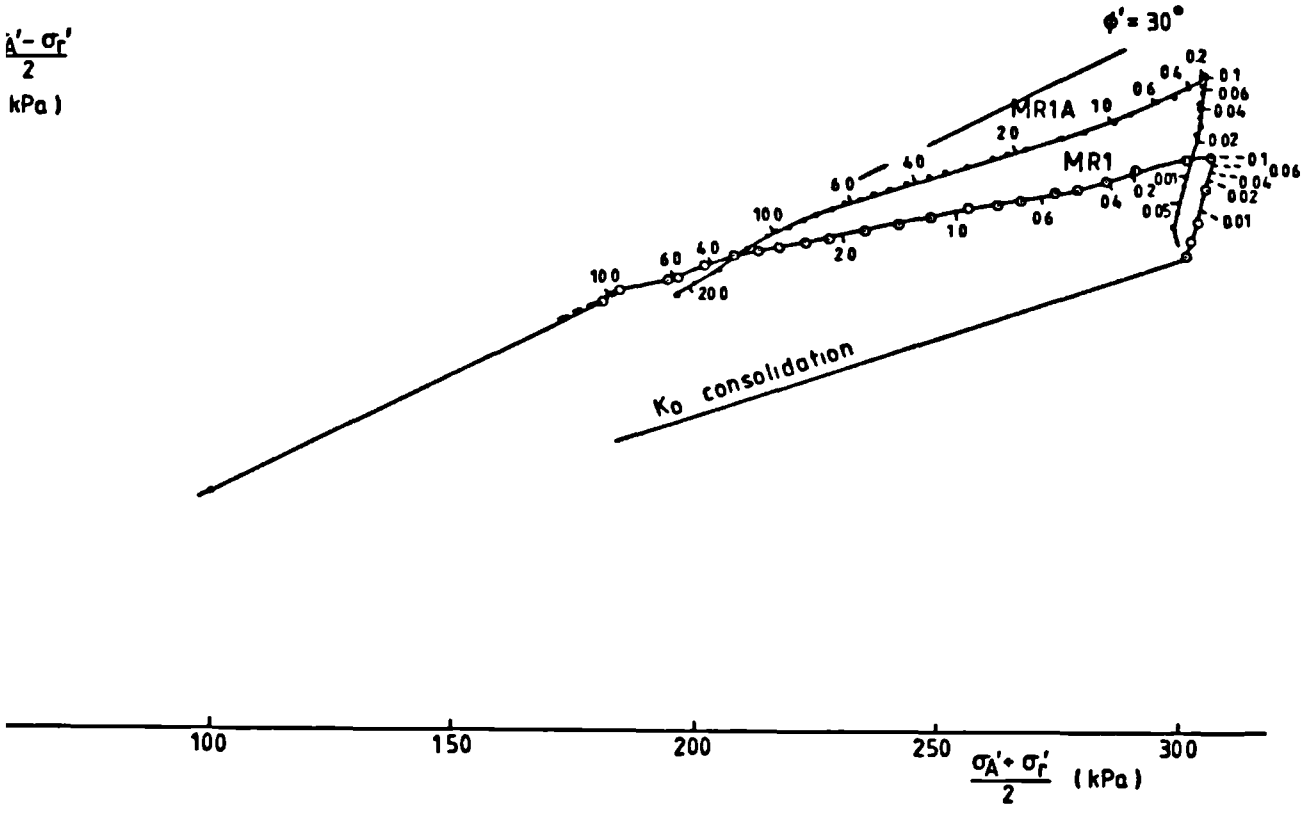


Figure 6.17 b). As above, showing effect of 20 days ageing for sample MR1A.

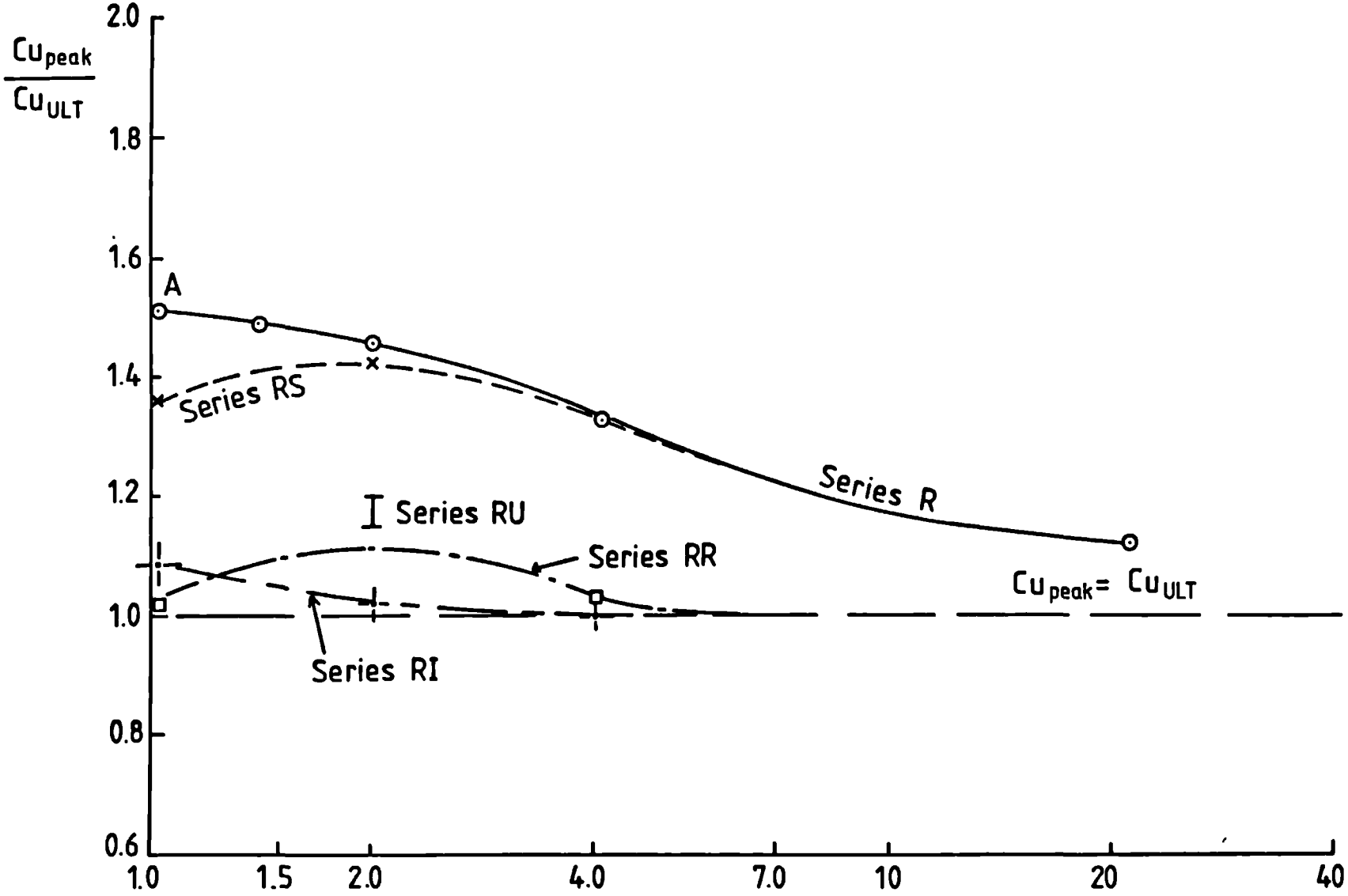


Figure 6.18. Undrained brittleness - OCR relationship for reconstituted Magnus clay.

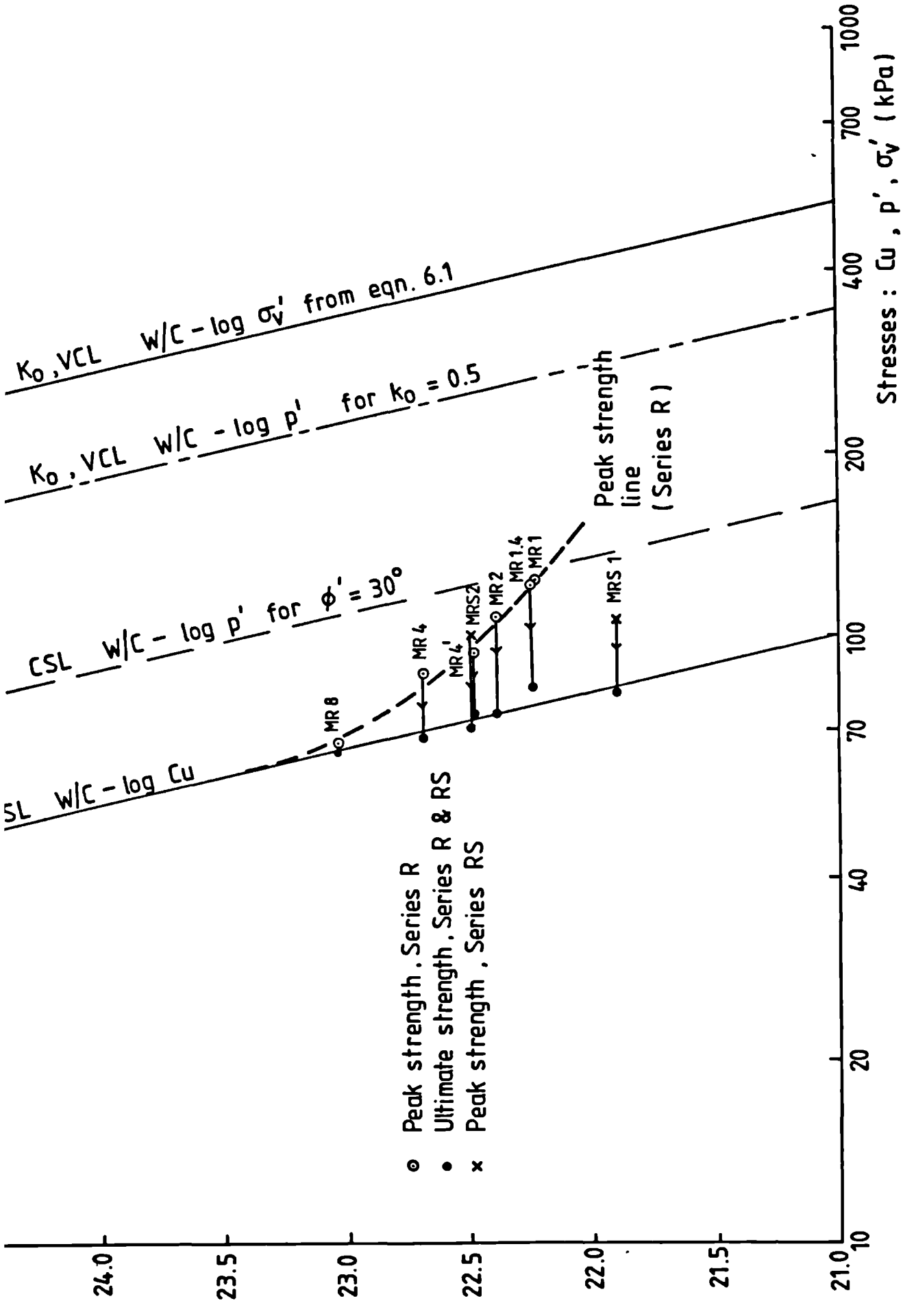
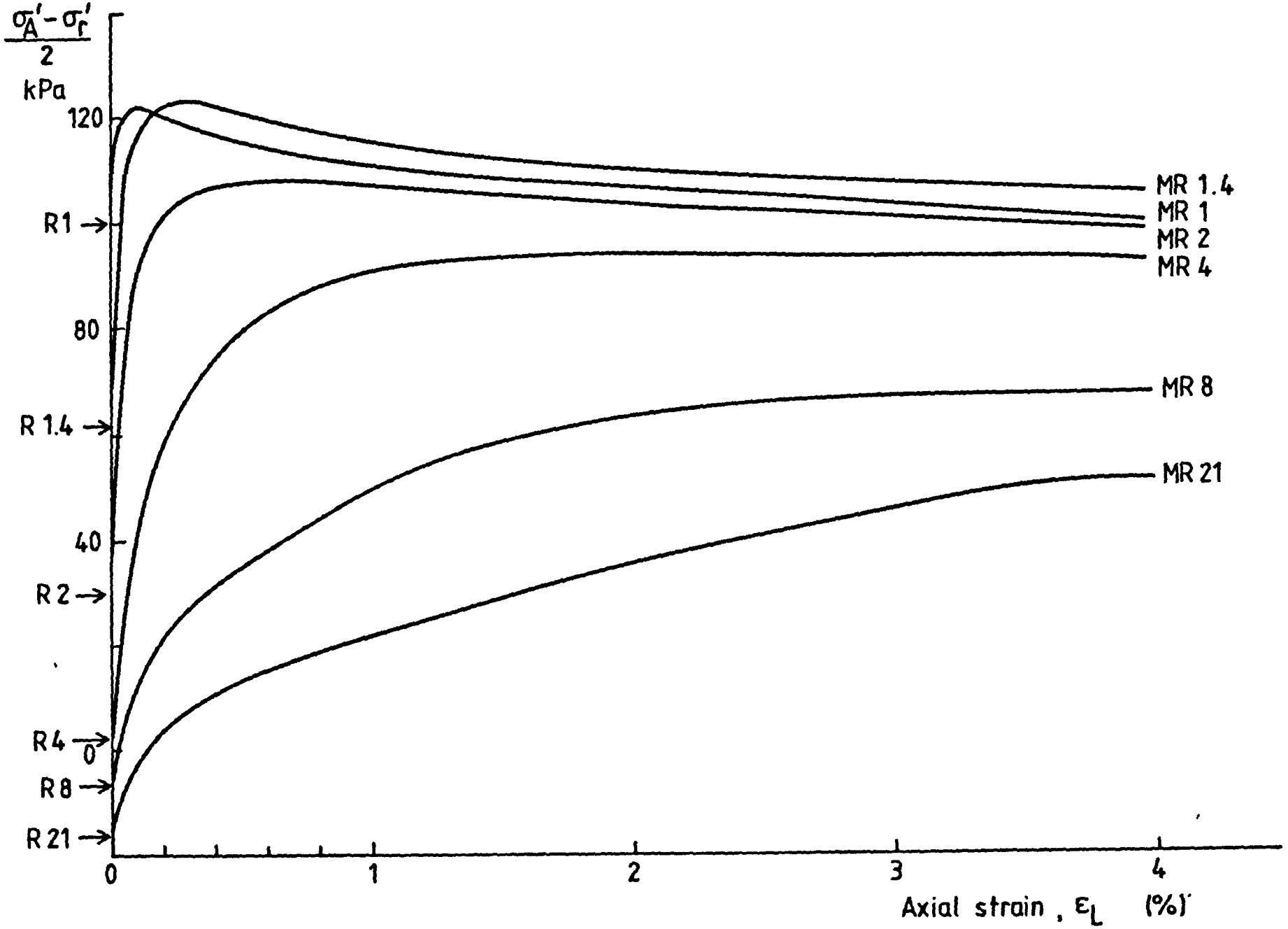


Figure 6.19. Strength - water content relationships.



Stress-strain data, series MR.

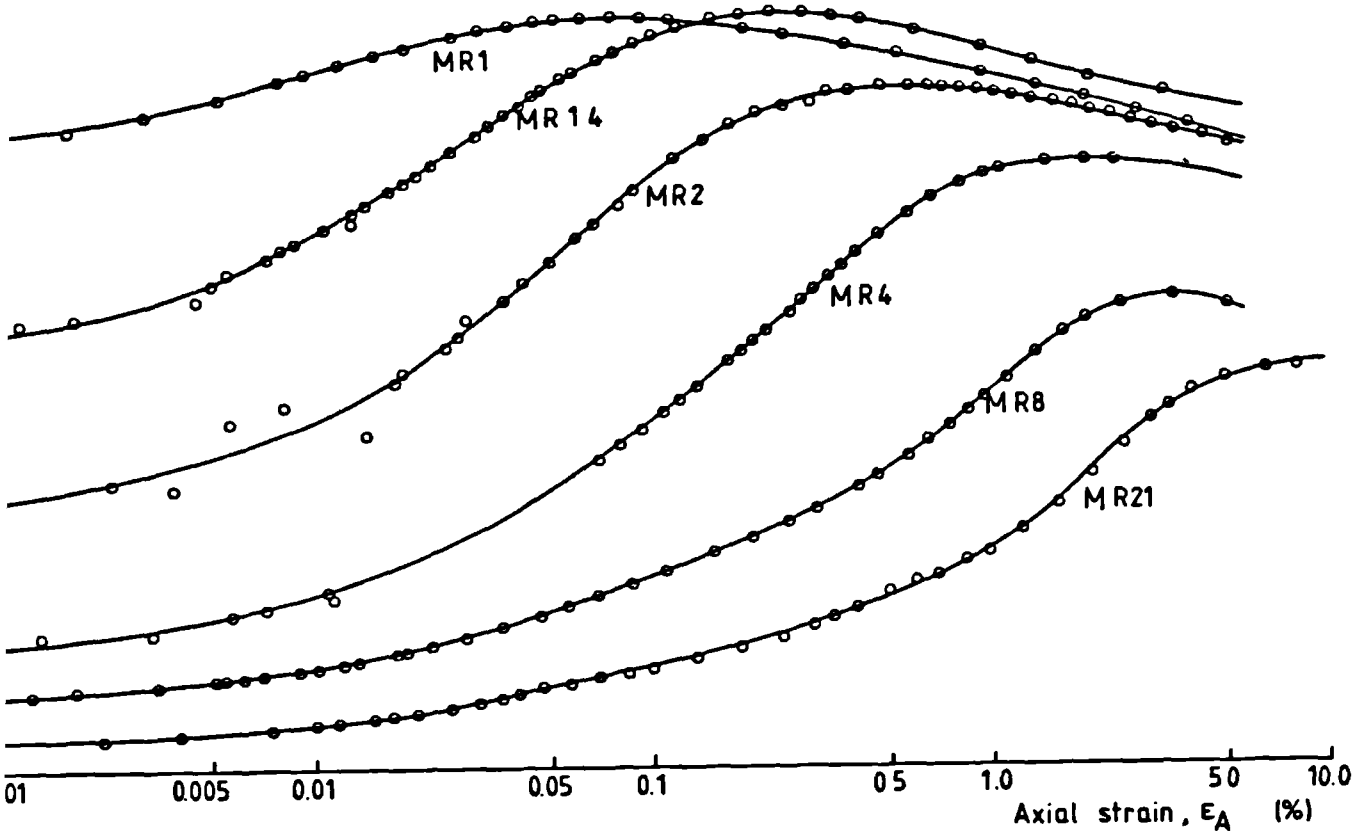


Figure 6.21 a). Stress - log strain data series MR.

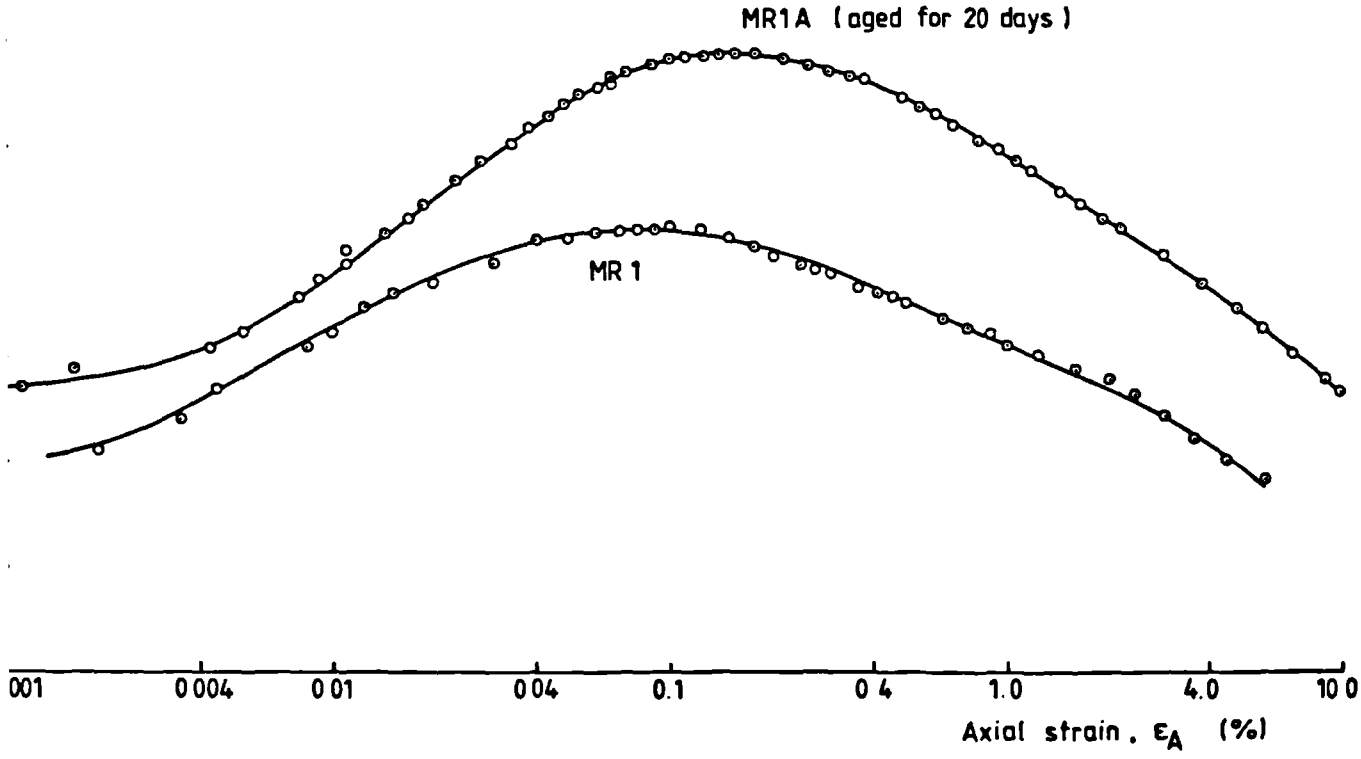


Figure 6.21 b). As above, showing effect of 20 days ageing for Sample MR1A.

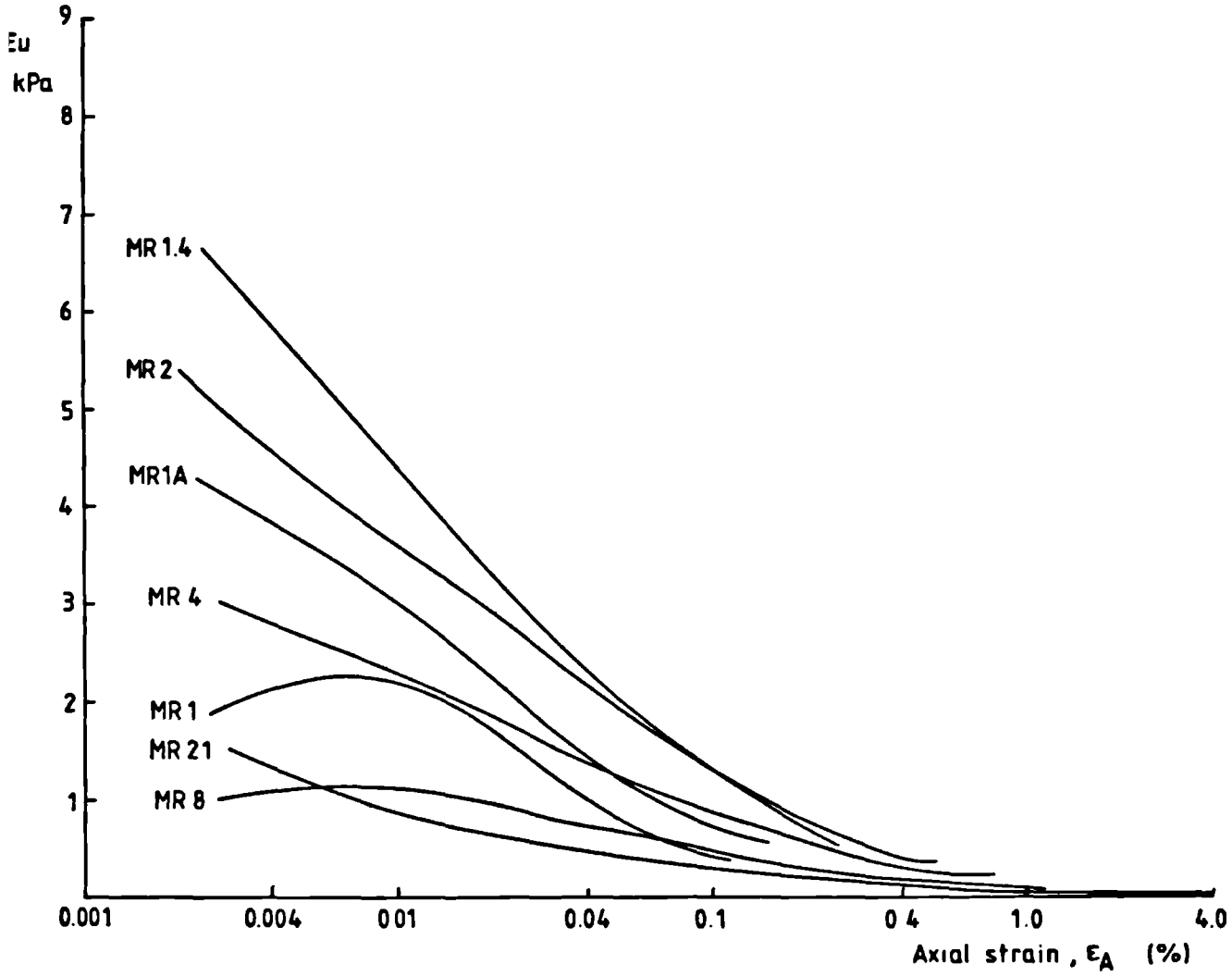


Figure 6.22. Secant modulus - strain characteristics.

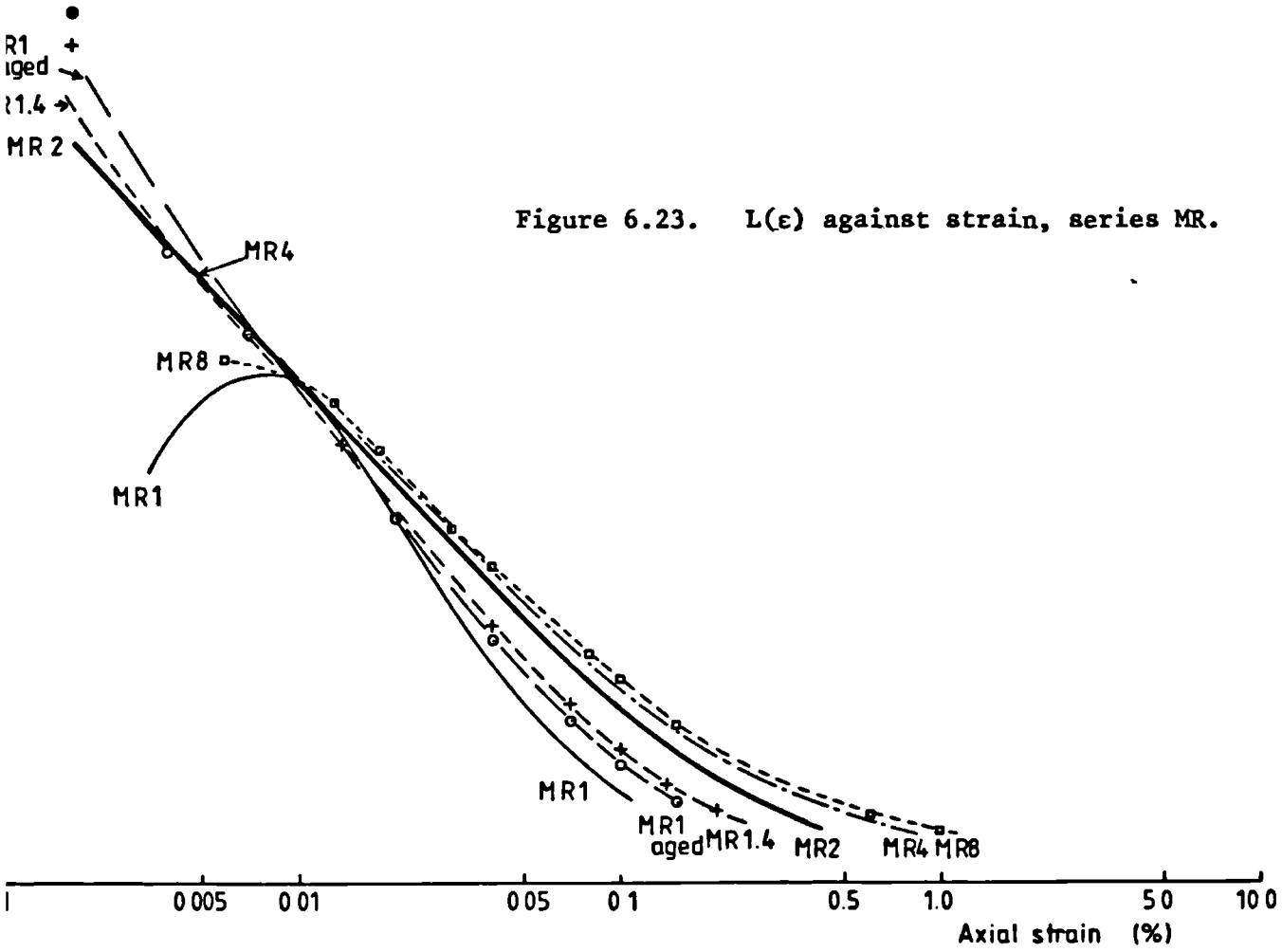


Figure 6.23. L(ε) against strain, series MR.

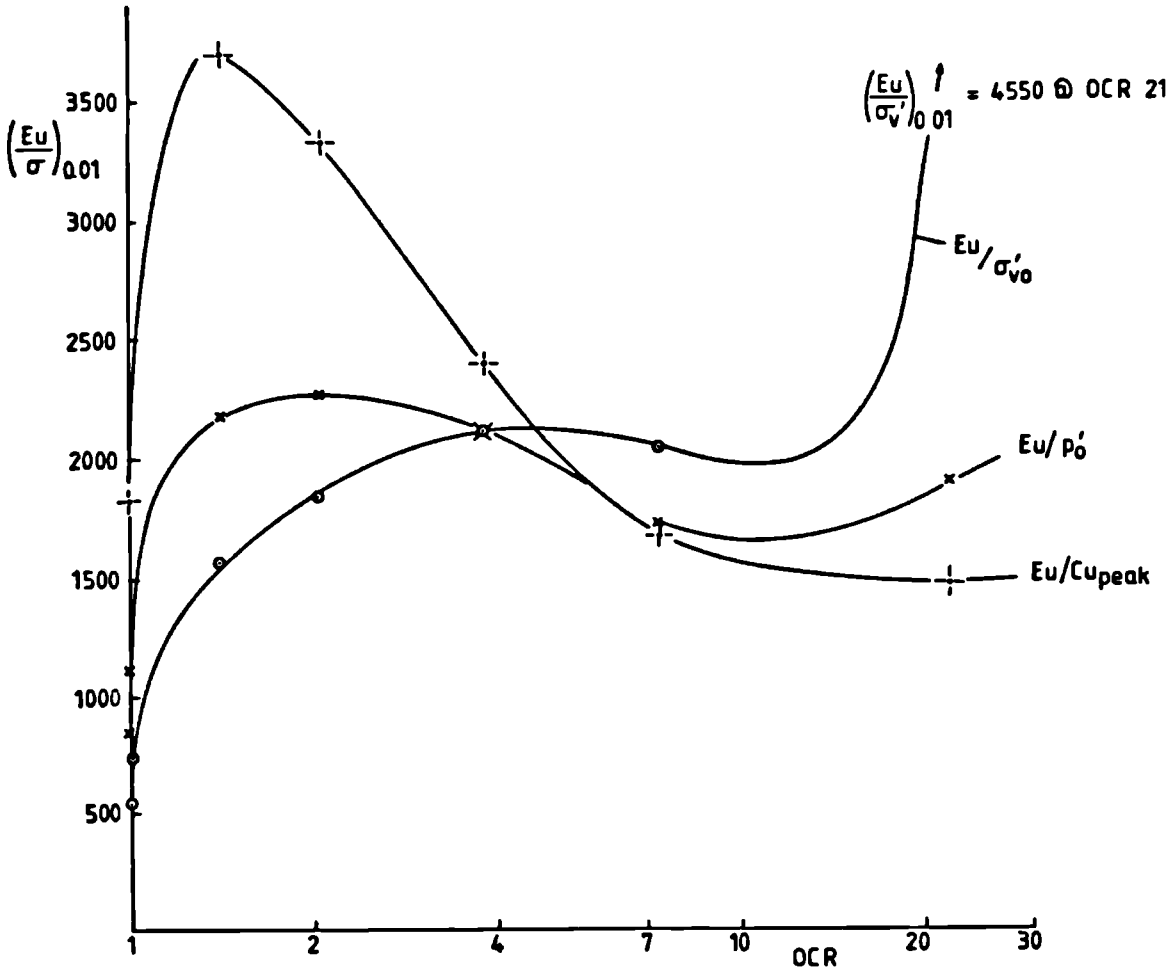


Figure 6.24. Normalised ratios of $E_{u/(\sigma_{0.01})}$ against OCR, series MR.

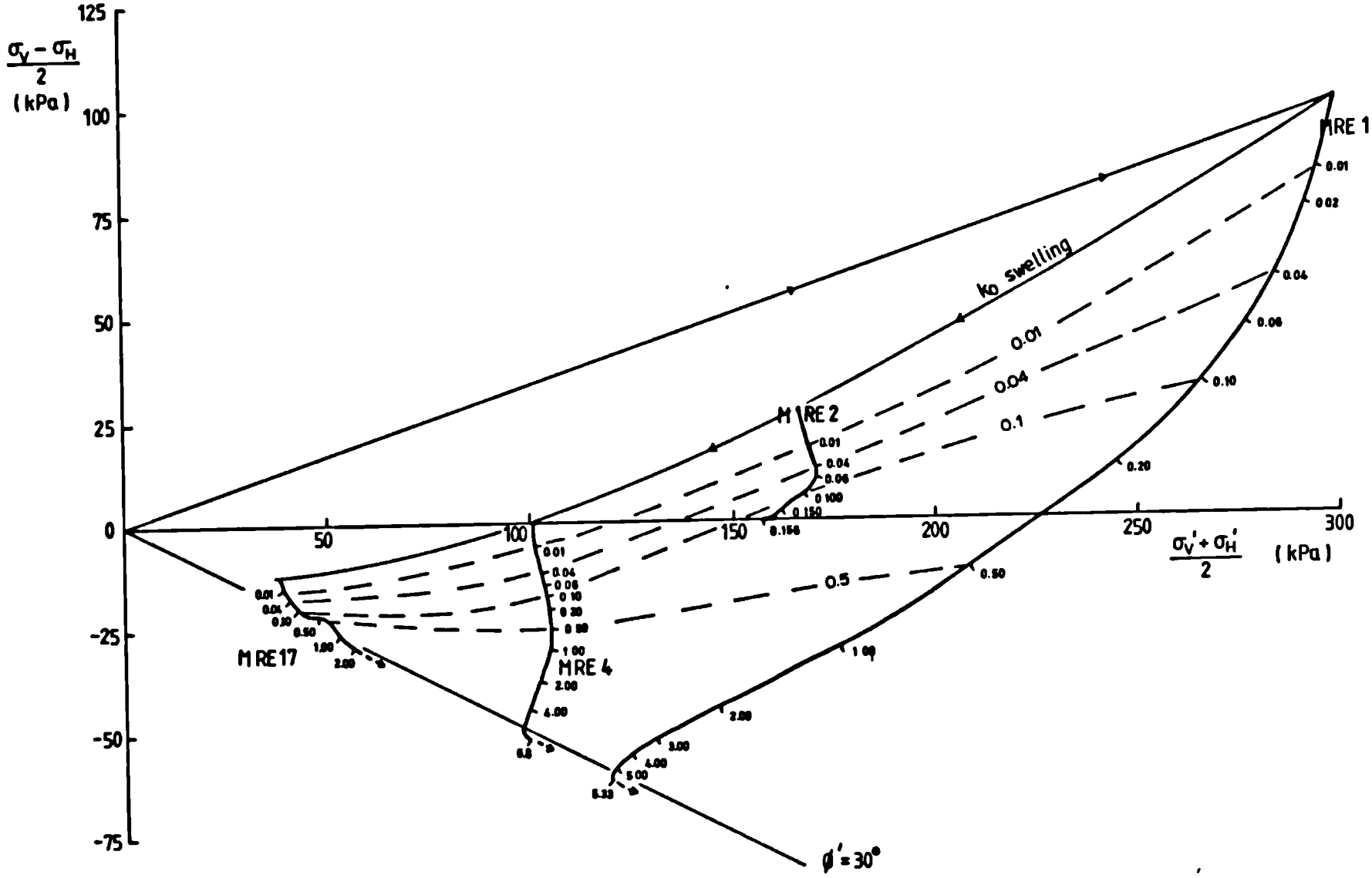


Figure 6.25. Effective stress paths during undrained shear, series MRE.

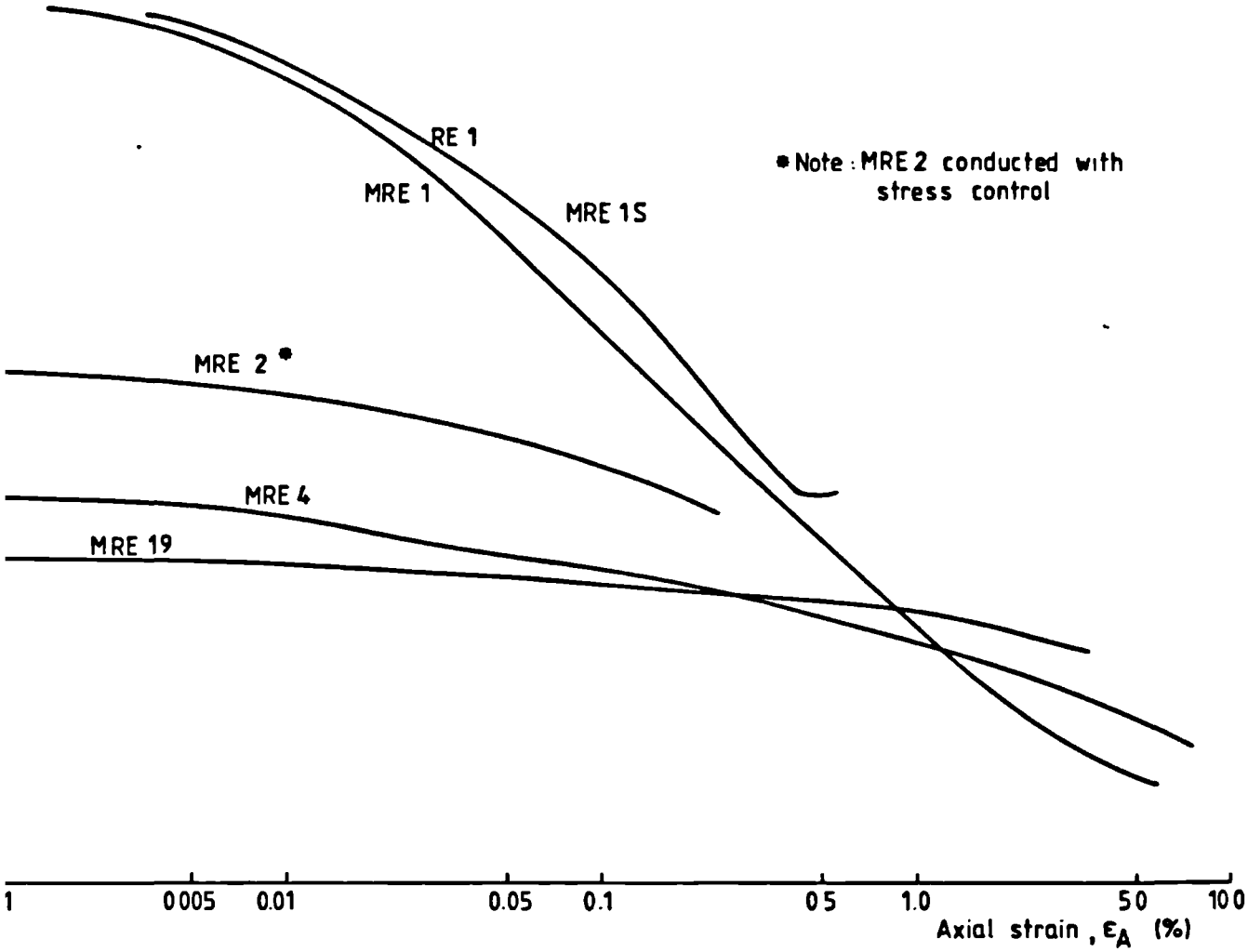
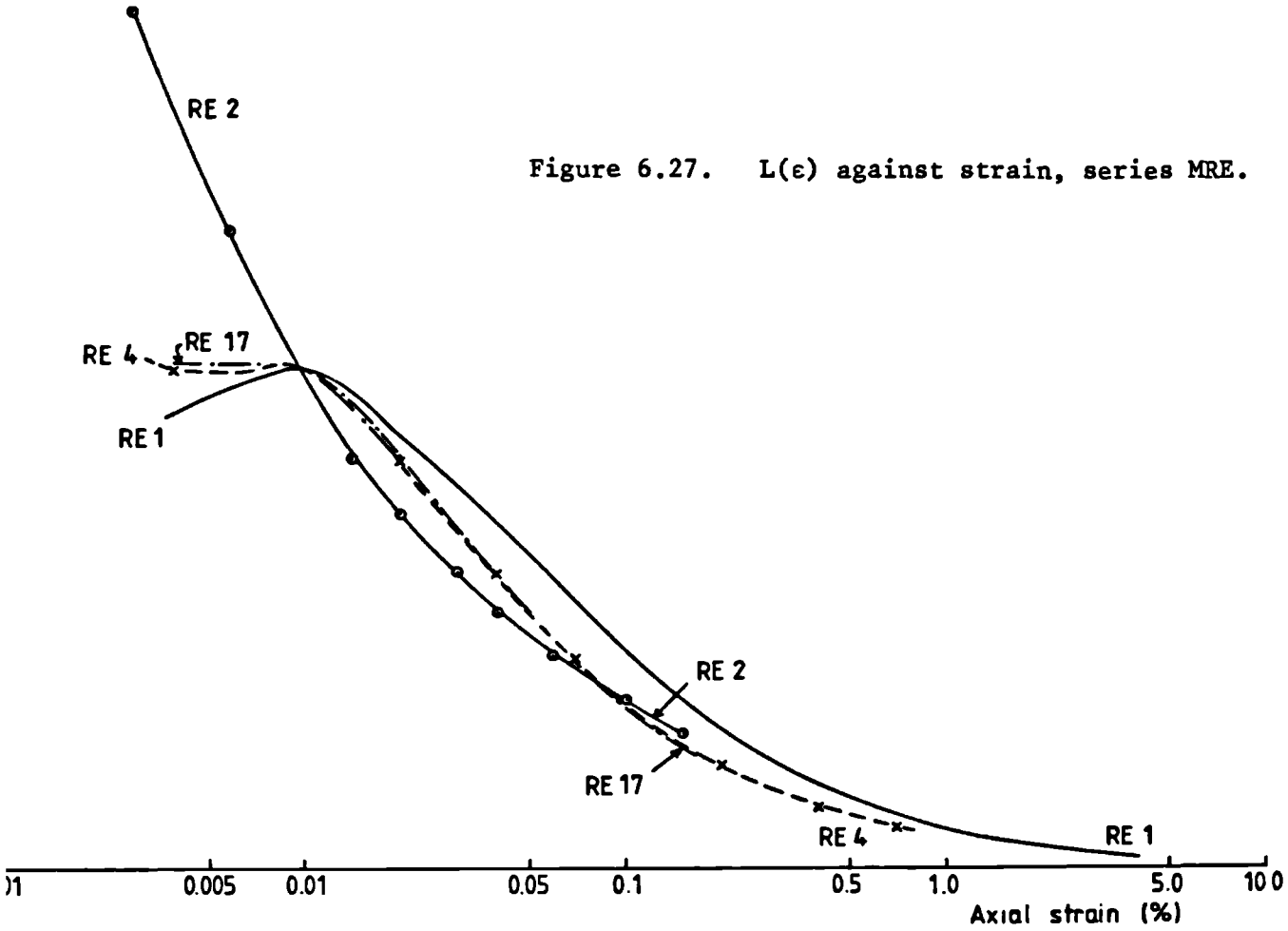


Figure 6.26. Stress - log strain data, series MRE.

Figure 6.27. L(ε) against strain, series MRE.



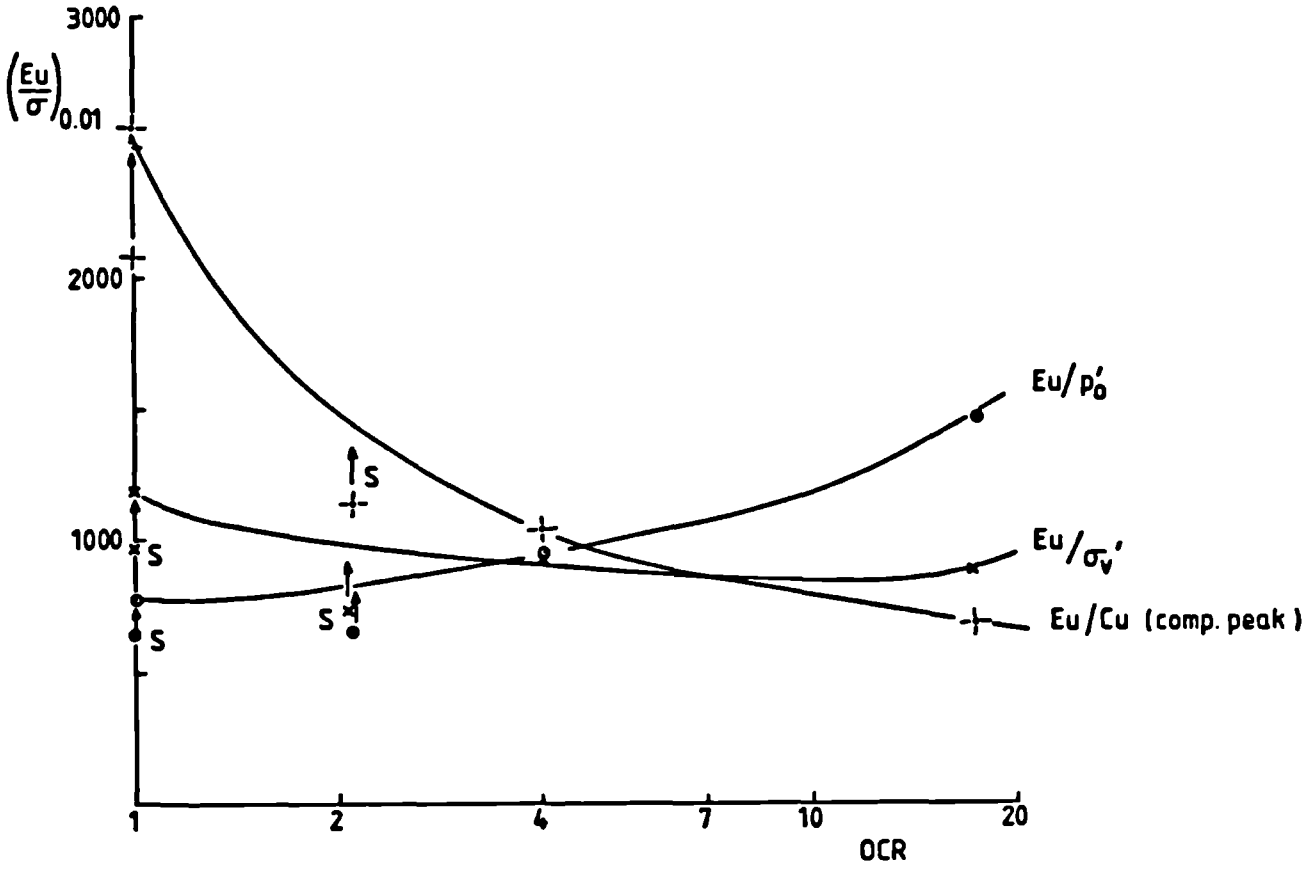


Figure 6.28. Normalised ratios of $E_{u(0.01)}$ against OCR, series MRE.

Figure 6.29. Effective stress paths, tests MRE 4 and MRE 4d.

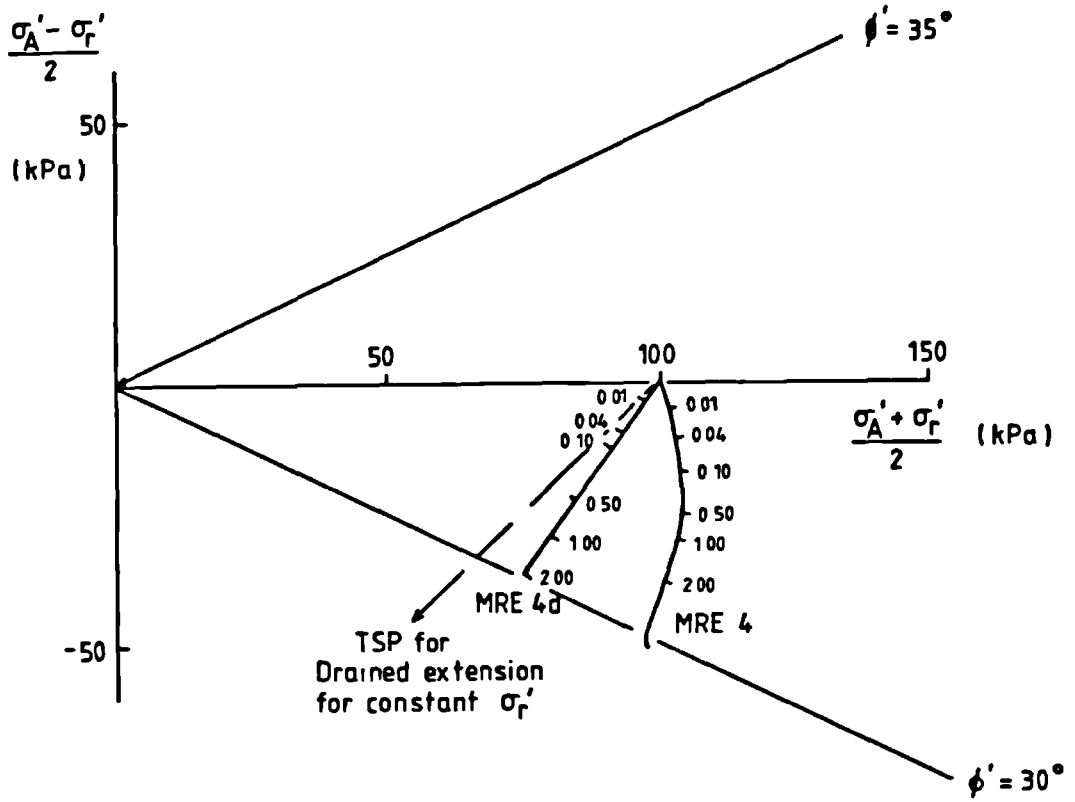
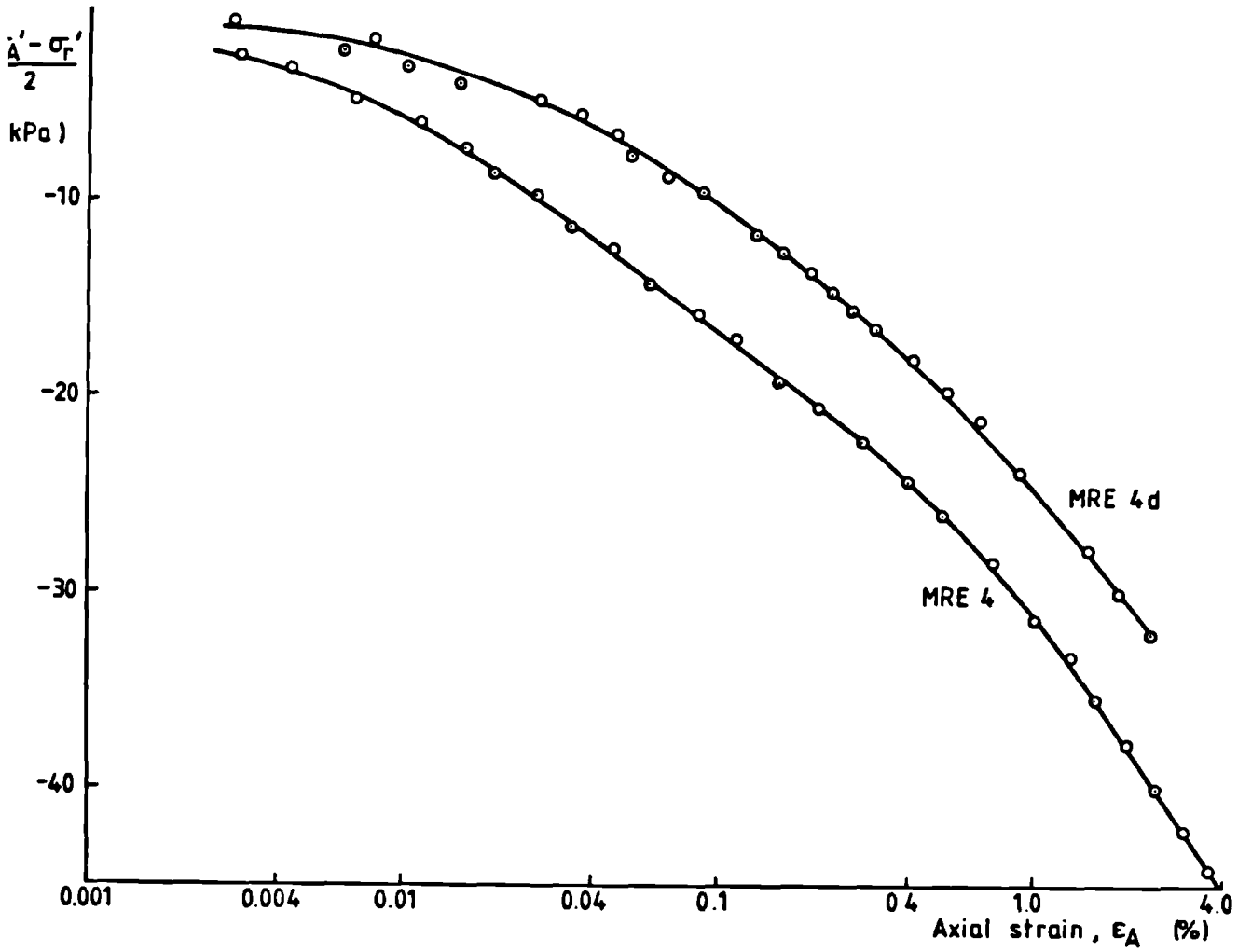


Figure 6.30. Stress - log strain data, tests MRE 4 and MRE 4d.



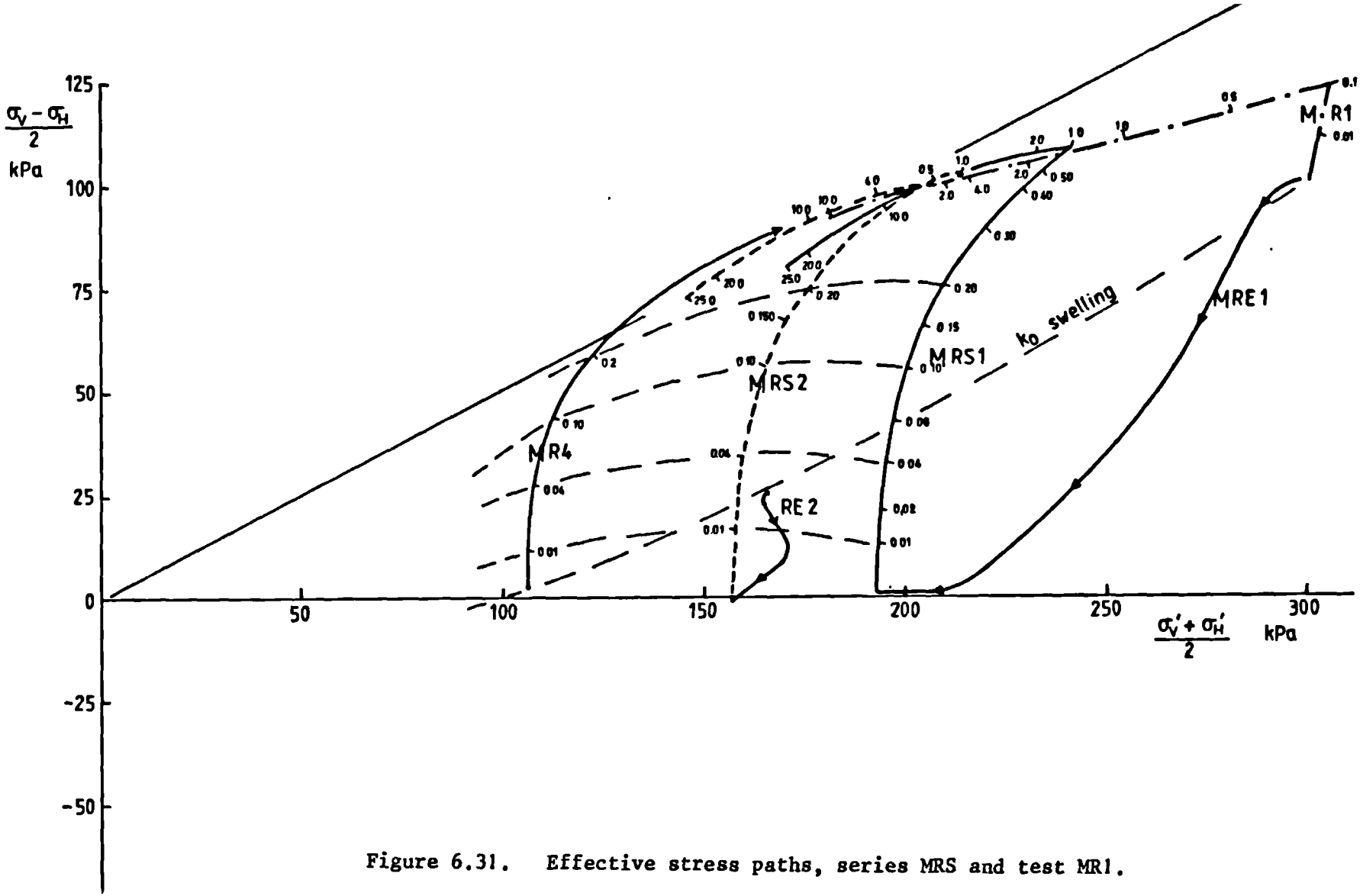


Figure 6.31. Effective stress paths, series MRS and test MR1.

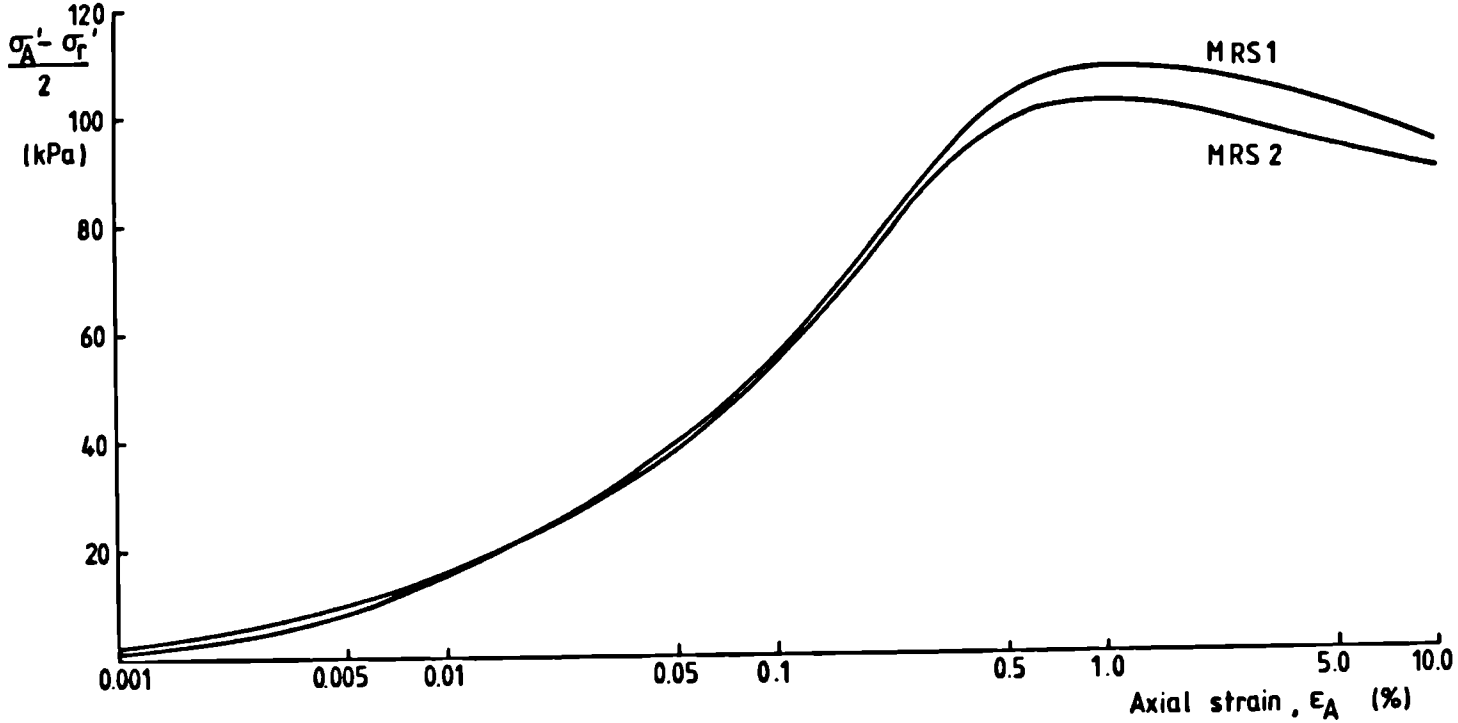


Figure 6.32. Stress - log strain data, series MRS.

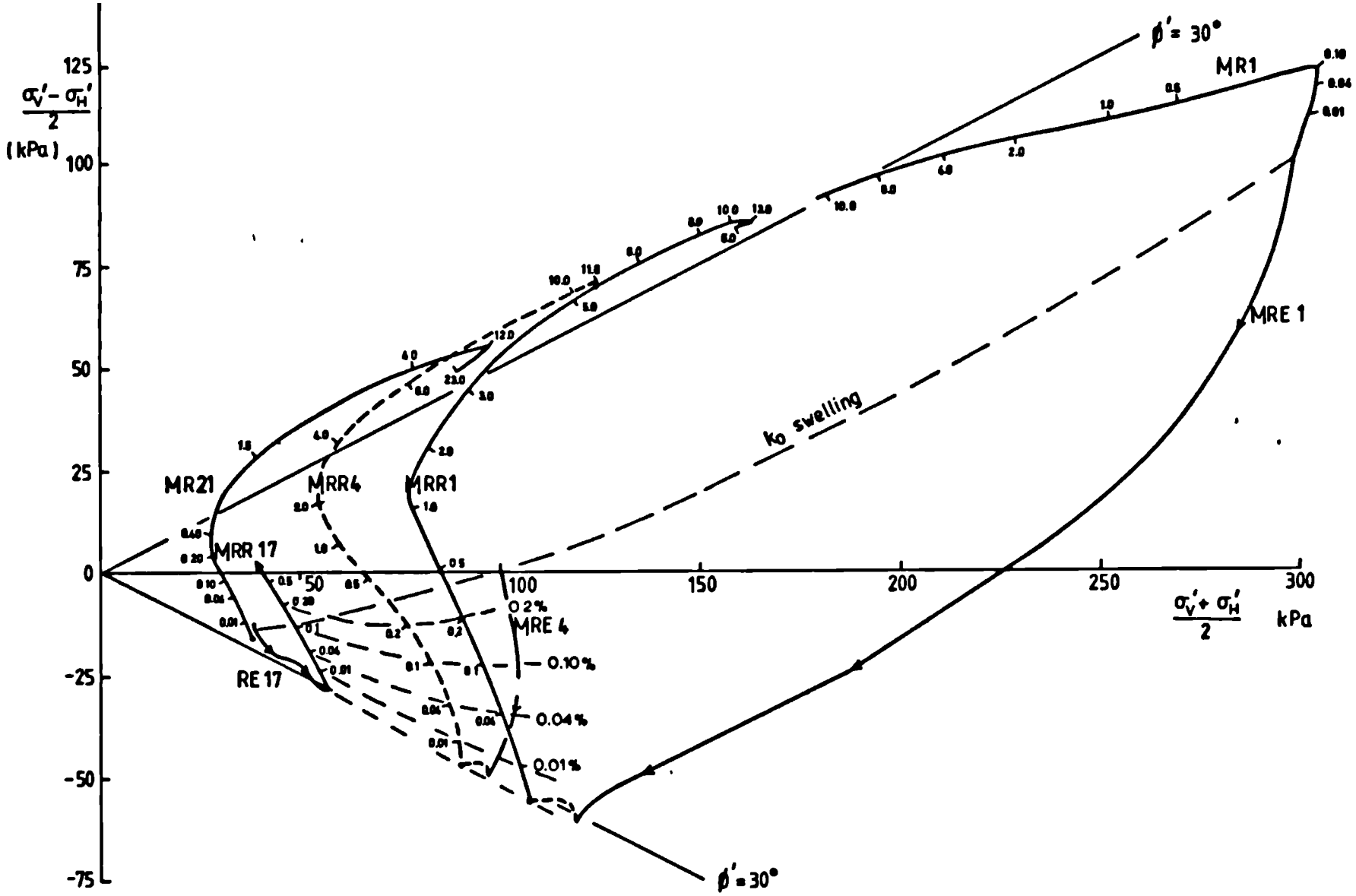
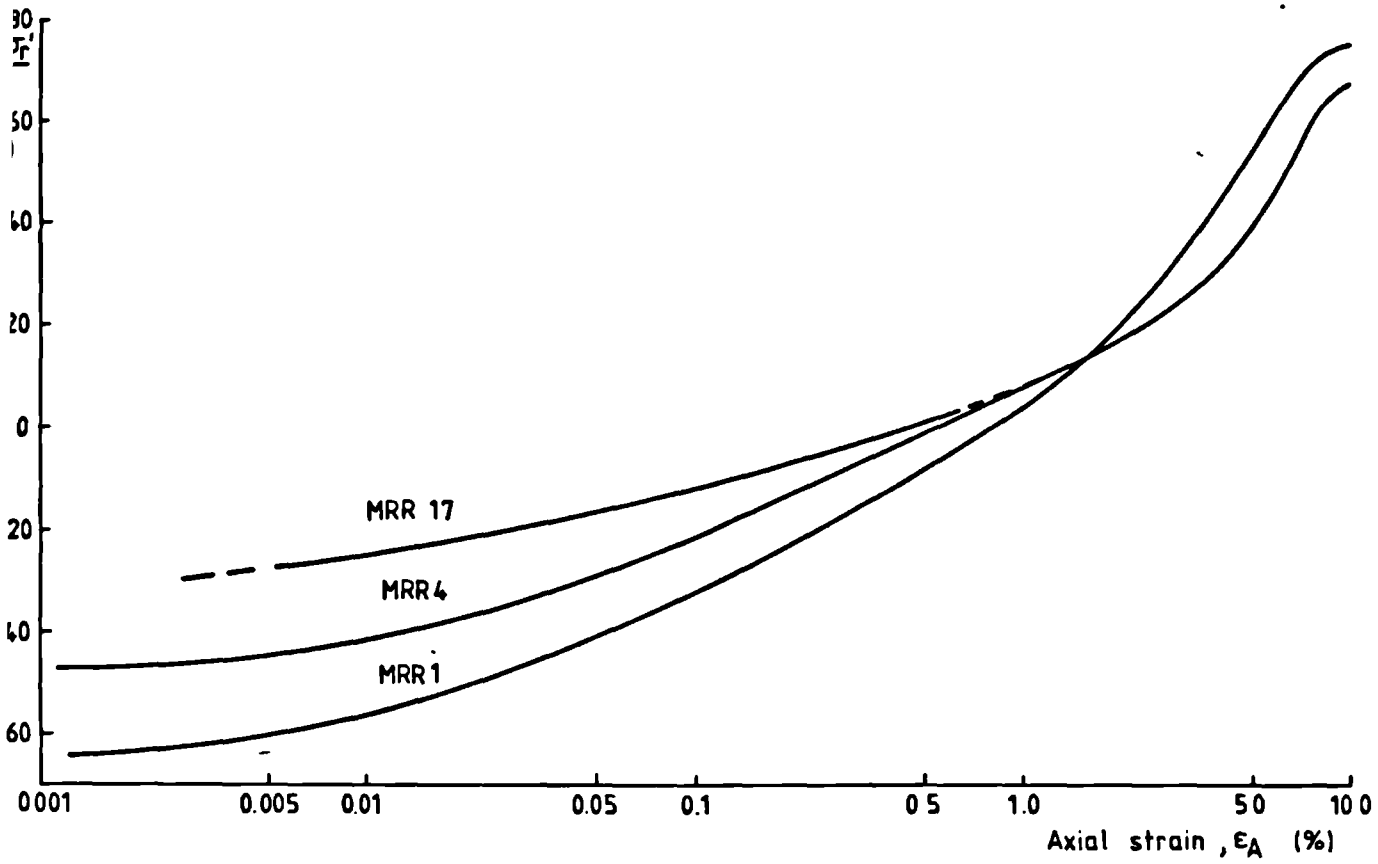


Figure 6.33. Effective stress paths, series MRR and test MR1.

Figure 6.34. Stress - log strain data, series MRR.



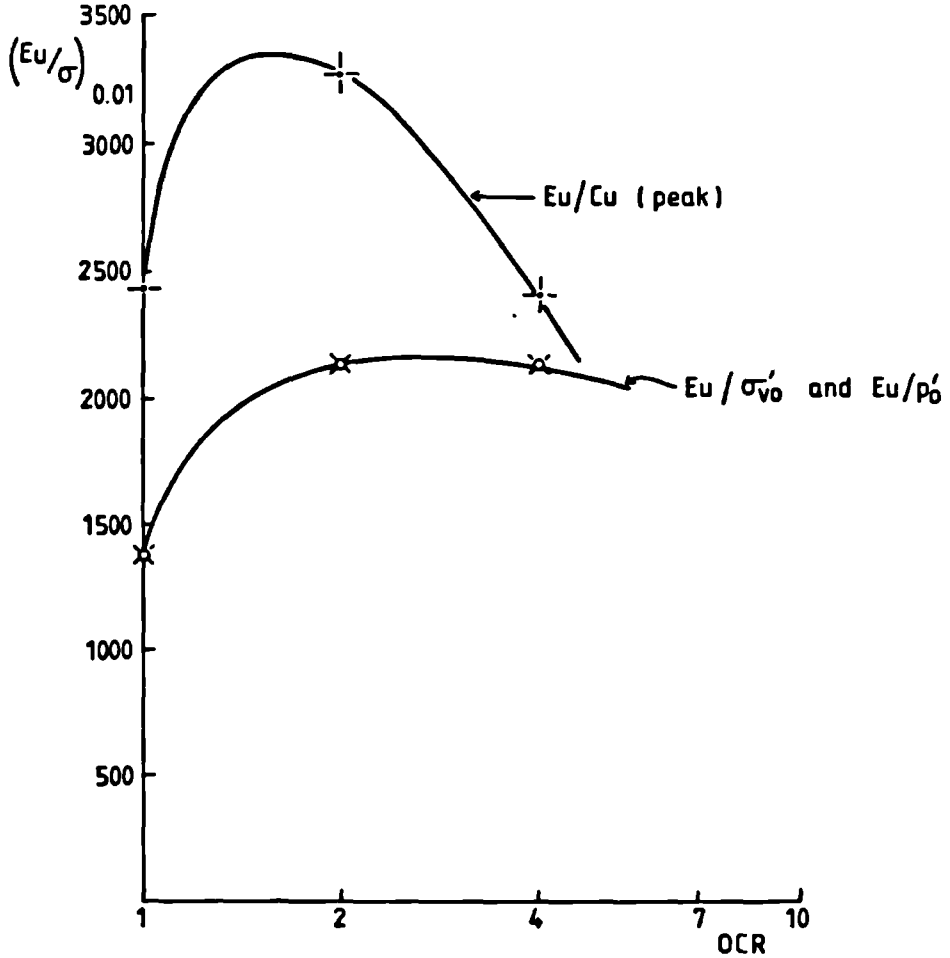


Figure 6.35. Normalised ratios of $E_{u(0.01)}$ against OCR, series MRS.

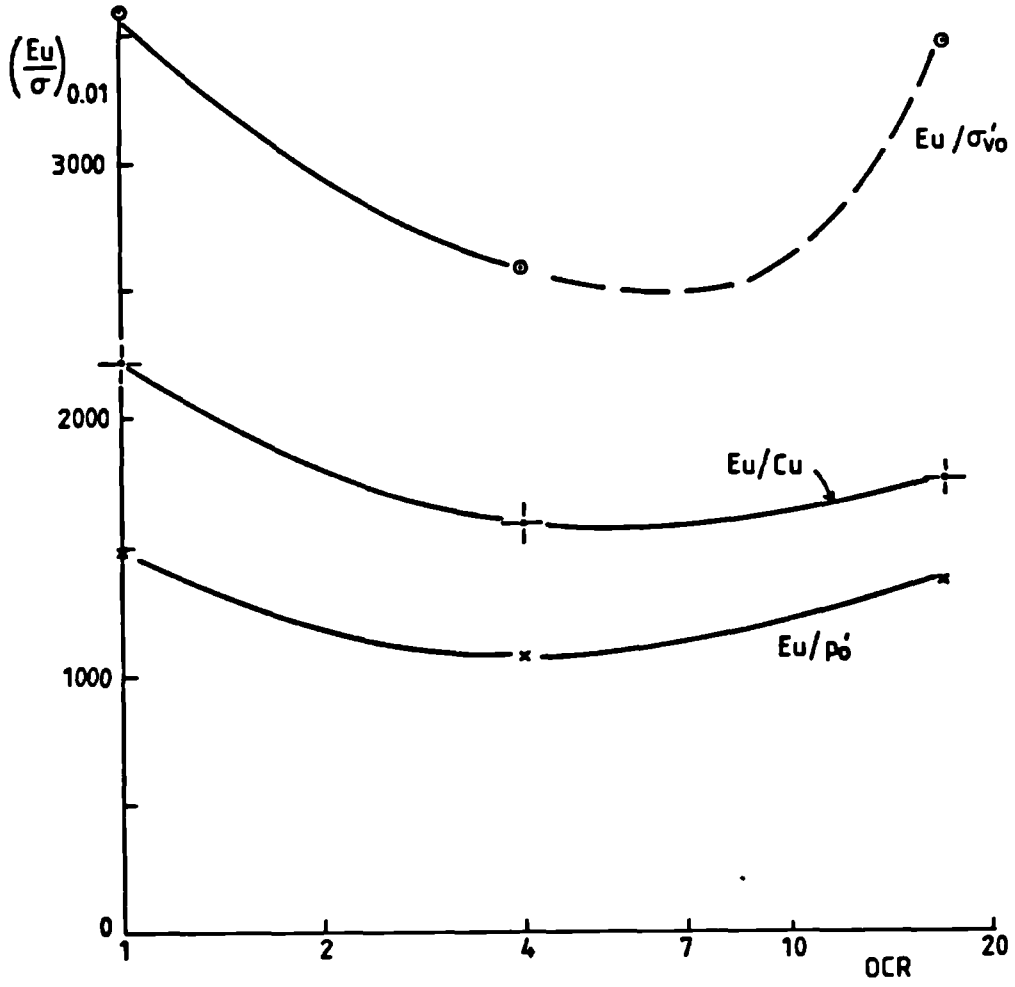
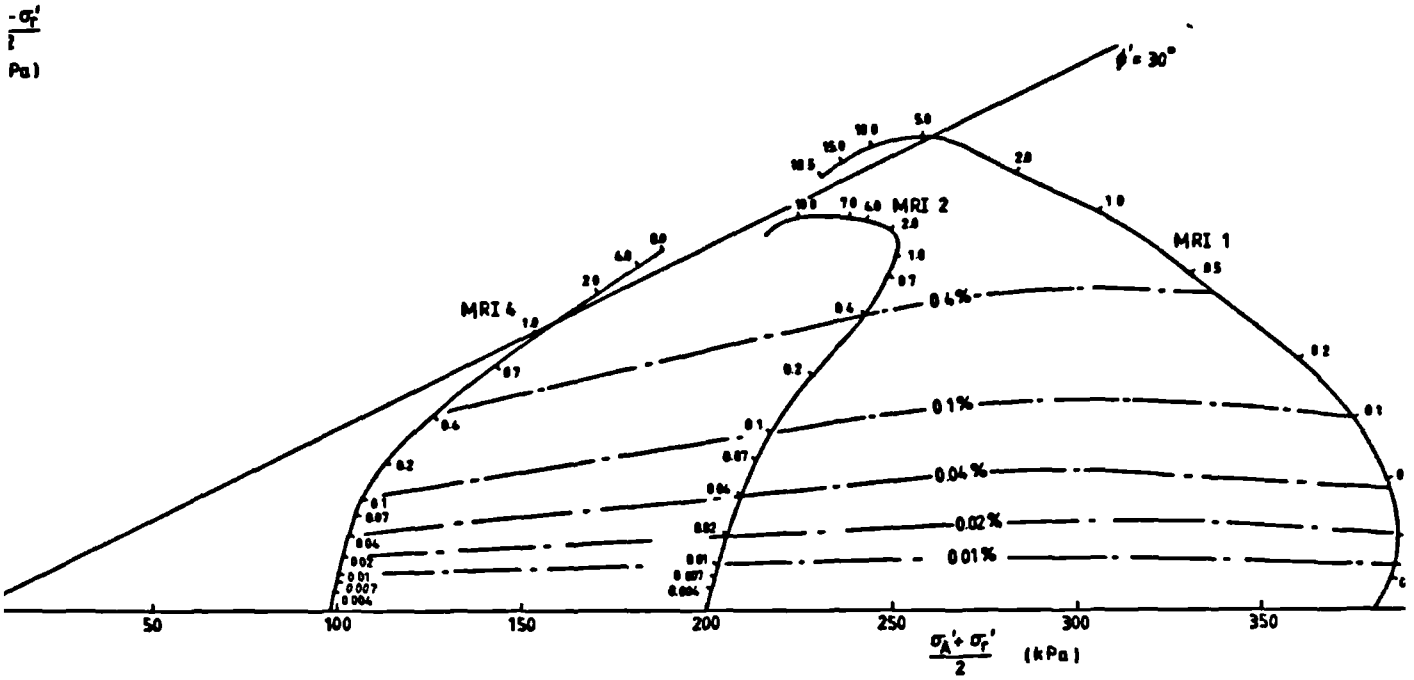


Figure 6.36. Normalised ratios of $E_{u(0.01)}$ against OCR, series MRR.

Figure 6.37. Effective stress paths, series MRI.



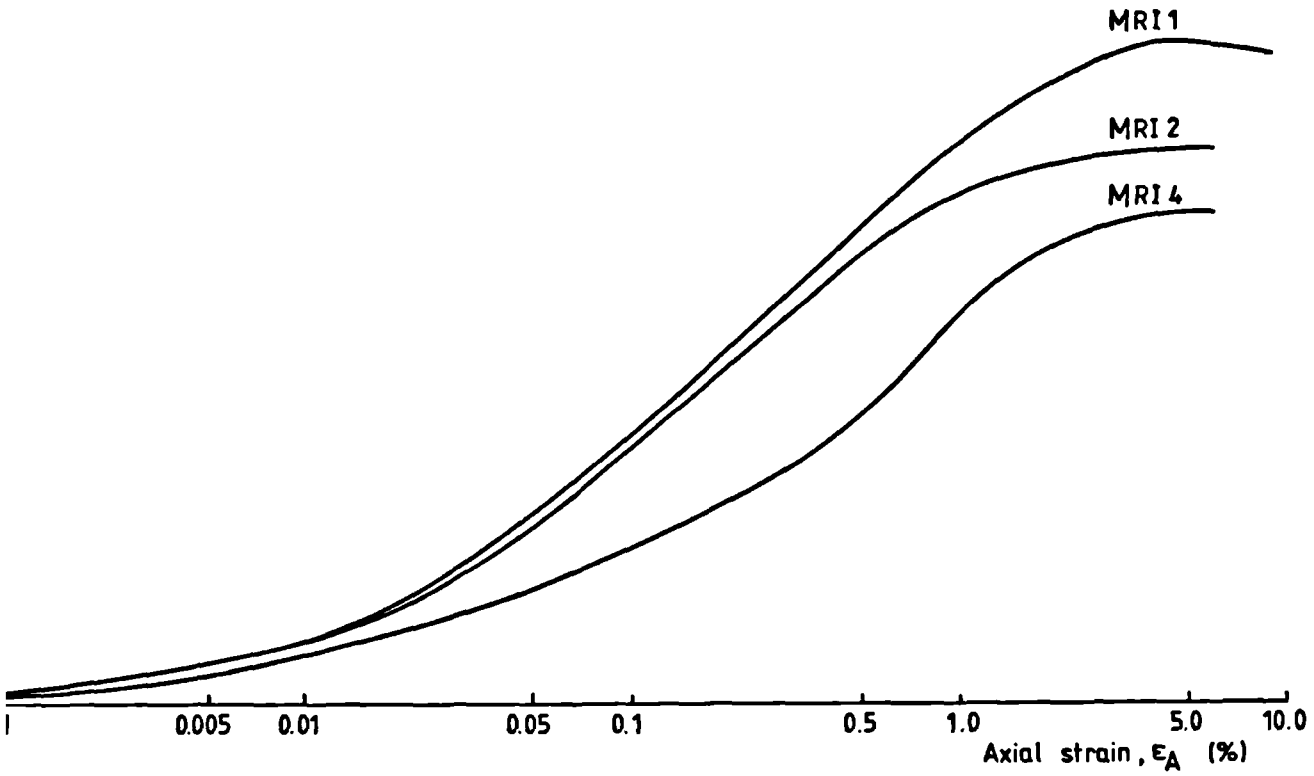
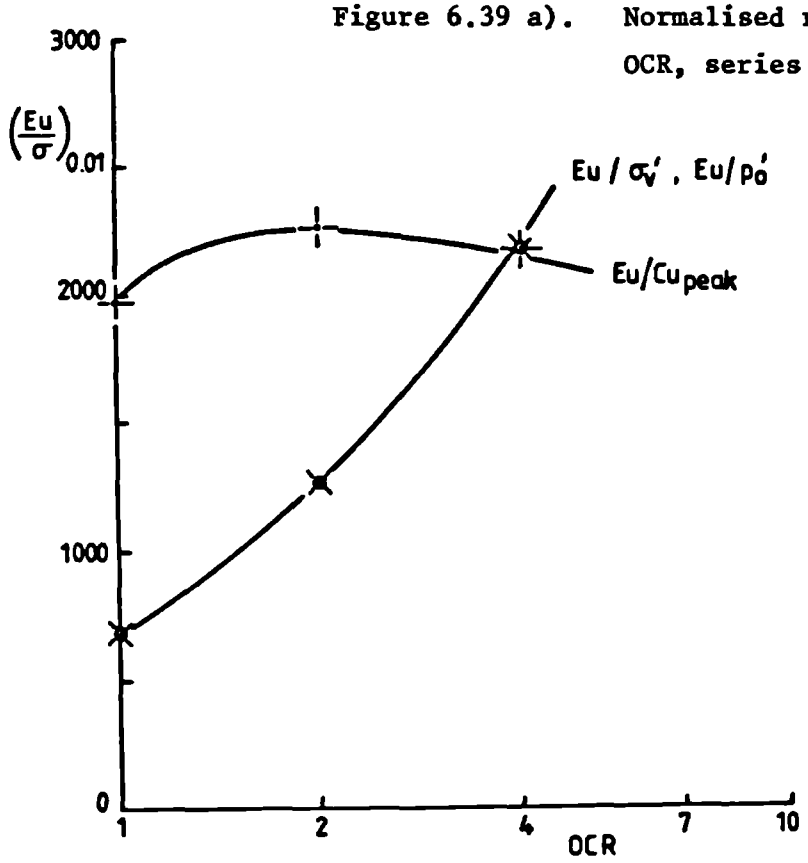


Figure 6.38. Stress - log strain data, series MRI.

Figure 6.39 a). Normalised ratios of $E_{u(0.01)}$ against OCR, series MRI.



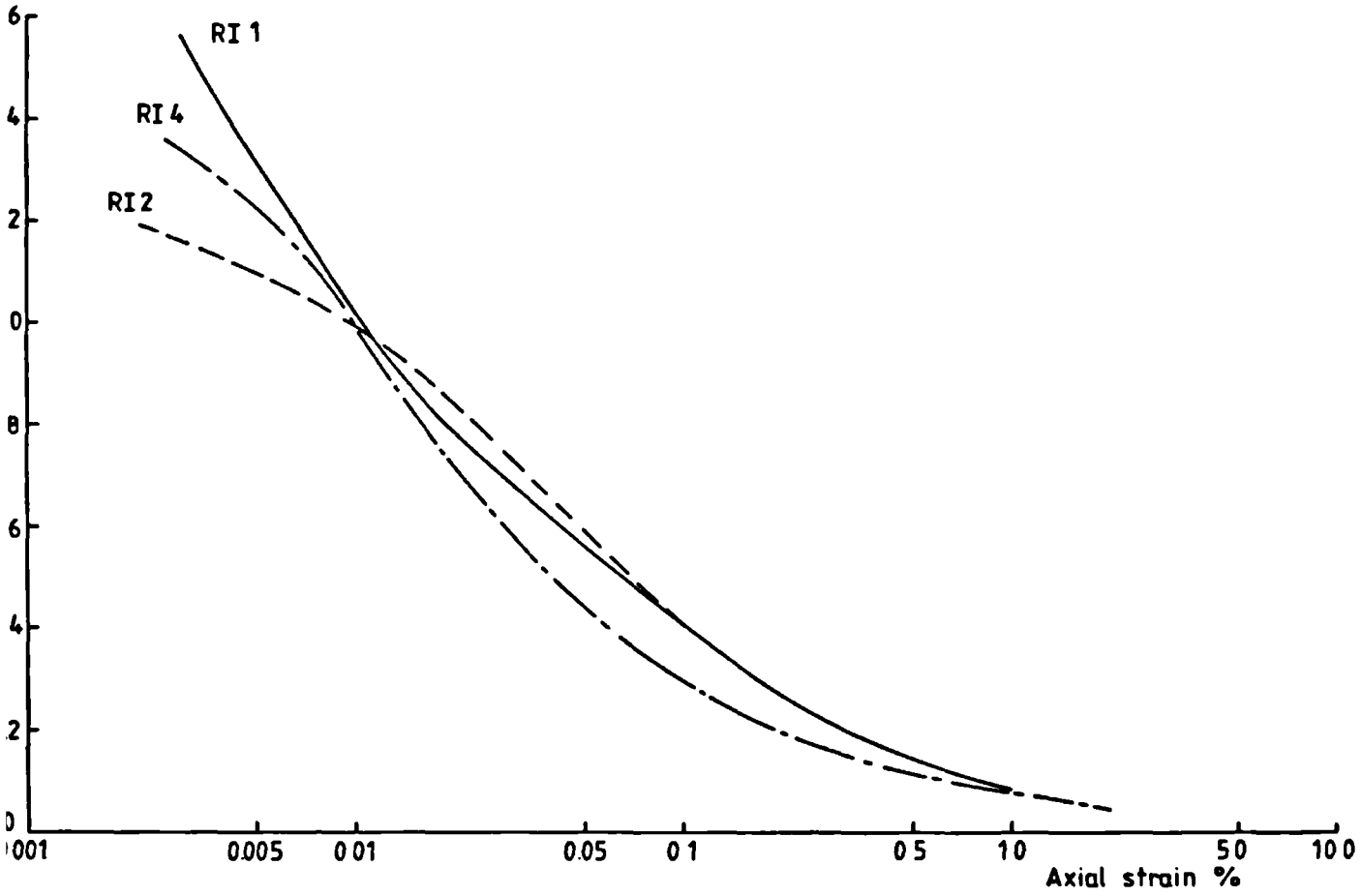


Figure 6.39 b). L(ε) against strain, series MRI.

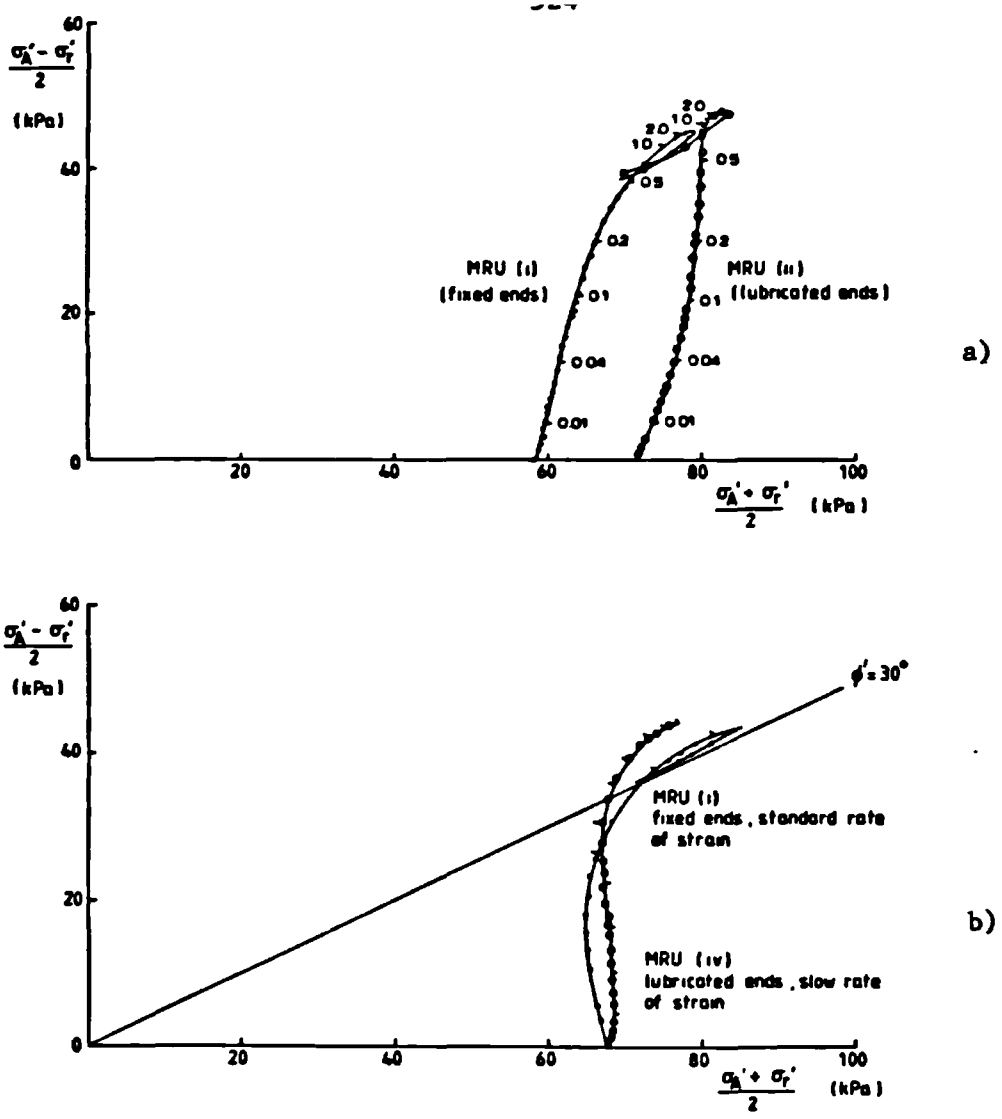


Figure 6.40. Effective stress paths, series MRU.

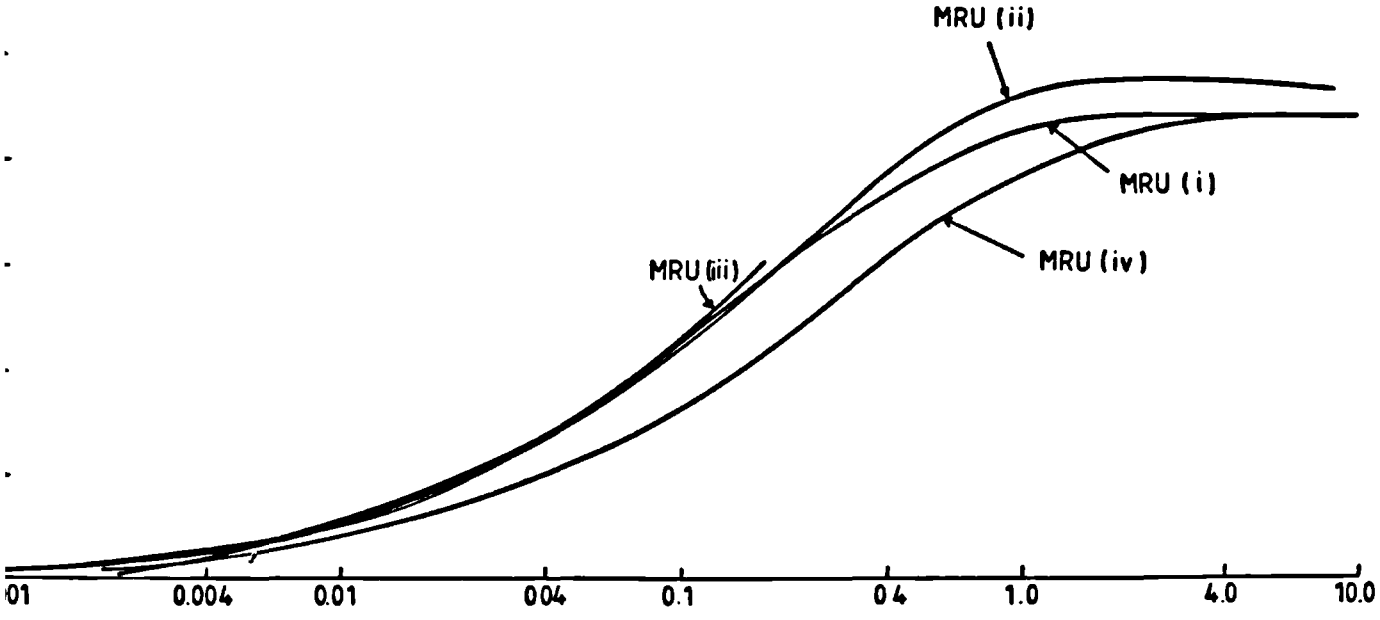


Figure 6.41. Stress - log strain data, series MRU.

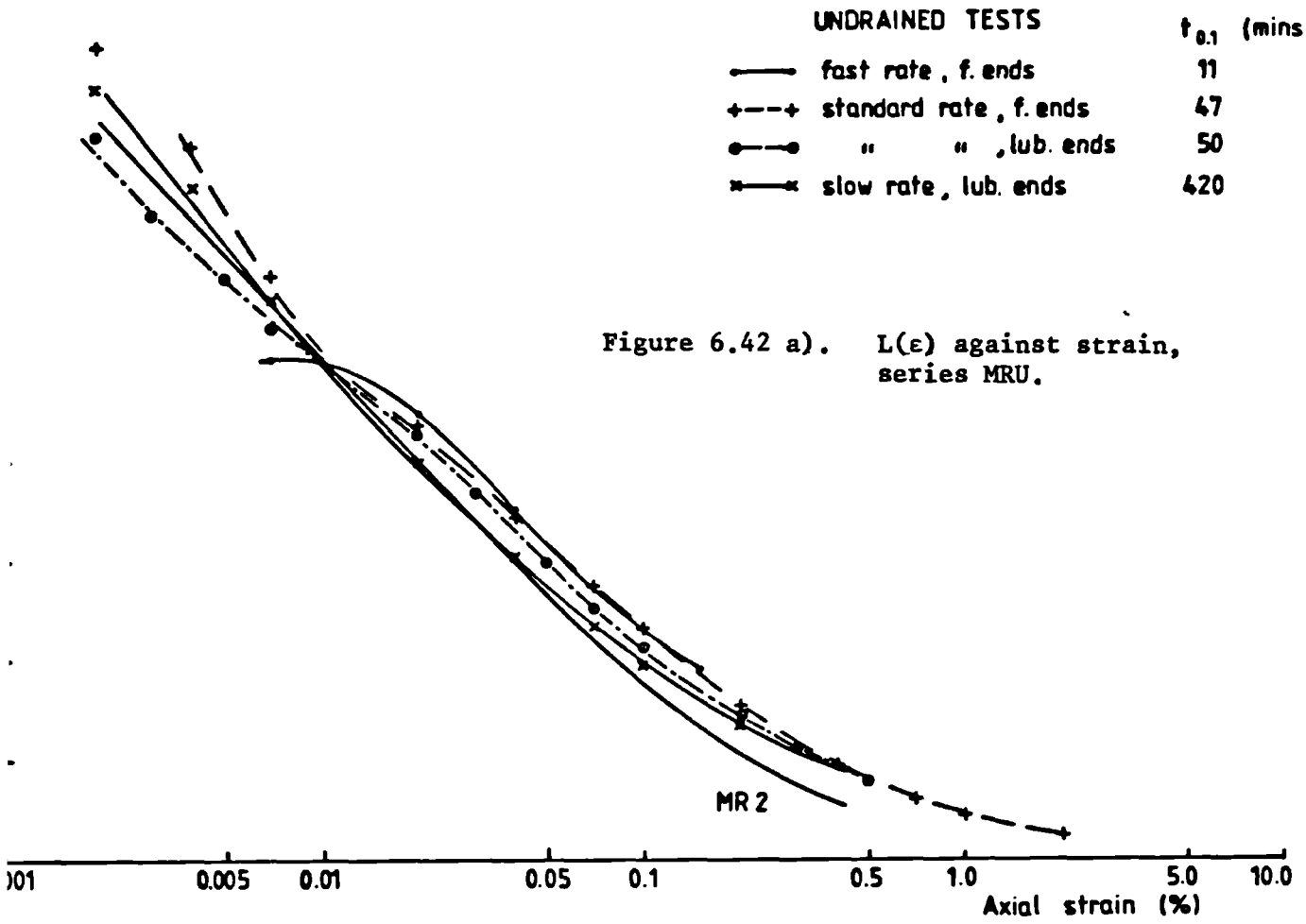


Figure 6.42 a). L(ε) against strain, series MRU.

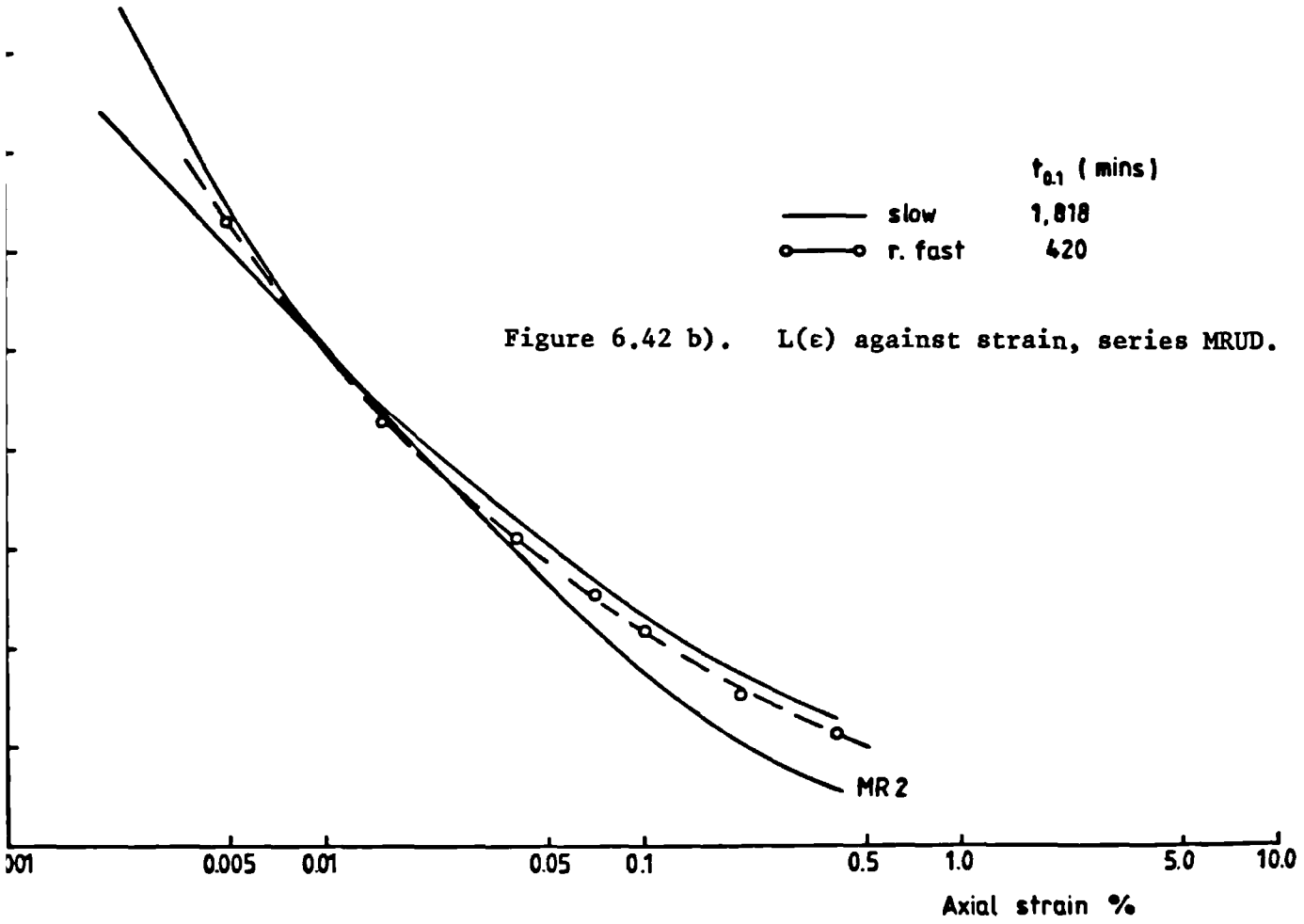
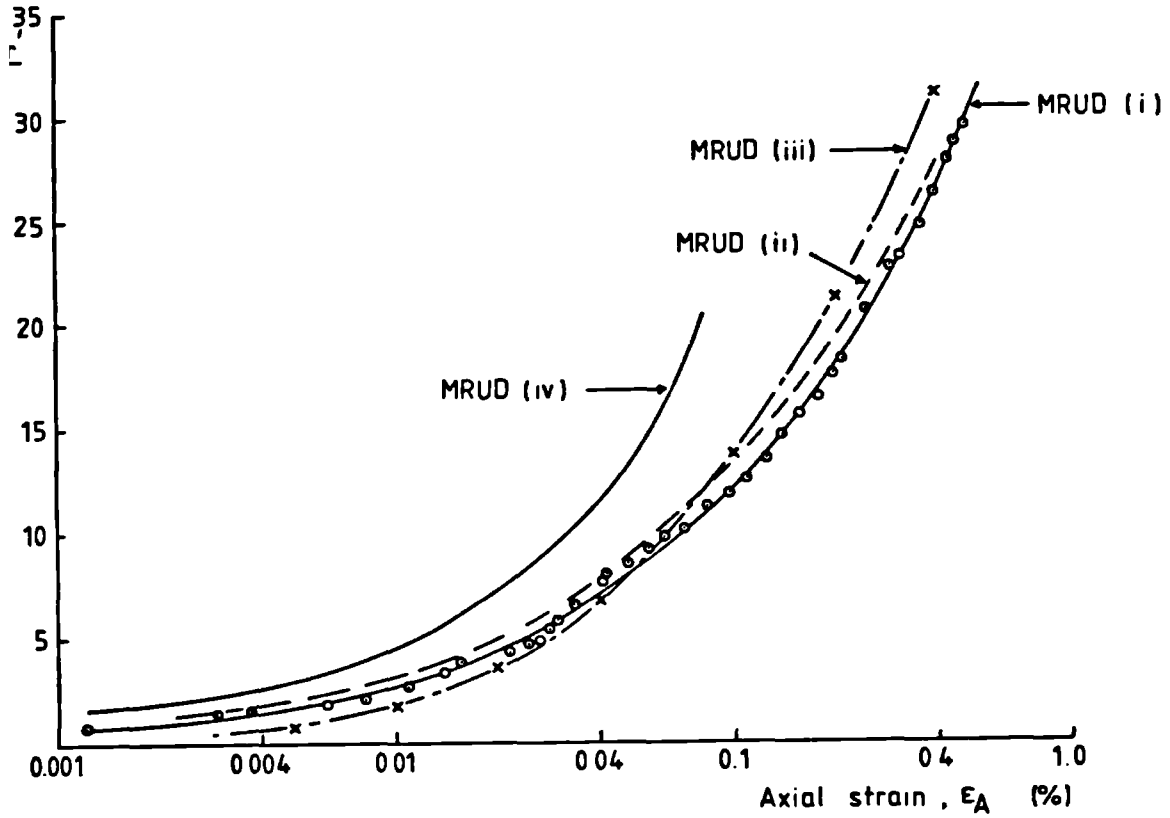


Figure 6.42 b). L(ε) against strain, series MRUD.

Figure 6.43. Stress - log strain data, series MRUD.



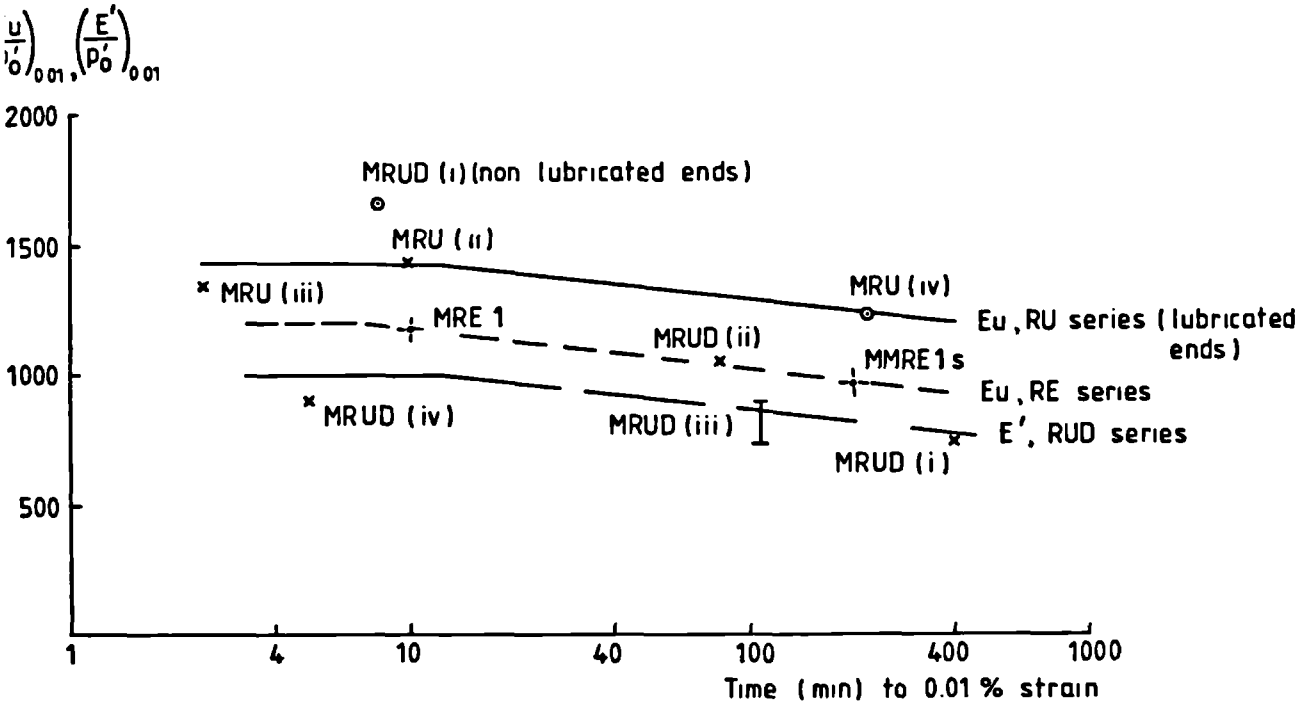


Figure 6.44. Summary of stiffness-rate effects, series MRU and MRUD.

Figure 6.45. Details of stress-strain loops, tests MRU(iii) and MRUD(iv).

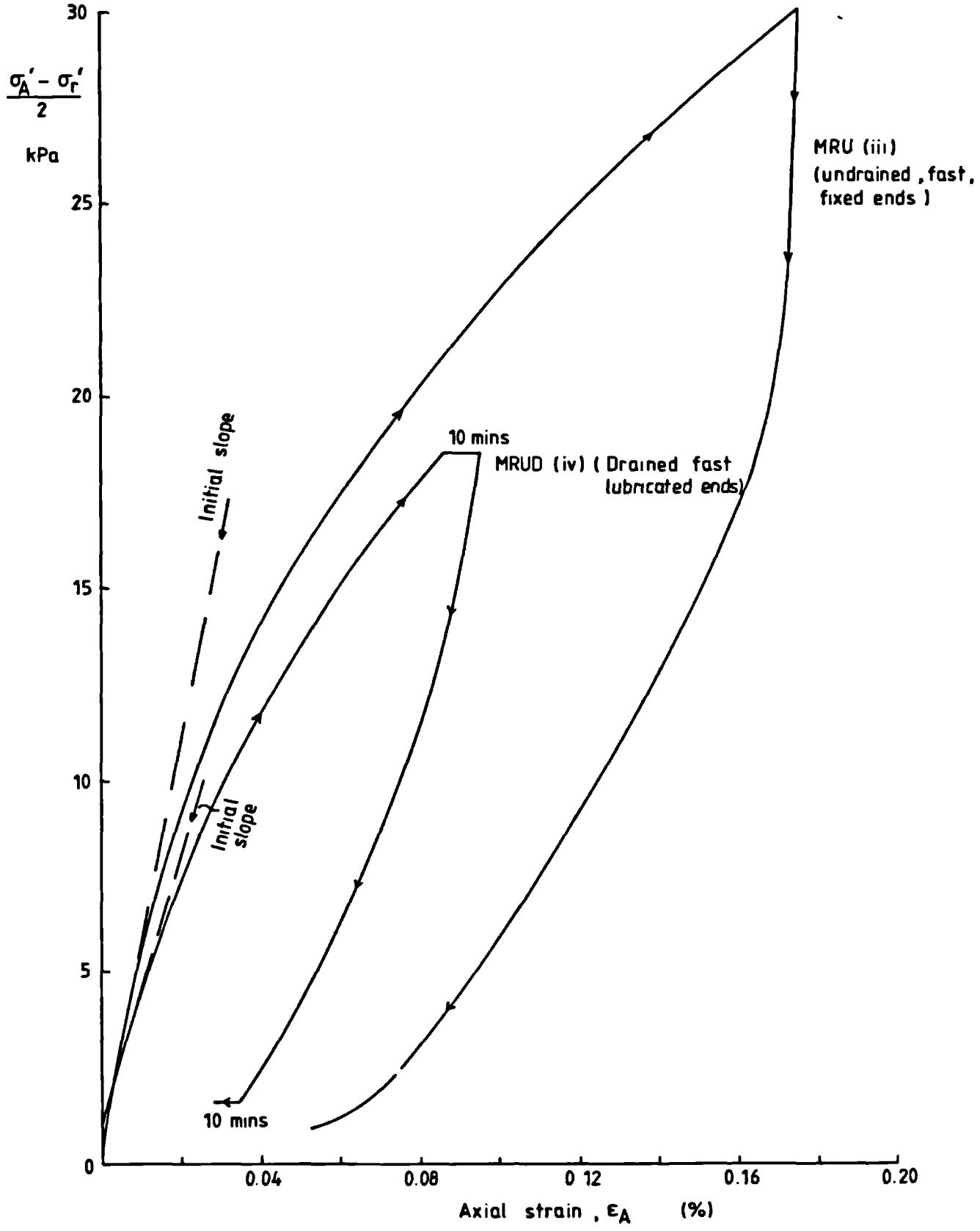
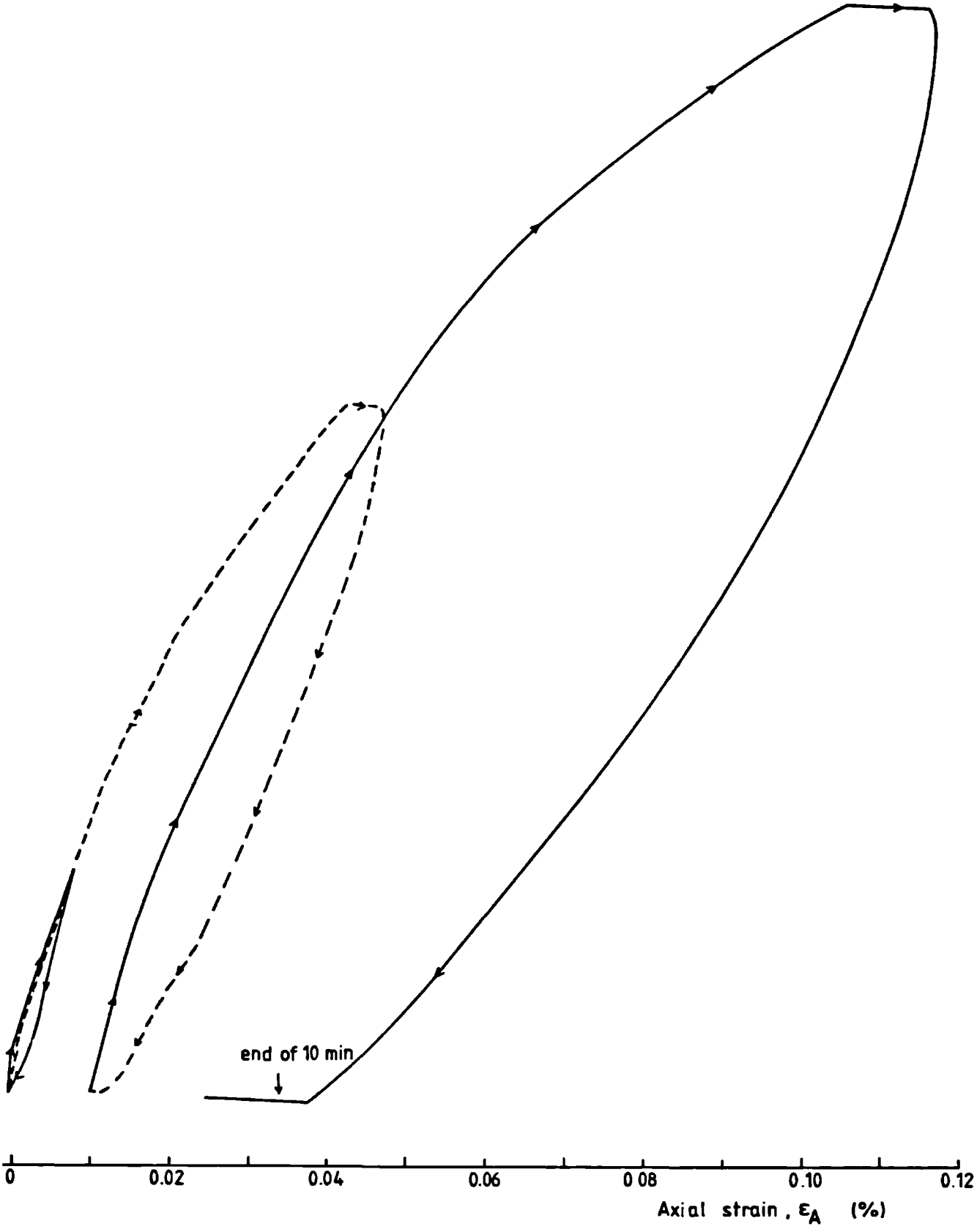


Figure 6.46. Details of stress-strain loops, test MRI2C.



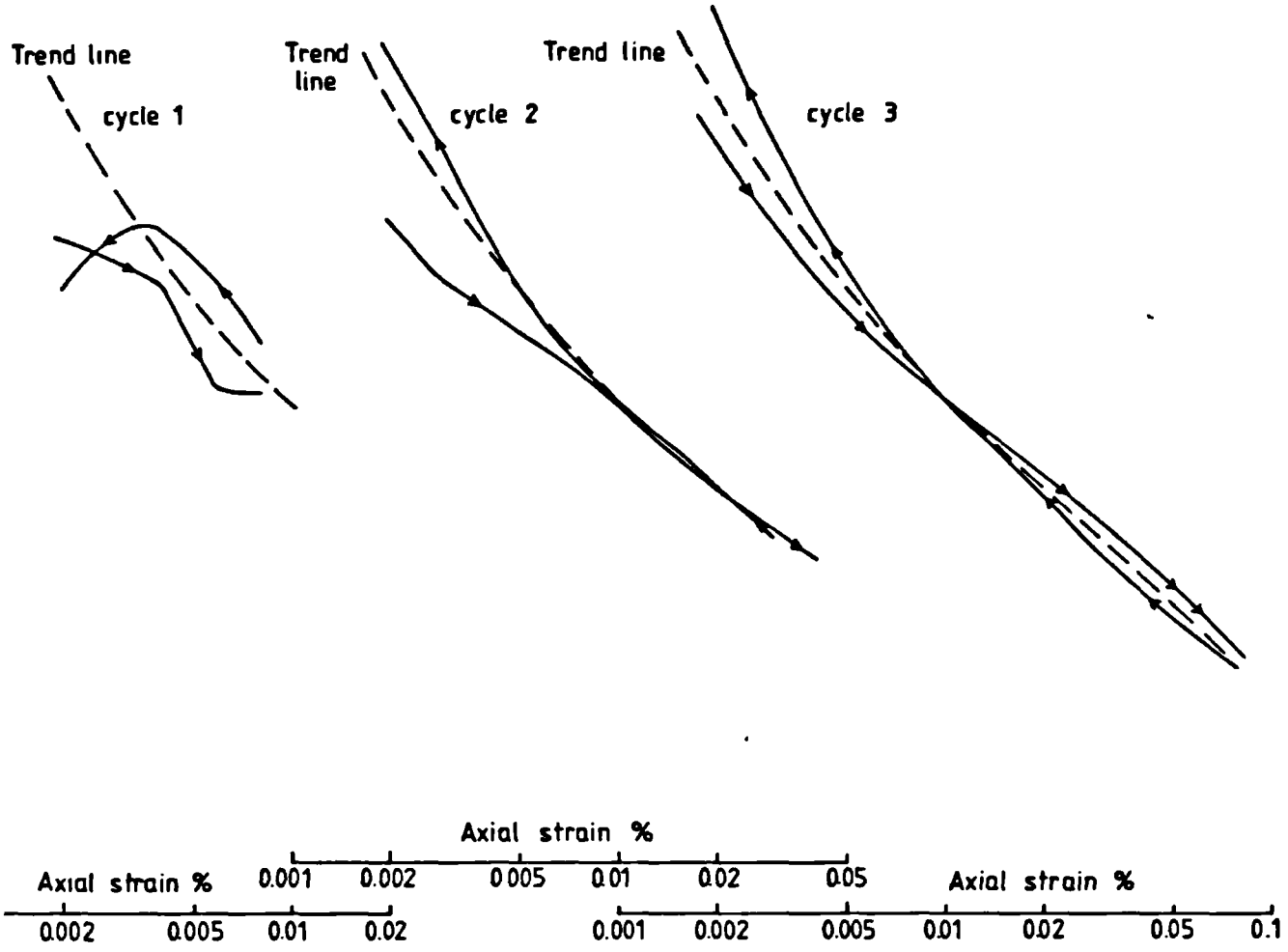


Figure 6.47. L(ε) against strain for three cycles of test MRI2C.

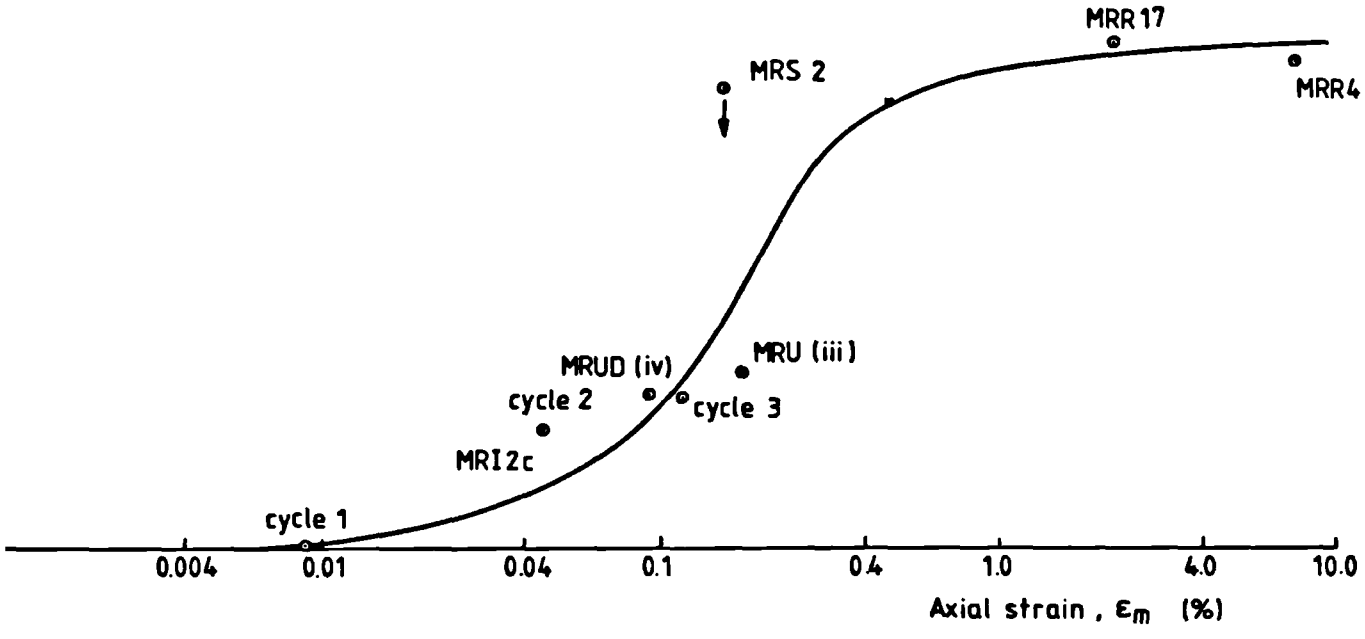


Figure 6.48. Ratios of plastic to total strains.

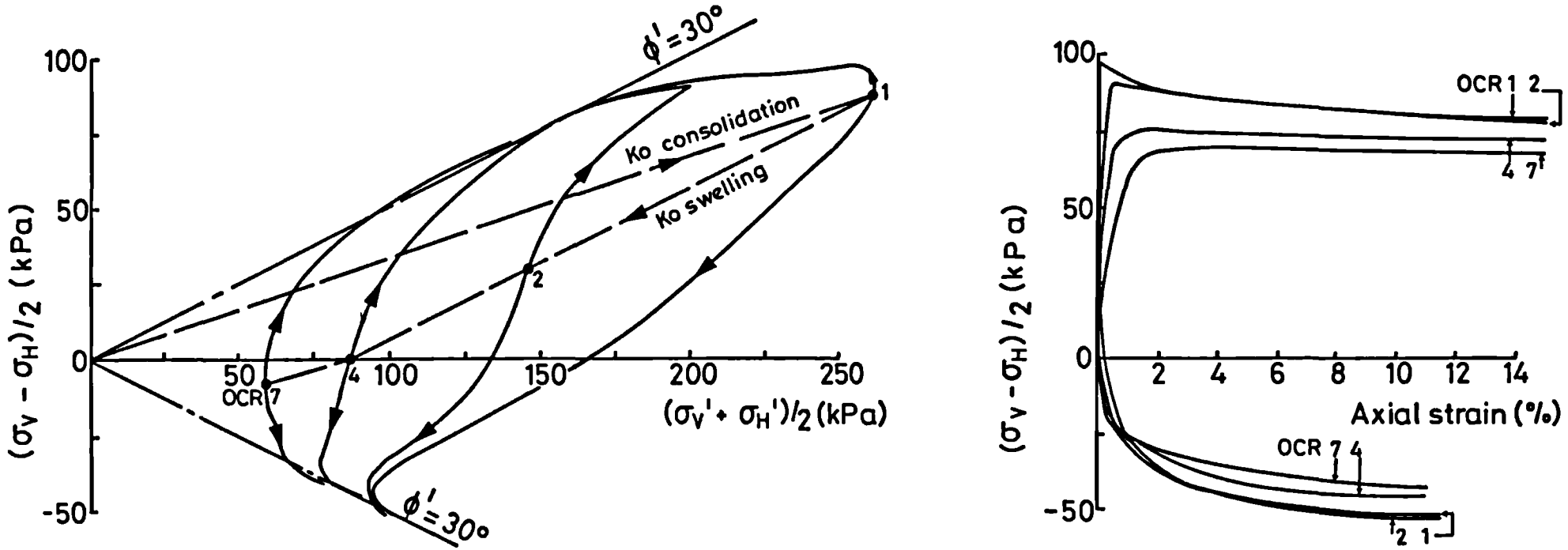


Figure 6.49. Summary of Lower Cromer Till characteristics in undrained compression and extension from K_o conditions, after Gens (1982).

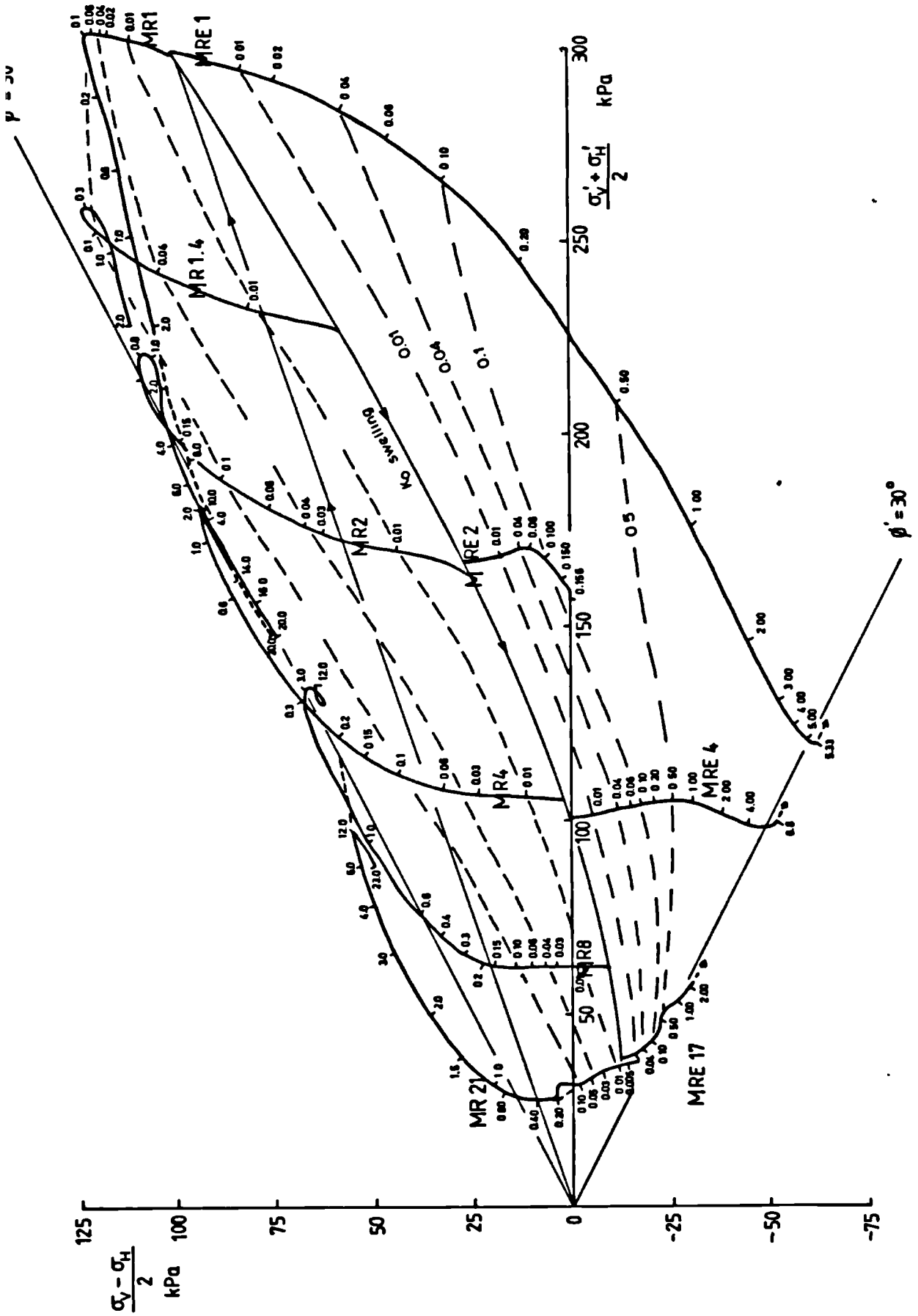


Figure 6.50. Summary of Magnus clay effective stress paths for series MR and MRE.

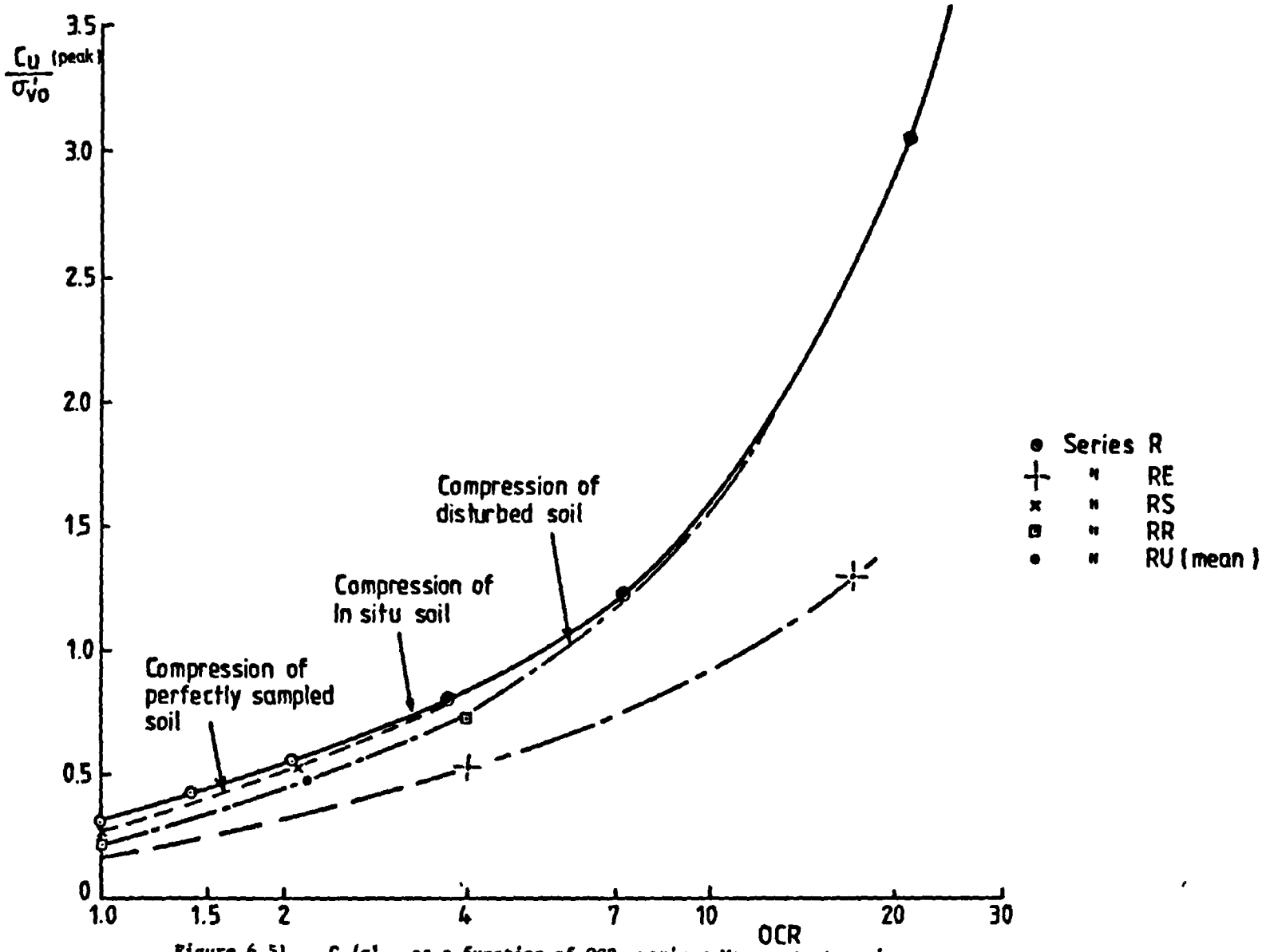


Figure 6.51. C_u/σ'_{vo} as a function of OCR, various Magnus test series.

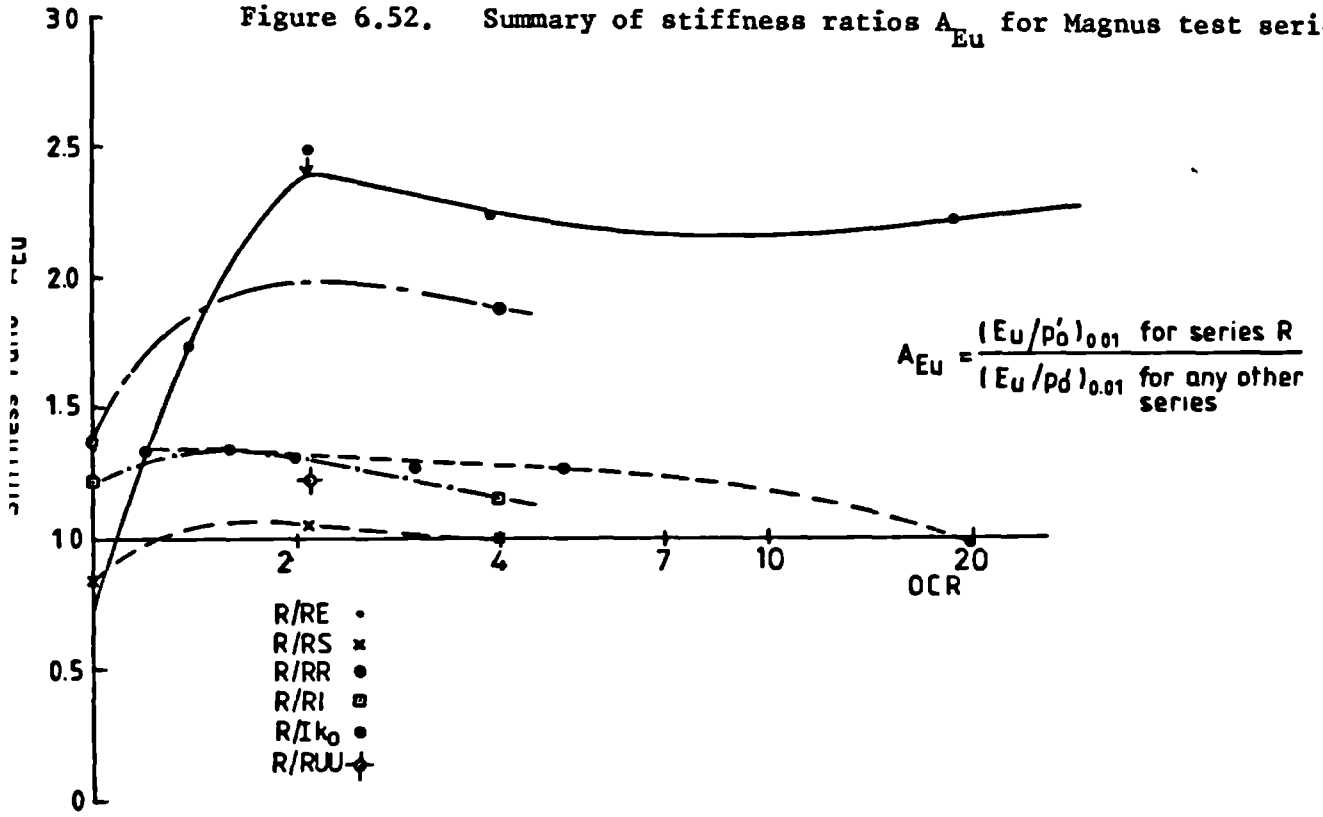


Figure 6.52. Summary of stiffness ratios A_{Eu} for Magnus test series.

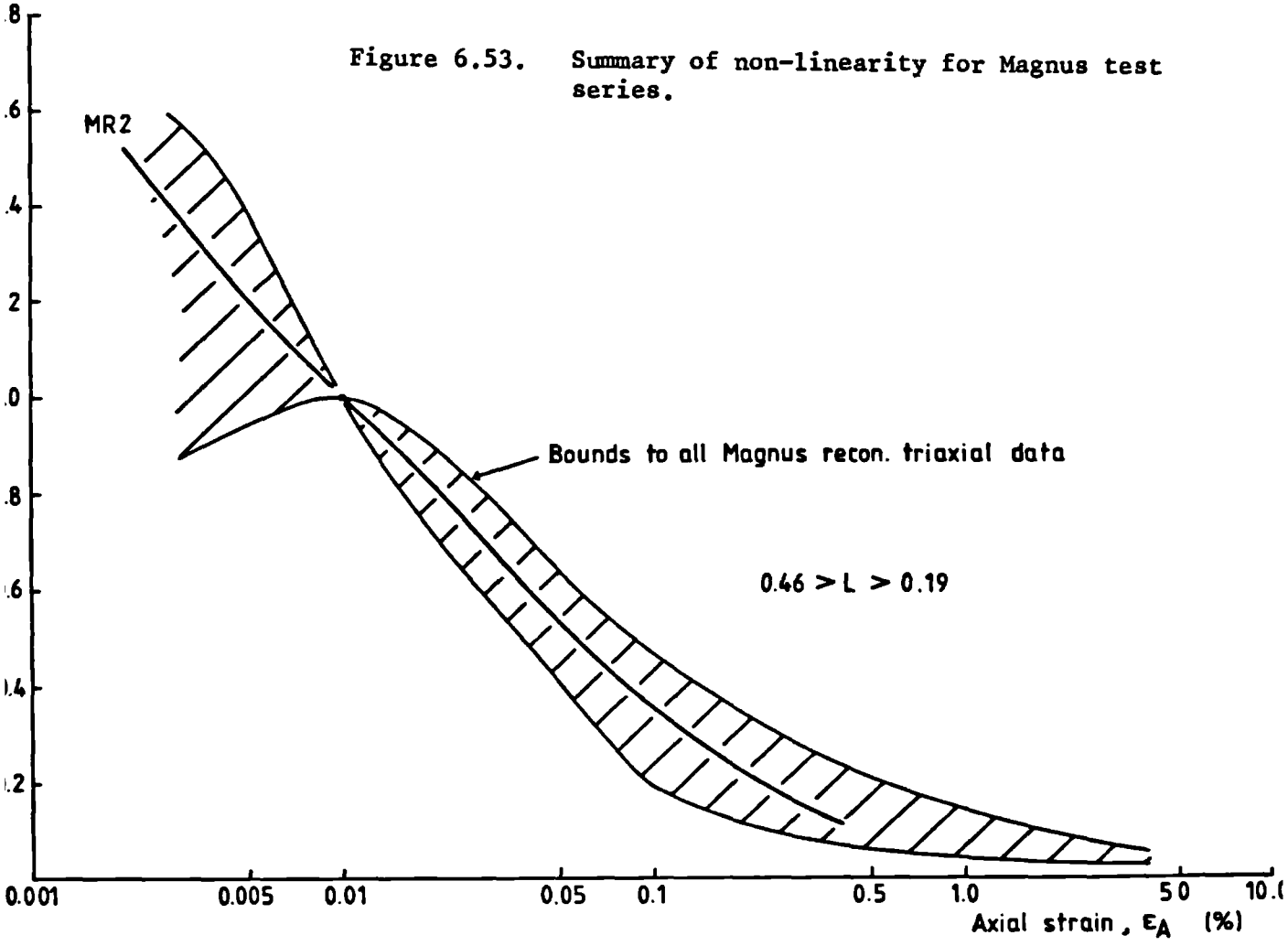


Figure 6.53. Summary of non-linearity for Magnus test series.

Figure 6.54. Summary of L(ε) for OCR 1.

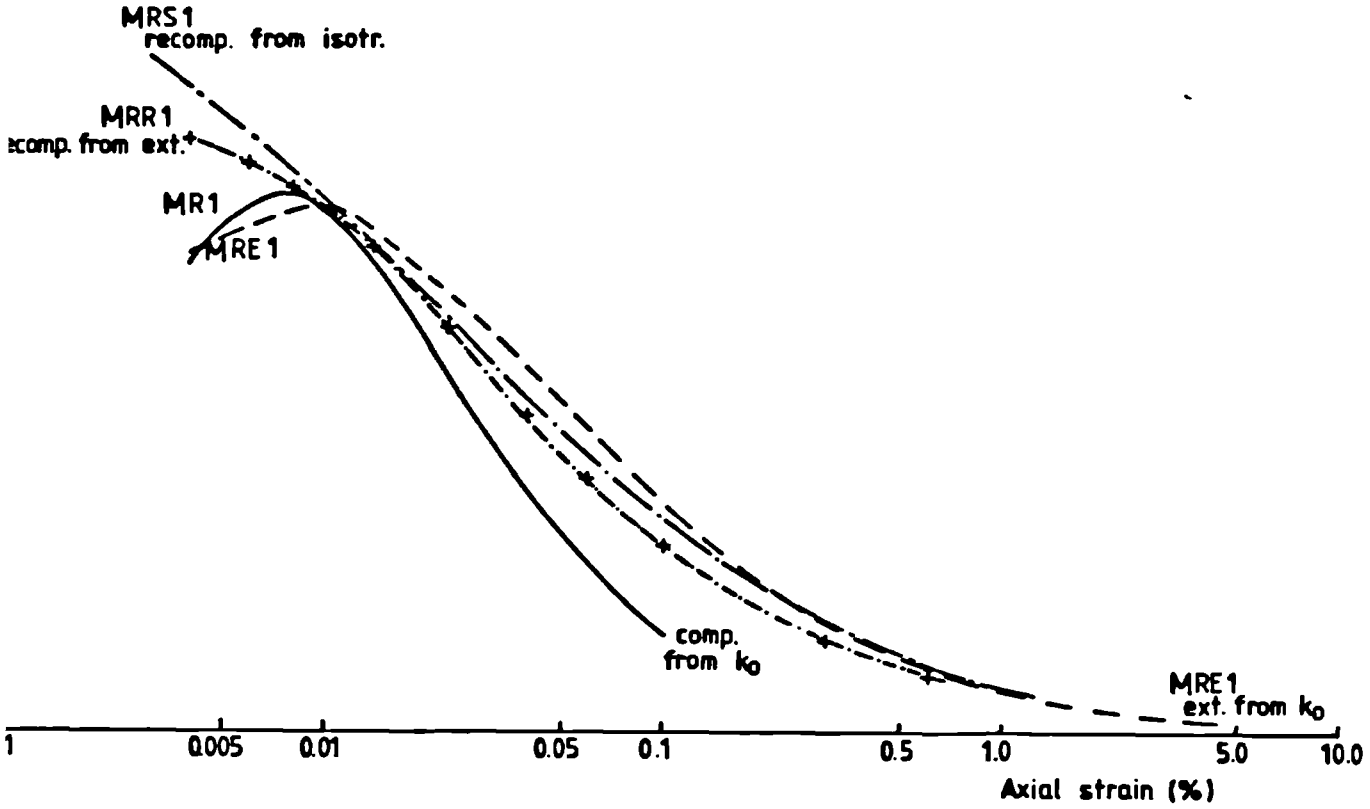
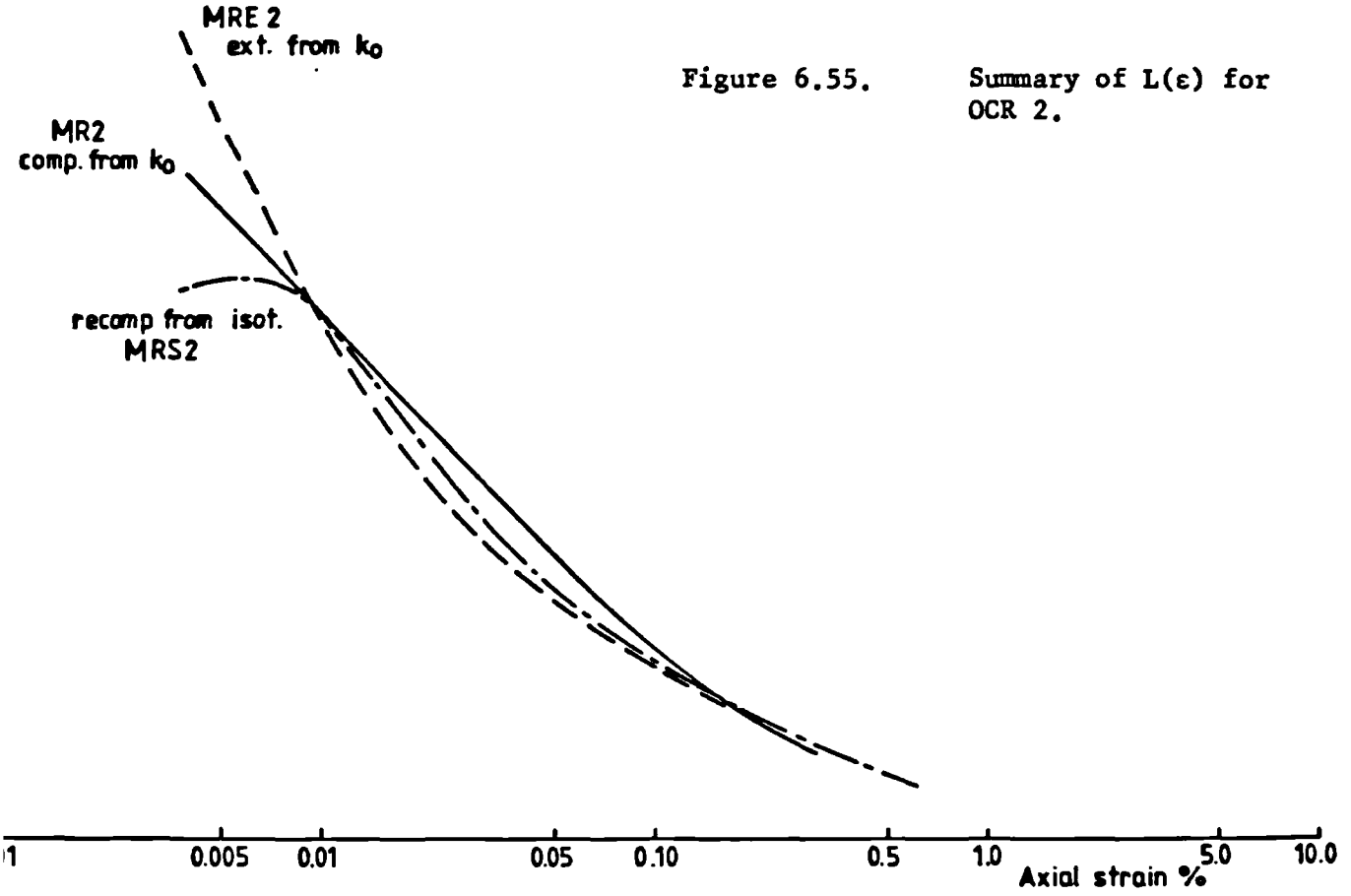


Figure 6.55. Summary of L(ε) for OCR 2.



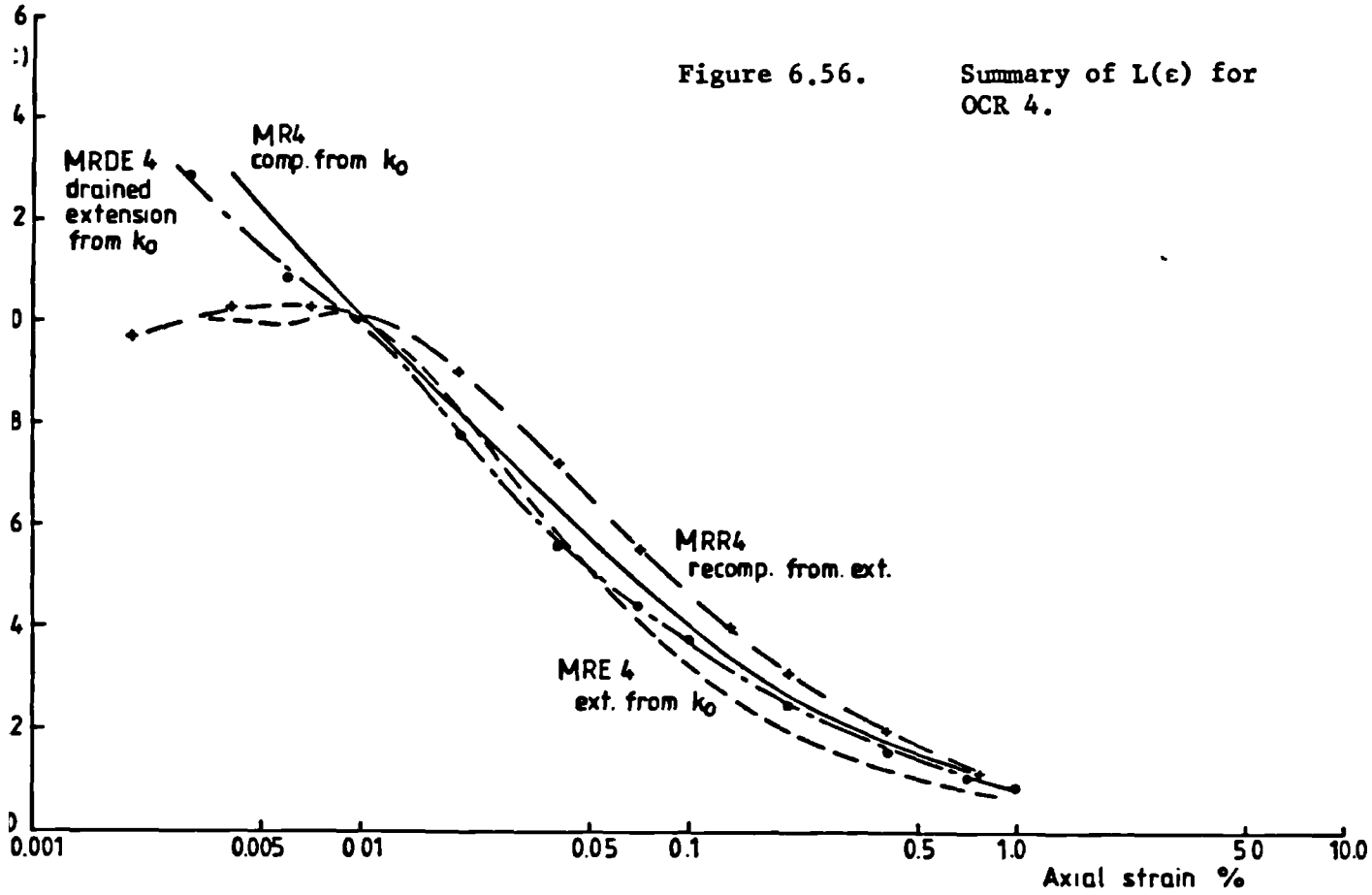


Figure 6.56. Summary of L(ε) for OCR 4.

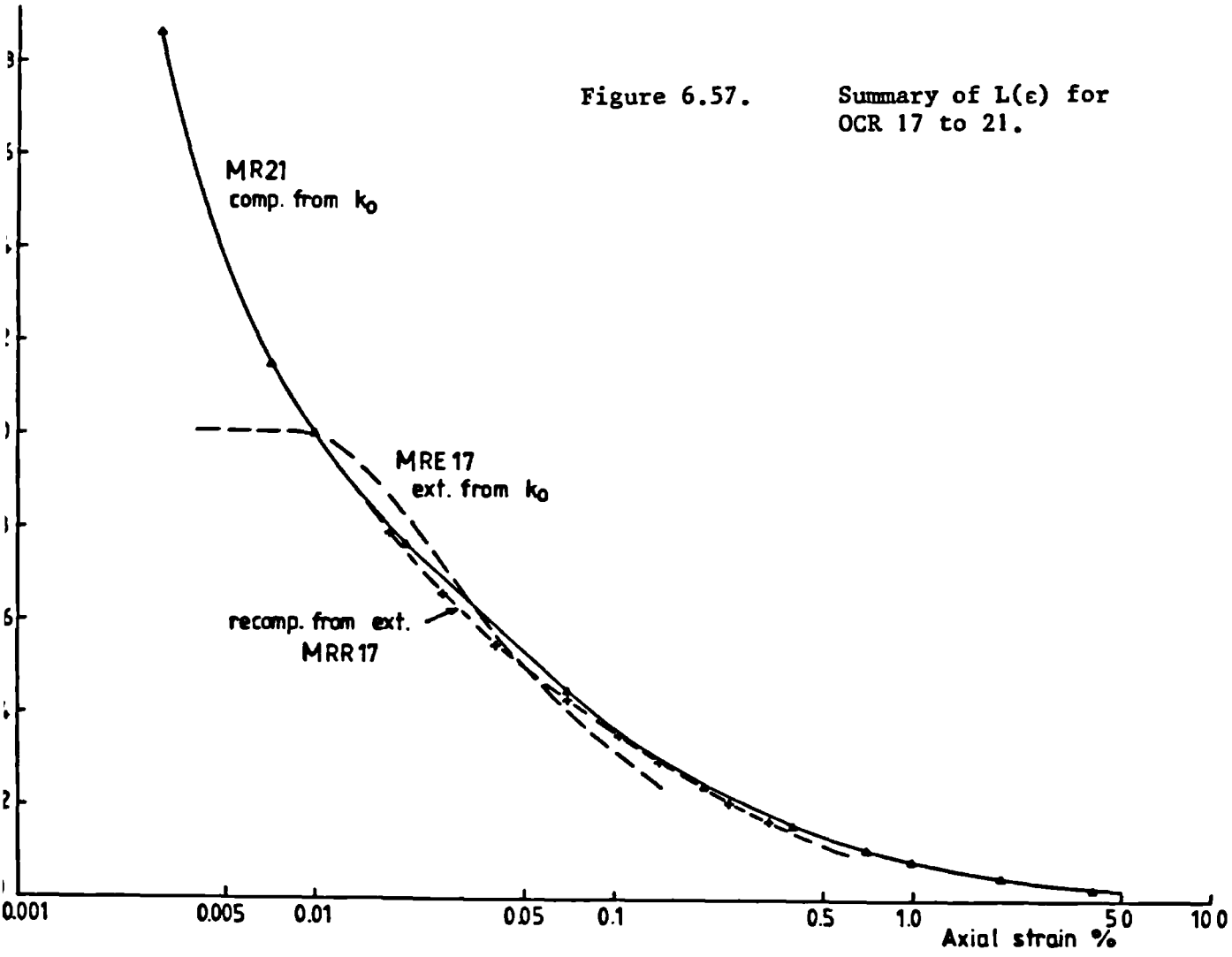


Figure 6.57. Summary of L(ε) for OCR 17 to 21.

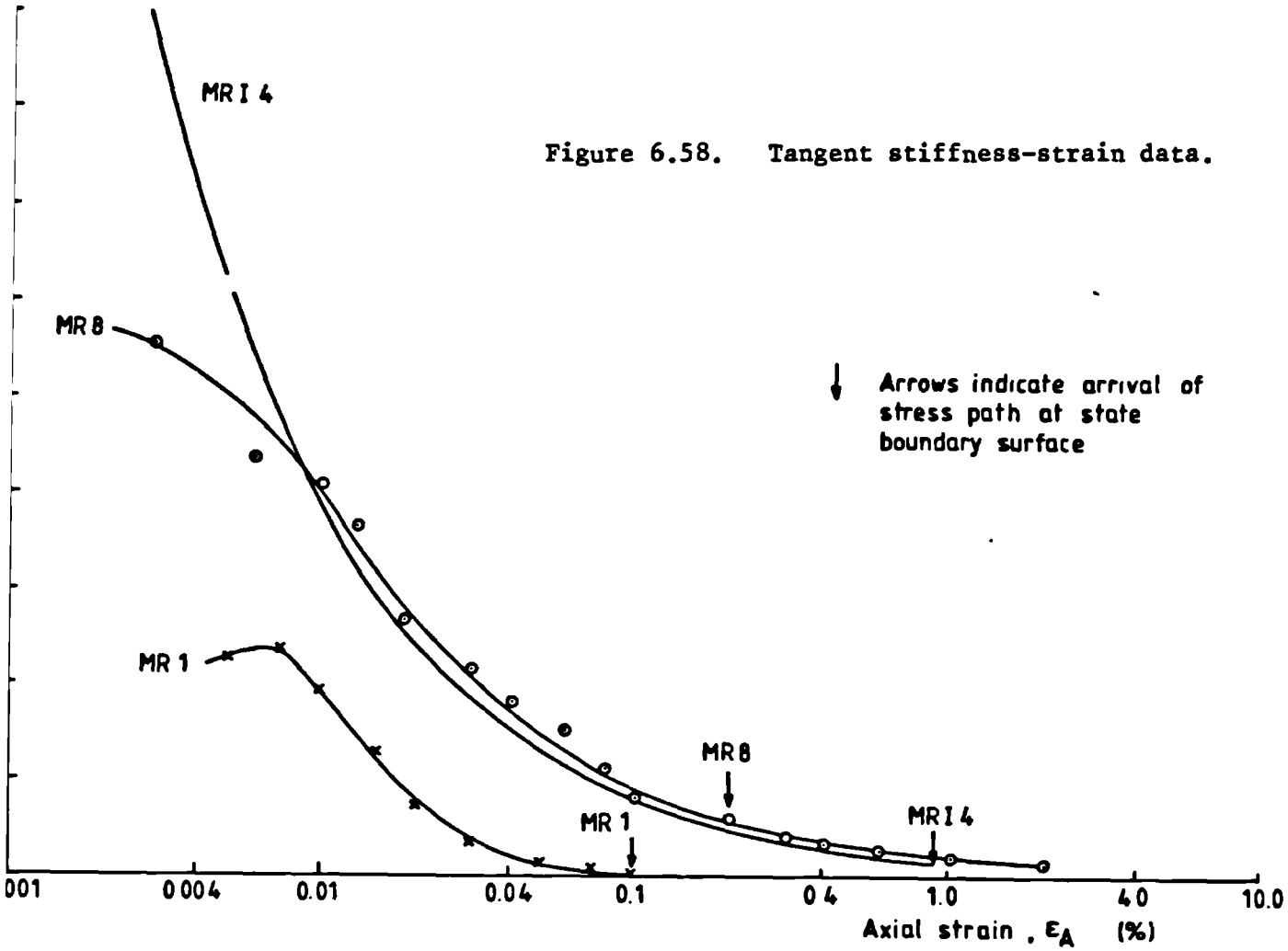


Figure 6.58. Tangent stiffness-strain data.

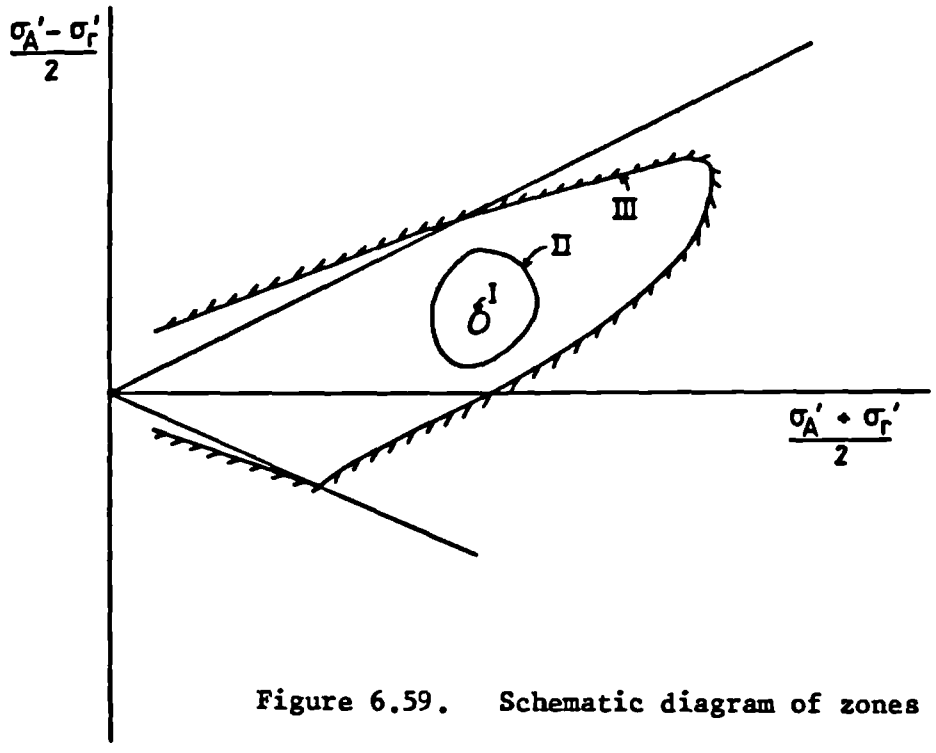


Figure 6.59. Schematic diagram of zones I, II and III.

Figure 6.60. Secant bulk modulus, volume strain data. Swelling portion of test MR8 at various OCR's.

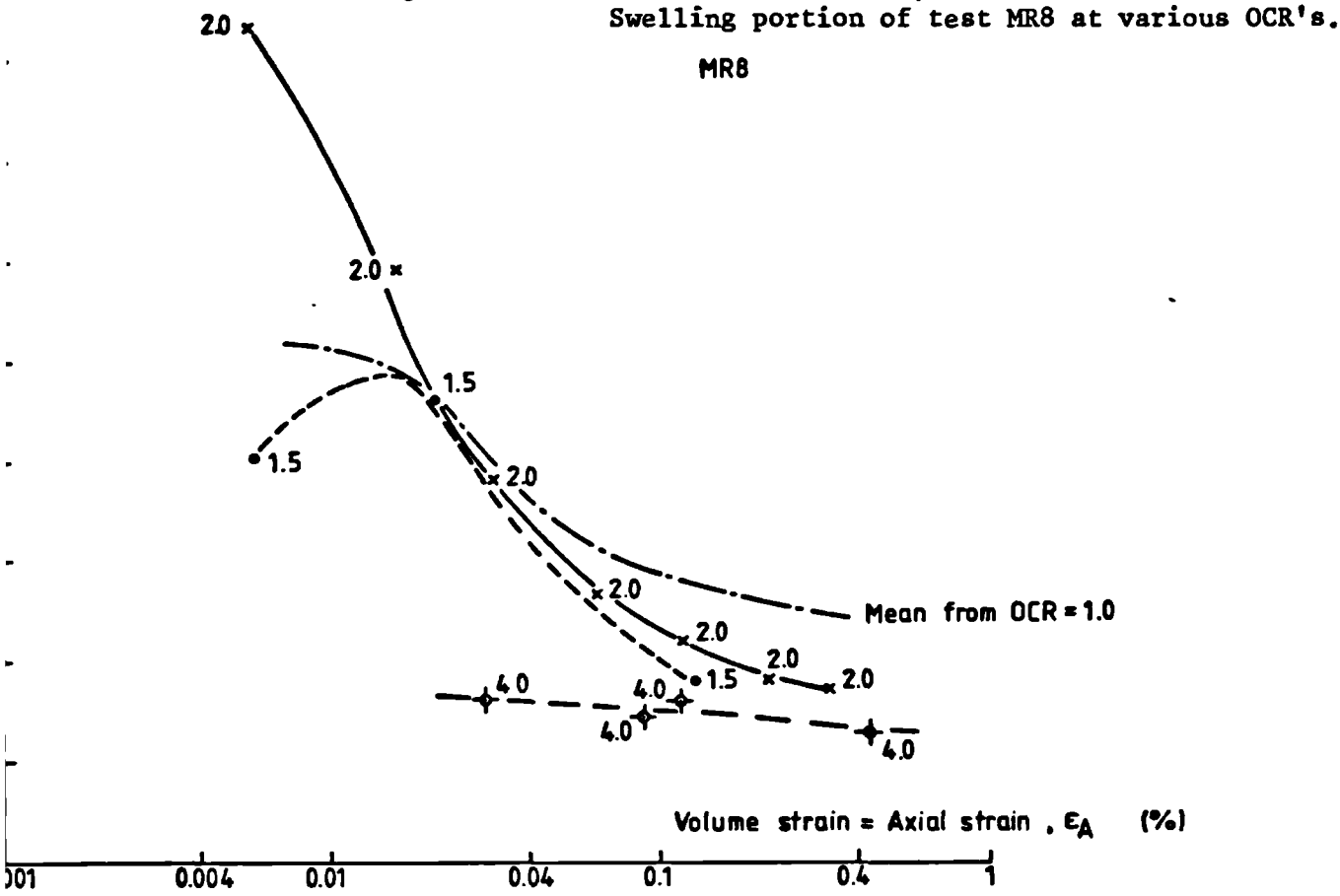
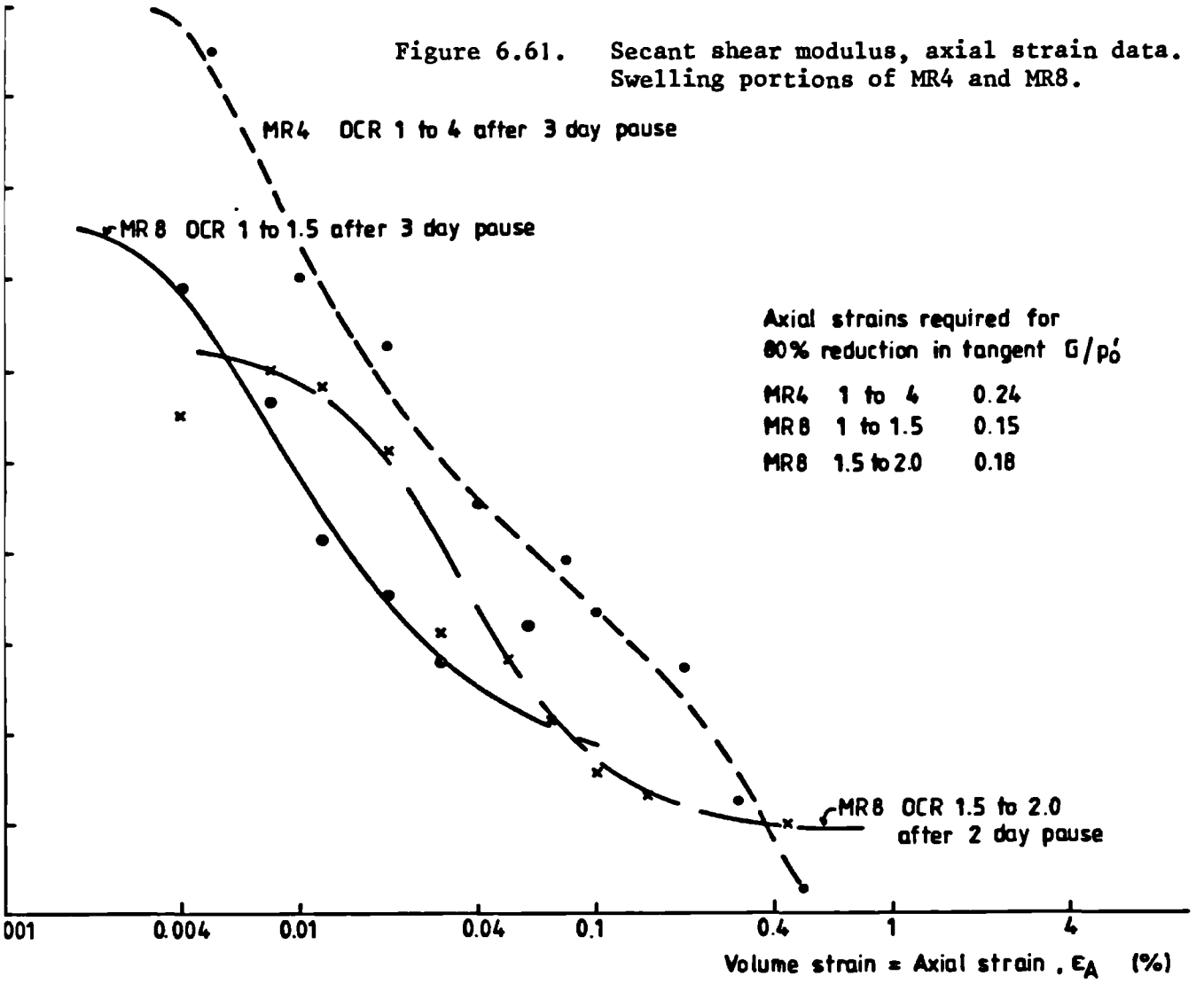


Figure 6.61. Secant shear modulus, axial strain data. Swelling portions of MR4 and MR8.



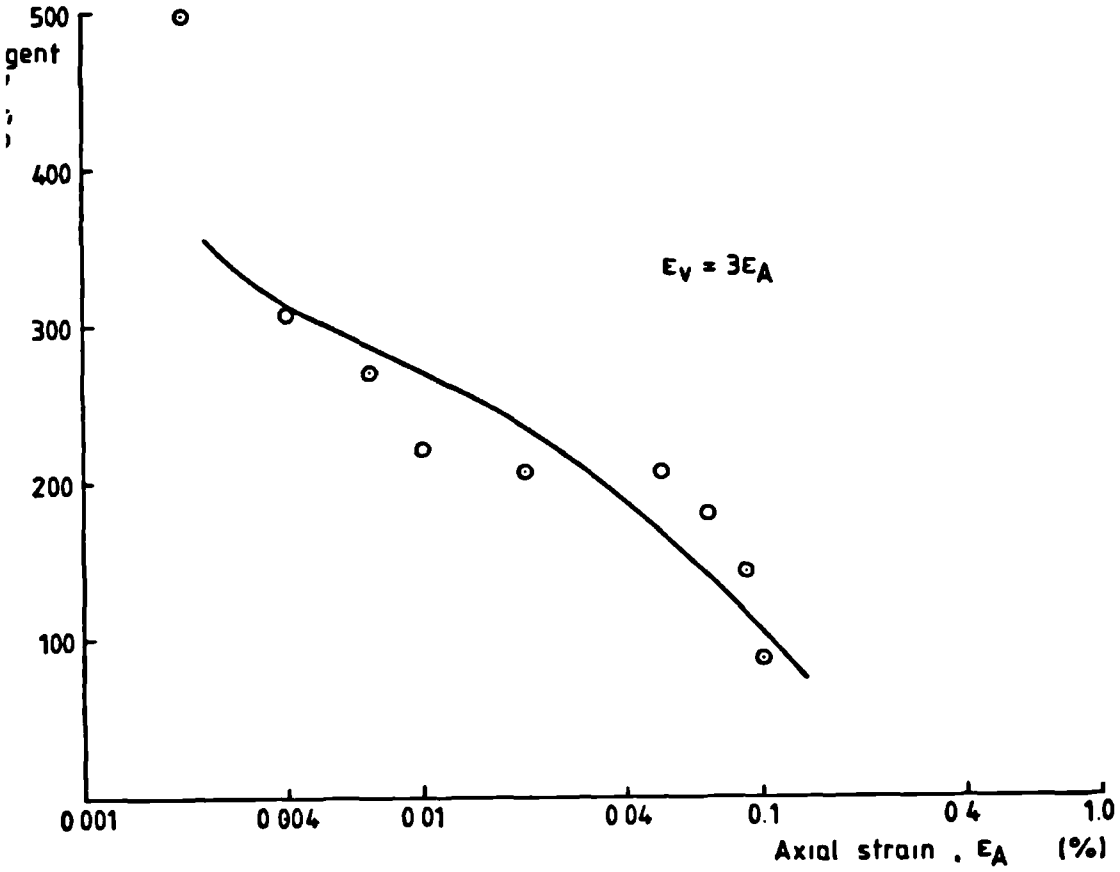


Figure 6.62. Tangent bulk modulus, volume strain data. Swelling portion of test MRI1.

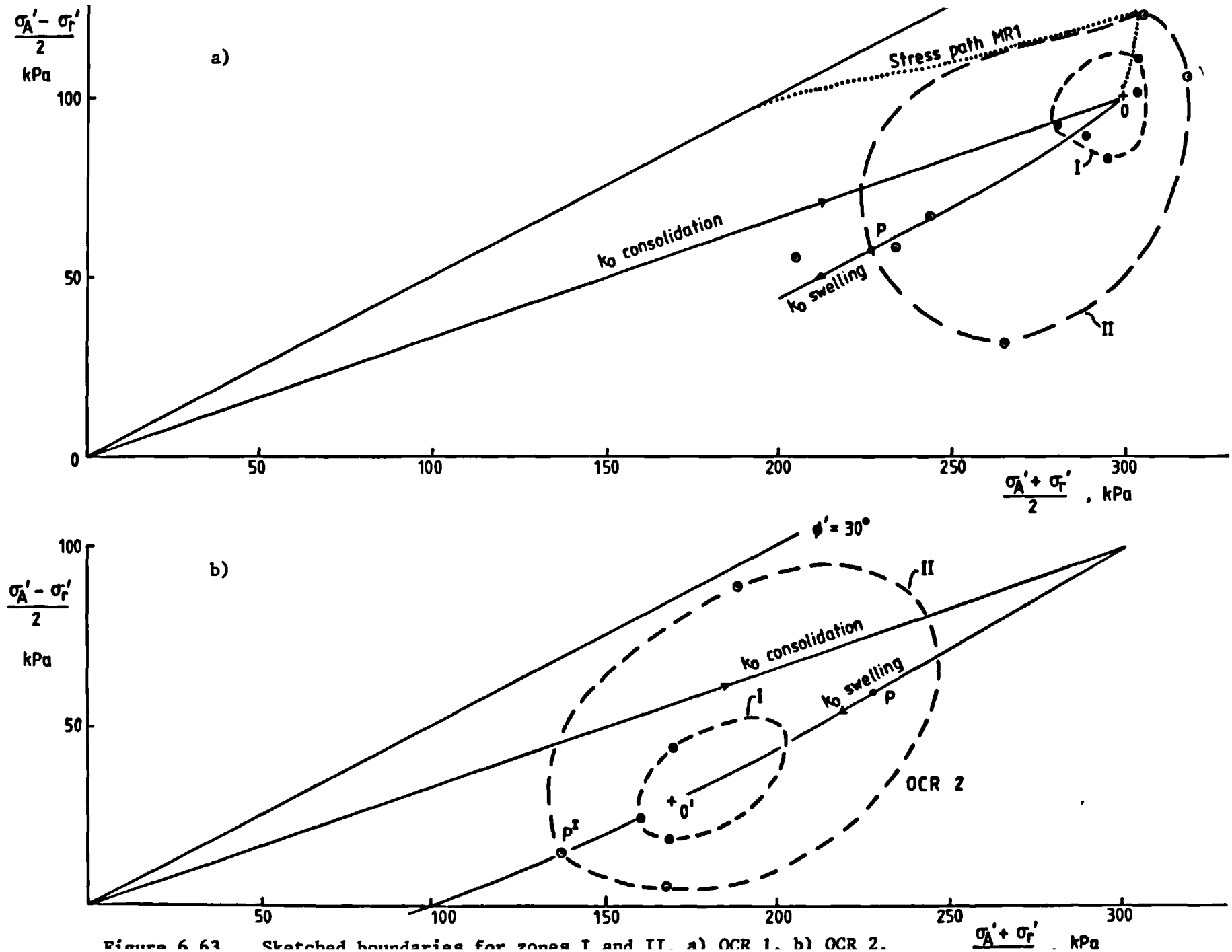


Figure 6.63 Sketched boundaries for zones I and II. a) OCR 1, b) OCR 2.

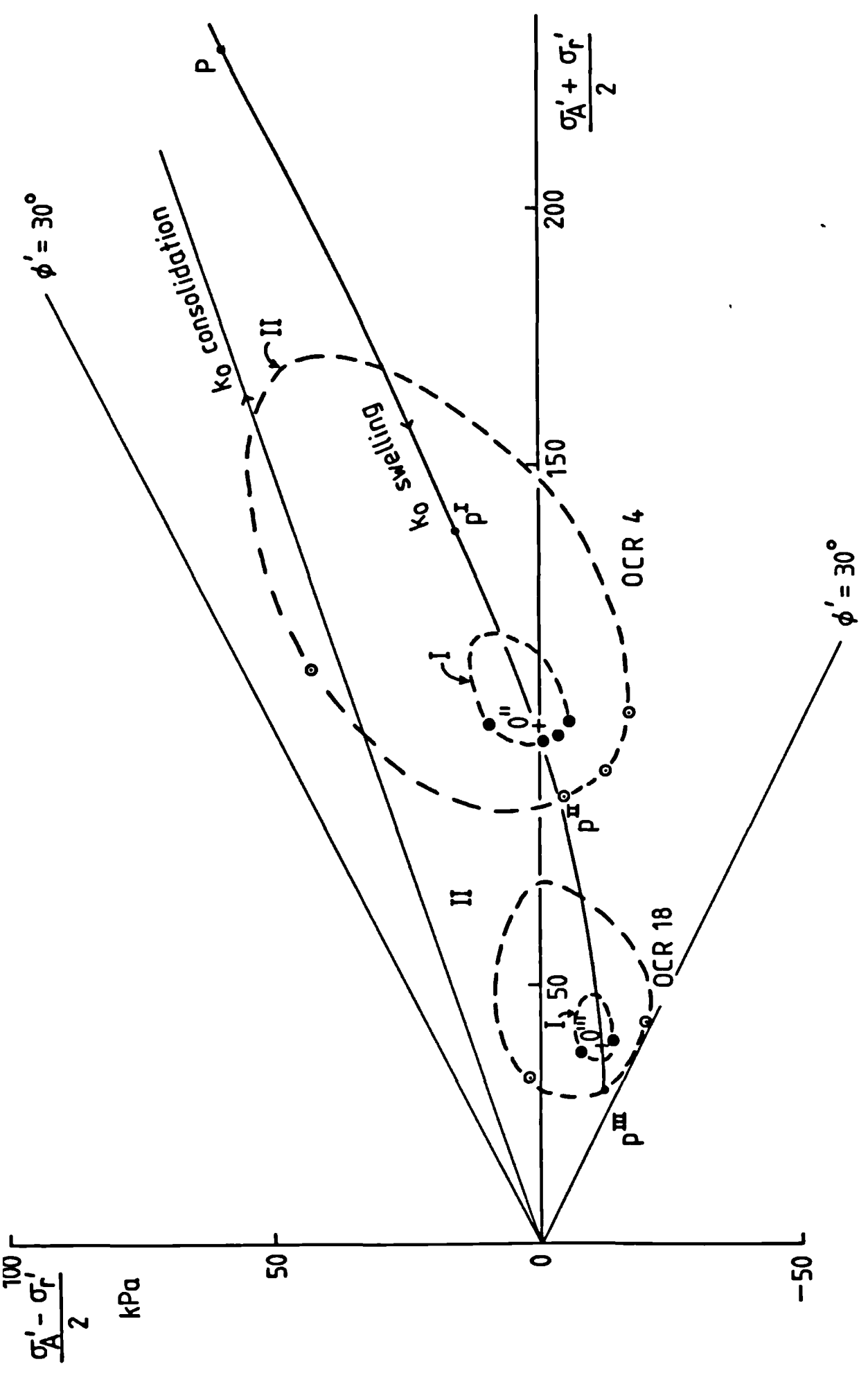


Figure 6.63 c). Sketched boundaries for zones I and II, OCR 4 and OCR 18.

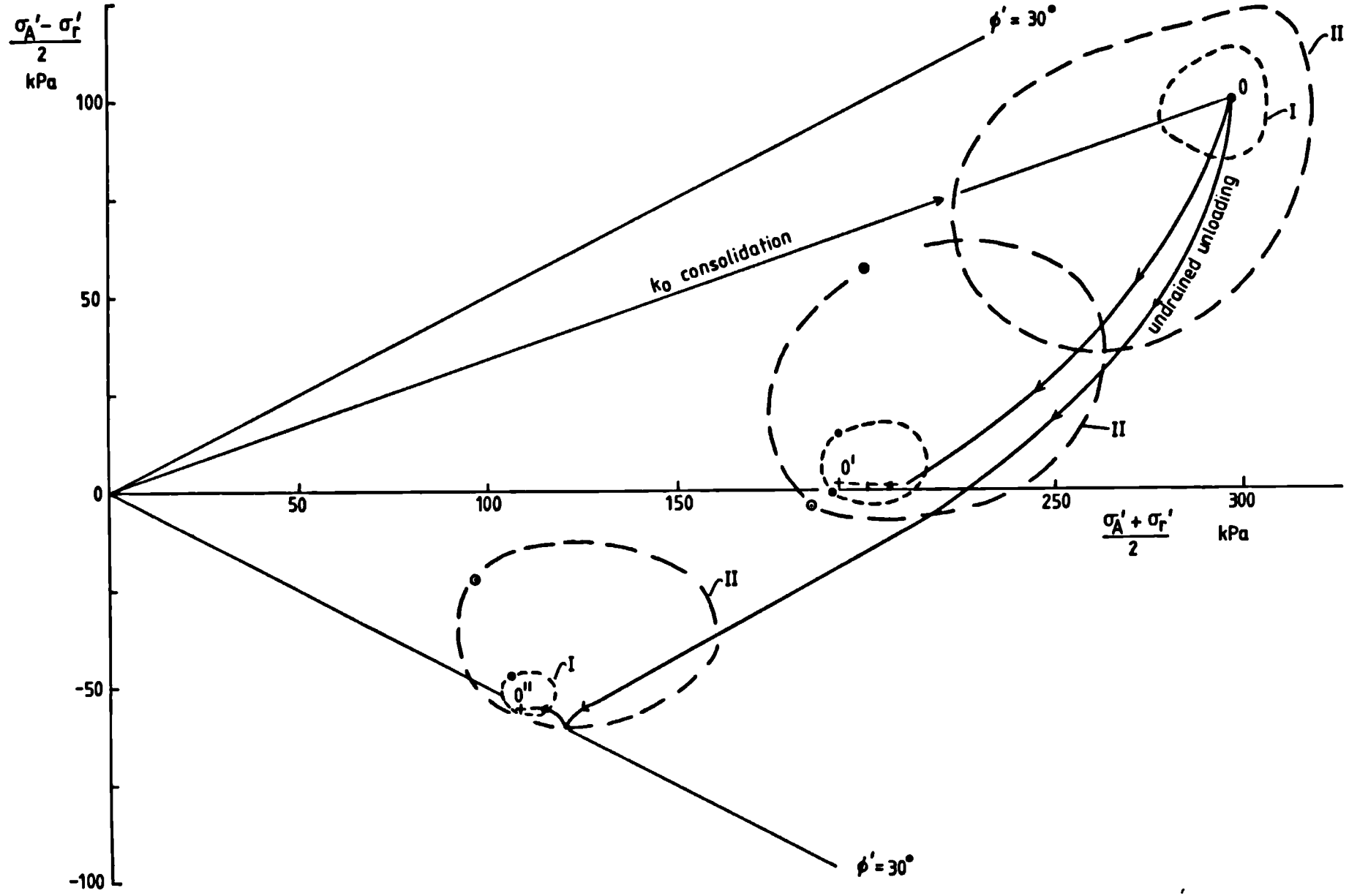


Figure 6.64. Sketched boundaries for zones I and II; OCR 1 at K_o condition, after perfect sampling, and after extension to 5% axial strain.

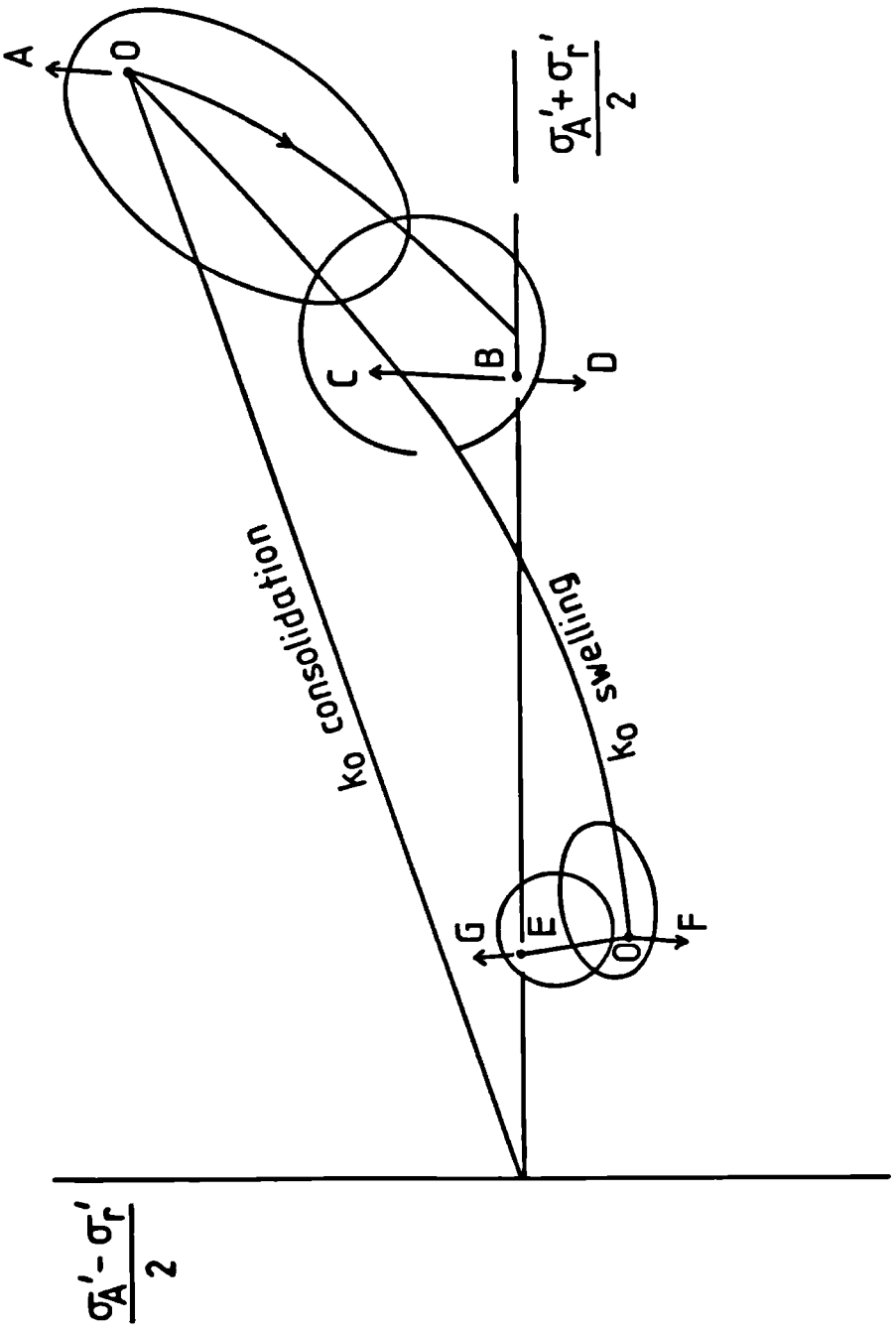


Figure 6.65. The effects of perfect sampling on stiffness anisotropy; schematic diagram.

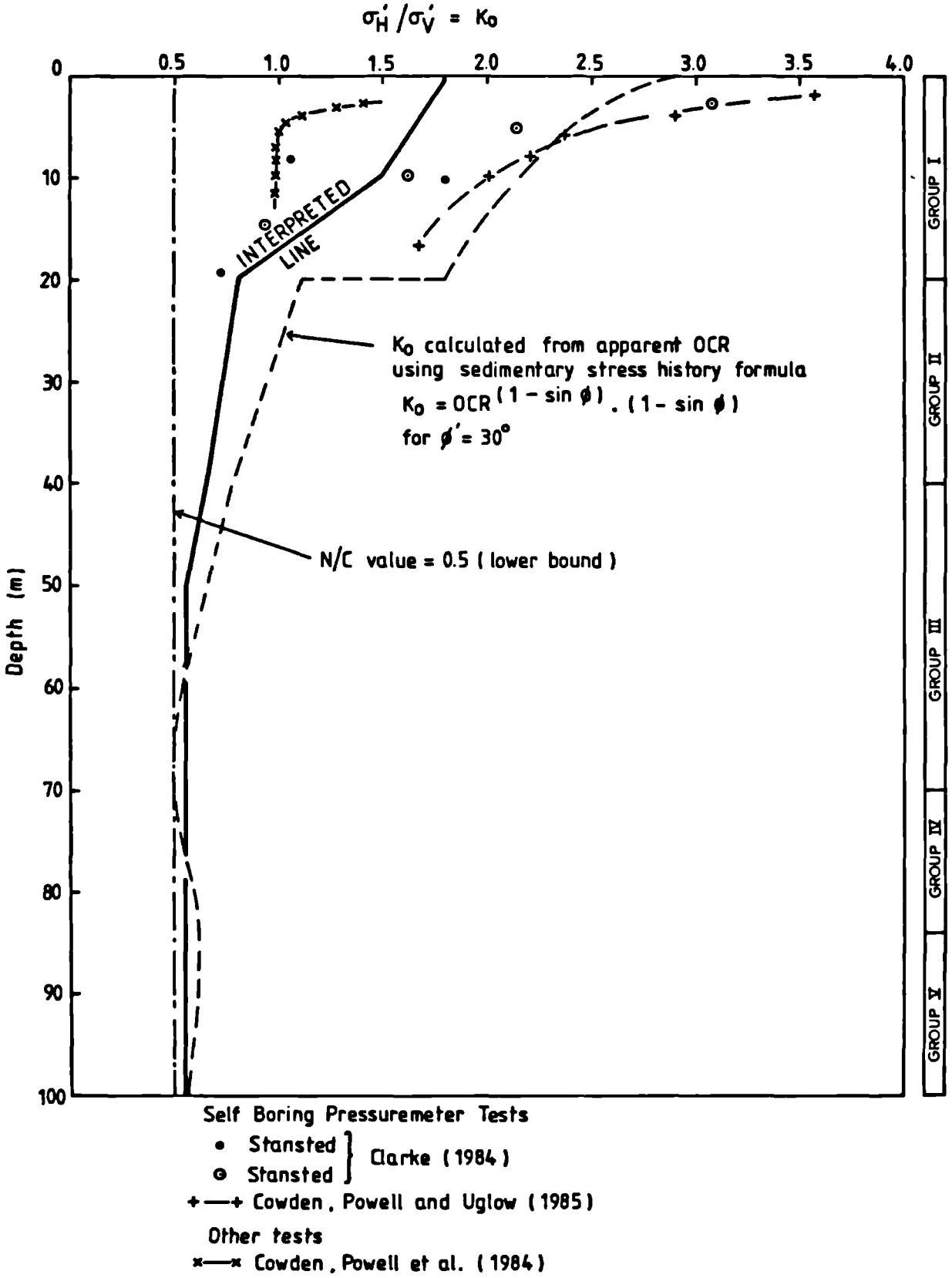


Figure 6.66. Variations of K_o with depth, various estimates.

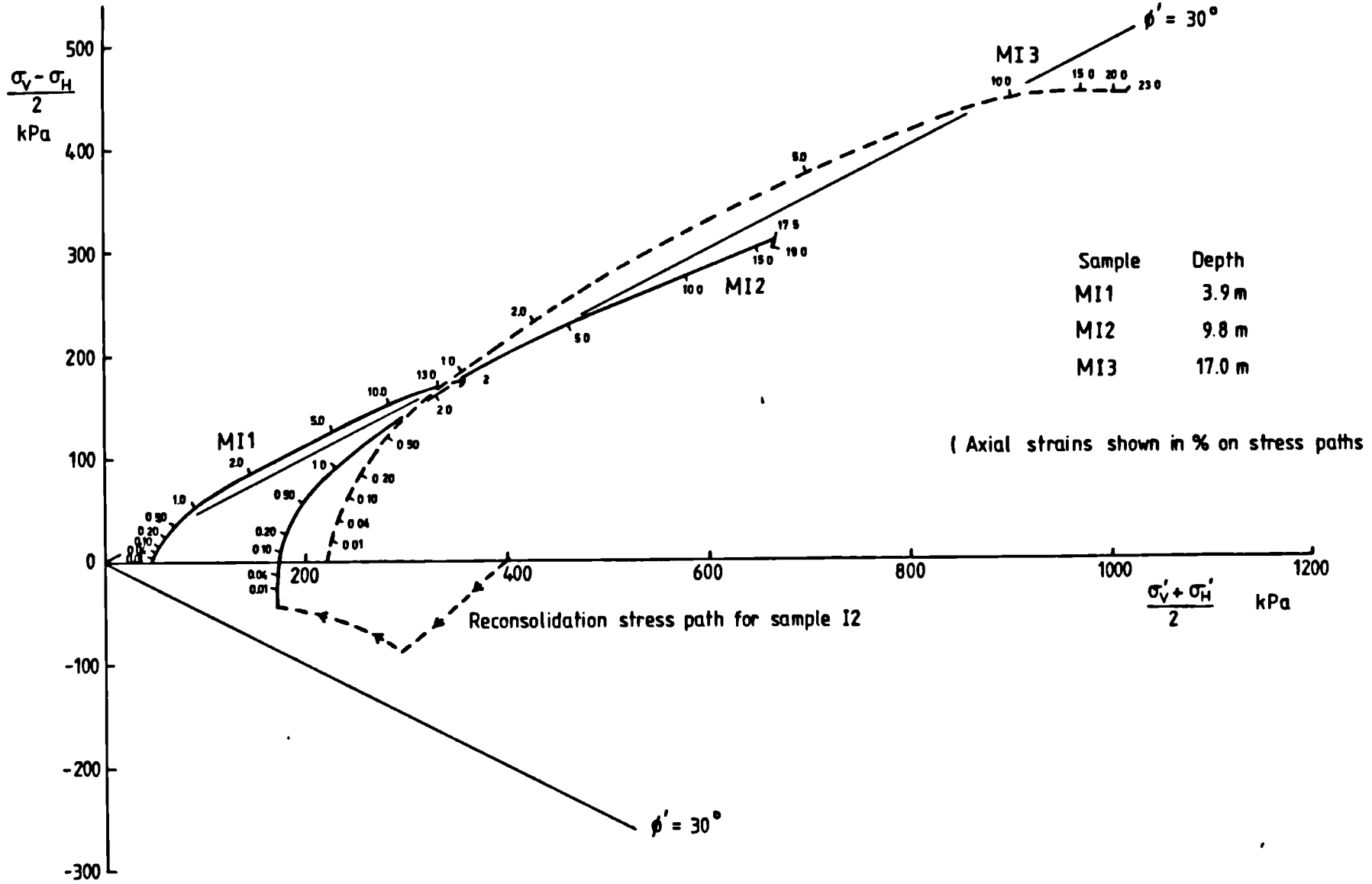


Figure 6.67. Effective stress paths, unconsolidated and K_o consolidated tests, Group I.

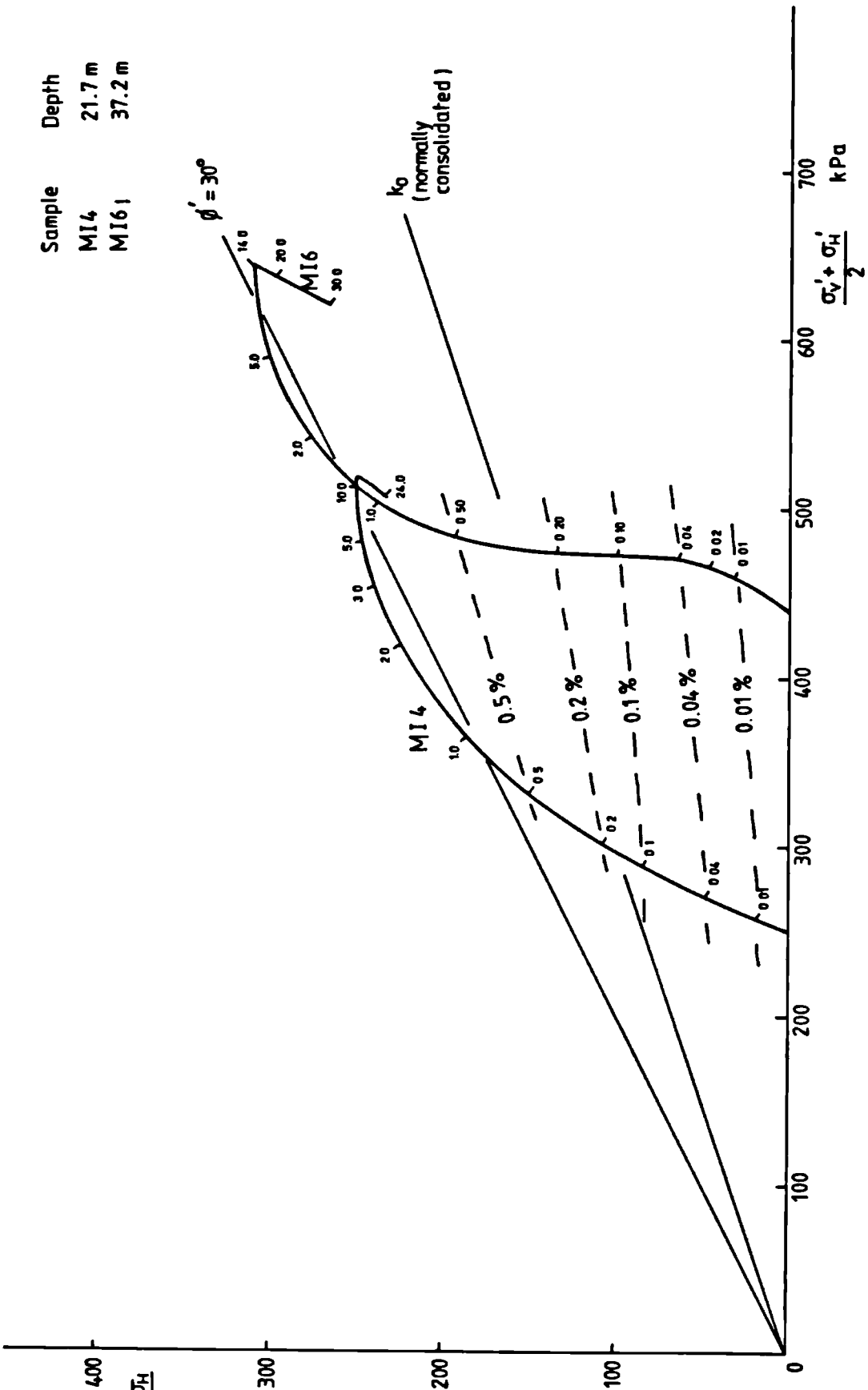


Figure 6.68. Effective stress paths, unconsolidated tests, Group II.

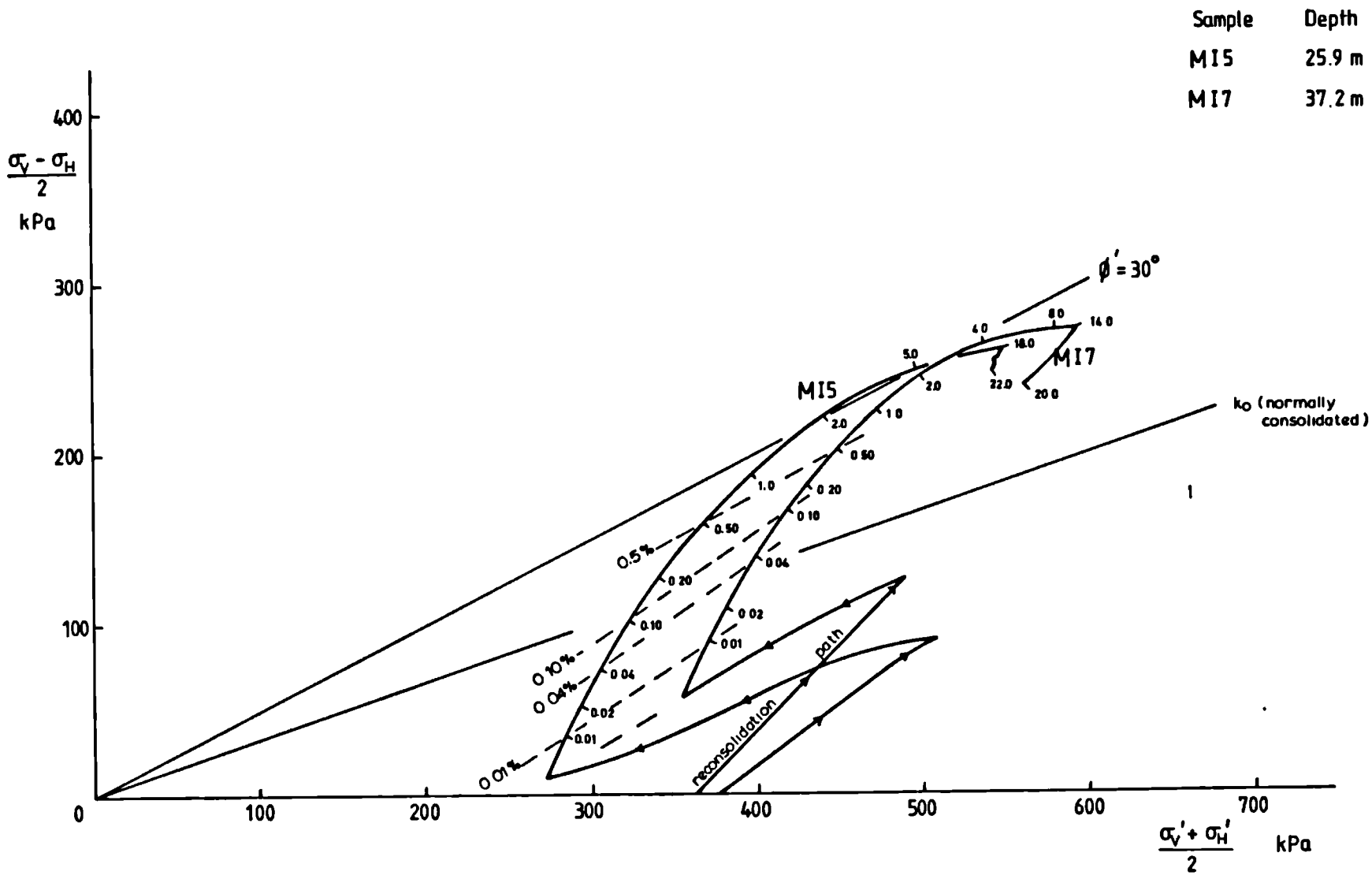


Figure 6.69. Effective stress paths, K_o consolidated tests, Group II.

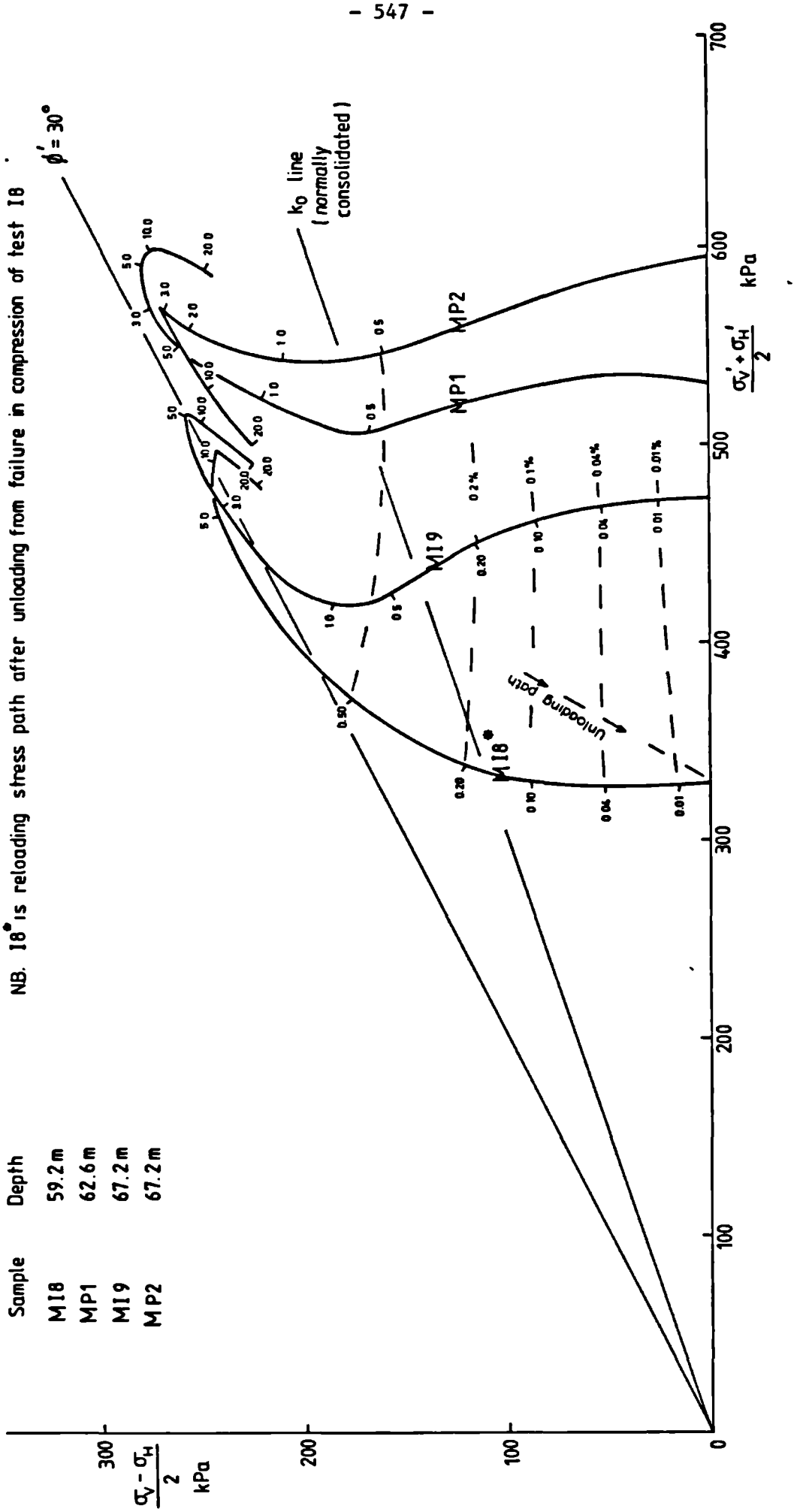


Figure 6.70. Effective stress paths, unconsolidated tests, Group III.

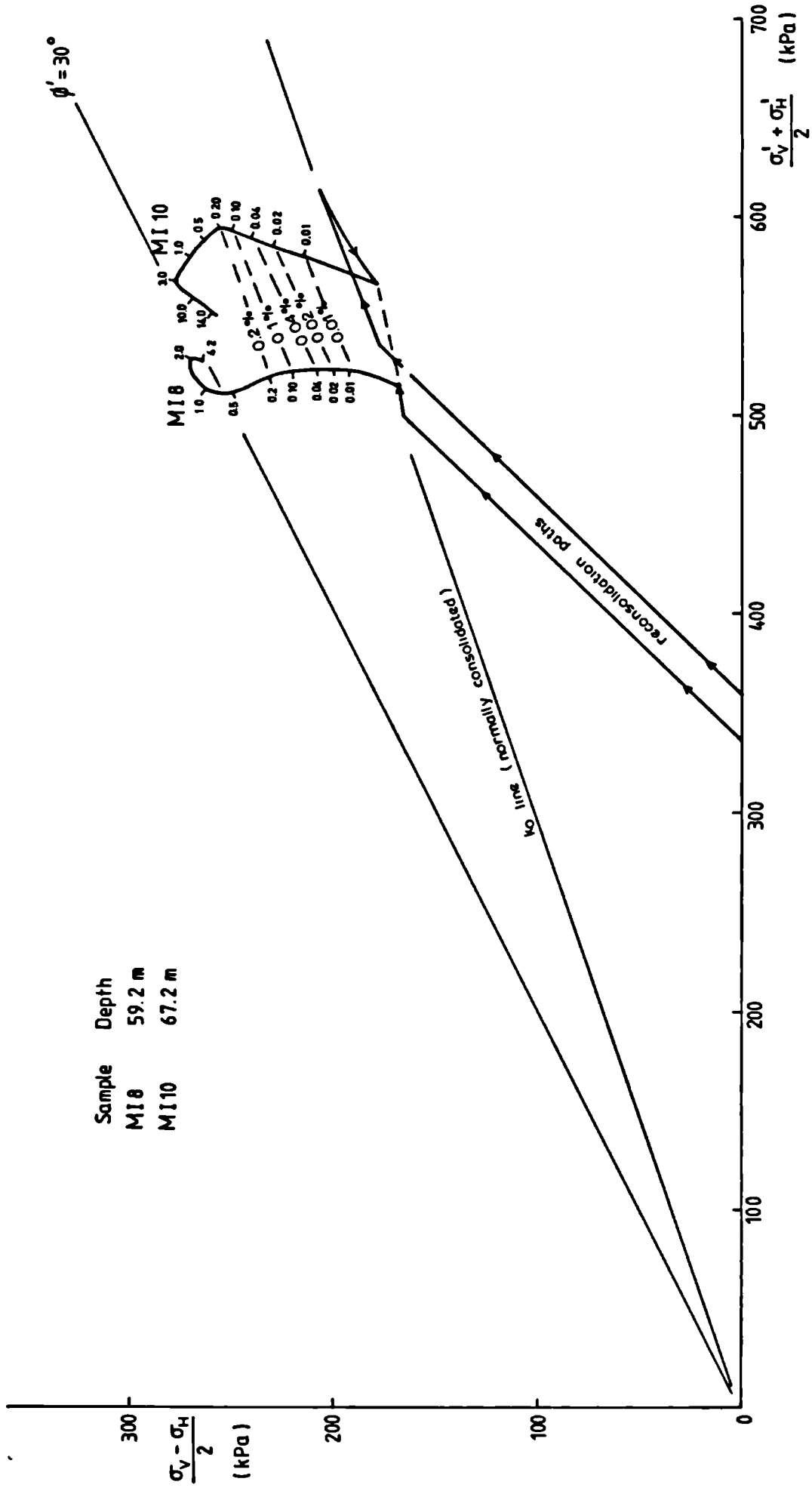


Figure 6.71. Effective stress paths, K_o consolidated tests, Group III.

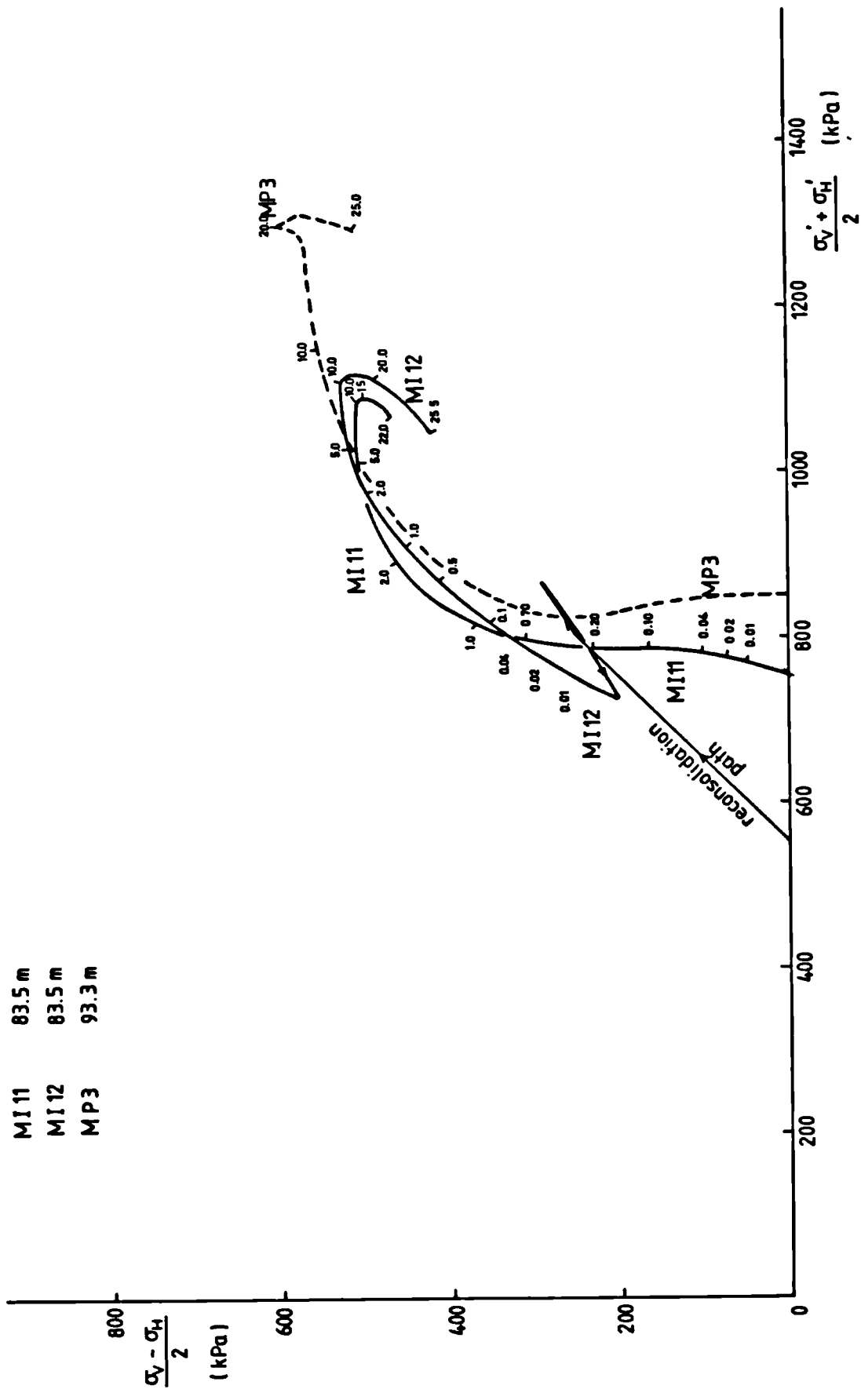
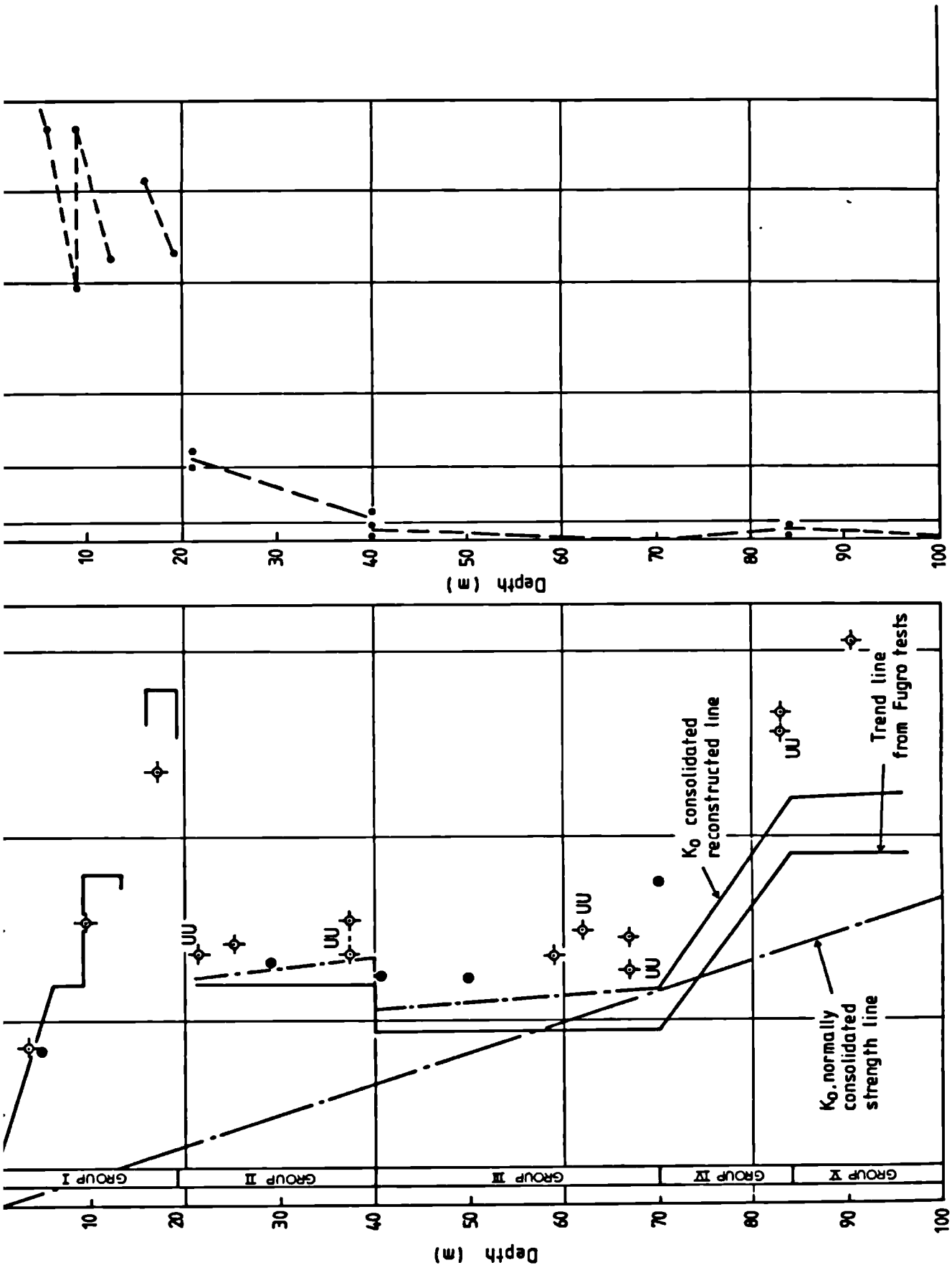


Figure 6.72. Effective stress paths, unconsolidated and K_o consolidated tests, Group IV.


Depth (m)
10
20
30
40
50
60
70
80
90
100
GROUP I
GROUP II
GROUP III
GROUP IV
GROUP V
UU
UU
UU
UU
UU
K_o consolidated reconstructed line
Trend line from Fugro tests
K_o normally consolidated strength line
I.C. Intact tests (UU denotes unconsolidated)
Push in pressuremeter test

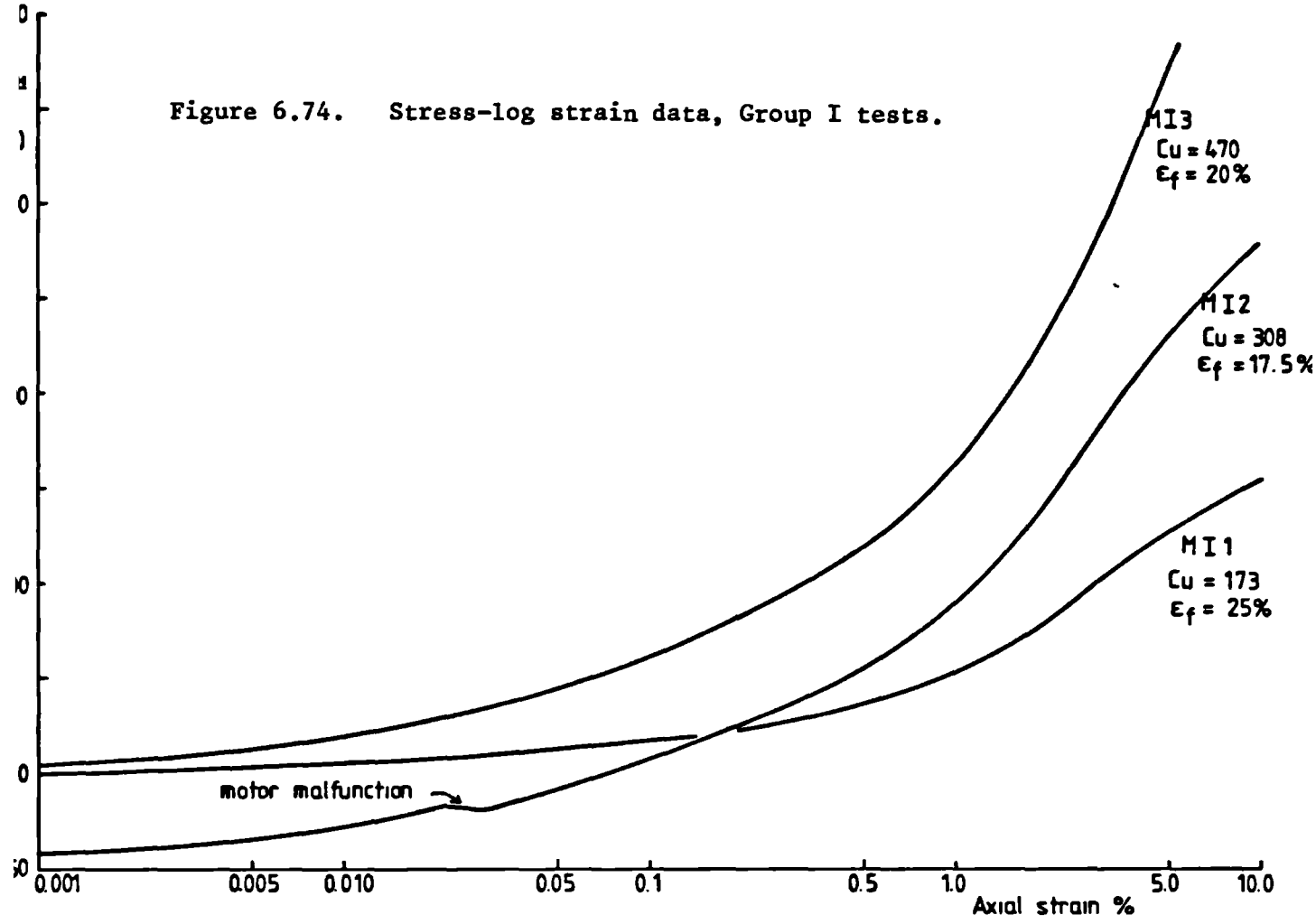


Figure 6.74. Stress-log strain data, Group I tests.

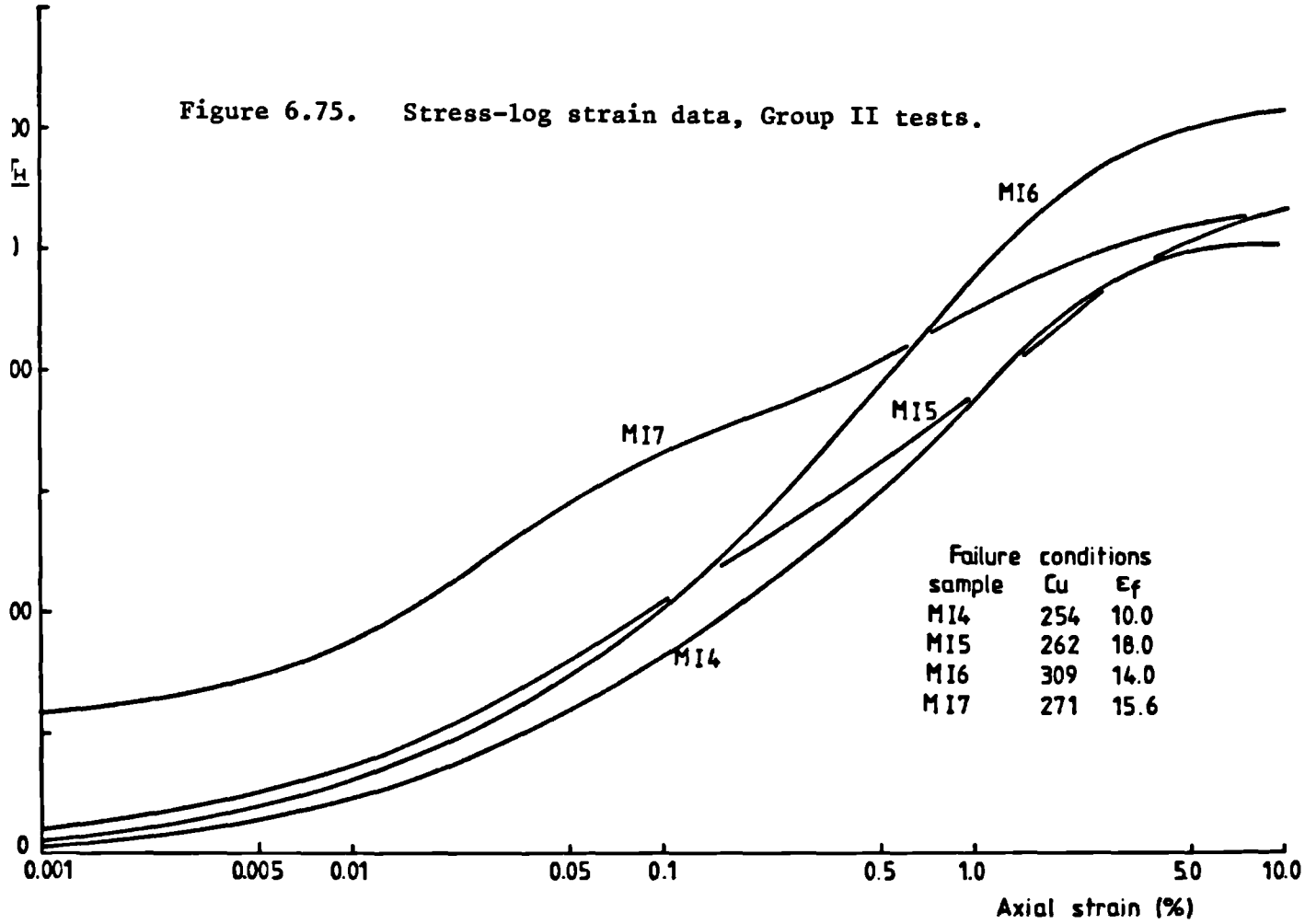


Figure 6.75. Stress-log strain data, Group II tests.

Figure 6.76. Stress-log strain data, Group III tests.

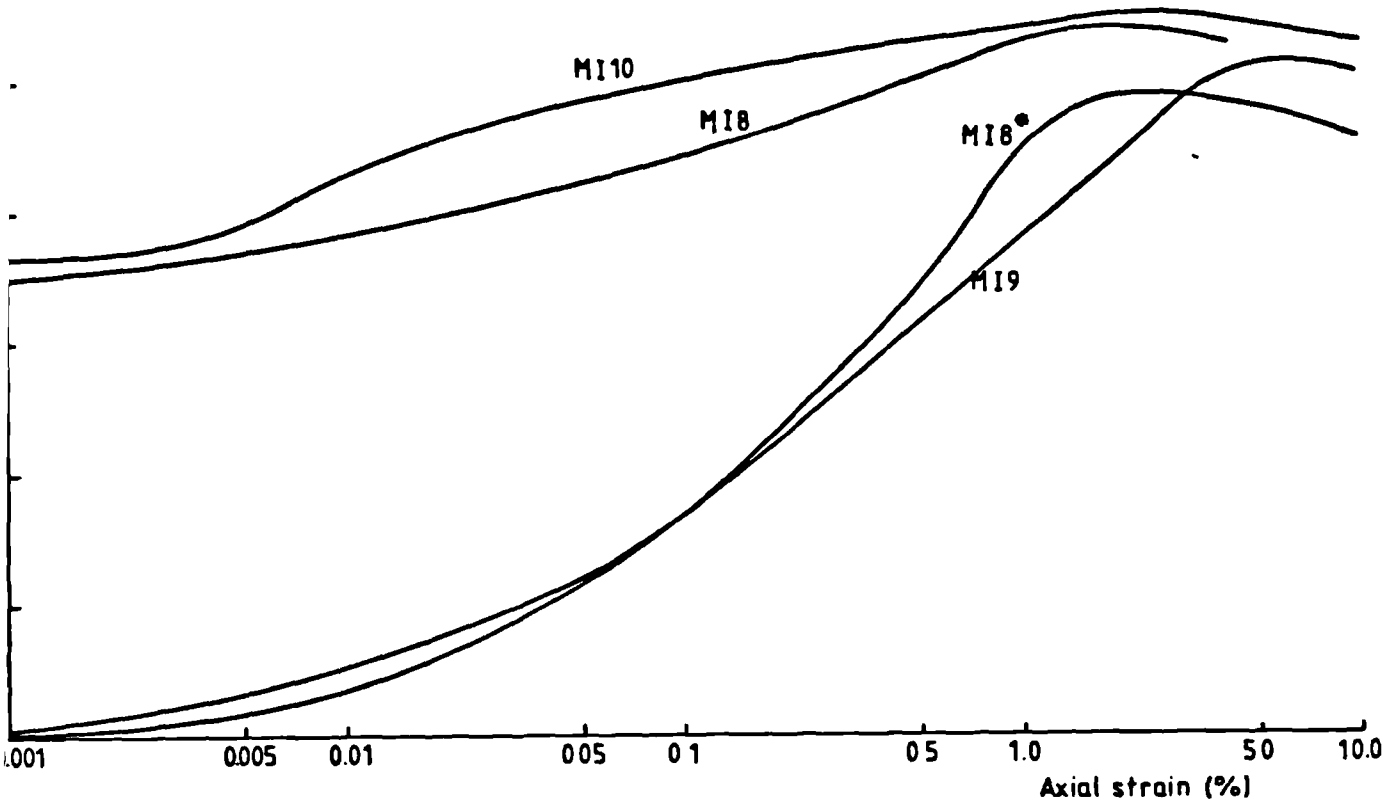
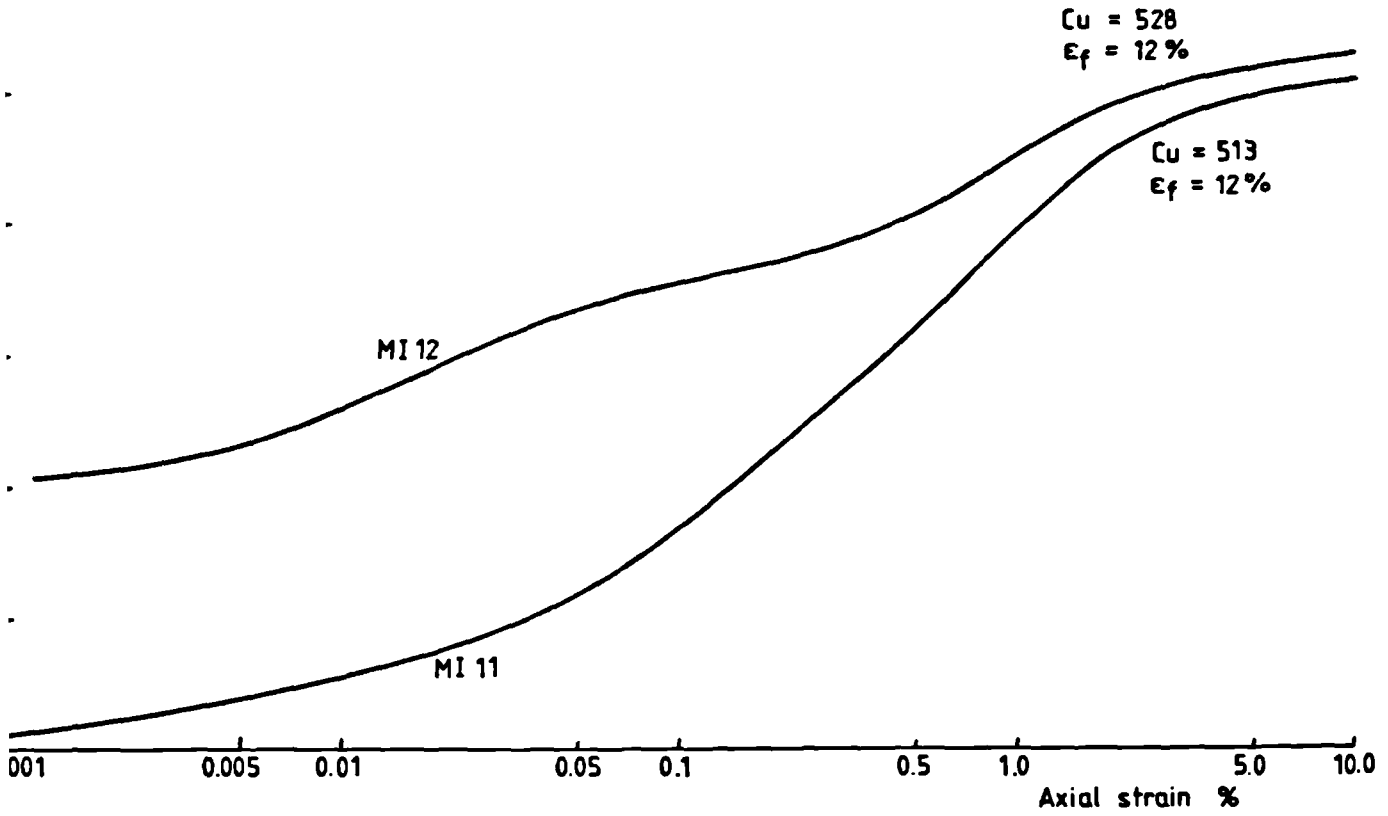


Figure 6.77. Stress-log strain data, Group IV tests.



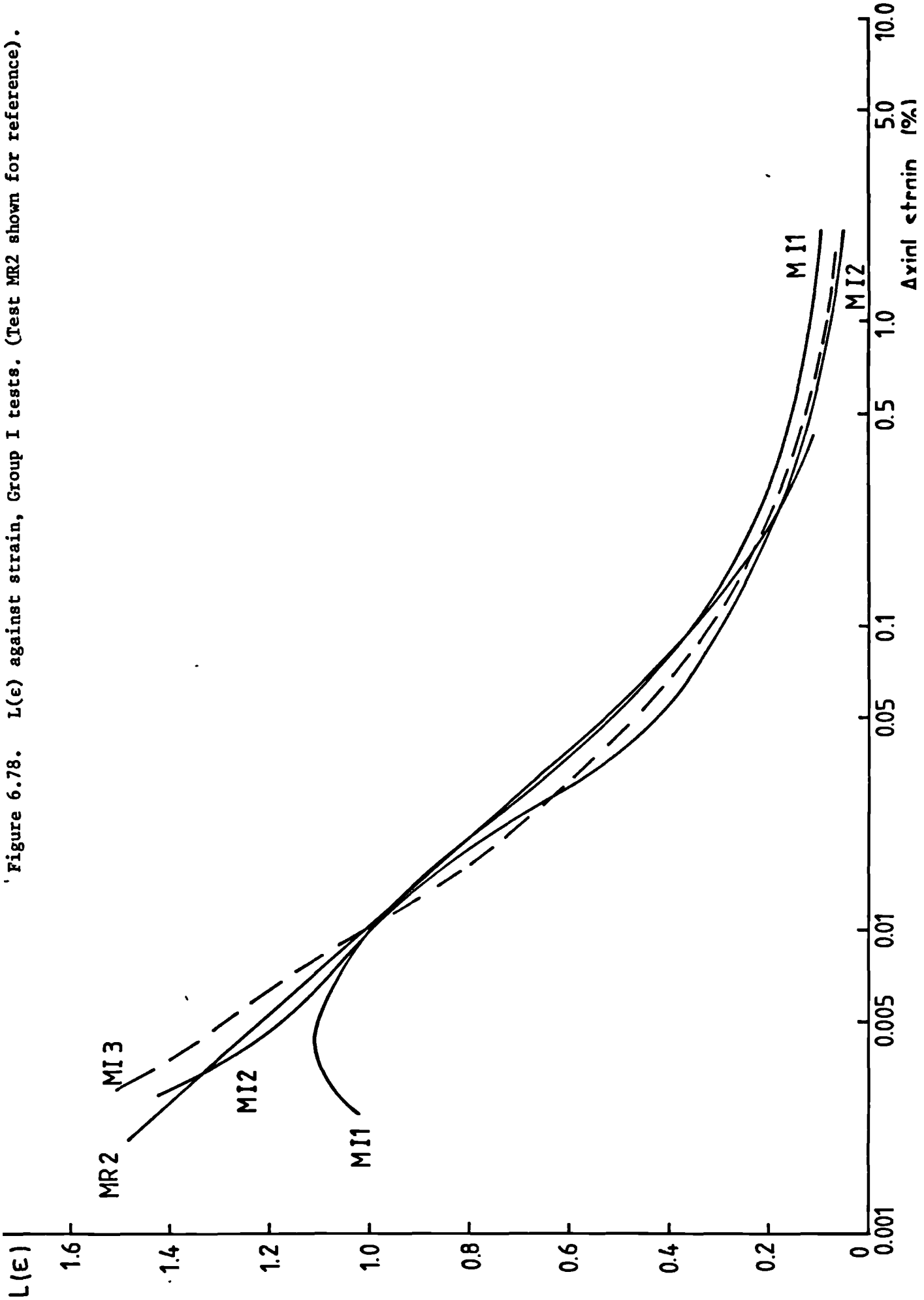


Figure 6.78. L(ε) against strain, Group I tests. (Test MR2 shown for reference).

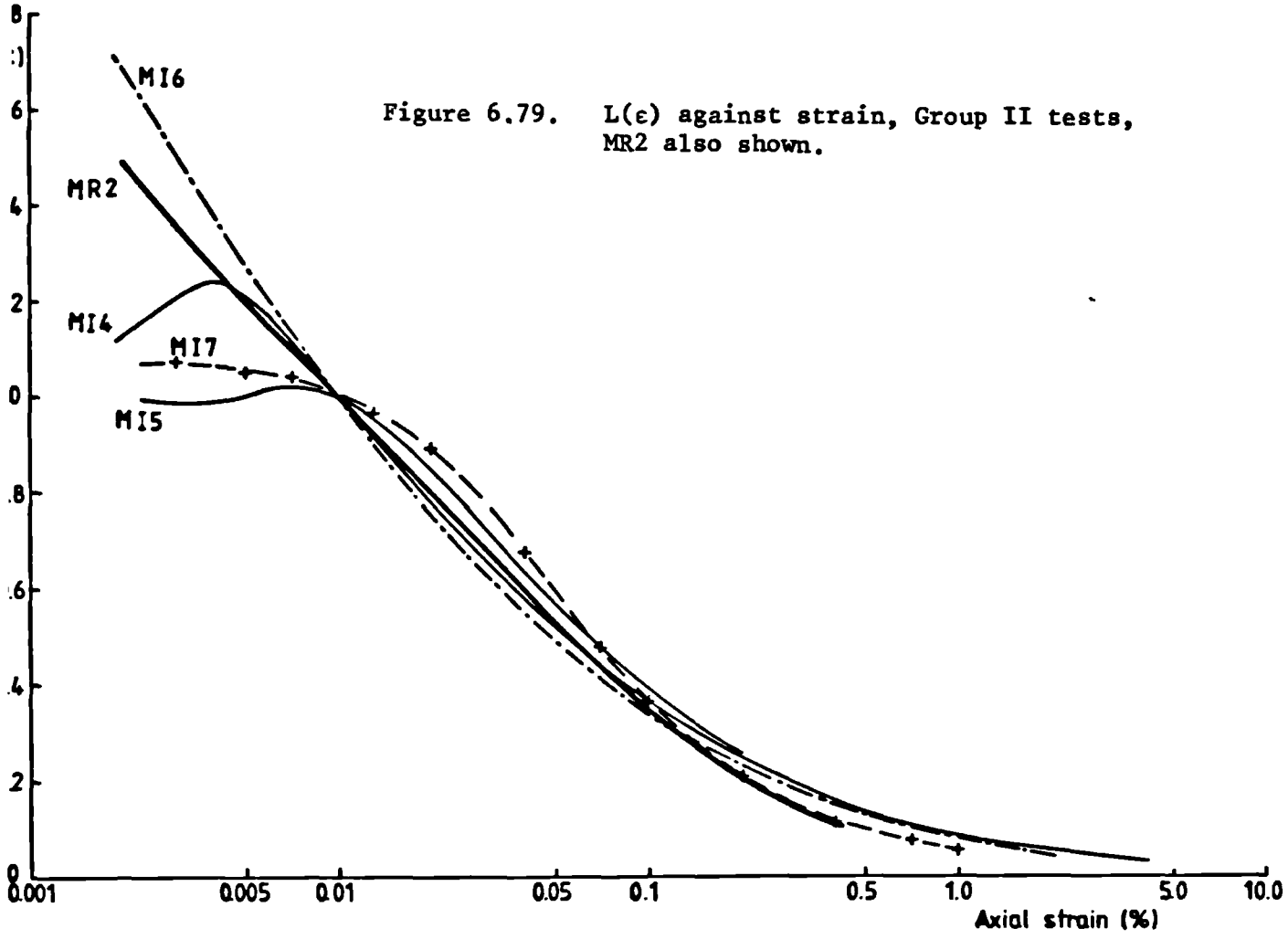


Figure 6.79. L(ε) against strain, Group II tests, MR2 also shown.

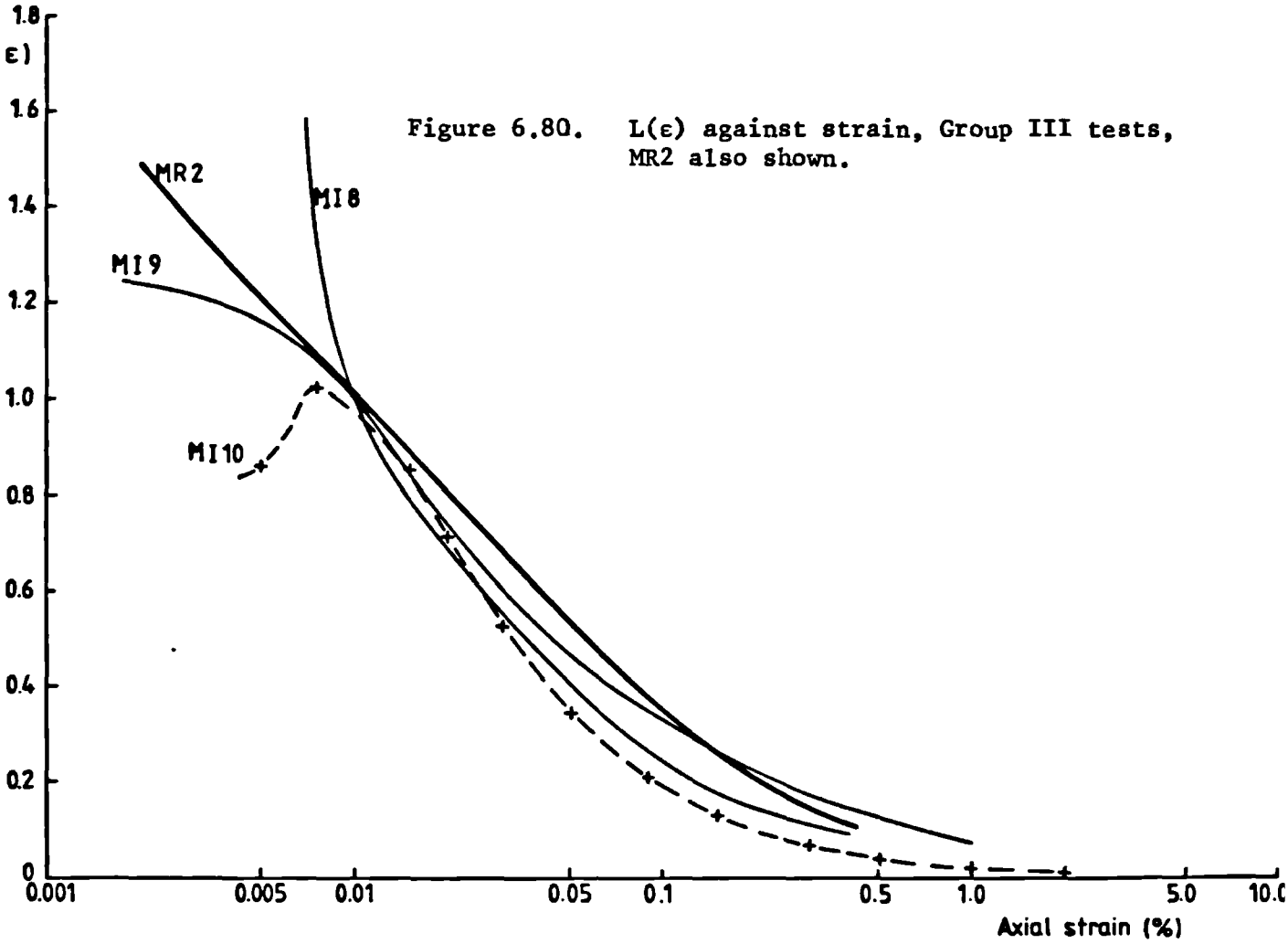


Figure 6.80. L(ε) against strain, Group III tests, MR2 also shown.

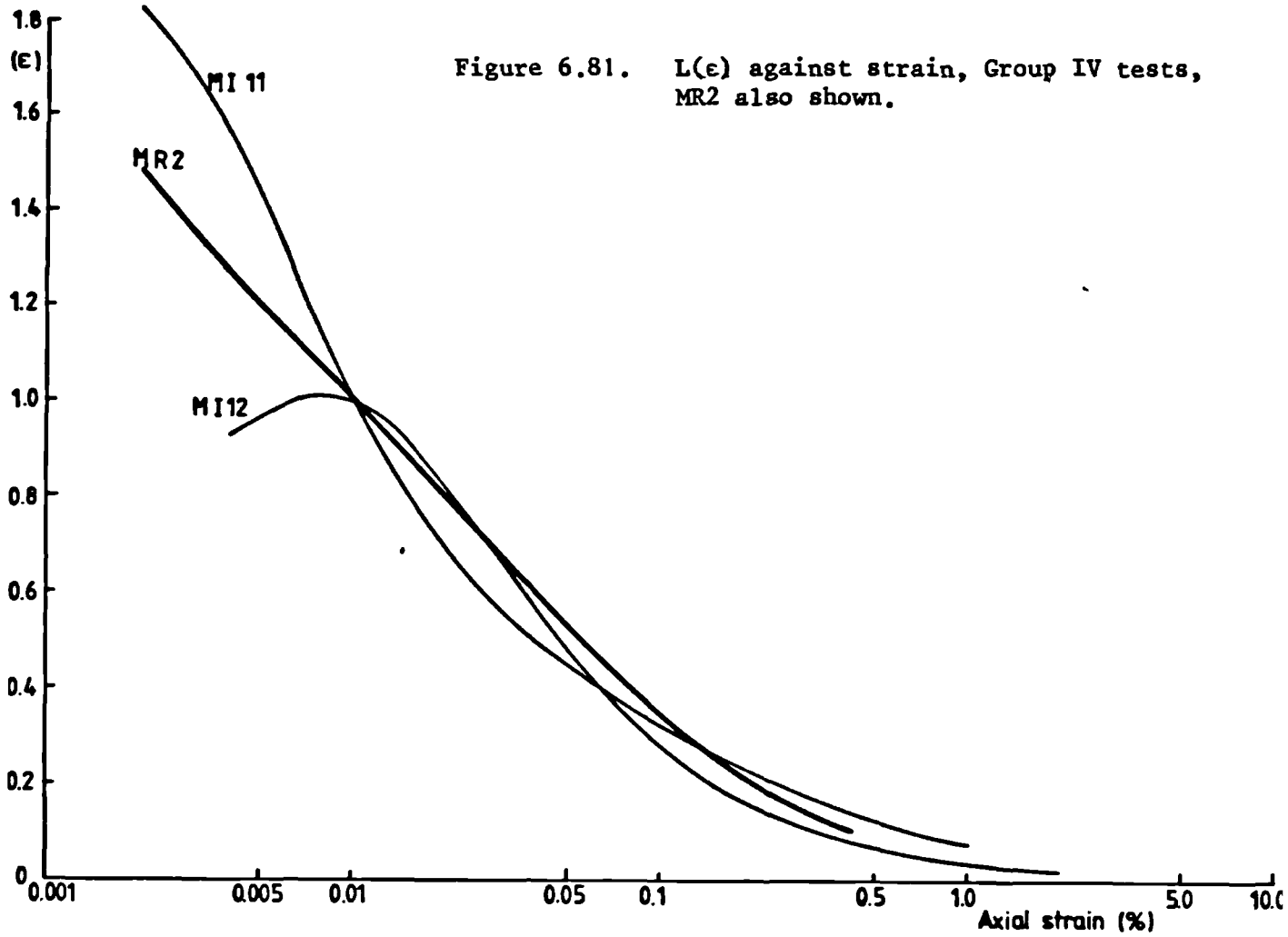


Figure 6.81. L(ε) against strain, Group IV tests, MR2 also shown.

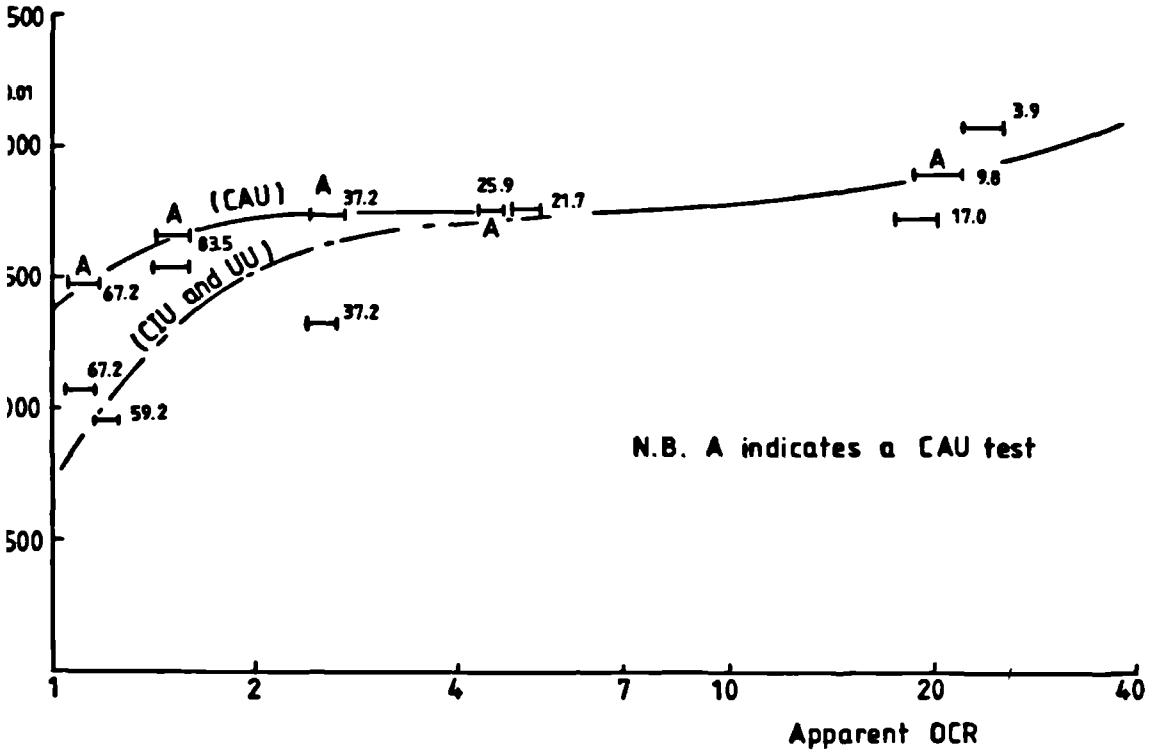


Figure 6.82. $(E_u p'_o)_{0.01}$ against apparent OCR, MI series, sample depths indicated in metres.

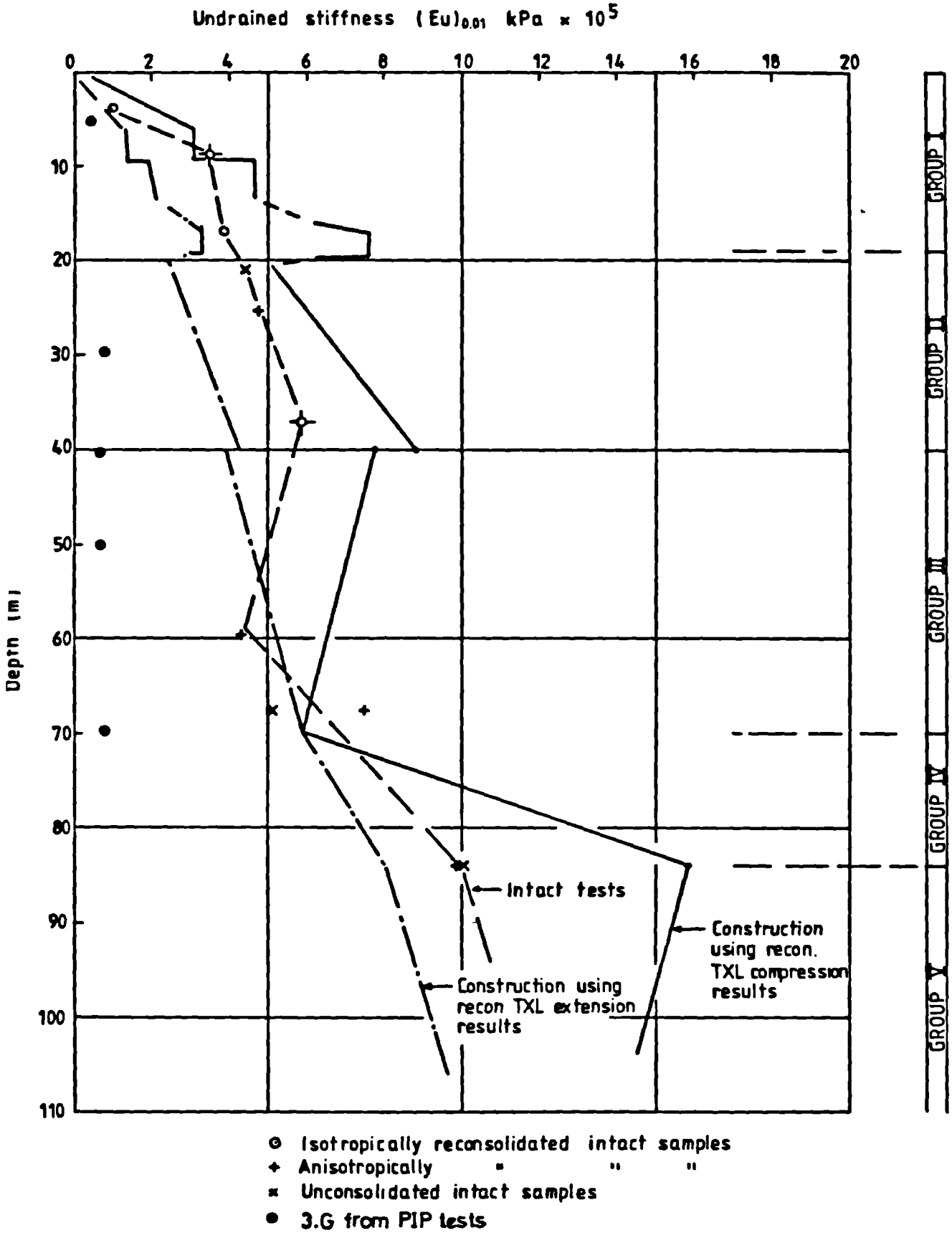


Figure 6.83. $E_{u(0.01)}$ plotted against depth for intact samples. Also shown are profiles constructed from reconstituted E_u/p'_o - OCR relationships, and 3.G interpreted from Push in Pressuremeter tests.

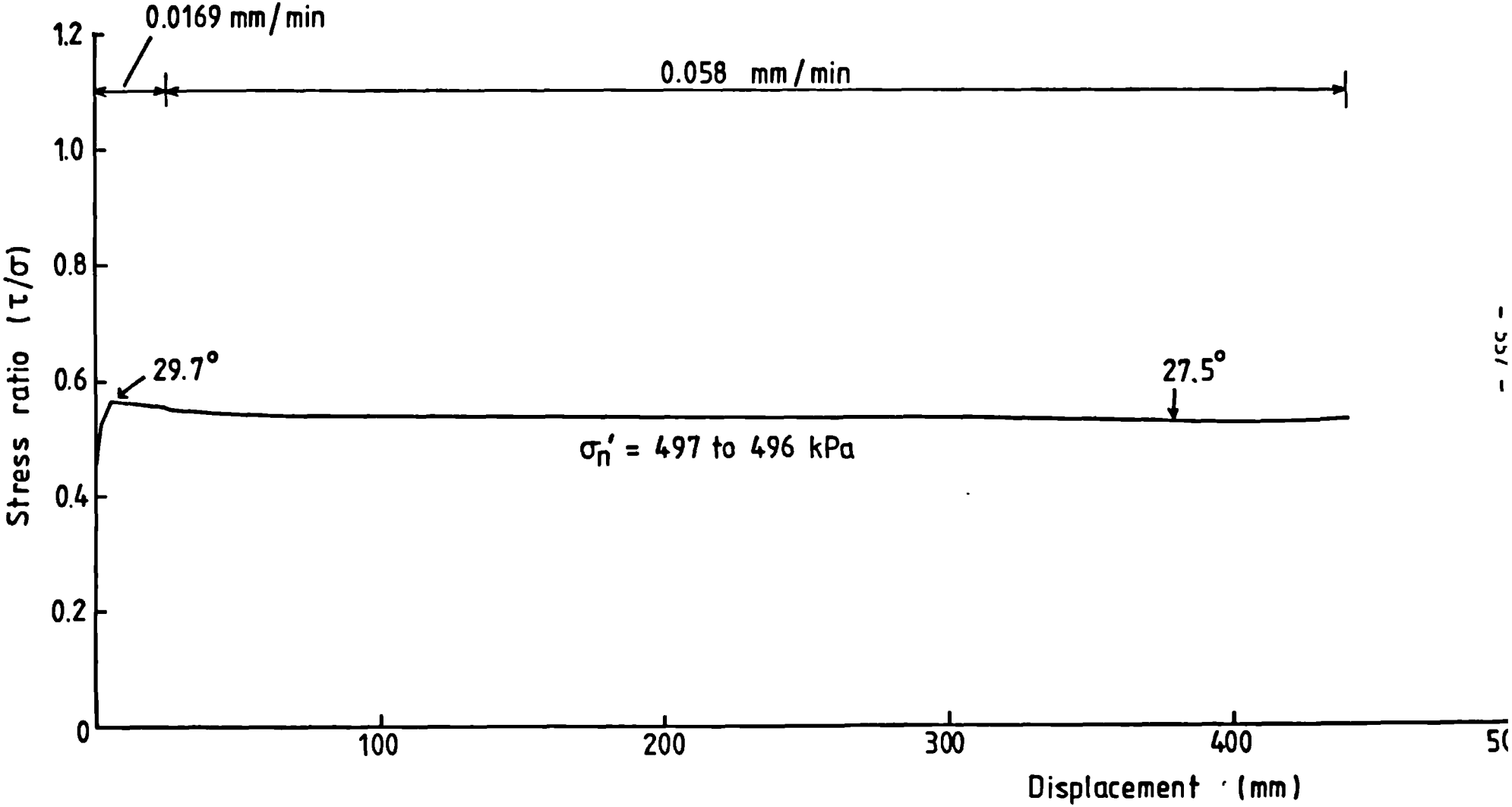


Figure 6.84. Soil-soil ring shear test on Magnus clay, after Lemos (1985).

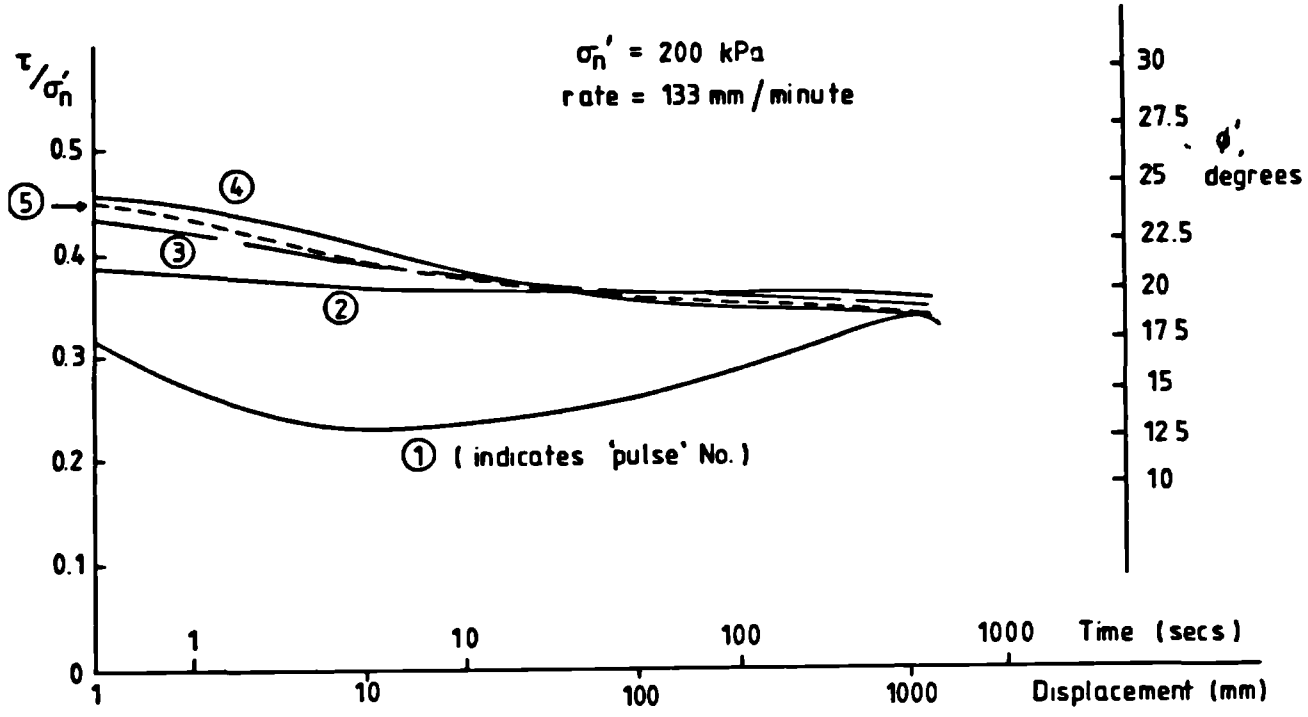


Figure 6.85. Soil-interface ring shear tests on Magnus clay; strength-displacement relationships for initial 5 pulses of shearing, after Lemos.

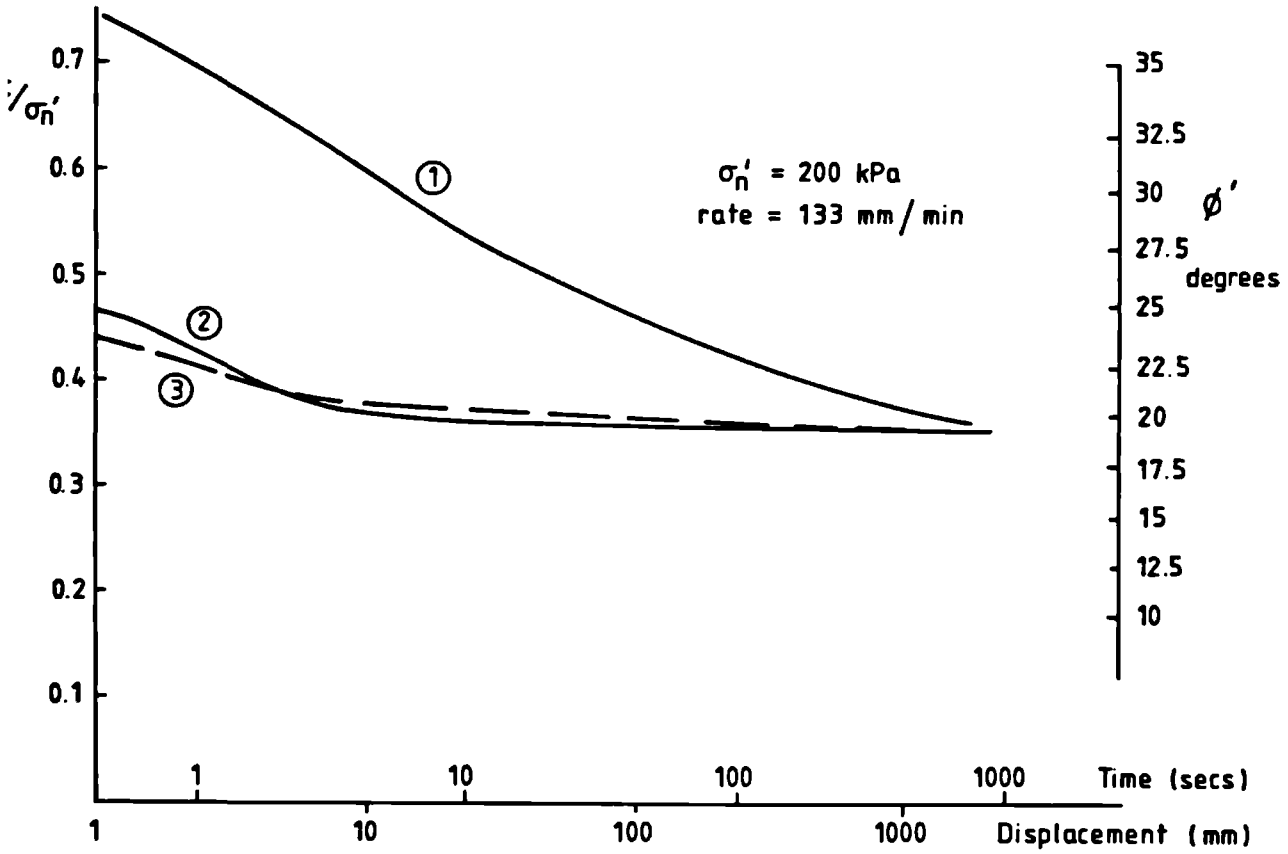


Figure 6.86. As above, further 5 pulses after slow shearing at σ'_n = 500 Kpa.

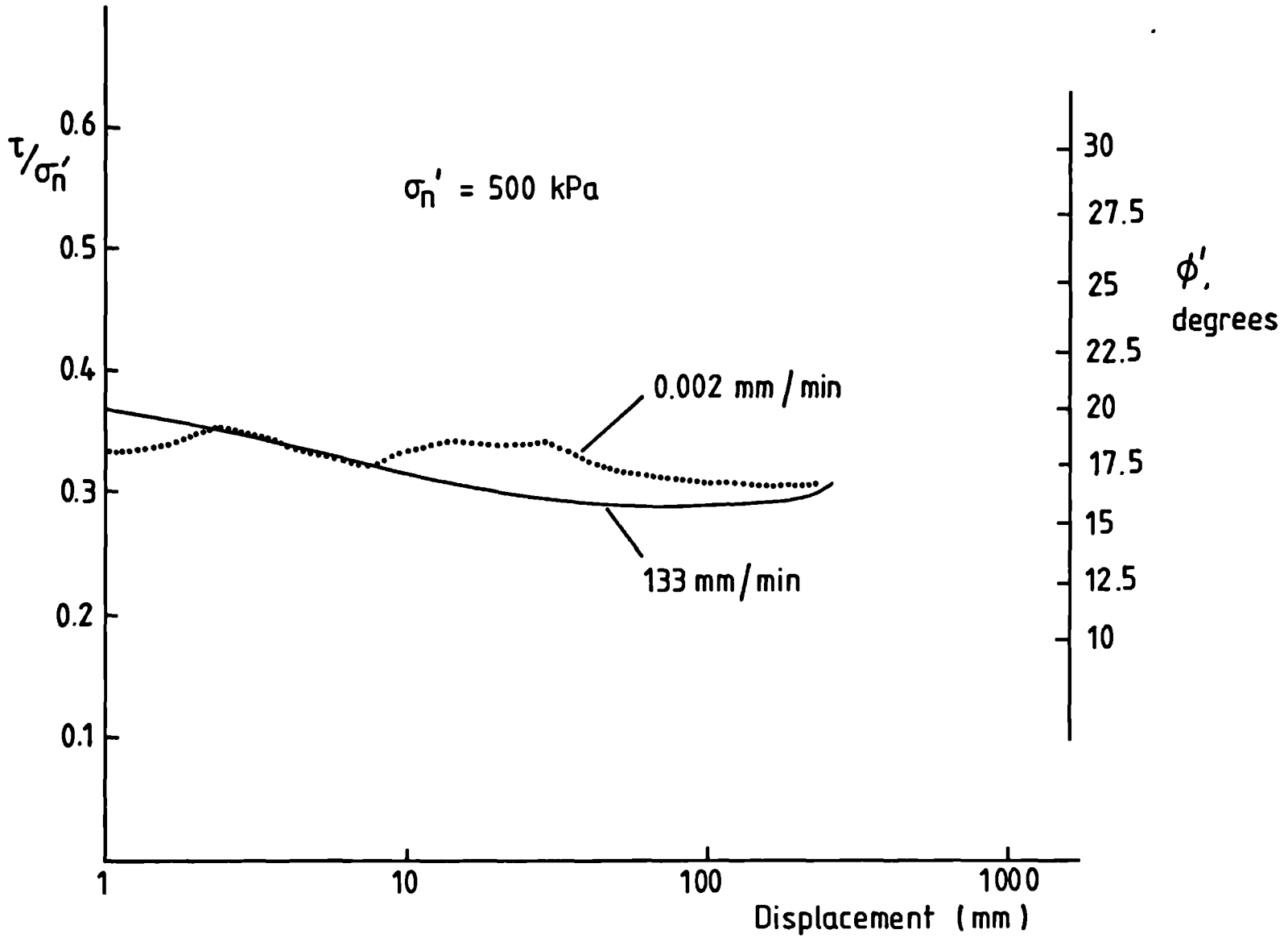


Figure 6.87. Soil-interface ring shear tests on Magnus clay : strength-displacement relationships for shearing at σ'_n = 500 Kpa after fast shear at σ'_n = 200 Kpa, after Lemos (1985).

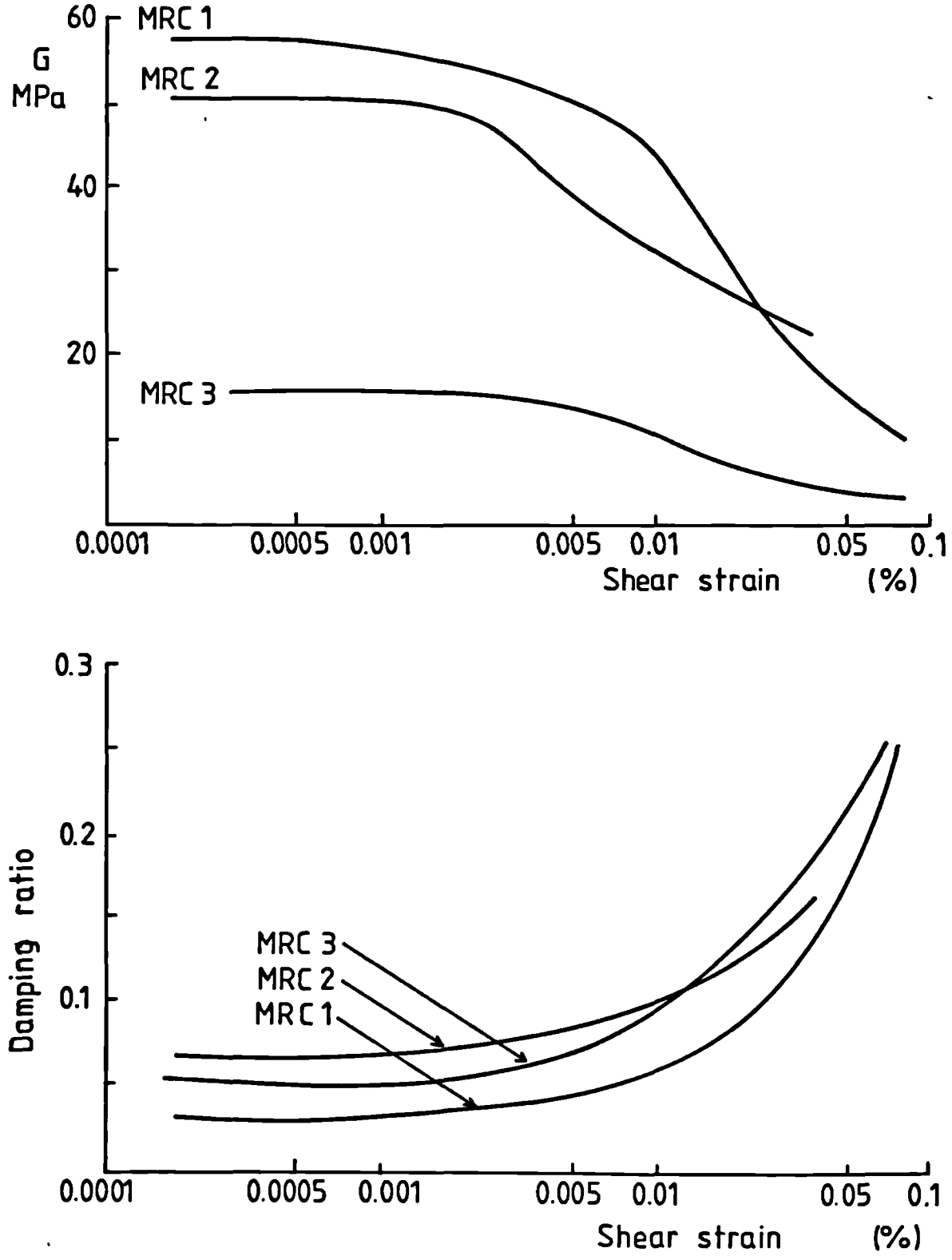


Figure 6.88. Resonant column test results, reconstituted Magnus clay, isotropically consolidated.

CHAPTER 7

Tables and Figures

Depth m	Water Content %	Liquid Limit %	Plastic Limit %	Plasticity Index %	Bulk Density kn/m3
1.4	30.0	85.4	28.1	57.3	19.05
2.4	26.5				19.68
2.7	27.8	78.8	28.3	50.5	19.27
3.5	29.7	86.4	28.8	57.6	19.02
4.1[1]	29.8	86.8	30.8	56.0	19.28
4.1[2]	-	67.6	25.9	41.7	-
4.6	25.7				19.53
5.1	31.2(?)	71.8	26.6	45.2	19.92
5.9	27.9				19.95
6.6	27.3	67.5	26.0	41.5	19.26
7.2	27.8				19.62
8.2	26.6	70.5	25.7	44.8	-
8.7	25.0				19.70
9.1	25.7				19.75
9.9	25.6	69.6	25.2	44.3	19.54

[1] In Disturbed London clay

[2] In Brown London clay.

Table 7.1. Variation of Index properties with depth

Test	Stress Range Kpa	e_1	c_c	c_s
LOED1	1,300 - 2,200	1.328	0.228	0.061
LOED2	1,300 - 2,200	1.280	0.206	0.041
LOED3	400 - 600	2.005	0.397	0.045
LOED3	10 - 400	2.312	0.545	-
Bell Common Sample	1,300 - 2,200	1.290	0.215	0.051

Table 7.2. Oedometer e - logσ'_v coefficients (e_1 is voids ratio for σ'_v = 1 Kpa for virgin compression curve)

Series	Description
LI	Unconsolidated, undrained compression tests on intact samples
LR	K_o consolidated, undrained, compression tests on reconstituted samples
LRE	K_o consolidated, undrained, extension tests on reconstituted samples
LRU	Various tests on reconstituted block samples.

Table 7.3. Description of Triaxial Test-Series.

Test No.	Depth m	p'_o Kpa	Cu peak Kpa	Cu ult Kpa	$E_{u(0.01)}$ Kpa	(Eu/p'_o) 0.01	L	$t_{0.1}$ mins
LI1	1.4	106.7	39.5	39.2	5.81×10^4	545	0.354	60
LI2	2.4	144.0	77.5	68.3	8.35×10^4	580	0.440	90
LI3	2.7	165.4	80.7	71	9.60×10^4	580	0.367	80
LI4	3.5	154	67.2	64	8.00×10^4	519	0.402	65
LI5	4.1	132	79	71	6.80×10^4	515	0.500	110
LI6	4.6	214.5	121.2	96	15.6×10^4	727	0.320	60
LI7	5.1	225.8	123	100	12.4×10^4	549	0.371	120
LI8	5.9	198	114	92	15.2×10^4	768	0.303	120
LI9	6.6	228.5	127.5	88	13.5×10^4	590	0.450	90
LI10	7.2	200	100	66	12.0×10^4	600	0.387	65
LI11	8.2	185.8	99.1	73	10.6×10^4	570	0.347	65
LI12	8.8	182.0	111.6	84	15.0×10^4	824	0.320	90
LI13	9.1	222	121.5	99	13.4×10^4	604	0.460	140
LI14	9.9	276	115	99	13.0×10^4	471	0.366	85

Table 7.4. Results for Series I tests

Layer	Mean $(E_u/p'_o)_{0.01}$	Mean L
Head	563	0.397
Disturbed London Clay	538	0.423
Brown London Clay	636	0.361
Blue London Clay	614	0.376
Mean of all samples	602	0.385

Table 7.5. Trends for stiffnesses at small strains, Series I.

Series	Test	σ'_{vc}kpa	OCR	Shearing Conditions
R	LR1	402	1	Undrained Compression
"	LR1.5	400	1.5	" "
"	LR3	399	3.0	" "
"	LR7	398	6.9	" "
RE	LRE1	397	1	Undrained Extension
"	LRE1.5	400	1.5	" "
"	LRE3	399	2.9	" "
"	LRE7	401	7.0	" "

Table 7.6. Tests on samples K_o consolidated in the triaxial cells

Test	Pre-shear Conditions		Strength		Stiffness			Strain rate
	p'_o Kpa	σ'_{vo} Kpa	Cu_p Kpa	Cu_{ult} Kpa	$E_{u(0.01)}$ Kpa	L	$(Eu/p'_o)_{0.01}$	$t_{0.1}$ Mins
LR1	292	401	106	78	1.41×10^5	0.319	482	38
LR1.5	225	267	93	79	1.90×10^5	0.418	844	10
LR3	148	132	79	68	1.30×10^5	0.416	880	123
LR7	93.4	58	75	70	9.9×10^4	0.480	1060	57
LRE 1	289	397	80	79	1.80×10^5	0.497	623	80
LREI.5	223	260	84	82	1.08×10^5	0.378	484	
LRE3	155	140	-	-	7.4×10^4	0.267	477	65
LRE7	84	58	46	40	3.54×10^4	0.377	421	50

Table 7.7. Summary of results from Series LR and LRE

Test Description	Test	p'_o	Stiffness			Strain rate
		Kpa	$E_{u(0.01)}$ Kpa	$(Eu/p'_o)_{0.01}$	L	$t_{0.01}$ Mins
Slow UU test	LRUU1	90	5.5×10^4	611	0.389	80
Standard rate " "	LRUU2	90	4.8×10^4	538	0.448	12
Fast " " "	LRUU3	89	6.1×10^4	685	0.438	2.5
Slow Drained test from		p'_o	$E'_{(0.01)}$	$(E'/p'_o)_{0.01}$	L	$t_{(0.01)}$ Mins
Unconsolidated conditions	LRUD1	83	4.0×10^4	480	0.316	450

Table 7.8. Summary of triaxial tests on unconsolidated samples; Series LRUU

	Pre-shear conditions			Stiffness parameters			
	p'_o Kpa	σ'_{vo} Kpa	OCR	G_{max} Kpa	$G_{(0.01)}$ Kpa	L	$(3G/p'_o)_{0.01}$
LCR 1	293	400	1.0	4.78×10^4	4.60×10^4	0.63	471
LCR 2	186	200	2.0	3.90×10^4	3.85×10^4	0.69	619

Table 7.9. Summary of results from K_o consolidated resonant column tests

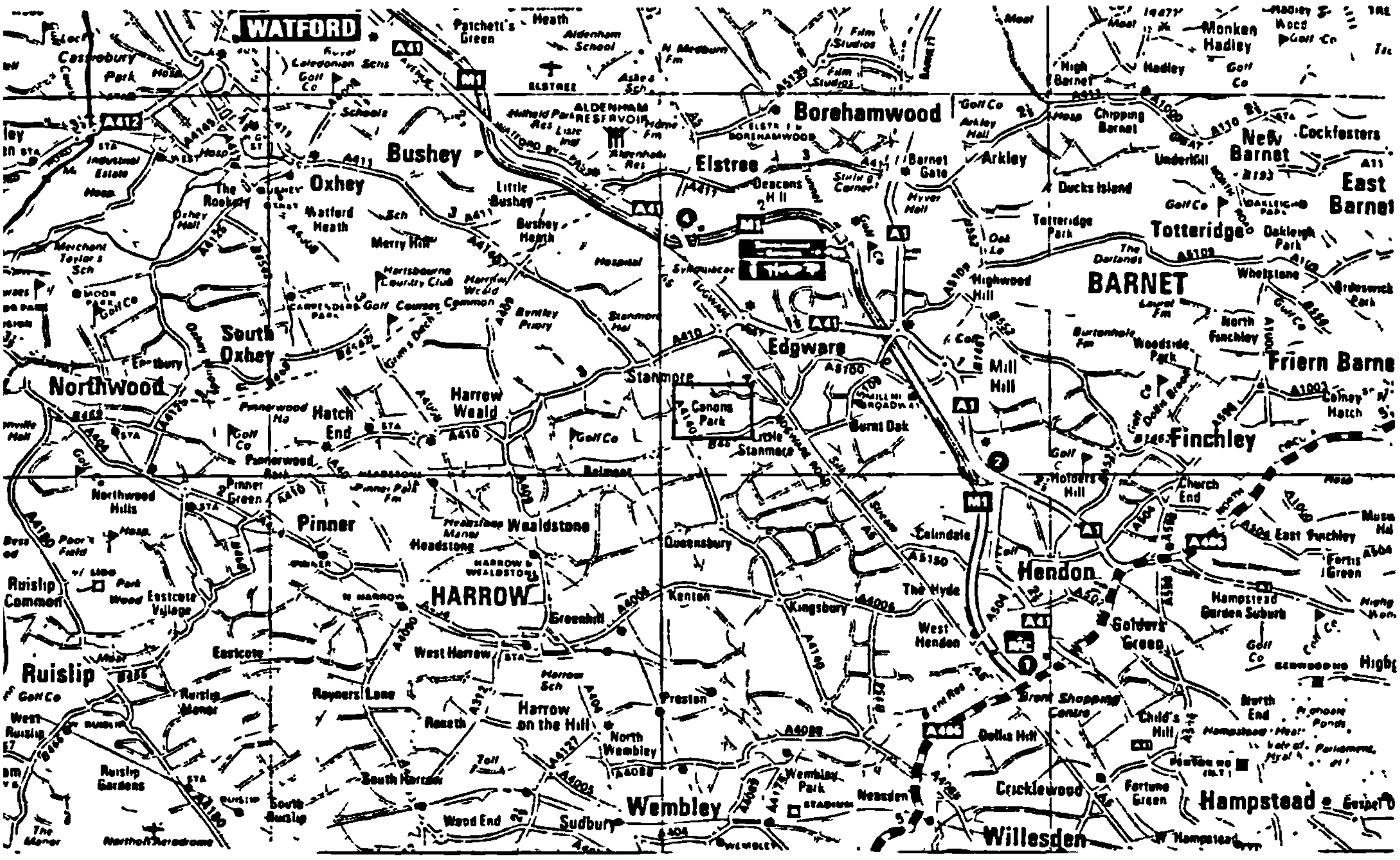
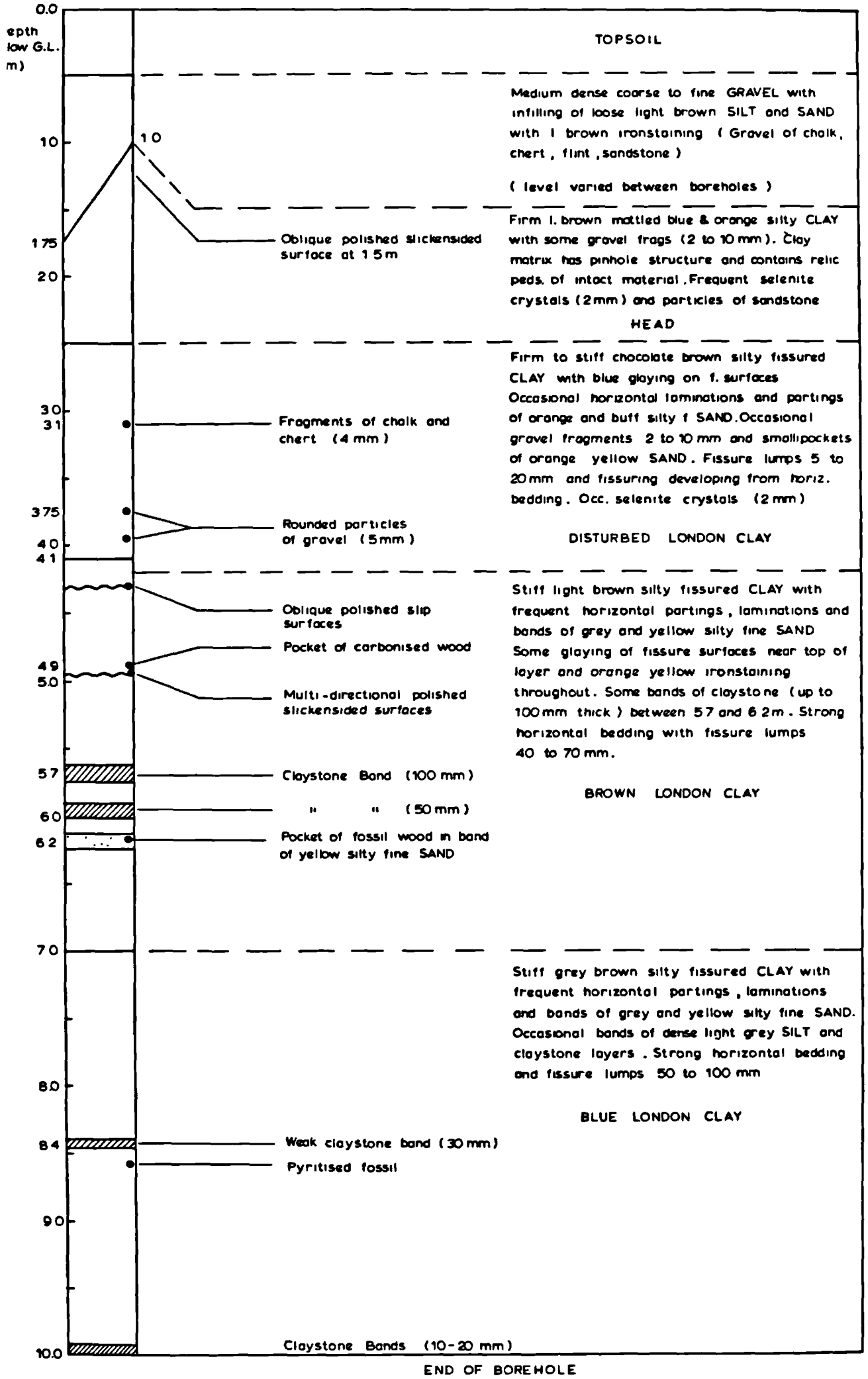


Figure 7.1. Location map for Canons Park.

Figure 7.2. Interpreted borehole log.



Figures 7.3, 7.4 and 7.5 (following 3 pages). Photographs of air dried samples from Canons Park.



1.2M



2.3M



3.7M



4.7M



6.8M



7.3M

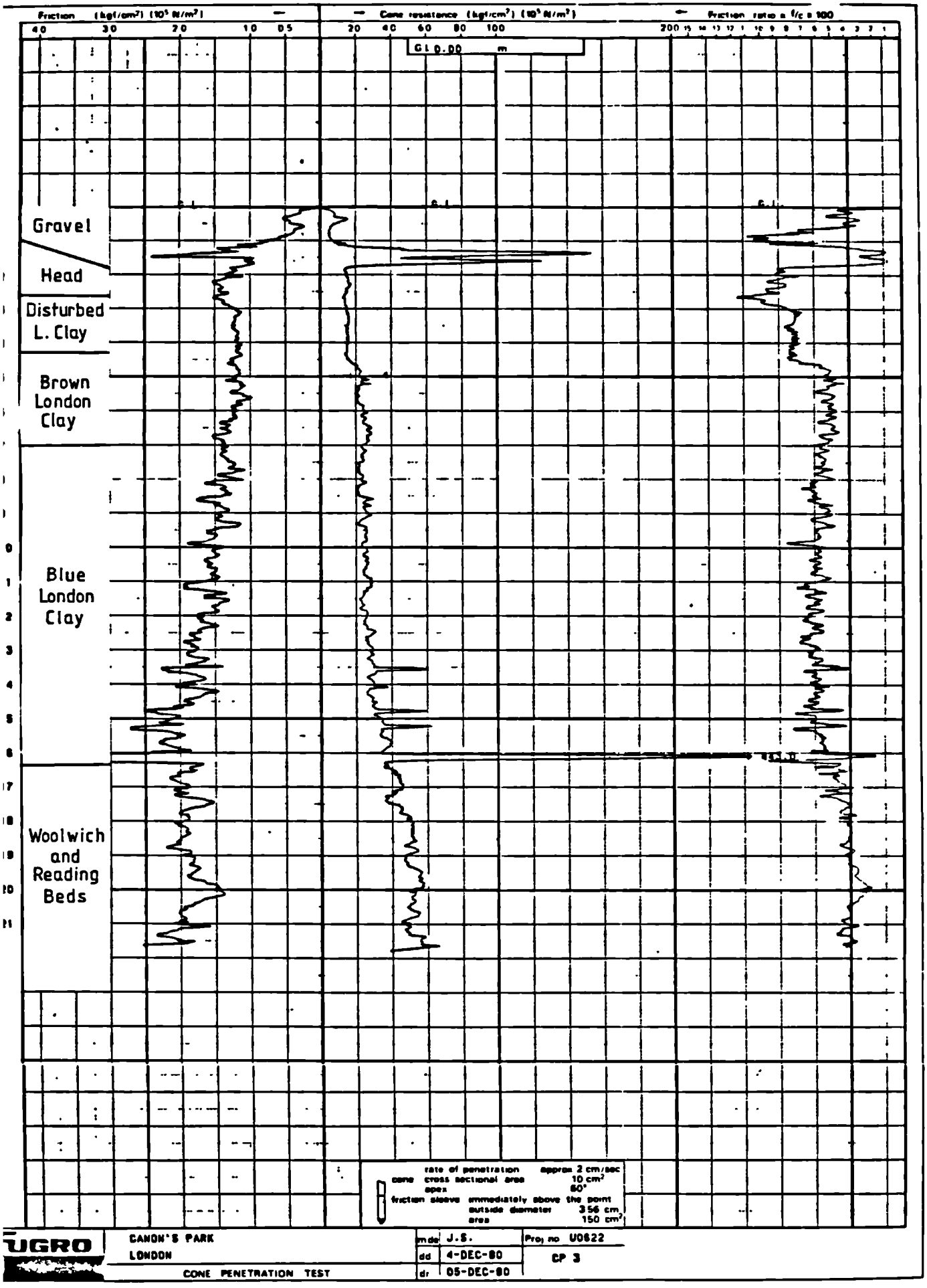


Figure 7.6. Cone test data and interpreted log.

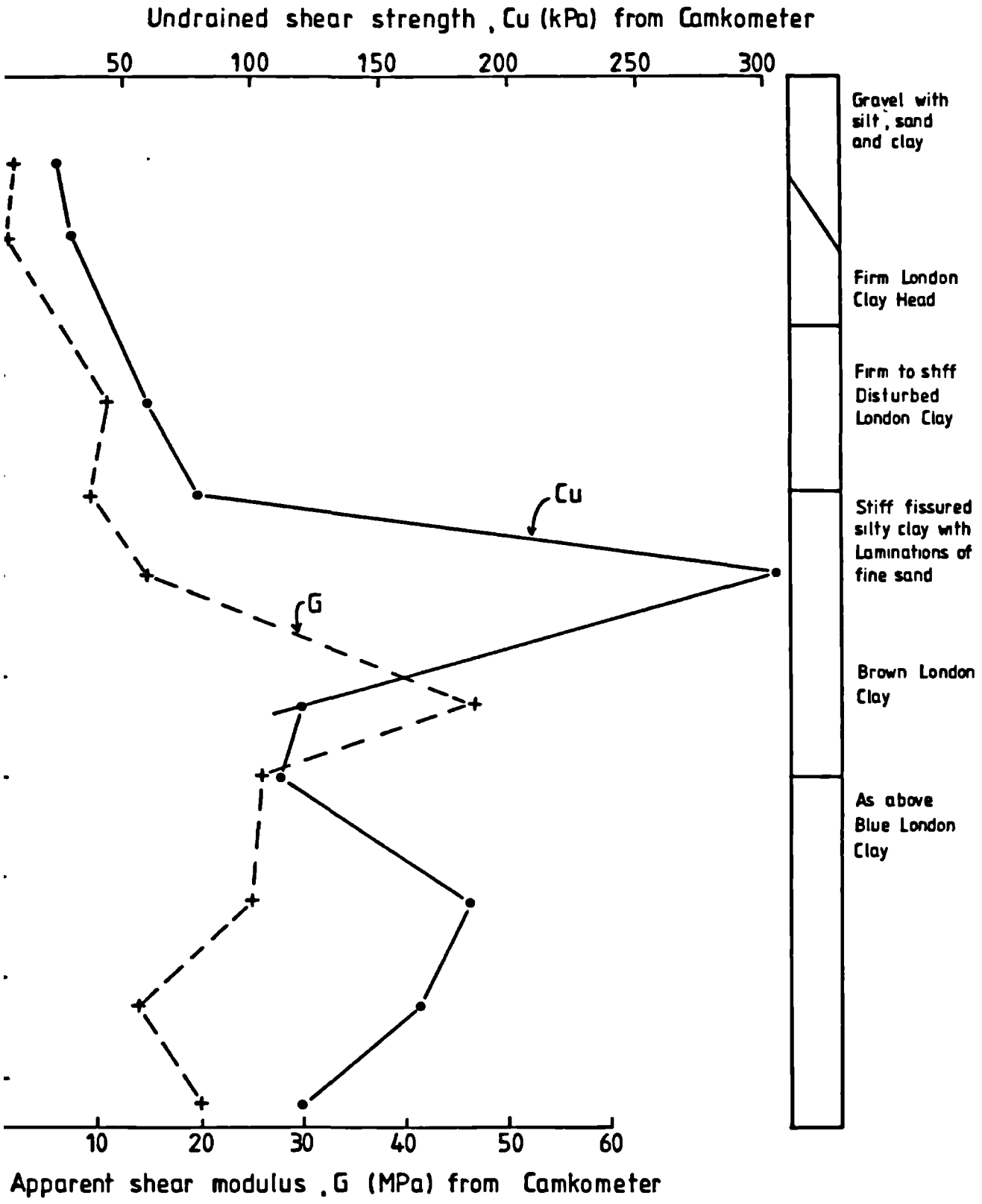


Figure 7.7. Self-boring pressuremeter results.

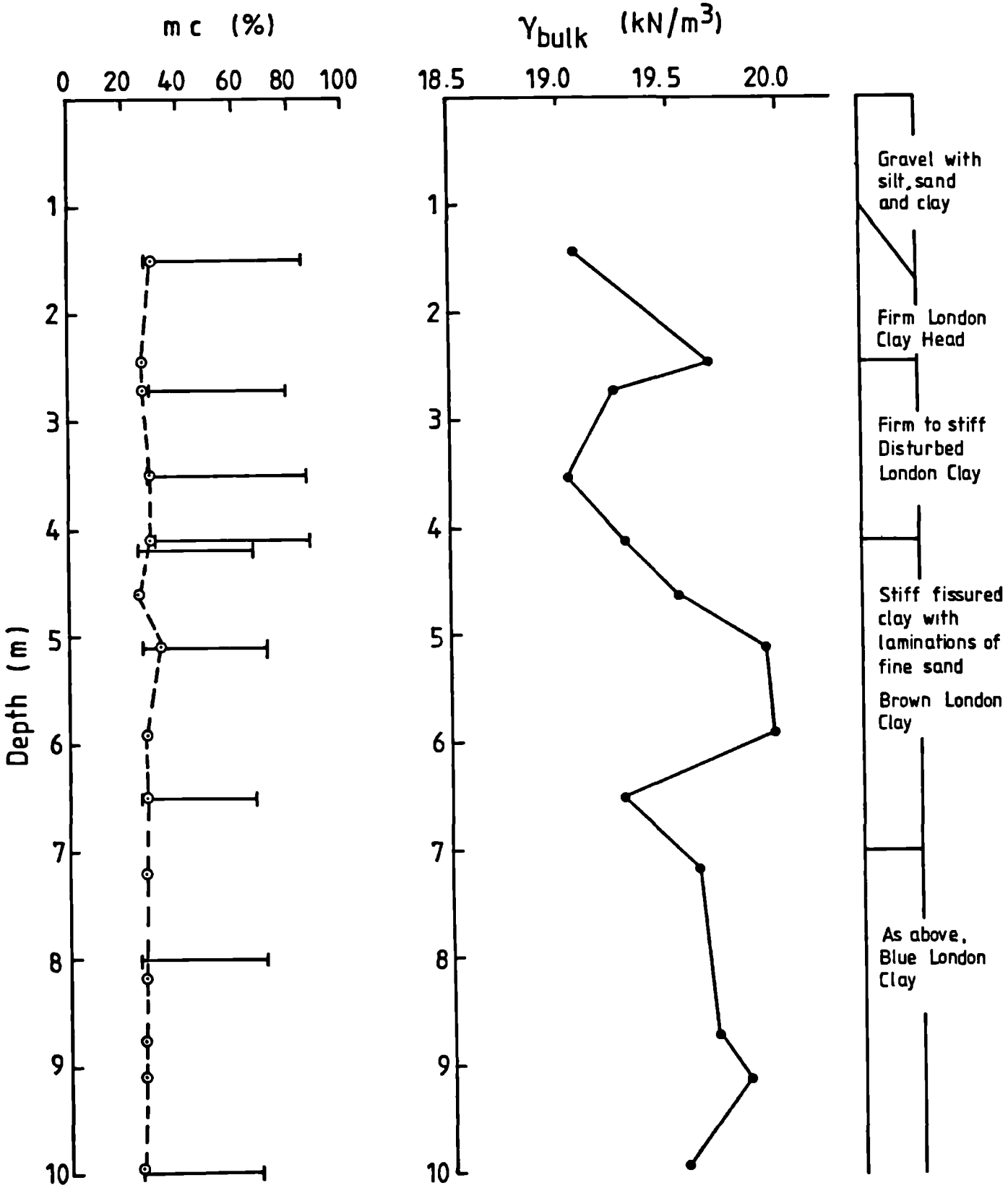
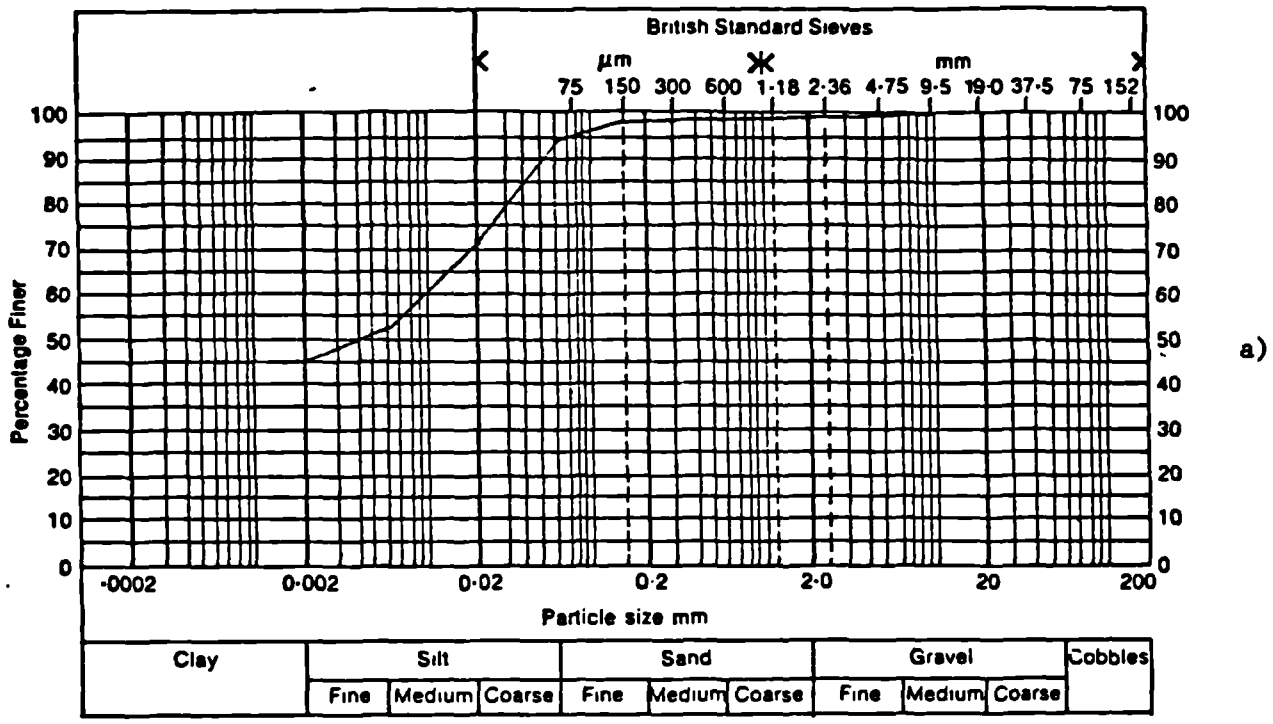
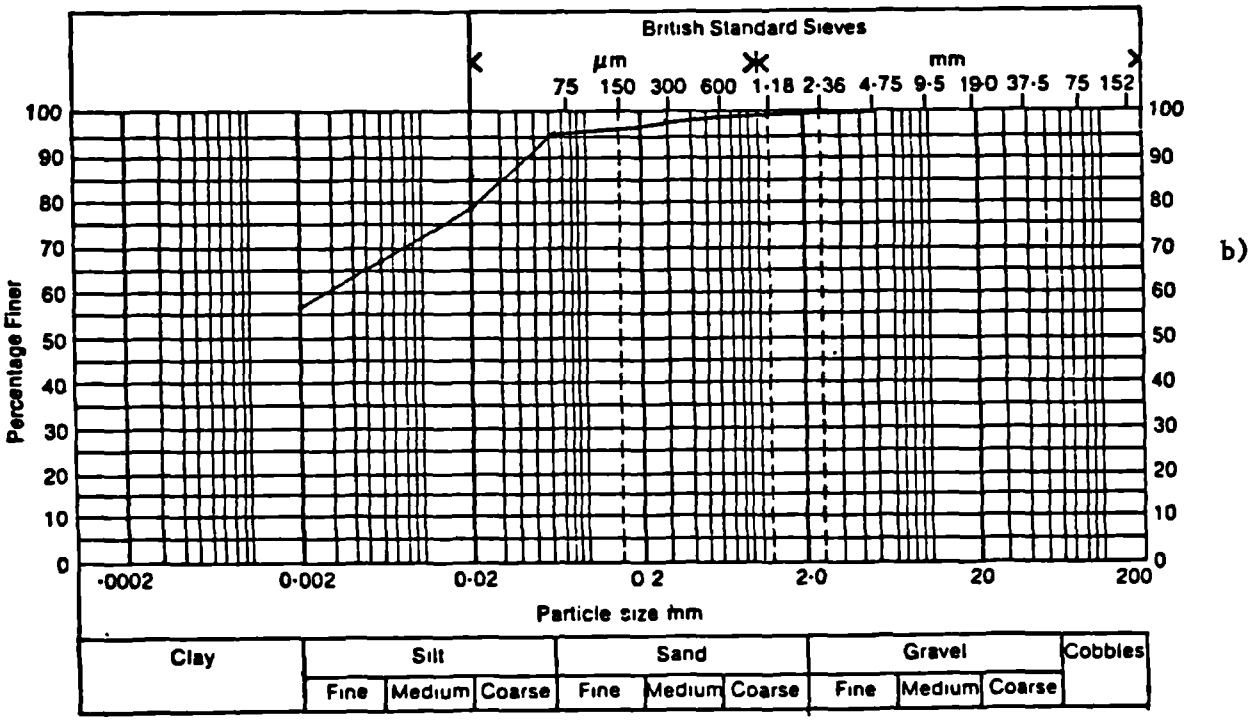


Figure 7.8. Profiles of index properties.

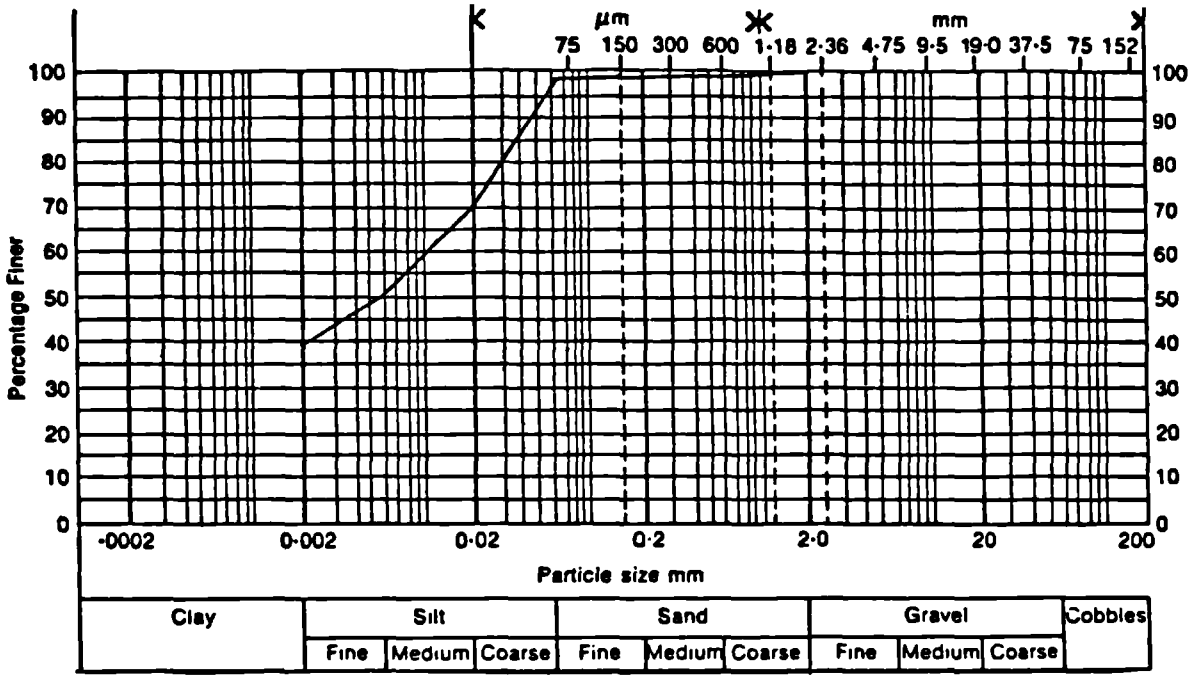


a)

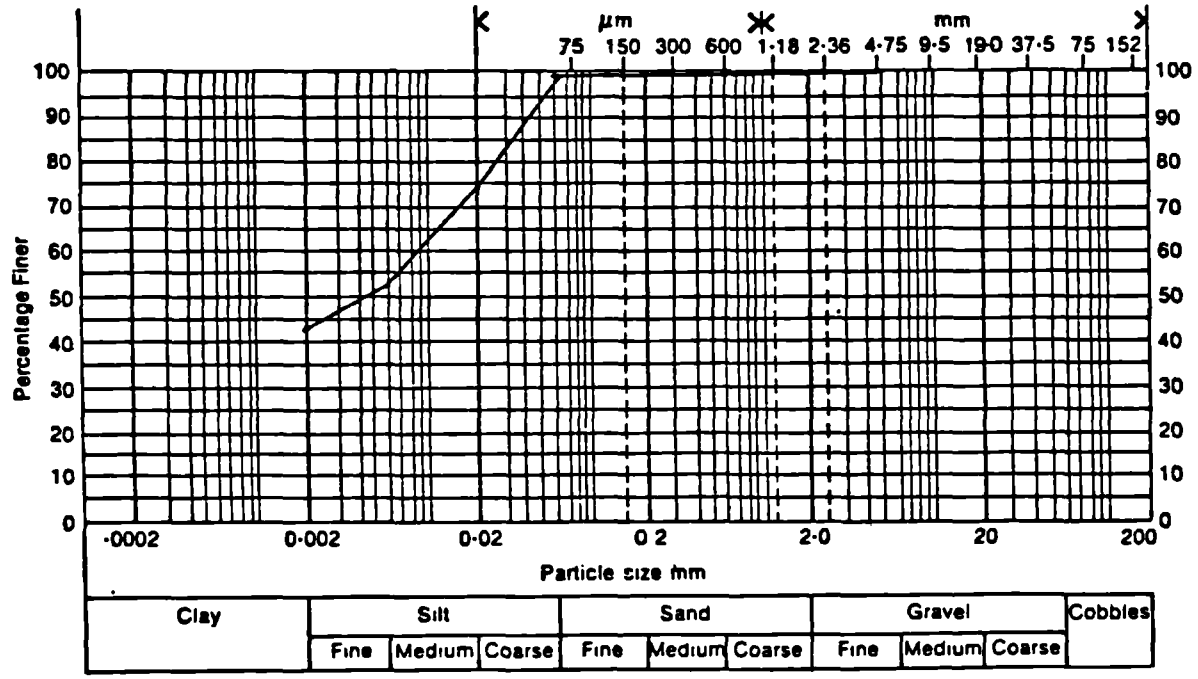


b)

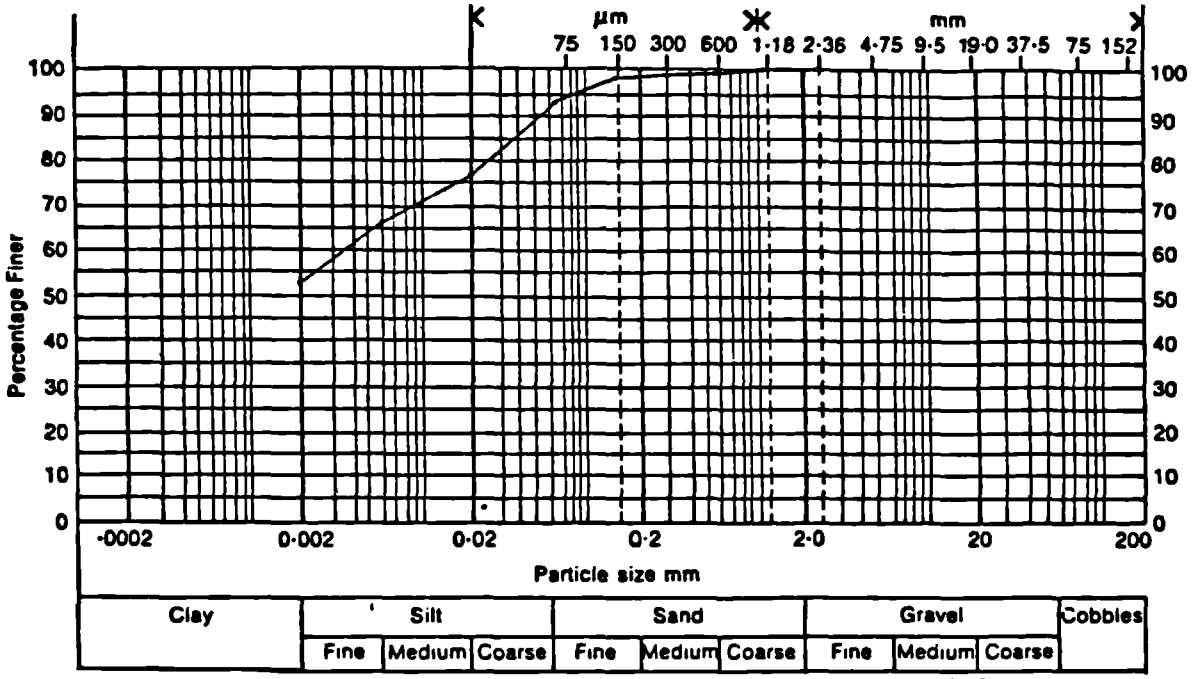
Figure 7.9. Grading curves; a) 2.3-2.9 metres, b) 4.0 metres.



c)



d)



e)

Figure 7.9. Grading curves; c) 4.3 metres, d) 6.3-6.9 metres, e) reconstituted soil mix.

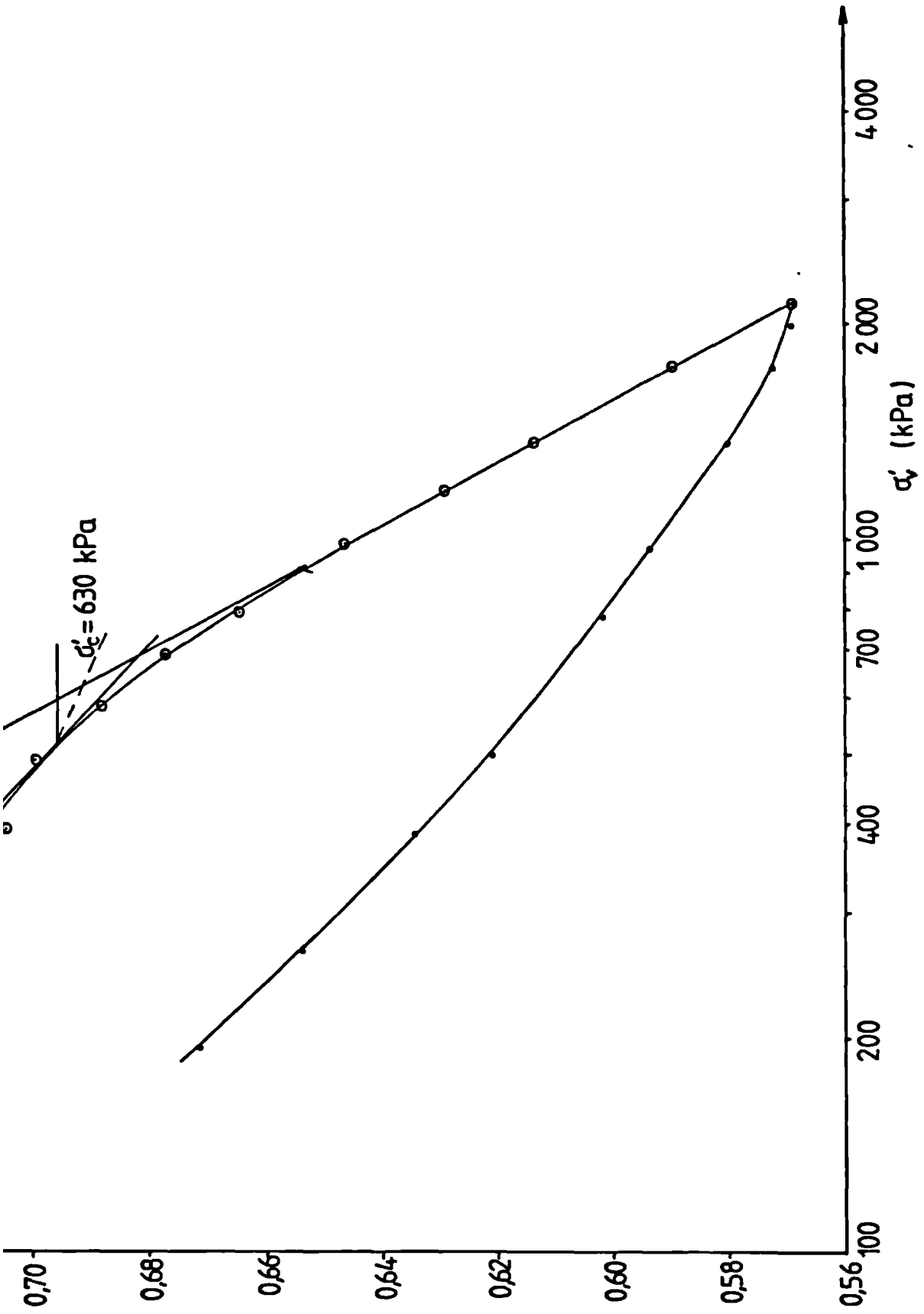


Figure 7.10. Voids ratio - σ'_v data LOED 1.

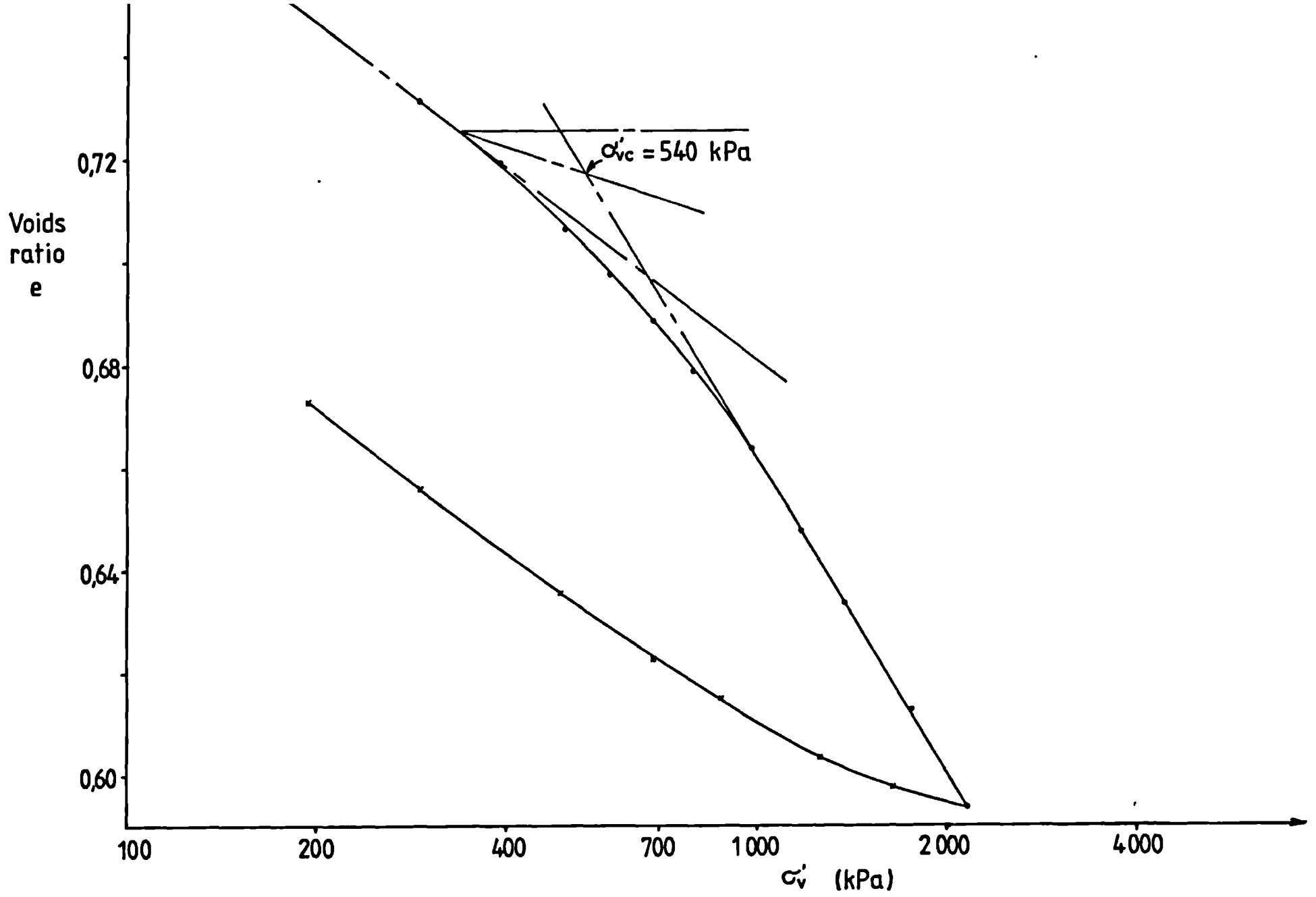


Figure 7.11. Voids ratio - σ'_v data LOED 2.

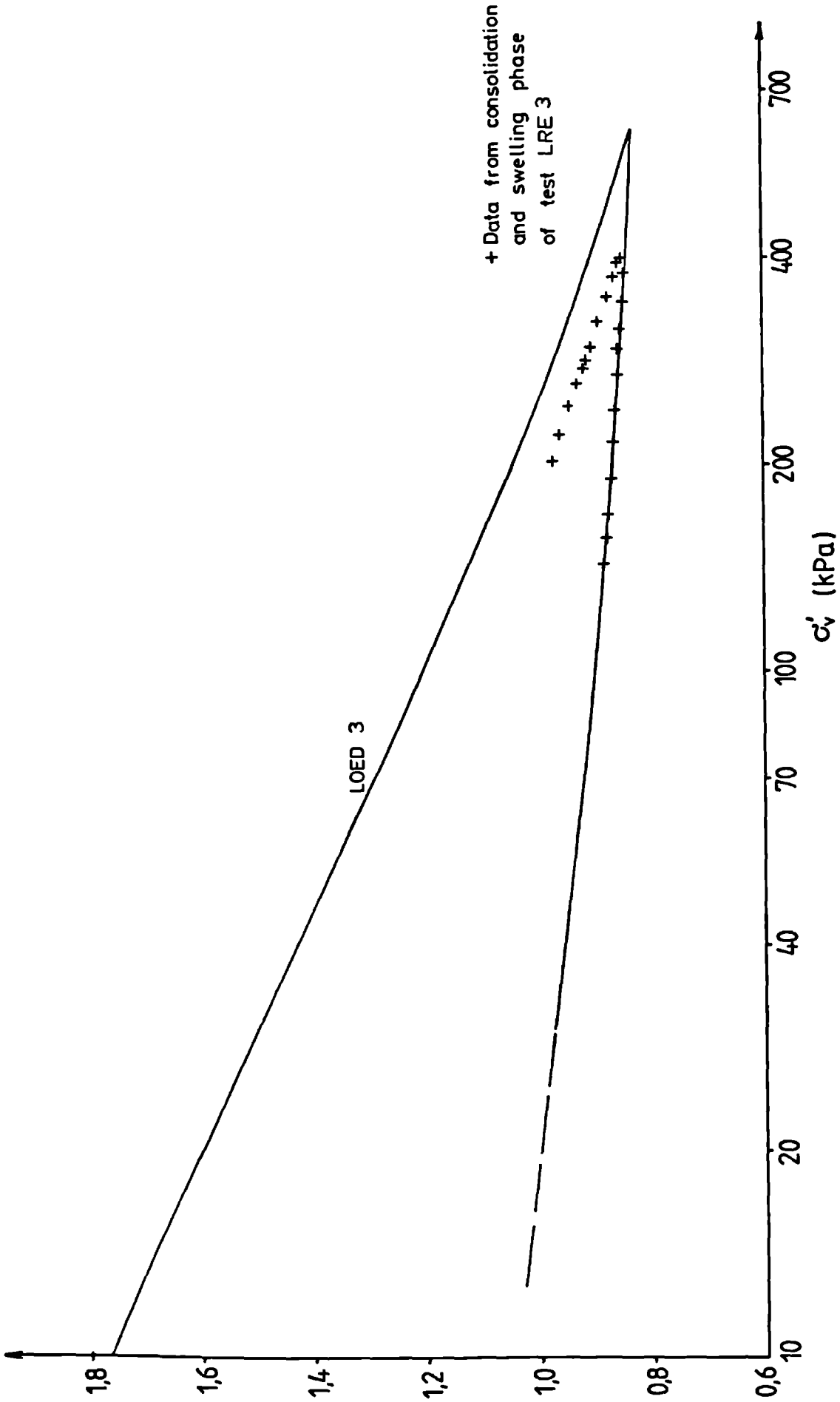


Figure 7.12. Voids ratio - σ'_v data LOED 3.

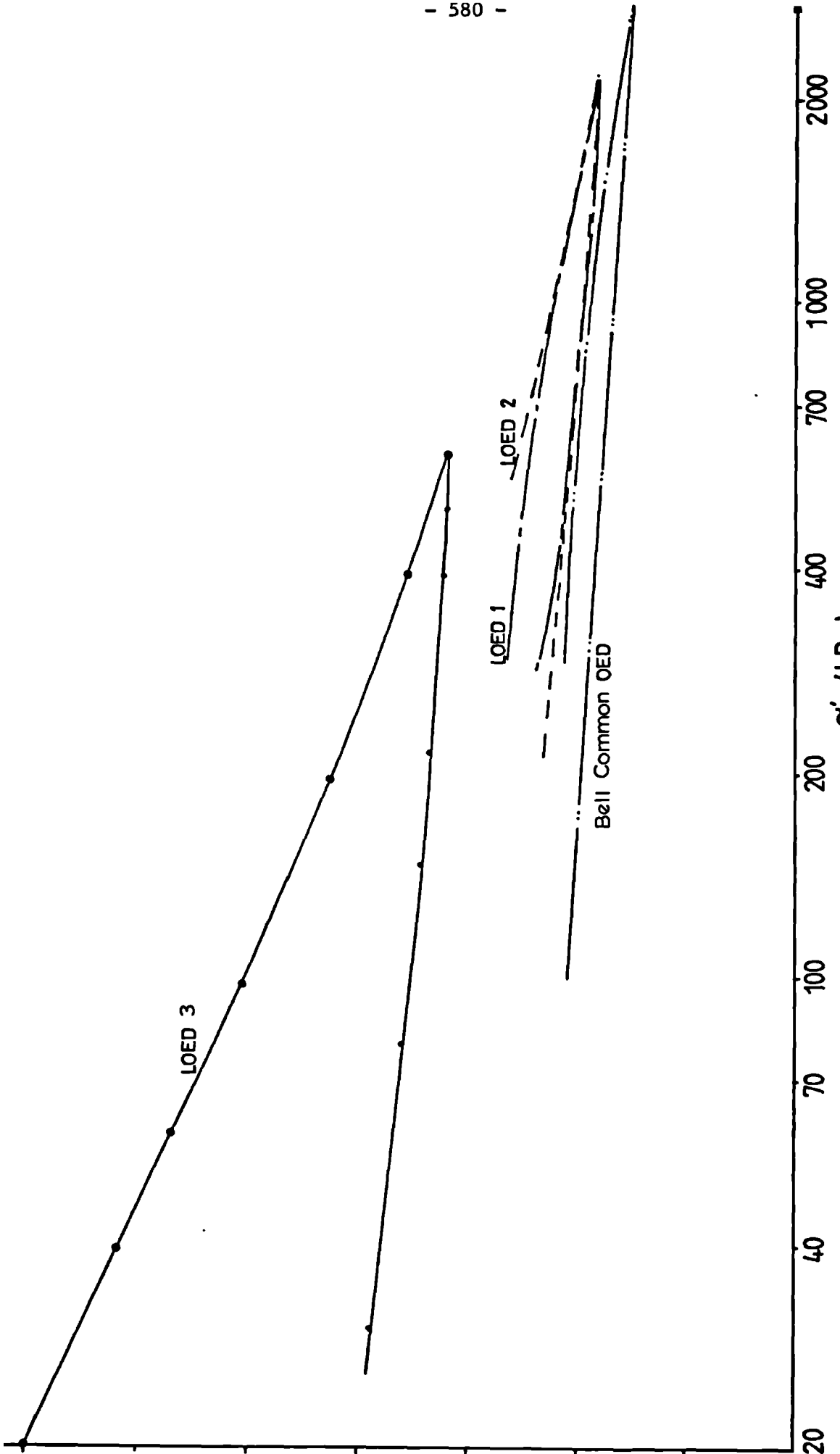


Figure 7.13. Voids ratio - σ'_v summary diagram.

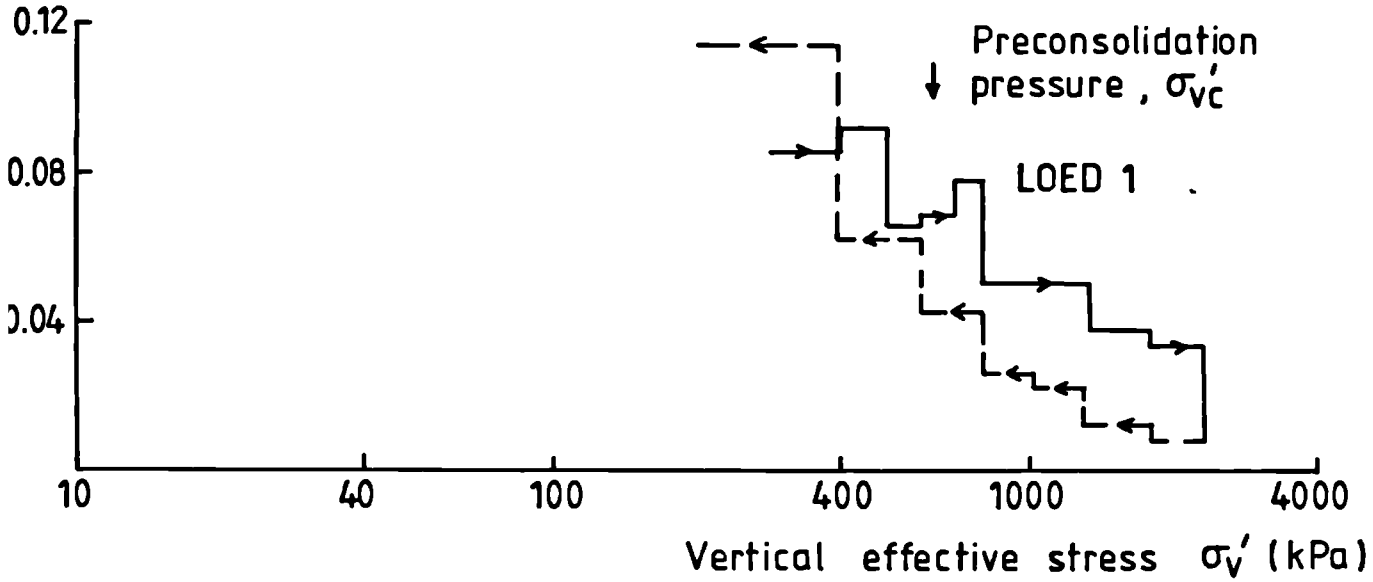


Figure 7.14. Compressibility data for LOED 1.

Figure 7.15. Voids ratio - σ'_v data LOED 3.

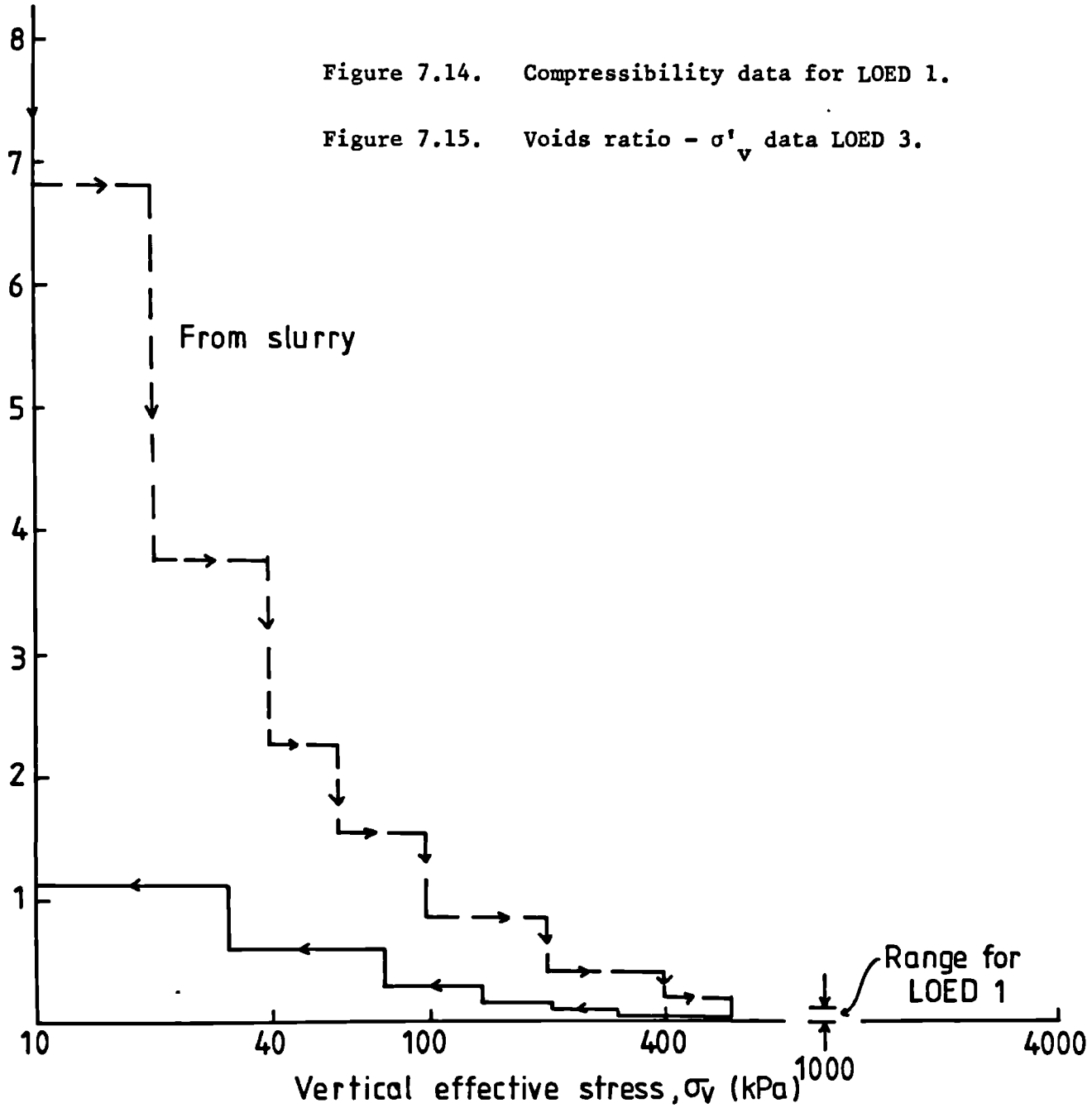
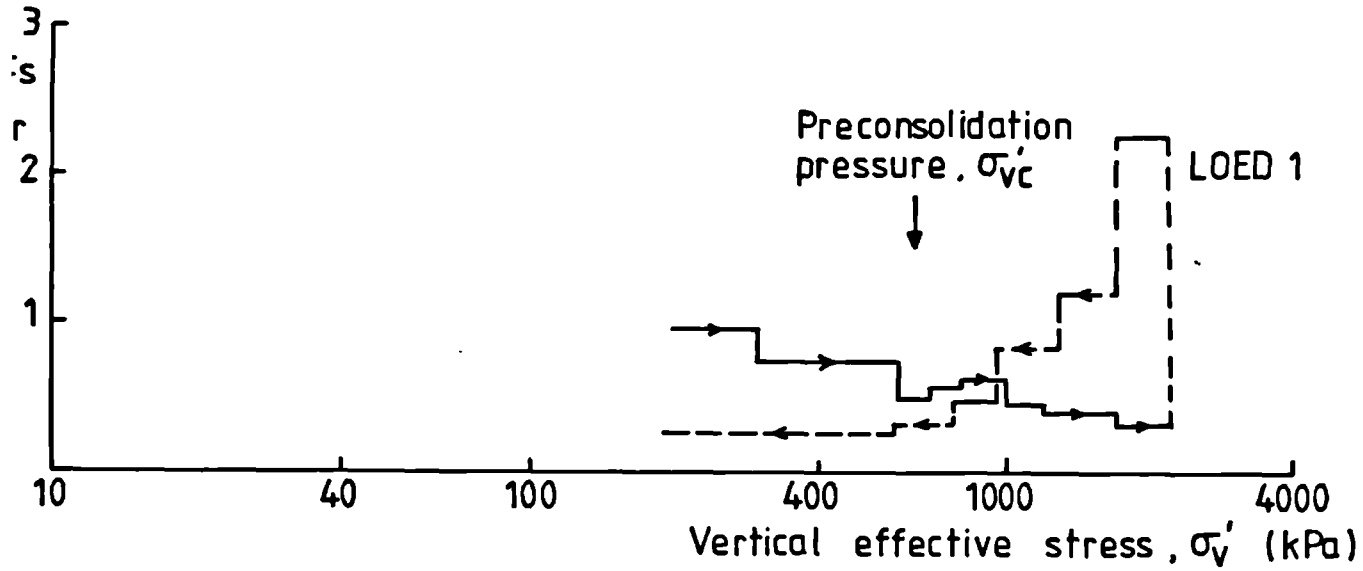
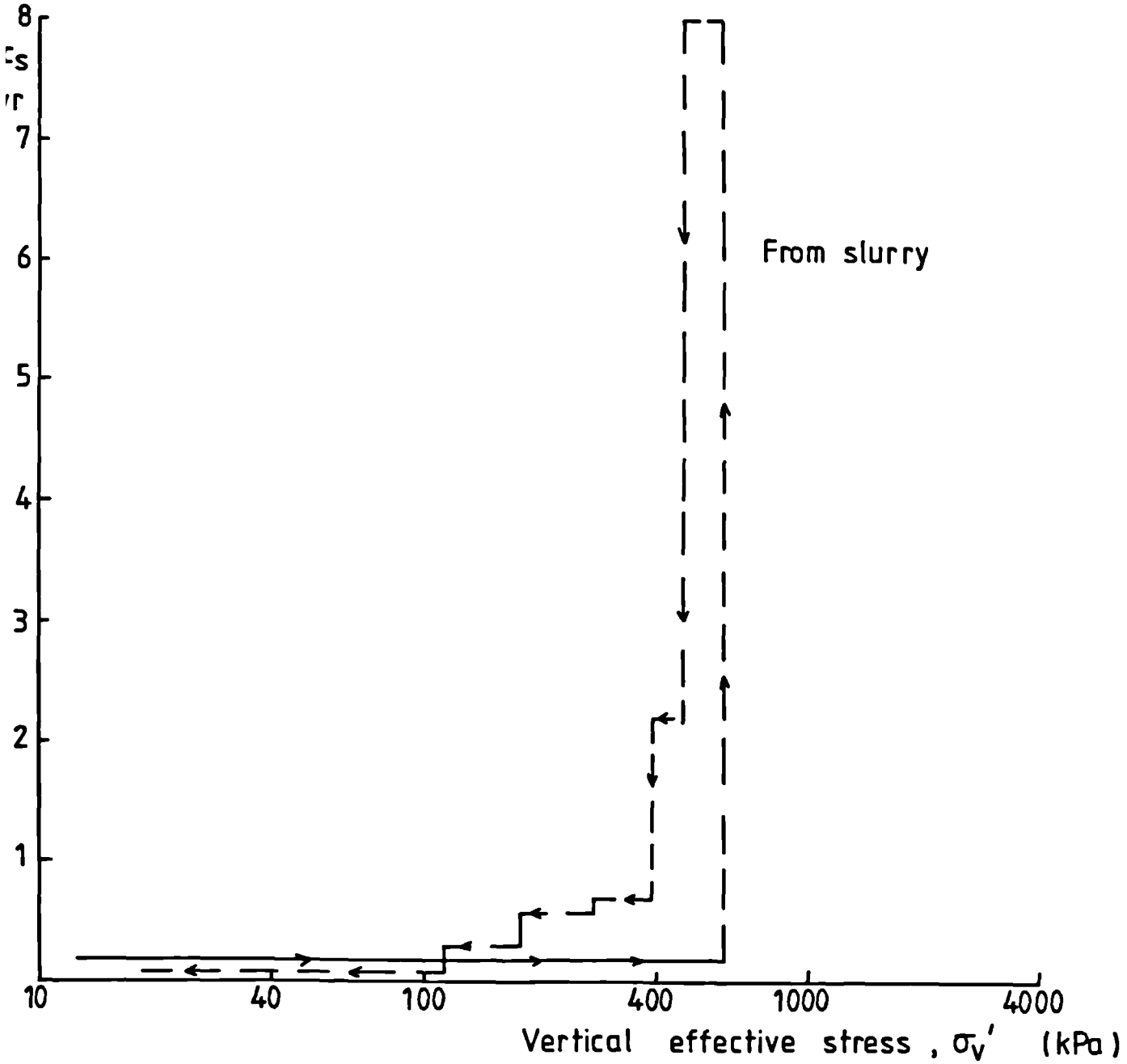


Figure 7.16. Consolidation rate data for LOED 1.





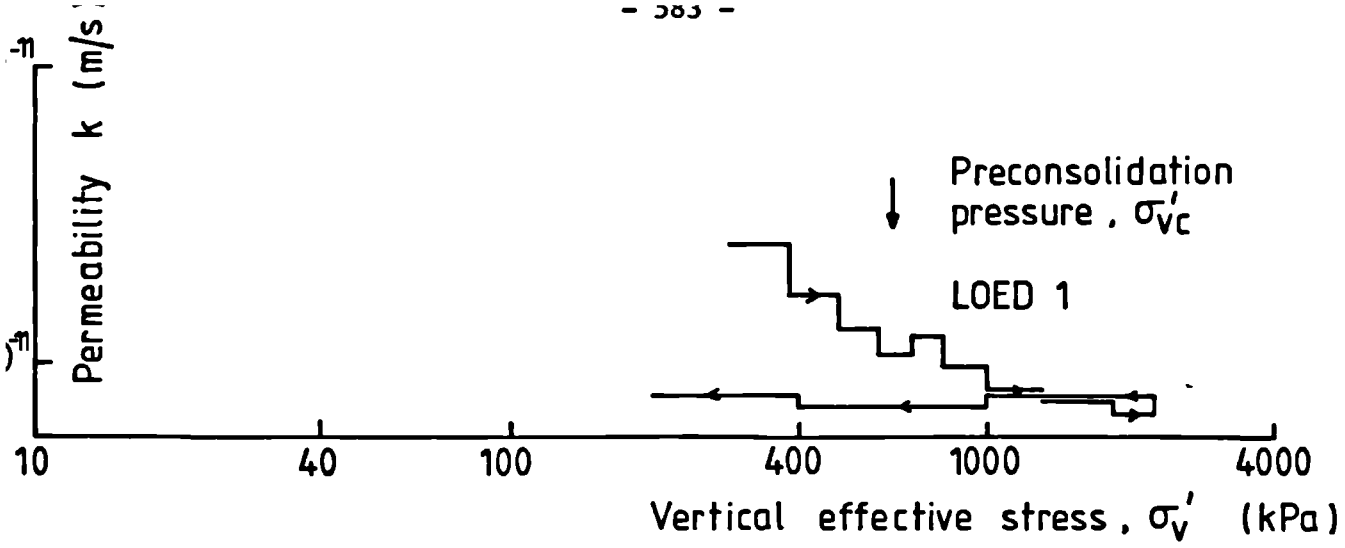
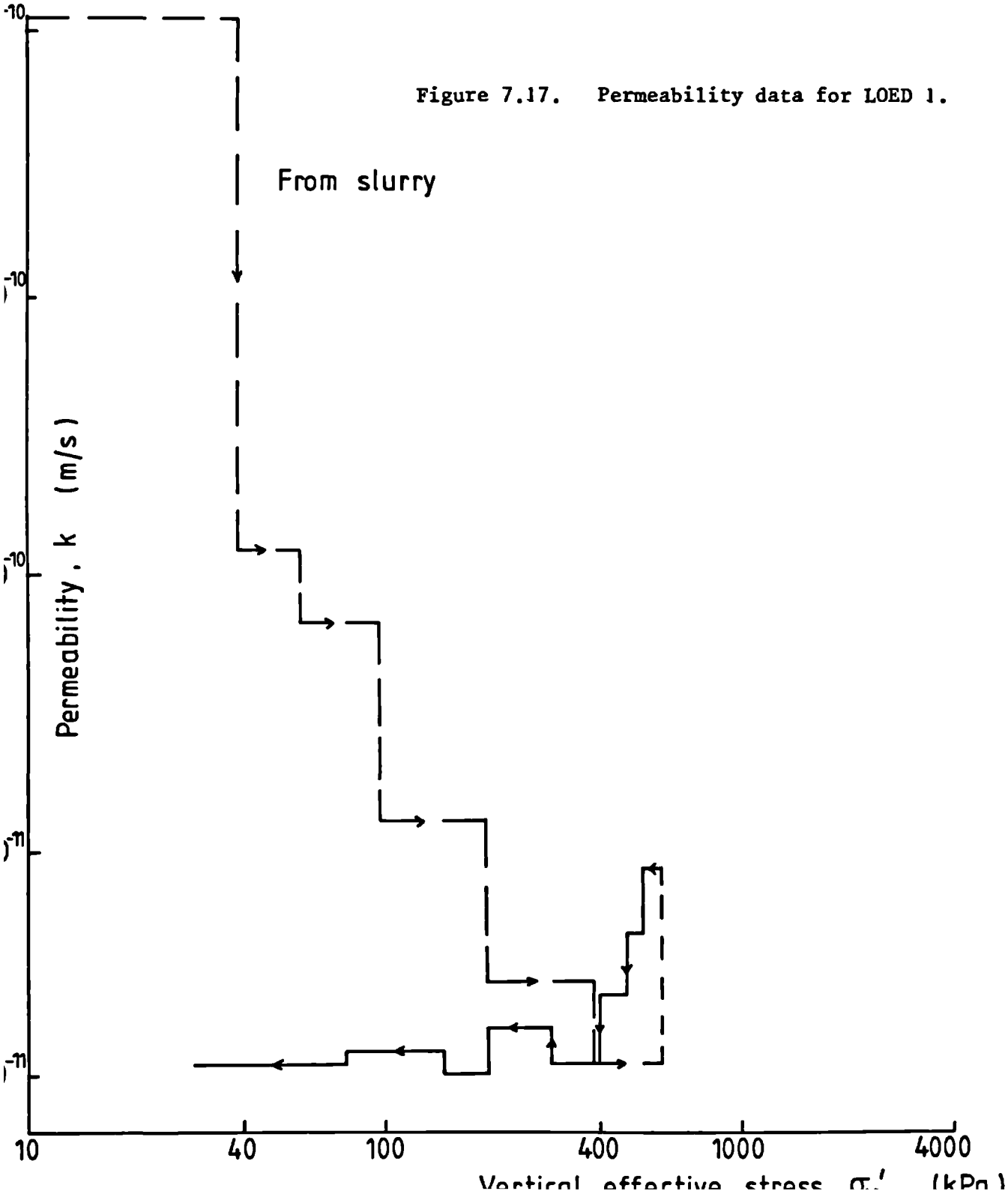


Figure 7.17. Permeability data for LOED 1.



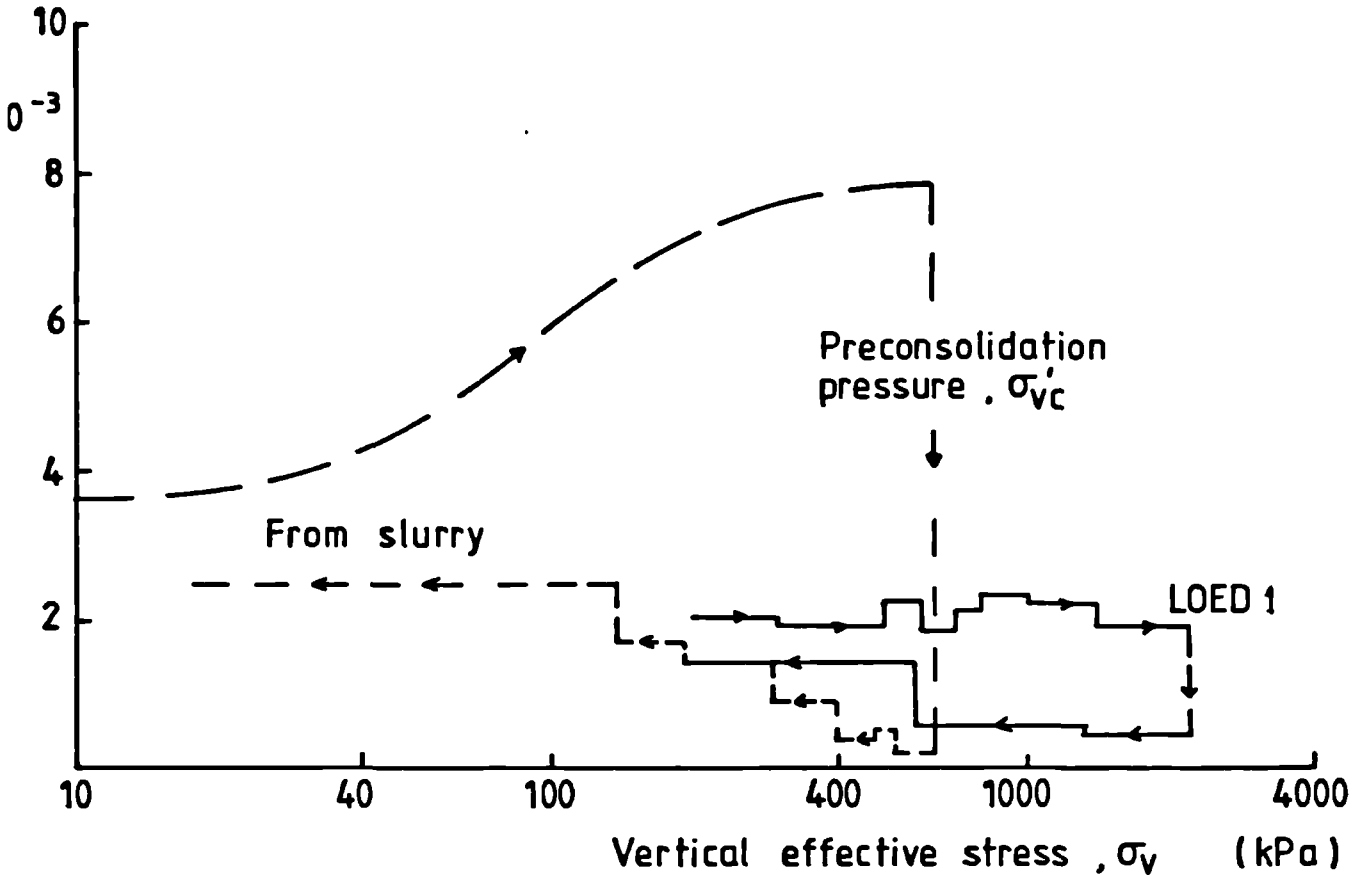


Figure 7.18. Secondary consolidation data for LOED 1 and LOED 3.

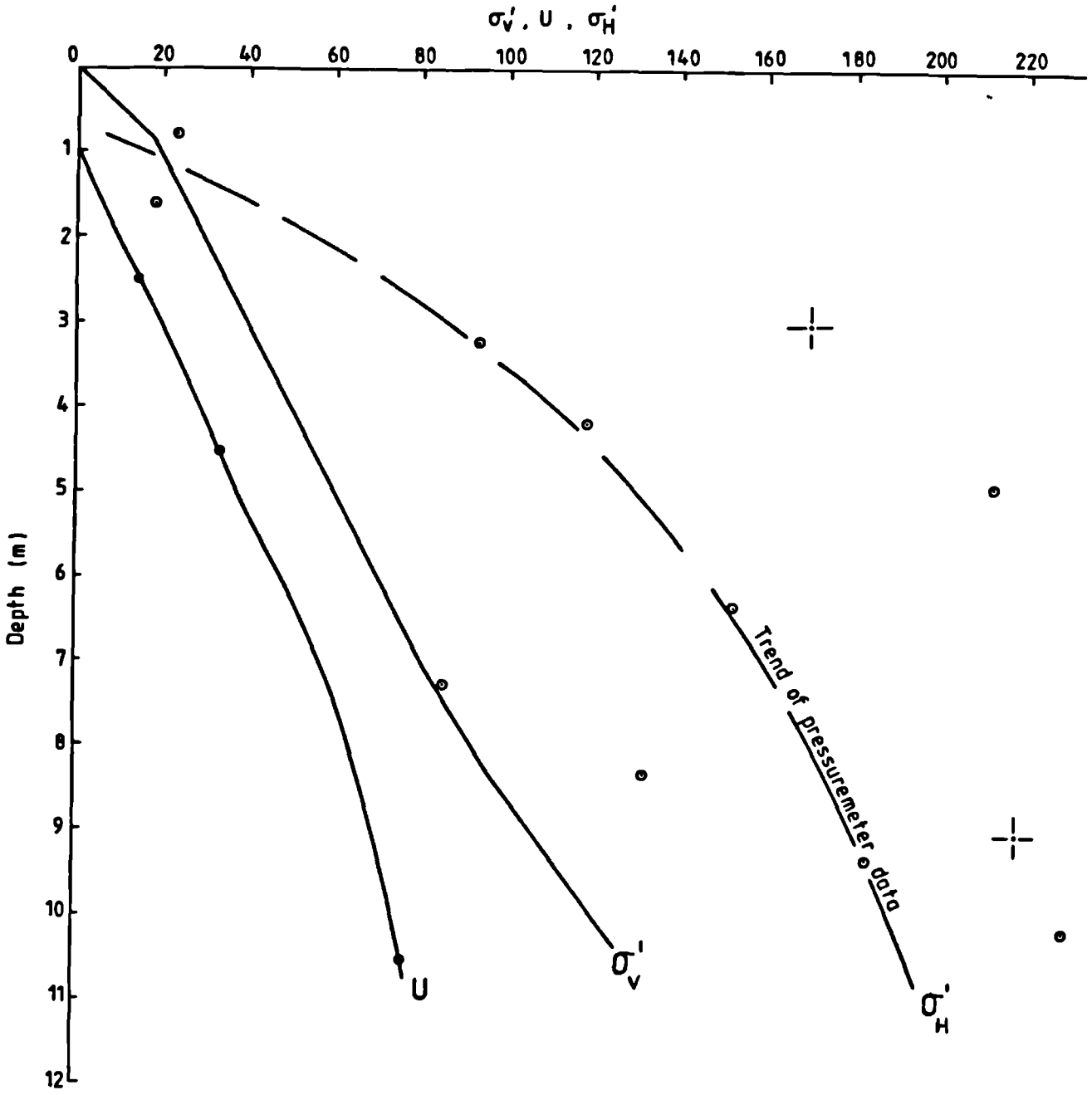


Figure 7.19. Insitu pressures at Canons Park.

⊙ Self boring Pressuremeter tests

● Piezometer data

Spade - cell data
(Tedd & Charles 1981)

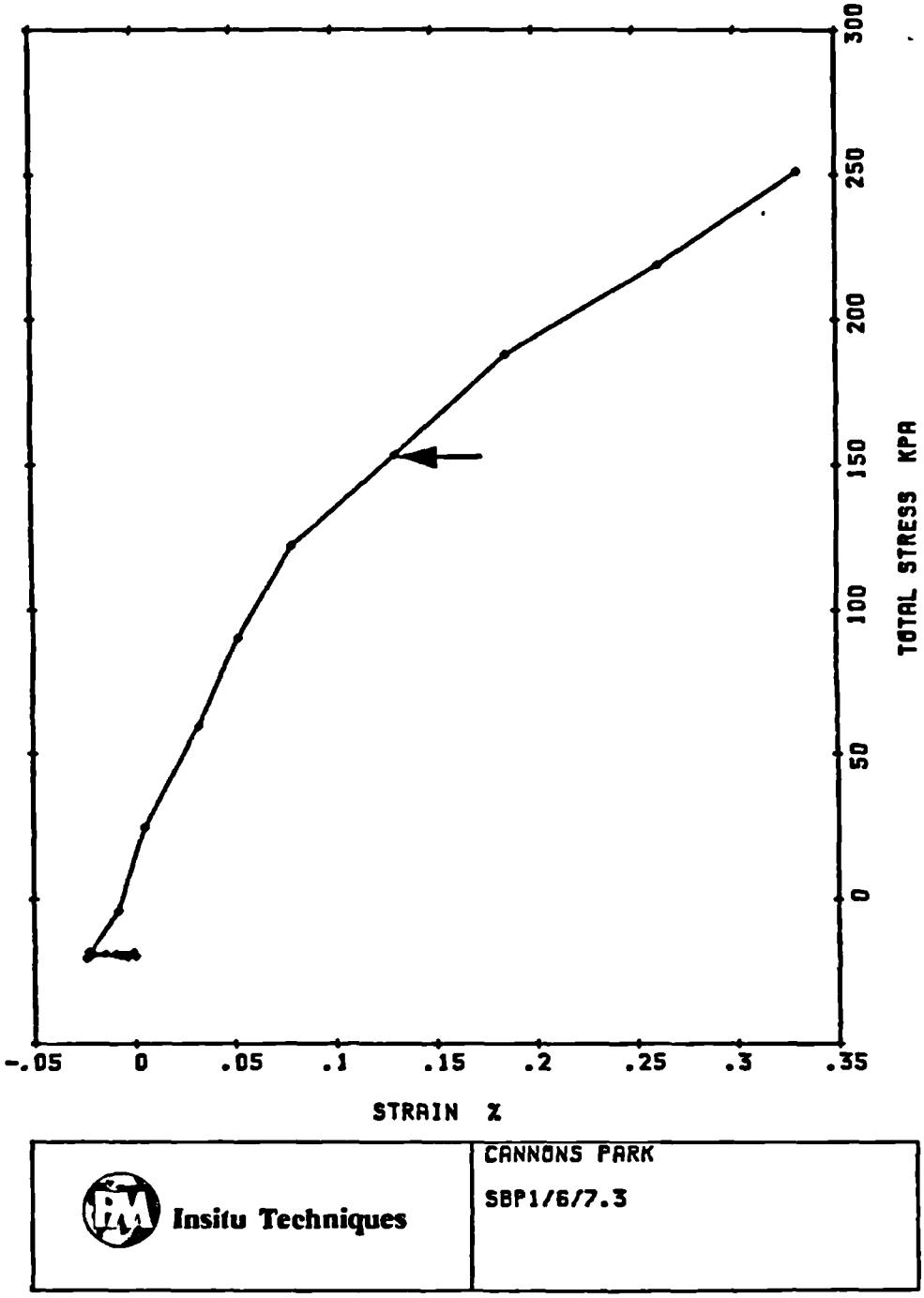


Figure 7.20. Self boring pressuremeter initial inflation curve, 7.3 metres depth.

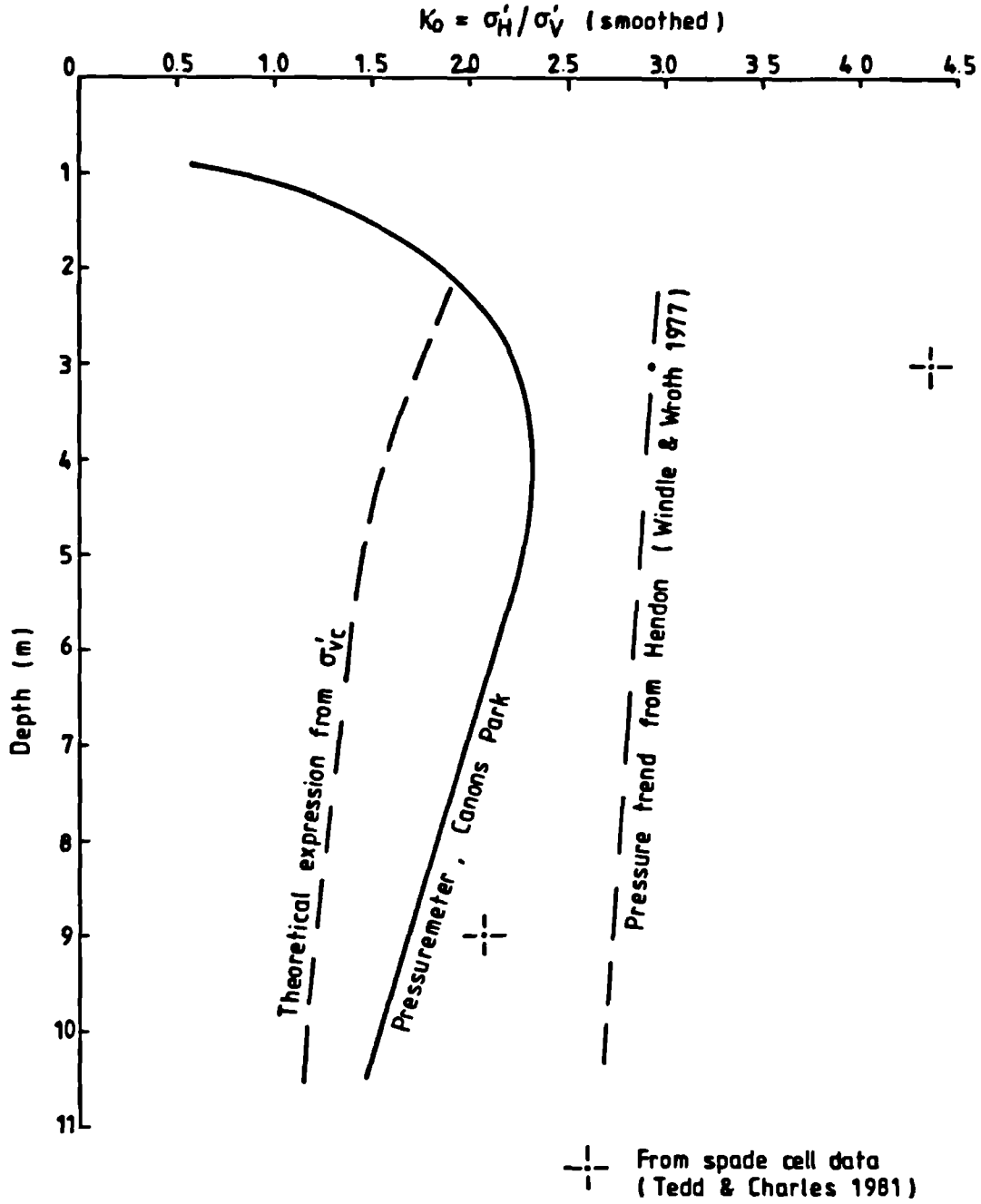
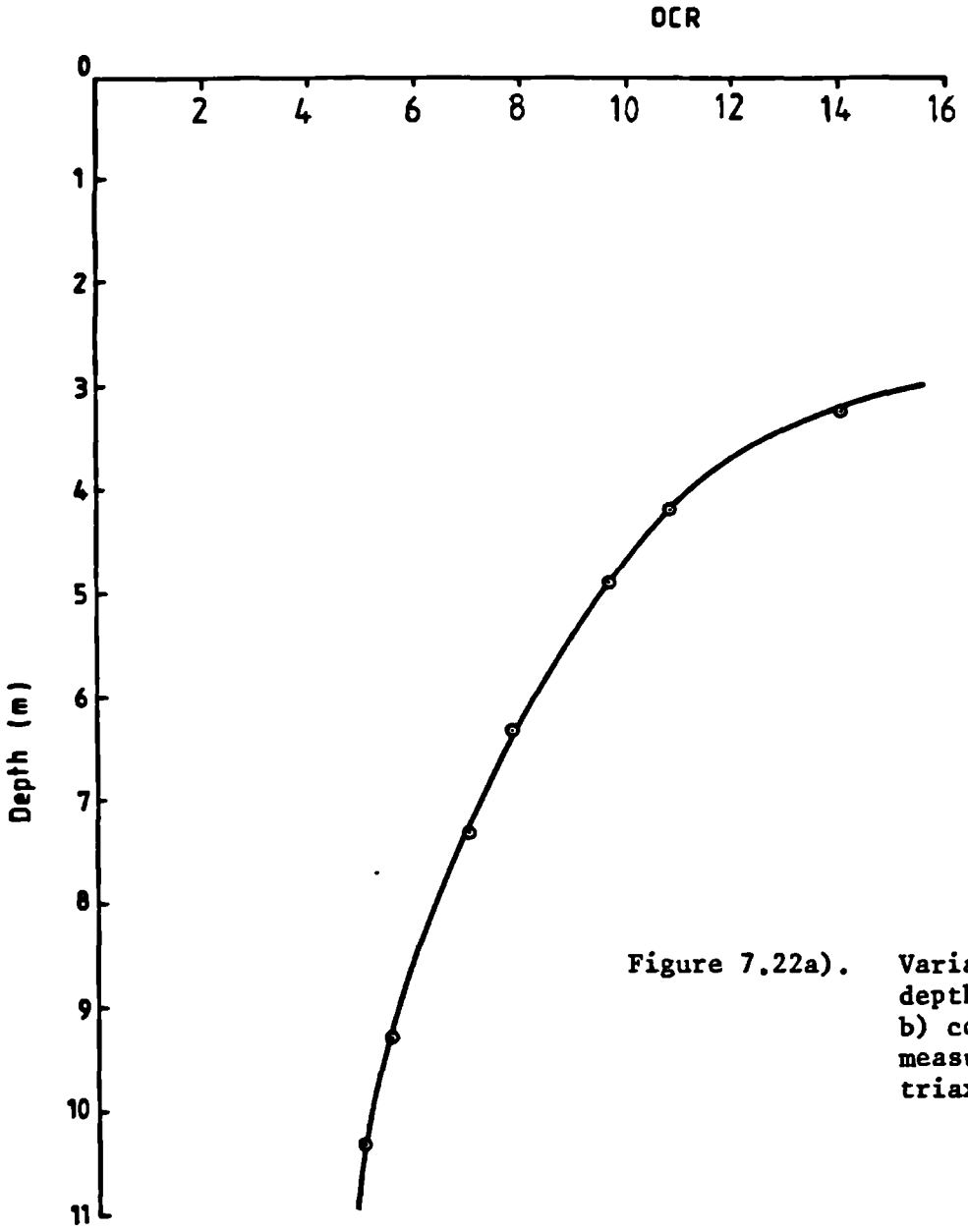


Figure 7.21. Variation of K_o with depth.



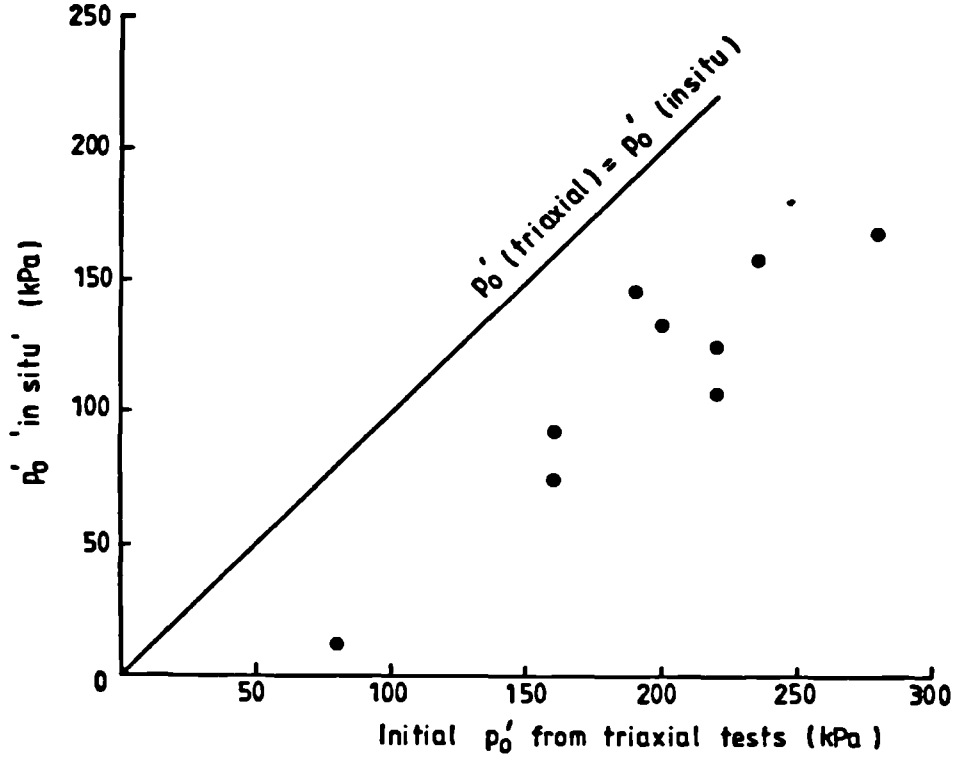


Figure 7.22a). Variation of OCR with depth (above) and b) comparison of p' measured insitu and in triaxial samples (belo

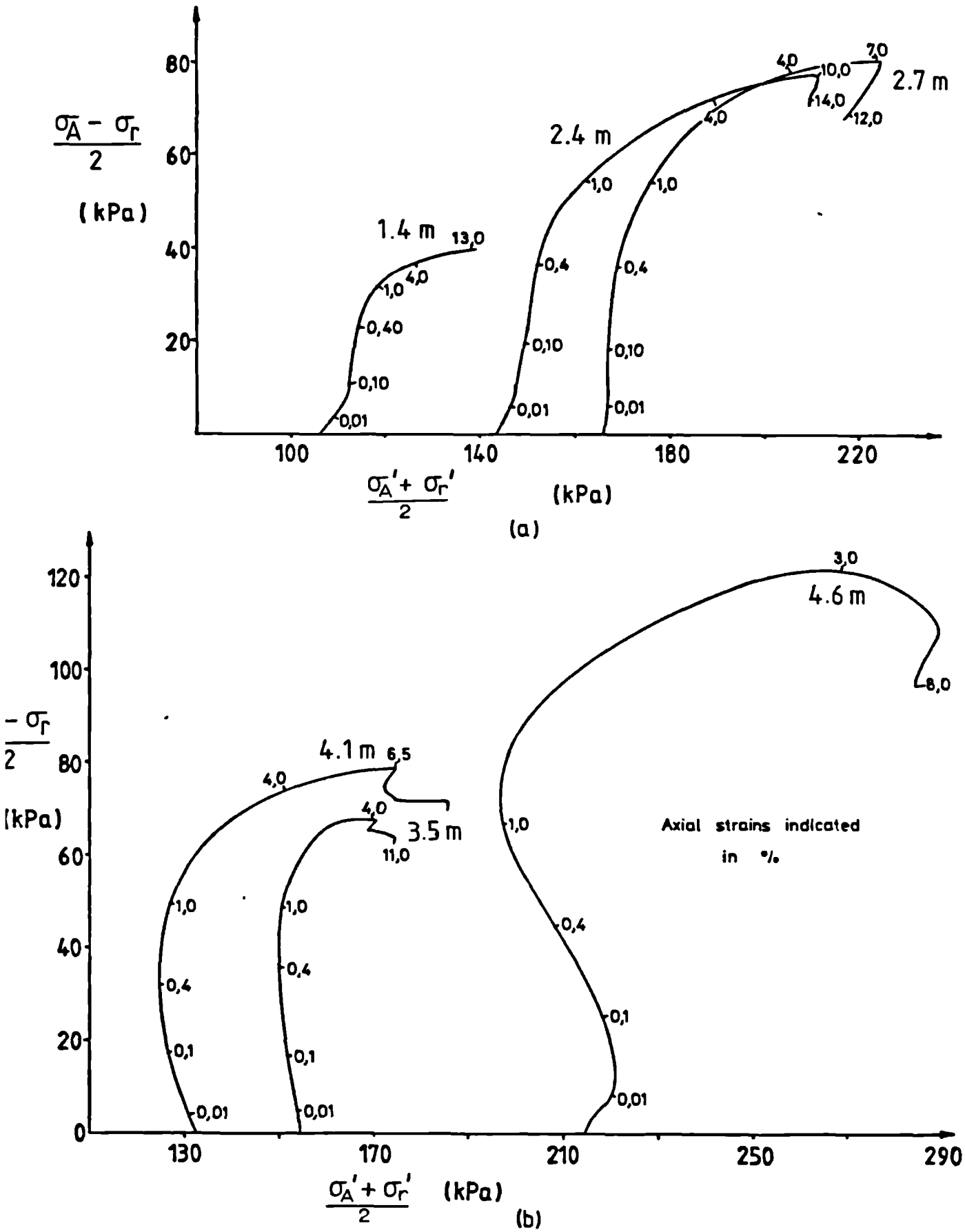
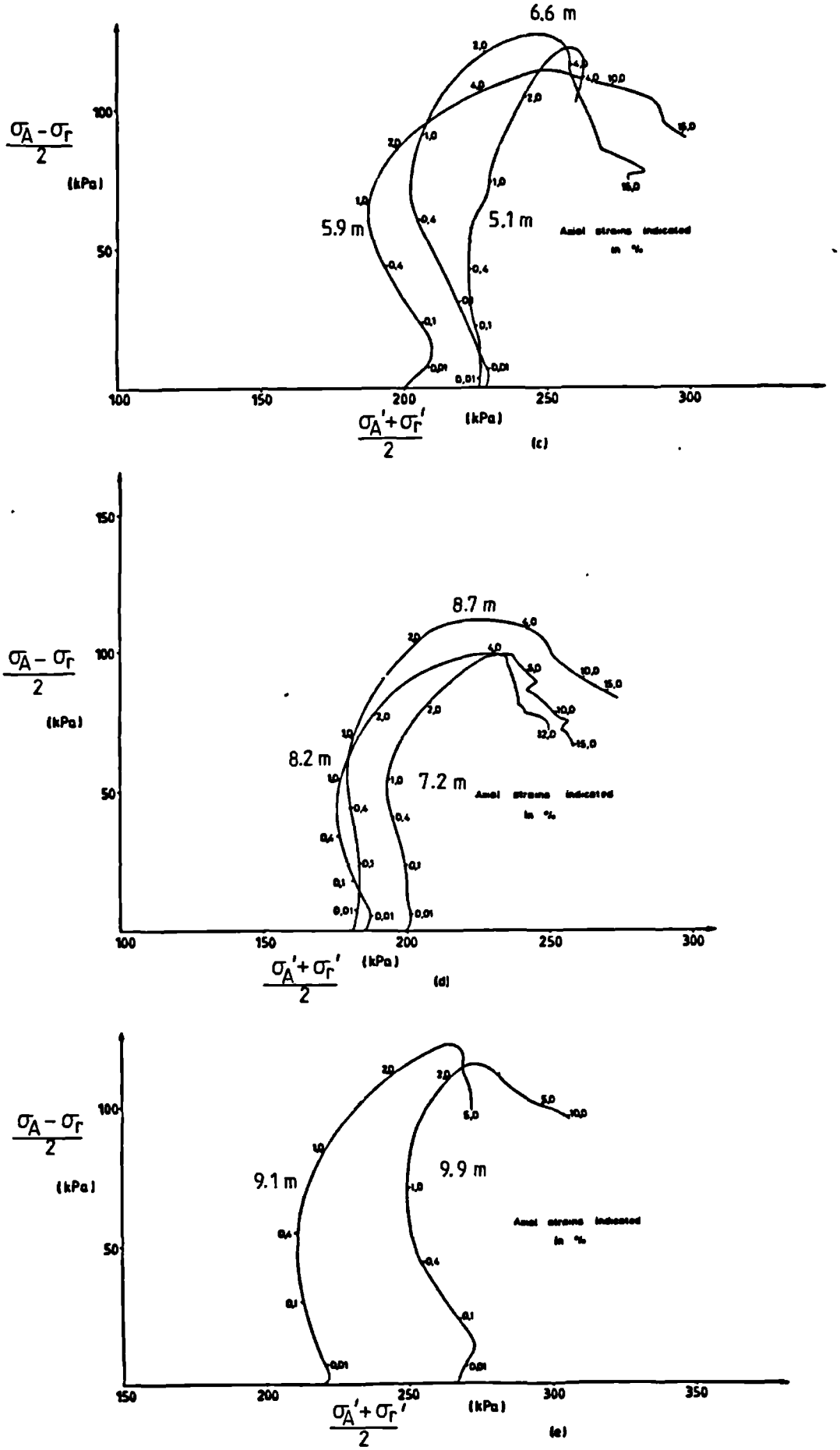
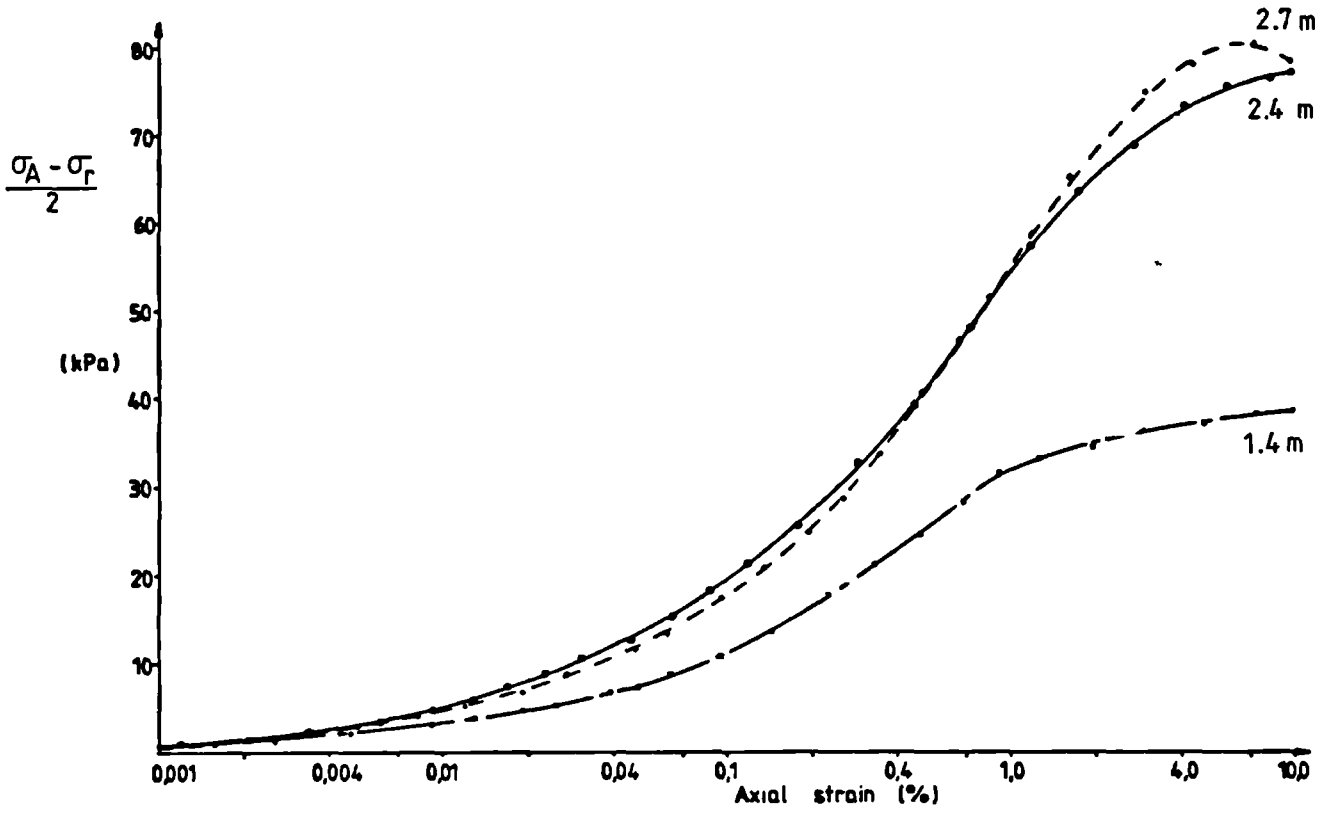


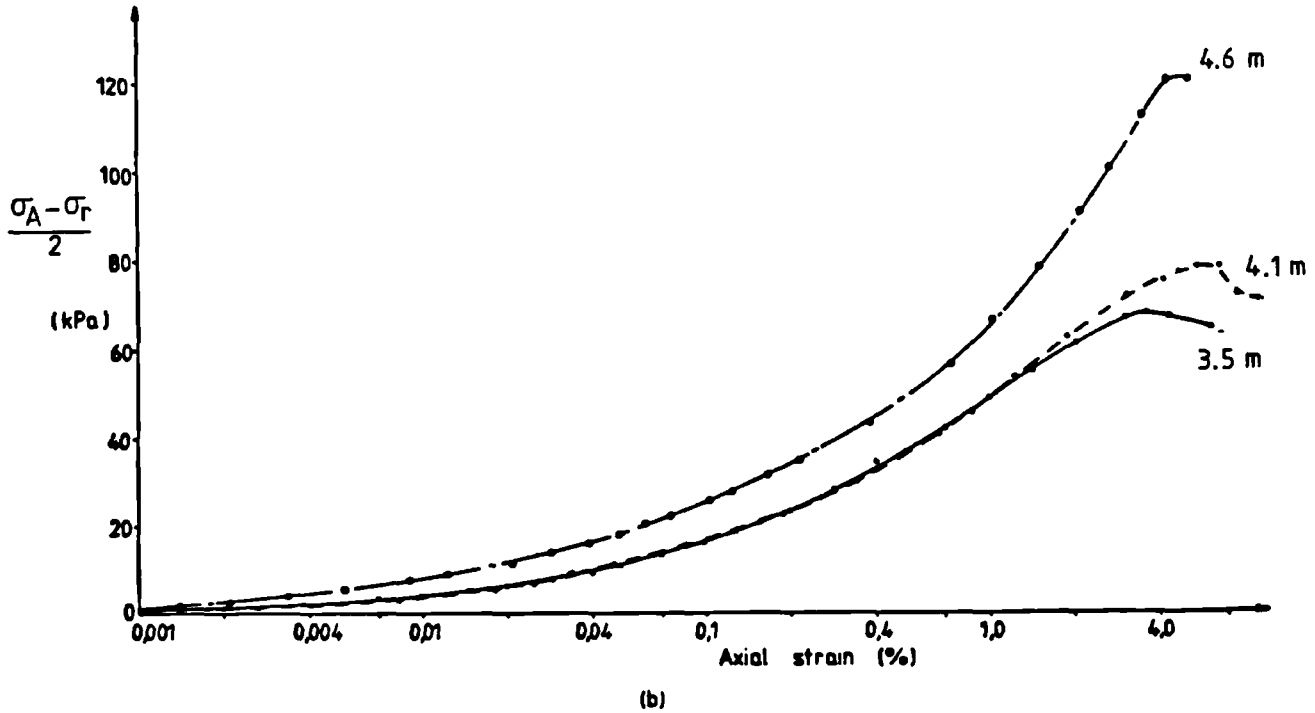
Figure 7.23. Stress paths for unconsolidated undrained tests on: (a) Head material and overlying gravel, (b) Disturbed London Clay



e 7.23. Stress paths for unconsolidated, undrained tests on: (c) Brown London Clay, (d) Blue London Clay 7.1–8.9m, (e) Blue London Clay 8.9–10.2m.



(a)



(b)

Figure 7.24. Stress strain curves corresponding to stress paths: in Figs. 7 23(a) and (b)

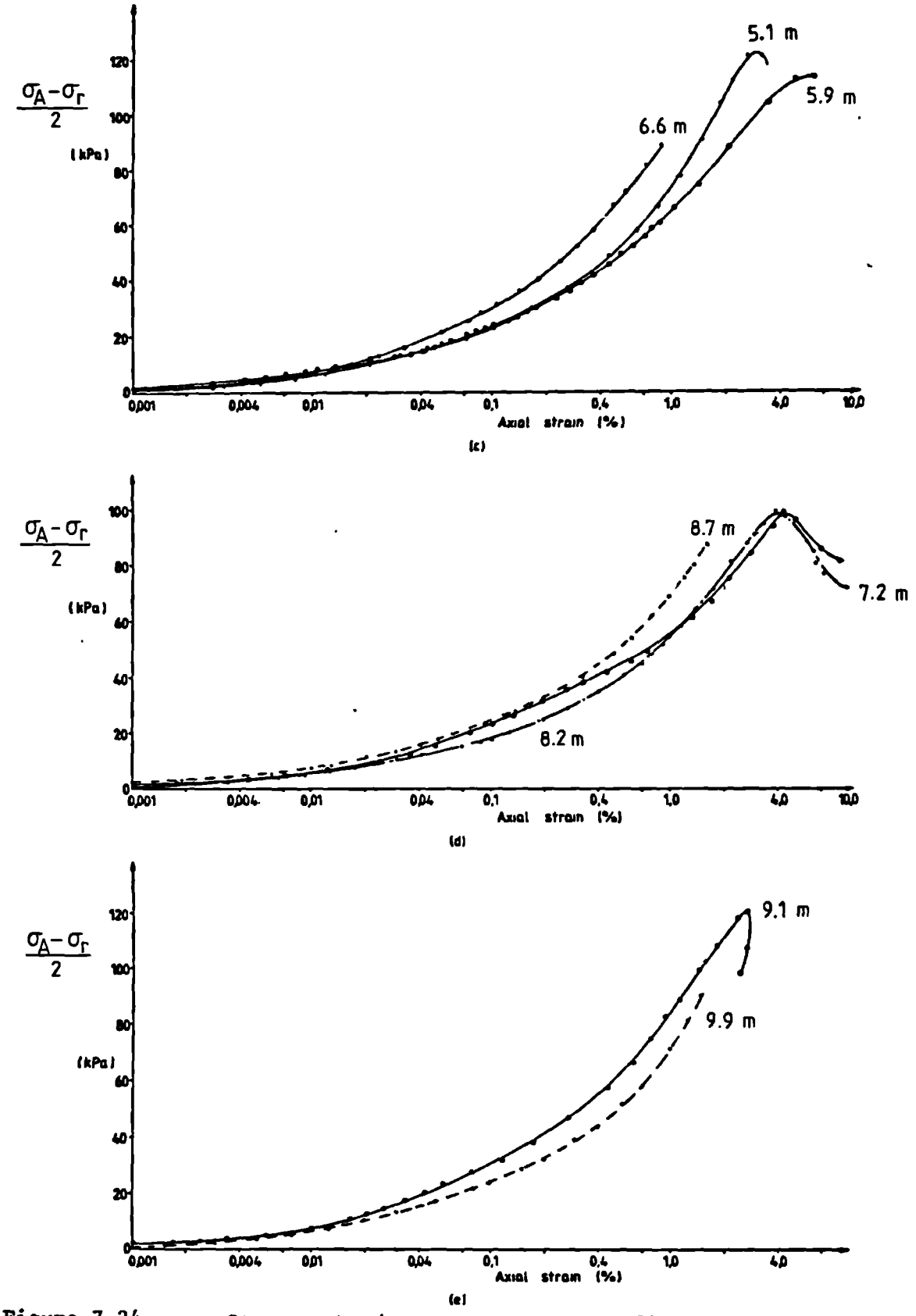
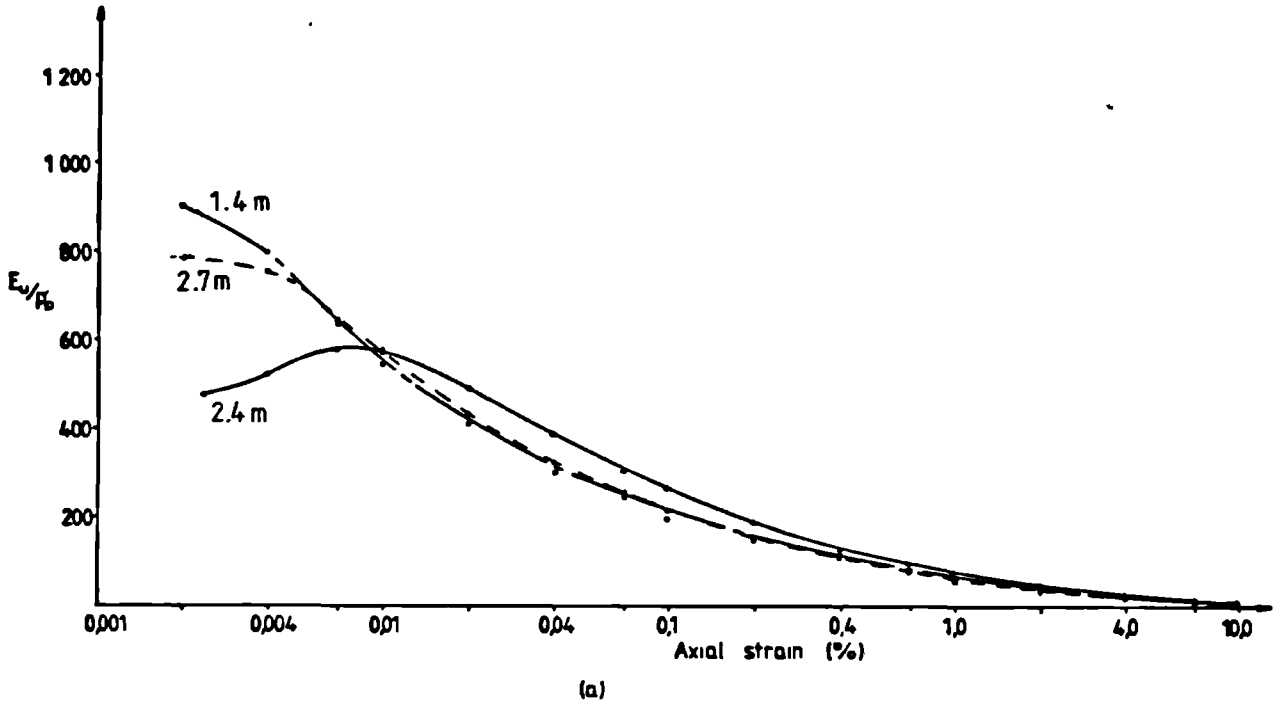
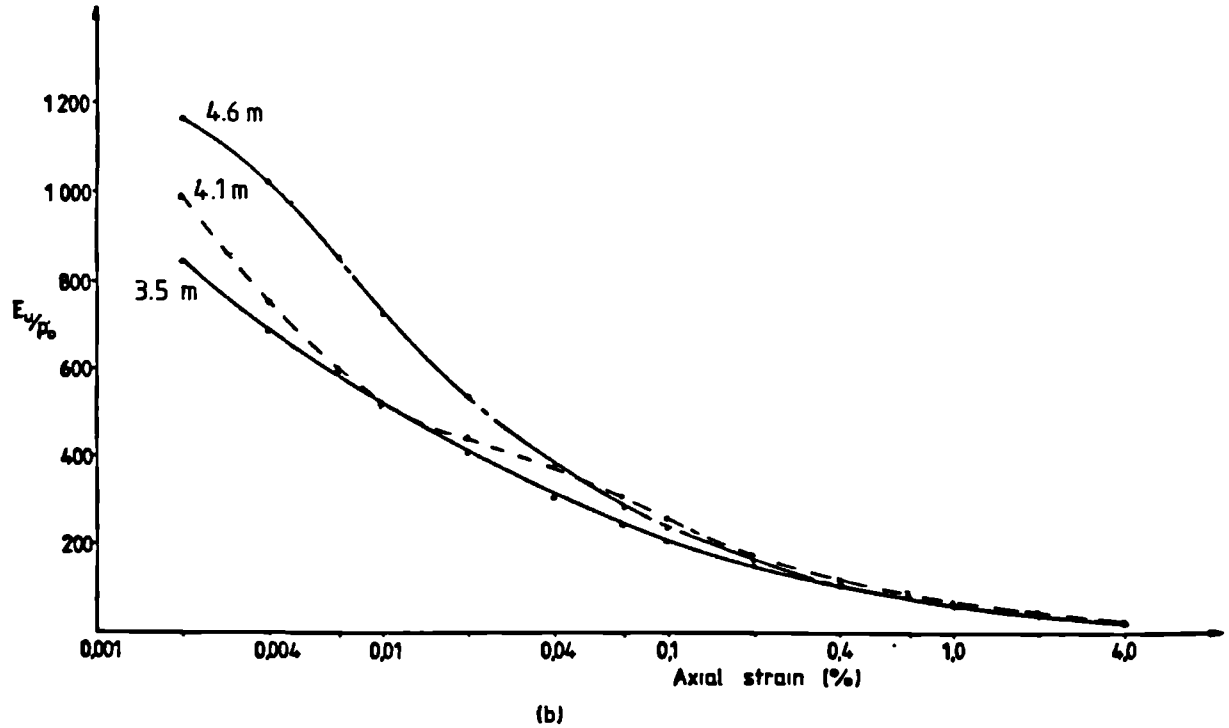


Figure 7.24. Stress strain curves corresponding to stress paths in Figs. 7.23(c),(d) and (e)

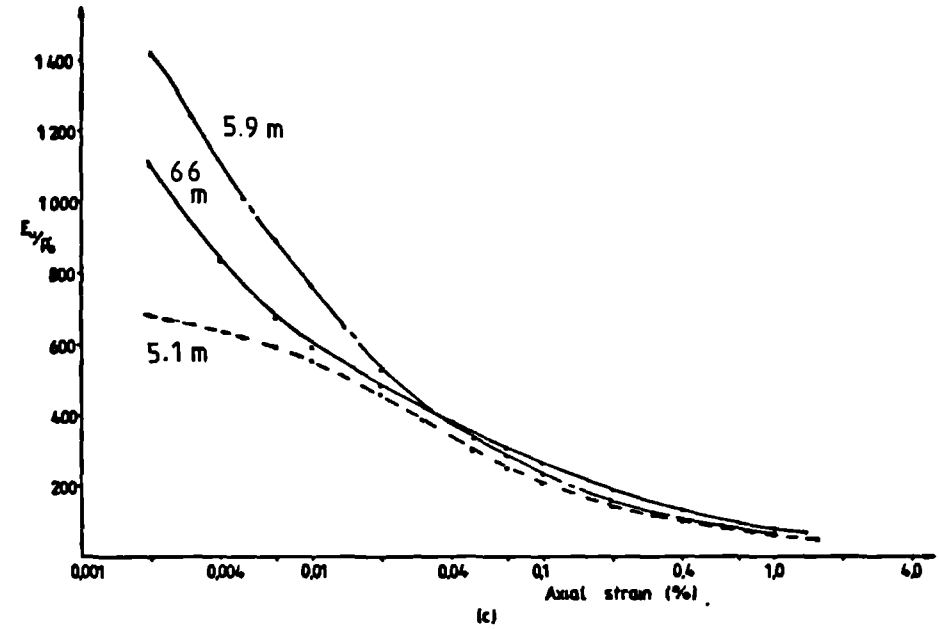


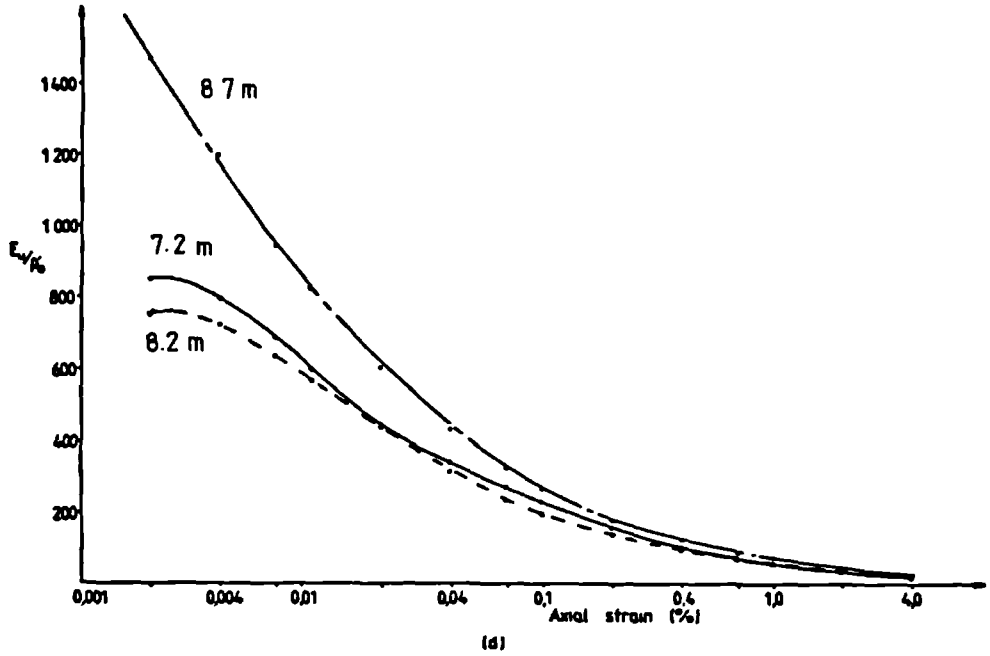
(a)

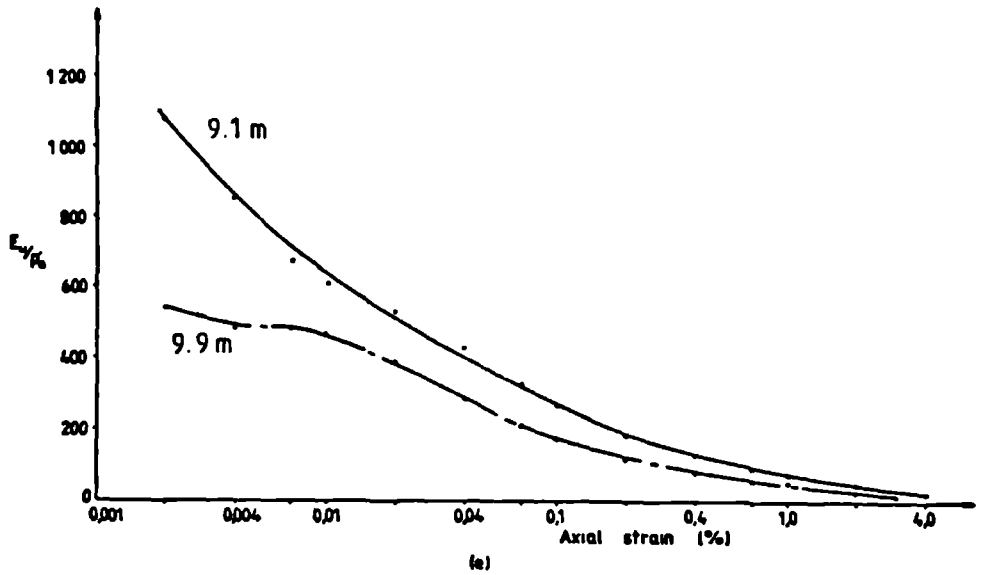


(b)

Figure 7.25. Plots of E_u/p'_o for corresponding stress paths in Figs. 7.23(a) and (b)







ure 7.25. Plots of E_u/p_o' vs. axial strain for corresponding stress paths in Figs. 7.23(c), (d) and (e)

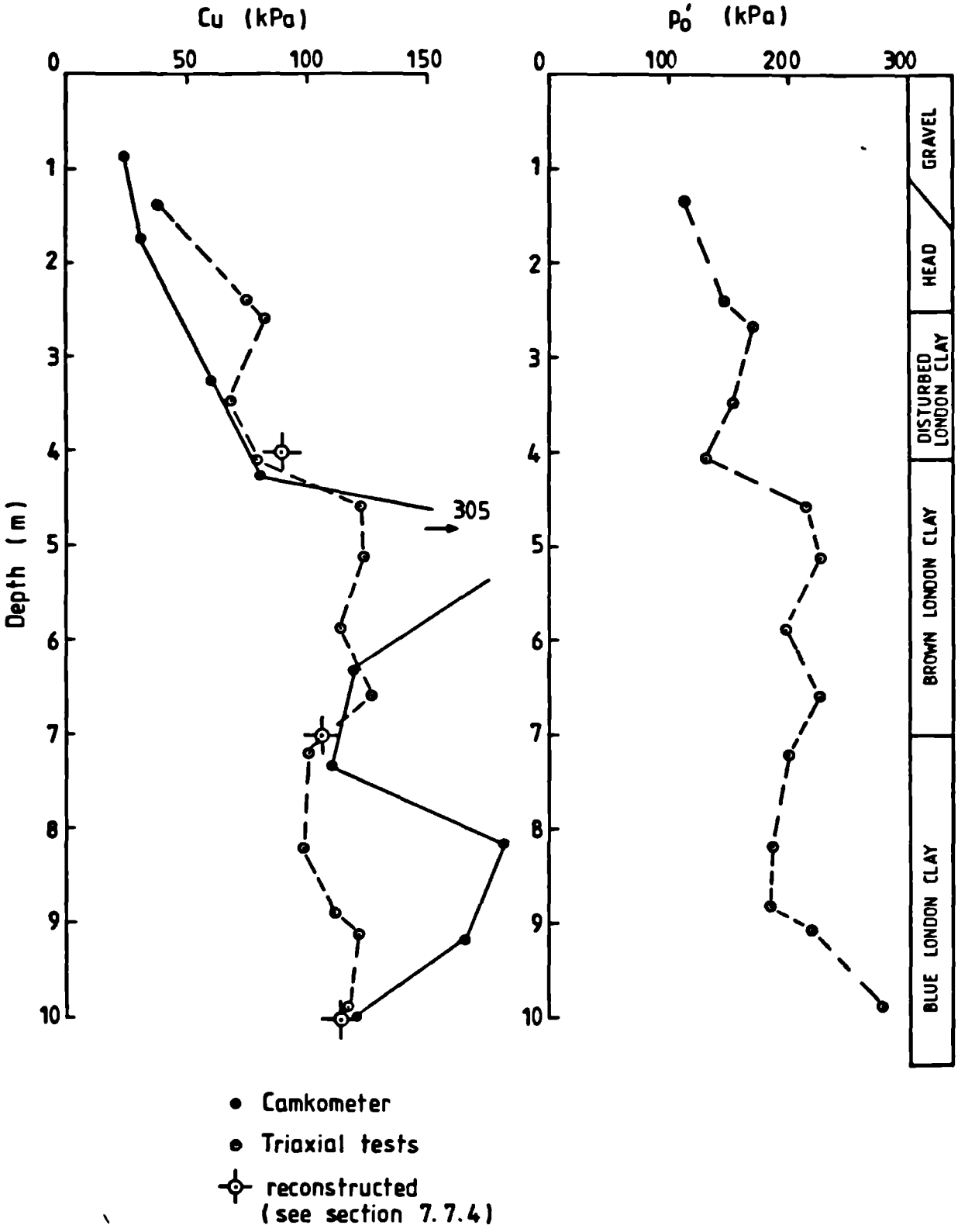


Figure 7.26. Shear strength - depth and p'_o depth profiles.

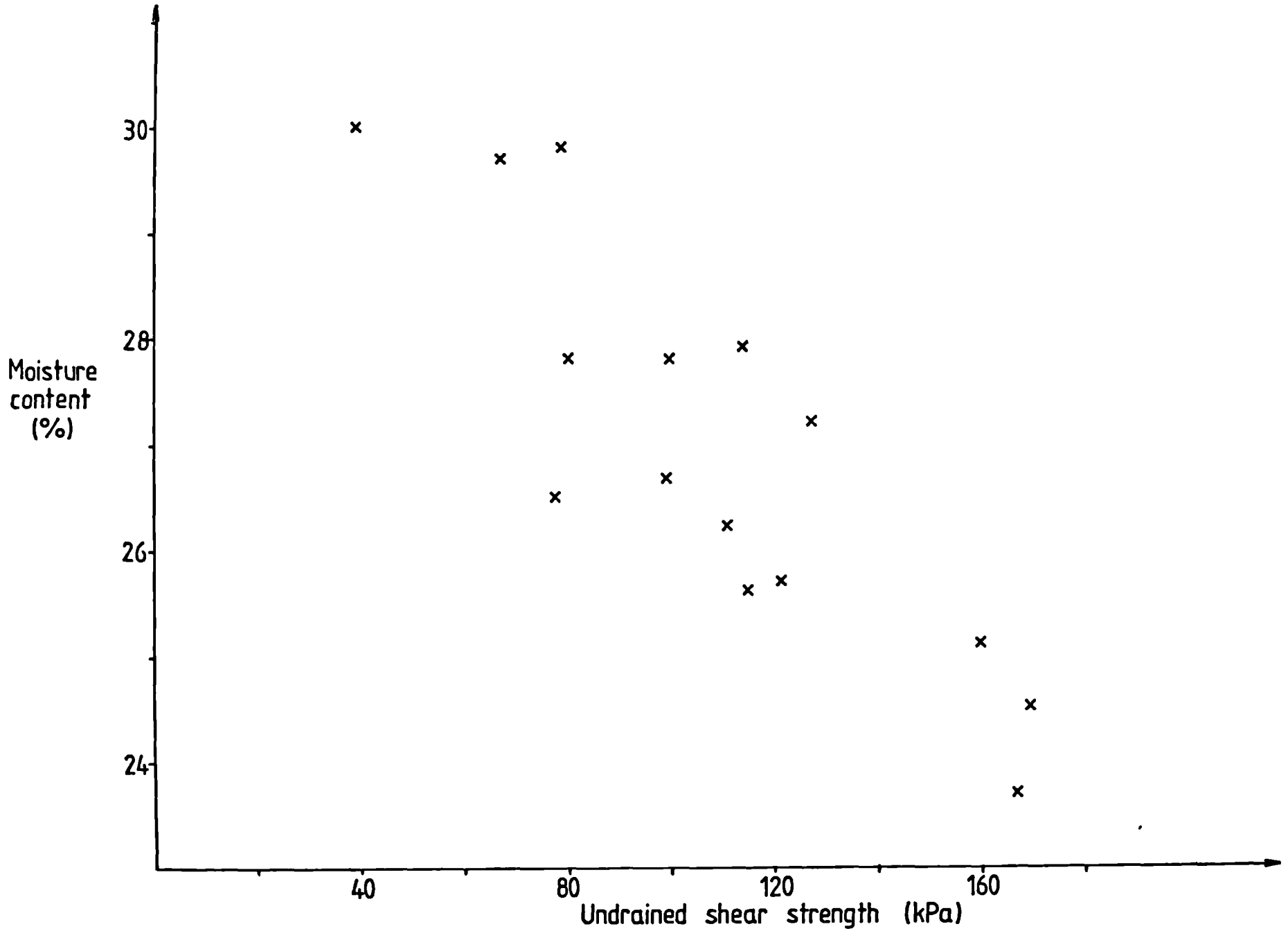


Figure 7.27. Cu - water content trends.

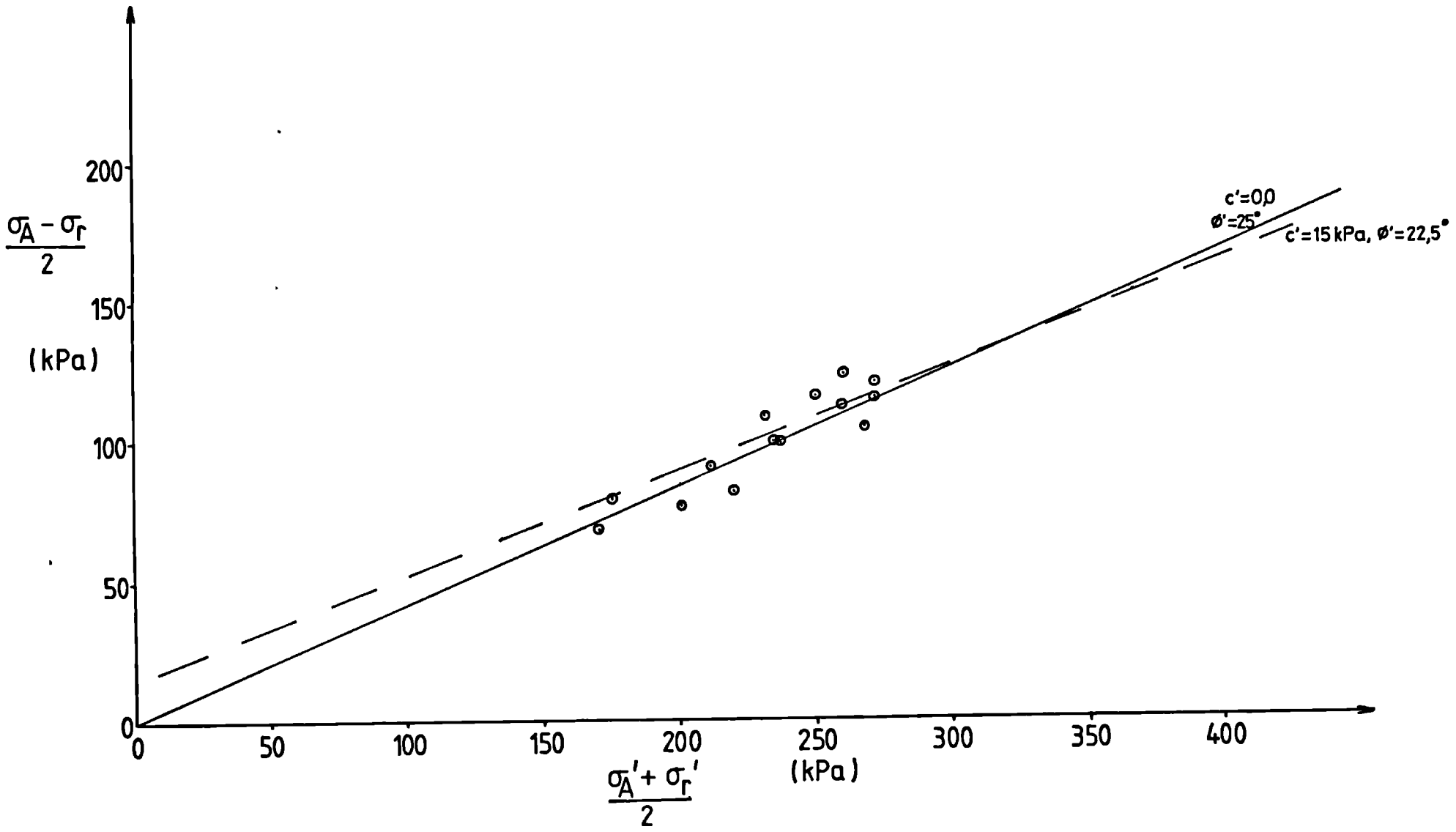


Figure 7.28. Failure conditions at peak strength, intact samples.

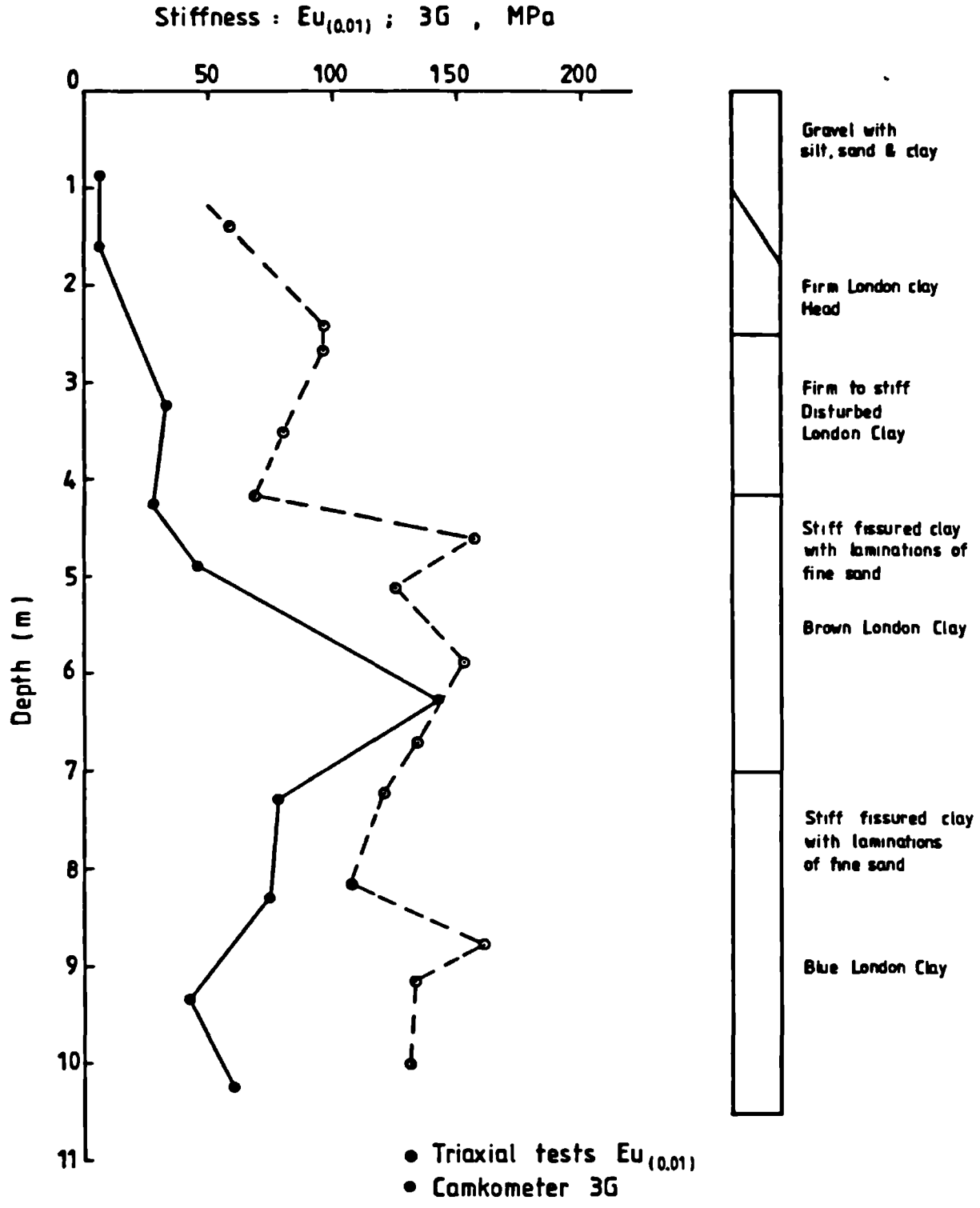


Figure 7.29. Stiffness - depth profiles.

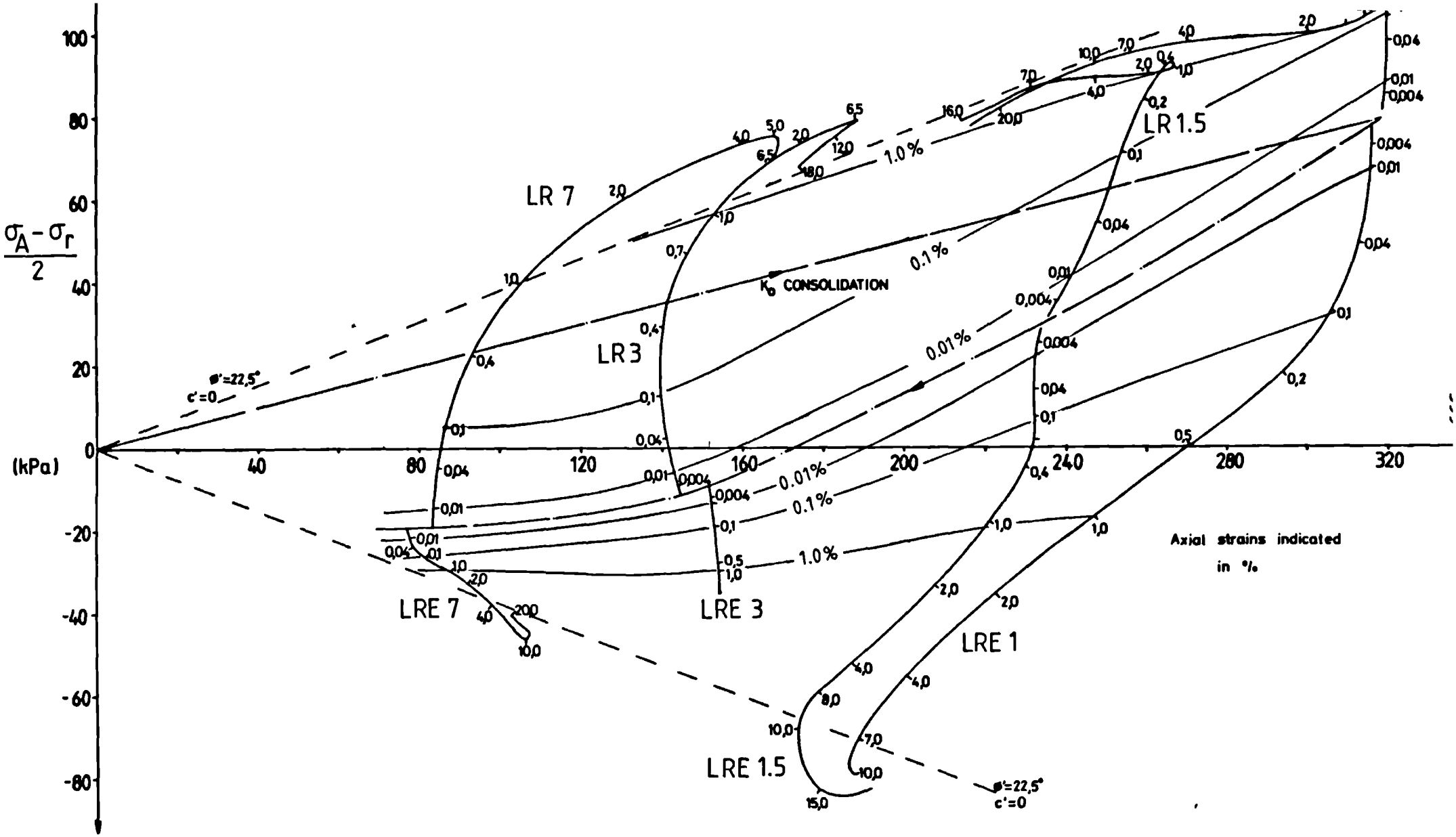


Figure 7.30. Effective stress paths for undrained portions of test series LR and LRE.

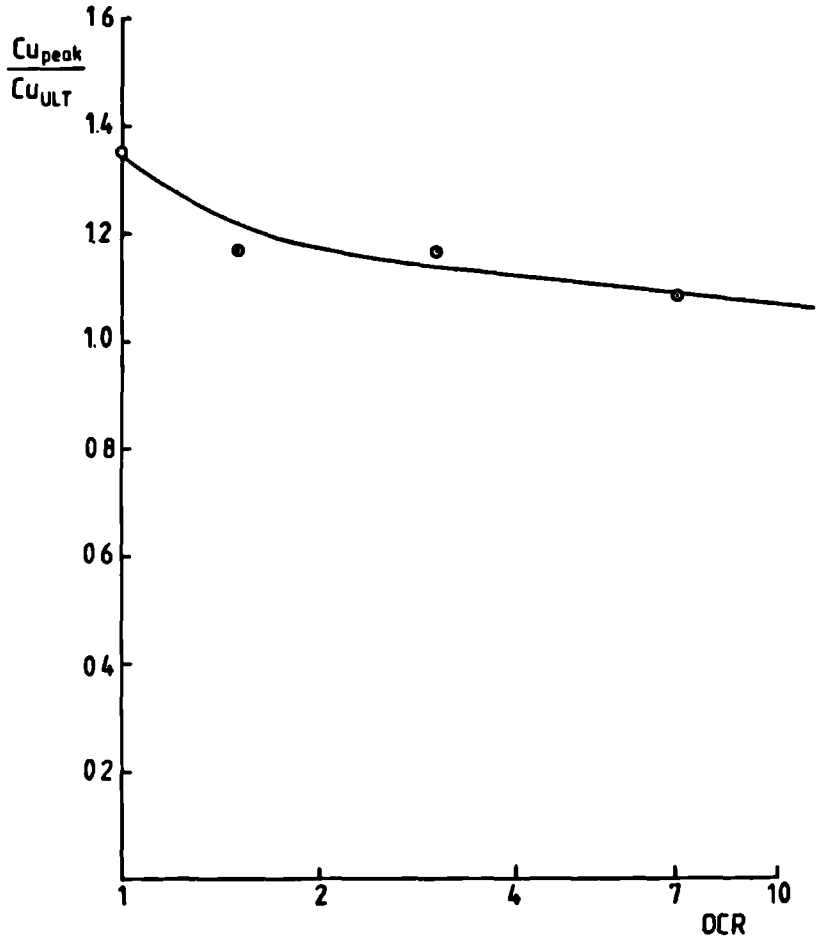


Figure 7.31a). Undrained brittleness - OCR trend for series LR.

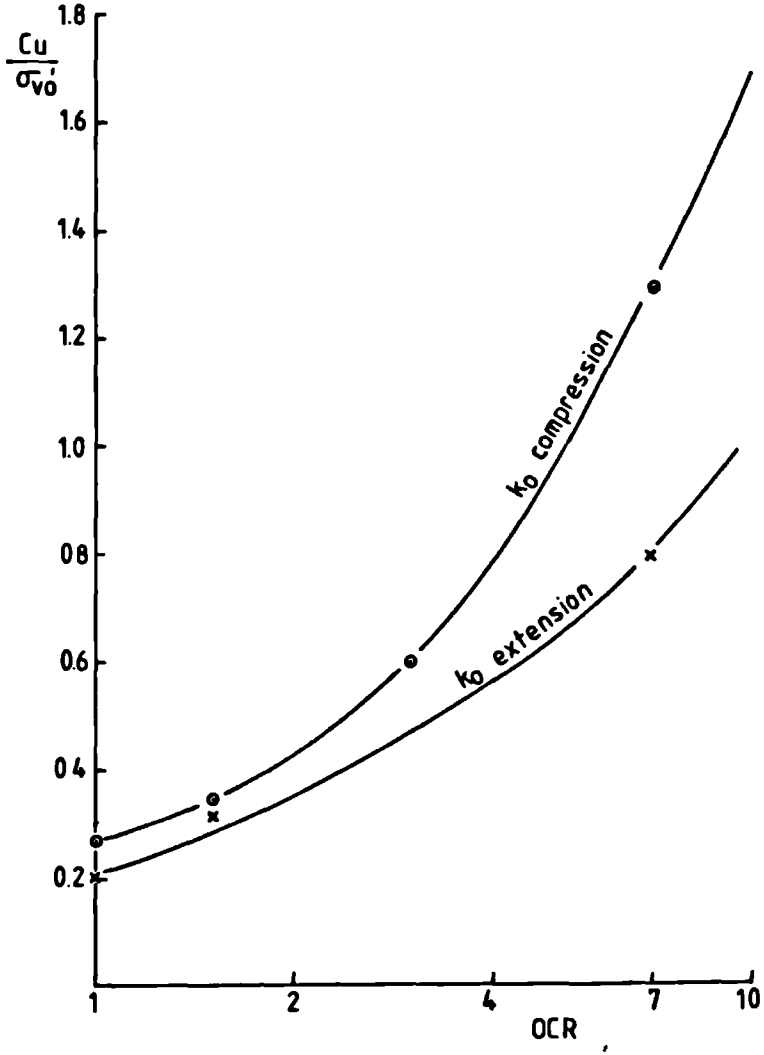


Figure 7.31b). Cu/σ'_{vo} - OCR trend for Series LR and LRE.

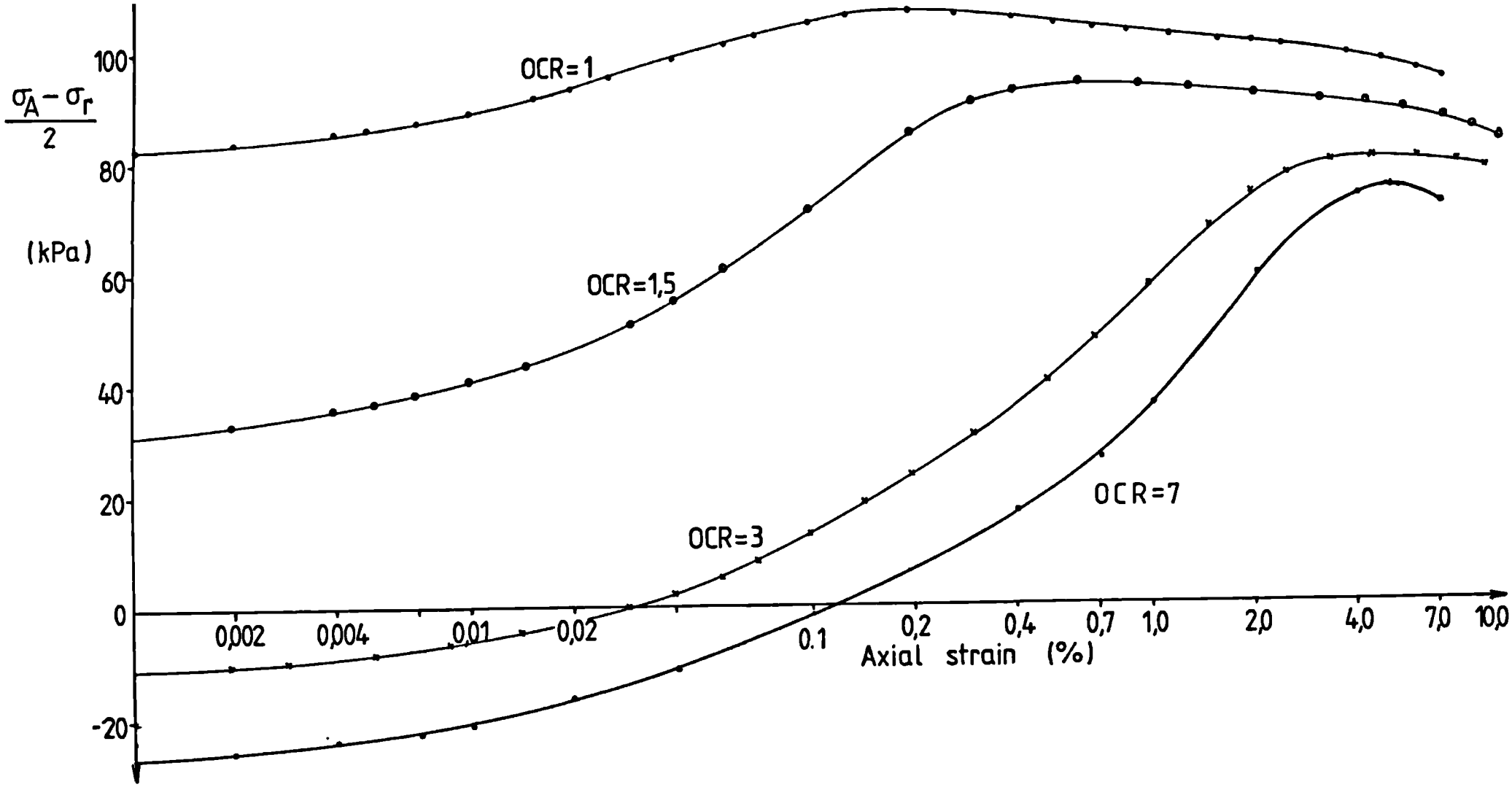


Figure 7.32. Stress - log strain data, Series LR.

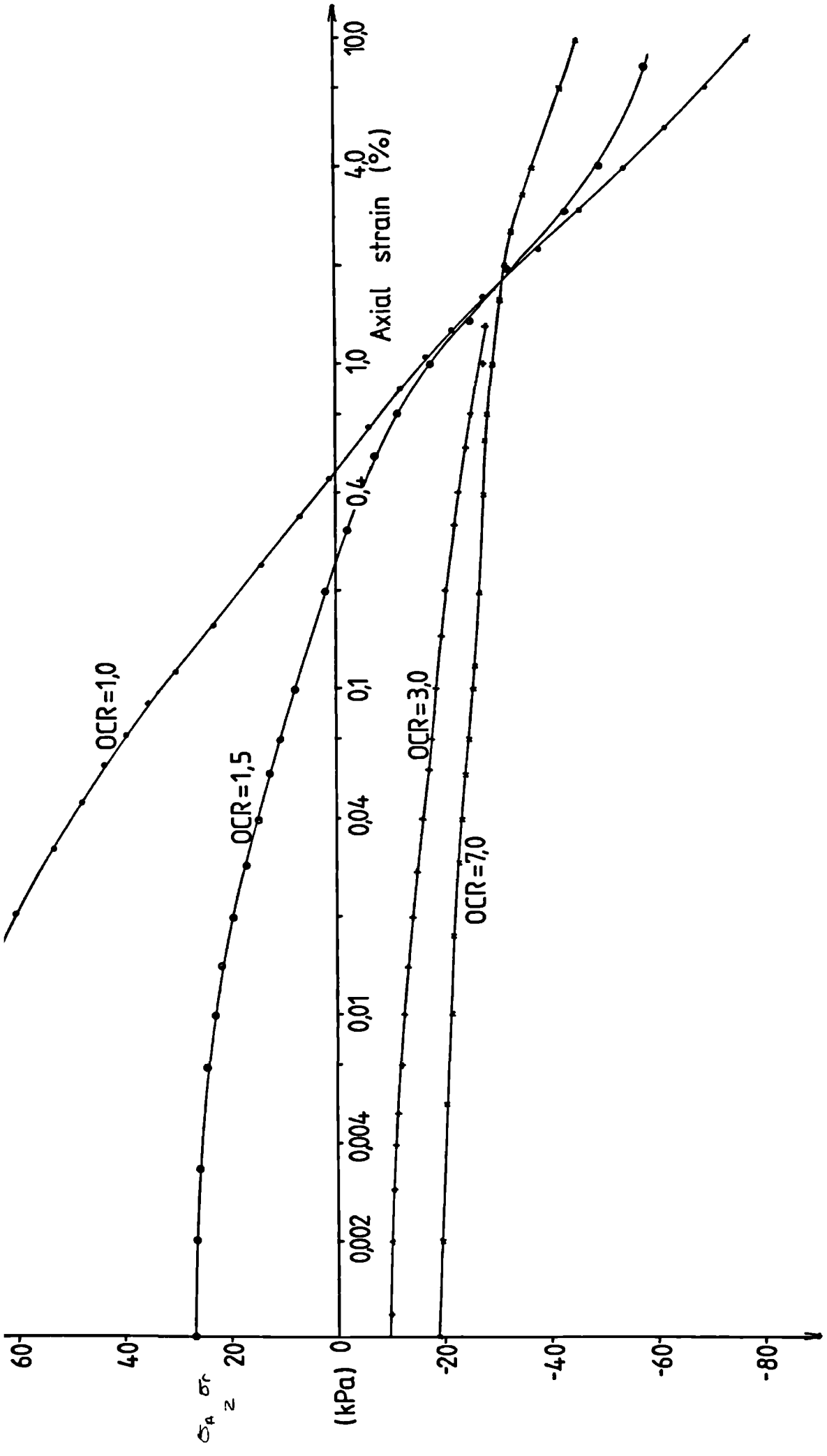


Figure 7.33. Stress - log strain data, Series LRE.

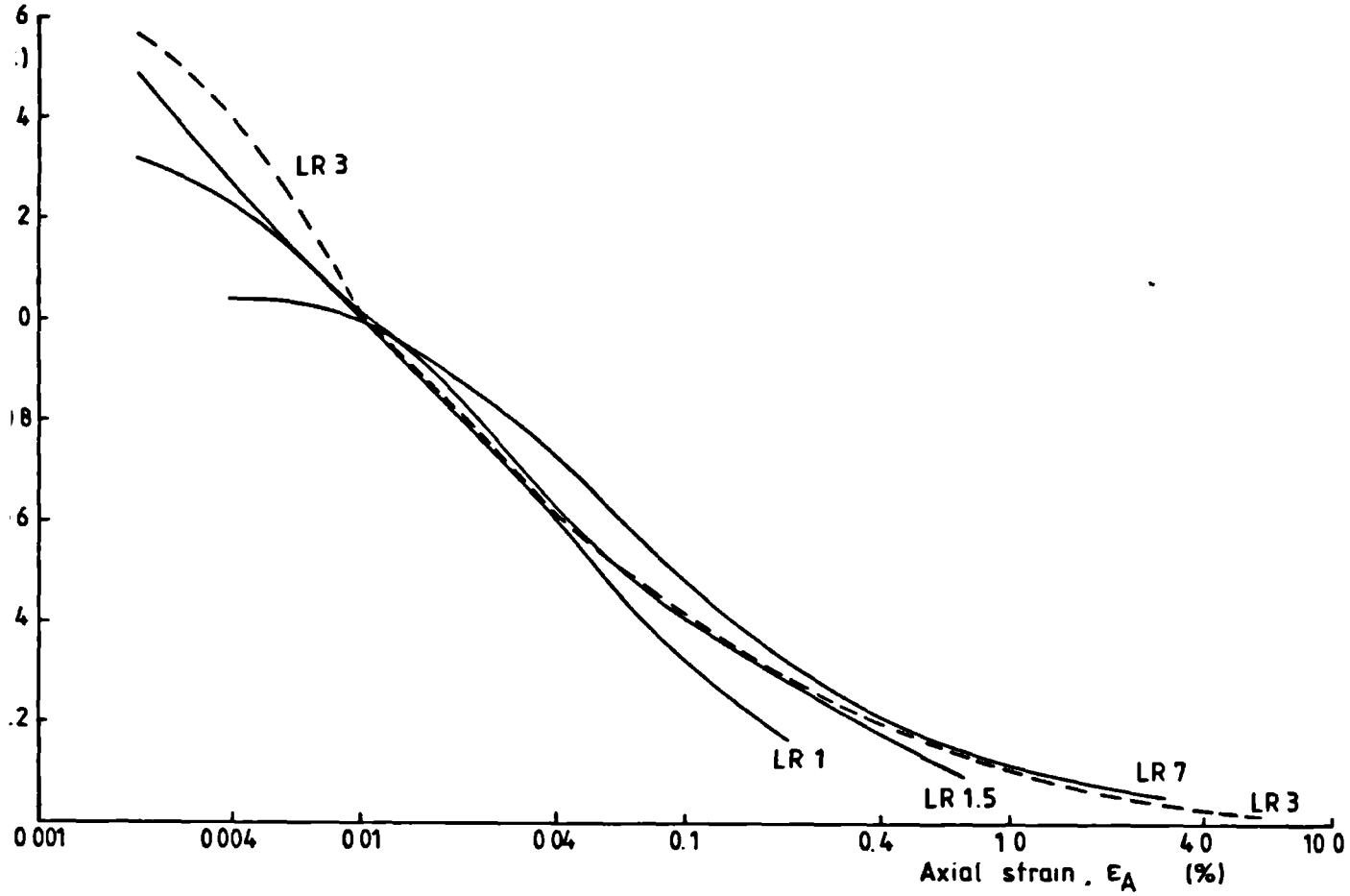
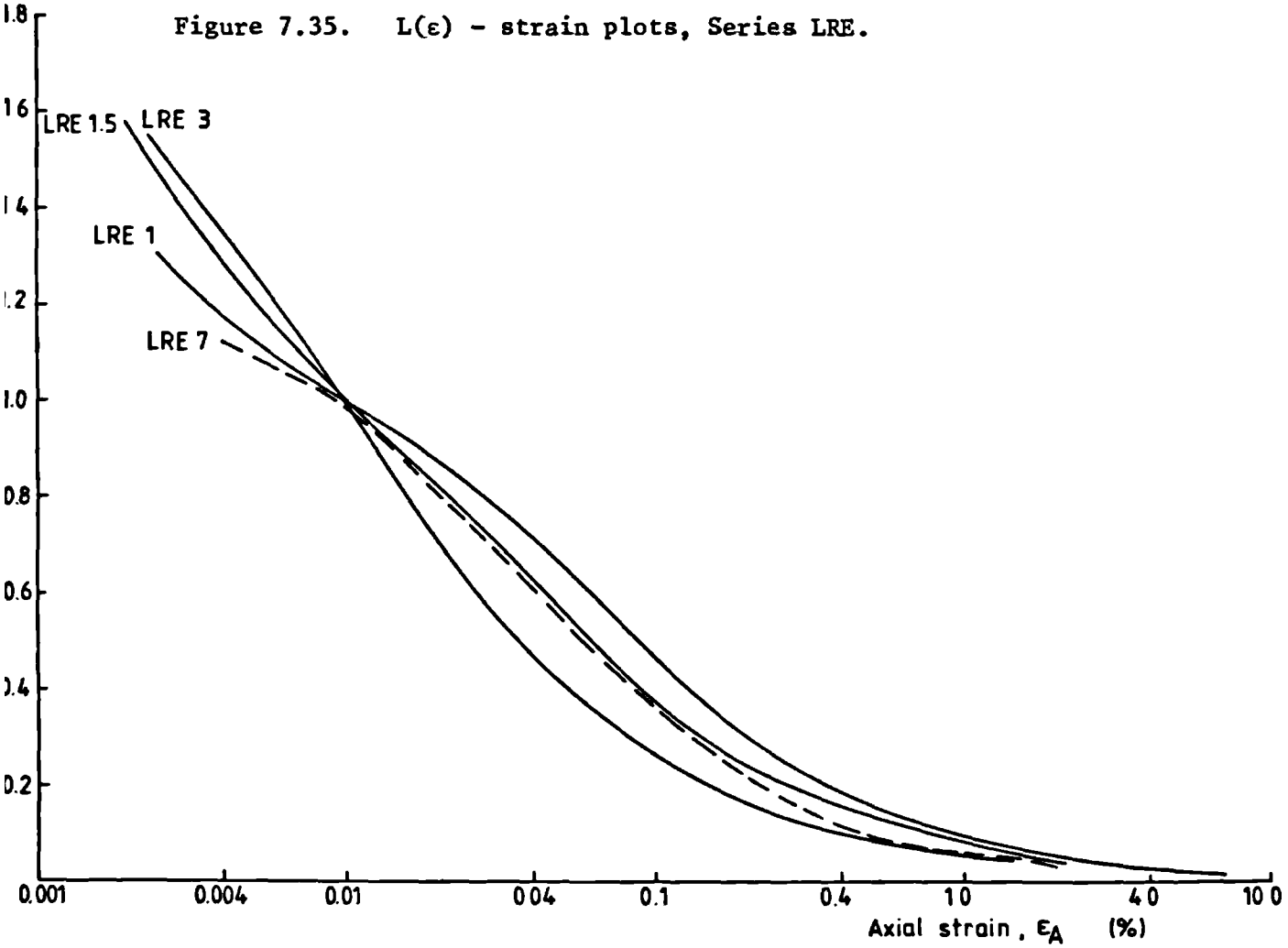


Figure 7.34. L(ε) - strain plots, Series LR.

Figure 7.35. L(ε) - strain plots, Series LRE.



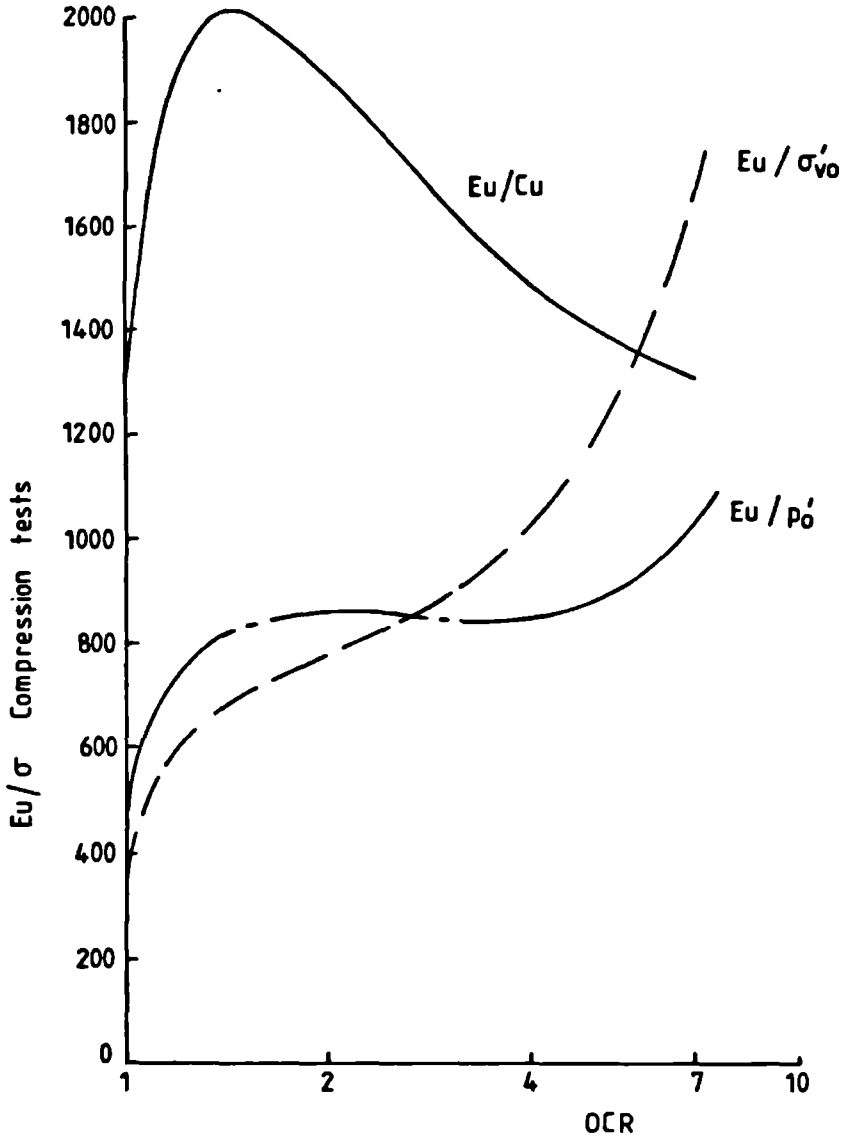
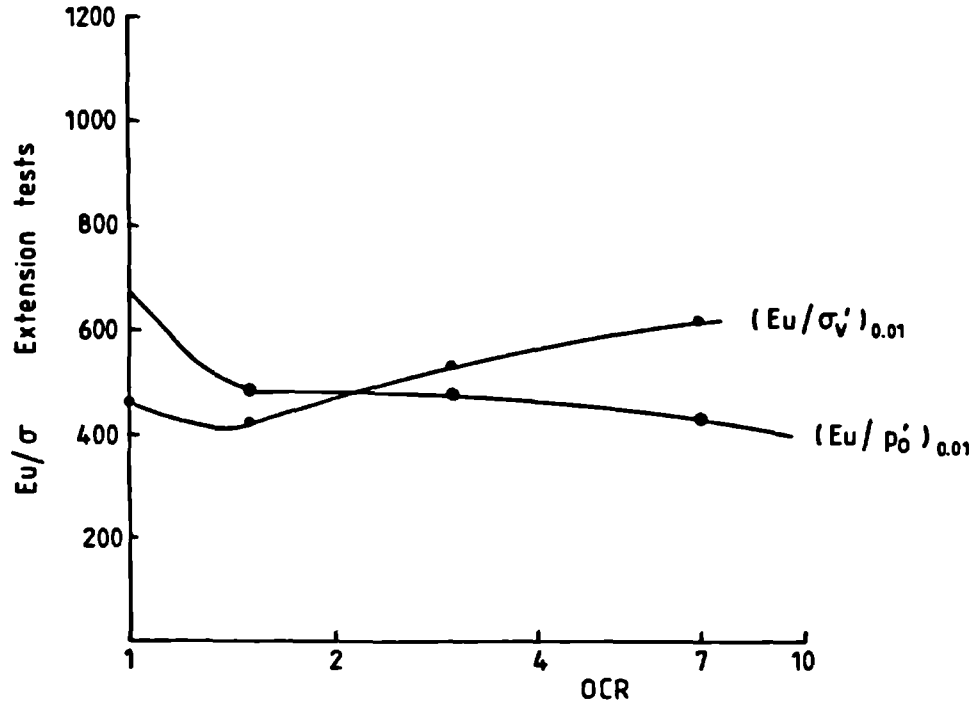


Figure 7.36. Normalised stiffness - OCR plots, Series LR.

Figure 7.37. Normalised stiffness - OCR plots, Series LRE.



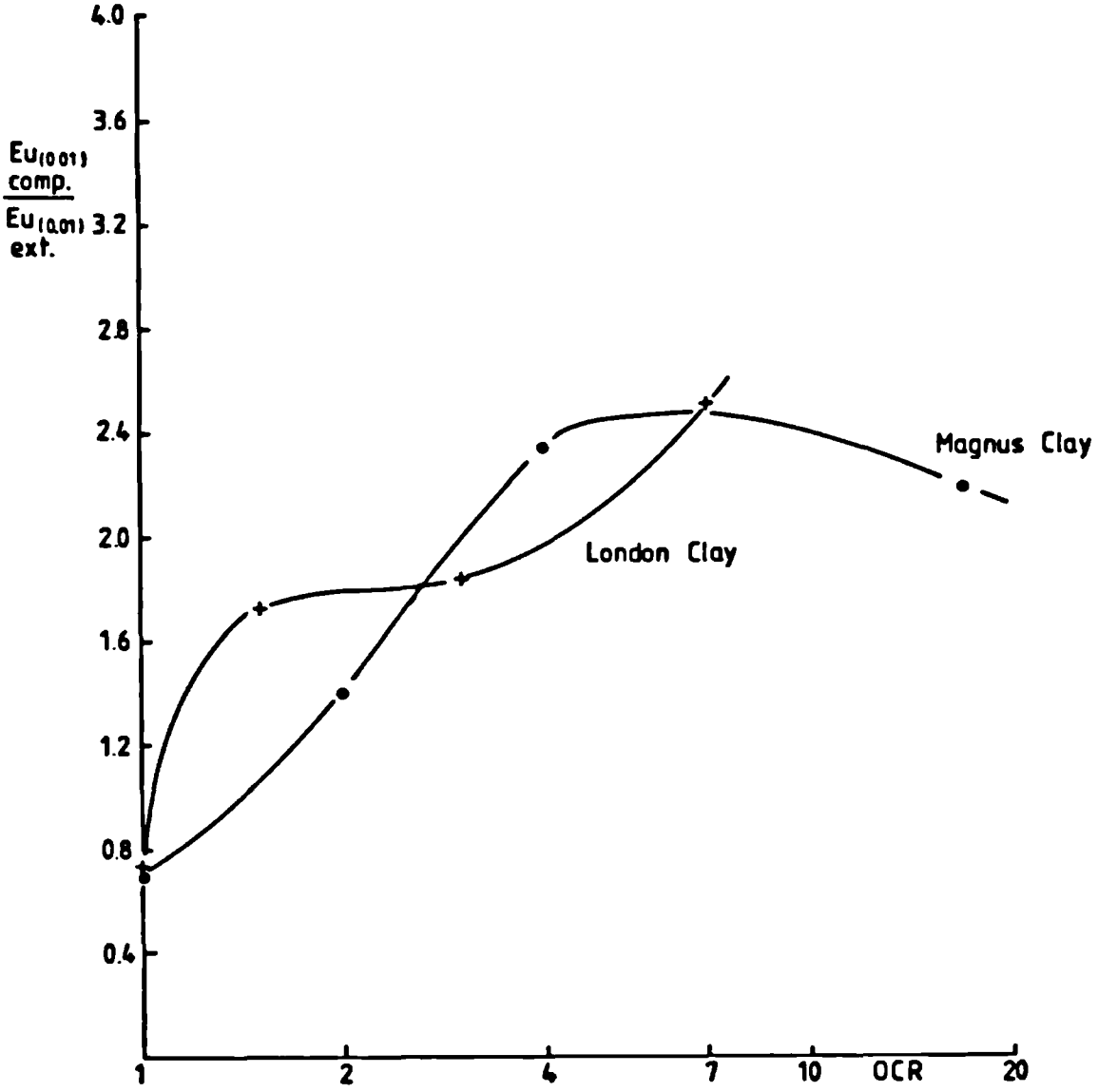


Figure 7.38. Comparisons of extension and compression stiffnesses, London clay and Magnus clay.

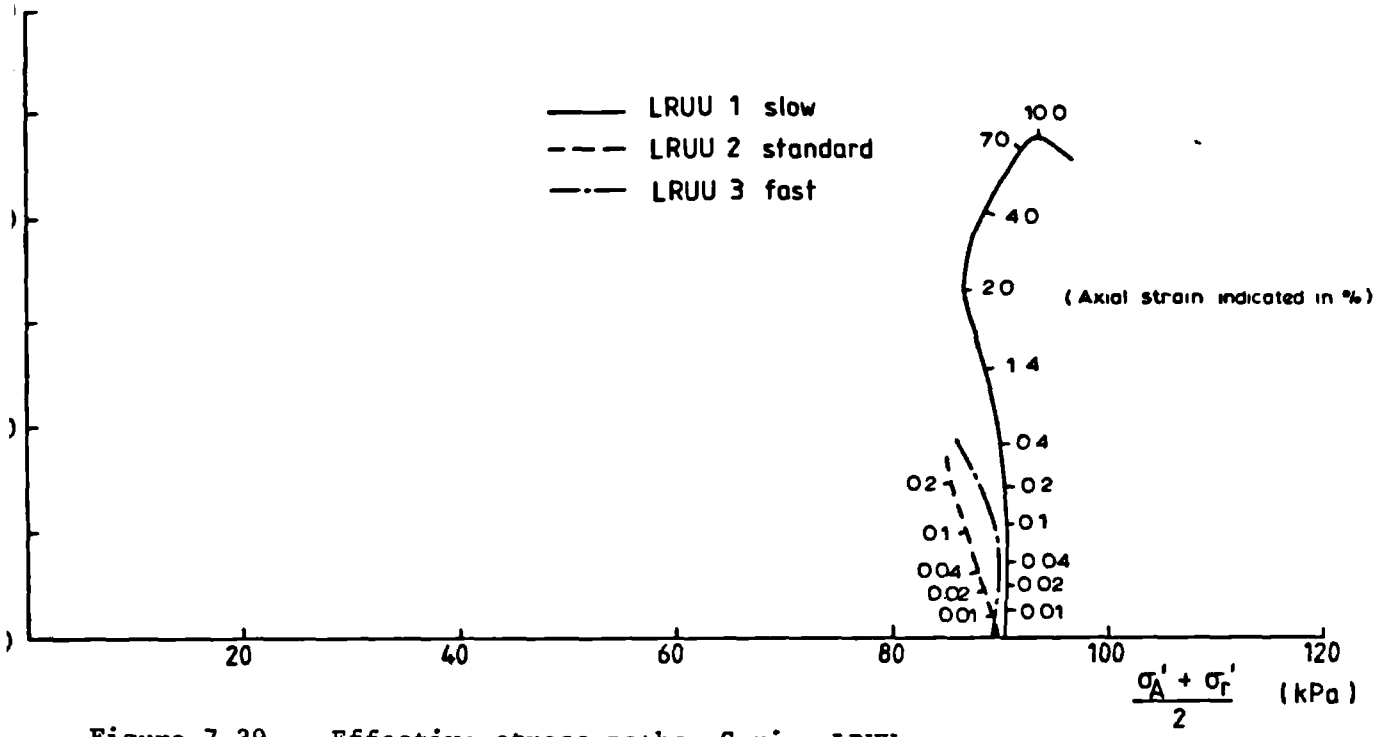


Figure 7.39. Effective stress paths, Series LRUU.

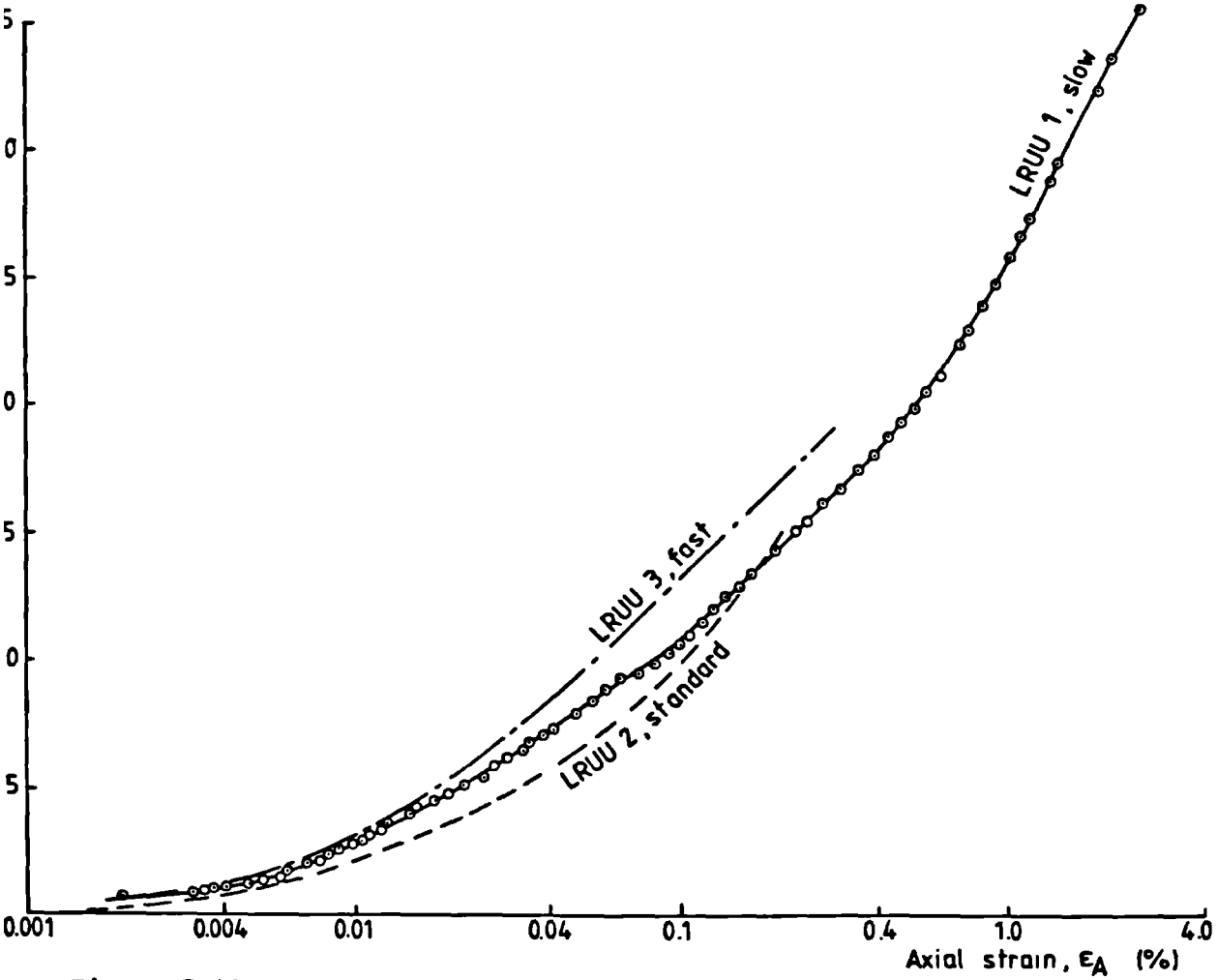
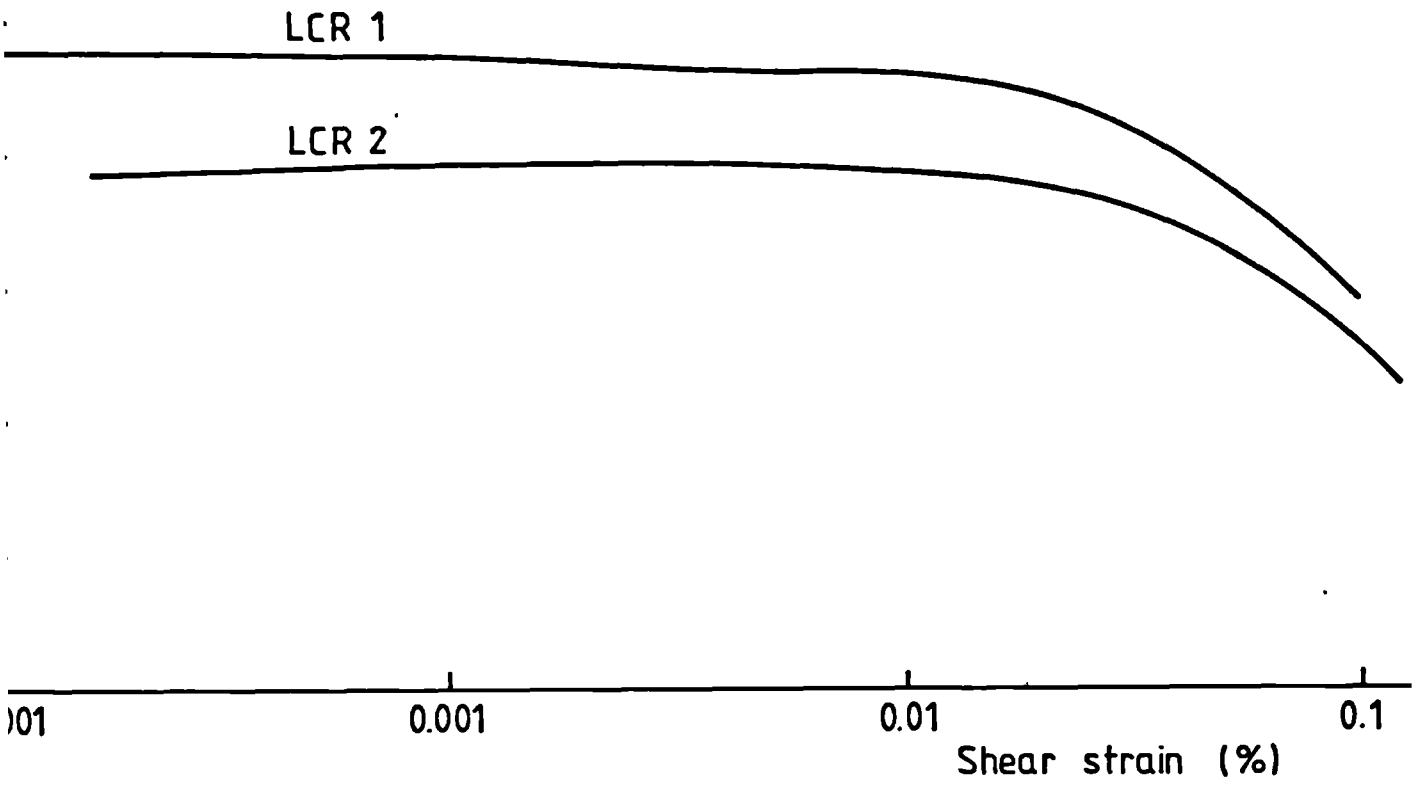


Figure 7.40. Stress - log strain data, Series LRUU.



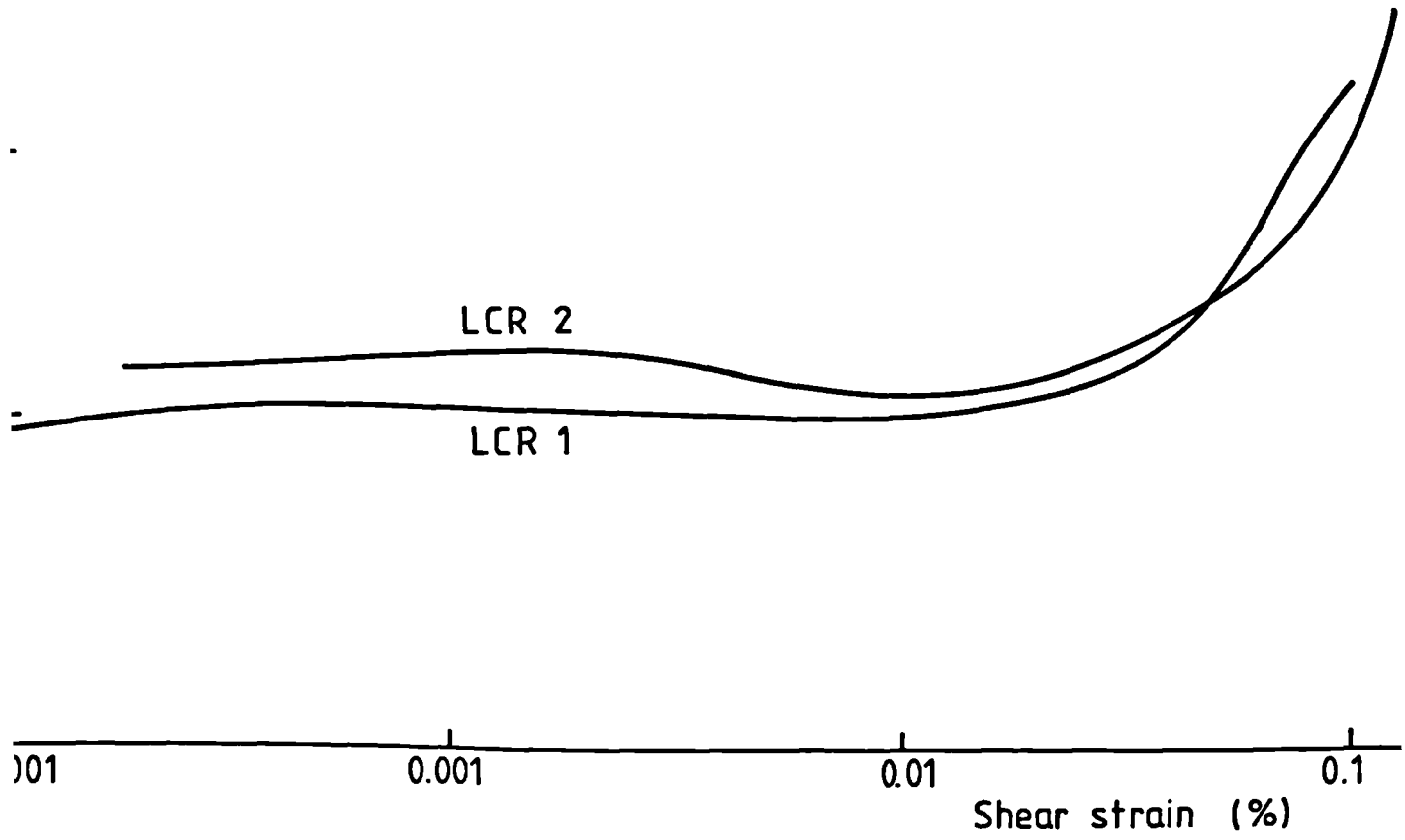
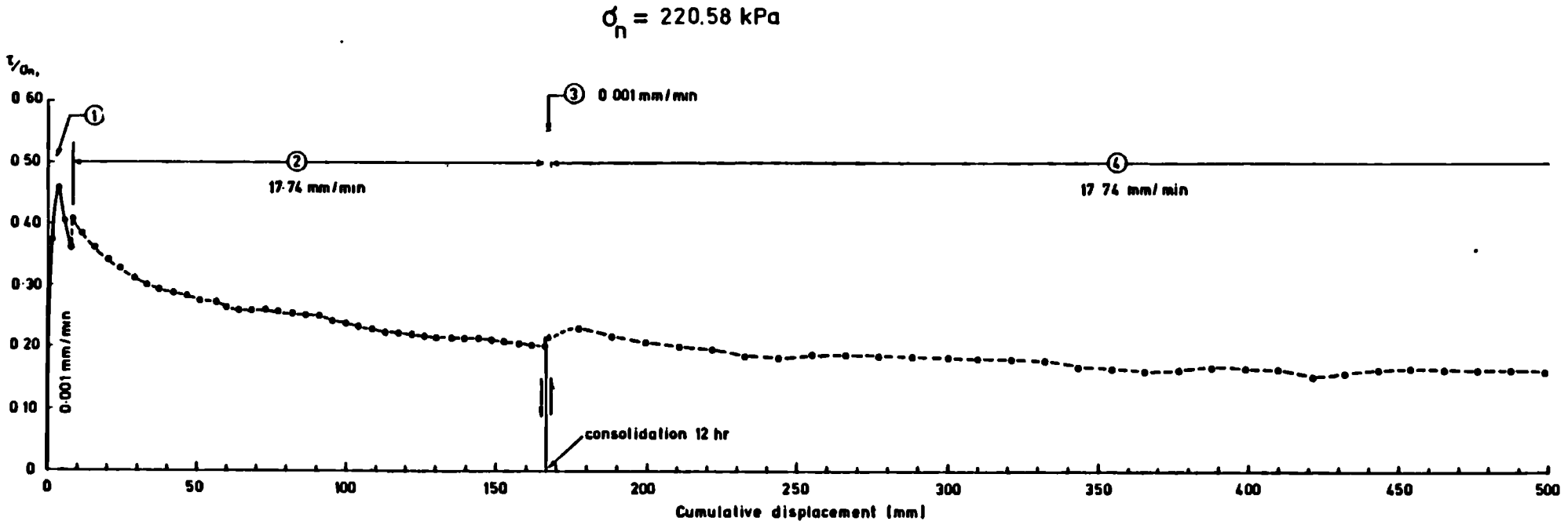


Figure 7.41. Resonant column test results for K_o consolidated, reconstituted London clay.



RING SHEAR TEST 19, LONDON CLAY (a)

Figure 7.42. Soil-soil ring shear tests, after Lupini (1980).

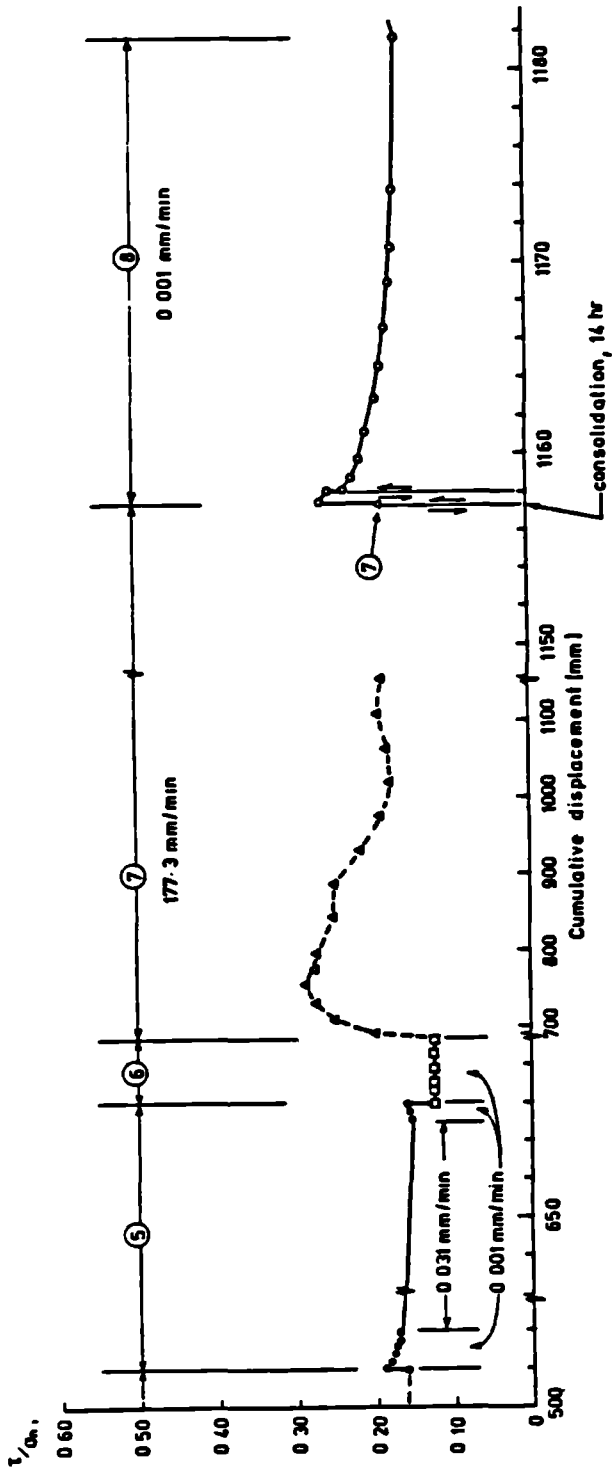


Figure 7.43. Soil-soil ring shear tests, after Lupini (1980).

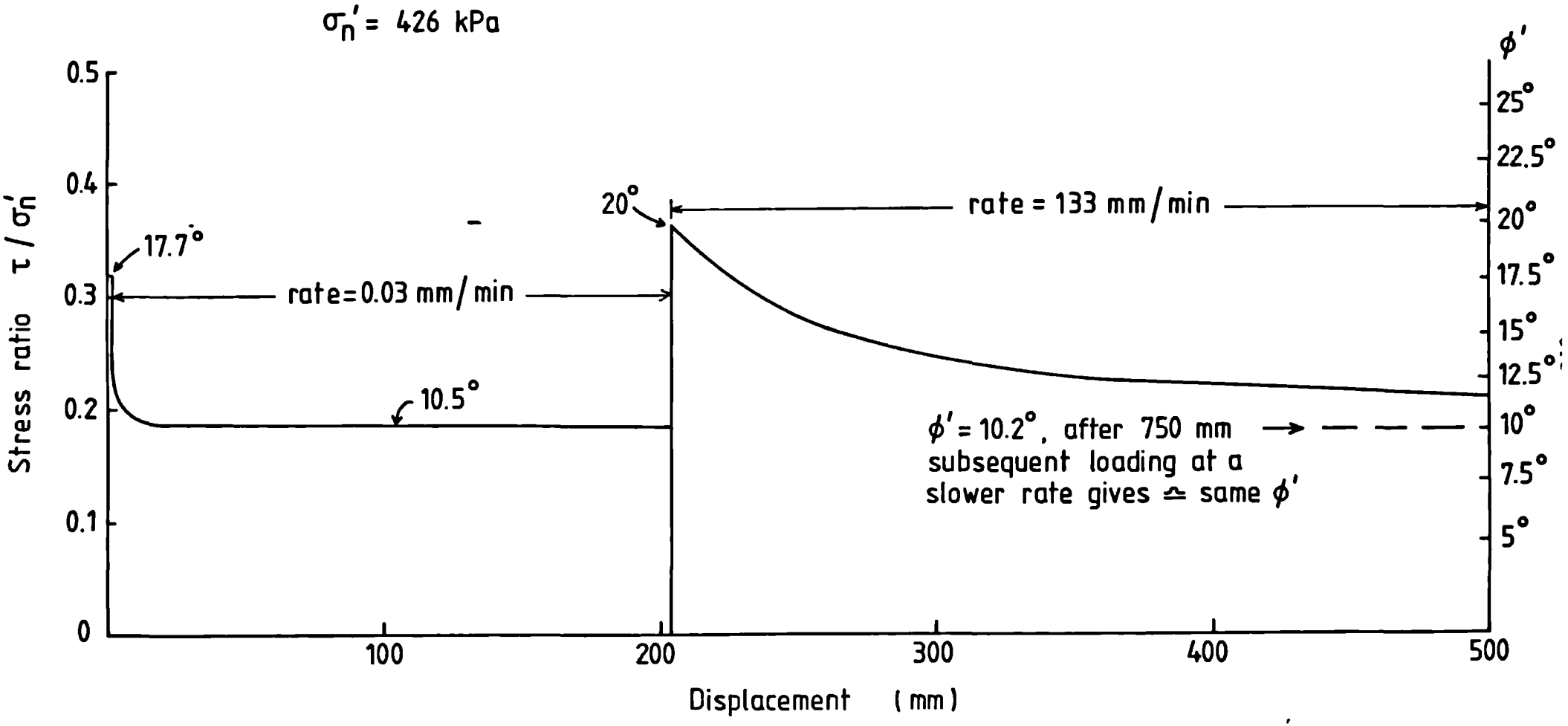


Figure 7.44. Soil-interface ring shear tests, after Lemos (1985).

CHAPTER 8

Tables and Figures

Test	A	B	C	α	β	ϵ_a min	ϵ_a max
R1	850	1000	0.008 %	2.023	0.5943	0.005%	0.20%
R2	3100	3200	0.0007%	1.349	0.6385	0.003%	0.20%
I2	1420	1380	0.009 %	2.098	0.5050	0.0045	1.5 %

Table 8.1. Non-linear soil parameters from 3 tests.

No. Plotted on Figure 8.34	Welt. and Healy Case No.	Pile Type	Length Metres	Diameter mm	Mean α -	Mean Cu Kpa	Range of P.I %
1	10	Bored, cast insitu	12.2	430	0.8	135	12-15
2	15	Bored, cast insitu	10.5	430	0.6	150	10-30
3	17	Driven, step taper	25.3	340	0.7	100	3-17
4	18	Driven, step taper	29.0	330	0.7	91	18-30
5	196	Driven, step taper	15.3	314	0.7	110	10-40
6	20	Driven, step taper	16.5	314	0.8	130	18-36
7	21a	Driven, step taper	11.6	340	1.0	200	23-30
8	26a	Bored, cast insitu	11.0	510	0.4	120	12-39
9	26b		18.0	430	0.5	180	12-39

Table 8.2. Summary of data from Weltman and Healy (1979)

(The mean values of α and Cu were interpreted by the writer from the original data)

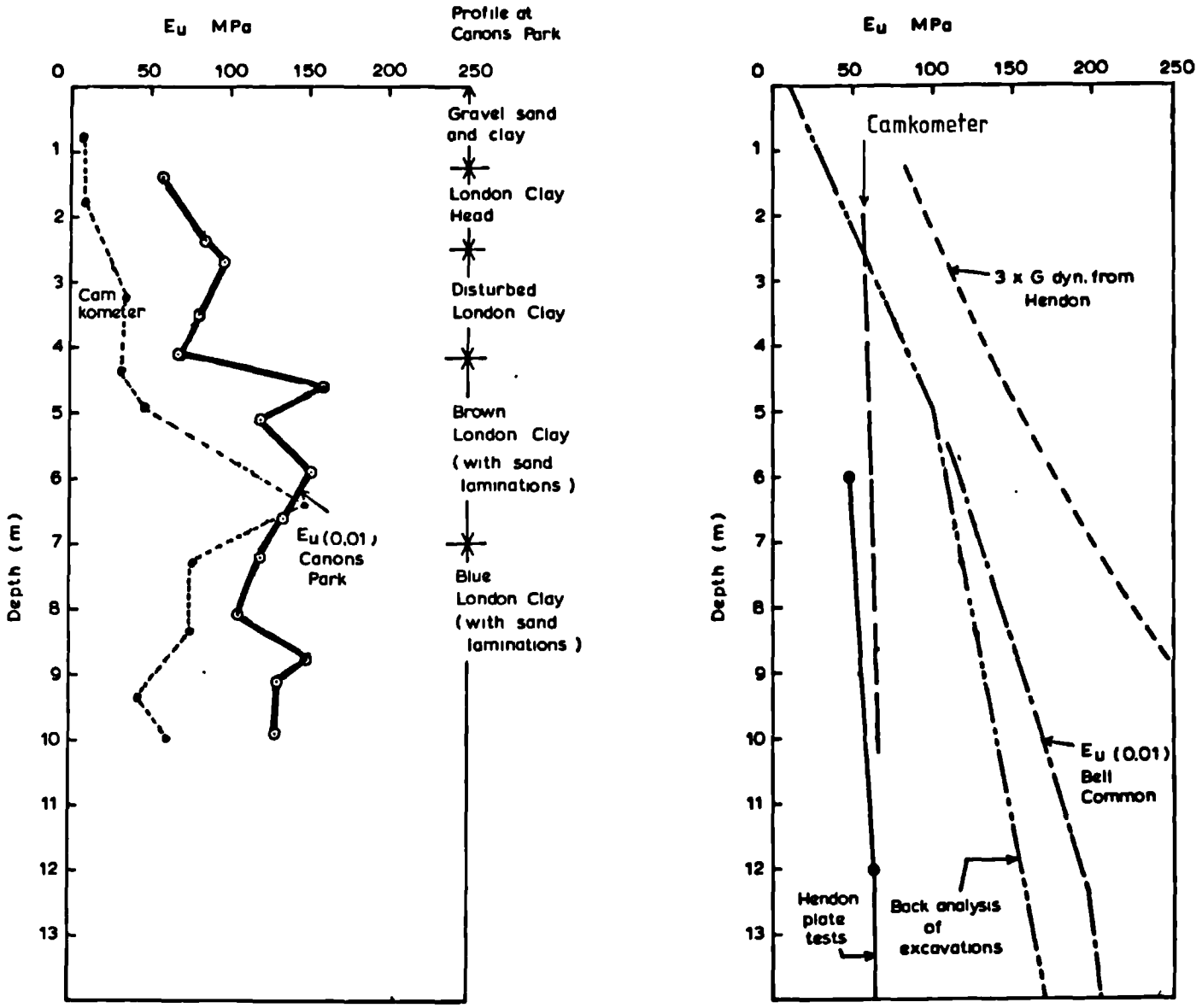


Figure 8.1. Stiffness profiles for London clay, left Canons Park data, I.C. intact triaxial tests and Camkometer, right data from other sites and Bell Common I.C. intact triaxial tests.

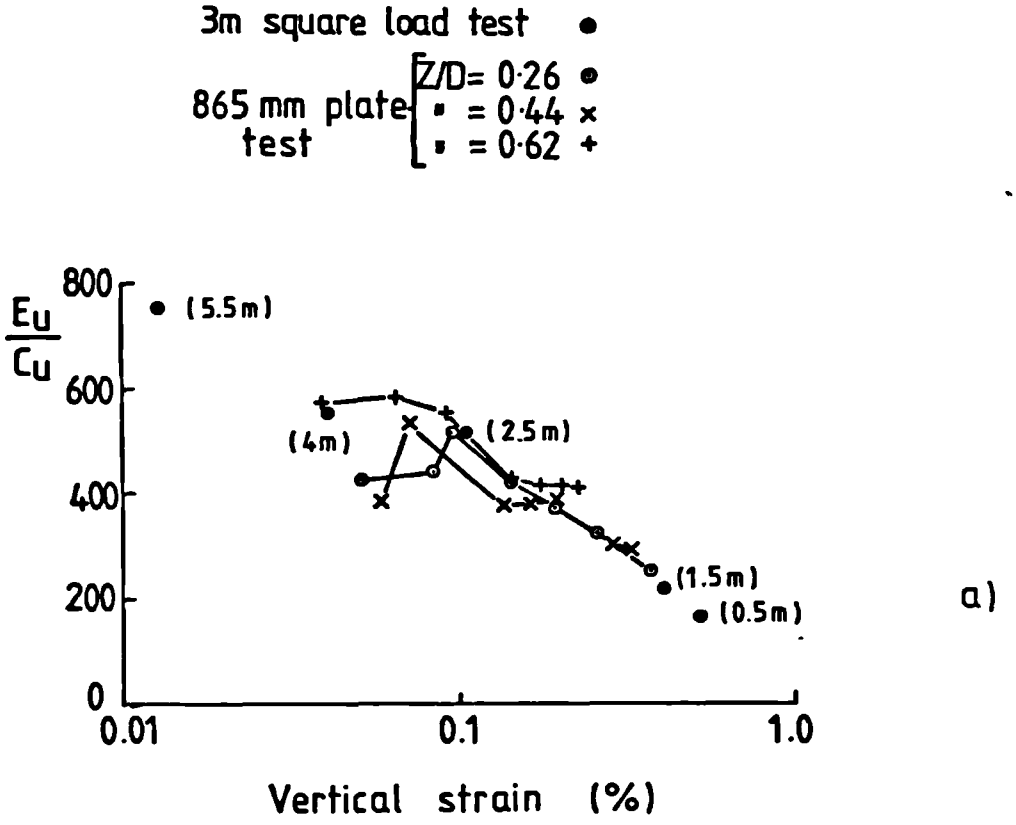
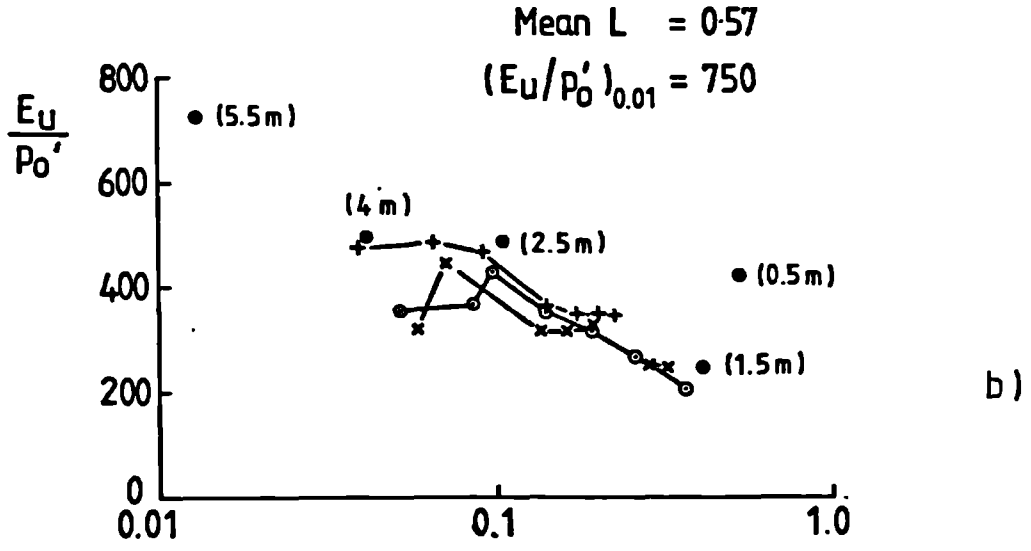


Figure 8.2. Instrumented plate loading and trial footing tests, Chelsea and Bracknell.



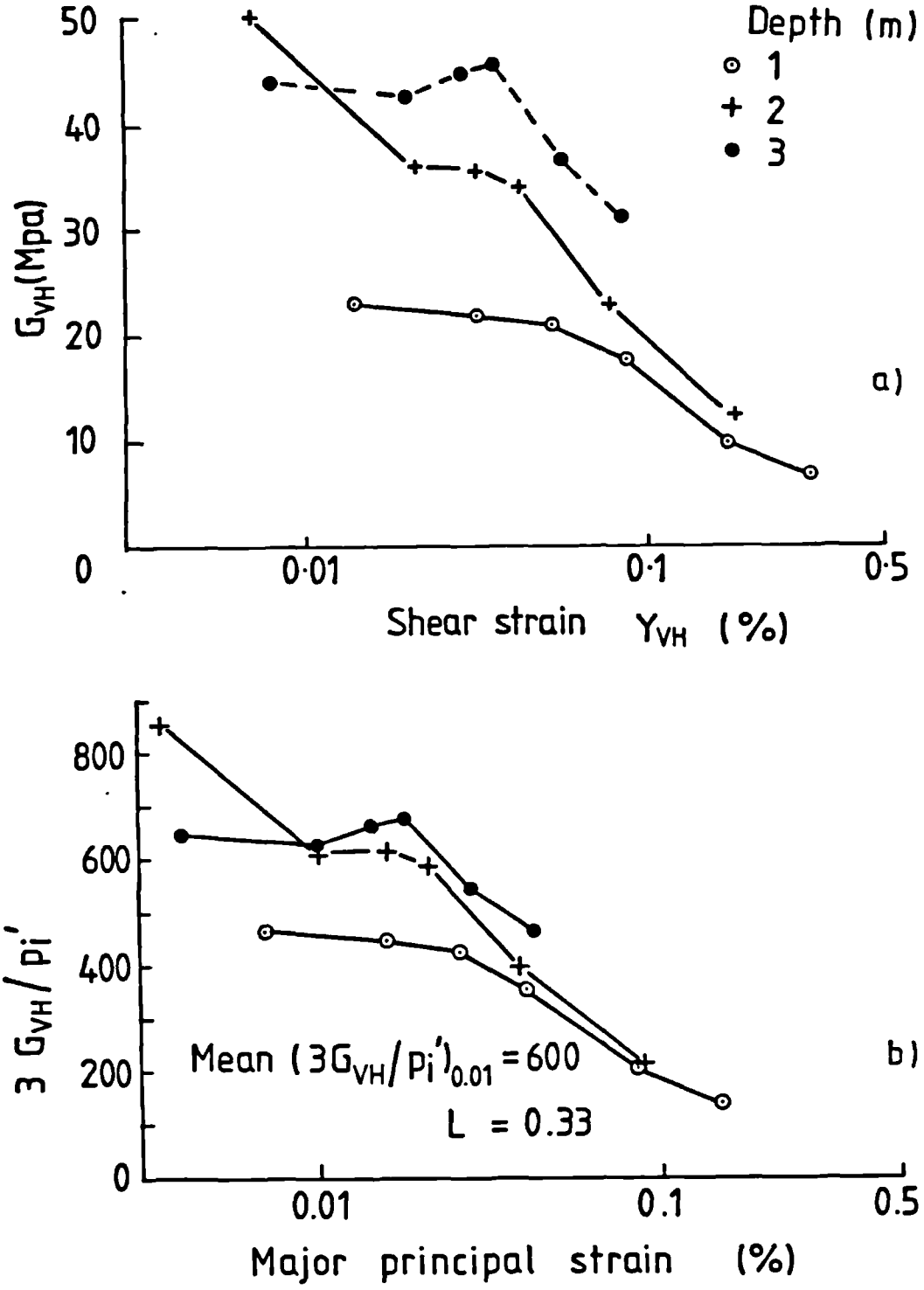


Figure 8.3. Instrumented pile loading test, Hendon.

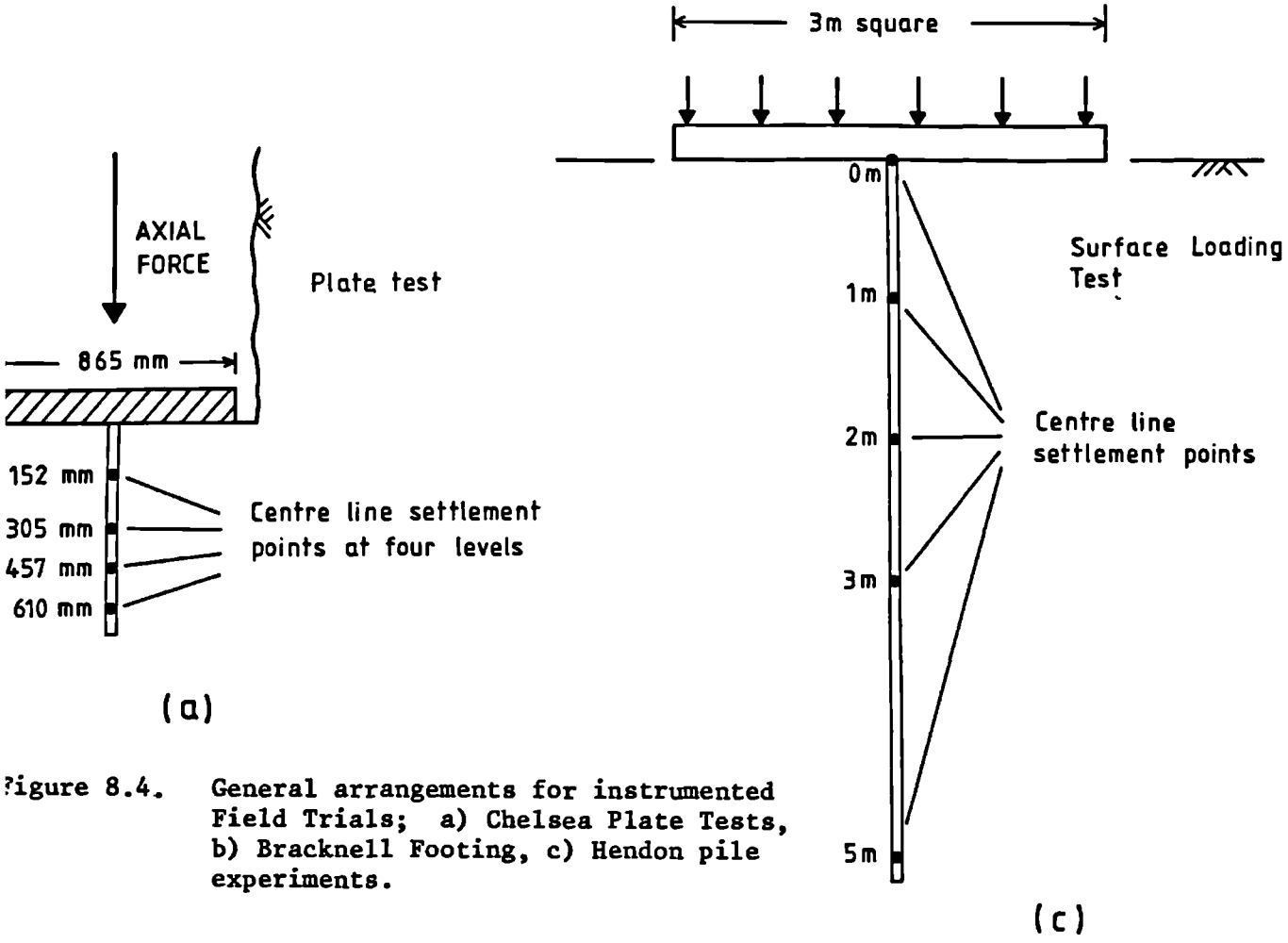
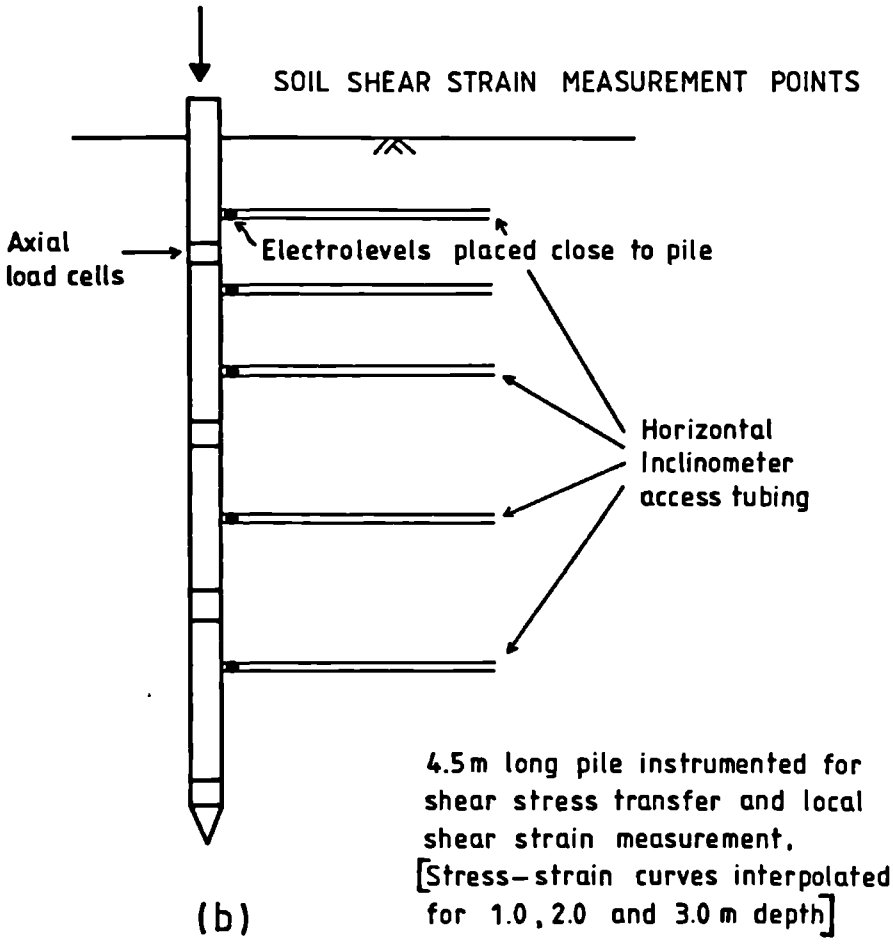


Figure 8.4. General arrangements for instrumented Field Trials; a) Chelsea Plate Tests, b) Bracknell Footing, c) Hendon pile experiments.



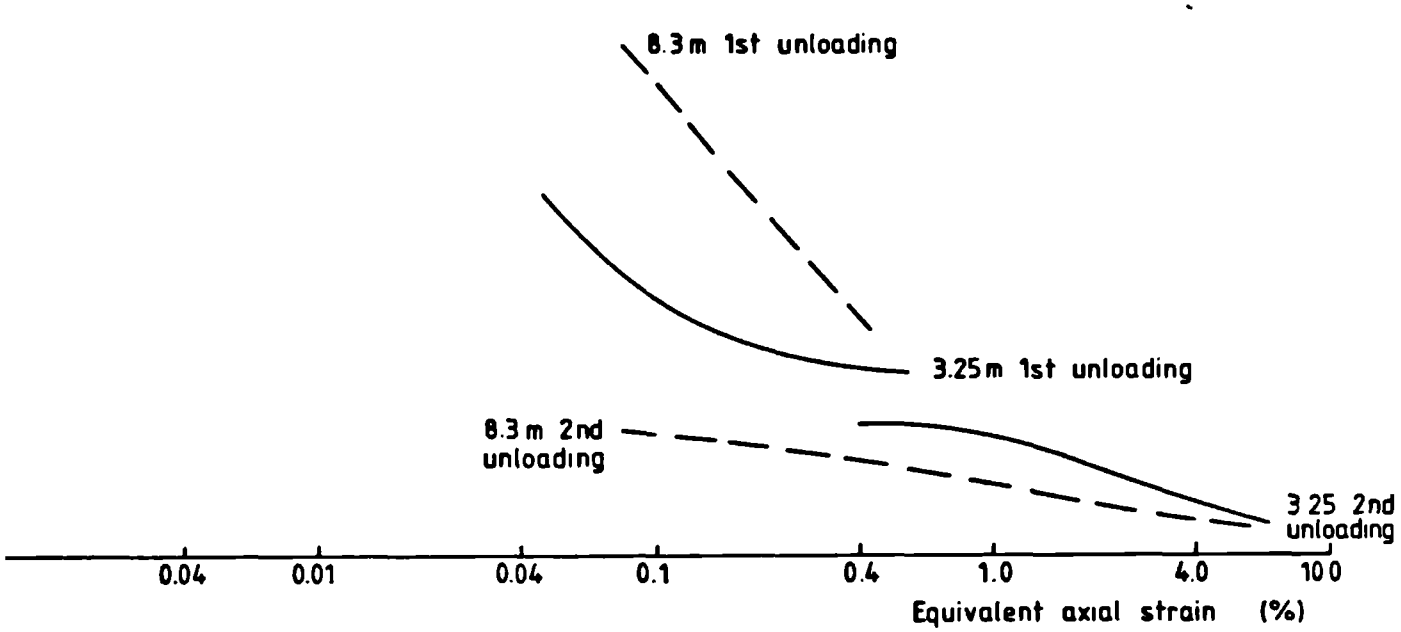


Figure 8.5a). Stiffness-strain characteristics deduced from Canons Park pressuremeter data by method of Palmer.

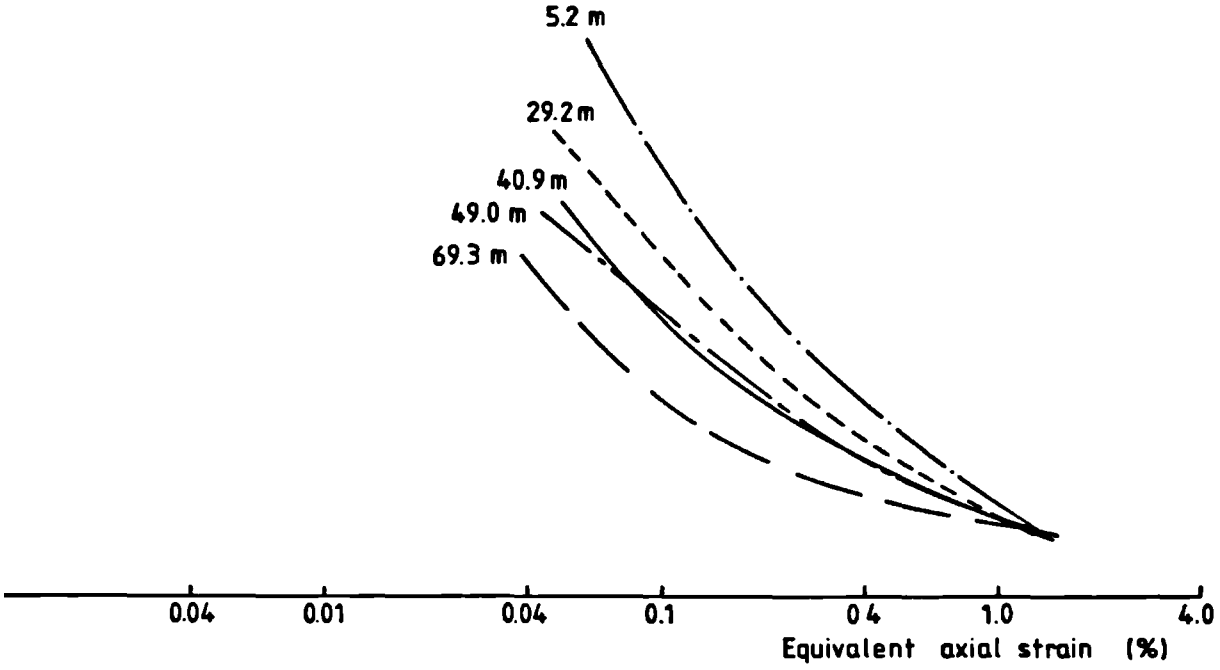


Figure 8.5b). Stiffness-strain characteristics deduced from Magnus pressuremeter data by method of Palmer.

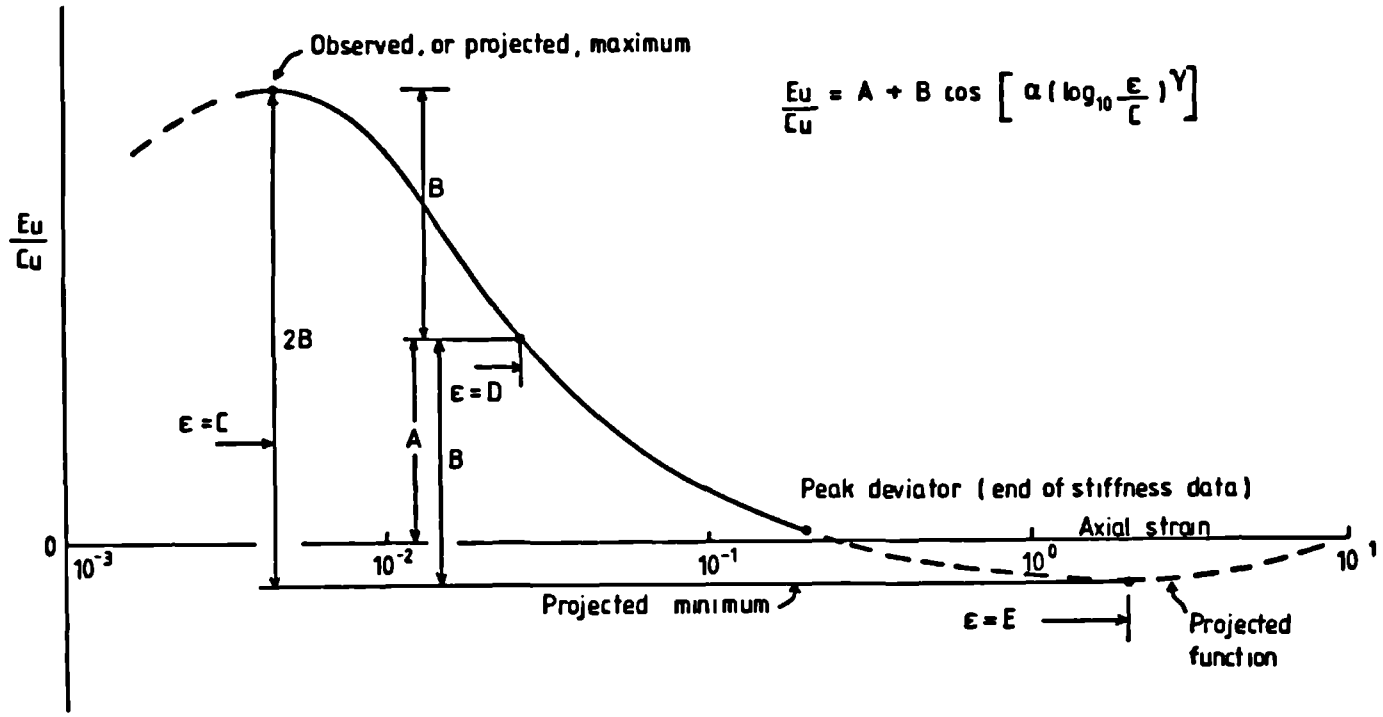


Figure 8.6 Curve fitting for stiffness-strain data.

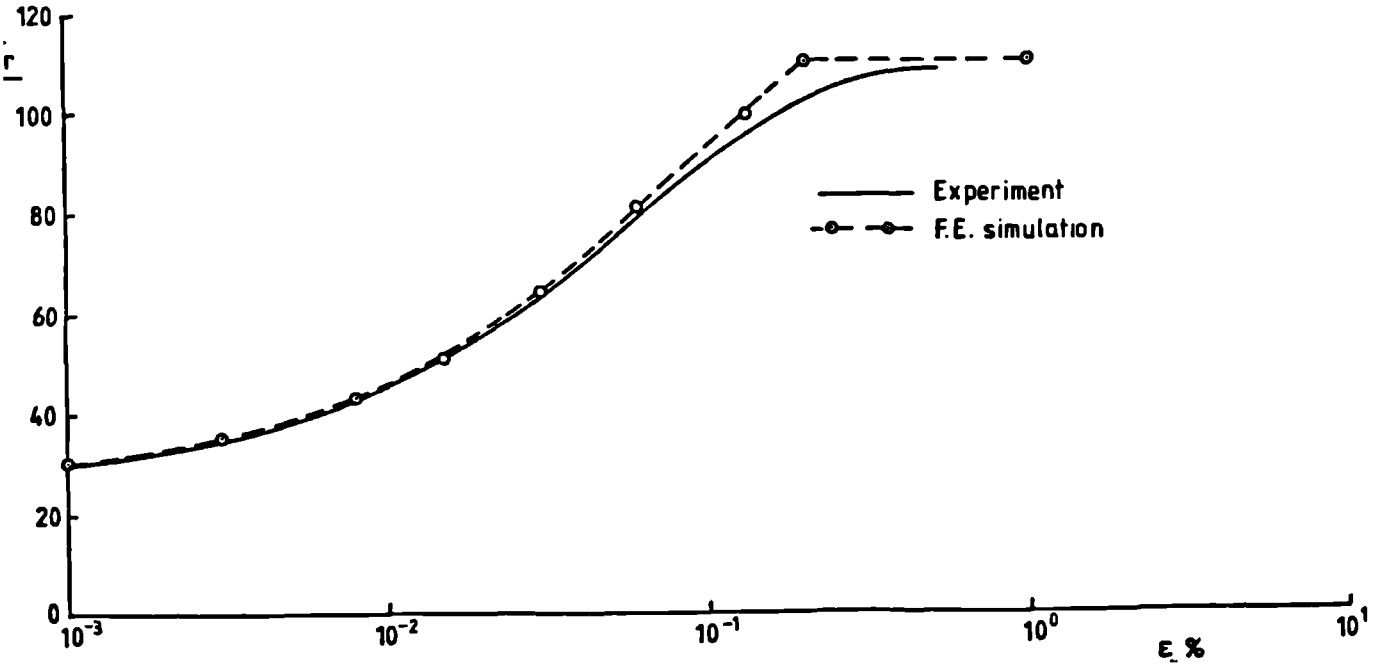


Figure 8.7 Stress-strain curves for experiment MR2.

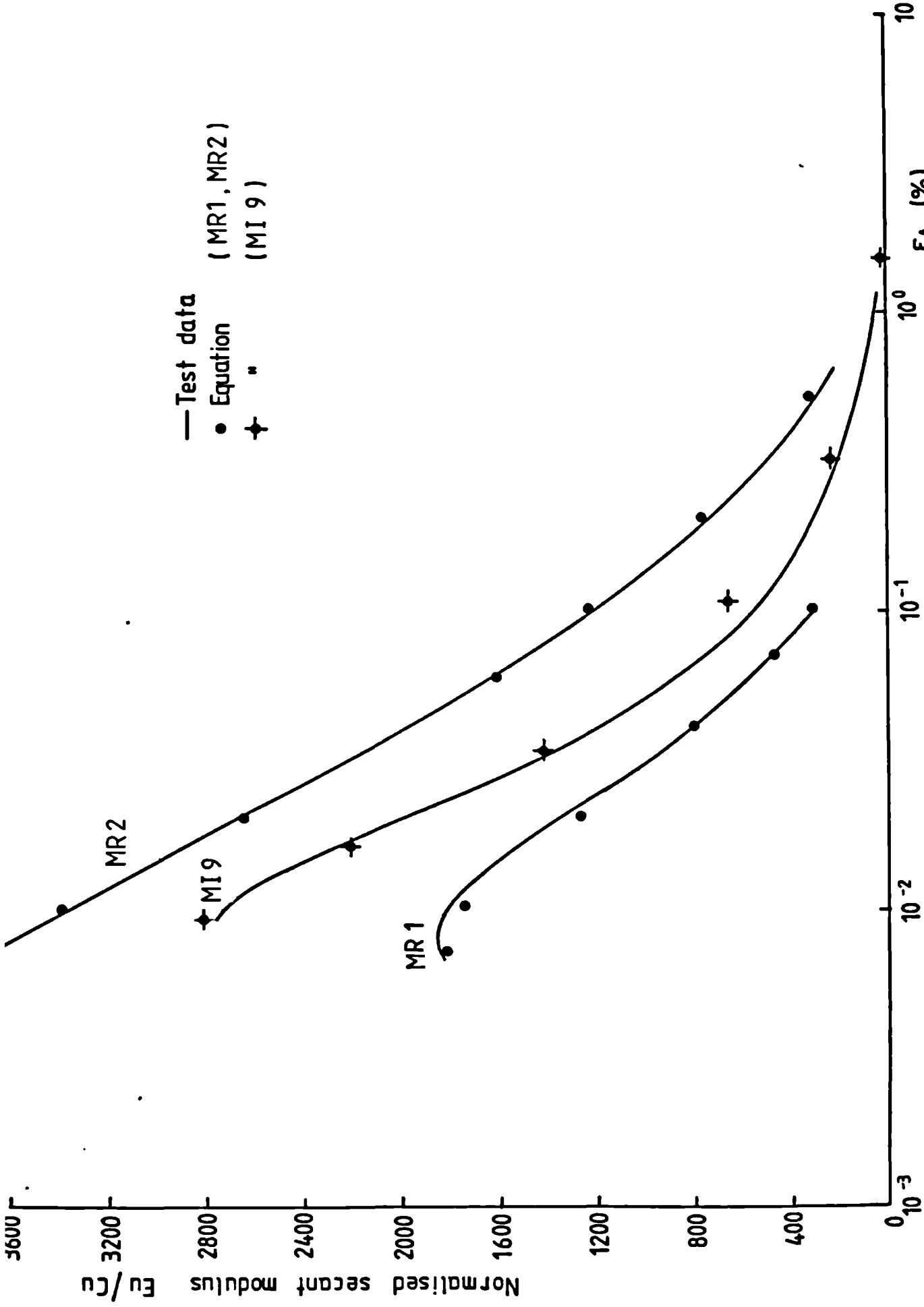
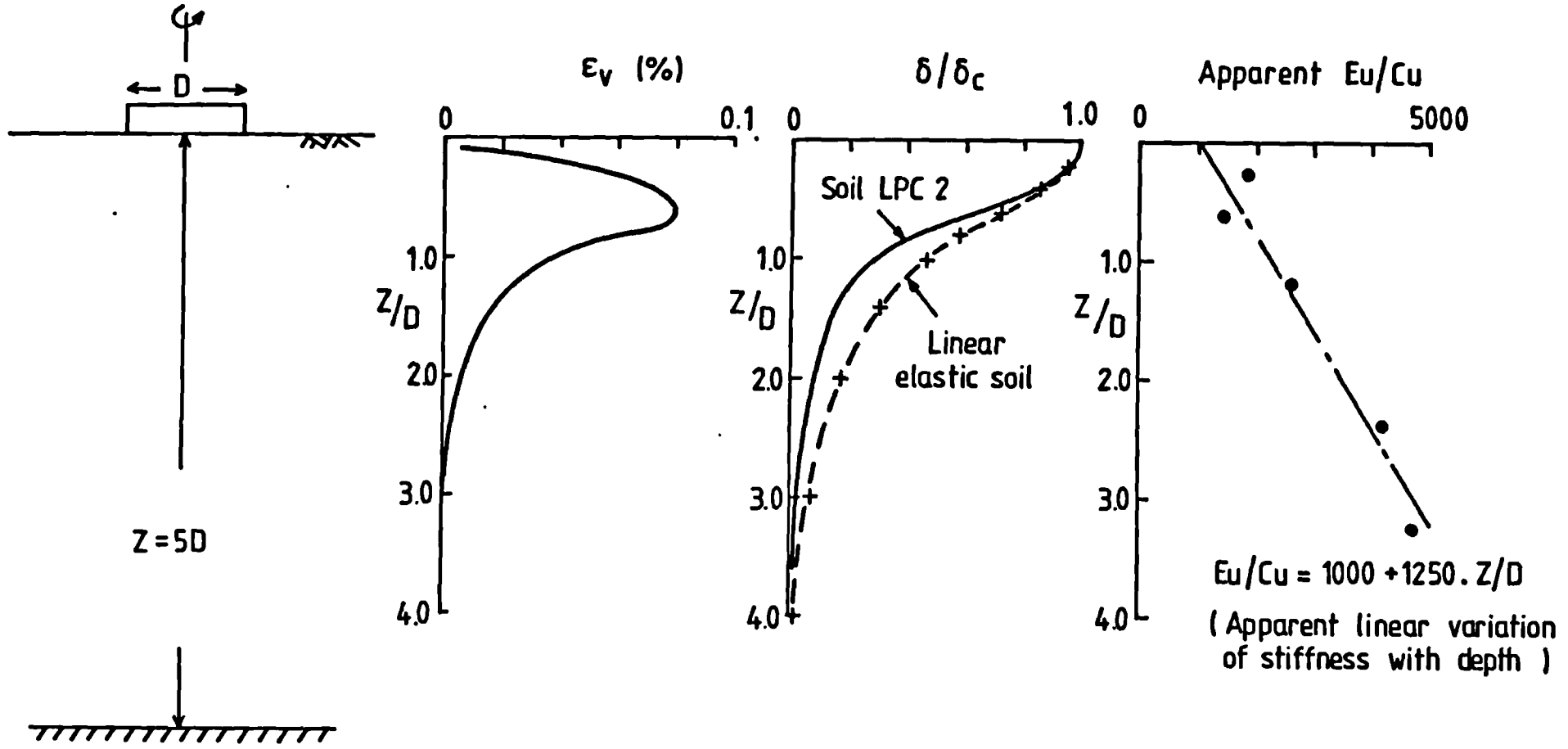


Figure 8.8 Comparisons between empirical equation and test data for three typical experiments.



a) Circular footing on a uniform layer of clay

b) Vertical strains deduced under ℄ assuming elastic stress distribution

c) Variations in settlement with depth for LPC 2 and a linear elastic soil assuming elastic stress distribution

d) Variation in apparent linear modulus with depth for LPC 2 using elastic stresses and strains from b)

Figure 8.9. Approximate variations of strain, settlement and apparent stiffness under centre line of rigid footing.

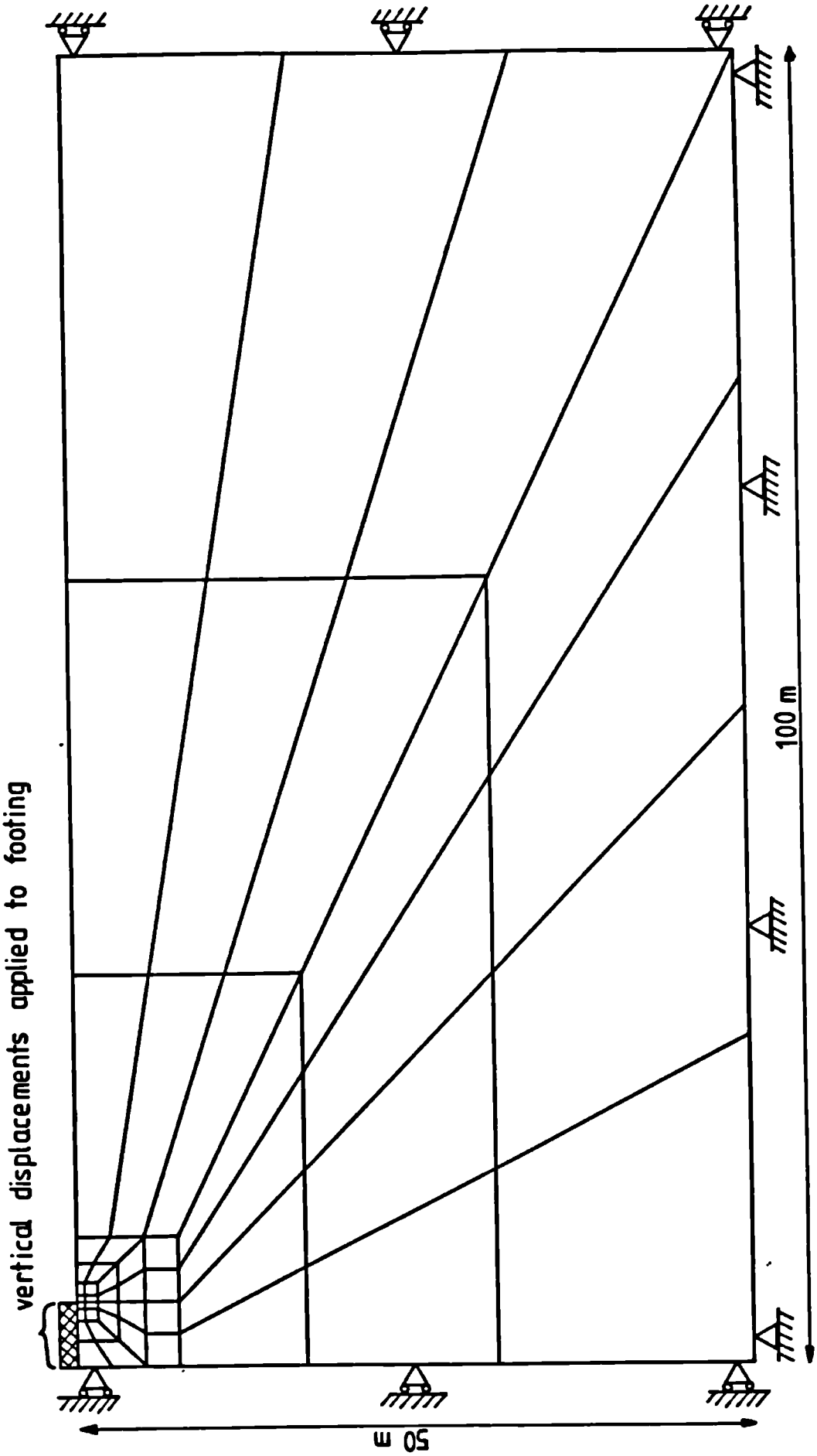


Figure 8.10. Finite Element Mesh for rigid footing, z/D = 0.5.

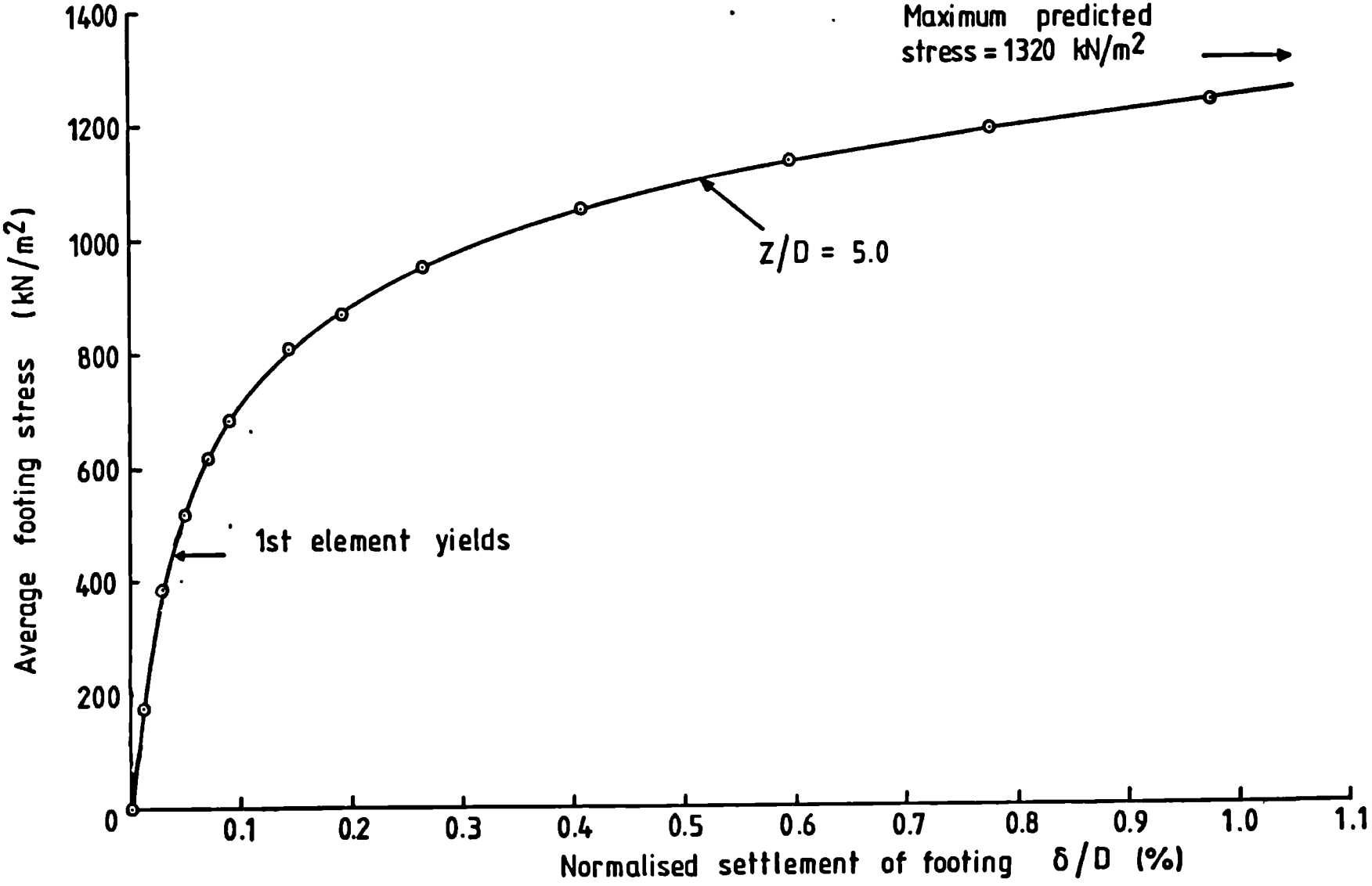


Figure 8.11. Load-displacement curve for rigid footing, z/D = 0.5.

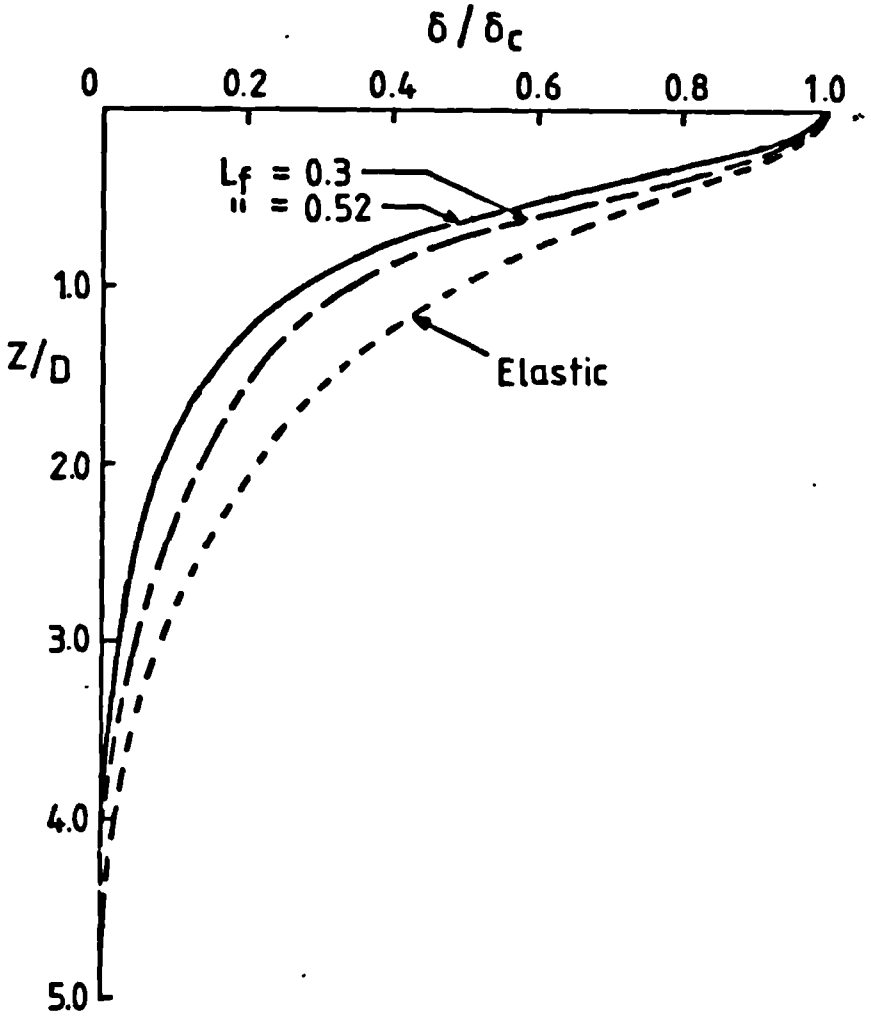


Figure 8.12.Profiles of normalised settlement with depth for rigid footing

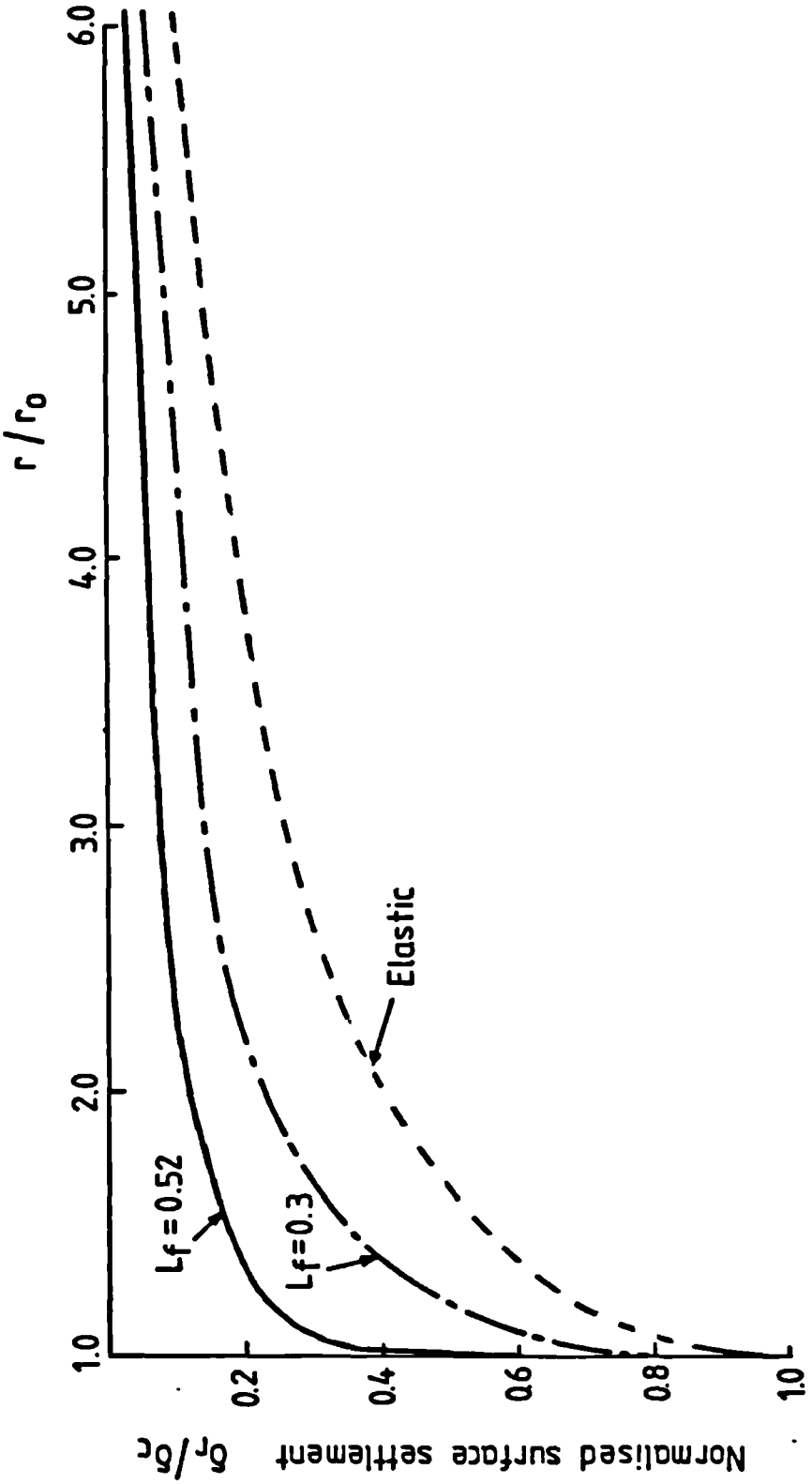
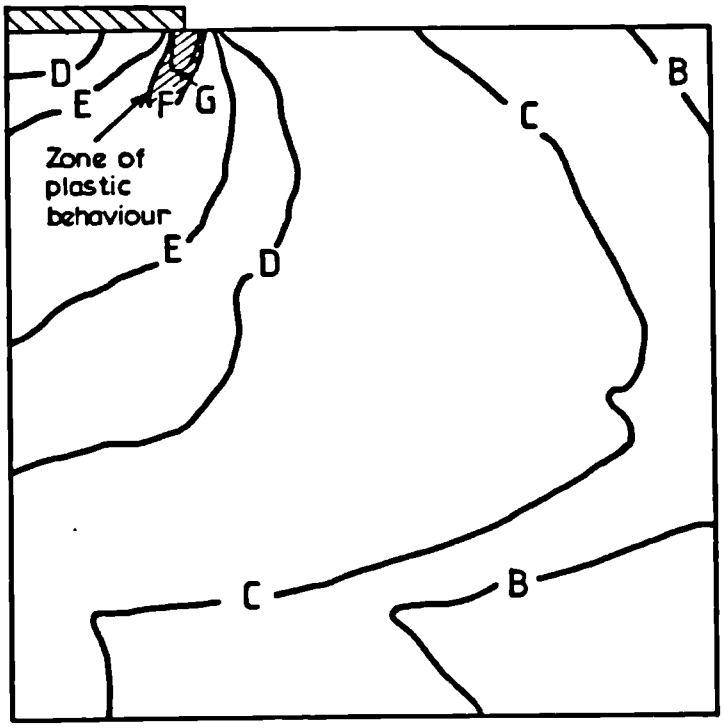


Figure 8.13. Surface displacement profiles for rigid footing, z/D = 0.5.



Contour level	E %
A	0.001
B	0.005
C	0.01
D	0.05
E	0.1
F	0.35
G	0.5

Figure 8.14. Contours of Deviatoric strain for rigid footing $Z/_D$ = 5.0, Lf = 0.5

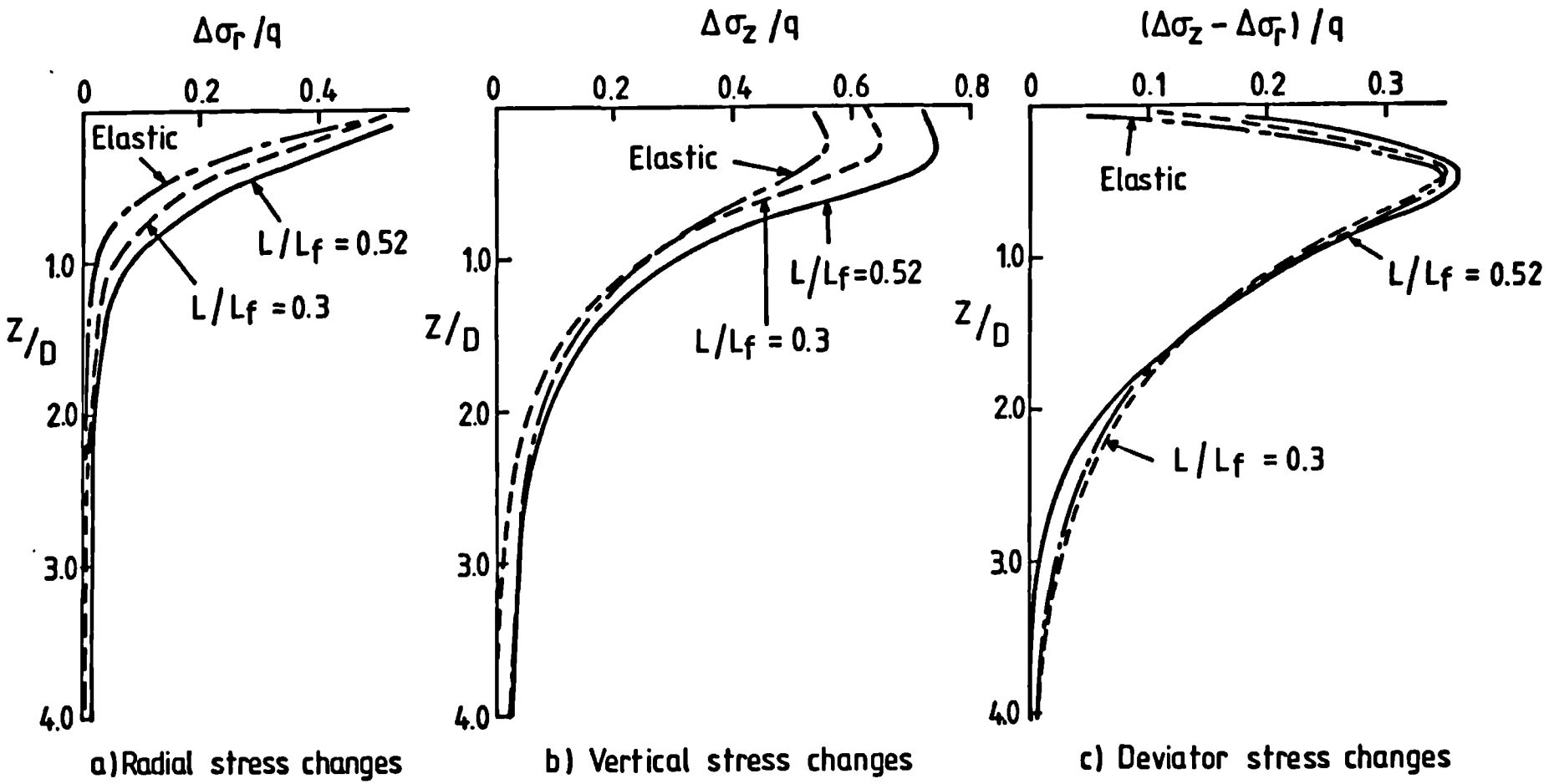


Figure 8.15. Profiles of stress changes induced by loading a rigid footing, z/D = 0.5.

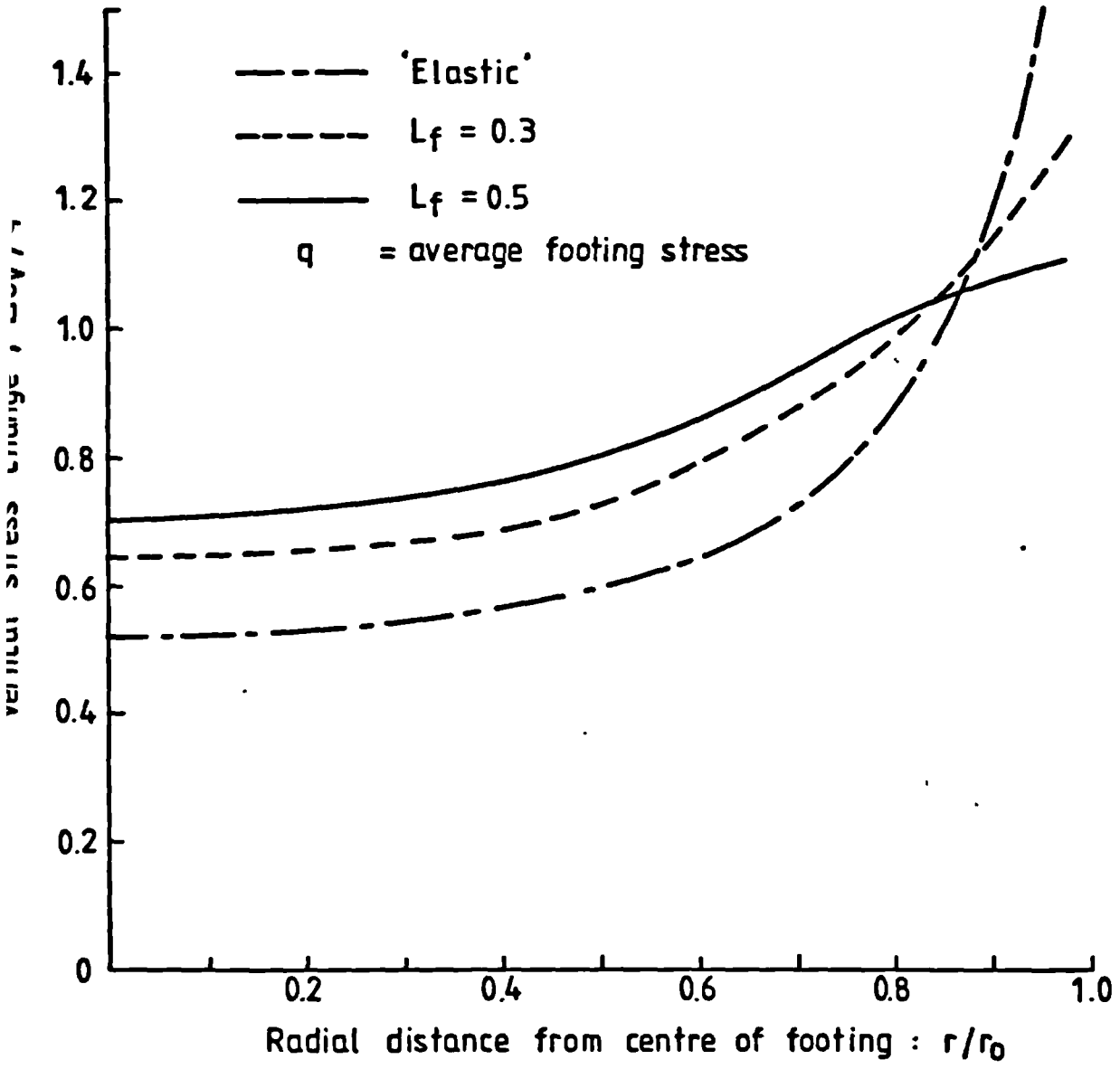


Figure 8.16. Vertical contact stresses under rigid footing $Z/_D$ = 5.0

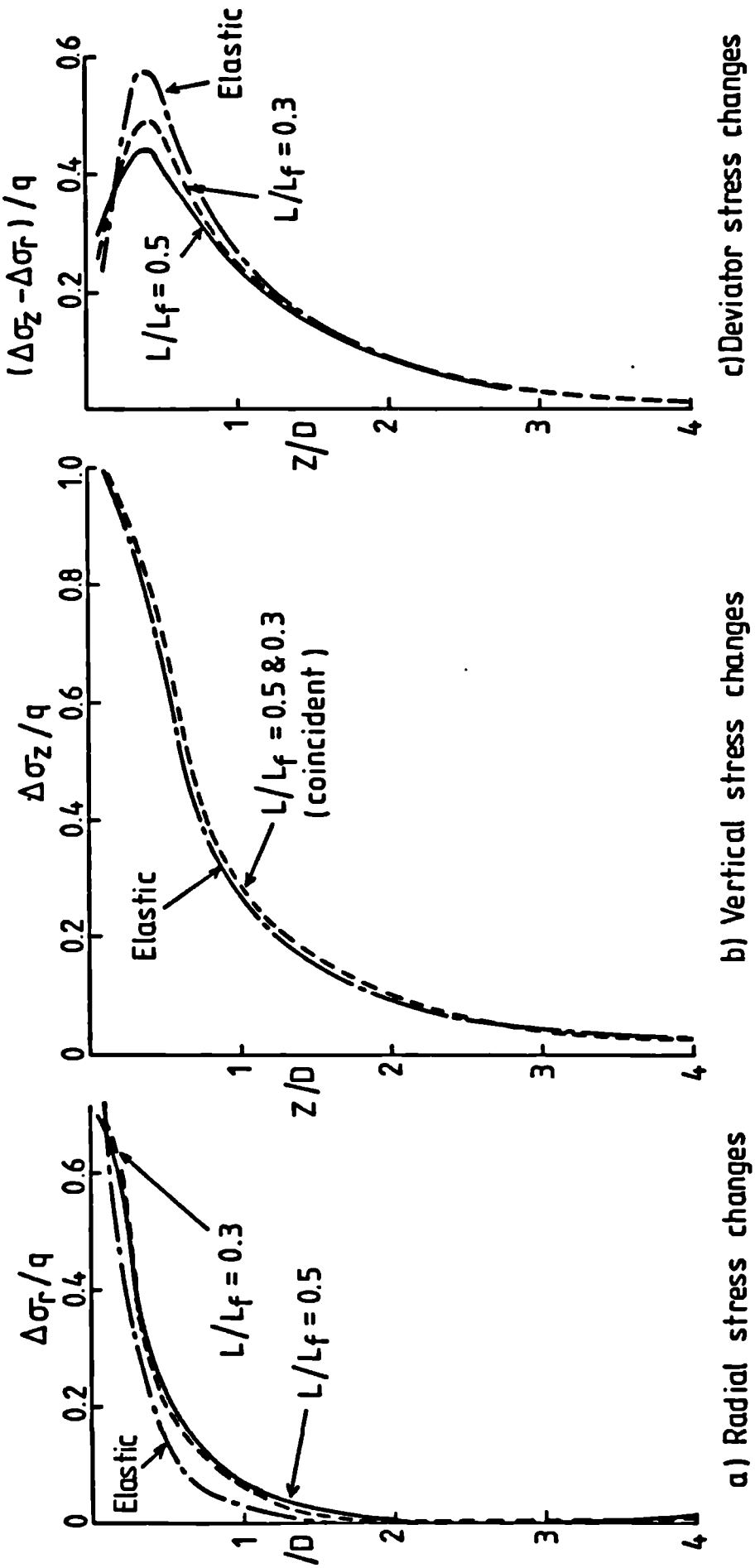


Figure 8.17. Profiles of stress changes induced by uniform surface loading, z/D = 0.5.

Figure 8.18. Pressure-inflation curve for a cylindrical cavity.

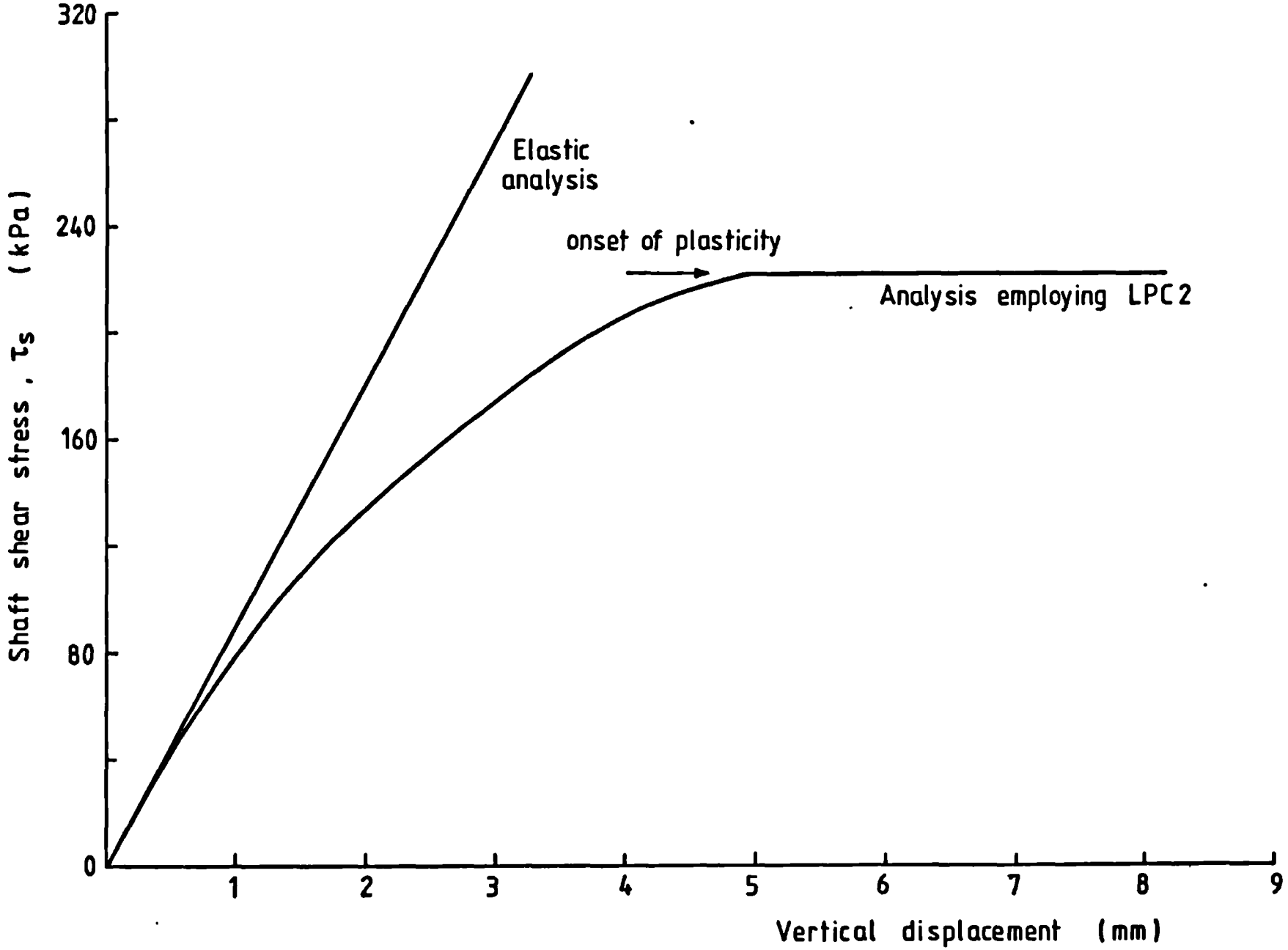


Figure 8.19. Shear stress-displacement curve for an element from a long pile.

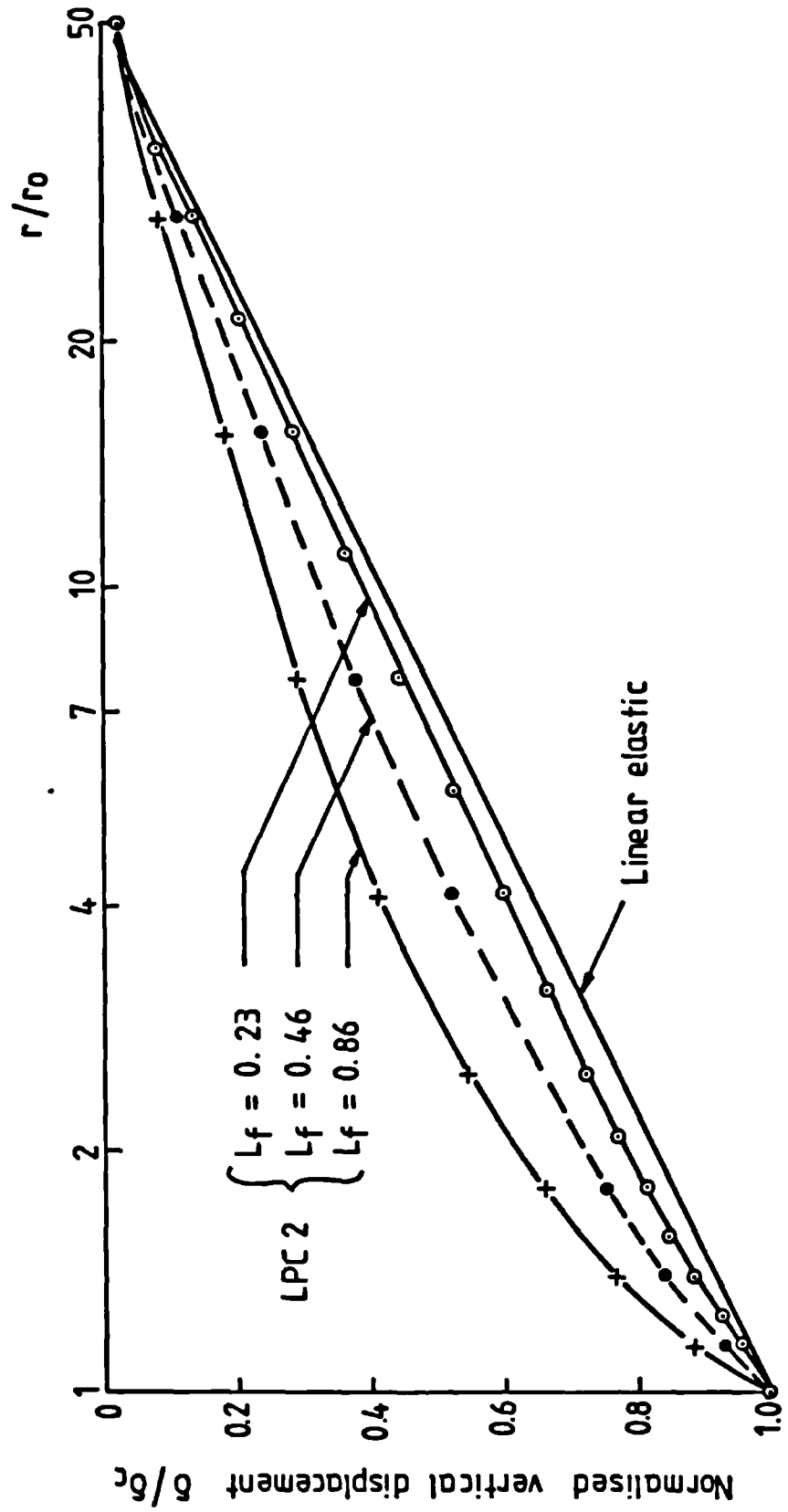


Figure 8.20. Vertical displacement profiles for an element from a long pile.

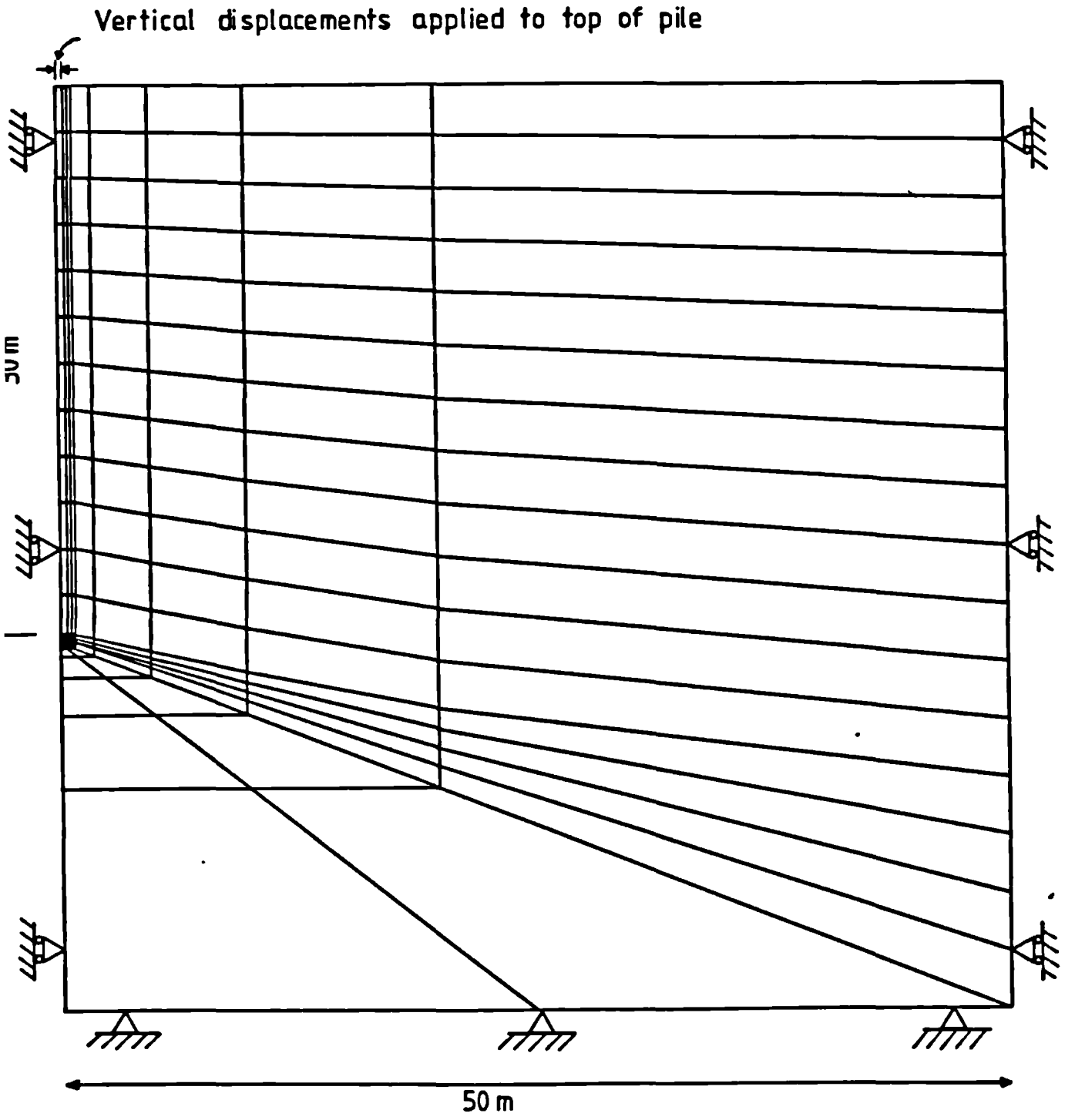


Figure 8.21 Finite element mesh for 30 m long pile.

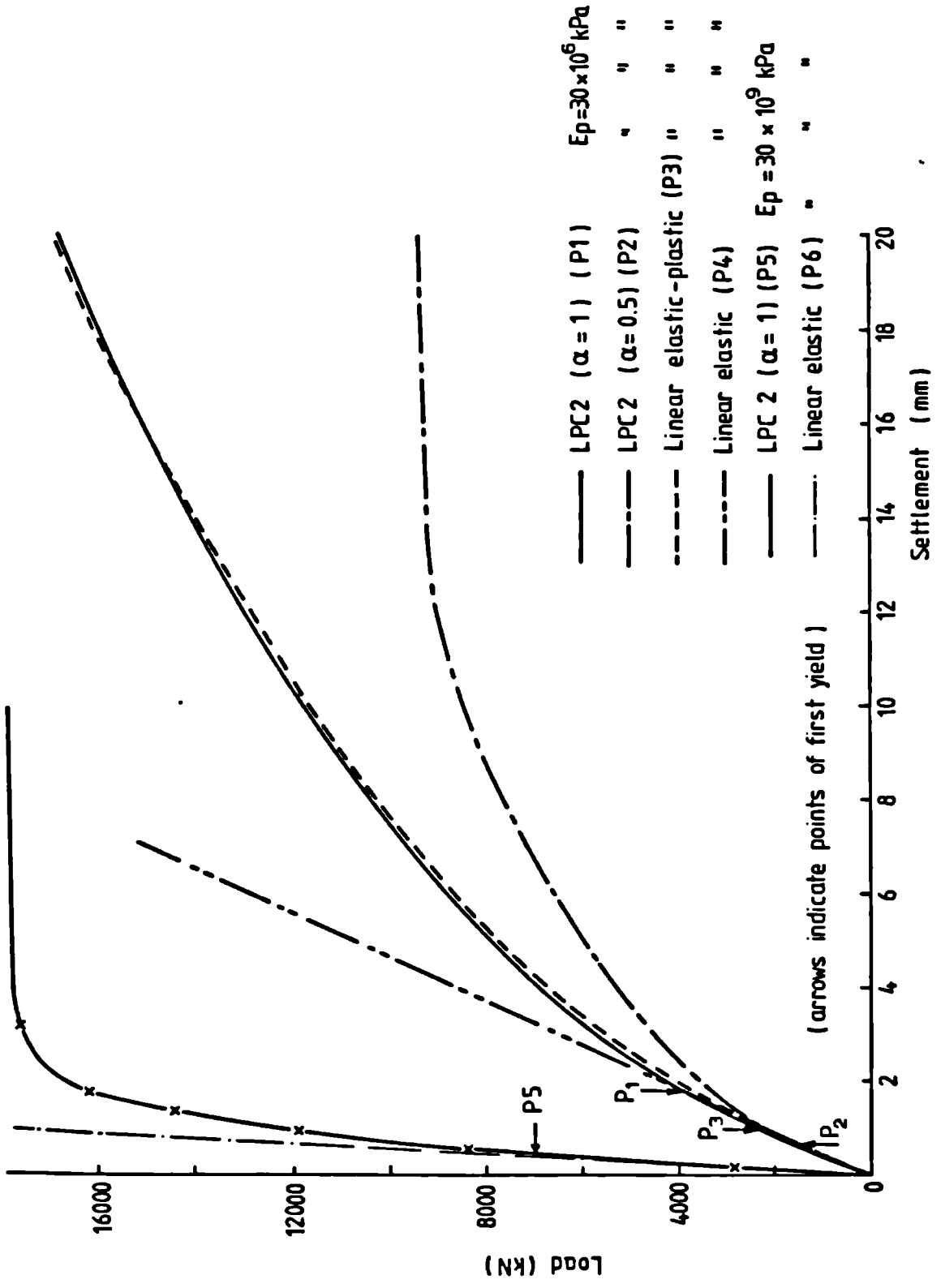
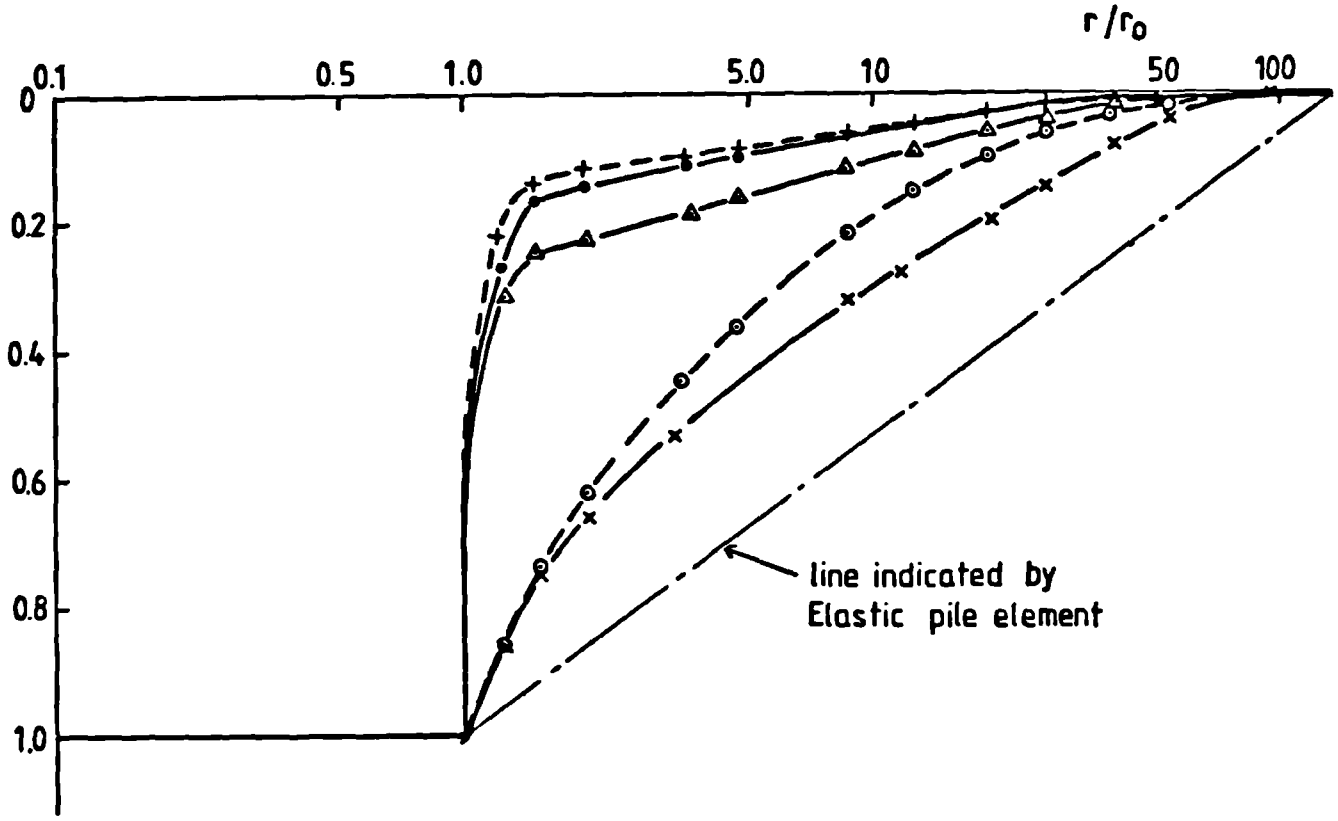


Figure 8.22. Load-settlement curves for 30 m long pile, various assumptions.



•——• LPC 2 ($\alpha = 1$), $L_f = 0.5$, $E_p = 30 \times 10^6$ P1

+——+ LPC 2 ($\alpha = 0.5$) $L_f = 0.5$, $E_p = 30 \times 10^6$ P2

△——△ Linear elastic-plastic, $L_f = 0.5$, $E_p = 30 \times 10^6$ P3

⊙——⊙ Linear elastic, $E_p = 30 \times 10^6$ P4

×——× As P1 but with $E_p = 30 \times 10^9$ P5

Figure 8.23 Normalised surface settlement profiles for 30 m long pile.

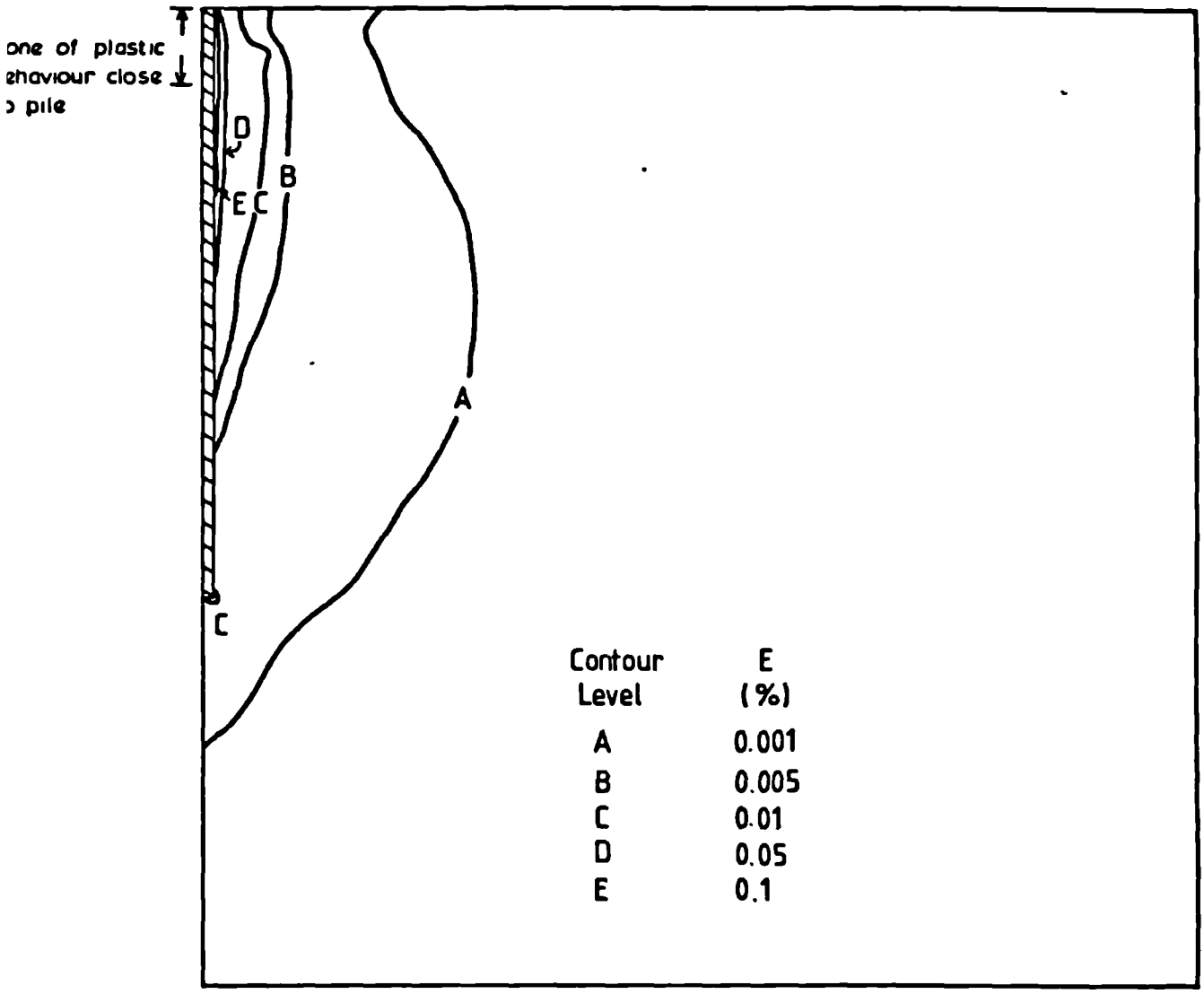


Figure 8.24 Deviatoric strain contours for Lf = 0.5 with 30 m long pile - Run P1.

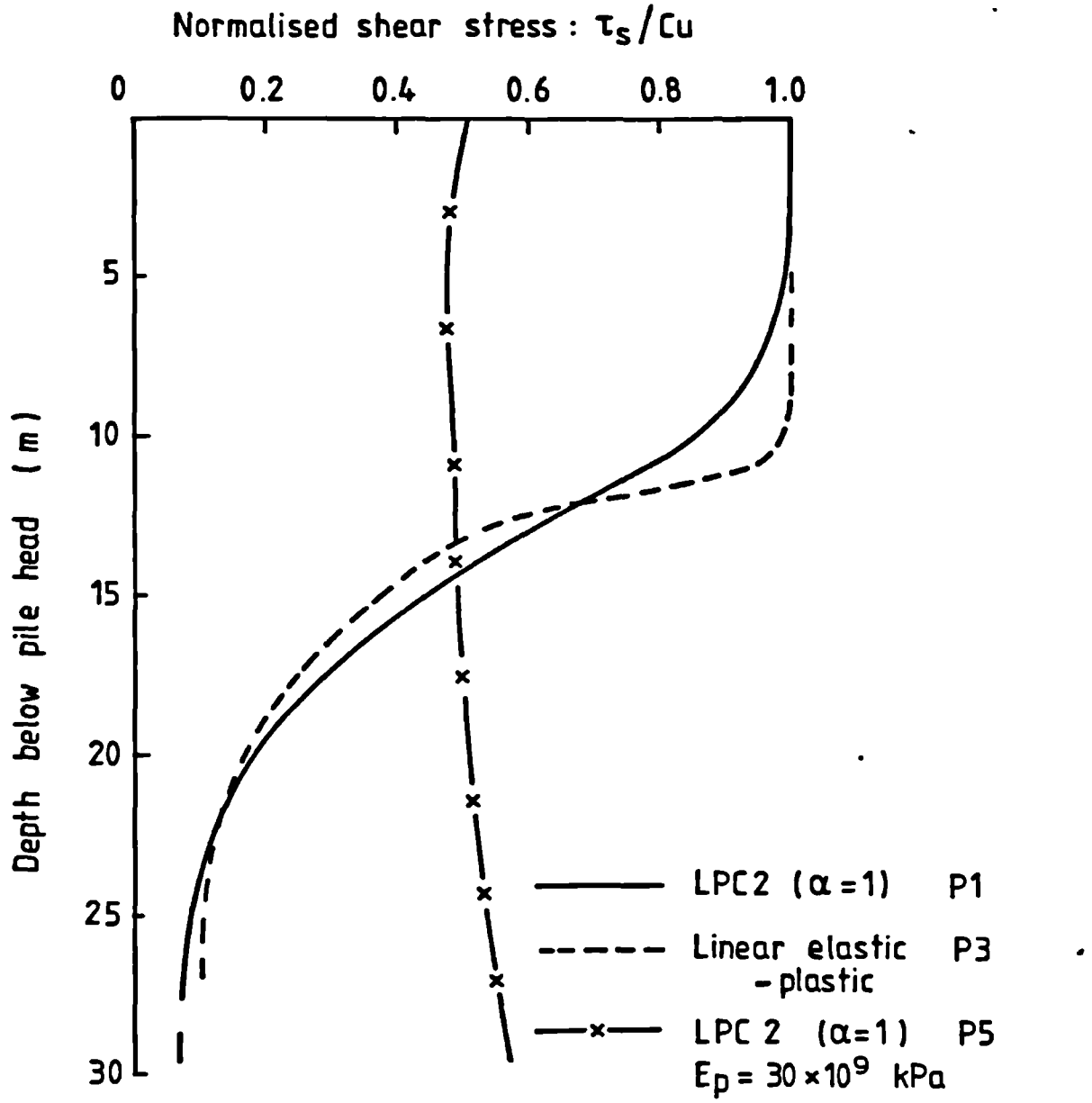


Figure8.25. Variation in shear stress with depth at Lf = 0.5. for 30 m long pile.

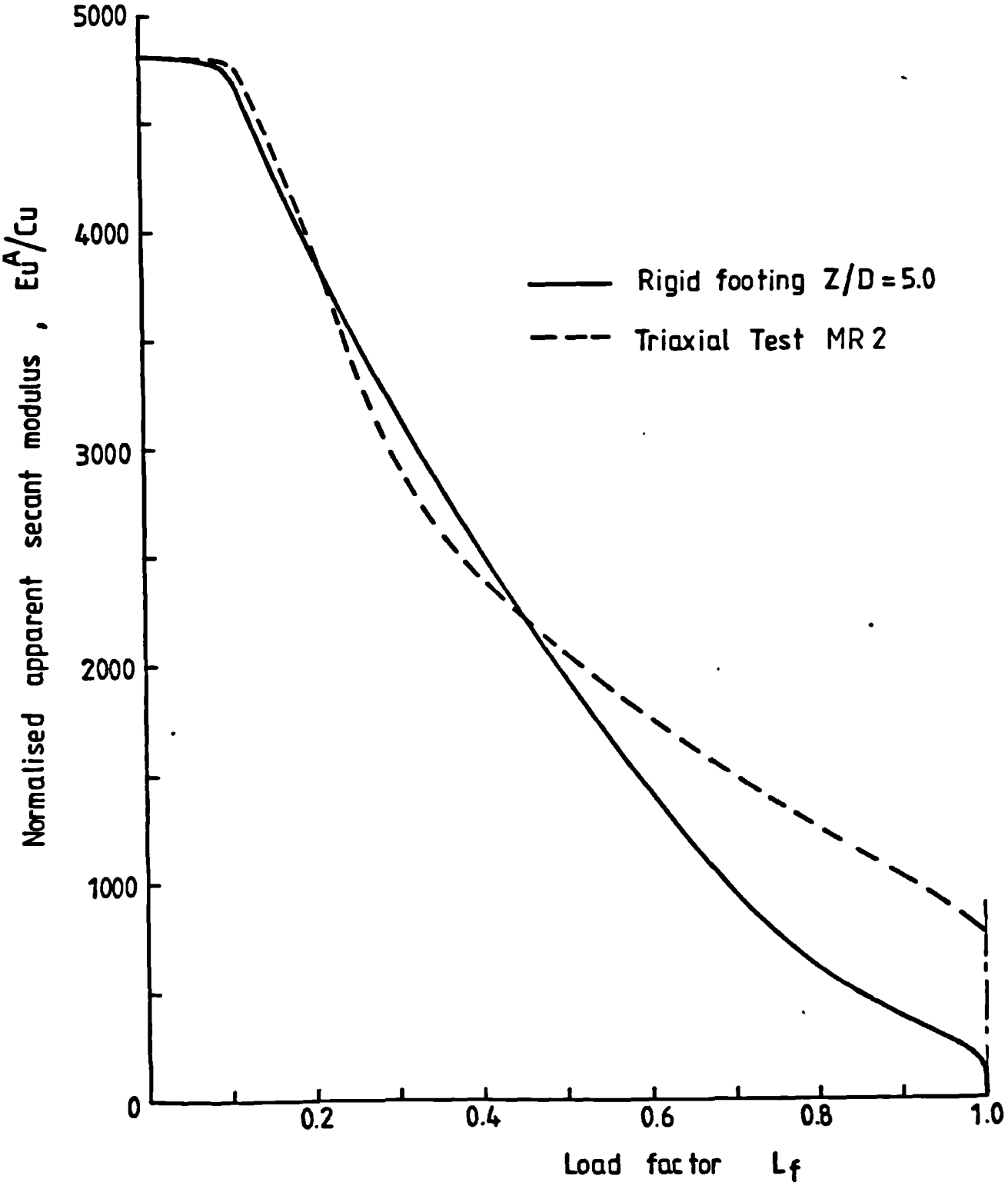


Figure 8.26 Variations of apparent modulus with load factor for a rigid footing and a triaxial sample.

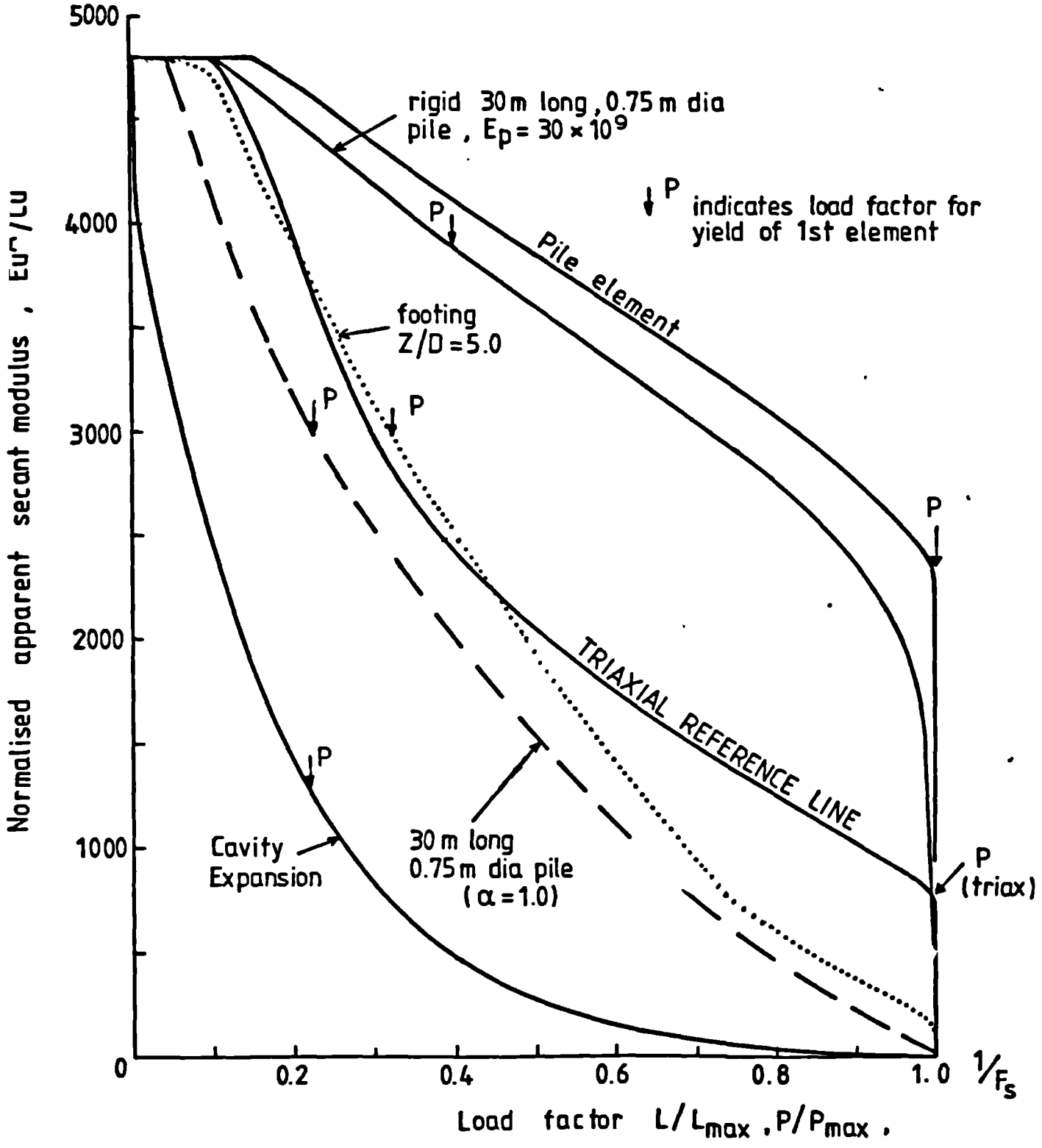


Figure 8.27. Summary plot for variation of apparent modulus with load factor.



Figure 8.28. Load-settlement curve for a bored pile, tested at Canons Park, after Price and Wardle (1982).

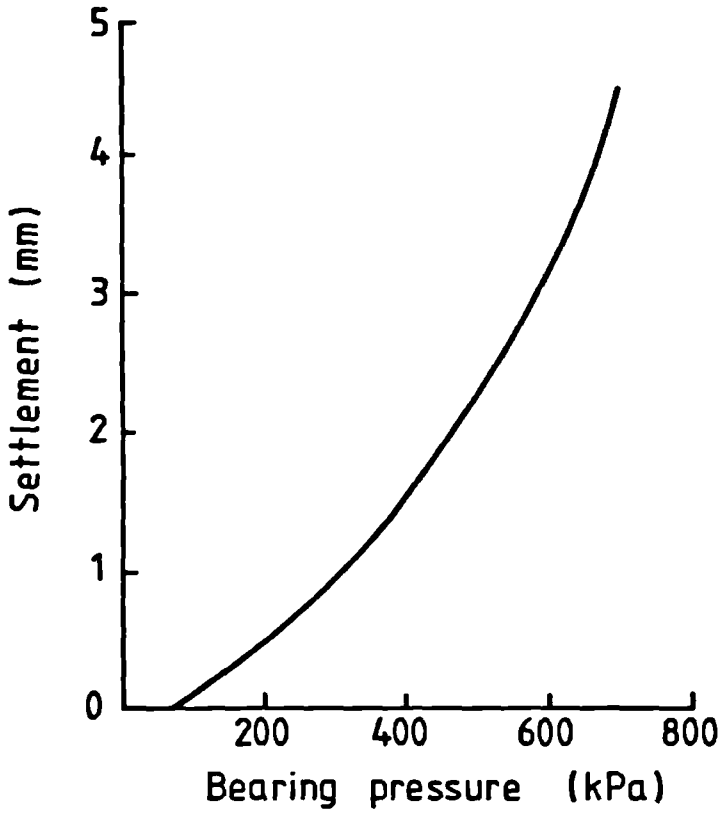


Figure 8.29. Load-settlement curve for a plate loading test at Chelsea.

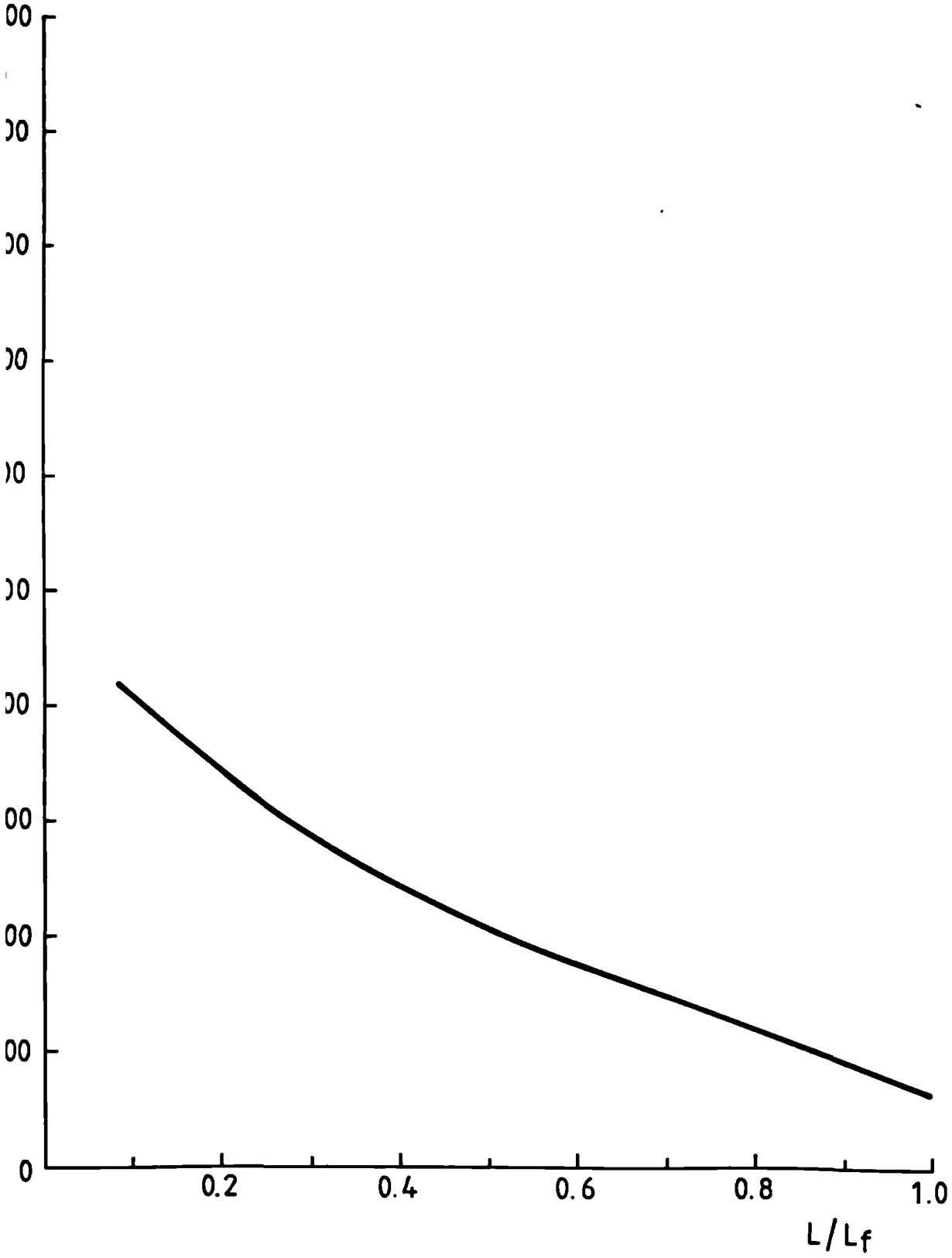


Figure 8.29 a). Variation of apparent modulus for plate loading test at Chelsea.

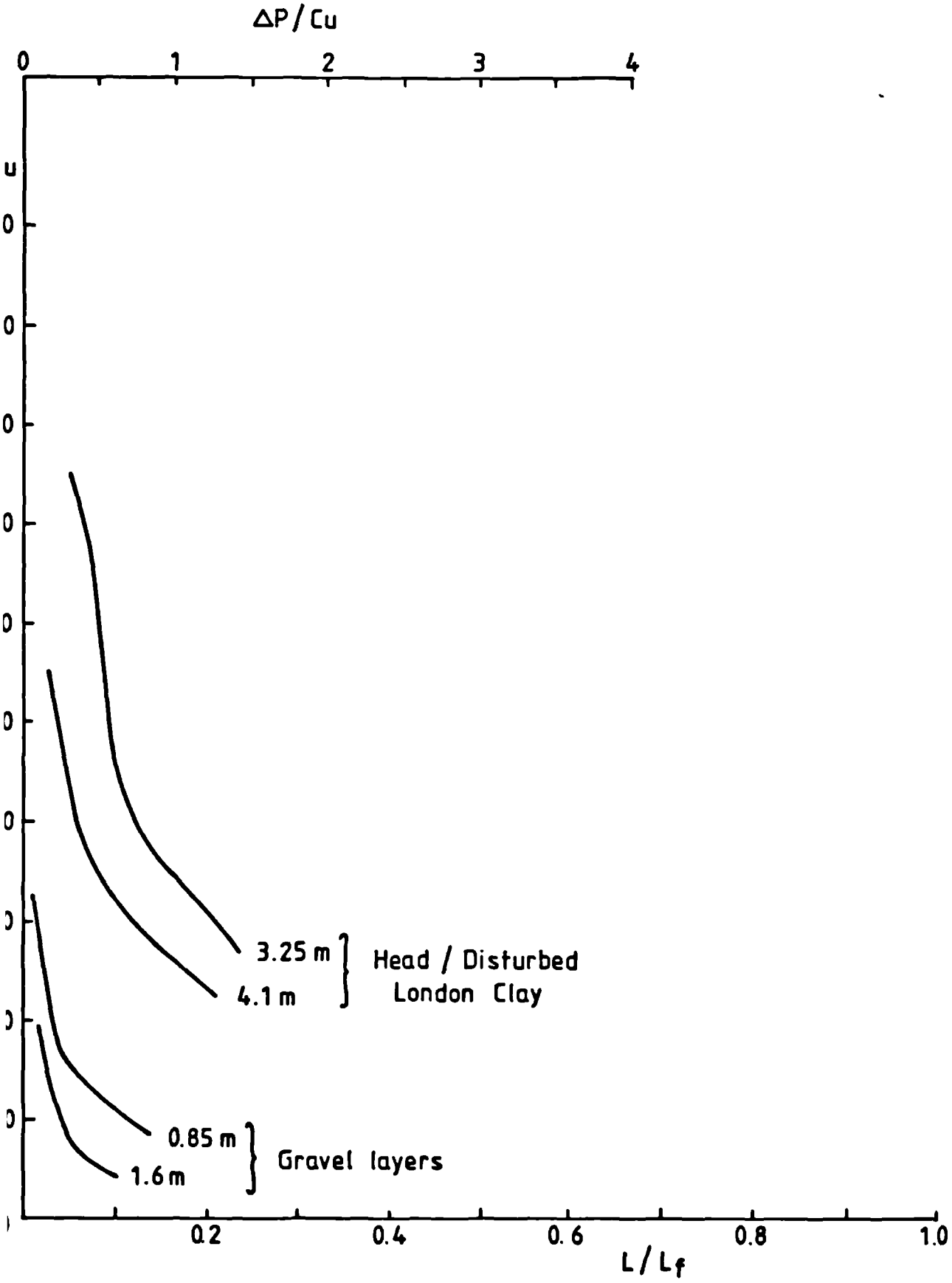


Figure 8.30a). Apparent modulus against load factor, Pressuremeter Tests Canons Park.

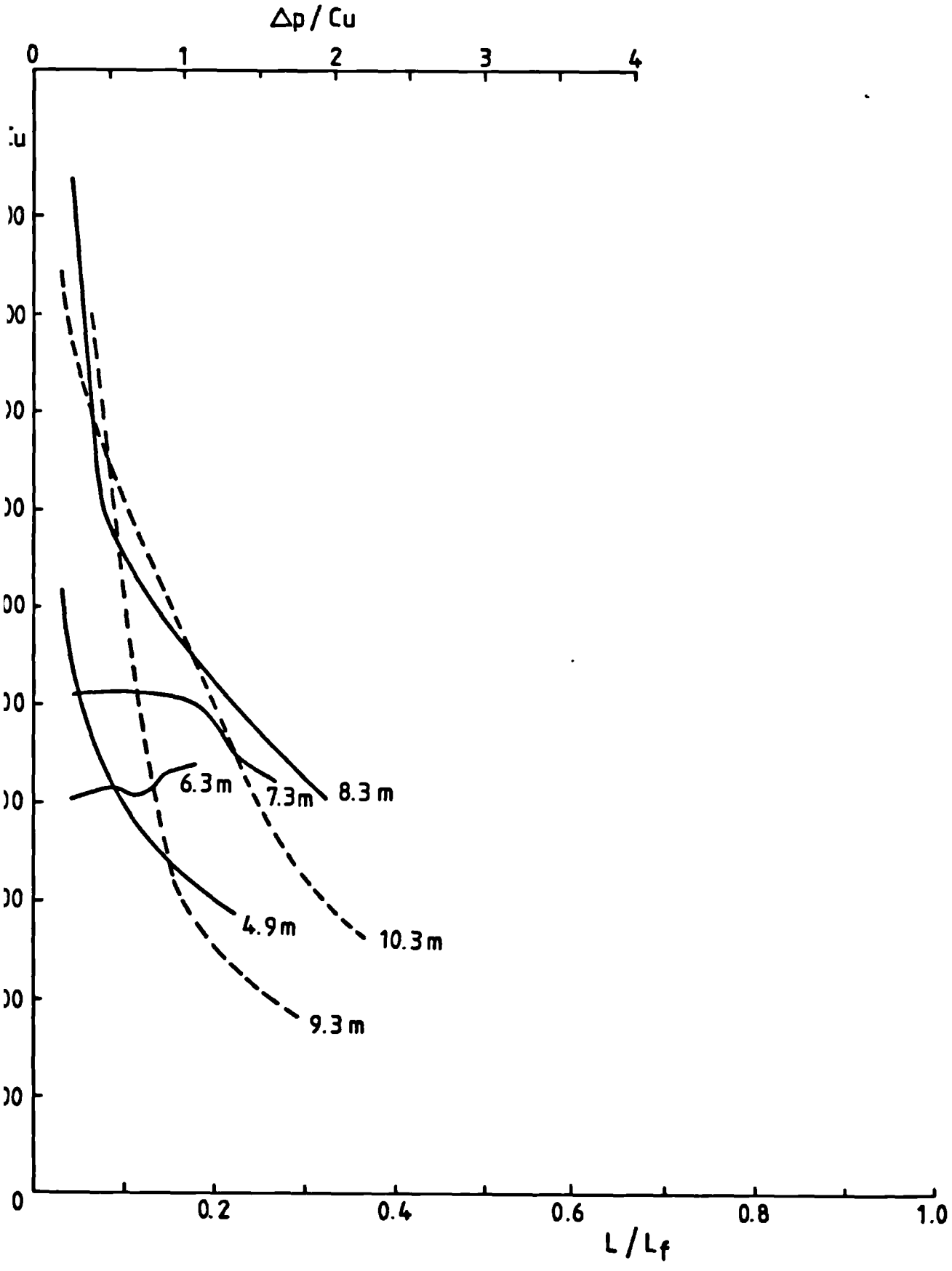


Figure 8.30b). Apparent modulus against load factor, Pressuremeter Tests Canons Park.

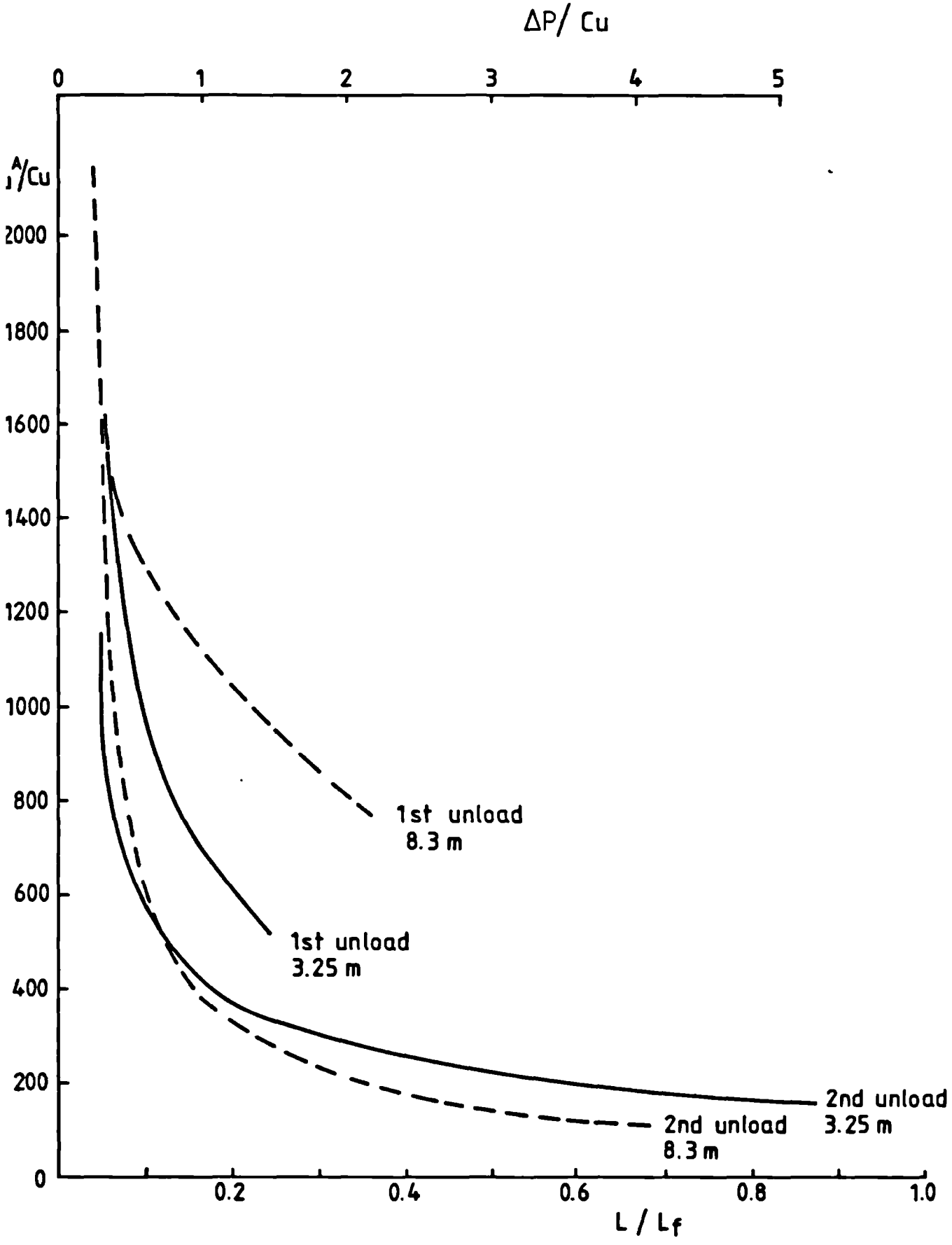


Figure 8.31. Apparent modulus against load factor, Pressuremeter Tests Canons Park.

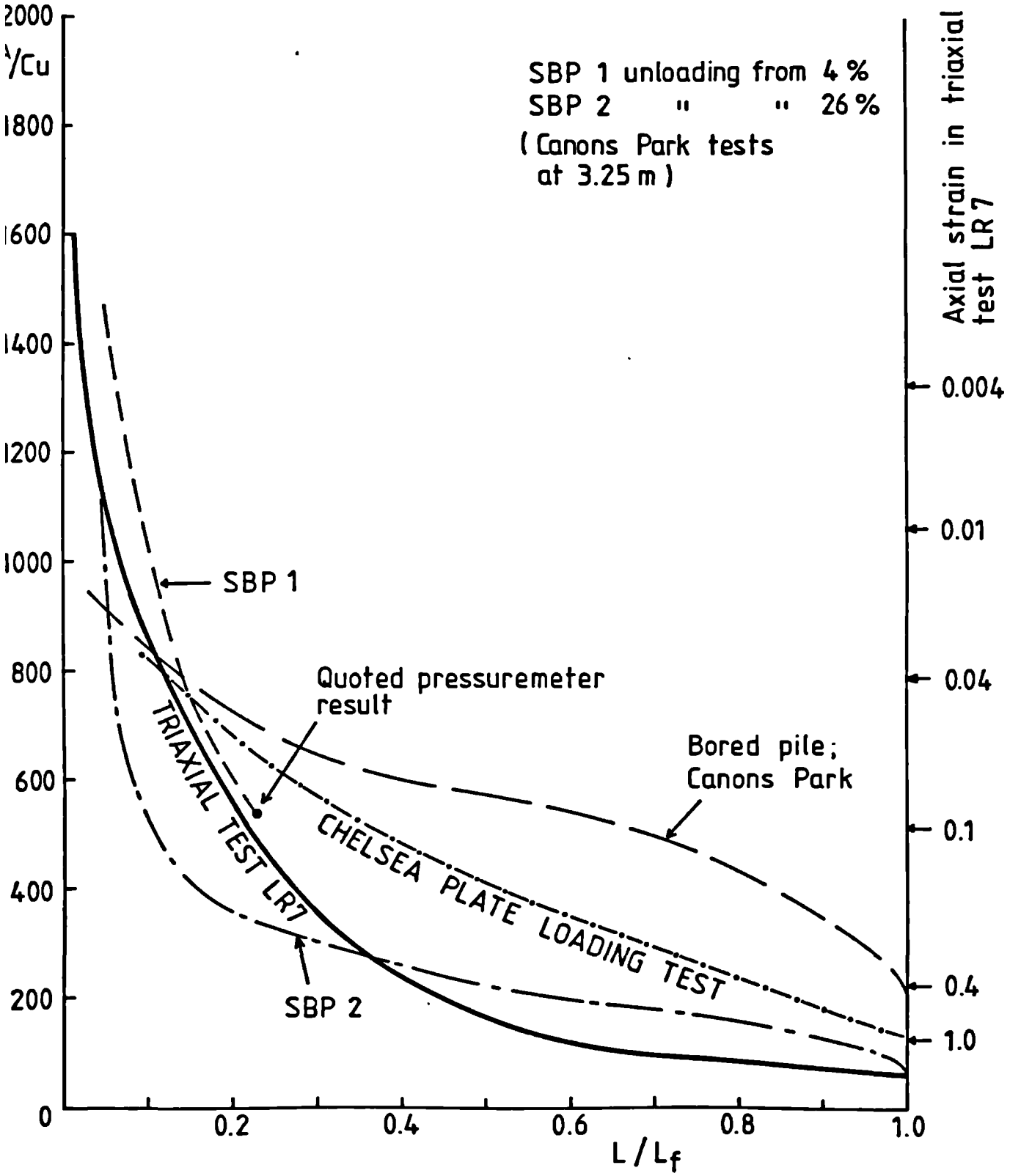


Figure 8.32. Summary of London clay field data - apparent modulus against load-factor.

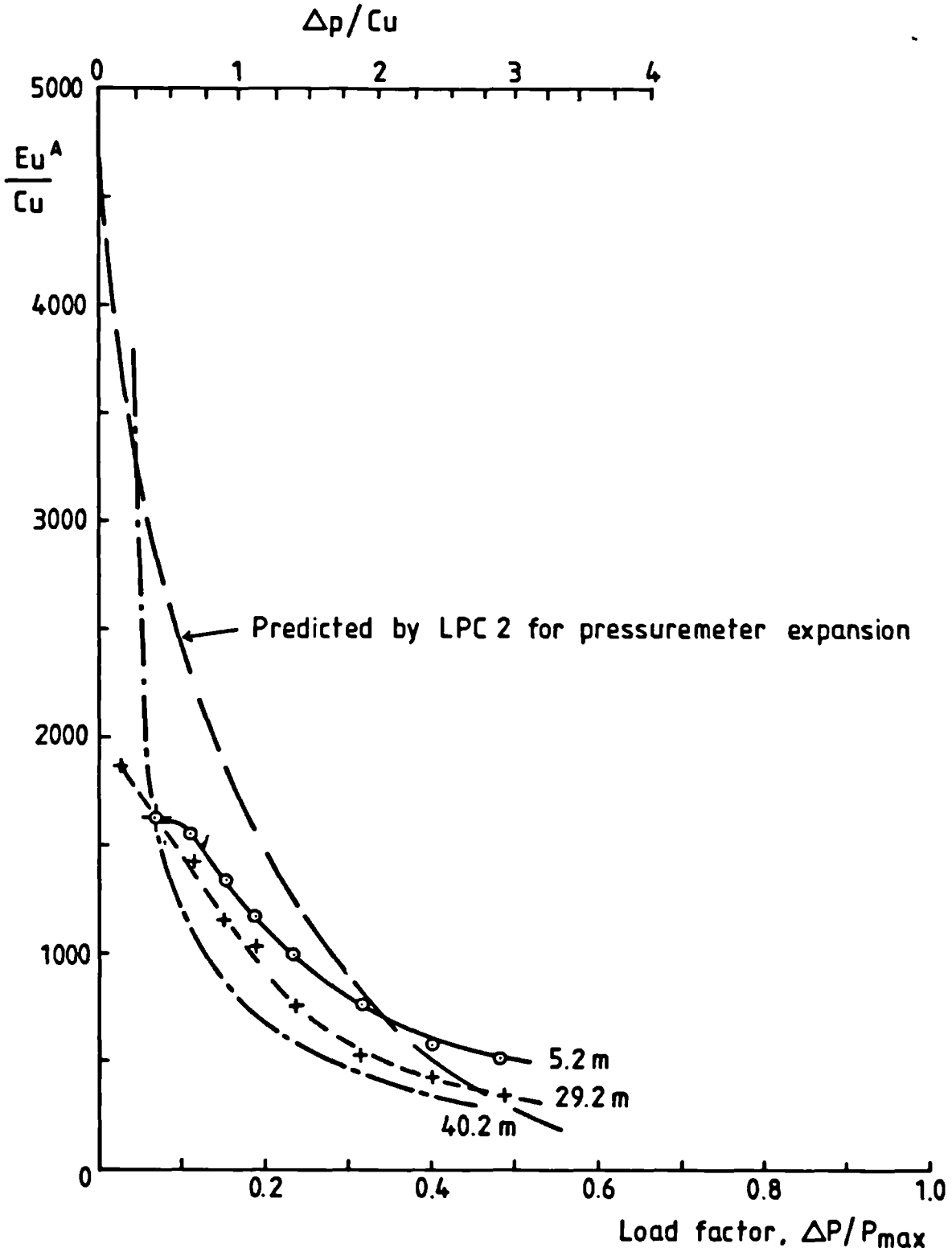


Figure 8.33 a). Apparent modulus against load factor, Magnus pressuremeter tests.

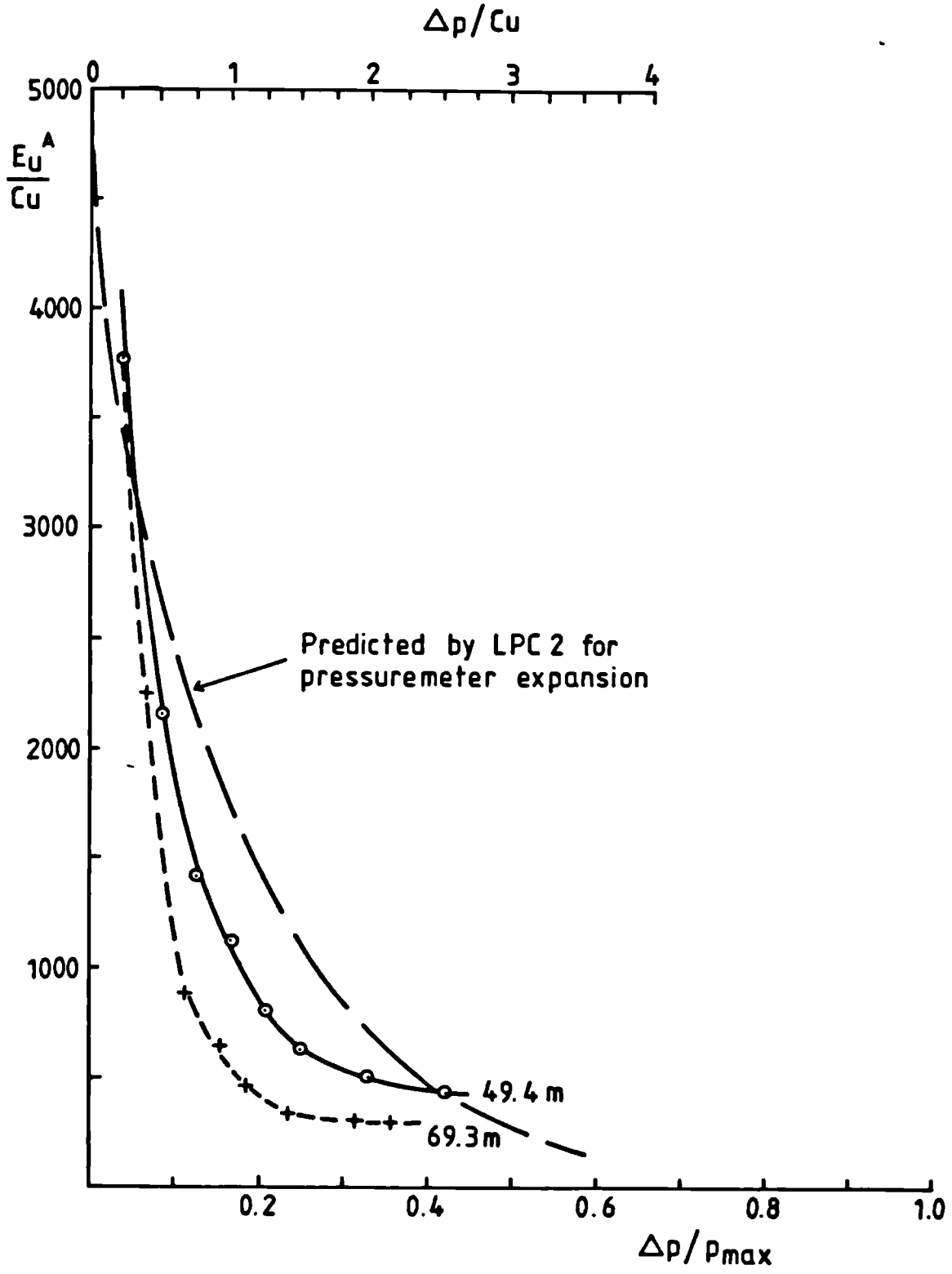


Figure 8.33 b). Apparent modulus against load factor, Magnus pressuremeter tests.

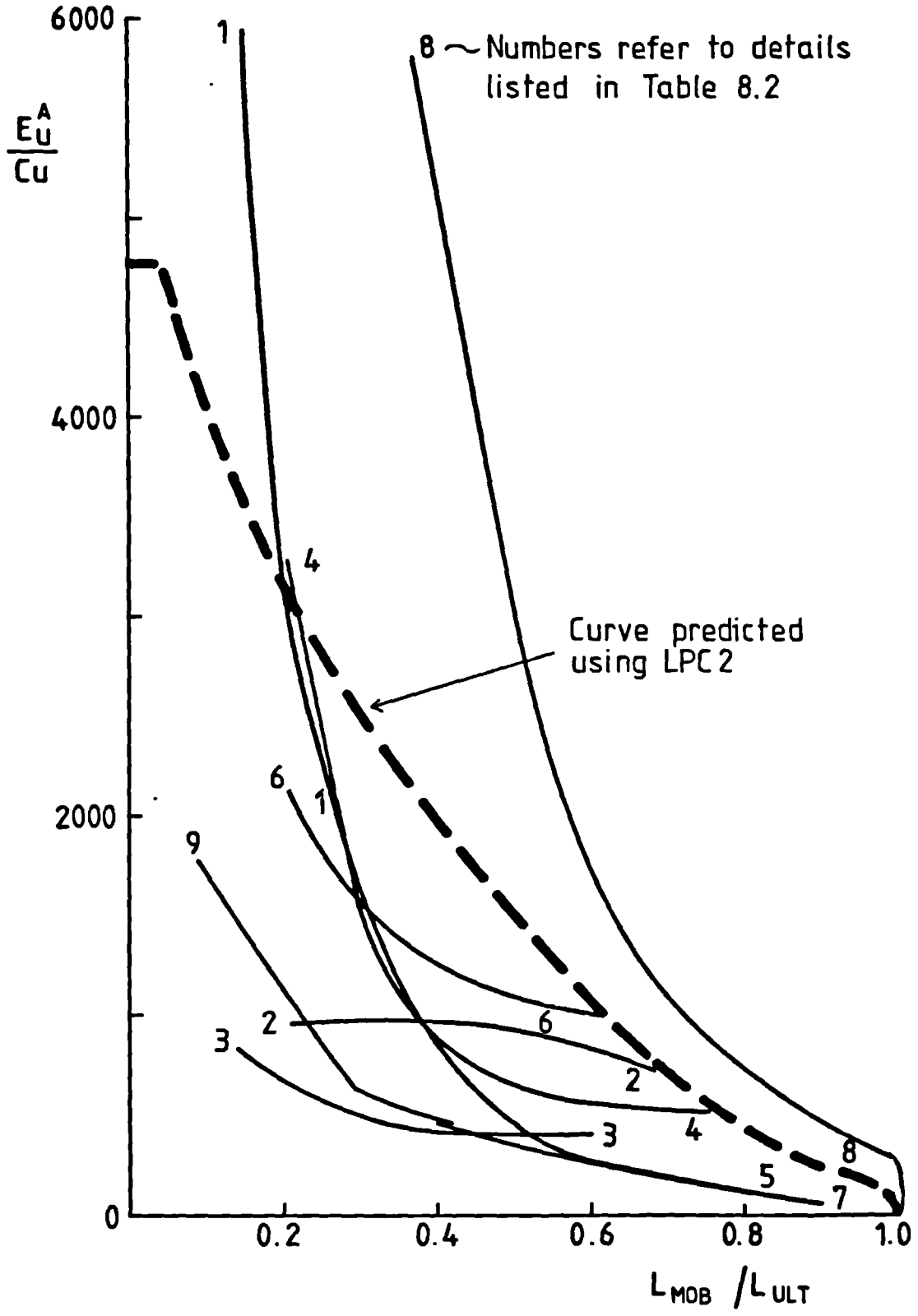


Figure 8.34. Apparent modulus against load factor, pile test data from Weltman and Healy (1978).

CHAPTER 9

Tables and Figures

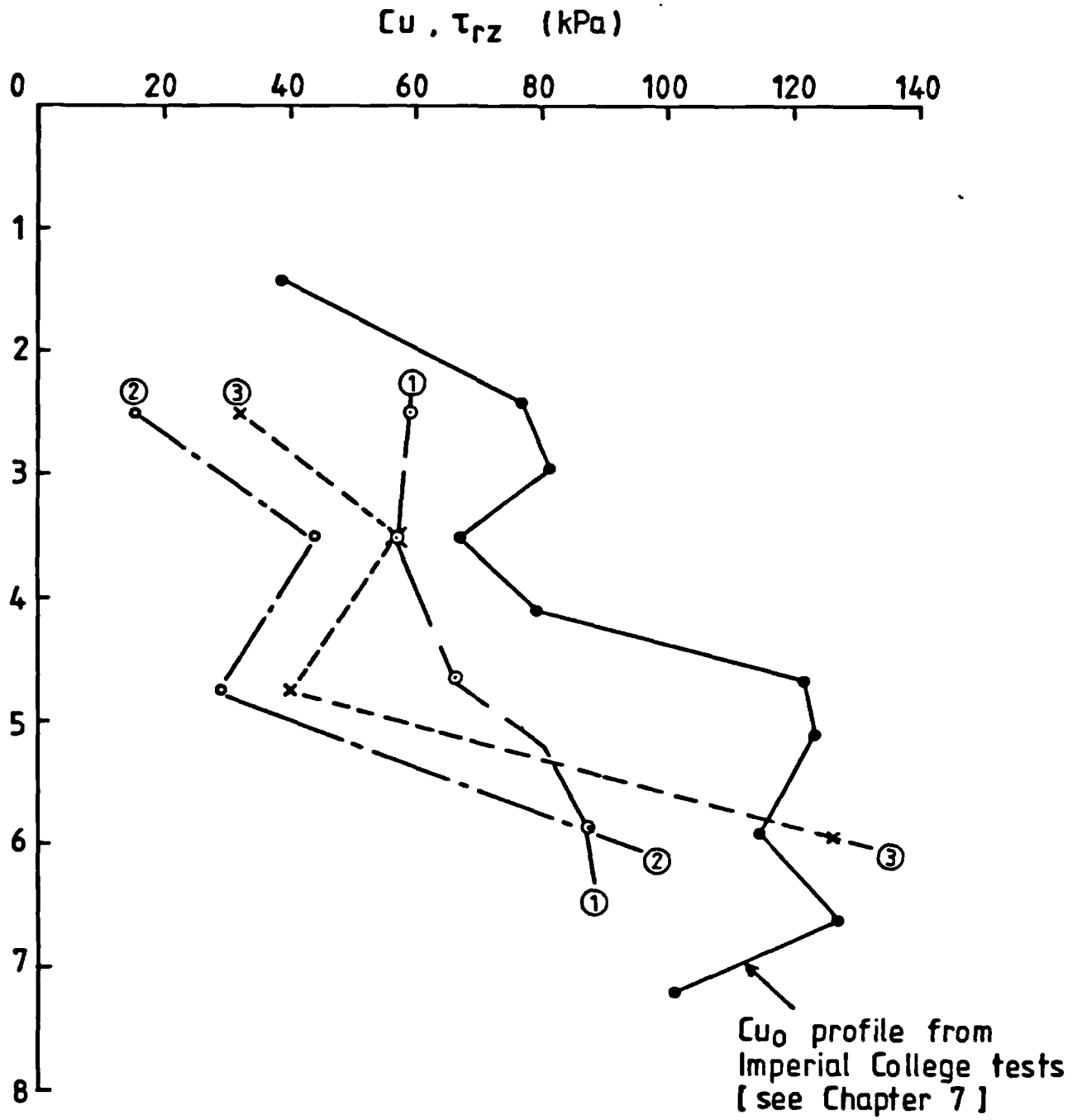
Transducer Type		Typical Constants
Axial Load Cell		
(i)	Compression load	$a_1 = 4.306$ KN, $a_2 = 4.611$ KN/MV, $a_3 = 0.167$ m^2
(ii)	Tension load	$a_1 = 1.882$ KN, $a_2 = 4.341$ KN/MV, $a_3 = 0.0157$ m^2
Local Load Cell		
(i)	Radial Stress	$b_1 = 193.9$ Kpa, $b_2 = 81.89$ Kpa/MV, $b_3 = 0.687$ Kpa/MV, $b_4 = 48.03$ Kpa/MV
(ii)	Shear Stress	$c_1 = 154.5$ " , $c_2 = 0.852$ " , $c_3 = 47.825$ " , $c_4 = 0.598$ "
(iii)	Moment/Area	$d_1 = 7.189$KN/M, $d_2 = 4.617$ KN/M , $d_3 = 0.197$ KN/M , $d_4 = -4.207$ KN/M
Druck pore pressure Transducer		
(i)	Pore pressure	Kpa = $e_1 + e_2.V$
		$e_1 = 66.87$ Kpa, $e_2 = -8.876$ Kpa/MV.

Table 9.1

Typical Calibration Factors for Transducers employed

Level (Metres depth)	τ_{rz} at peak Kpa	σ'_r required Kpa	Projected σ'_r before loading, Kpa	Stress changes during tension loading, Kpa	
				Δu (measured)	$\Delta\sigma_r$ (required)
3	65	178	70	- 50	+ 58
4	97	266	125	- 10	+ 131
5	110	302	265	+ 70	+ 107

Table 9.2



① Max τ_{rz} for lowest section passing given level during jacking
② " " for given level at end of jacking
③ " " " " " during CRP test

after Price and Wardle (1982)

Figure 9.1. Shear stress-depth distributions for a jacked pile at Canons Park, after Price and Wardle (1982).

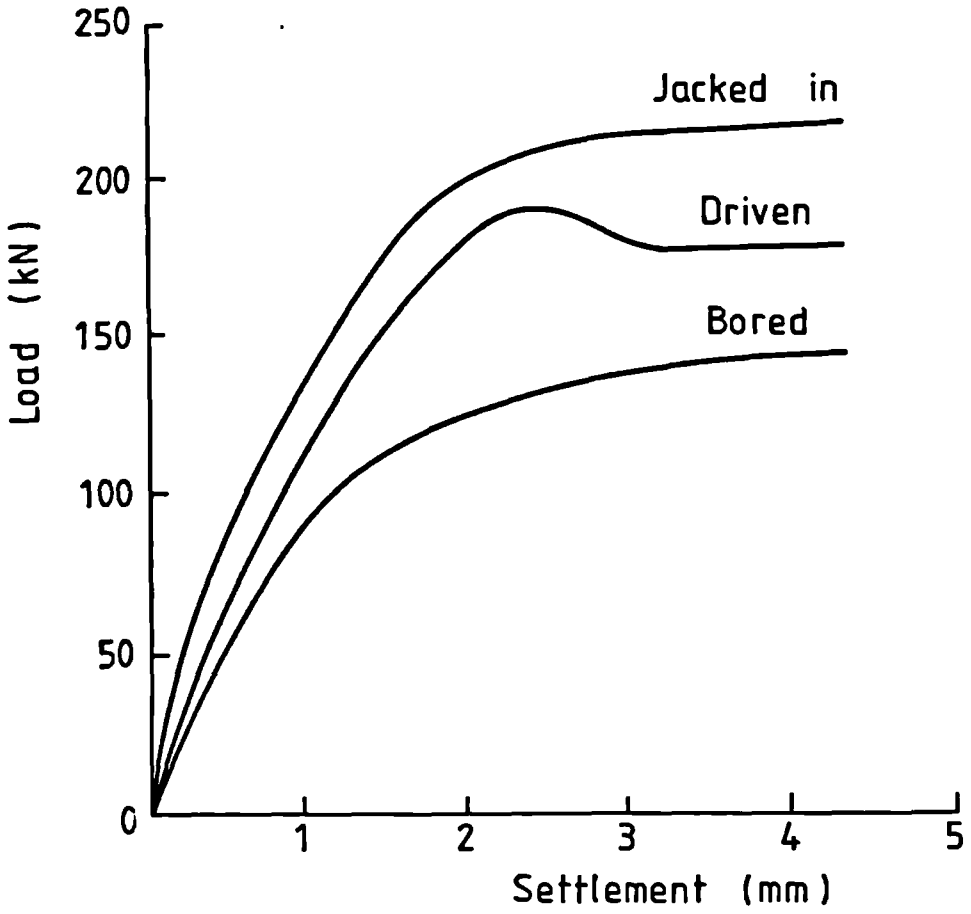


Figure 9.2. Load-settlement for three types of pile at Canons Park, (0 to 5 mm only).

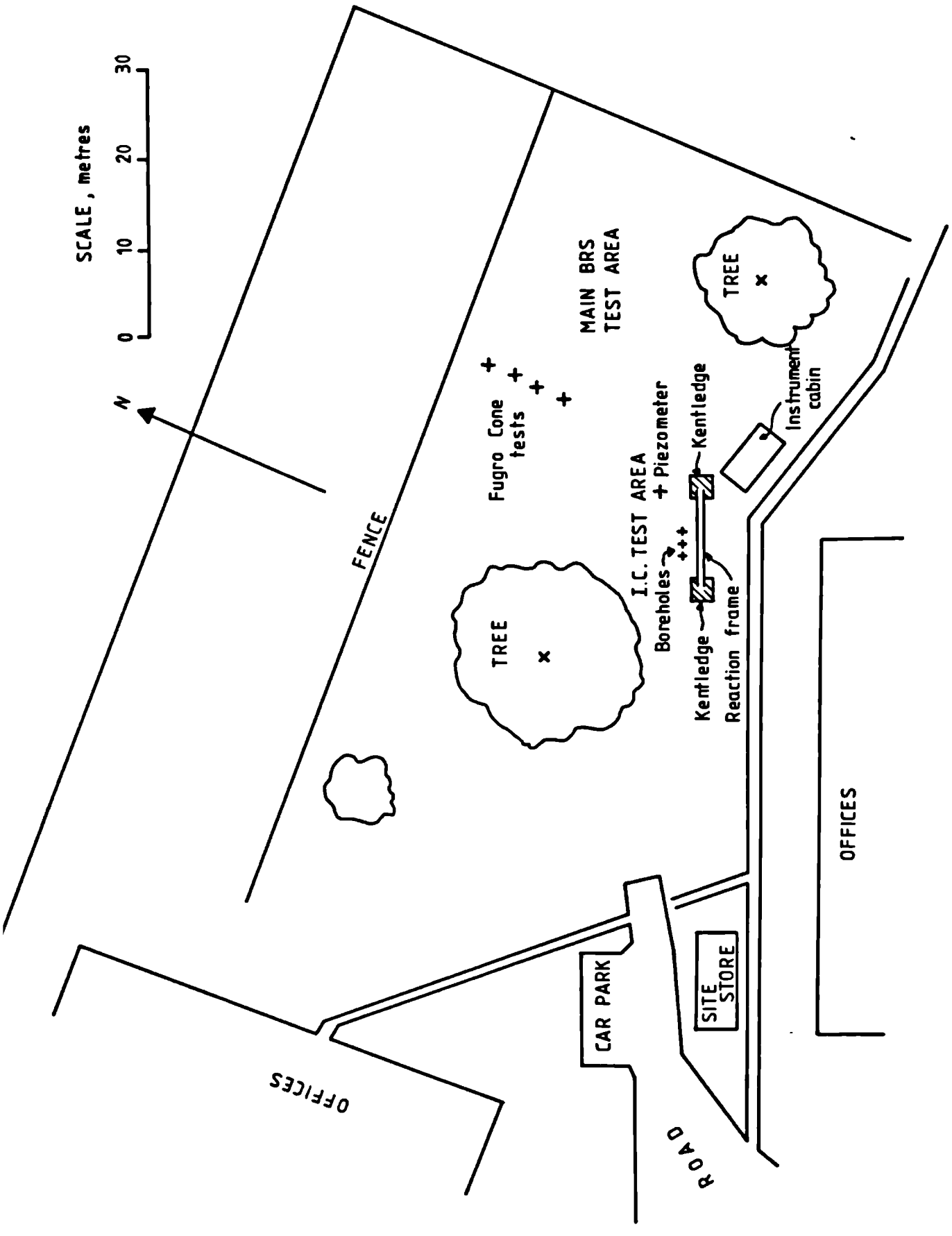


Figure 9.3. Site Map, Canons Park.

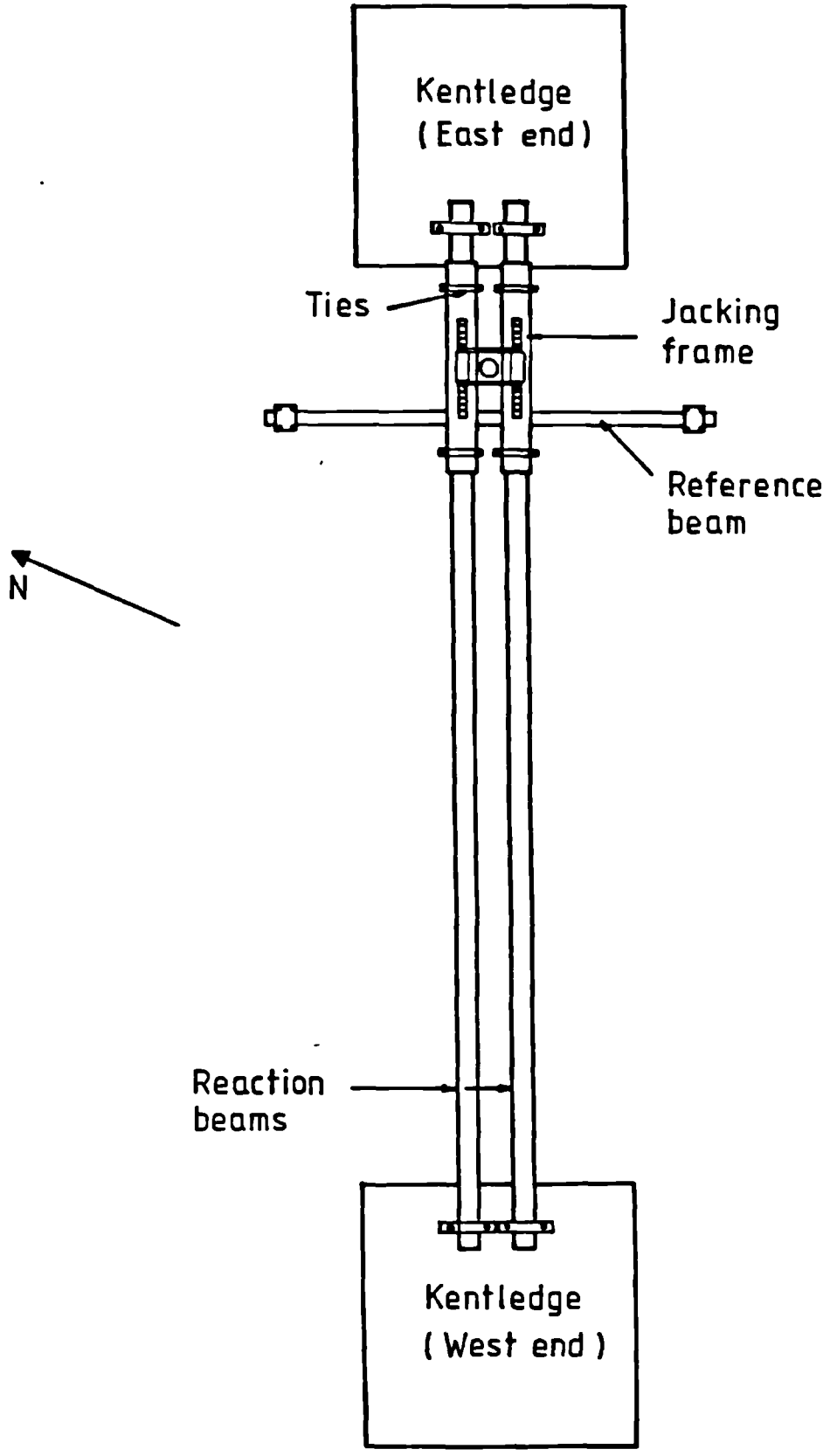


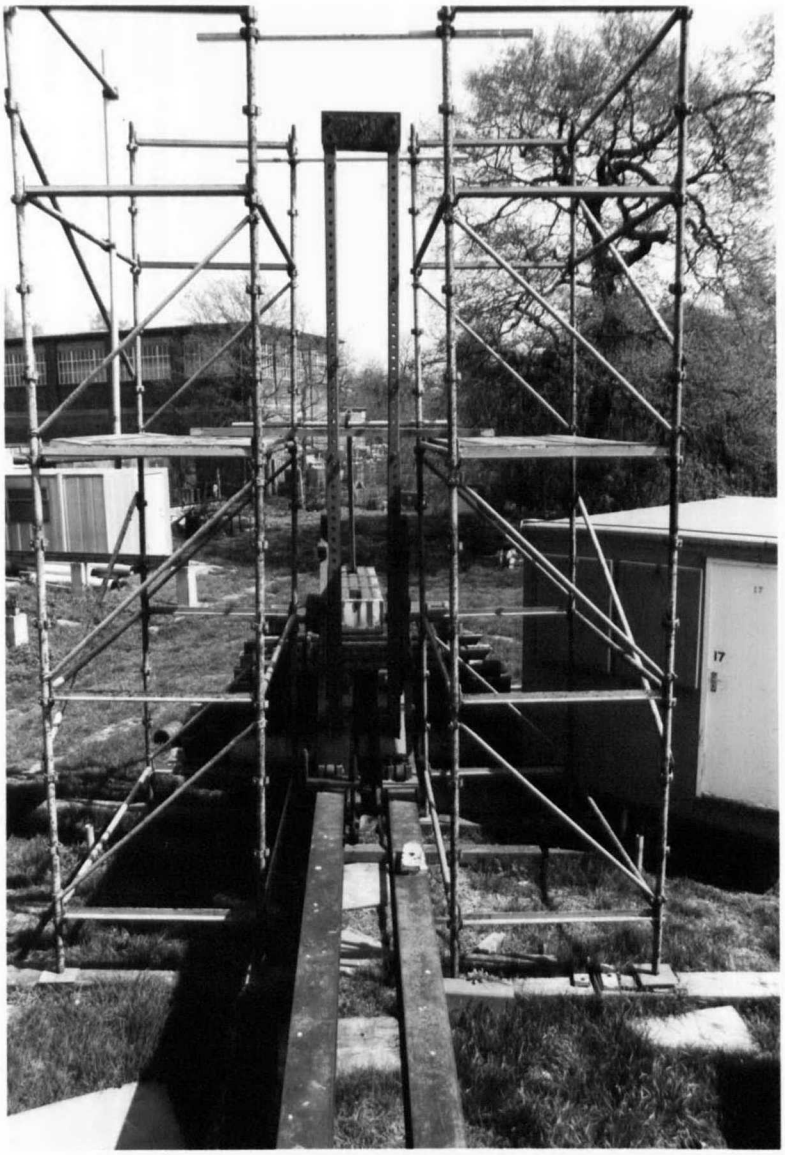
Figure 9.4. Pile loading frame and reaction arrangement.

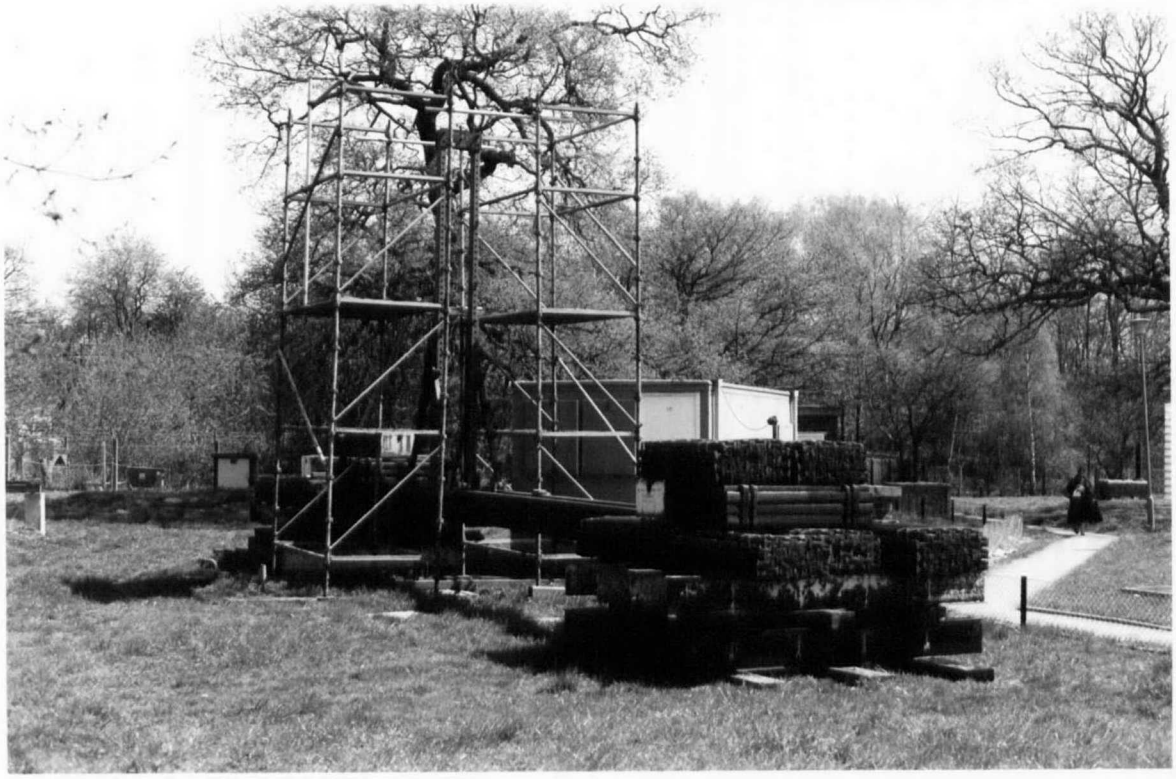
OPPOSITE

Figure 9.5. Pile testing arrangements at Canons Park.

TOP - Loading frame, reaction beams and instrument cabin

BOTTOM - General view showing stacked kentledge and test-bed position.





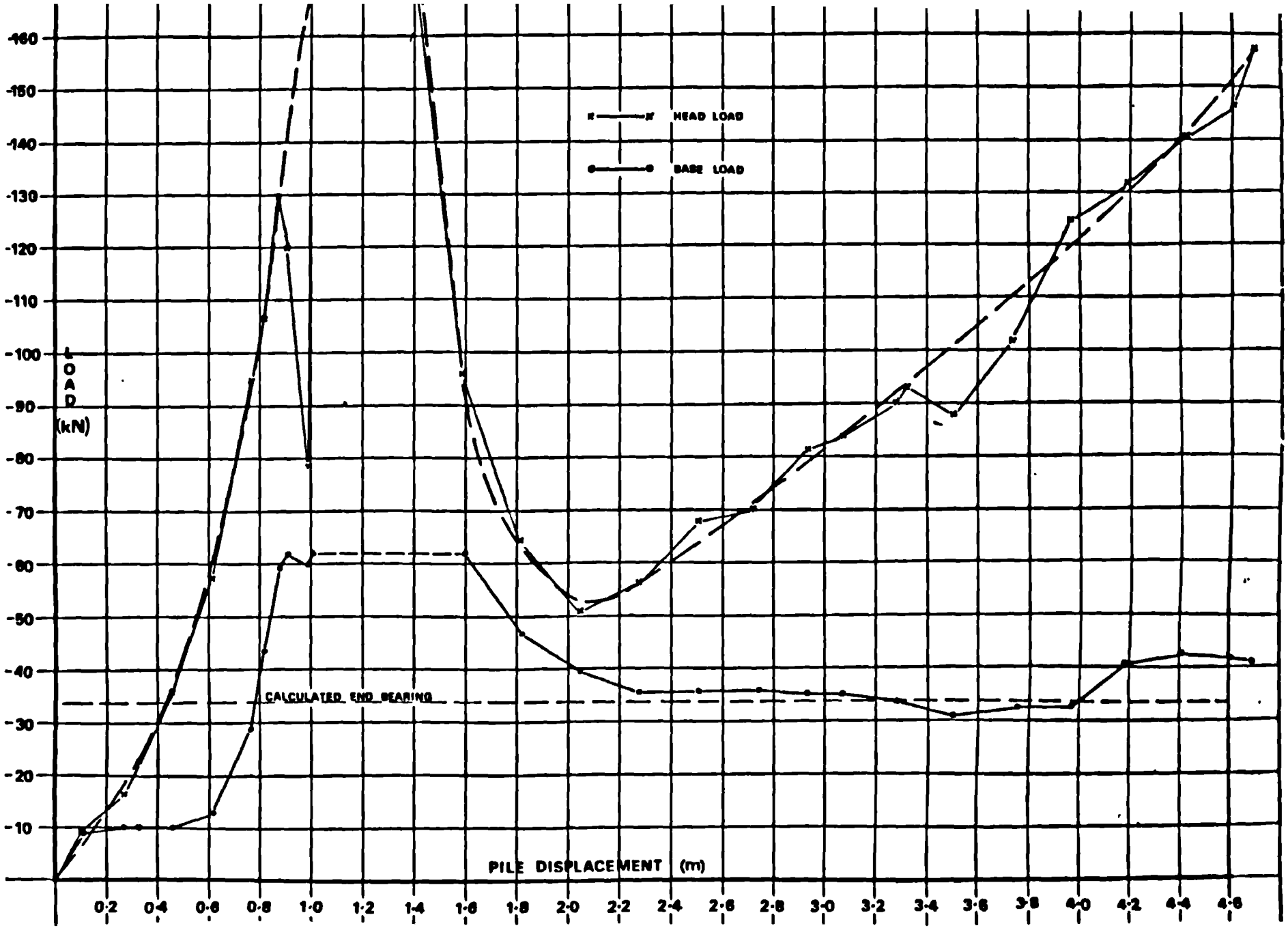


Figure 9.6 Jacking force - displacement record for a 170 mm diameter steel pile after Kitching(198

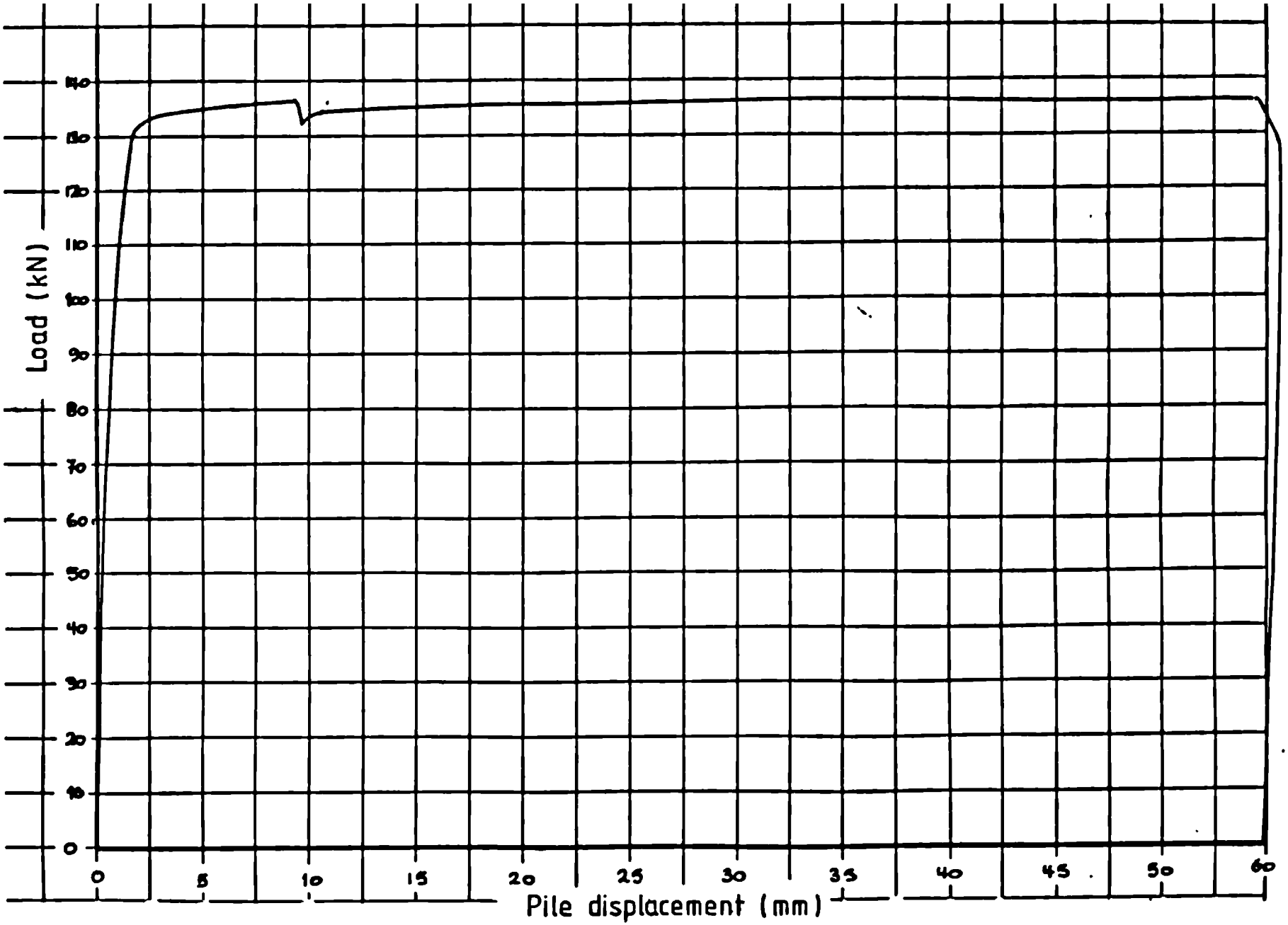


Figure 9.7. Load test record for a jacked pile, after Kitching (1983).

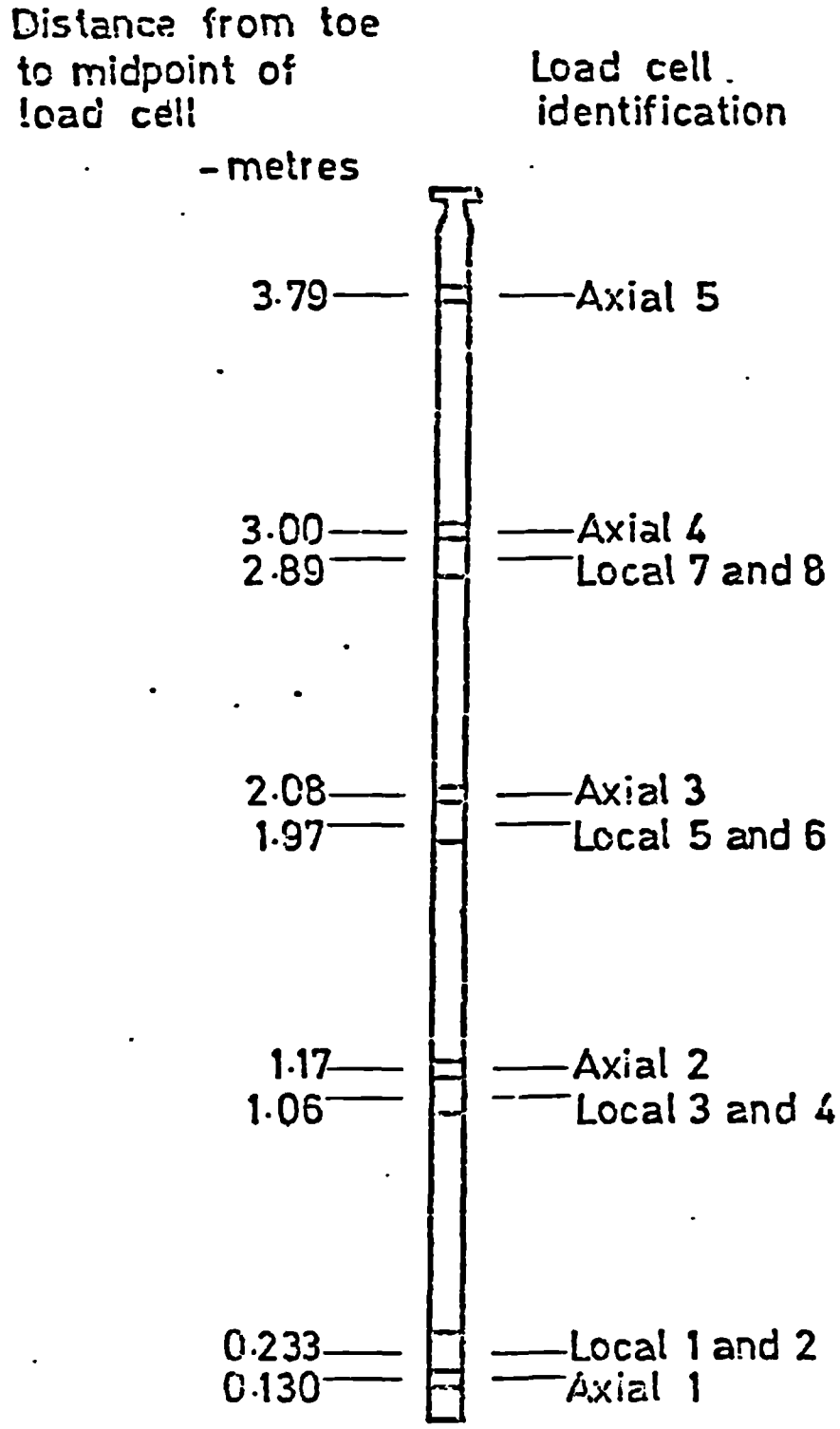


Figure 9.8. Identification and Location of Load Cells

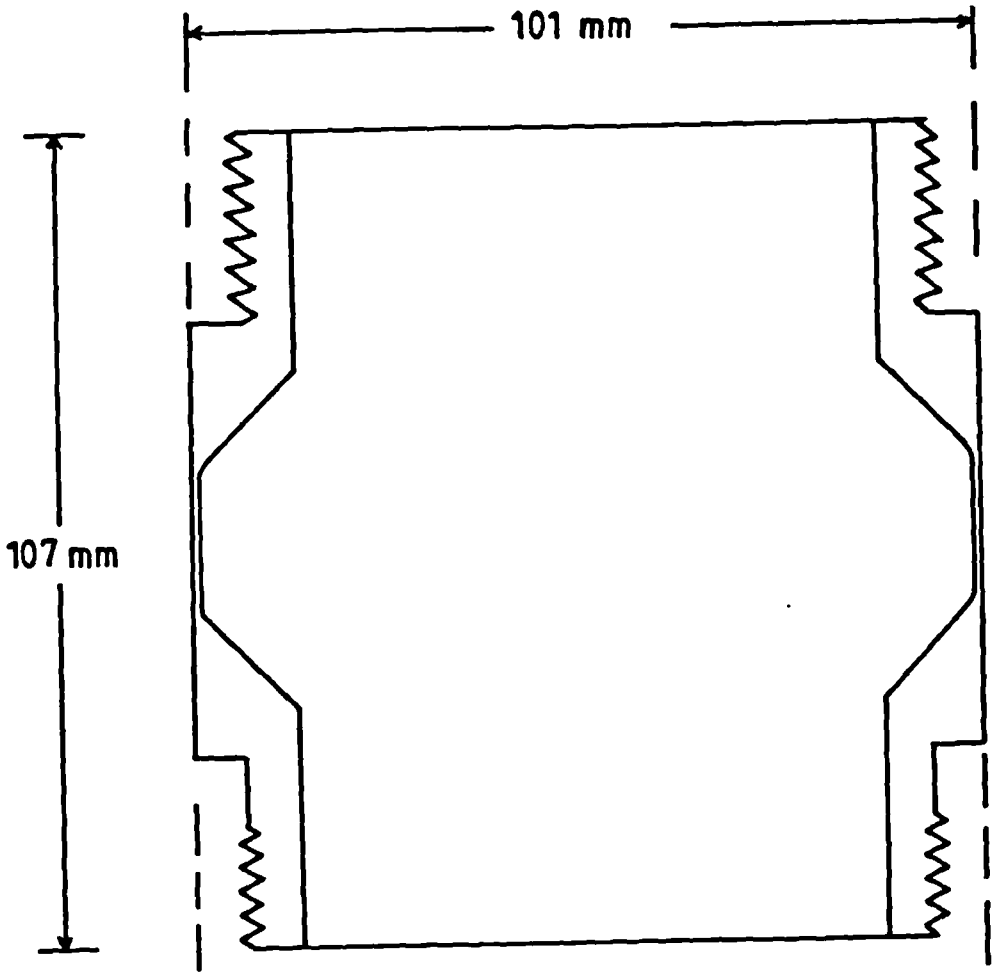


Figure 9.9. Long section through axial load cell.

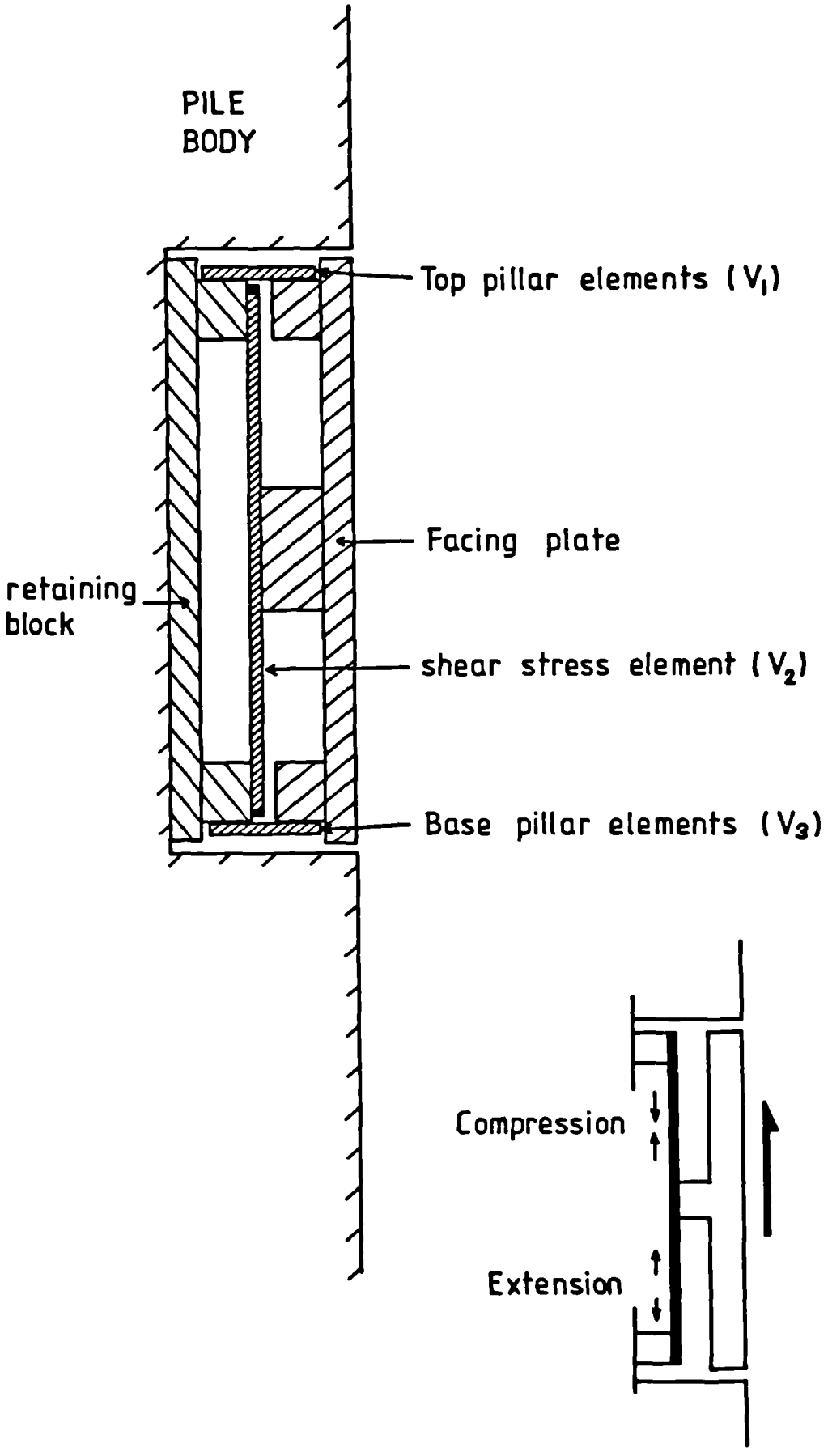
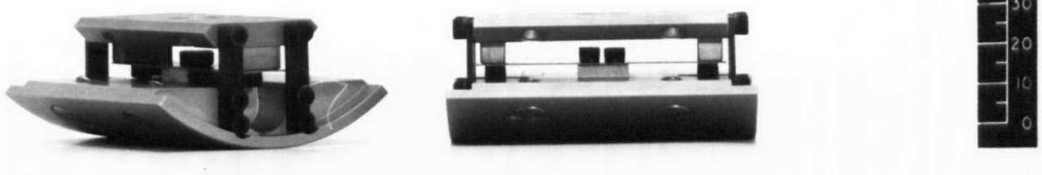


Figure 9.10. Schematic diagram of a local load cell.


MMS
50
40
30
20
10
0


MMS
50
40
30
20
10
0

OPPOSITE

Figure 9.12. General view of local load cell body and sensing components.


MMS
50
40
30
20
10
0

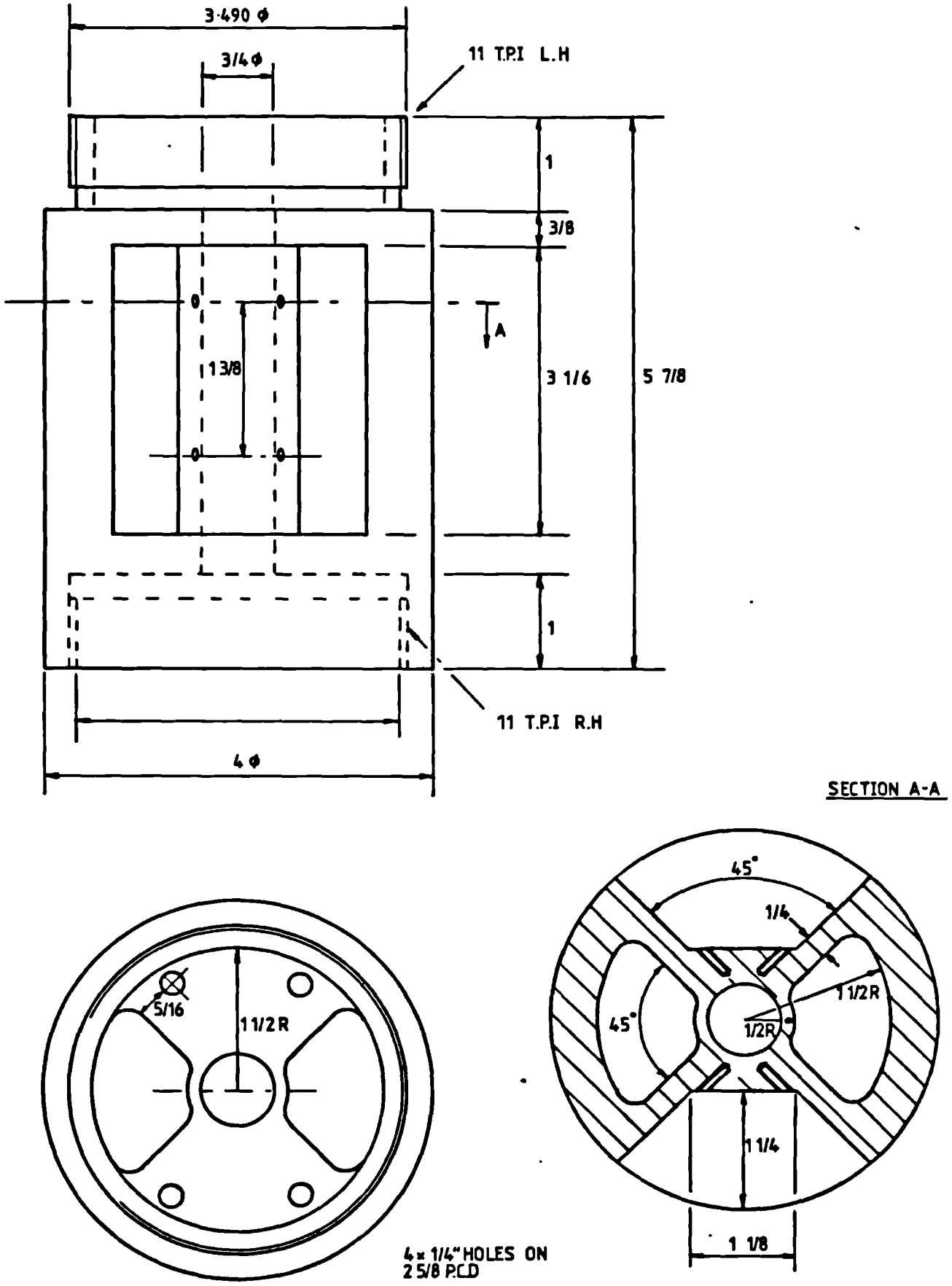
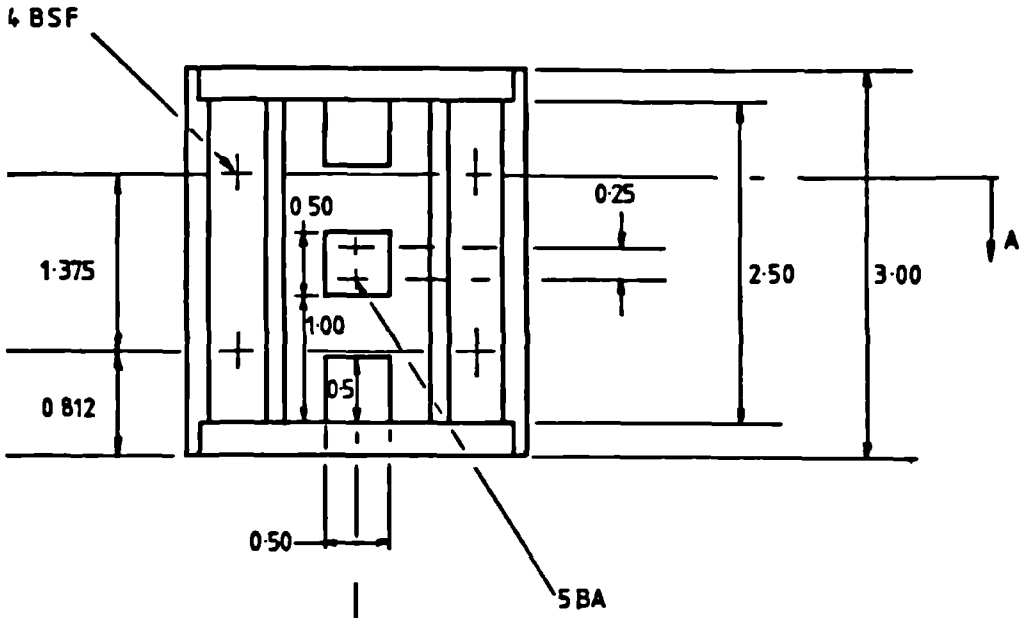
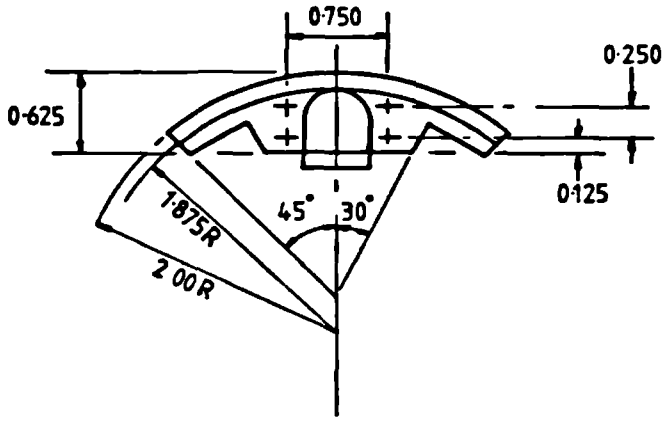
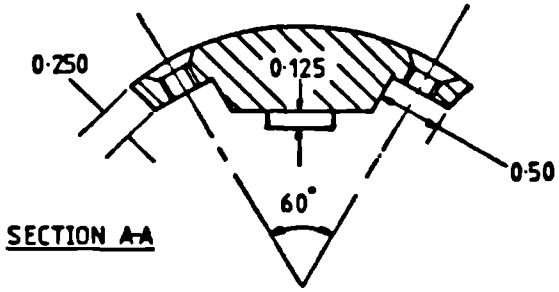


Figure 9.13. Local load cell body, dims. in Imperial units.







SECTION A-A

STAINLESS STEEL

Figure 9.14. Local load cell facing plate, dims. in Imperial units.

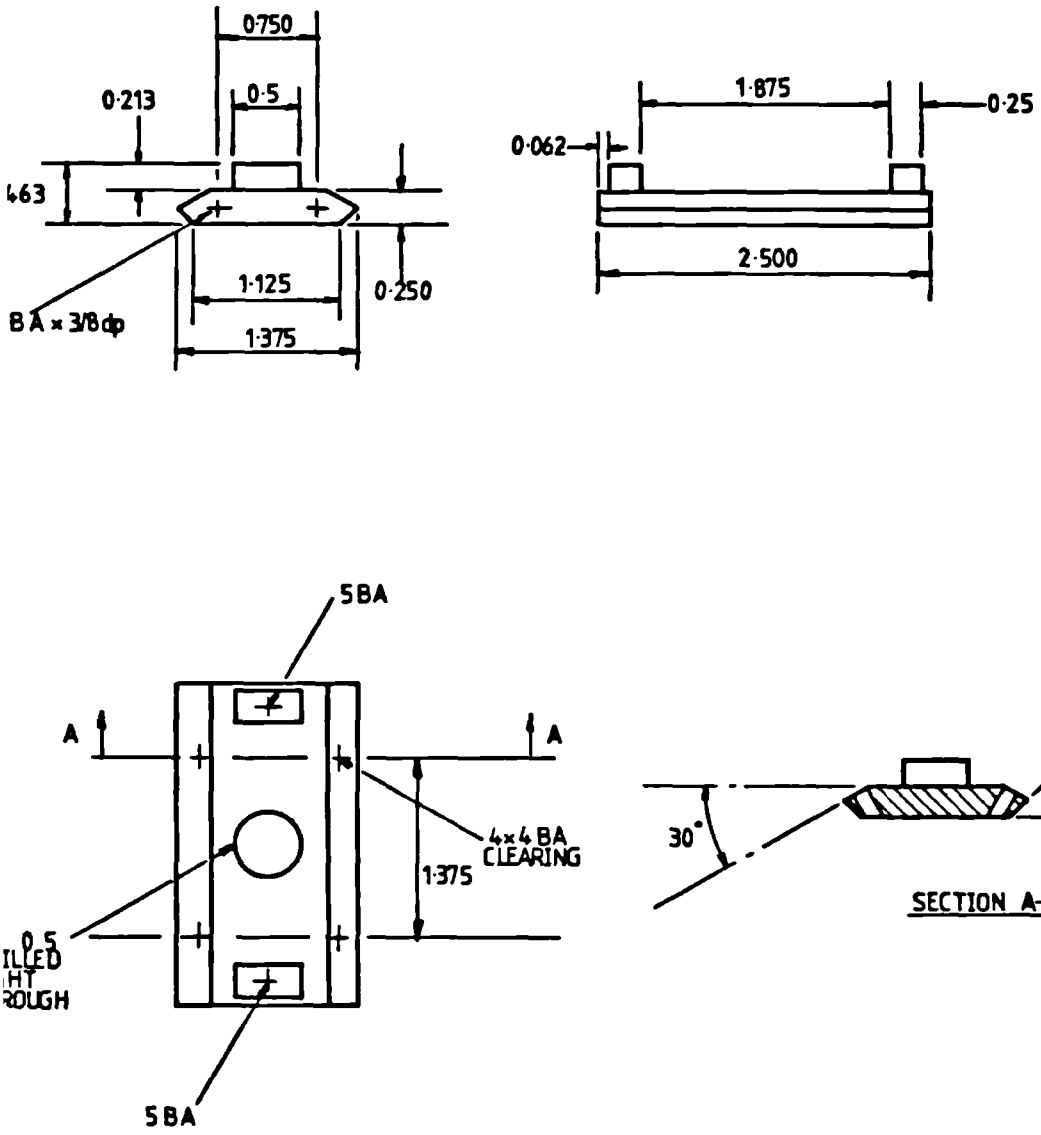


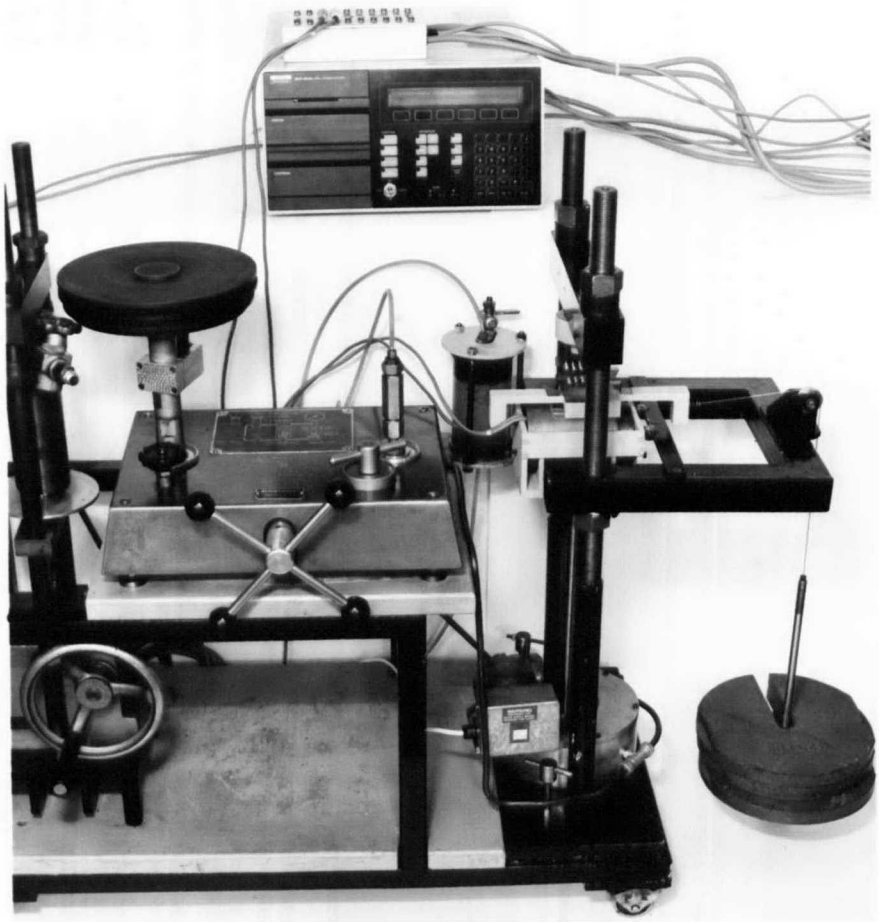
Figure 9.15. Local load cell backing piece, dims. in Imperial units.

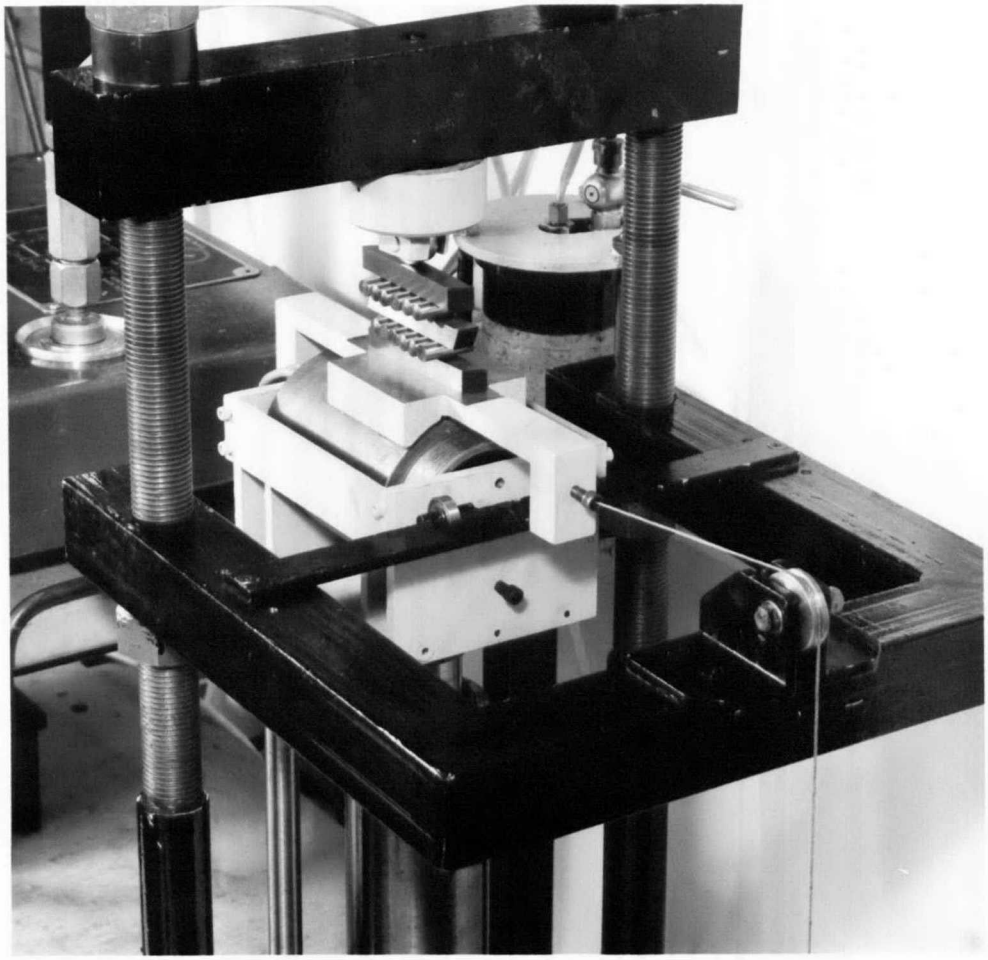
OPPOSITE

Figure 9.16. Local load cell undergoing calibration.

TOP - Dead weight test apparatus and orion data logger.

BOTTOM - Detail of load cell in cradle with load bearing in place and horizontal force being applied.





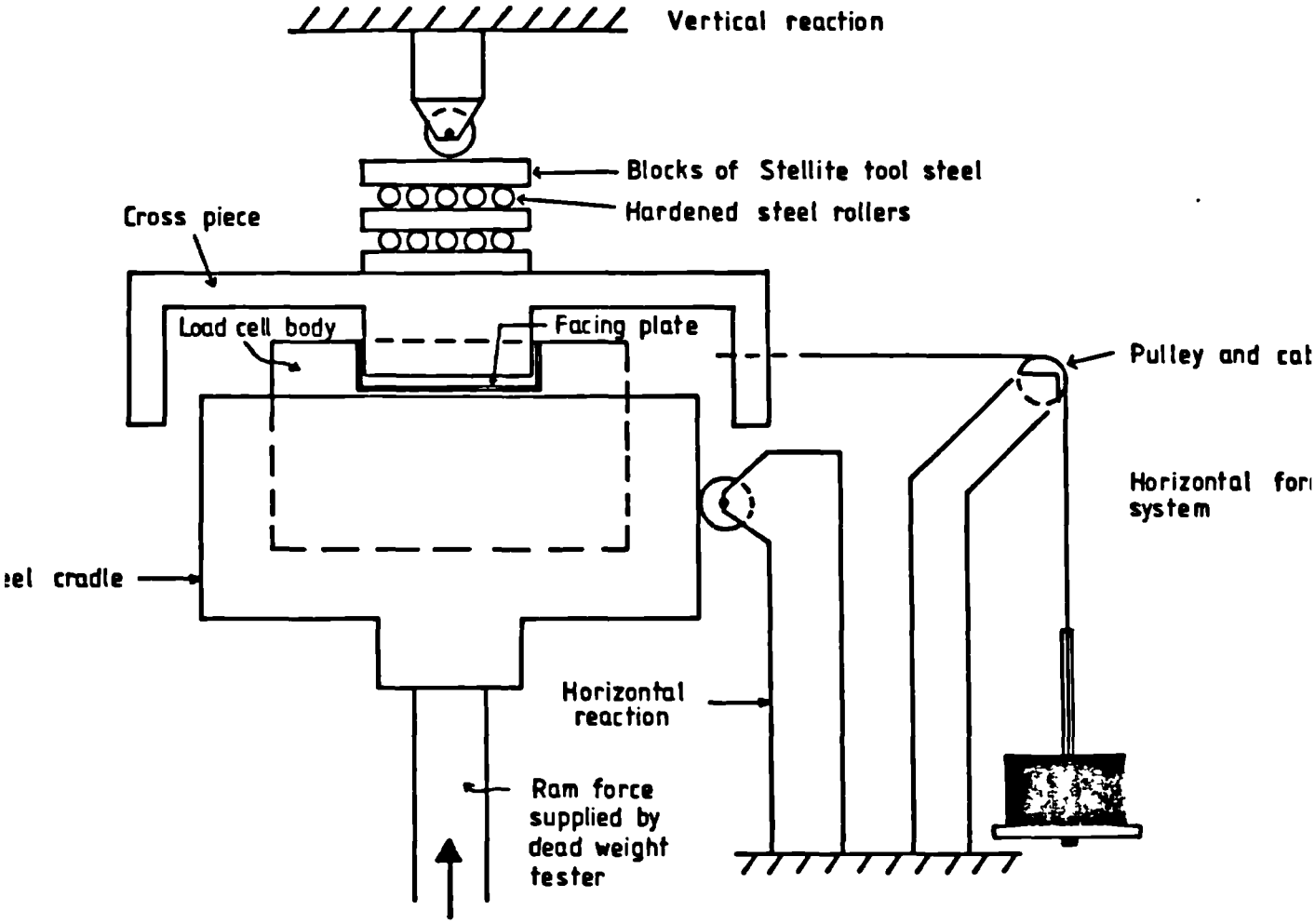


Figure 9.17. Schematic diagram of local load cell calibrator.

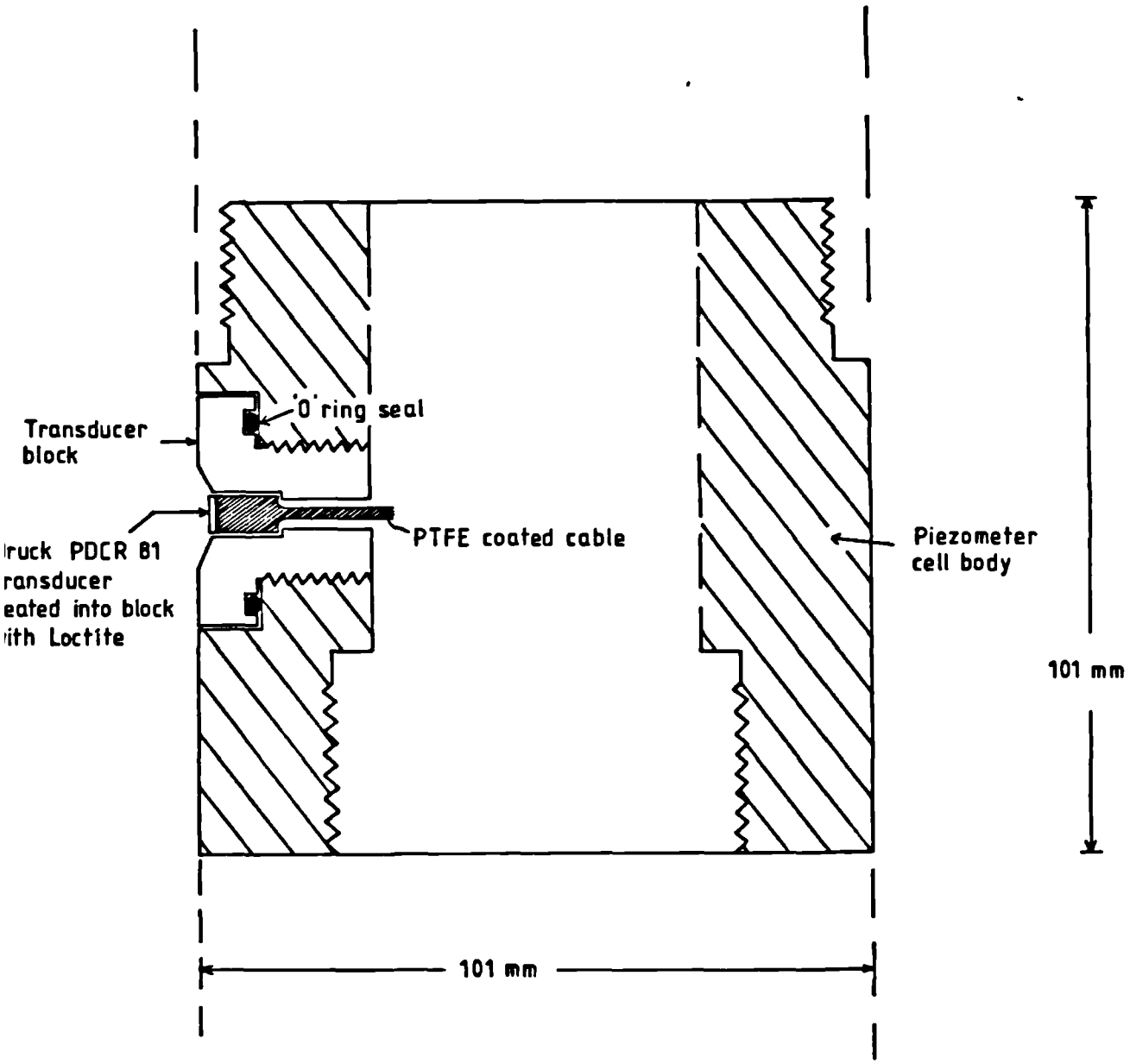


Figure 9.18. Piezometer cells.

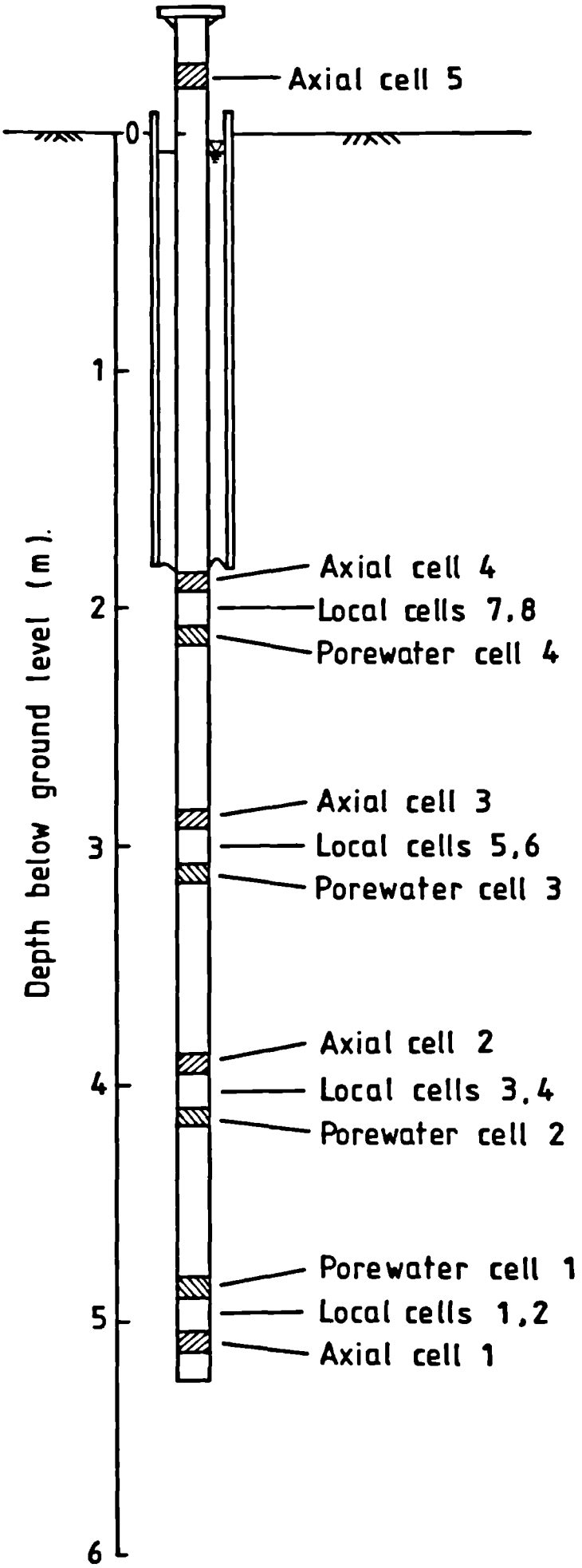


Figure 9.19. Configuration of instrumentation for pilot test at Canons Park.

0.23 m above tip
2.22 m above tip
0
100
200
300
400
2
3
4
5
Instrument depth below G.L. (m)

0.23 m above tip
1.22 m above tip
0
100
200
300
400
500
600
2
3
4
5
Instrument depth below G.L.(m)

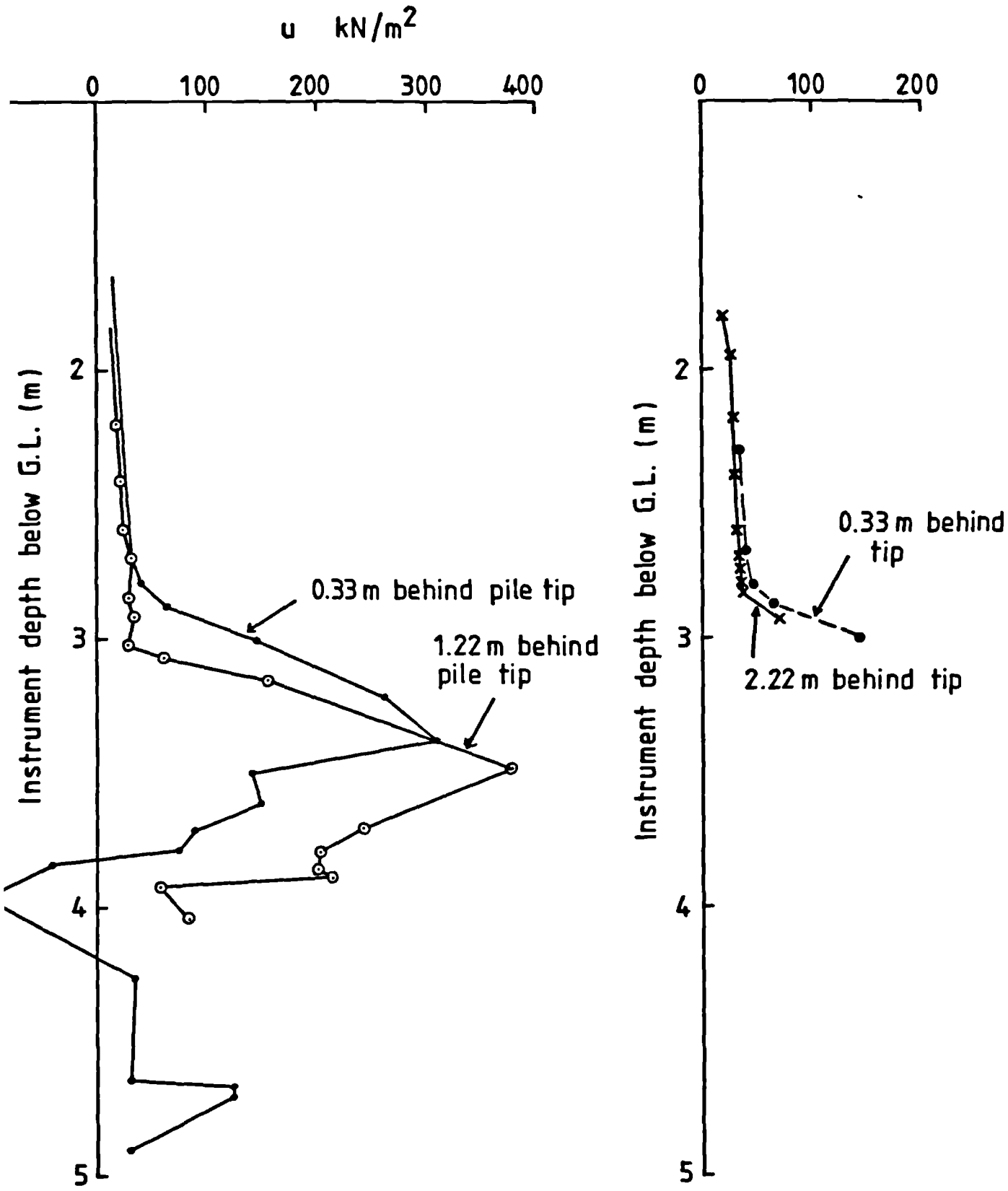


Figure 9.21. Variations of pωp with depth during installation, traces for individual cells.

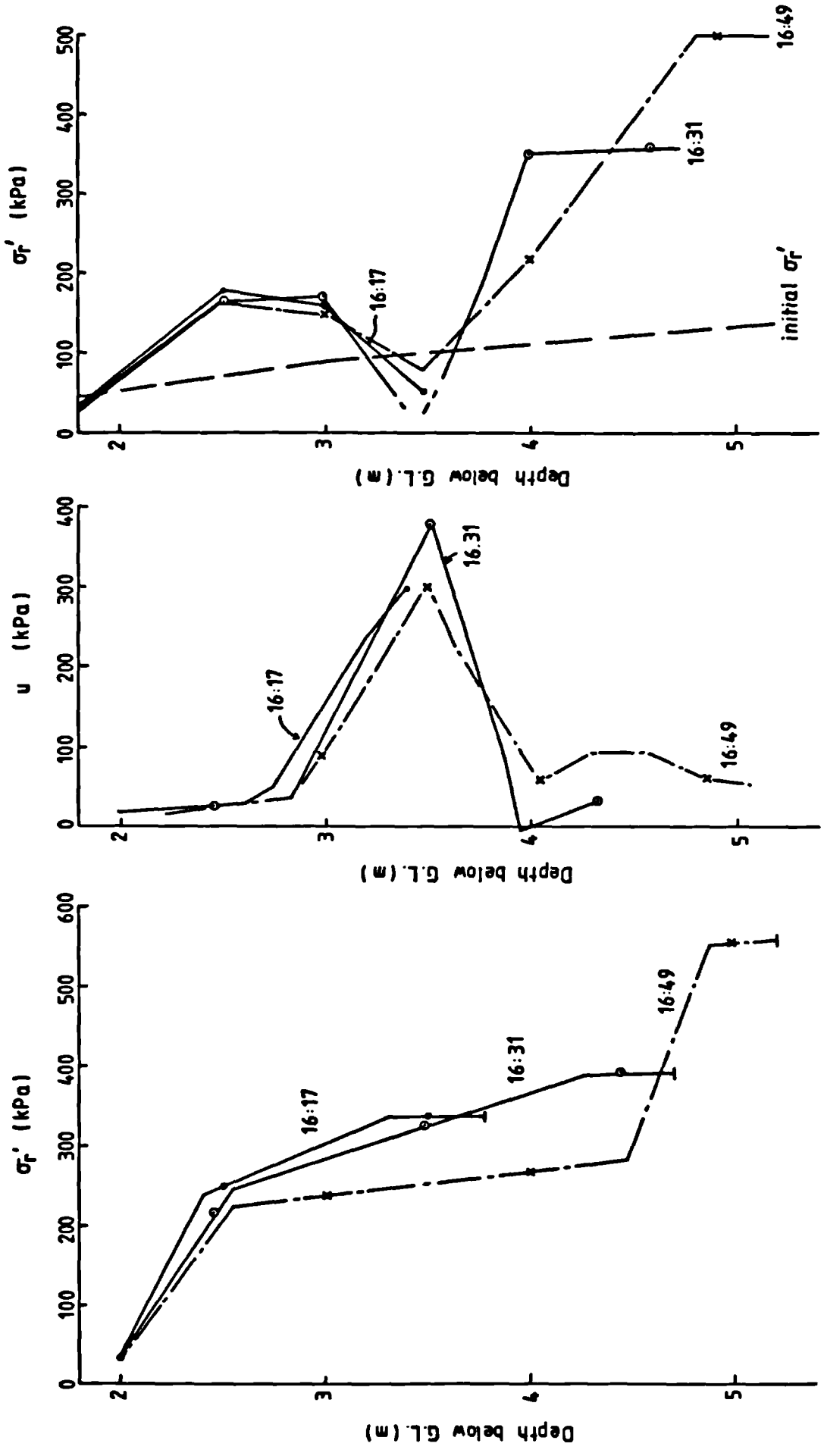


Figure 9.22. Variations of σ_r and pwp with depth for given depths of penetration.

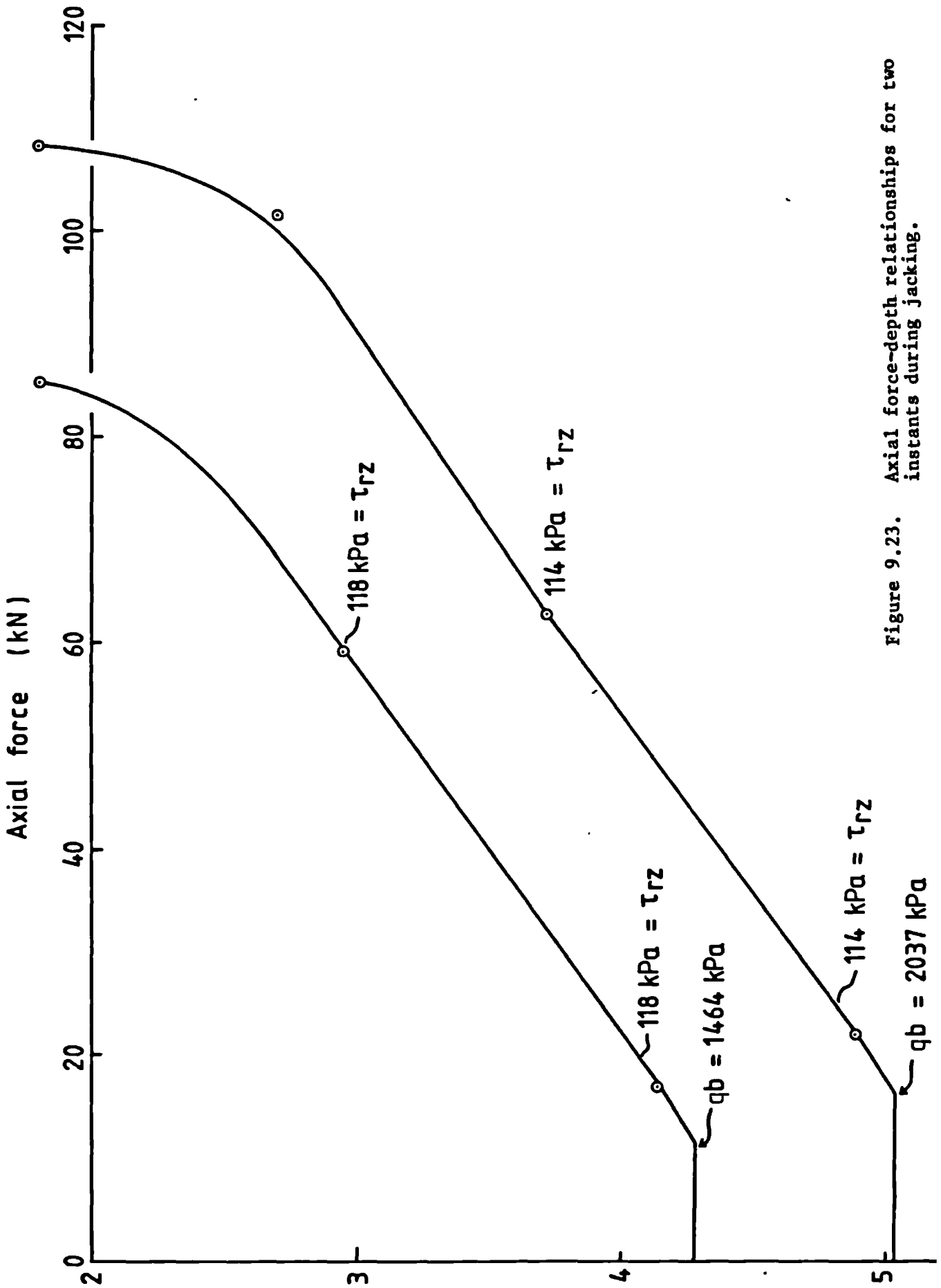


Figure 9.23. Axial force-depth relationships for two instants during jacking.

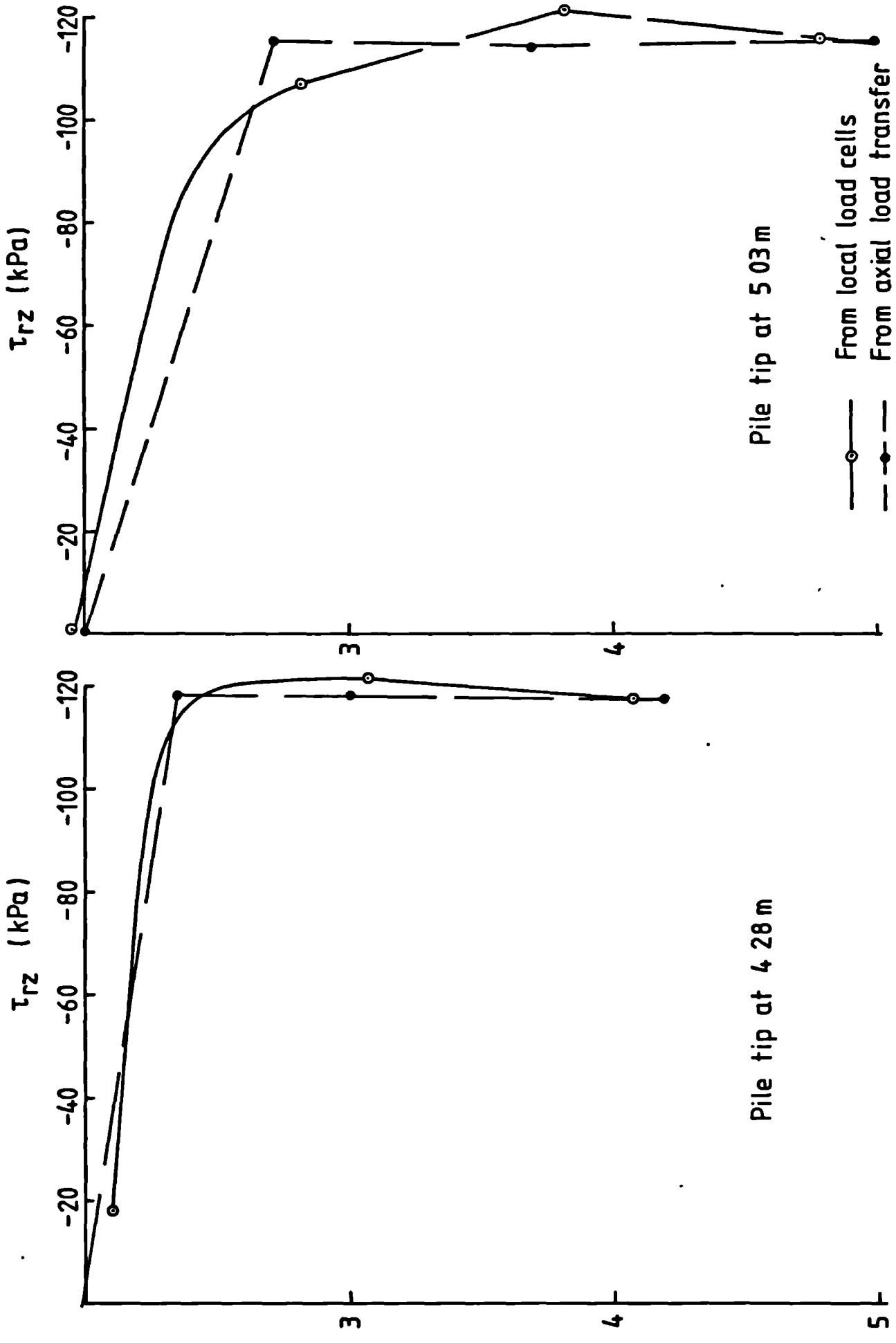


Figure 9.24. Shear stress-depth relationships for two instants during jacking.

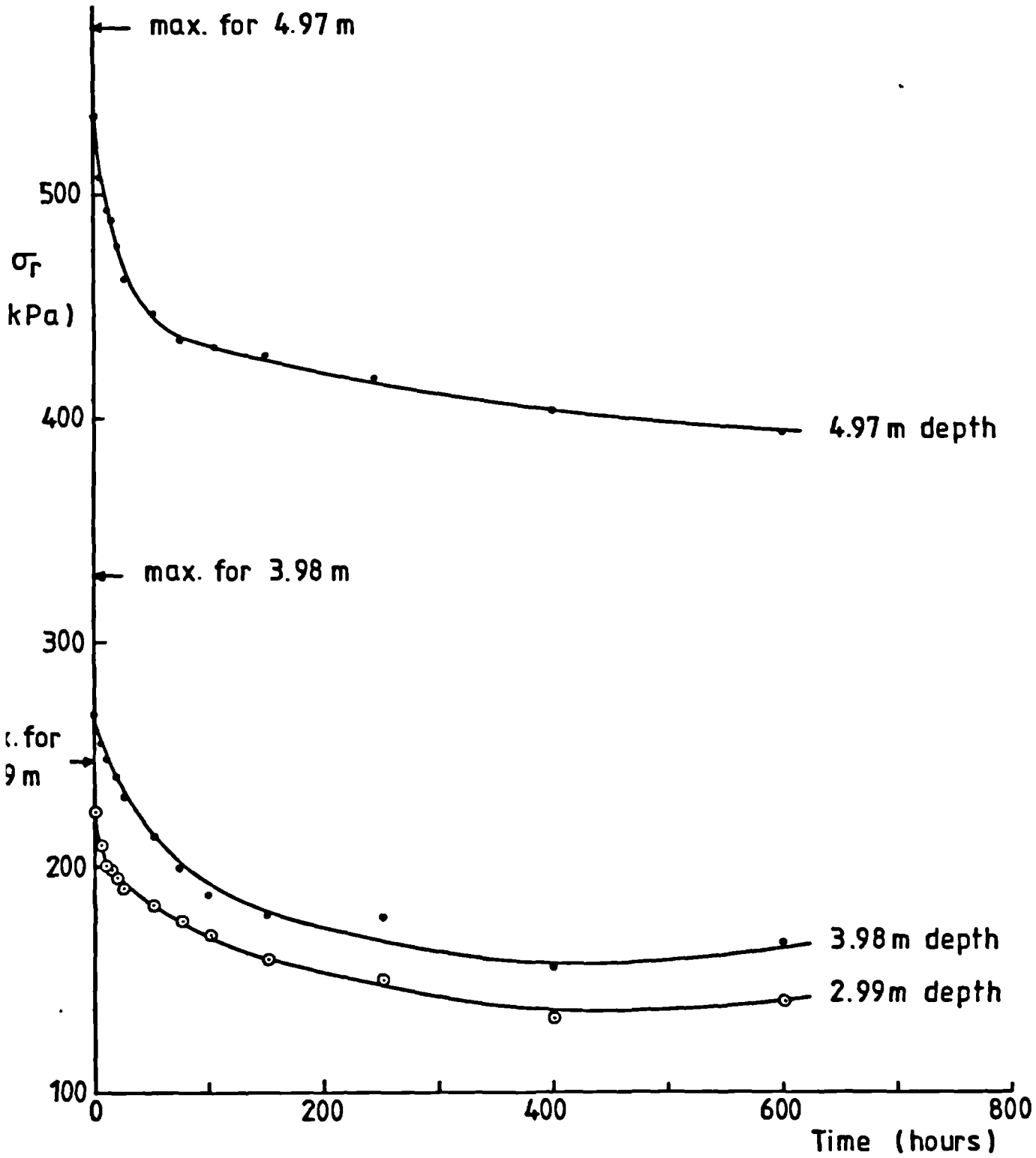


Figure 9.25. Variations of σ_r with time after installation.

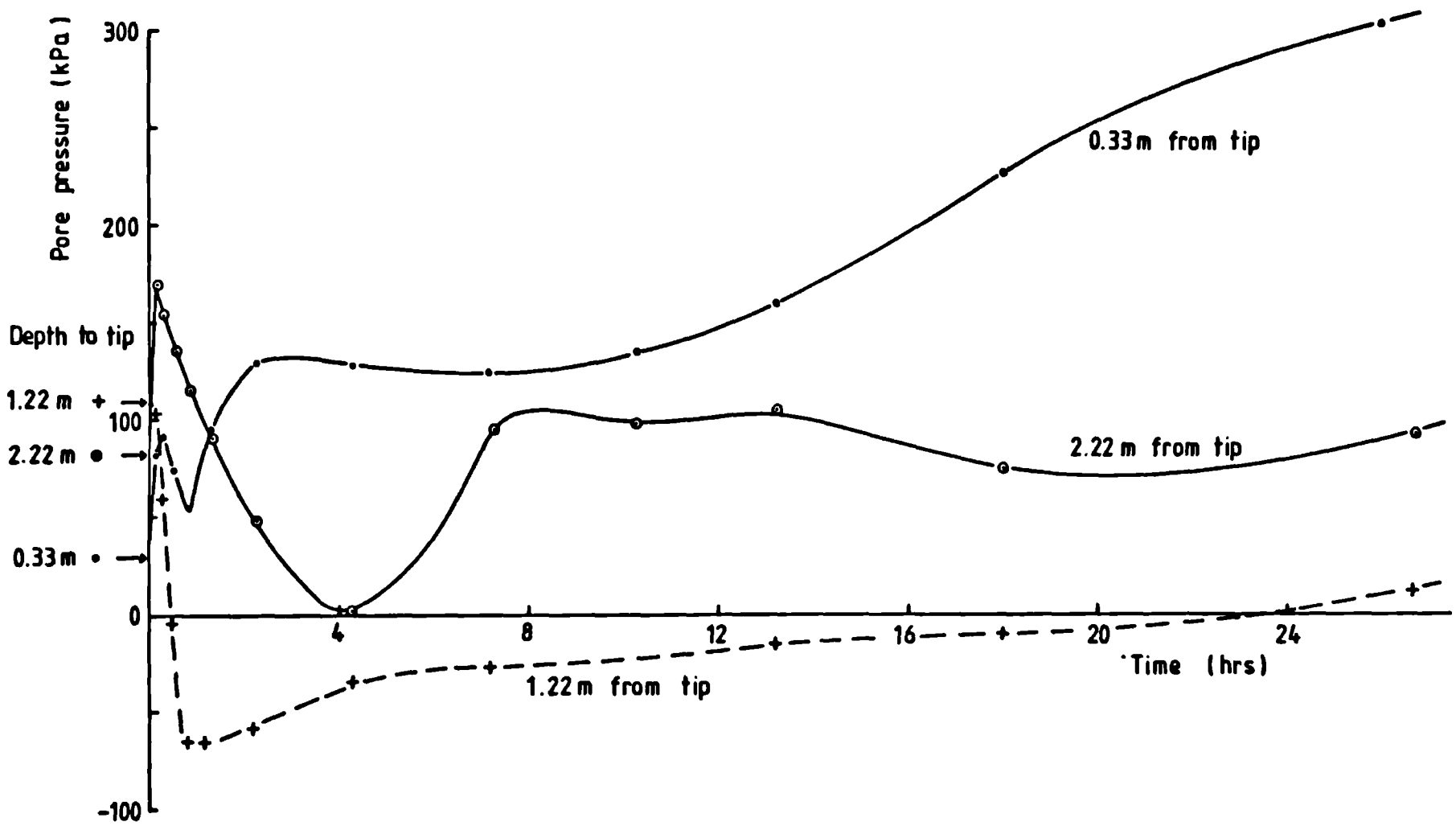


Figure 9.26. Variations of pwp for 24 hrs after installation.

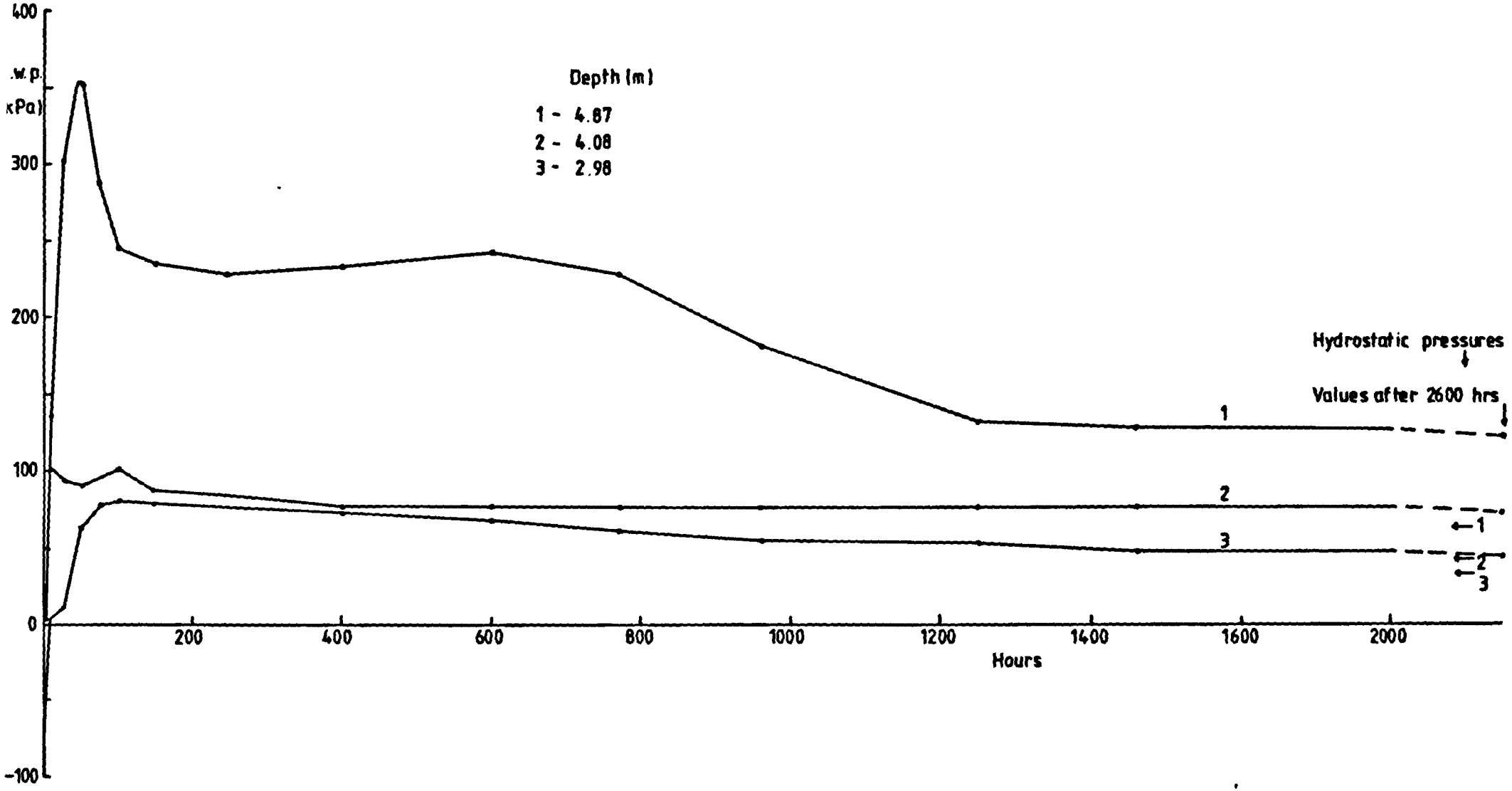


Figure 9.27. Variations of pwp for 2,500 hrs after installation.

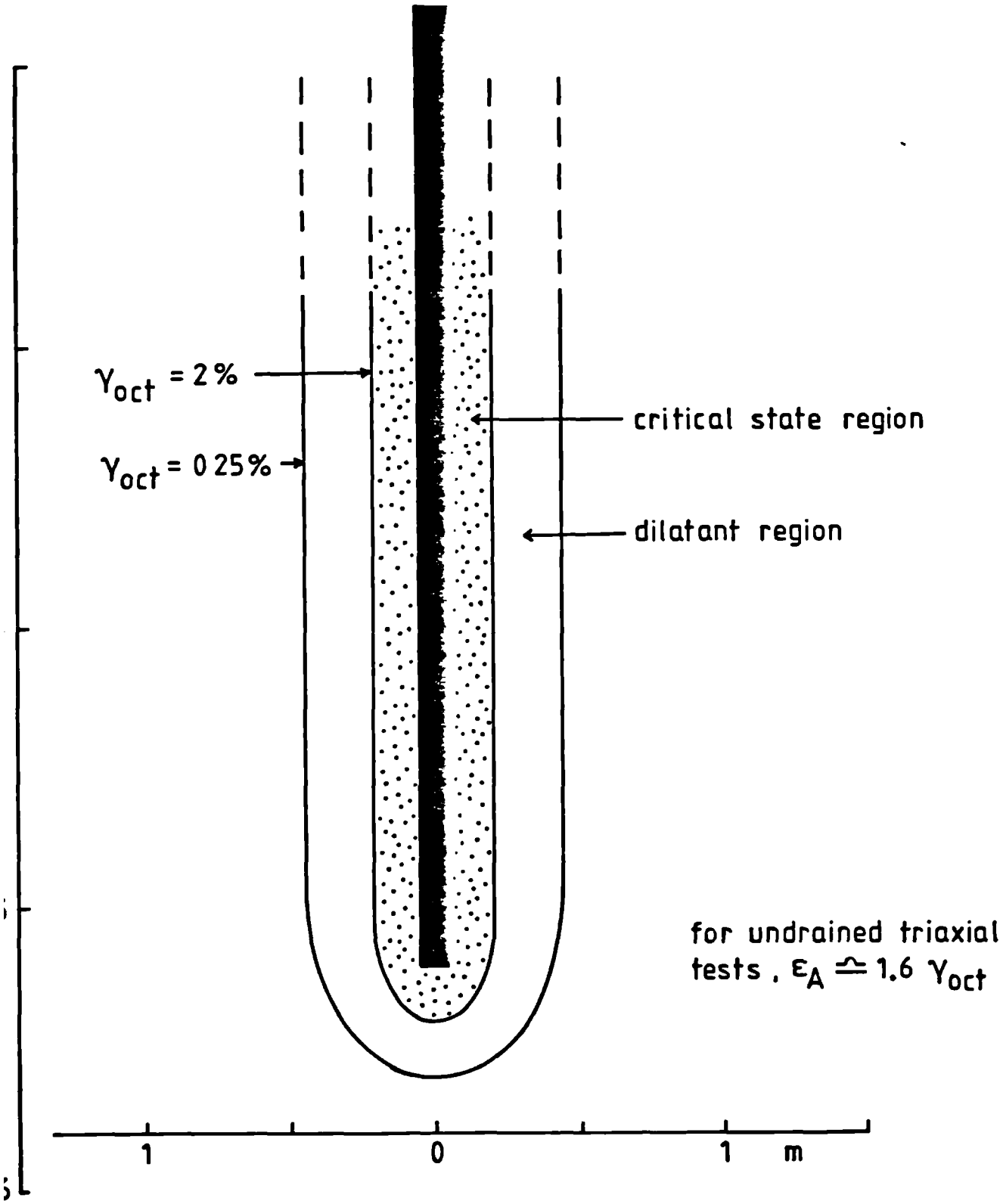


Figure 9.28. Predictions of extent of dilatant zone during installation.

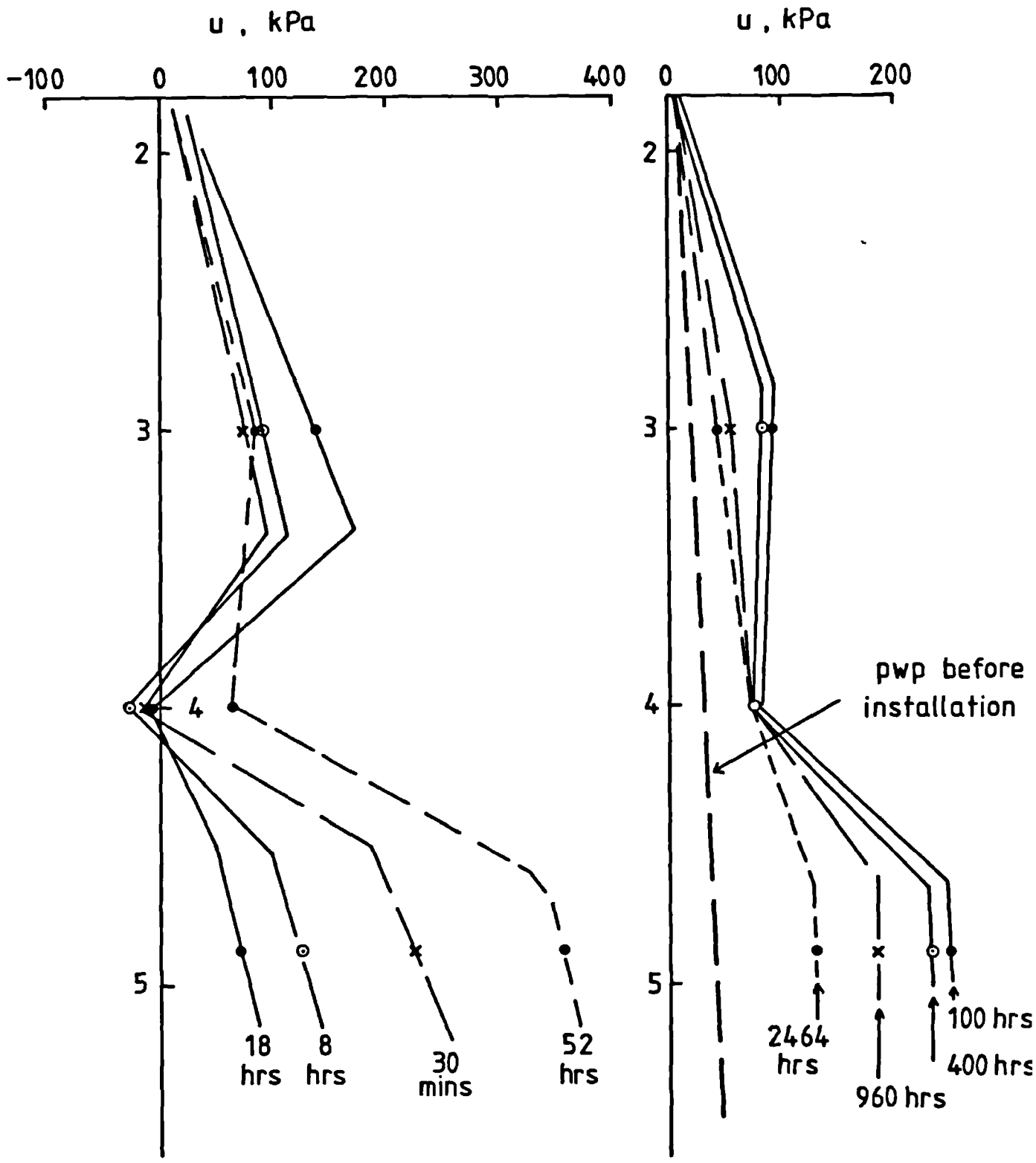


Figure 9.29. Profiles of pwp at given times after installation.

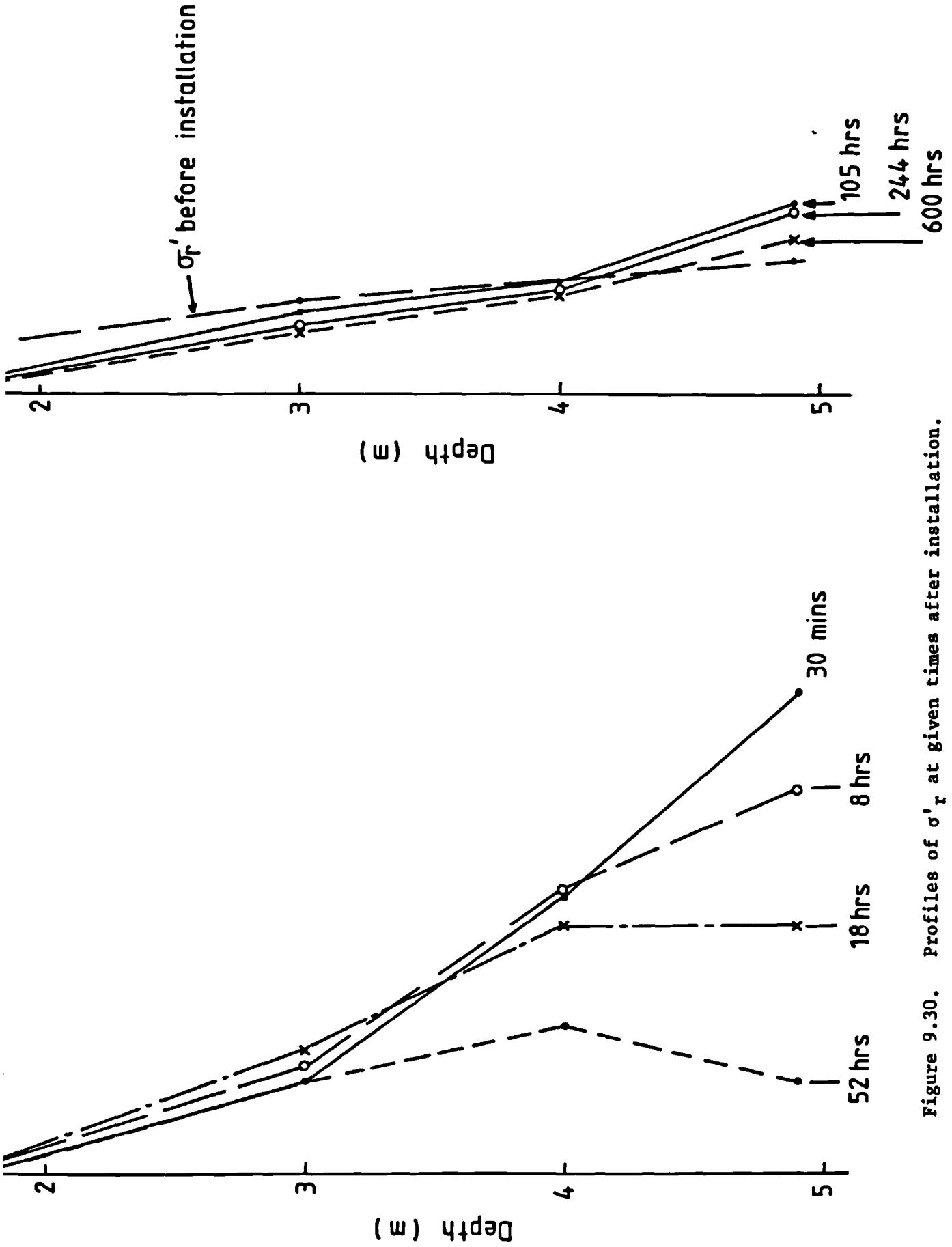


Figure 9.30. Profiles of σ'_r at given times after installation.

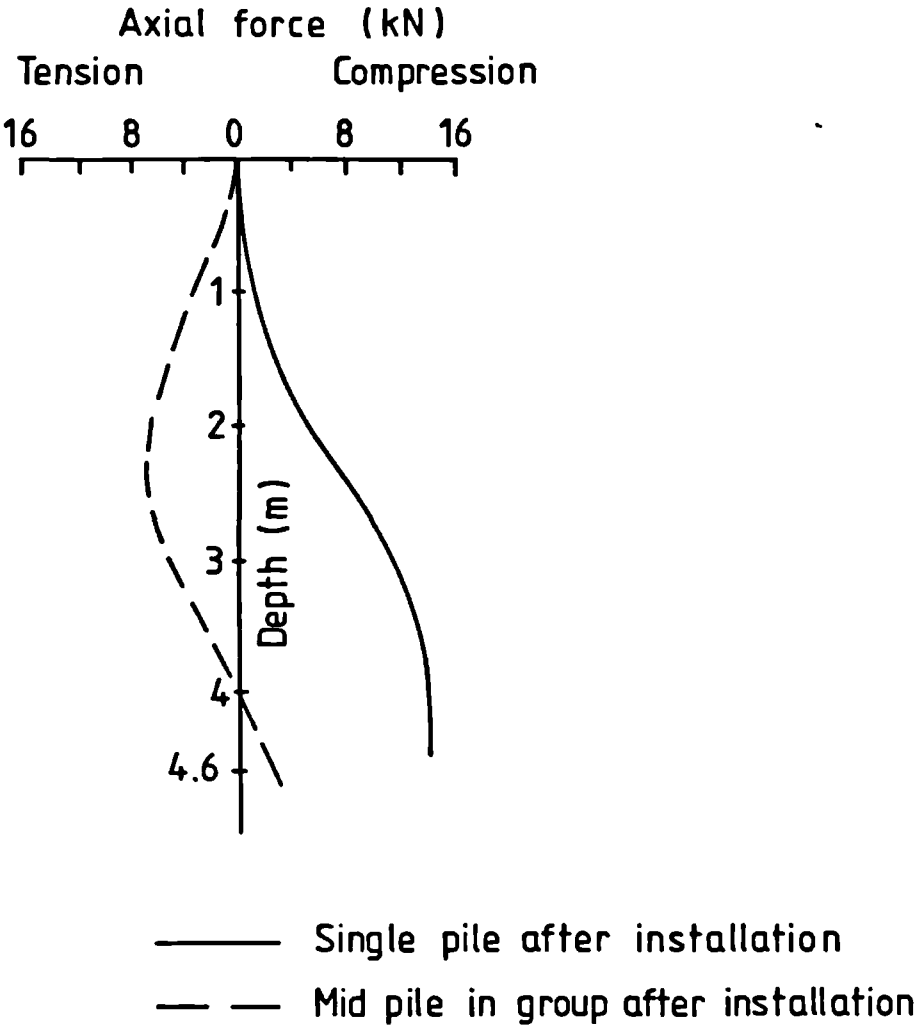


Figure 9.31. Residual stresses after installation (from Cooke et al., 1979).

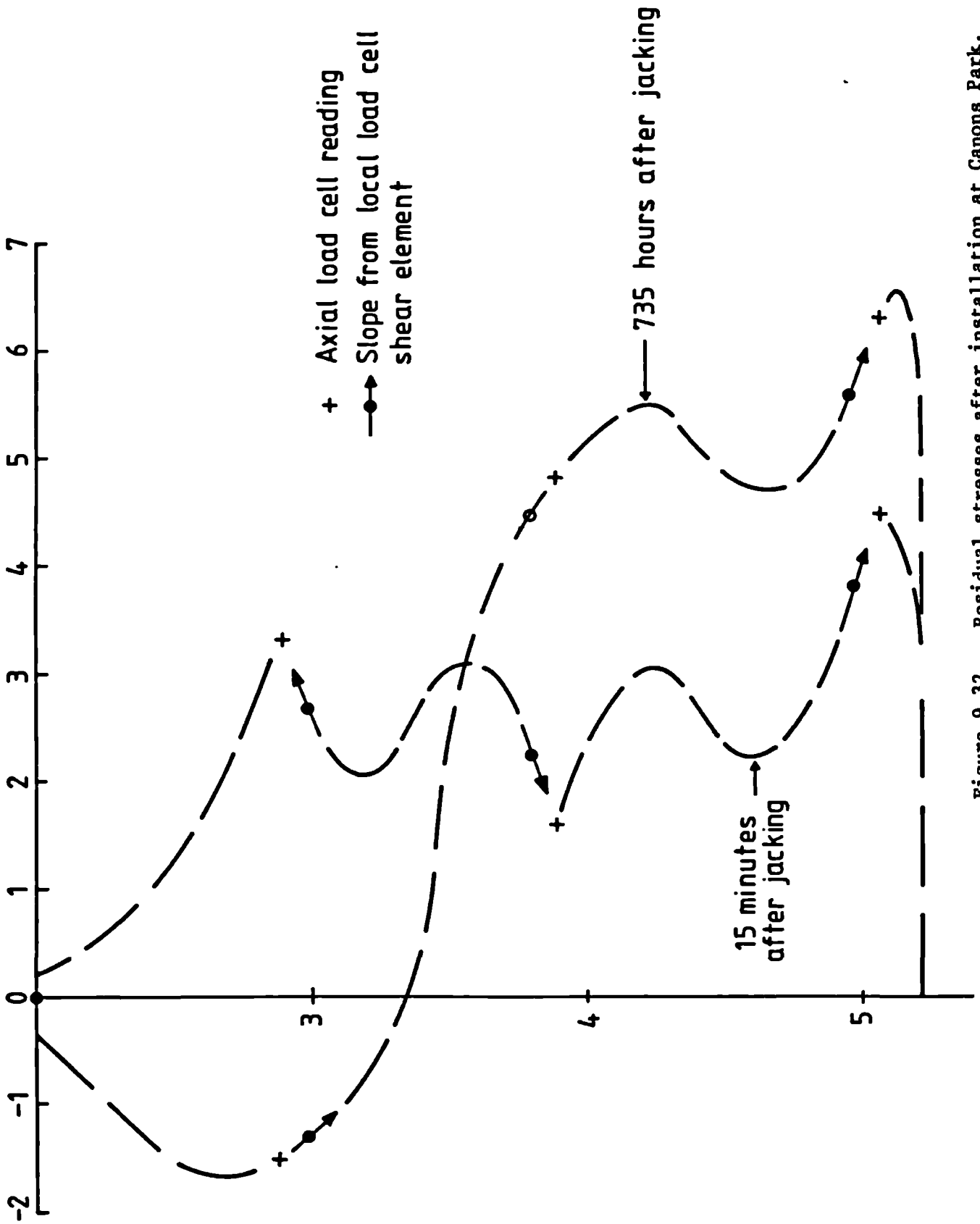


Figure 9.32. Residual stresses after installation at Canons Park.

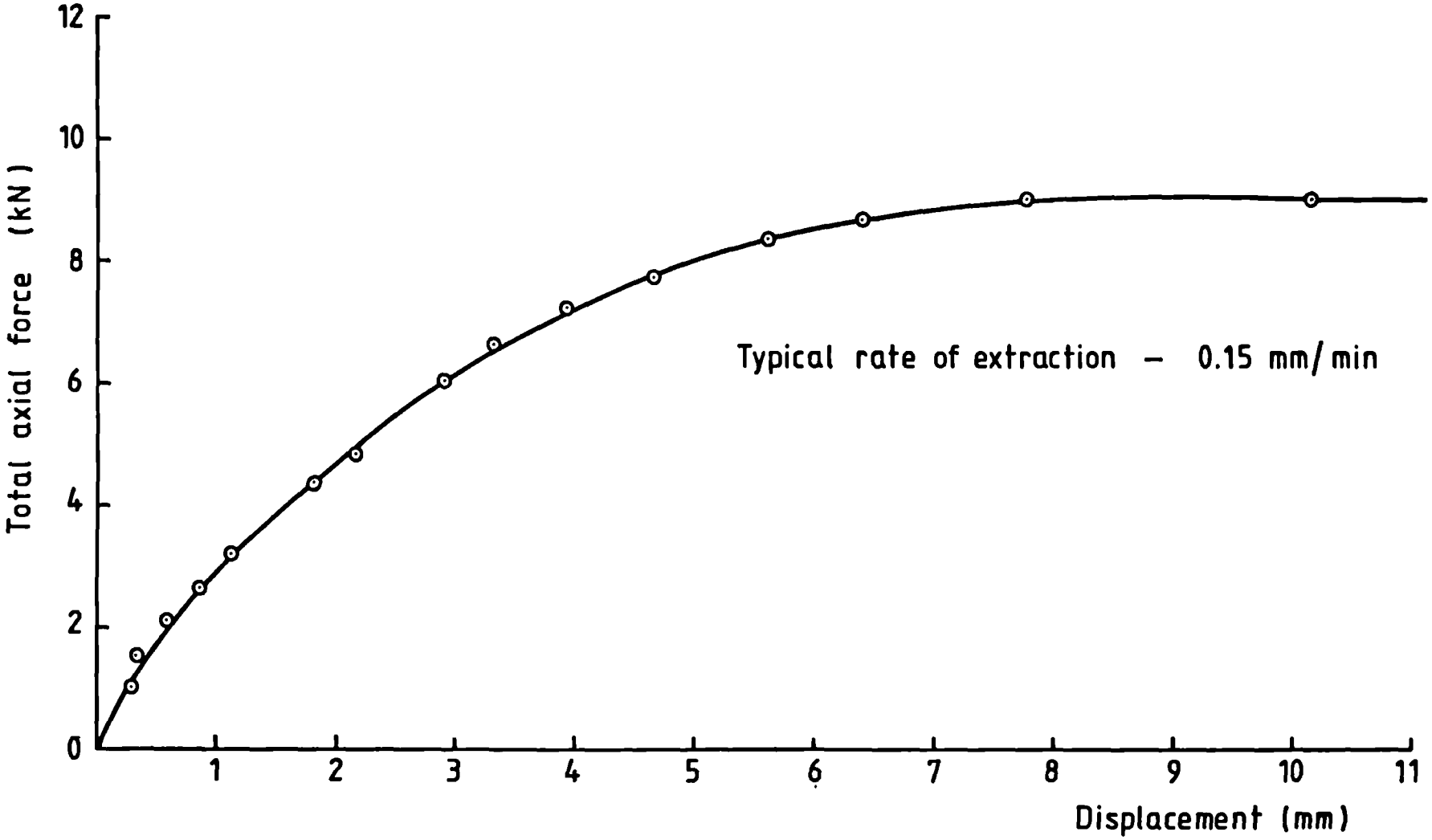


Figure 9.33. Load-displacement curve, tension test at Canons Park (with buckled load cell).

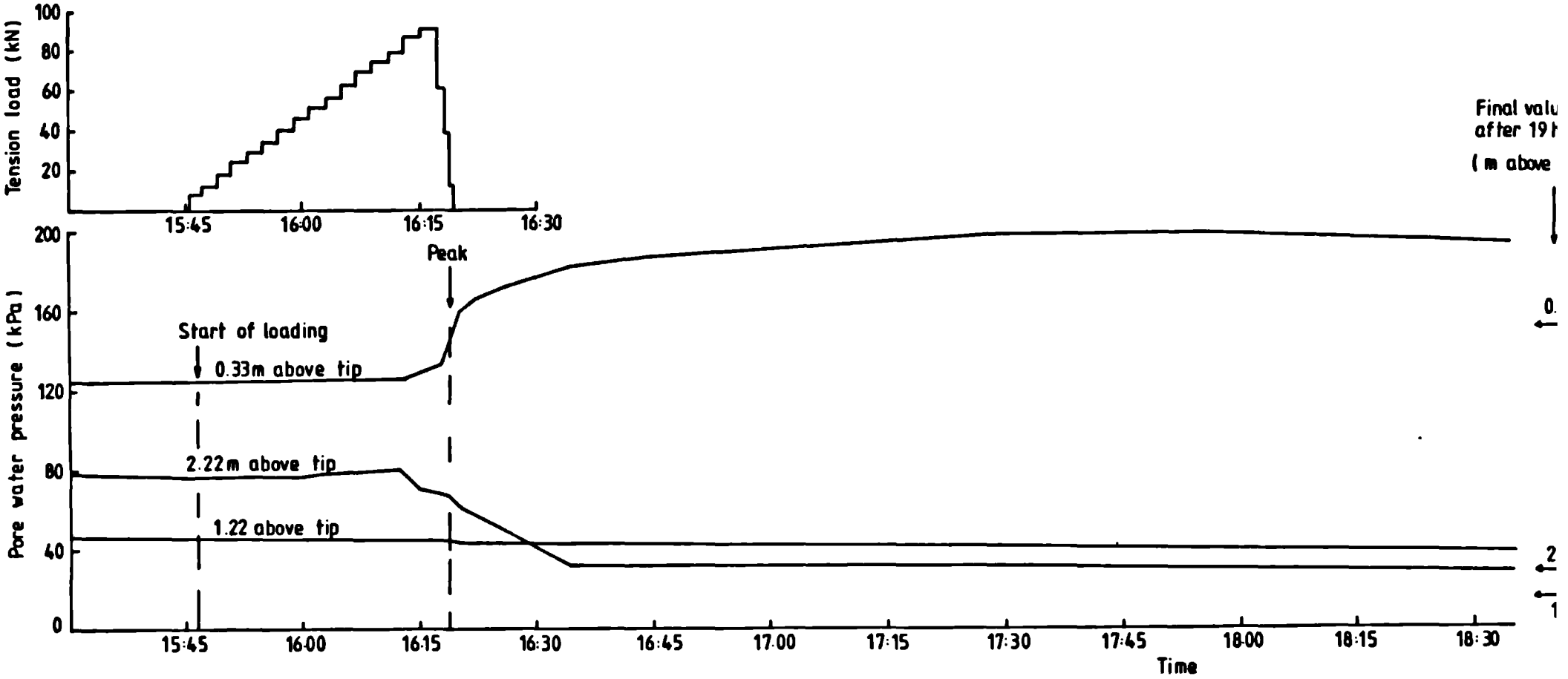


Figure 9.34. Variations of load and pwp with time for tension test at Canons Park.

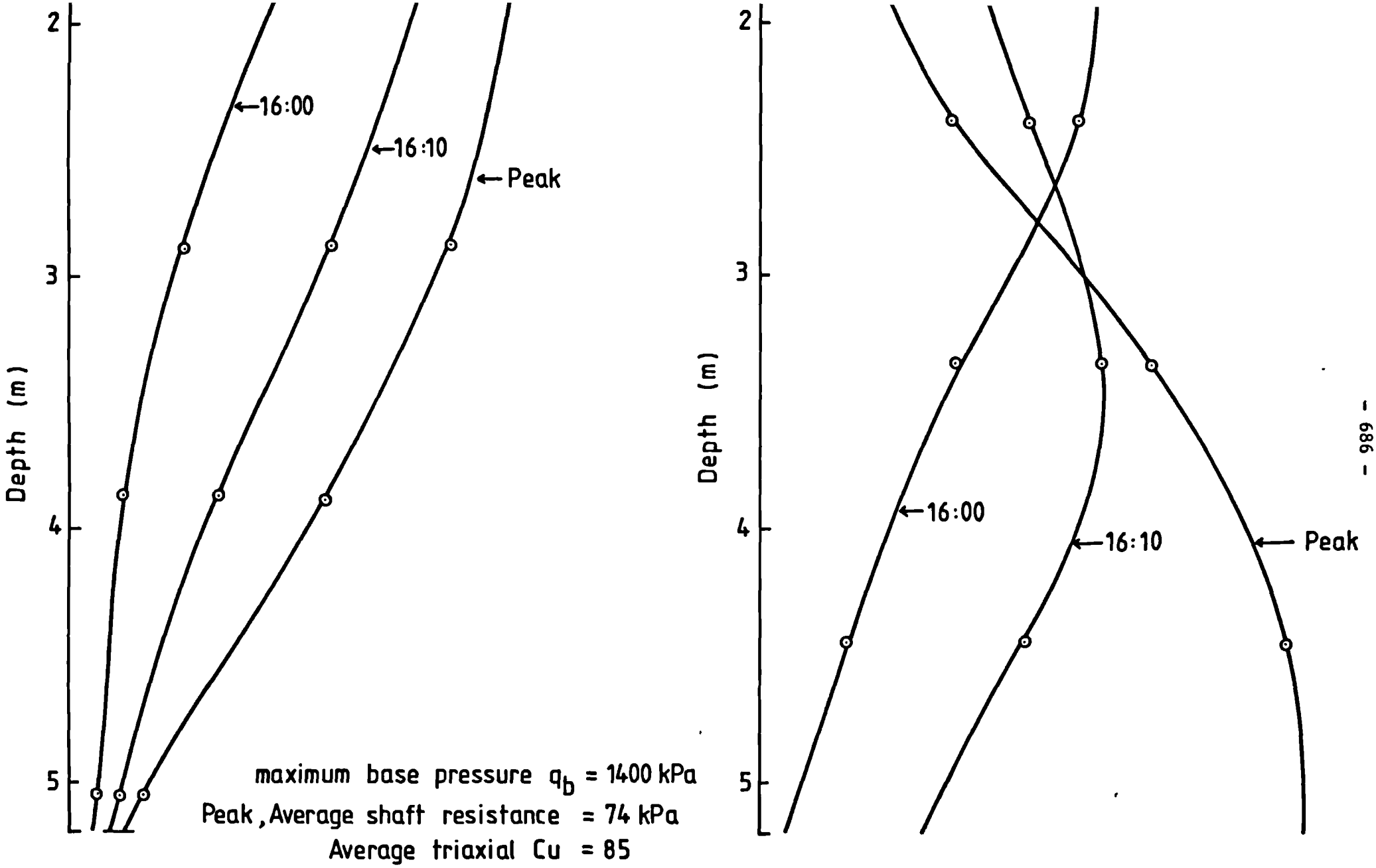


Figure 9.35. Variations of axial load and shear stress with depth for three stages of the tension test.

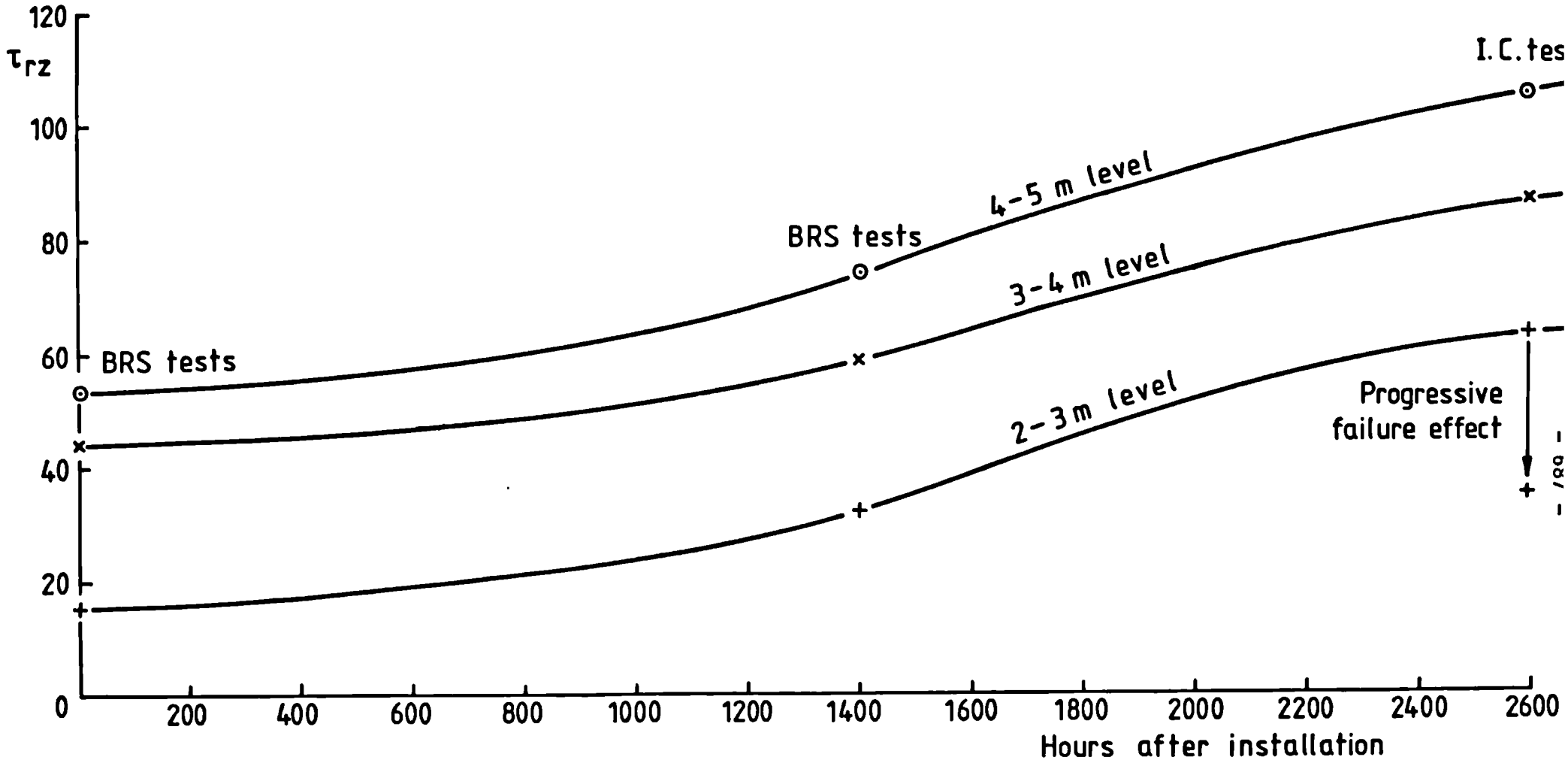


Figure 9.36. Dependence of shaft capacity on set-up time.

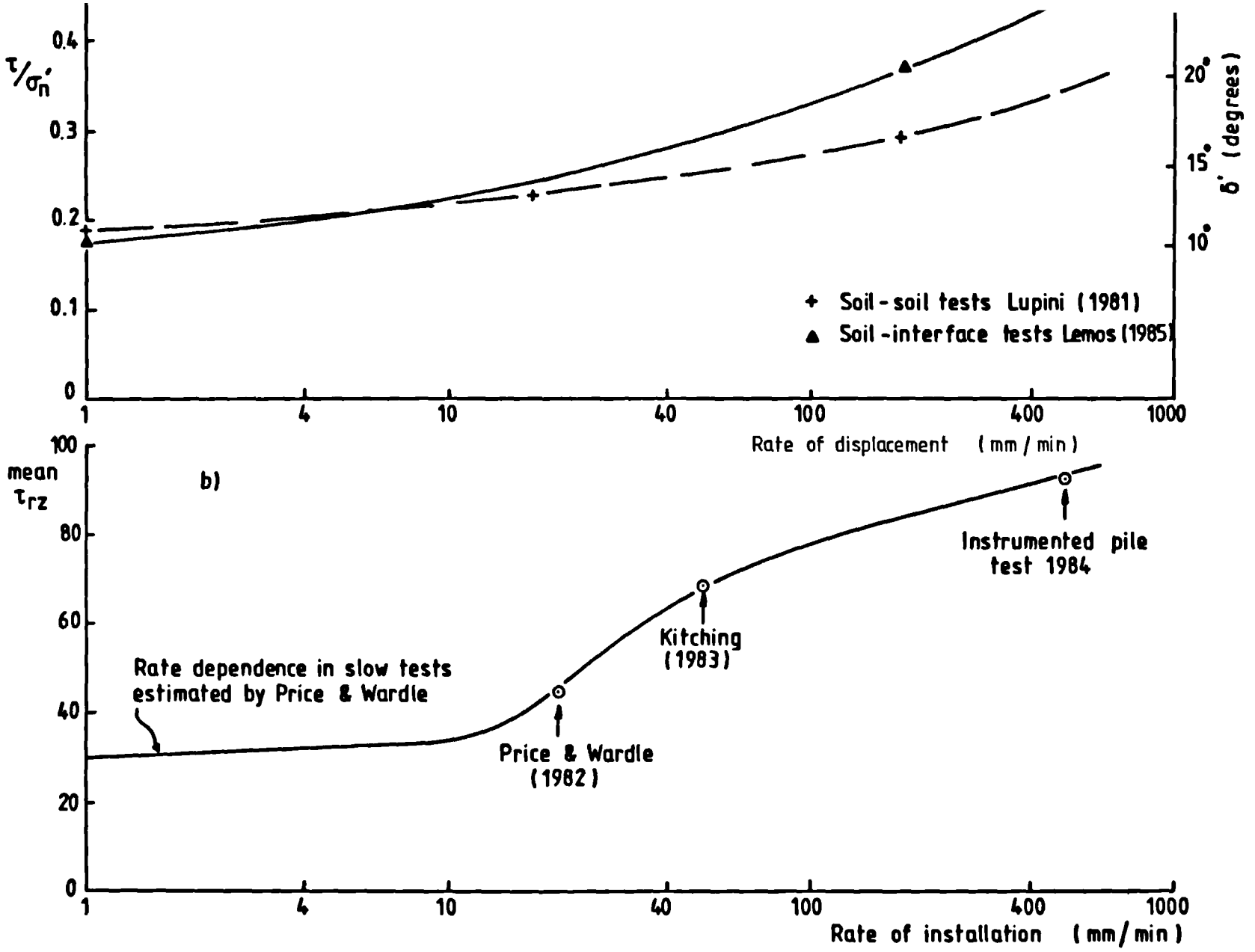


Figure 9.37. Variations of shaft resistance and residual shear strength on rate of shearing displacement.

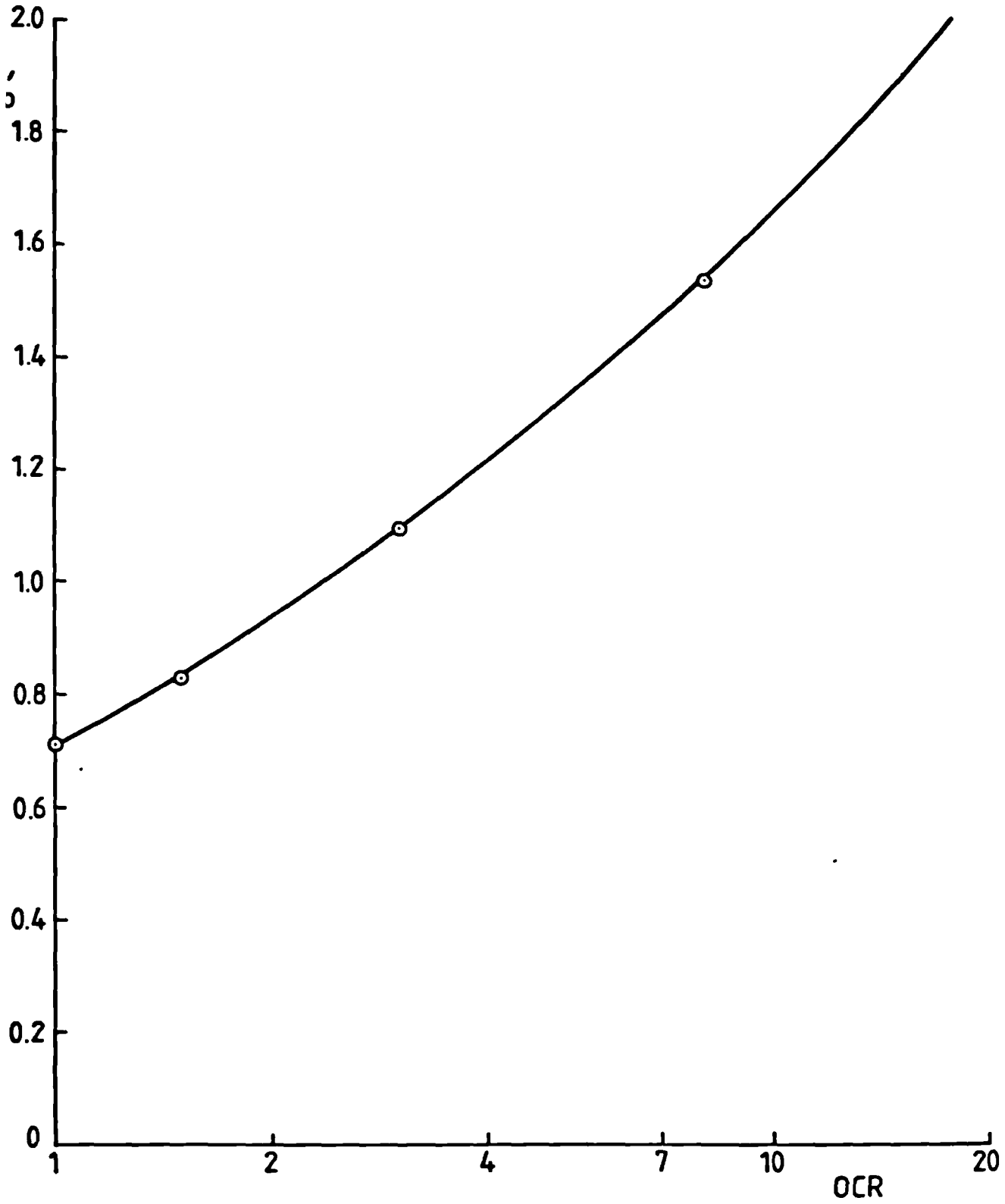


Figure 9.38. Dependence of p'_{cs}/p'_{o} on OCR, from Chapter 7.

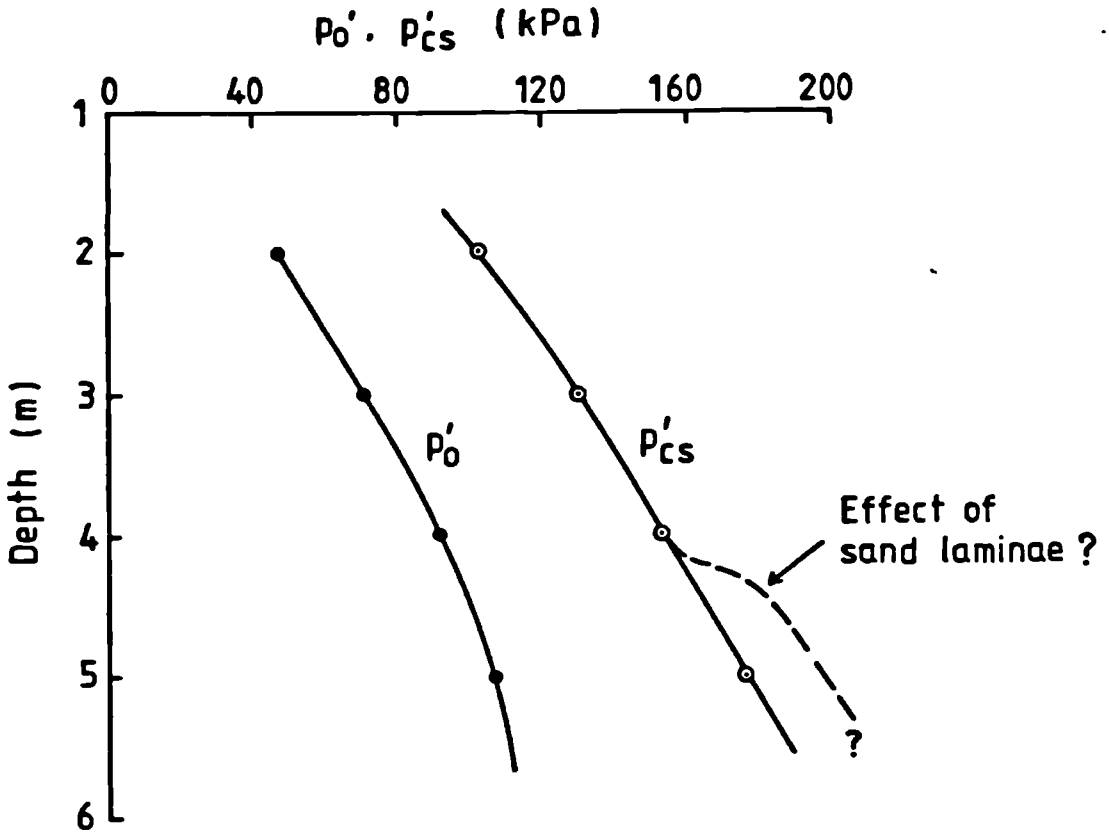


Figure 9.39. Variation of p'_{cs} with depth.

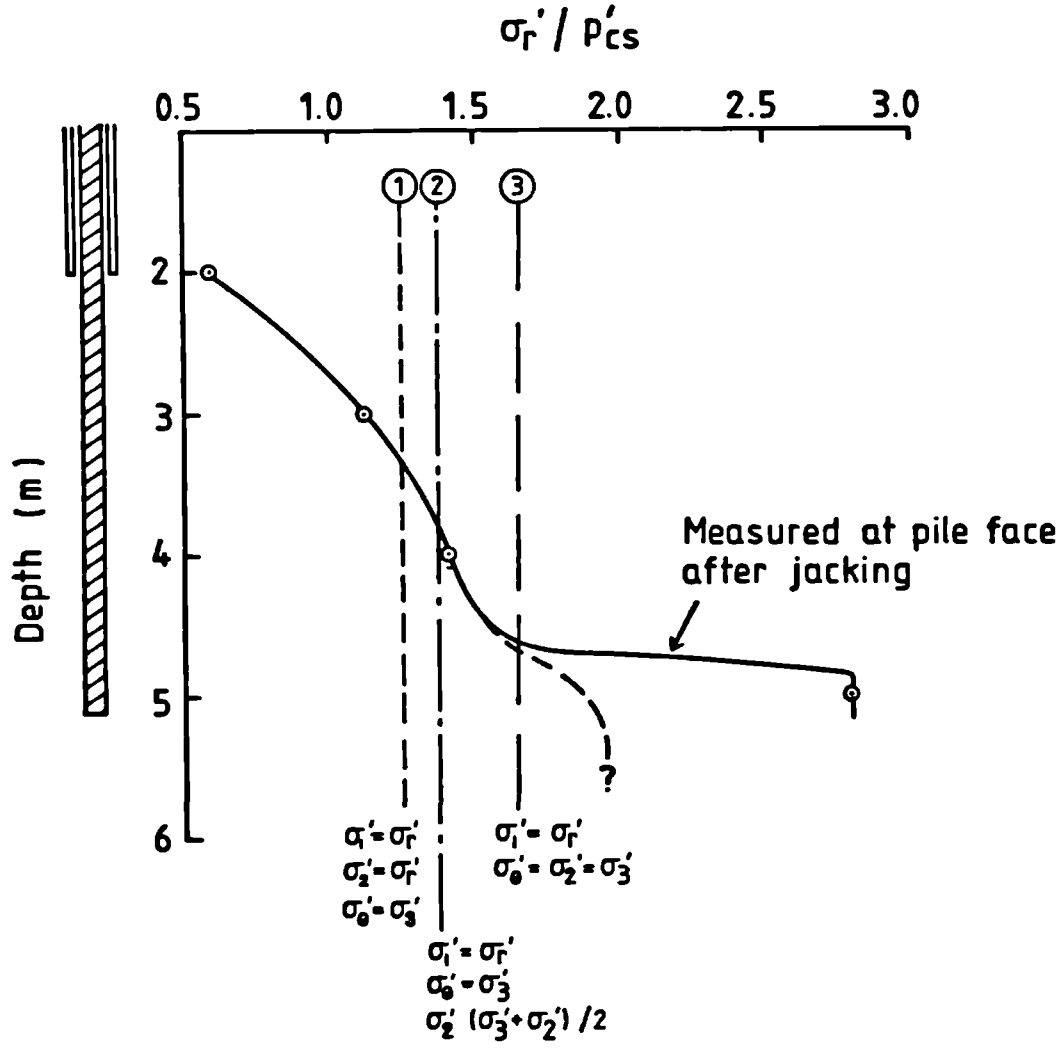


Figure 9.40. Variation of σ'_r/p'_{cs} with depth, with limiting

CHAPTER 10

Tables and Figures

(a) Parameters for Non-linear Modulus, Equations 10.1 and 10.2

A = 623	A' = 587
B = 643	B' = 412
C = 0.0007%	C' = 0.0007%
α = 1.349	α' = 1.400
α = 0.6385	γ' = 0.797

$\text{Min } \frac{E}{\sqrt{3}} = \varepsilon_{a\ min} = 0.003\%$ $\qquad \varepsilon_{v\ min} = 0.003\%$

$\text{Max } \frac{E}{\sqrt{3}} = \varepsilon_{a\ max} = 0.25\%$ $\qquad \varepsilon_{v\ max} = 0.2\%$

(b) Parameters for Modified Cam Clay, Variant , See Appendix

v_1 = 2.25

λ = 0.10

k = 0.0077 (0.03 for OCR 8)

$\blacklozenge$ = 30°

Hvorslev surface gradient w.r.t. horizontal = 7.5%

Table 10.1. Parameters for Element Test Studies

Group	Depth range	v_1	λ	k	γ' (KN/m^3)
I	0 - 20 m	2.00	0.078	0.0260	12.0
II	20 - 40 m	2.10	0.083	0.0110	11.3
III	40 - 70 m	2.25	0.100	0.0077	10.7
IV	70 - 82 m	2.20	0.091	0.0070	11.1
V	82 - 170 m	2.20	0.091	0.0070	11.1

Table 10.2. Parameters for Layers I to V

Group	C_{vs}	Time factor, T_v		% dissipation	
	m^2/yr	6 months	10 years	6 months	10 years.
I	2	0.88	17.6	30	90
II	6	2.64	52.8	50	95
III	12	5.28	105.6	70	100
IV	12	5.28	105.6	70	100

Table 10.3. Estimates of the rate of equilibration after pile installation

Soil Group	σ'_r/σ'_r initial	
	6 months after Installation	10 years after Installation
I	1.0	1.5
II	1.0	1.5
III	0.9	1.2
IV	0.9	1.2

Table 10.4. Estimates of radial effective stress changes at pile face, for two stages after installation

Layer	Stresses at pile face σ'_z/σ'_{zo}	σ'_r/σ'_{zo}	$\sigma'_\theta/\sigma'_{zo}$	Undisturbed K_o
I 0 - 10 m	1.65	1.4	1.2	1.62
I 10 - 20 m	1.15	1.1	1.0	0.95
II	1.30	0.72	0.60	0.72
III	1.0	0.50	0.45	0.55
IV	1.0	0.50	0.45	0.55
V	1.0	0.55	0.55	0.55

Table 10.5. Effective stresses at the pile face, 6 months after installation

Layer	Stresses at pile face σ'_z/σ'_{zo}	σ'_r/σ'_{zo}	$\sigma'_\theta/\sigma'_{zo}$	Undisturbed K_o
I 0 - 10 m	1.80	2.50	1.60	1.65
I 10 - 20 m	1.80	2.00	1.40	0.95
II	1.7	1.08	0.90	0.72
III	1.4	0.70	0.46	0.55
IV	1.4	0.70	0.46	0.55
V	1.0	0.55	0.55	0.55

Table 10.6. Effective stresses at the pile face, 10 years after installation

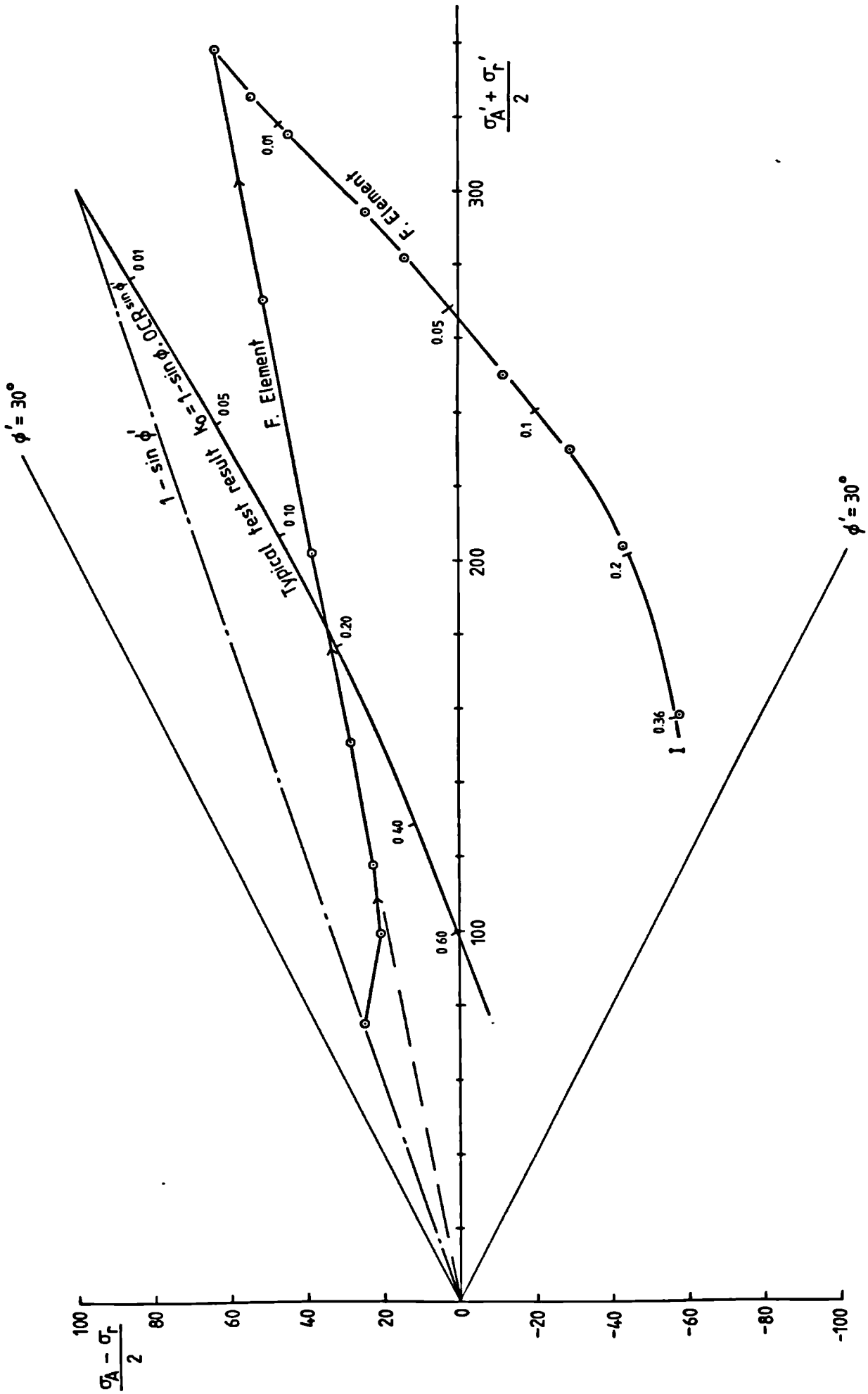


Figure 10.1. Finite element predictions; stress paths for K_o compression and swelling.

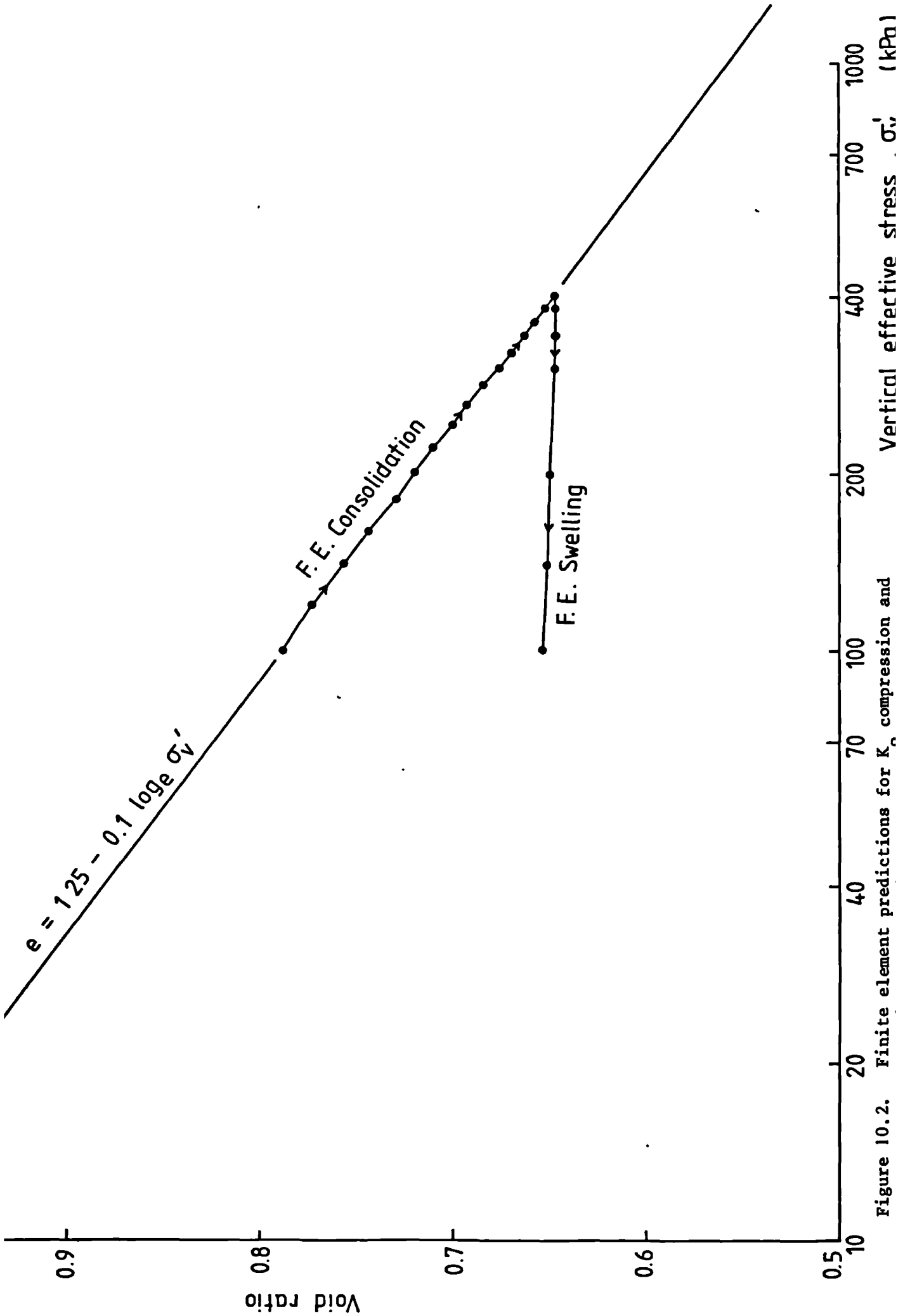


Figure 10.2. Finite element predictions for K_o compression and

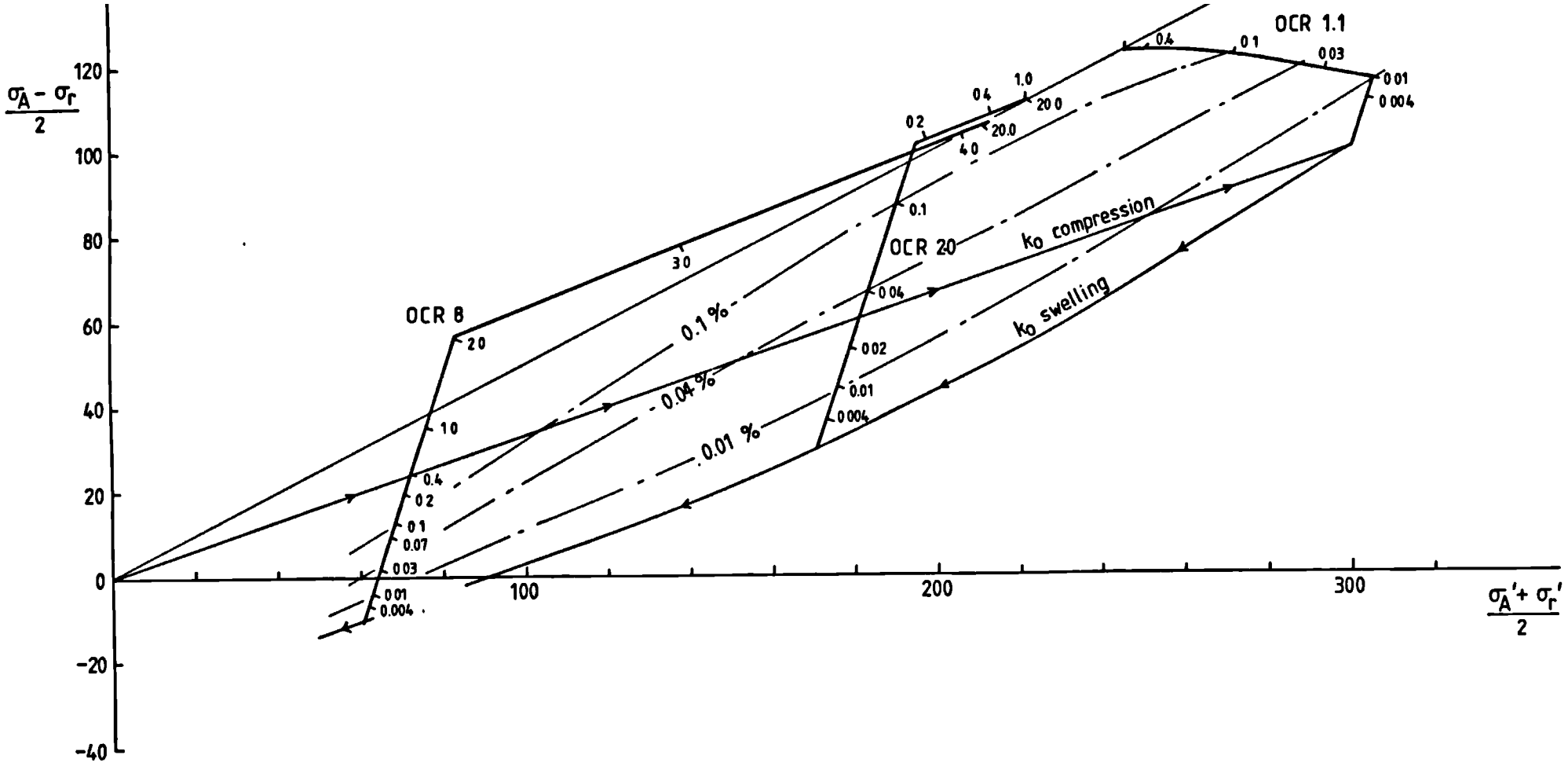


Figure 10.3. Finite element predictions; stress paths and strains for undrained compression at three OCR's.

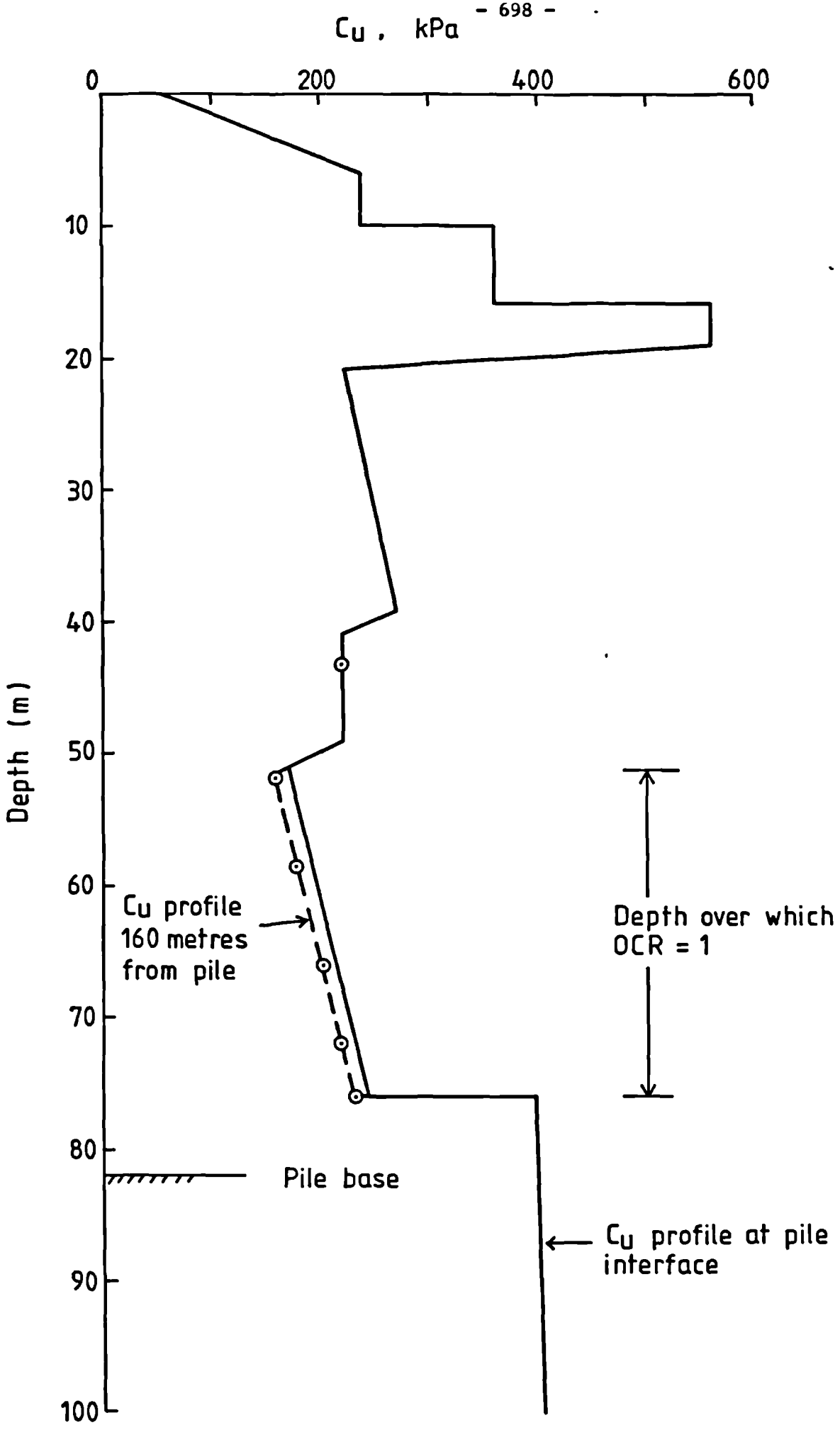


Figure 10.4. C_u - depth variations; Runs A and B.

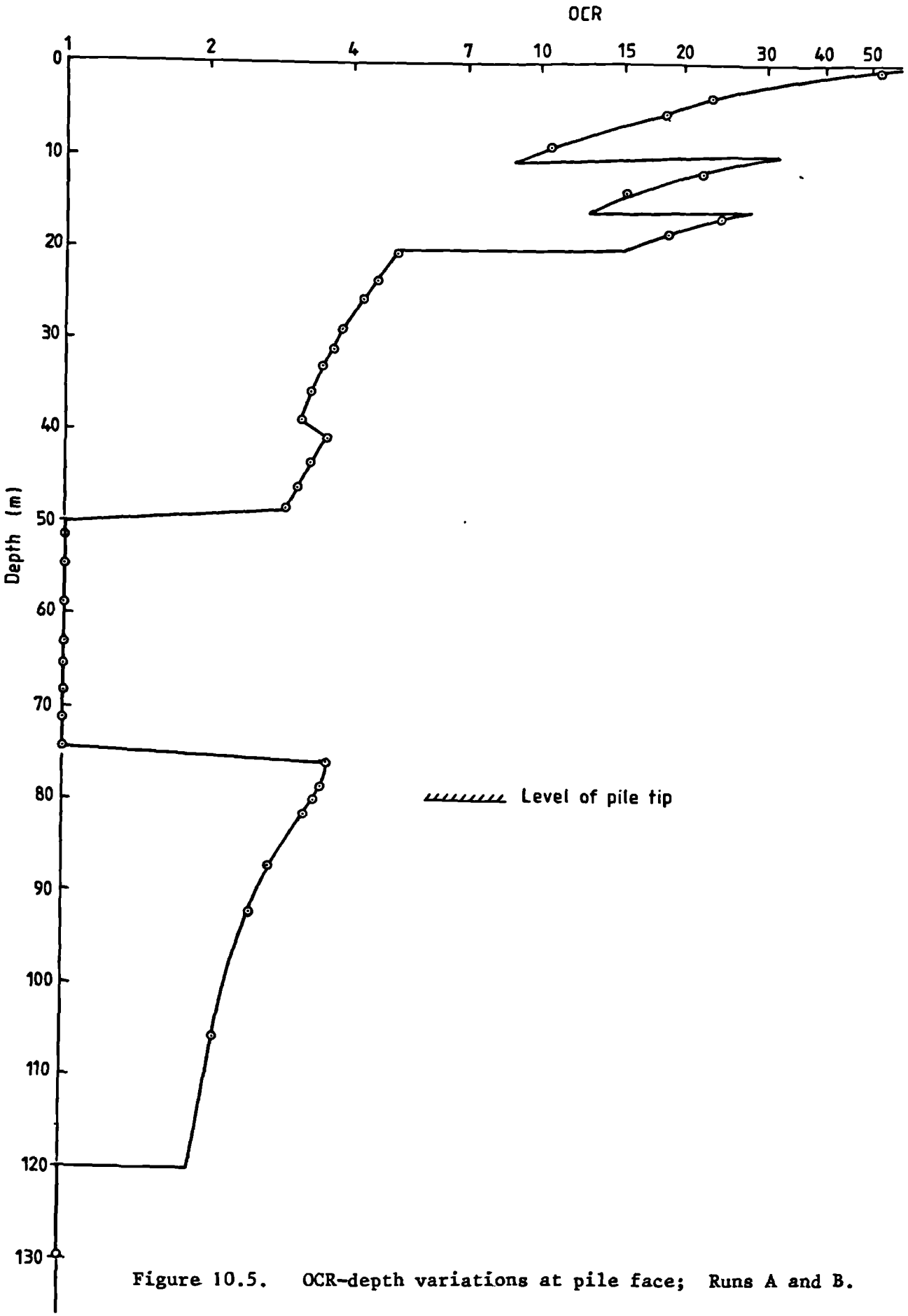


Figure 10.5. OCR-depth variations at pile face; Runs A and B.

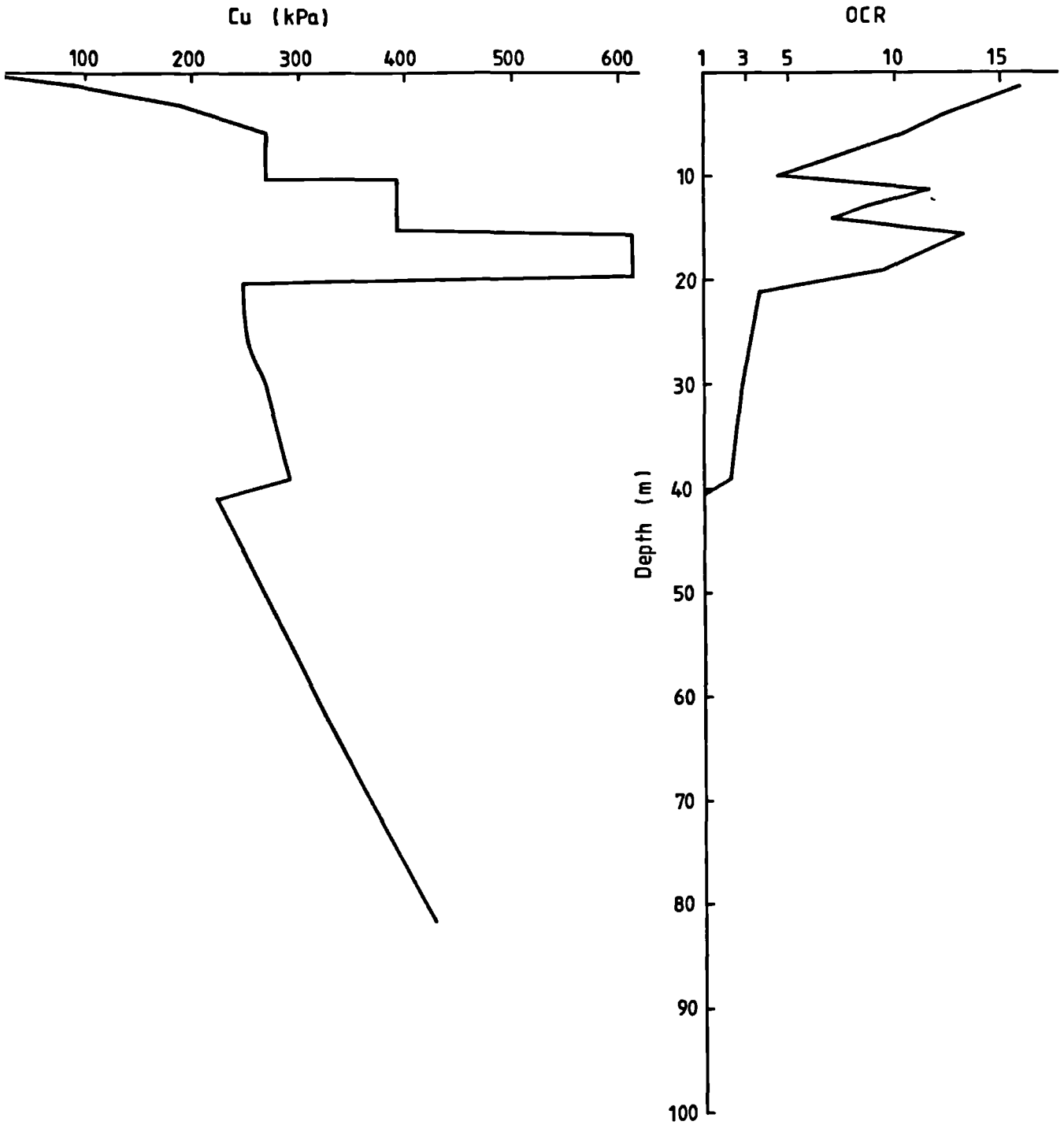


Figure 10.6. C_u and OCR variations at pile face; Run C.

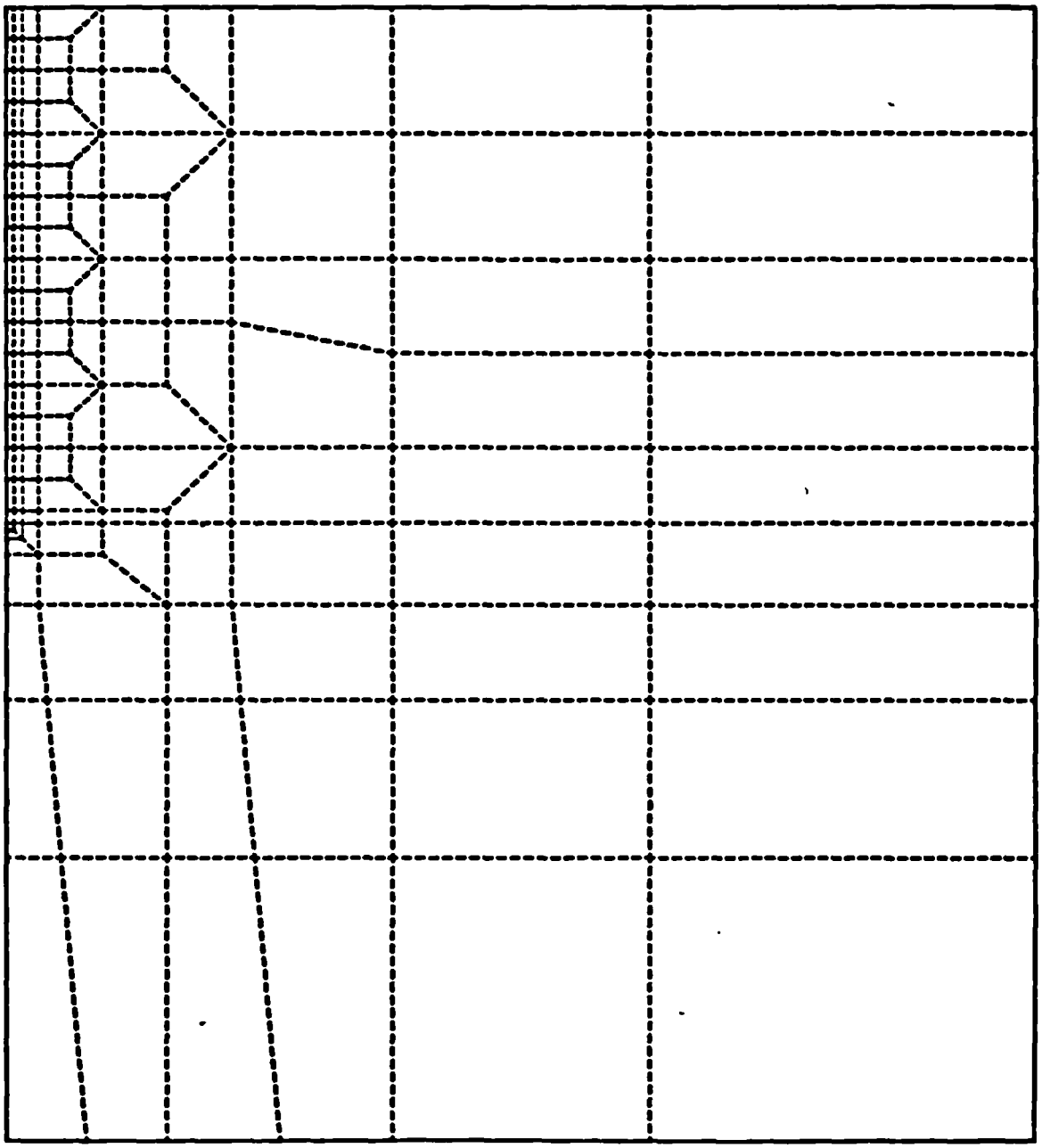


Figure 10.7.

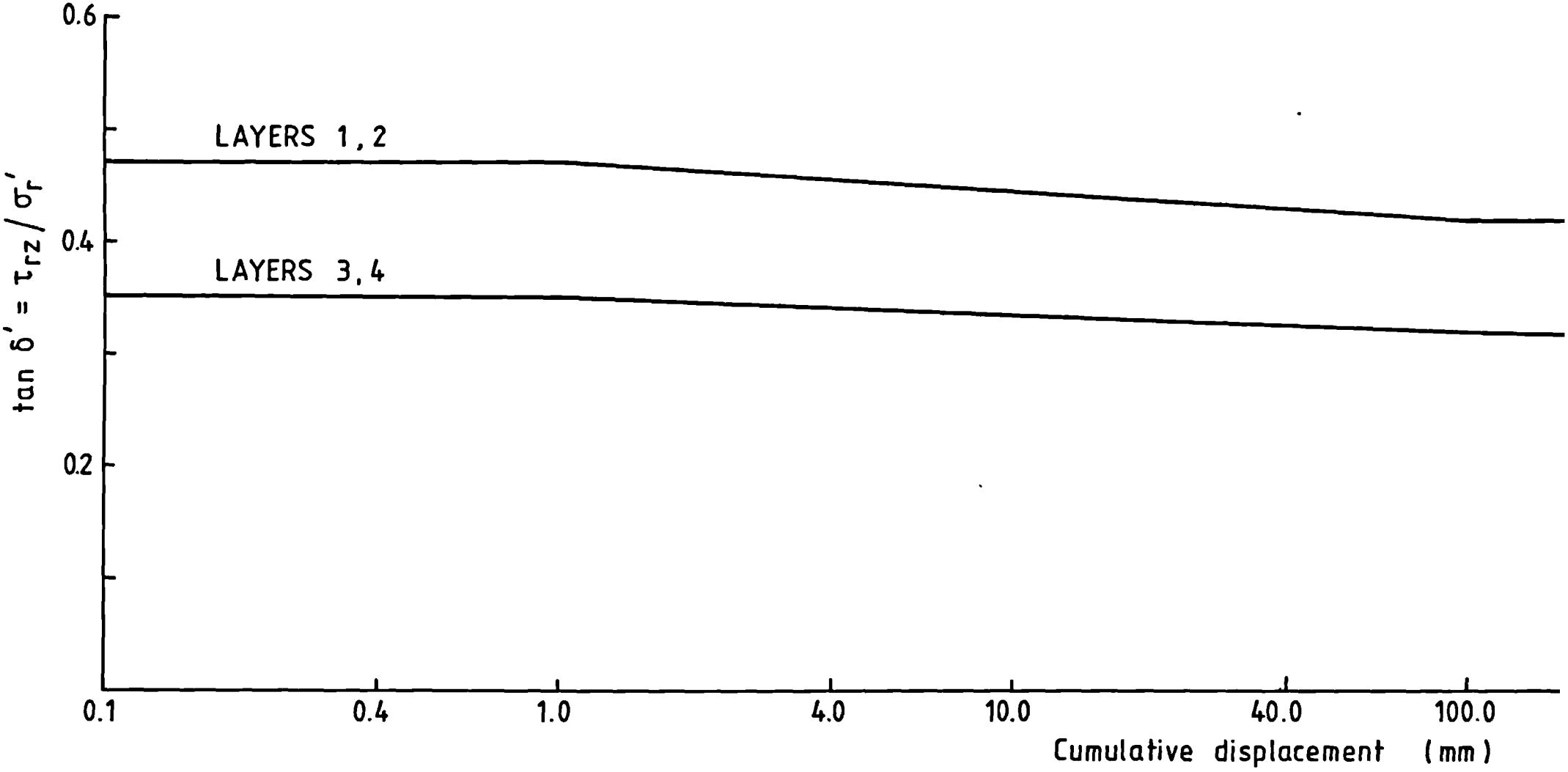


Figure 10.8. Interface skin friction characteristics specified for Runs B and C.

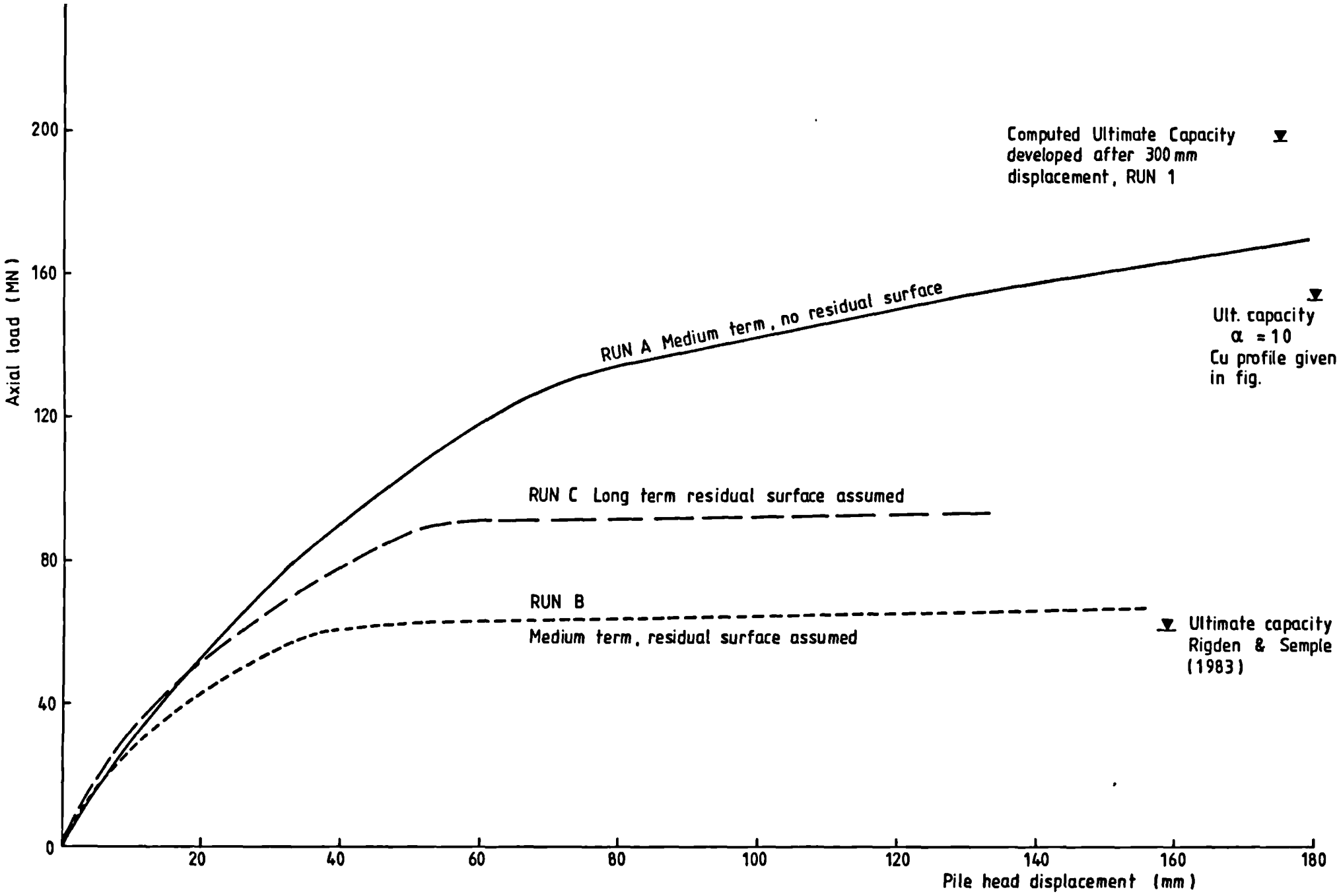


Figure 10.9. Single pile load-displacement curves for Runs A, B and C.

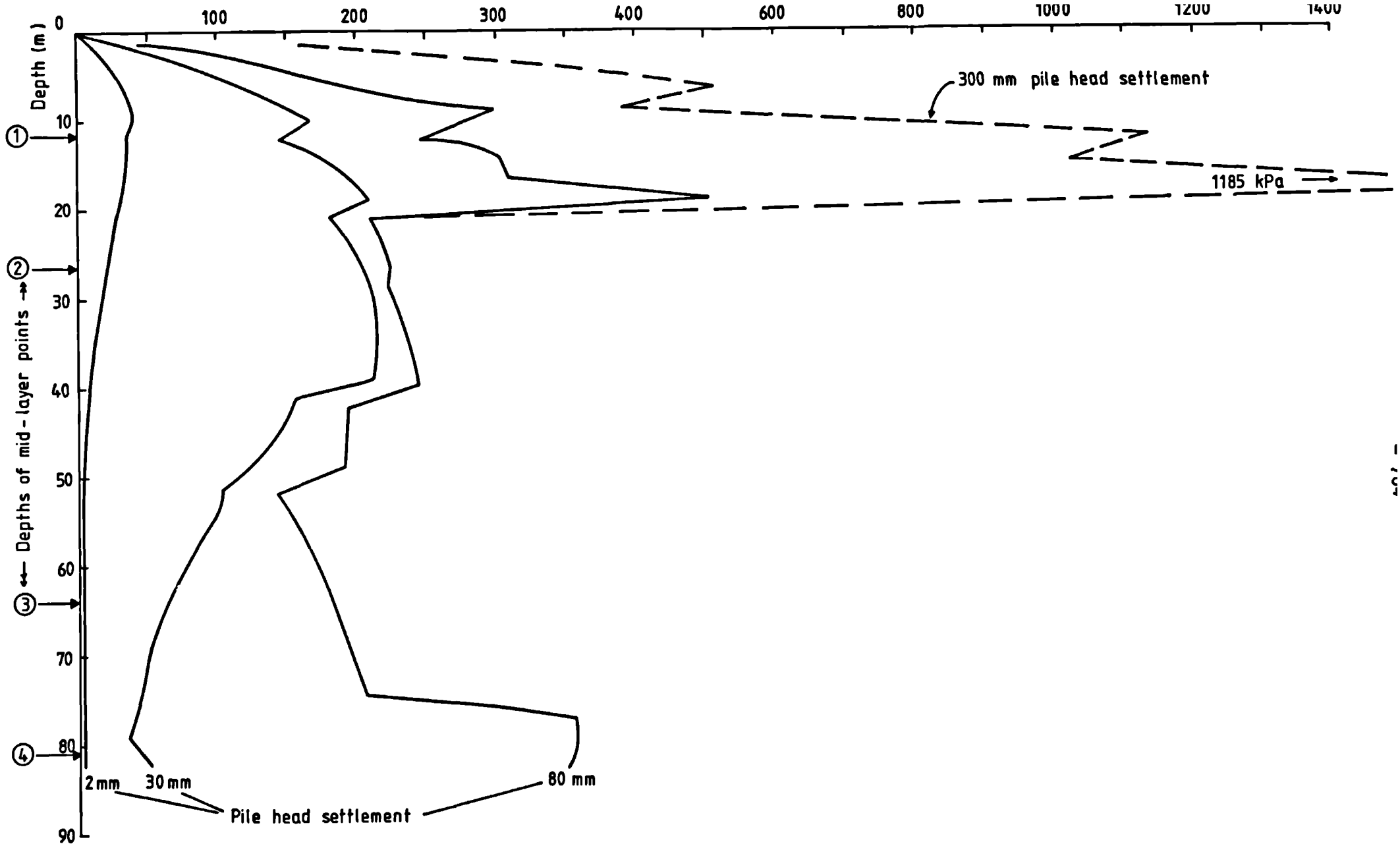


Figure 10.10. Skin friction-depth plots for Run A at three displacements.

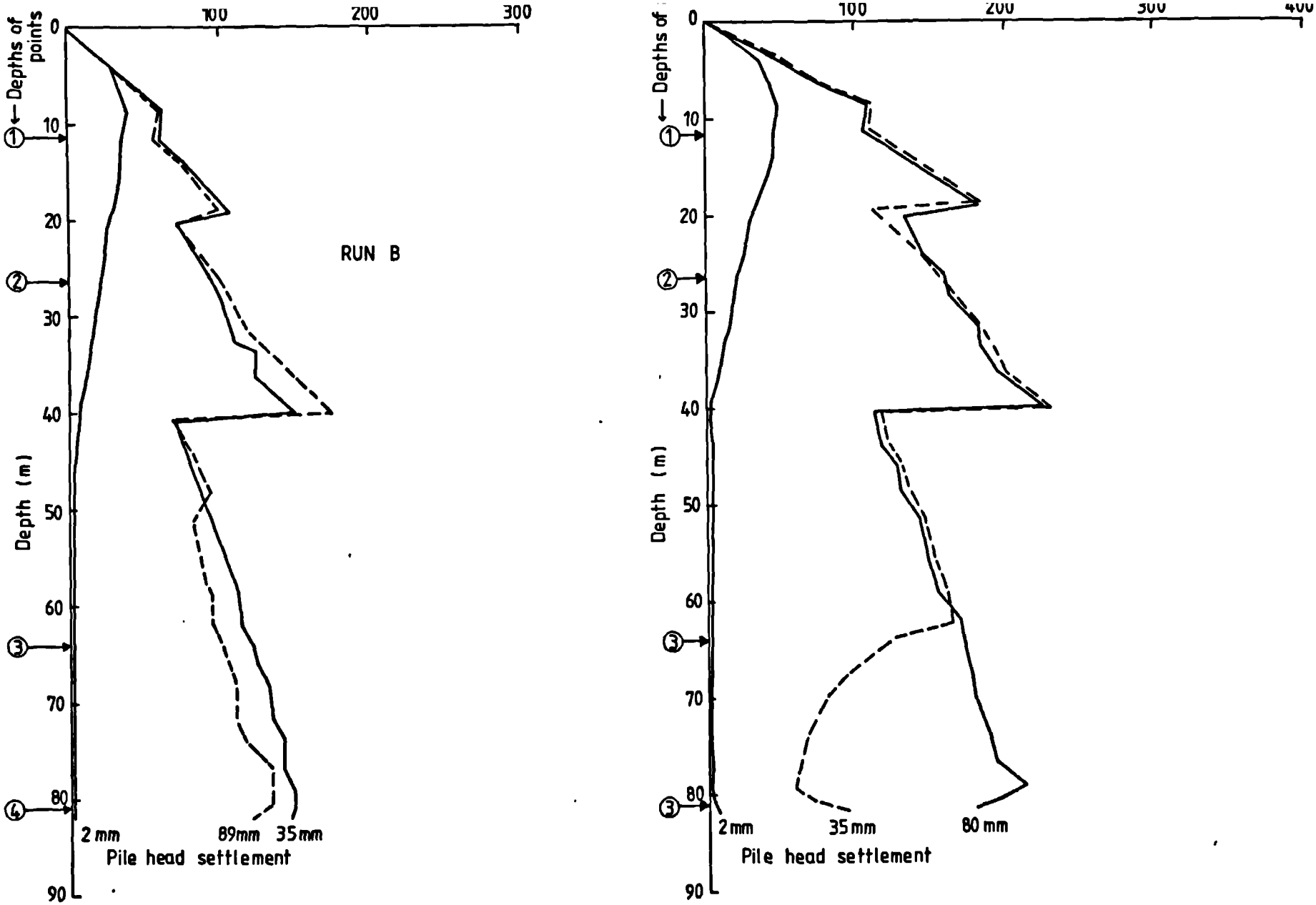
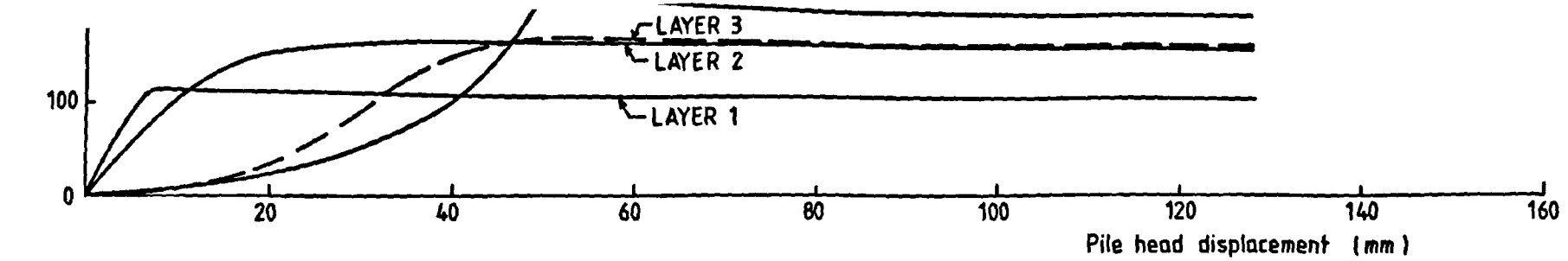
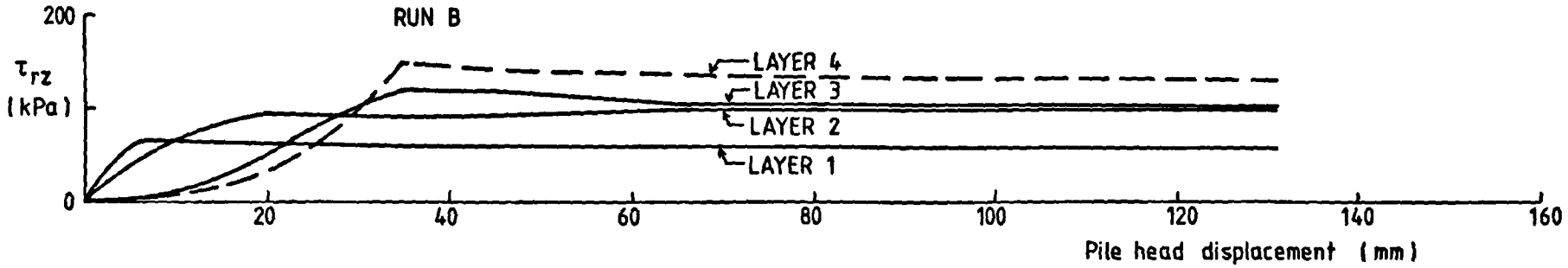
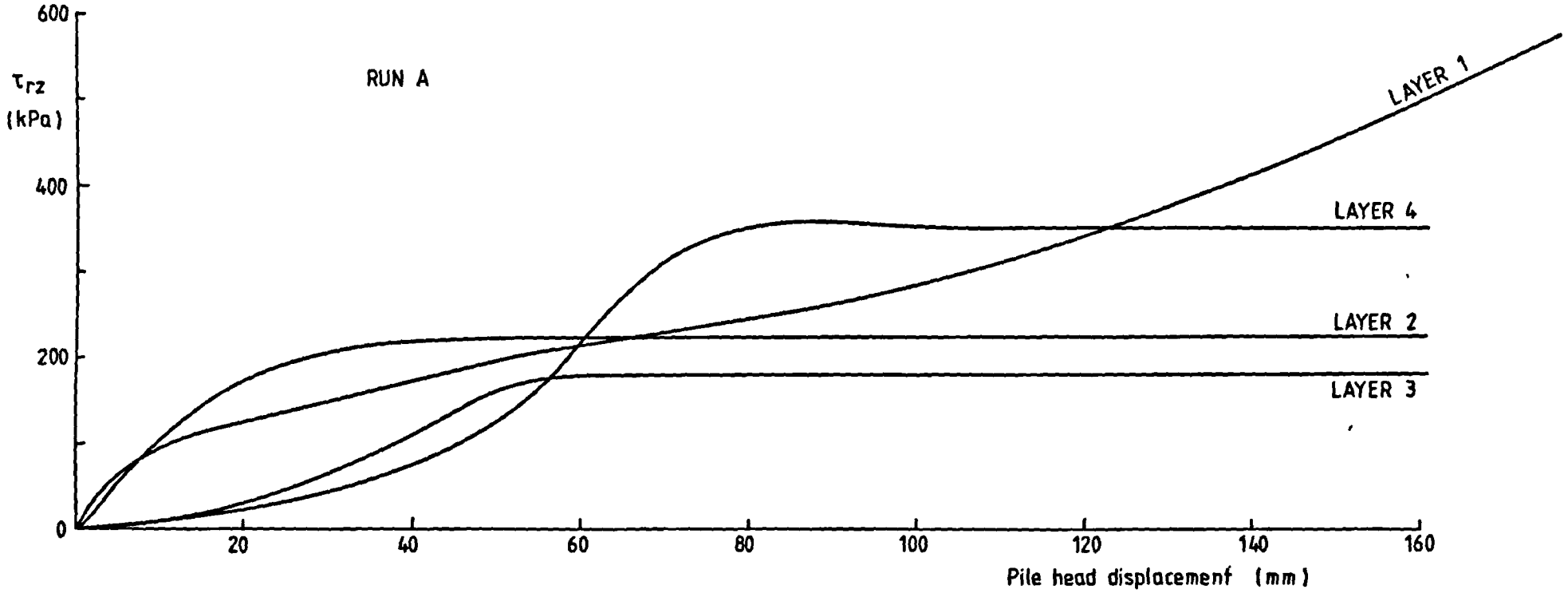


Figure 10.11. Skin friction-depth plots for Runs B and C at three displacements.


LAYER 3
LAYER 2
LAYER 1
100
0
20
40
60
80
100
120
140
160
Pile head displacement (mm)


RUN B
200
τ_{rz}
(kPa)
LAYER 4
LAYER 3
LAYER 2
LAYER 1
0
20
40
60
80
100
120
140
160
Pile head displacement (mm)


600
τ_{rz}
(kPa)
RUN A
LAYER 1
400
LAYER 4
LAYER 2
200
LAYER 3
0
20
40
60
80
100
120
140
160
Pile head displacement (mm)

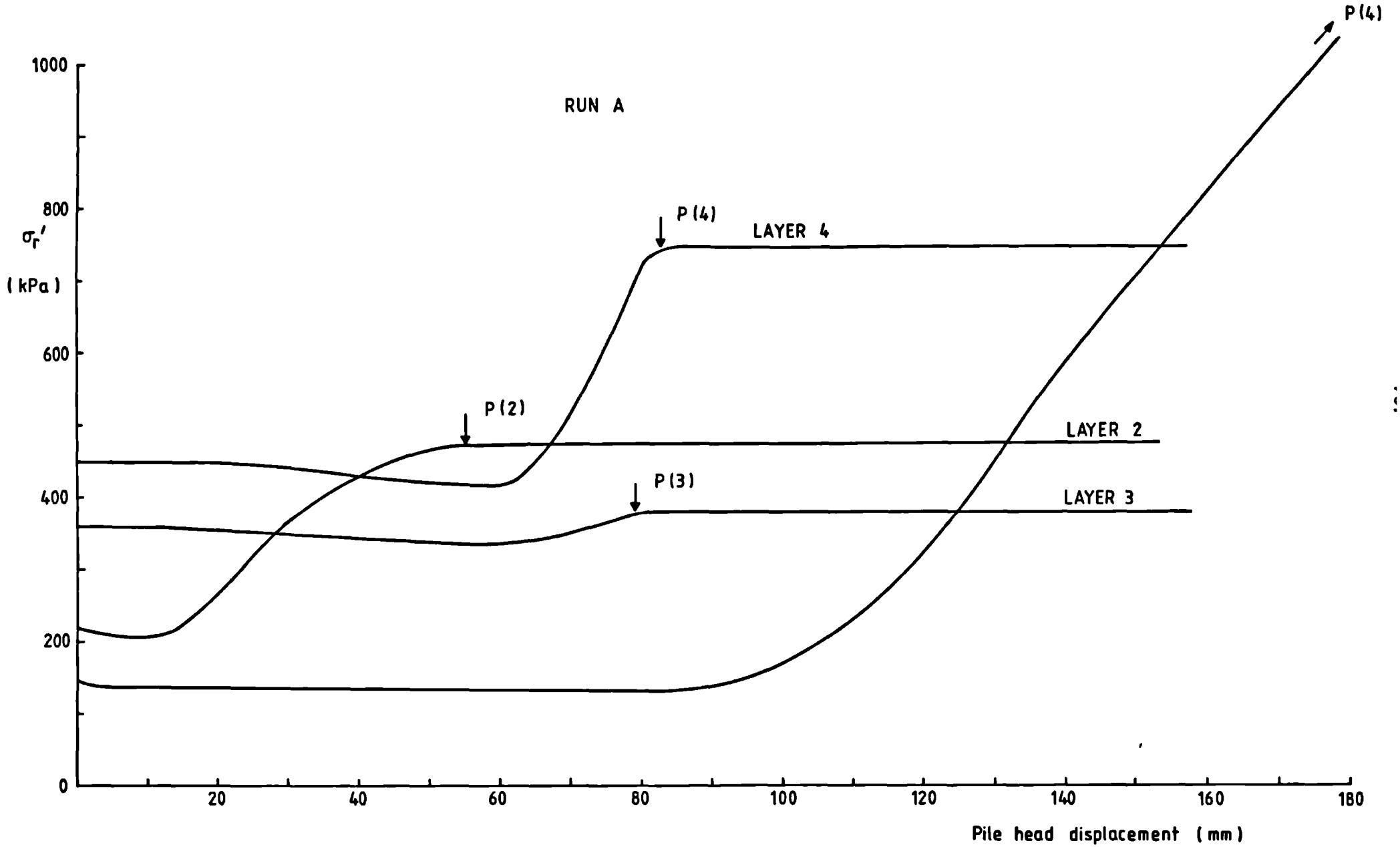
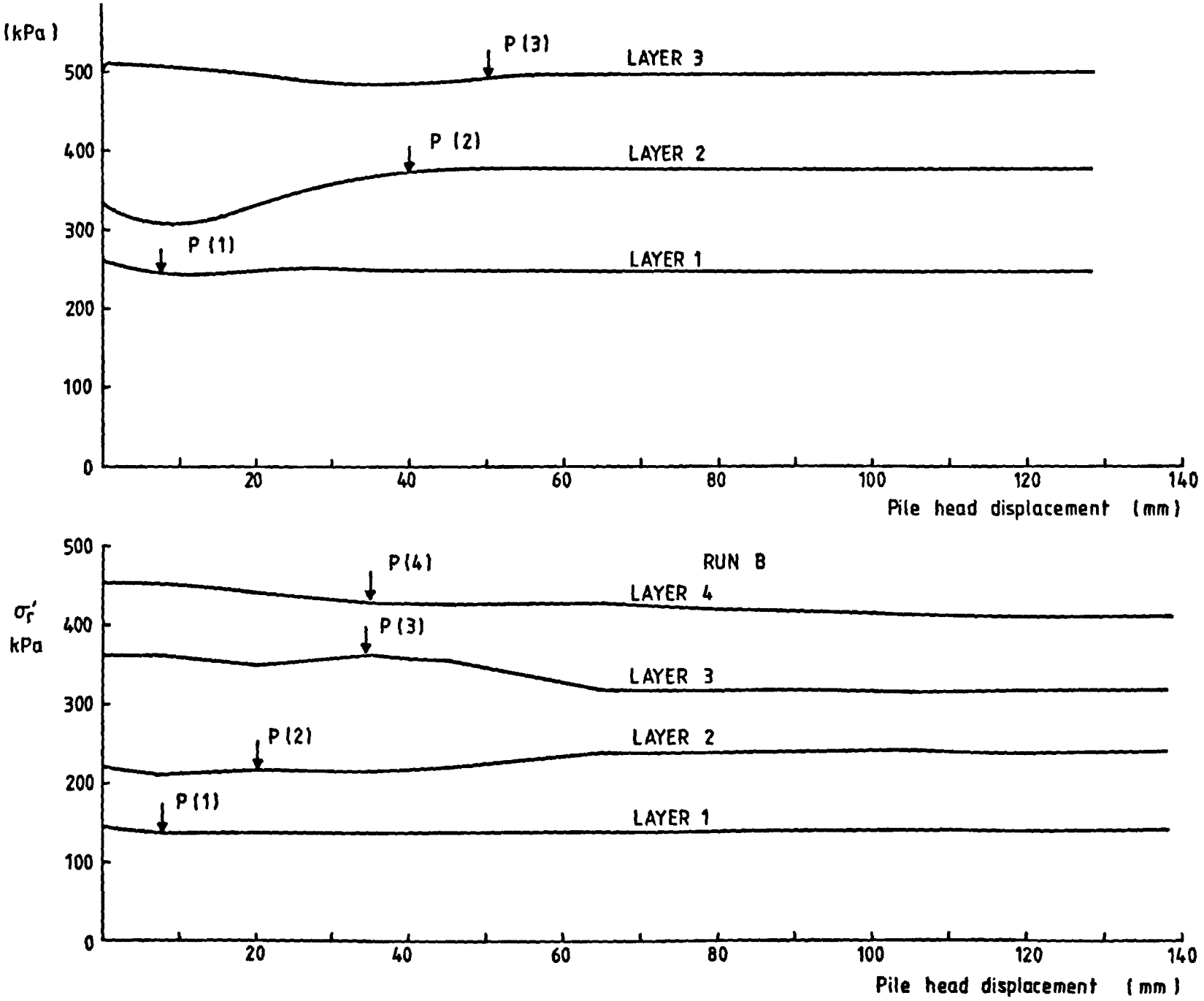
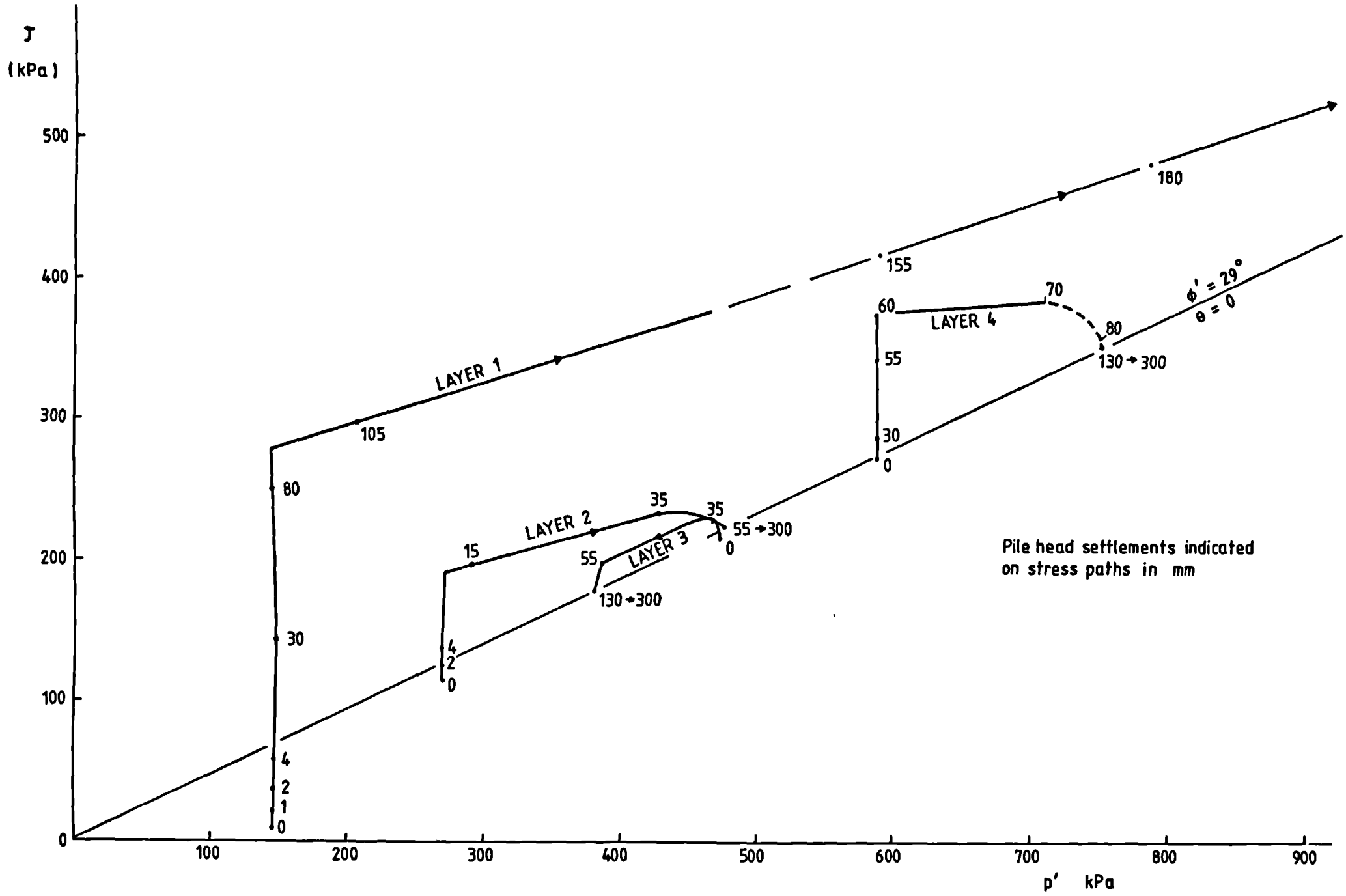


Figure 10.13. Development of σ'_r with displacement; Run A.



with displacement: Runs B and C.



Effective stress paths followed by four typical points with displacements indicated: Run A

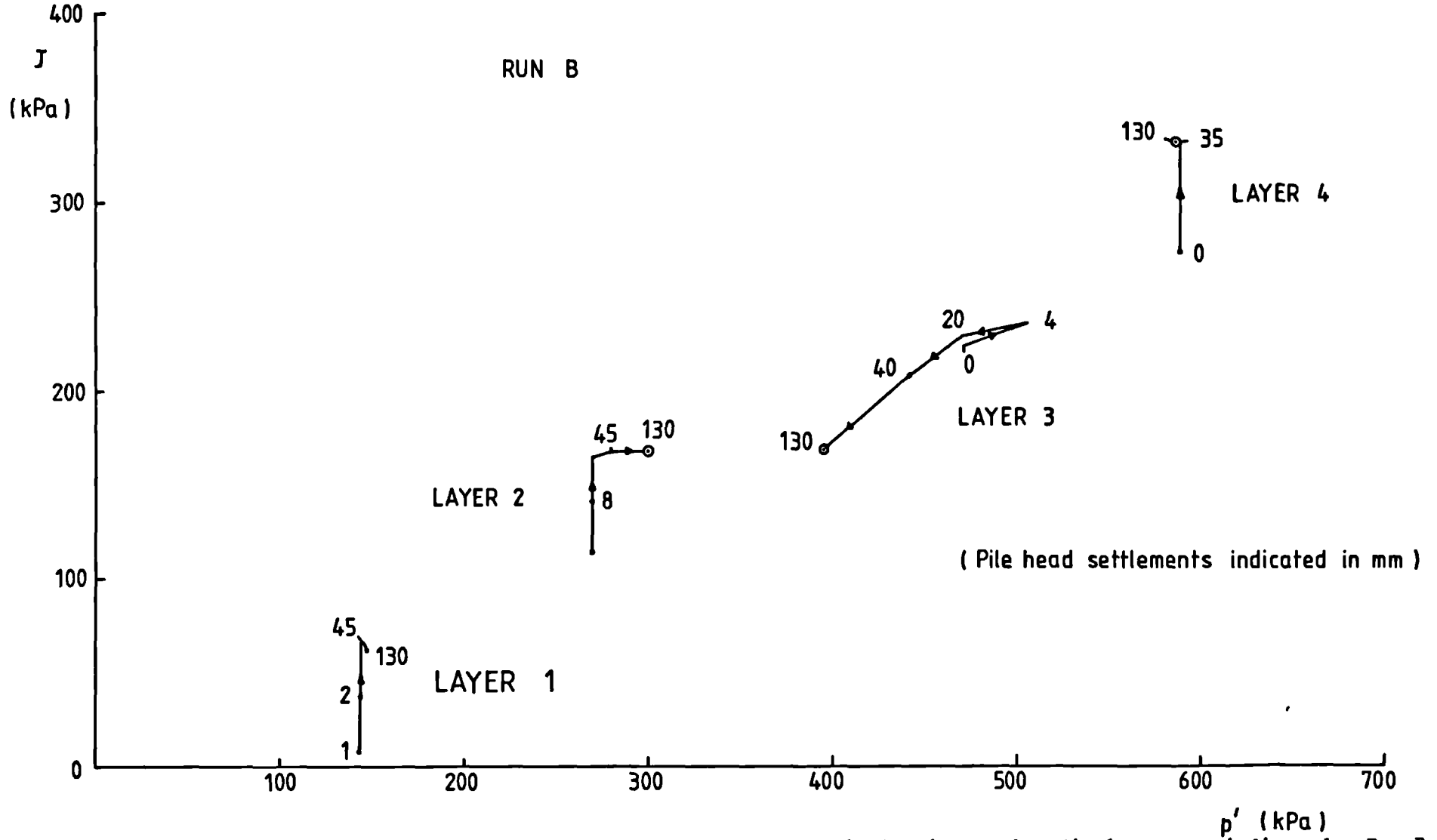


Figure 10.16. Effective stress paths followed by four typical points, with displacements indicated; Run B.

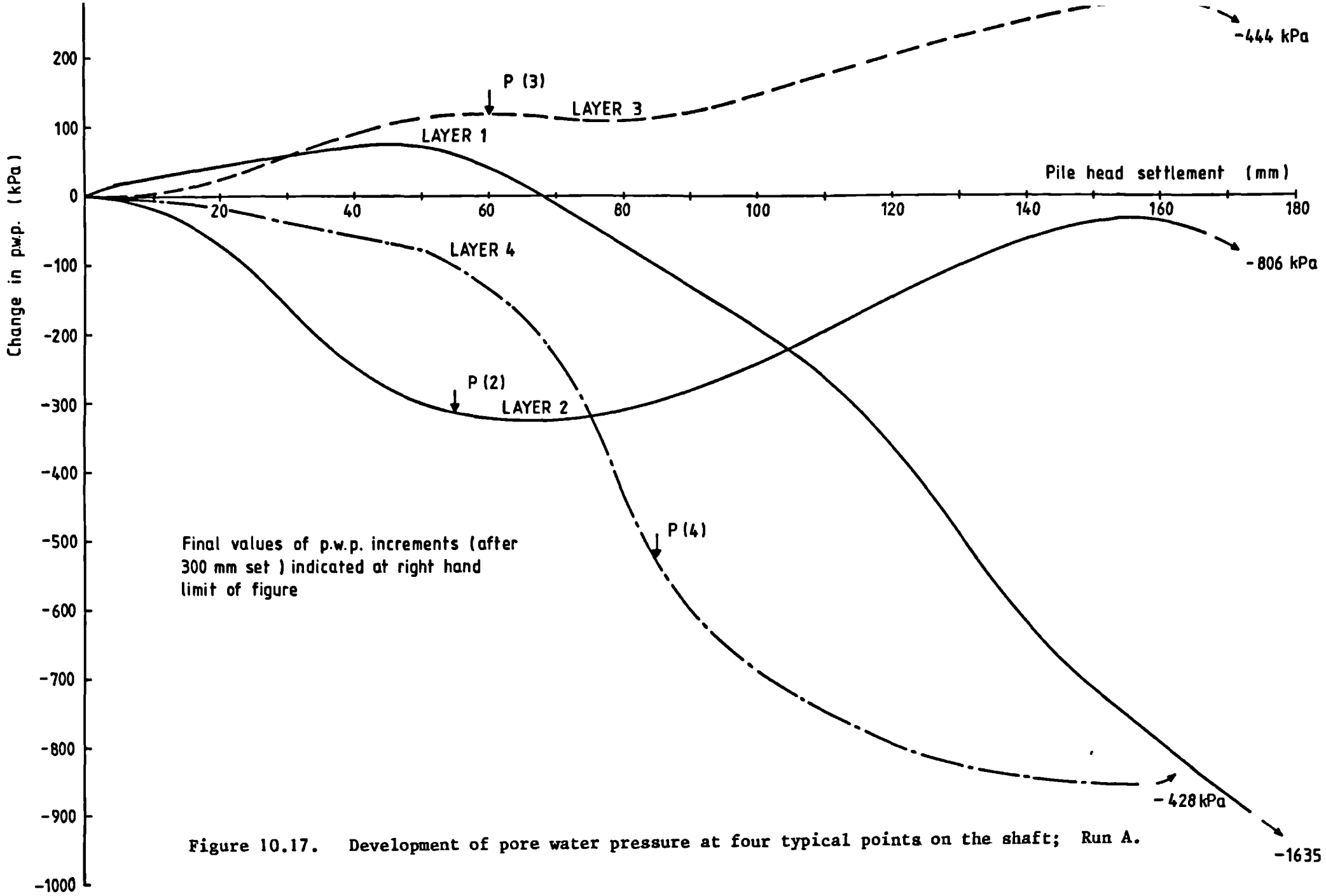


Figure 10.17. Development of pore water pressure at four typical points on the shaft; Run A.

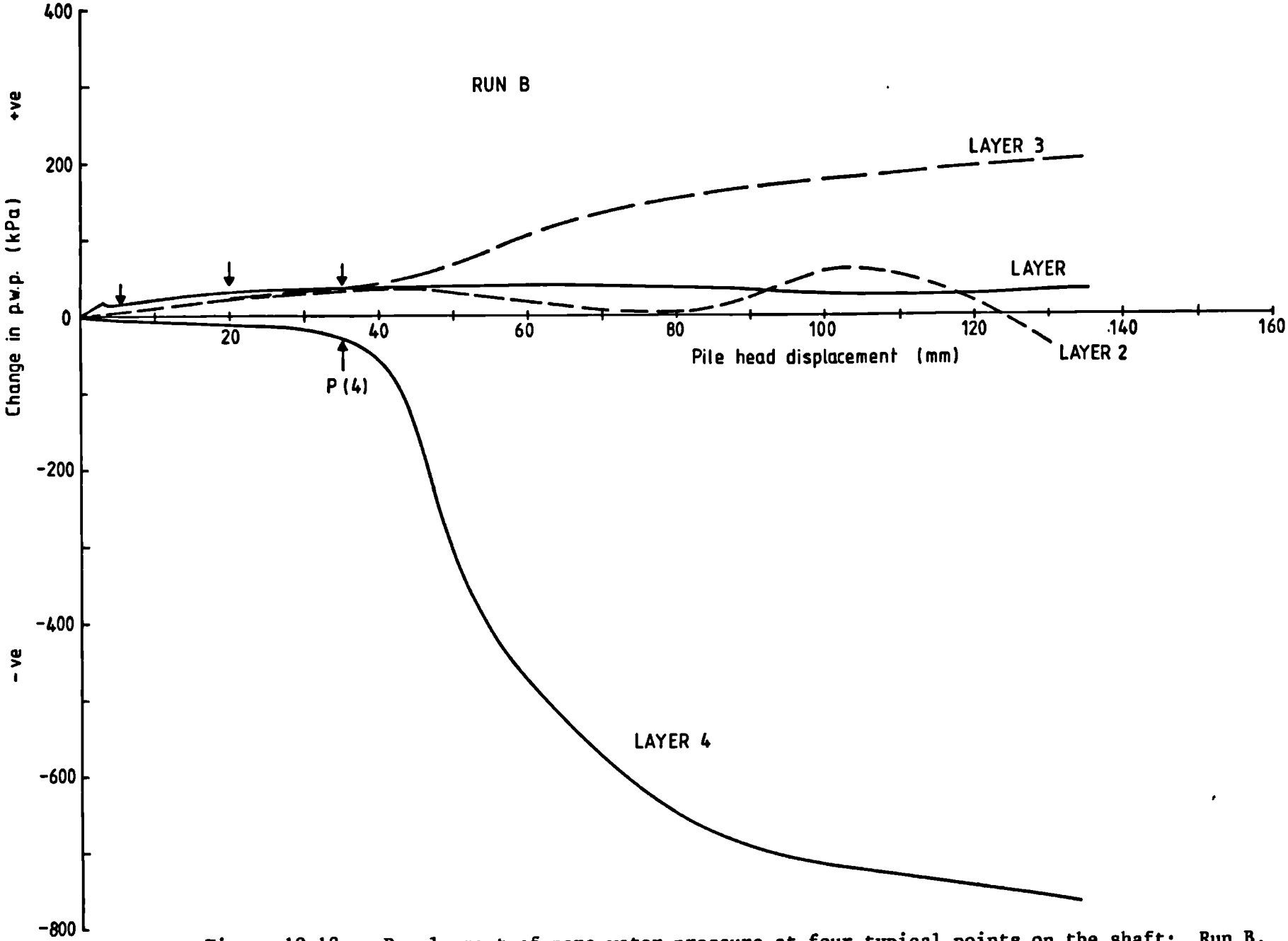


Figure 10.18. Development of pore water pressure at four typical points on the shaft; Run B.

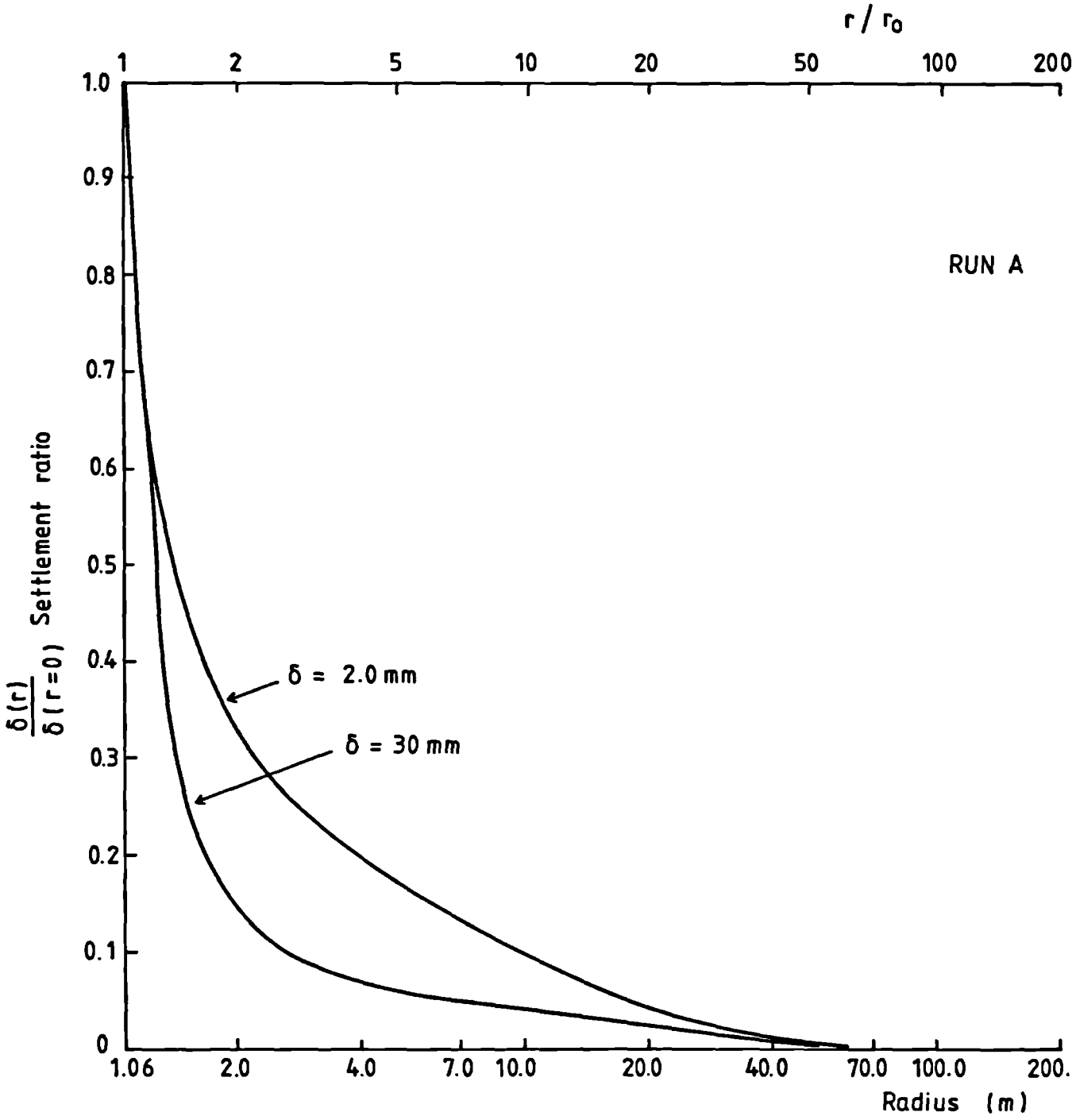


Figure 10.19. Profiles of ground surface displacement at two settlements; Run A.

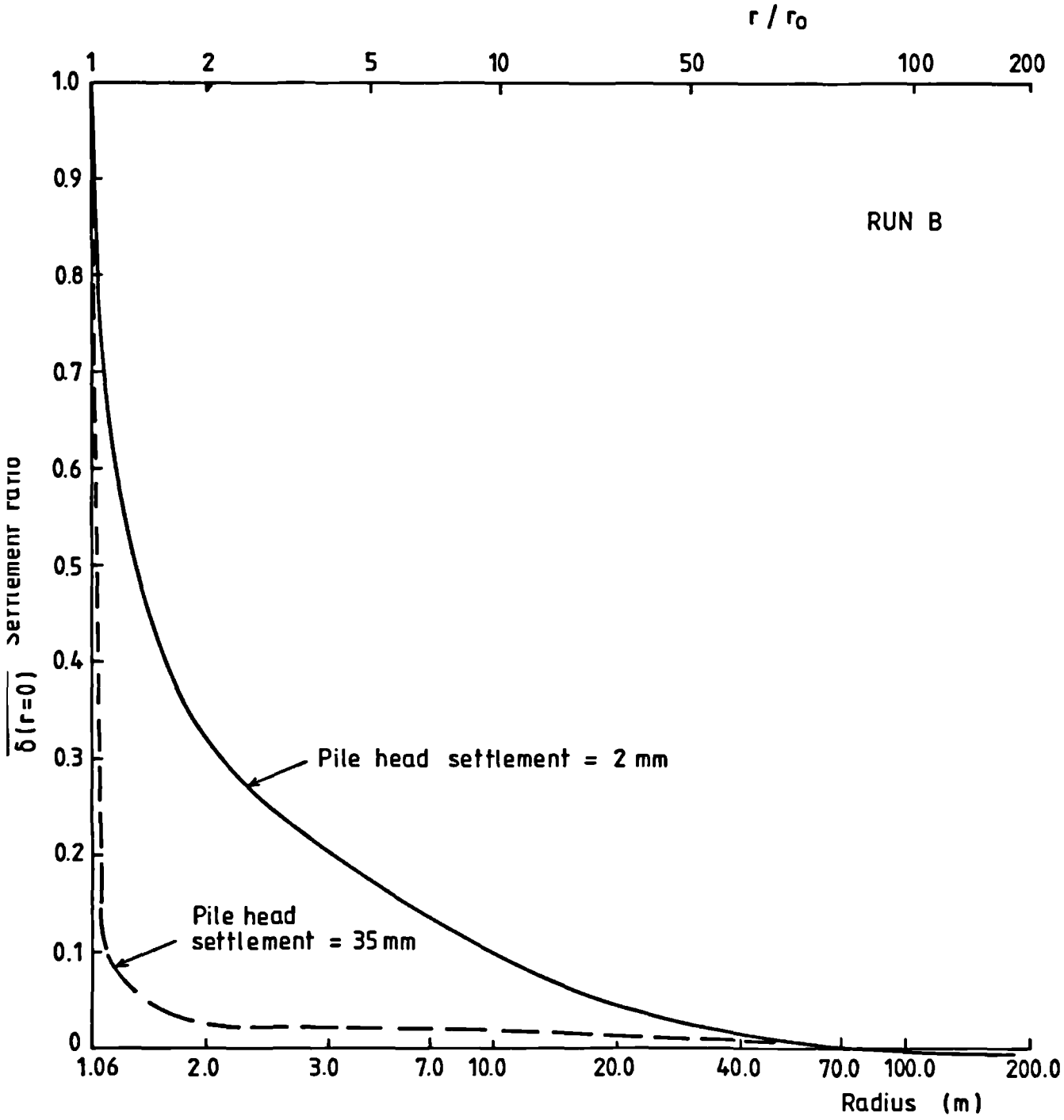


Figure 10.20. Profiles of ground surface displacement at two settlements; Run B.

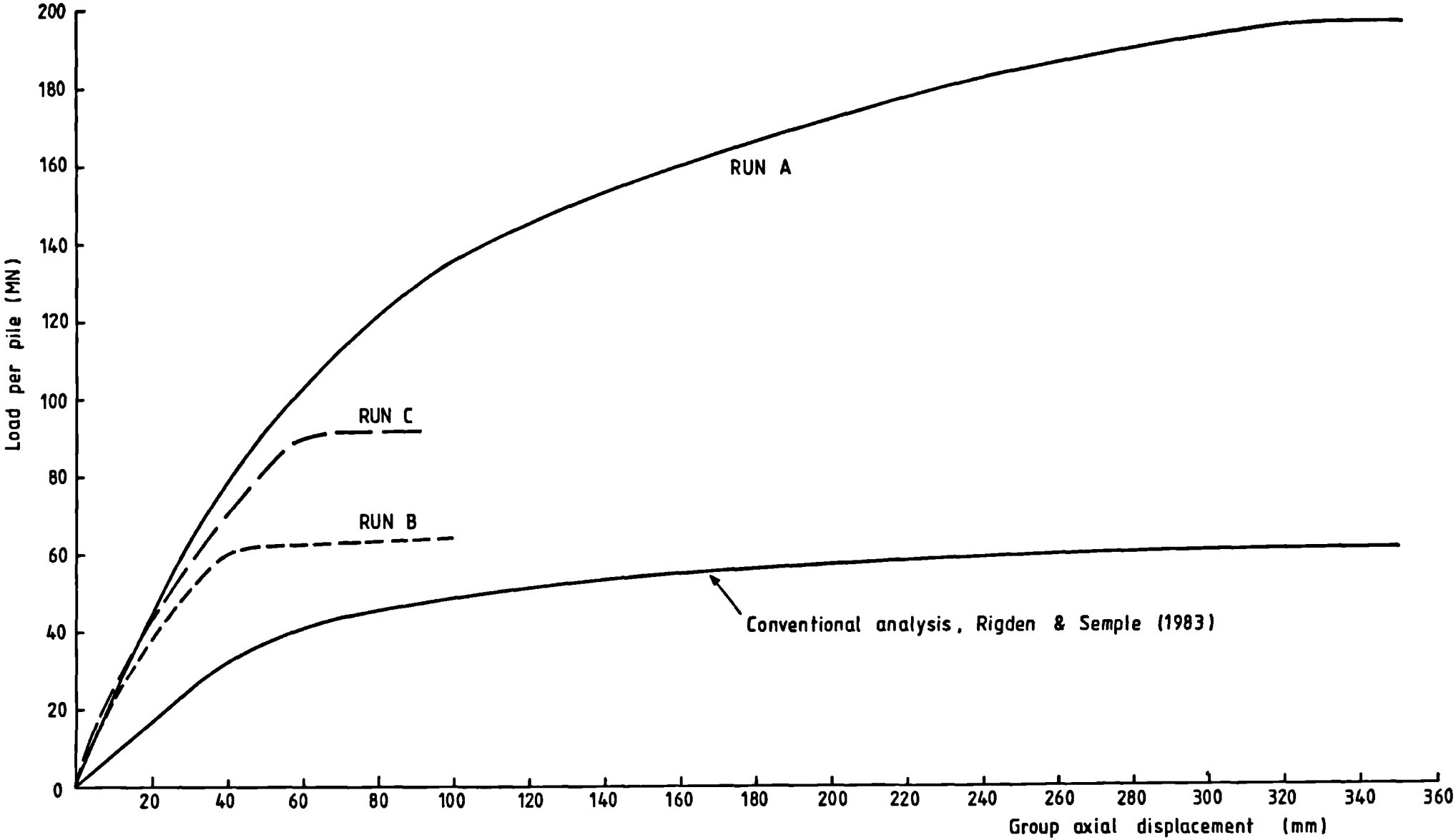


Figure 10.21. Group load-displacement curves; Runs A, B and C.

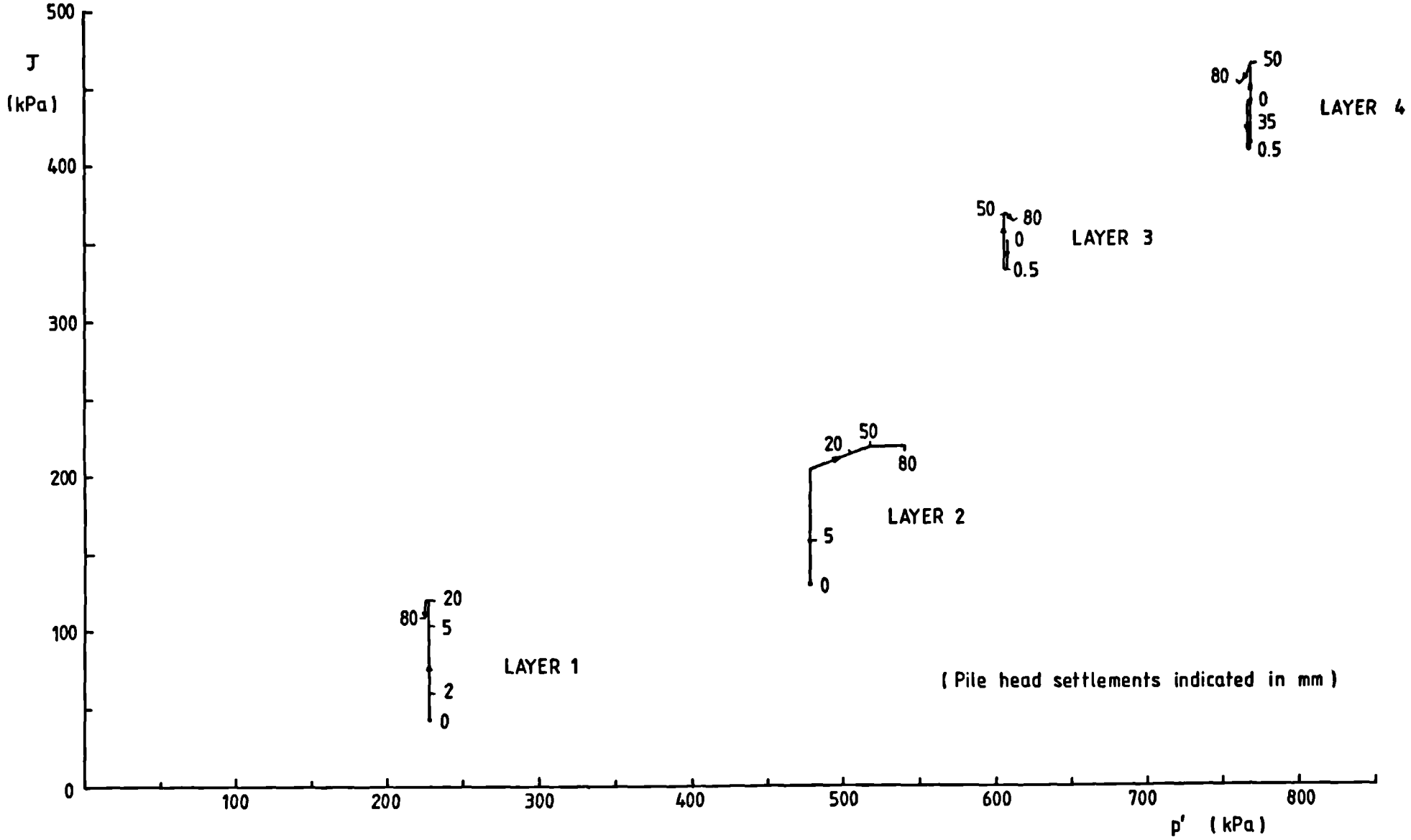


Figure 10.22. Effective stress paths followed by four typical points, with displacements indicated; Run C.

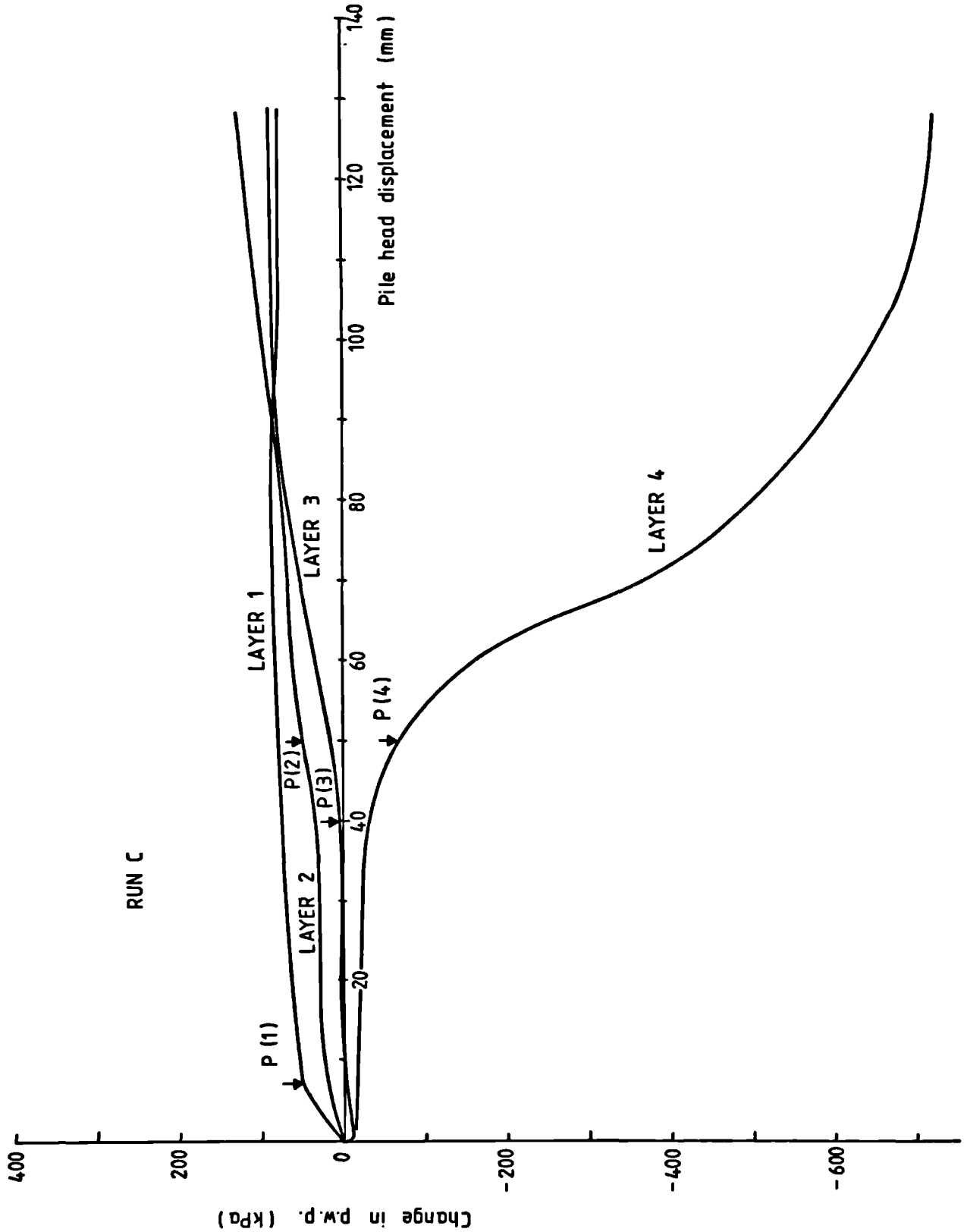


Figure 10.23. Development of pore water pressure at four typical points on the pile shaft; Run C.

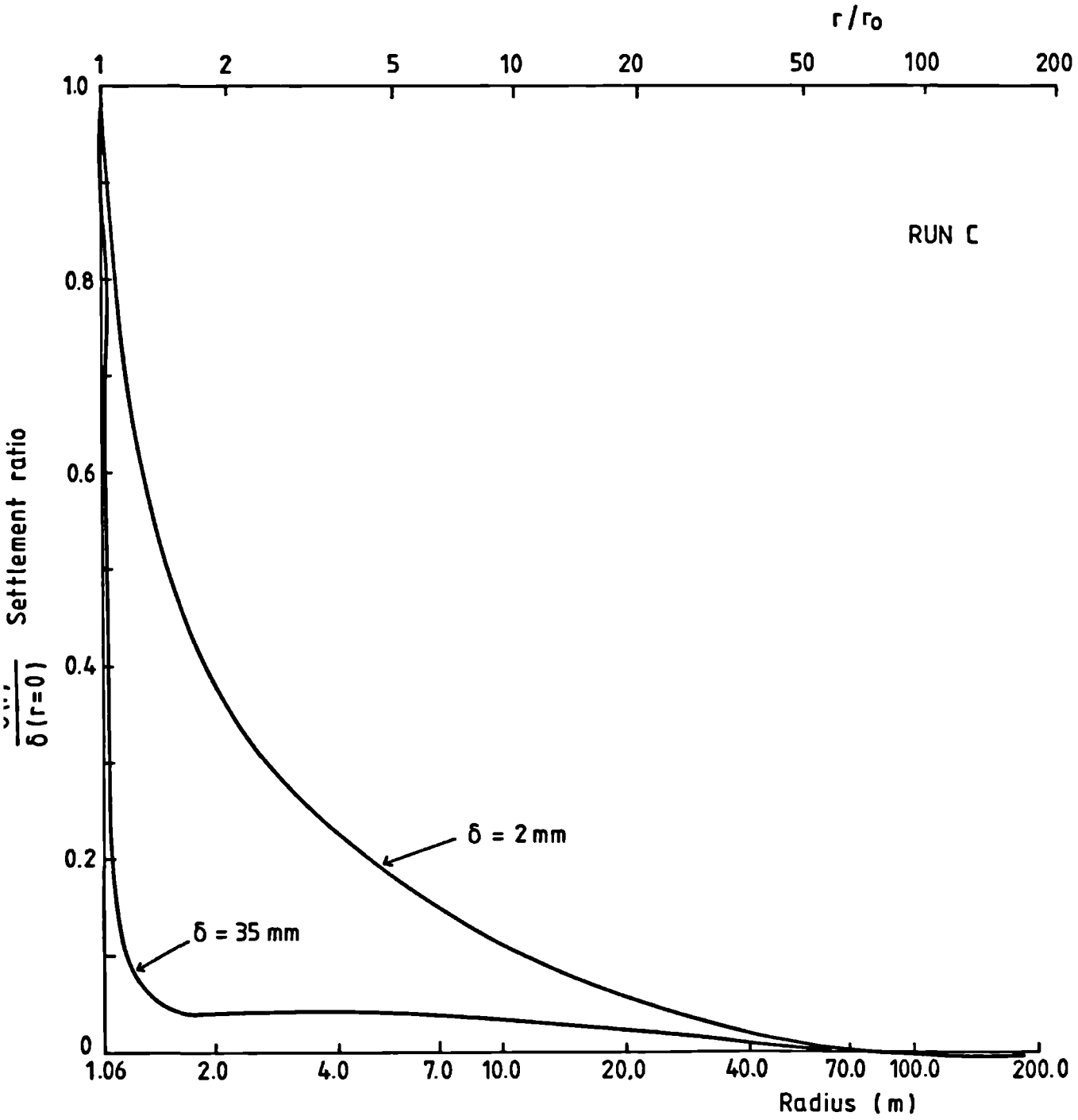


Figure 10.24. Profiles of ground displacement at two settlements; Run C.

CHAPTER 11

Tables and Figures

Depth	Layer	Undisturbed K_o	Cu		σ'_r/σ'_{zo} (Pile Face)	$\sigma'_\theta/\sigma'_{zo}$ (Pile Face)	σ'_z/σ'_{zo} (Pile Face)
			at pile face	undisturbed			
0 - 9m	A	1.6	120 - 210	110 - 190	2.50	1.60	1.80
9 - 14m	B	1.4	SAND		2.20	1.50	1.80
14 - 25m	C	0.9	310	280	1.70	1.25	1.75
25 - 37m	D	0.75	SAND		1.20	0.90	1.60
37 - 60m	E	0.6	250	200	0.75	0.60	1.30
60 - 73m	F	0.6	SAND		0.60	0.60	1.00
73 +	G	0.6	OCR = 1.0	OCR = 1.0	0.60	0.60	1.00

Table 11.1. Soil Stresses for Finite Element Calculations at Hutton Site, long-term

Layer	Depth (metres)	γ', kn/m^3	λ	k	e_1	ϕ'	δ'	ν'
A	0 - 9	9.8	0.076	0.026	0.9	30°	as Magnus Layers I, II	-
B	9 - 14	11.0	-	SAND -	-	35°	24°	15°
C	14 - 25	10.8	0.120	0.020	1.5	28°	as A	-
D	25 - 37	11.0	-	SAND -	-	35°	24°	15°
E	37 - 60	9.5	0.130	0.010	1.7	27°	as Magnus Layers III, IV	-
F	60 - 73	11.0	-	SAND -	-	35°	-	15°
G	73 →	10.7	0.130	0.010	1.7	30°	-	-

Table 11.2. Soil parameters for Finite Element Calculations at Hutton site, long-term (note : non-linear stiffness descriptions are same as for Magnus profile).

Gauge	Change in Eccentricity	Change in Pullout with 3,000 tonnes total load, mm	Rotational stiffness tonne m/radian
SG2L	2.3 to 0.77M	- 0.28	146×10^6
"	0.77 to 0.00	- 0.13	150×10^6
SG3R	2.3 to 0.77	- 0.35	112×10^6
"	0.77 to 0.00	- 0.21	93×10^6
SG4L	2.3 to 0.77	- 0.32	122×10^6
"	0.77 to 0.00	- 0.20	98×10^6

Table 11.3. Rotational stiffnesses calculated for pile groups

(N.B. Active pots are assumed to be offset from group centre by 8.5M along X-X^1)

Quantity	Prediction (based on F.E. analyses)	Measurements	
		Template F1	Template F2
Uplift at 3,200 tonnes[1] w.r.t. a remote datum	1.87 mm	not observed	1.78 mm
As above, w.r.t. a local datum	0.96 mm	1.20 mm	0.85 mm
Moment-rotation stiffness of pile group, w.r.t. a remote datum	113 x 10^6 tonne m/radian	not observed	93 to 112 x 10^6 tonne m/radian
As above, w.r.t. a local datum	163 x 10^6 tonne m/radian	146 to 150 x 10^6 tonne m/radian	98 to 122 x 10^6 tonne m/radian

Table 11.4. Comparisons between predictions and measurements for the Hutton TLP pile group

[1] This is a group load, equivalent to 4 MN per pile.

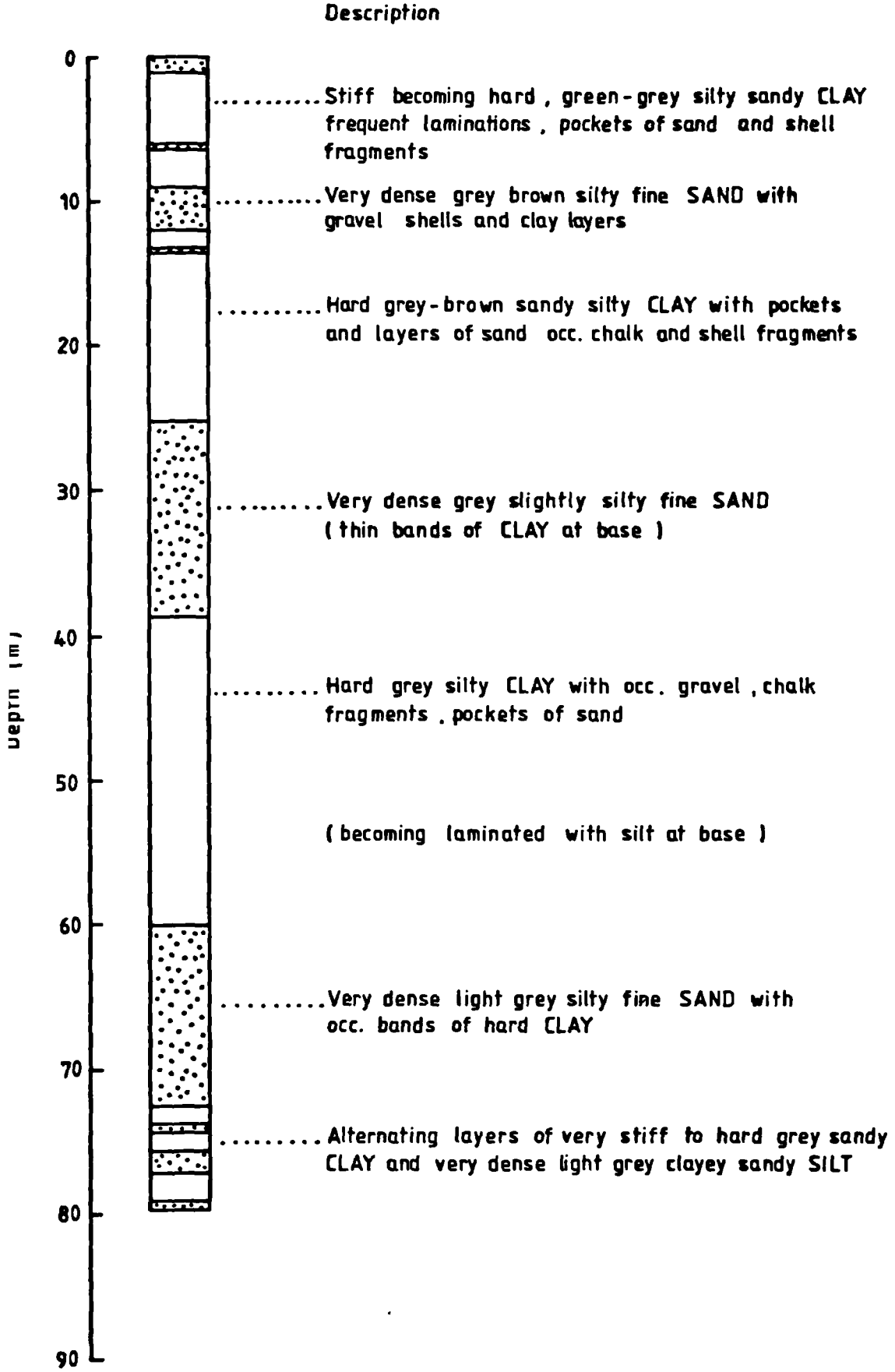


Figure 11.1. Simplified borehole log B1/B1A.

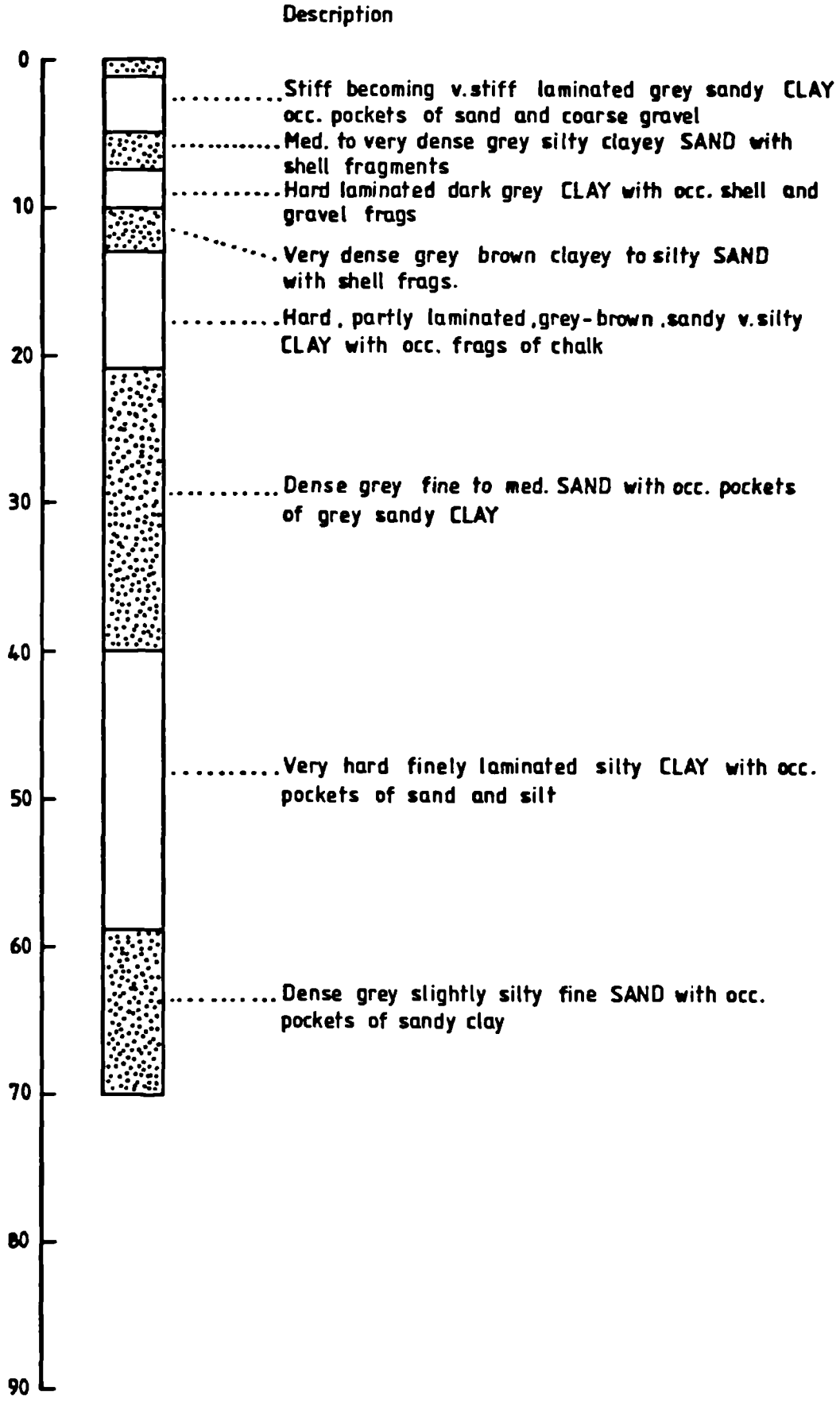


Figure 11.2. Simplified borehole log B2/B2A.

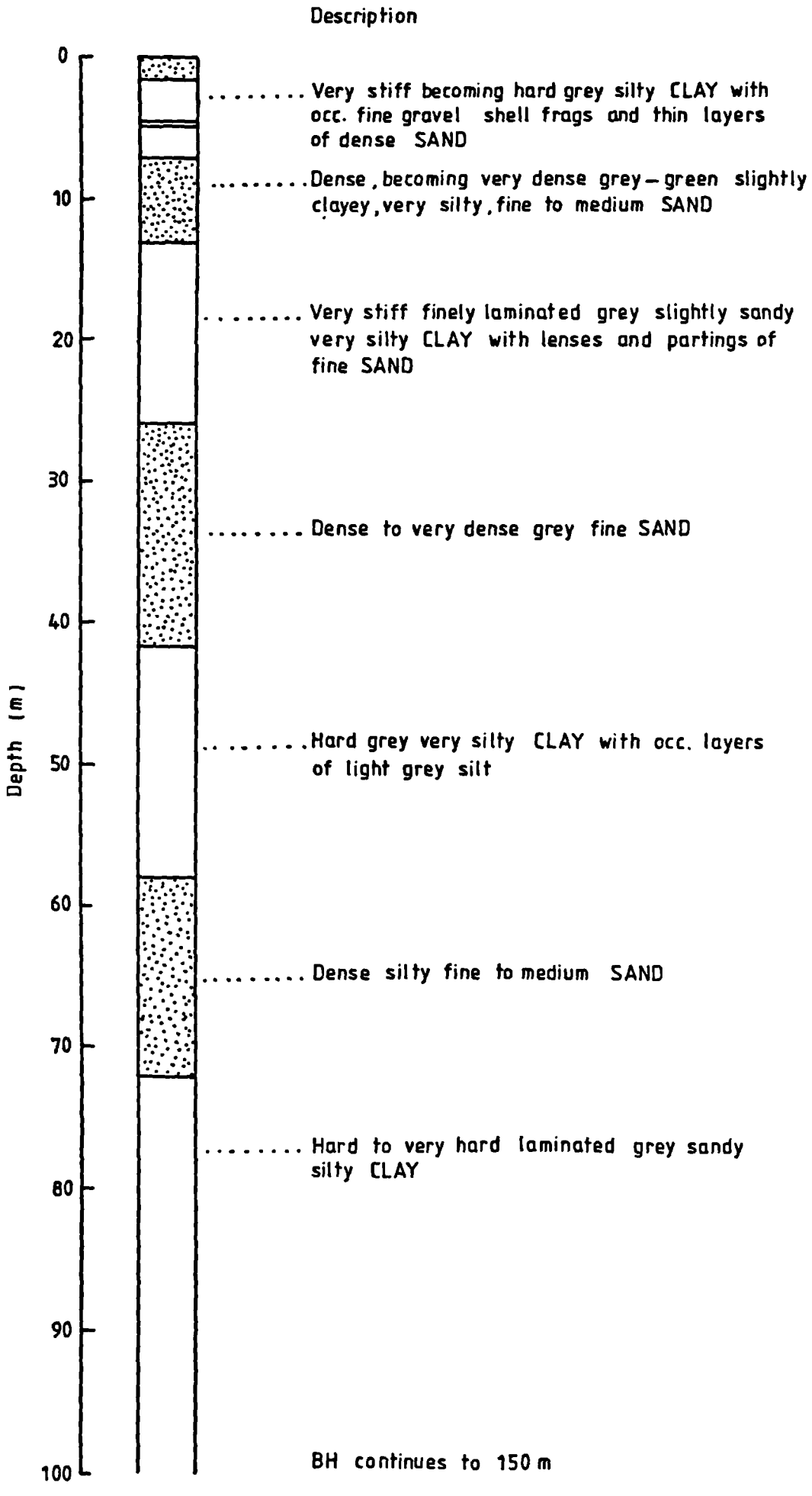


Figure 11.3. Simplified borehole log B4/B4A.

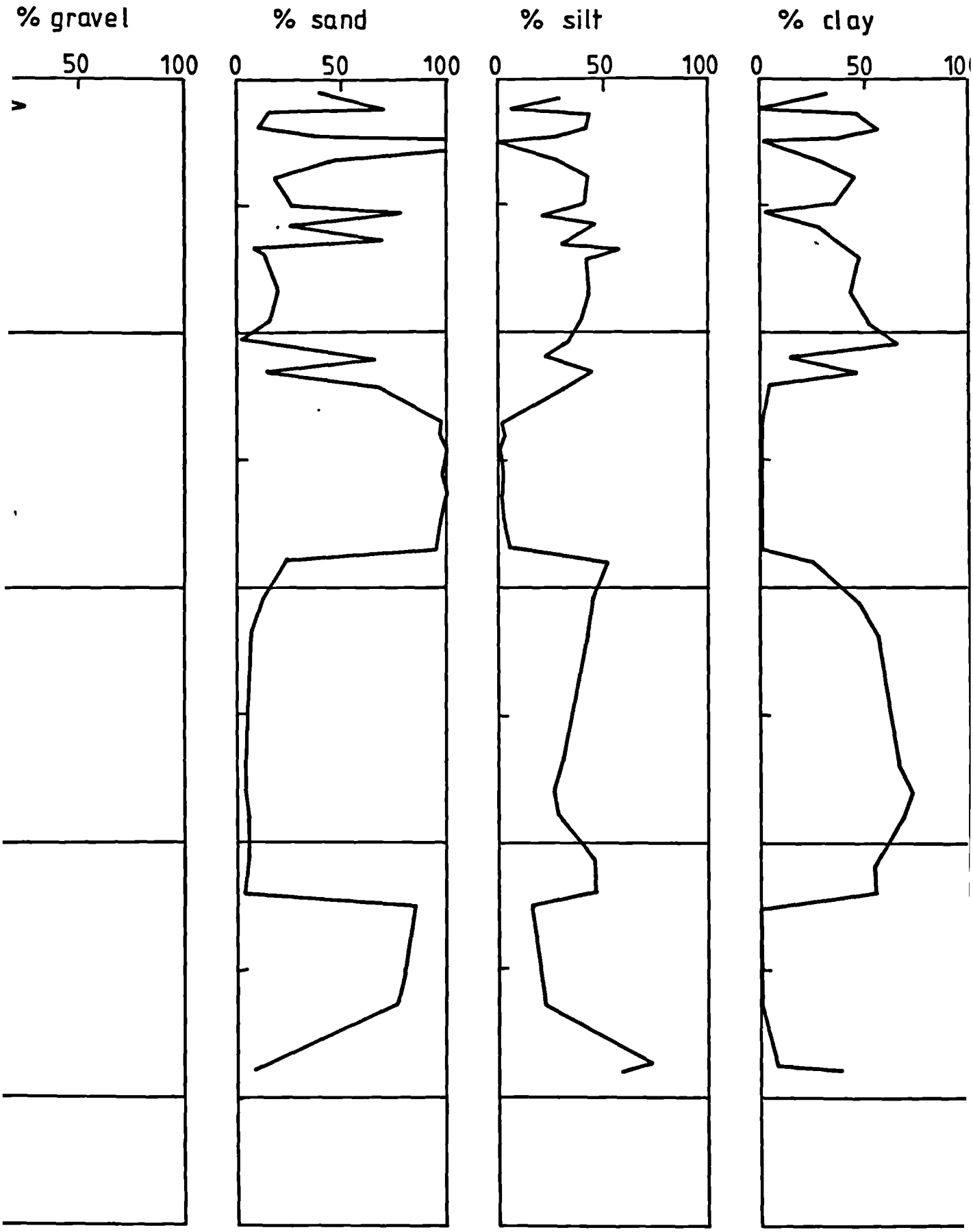


Figure 11.4. Summary of grading variations with depth.

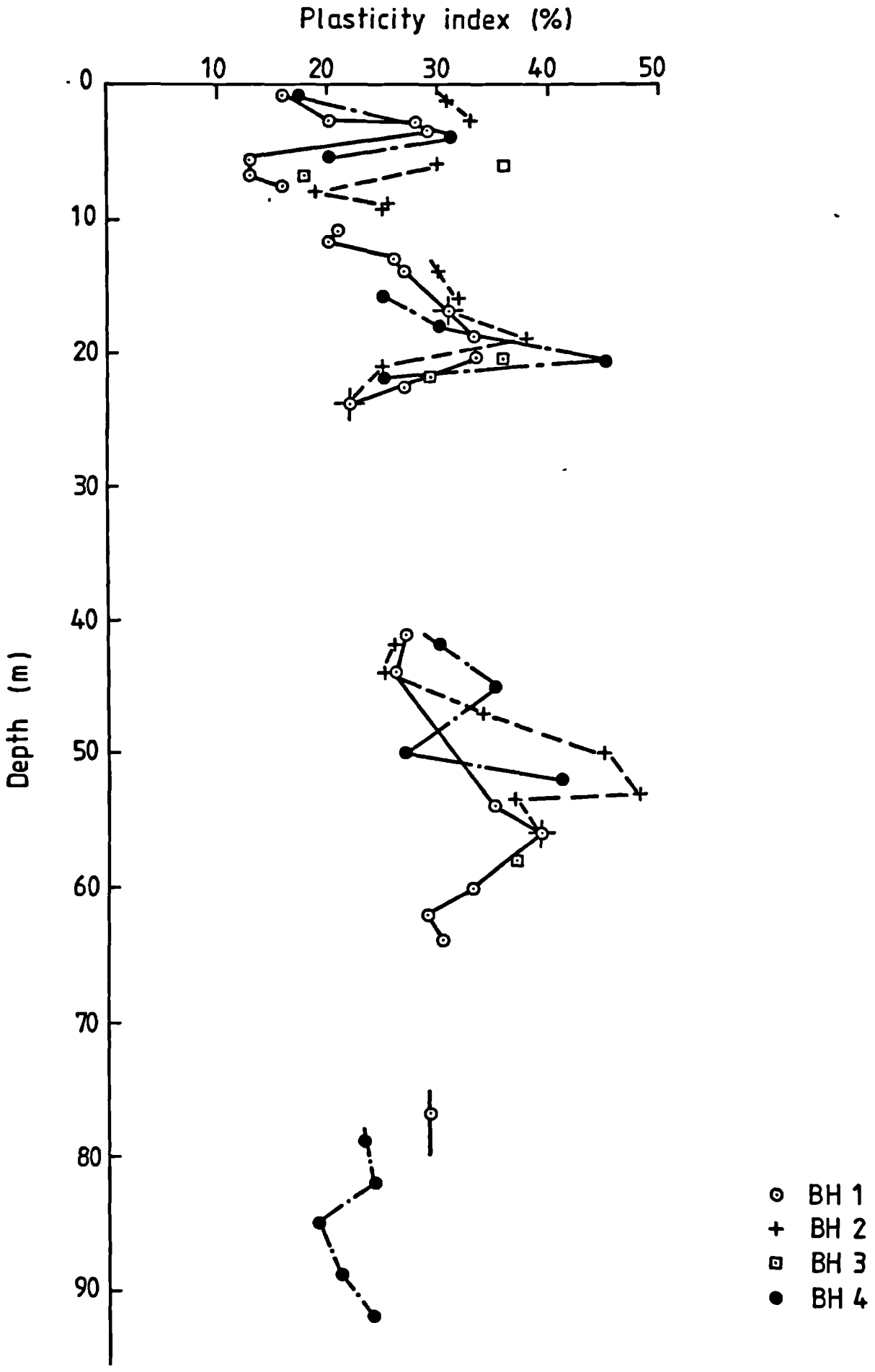


Figure 11.5. Summary of P.I. variations with depth.

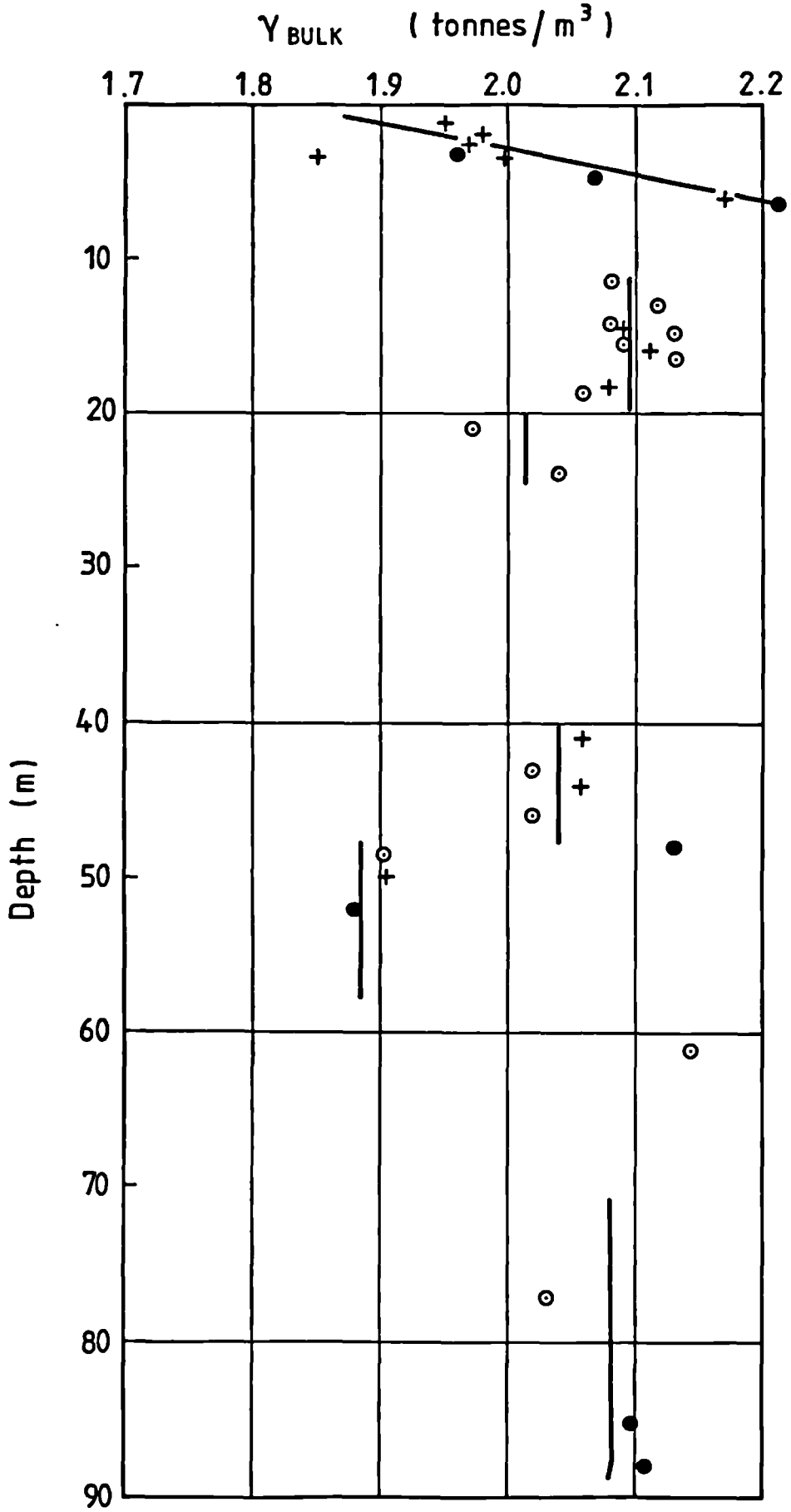


Figure 11.6. Summary of γ_{bulk} variations with depth (for legend see 11.5).

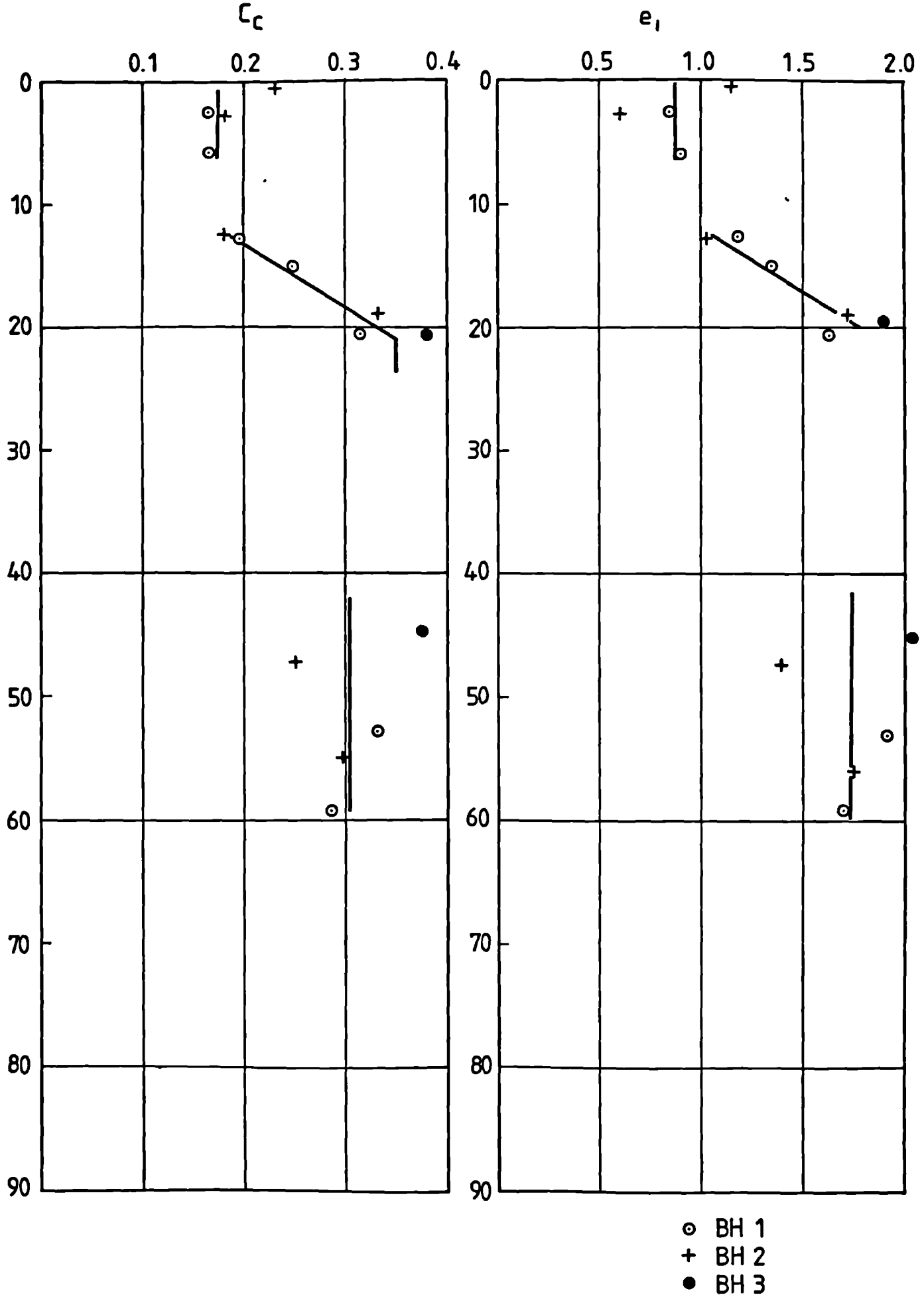


Figure 11.7. Variations with depth of oedometer compression characteristics; loading from 1,600 to 3,200 Kpa.

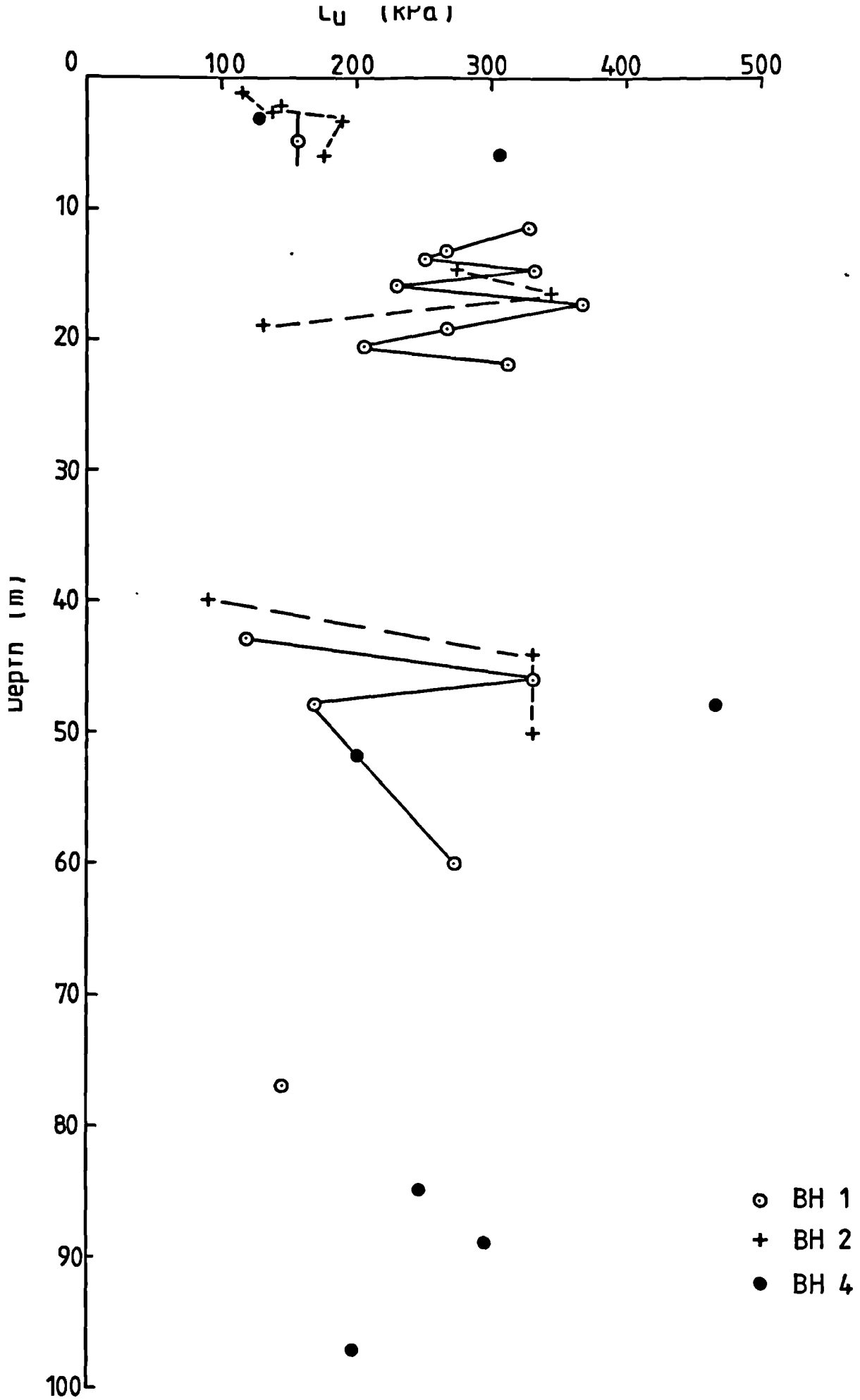


Figure 11.8. Variations of Cu with depth.

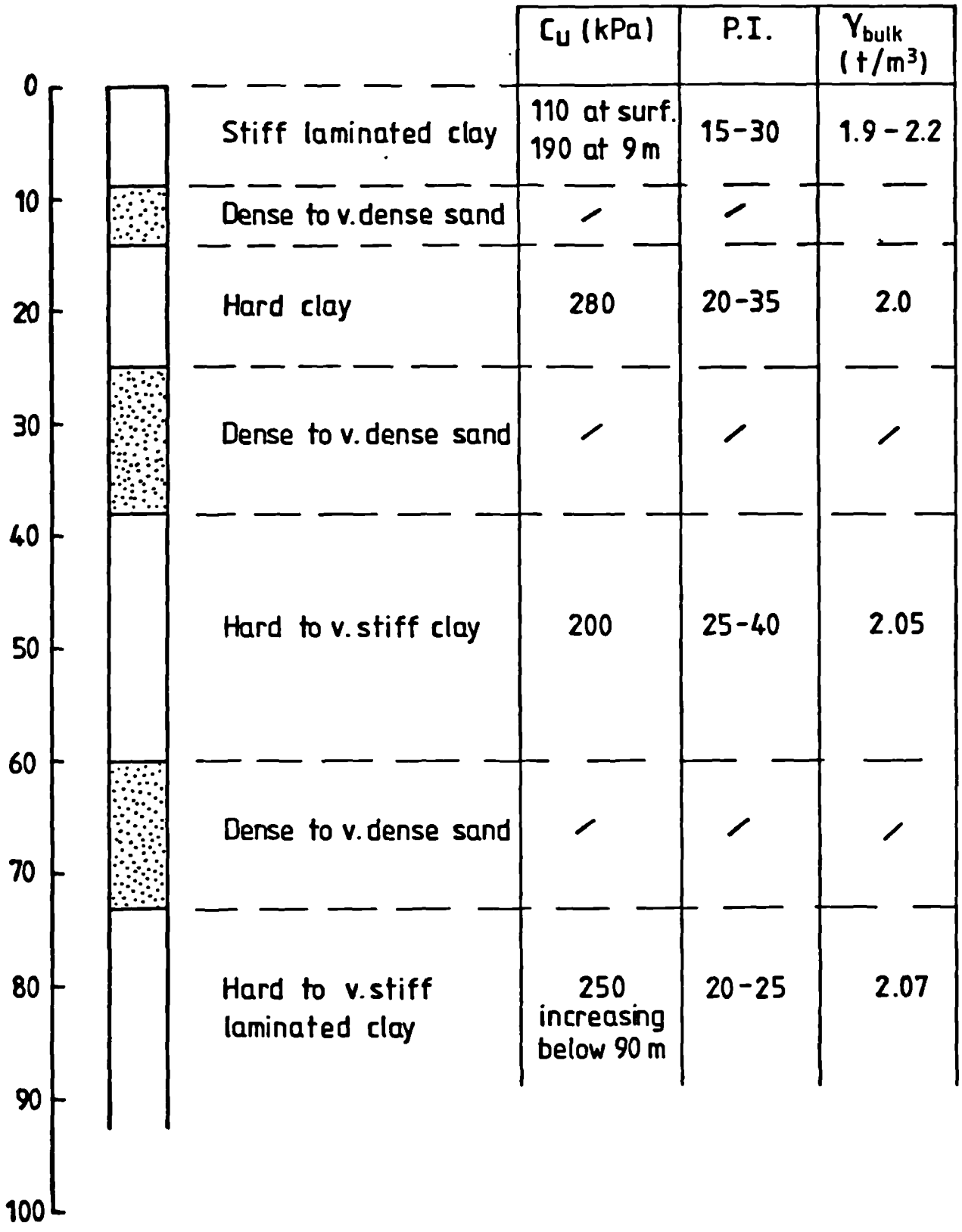


Figure 11.9. Simplified 'typical' Hutton profile.

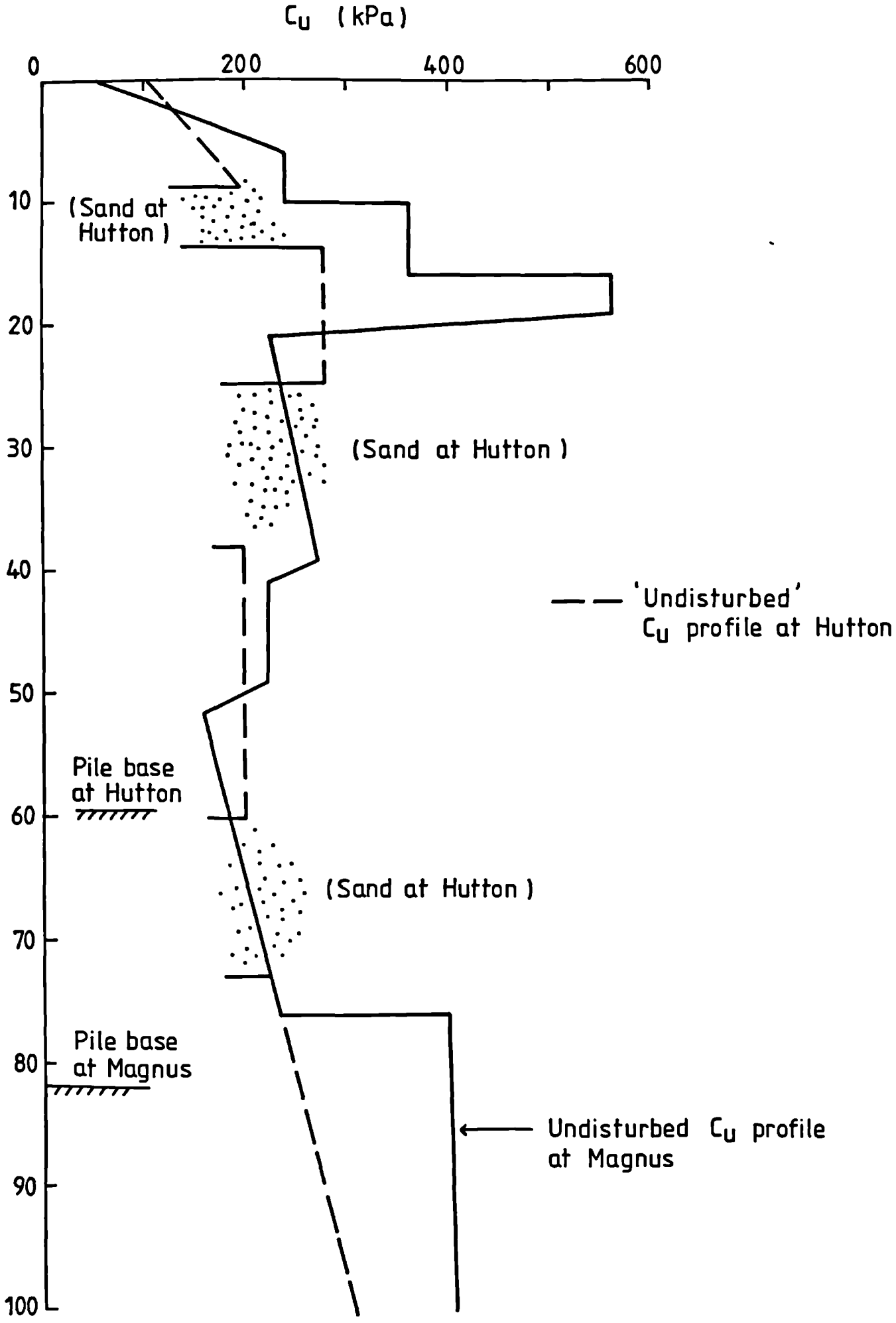
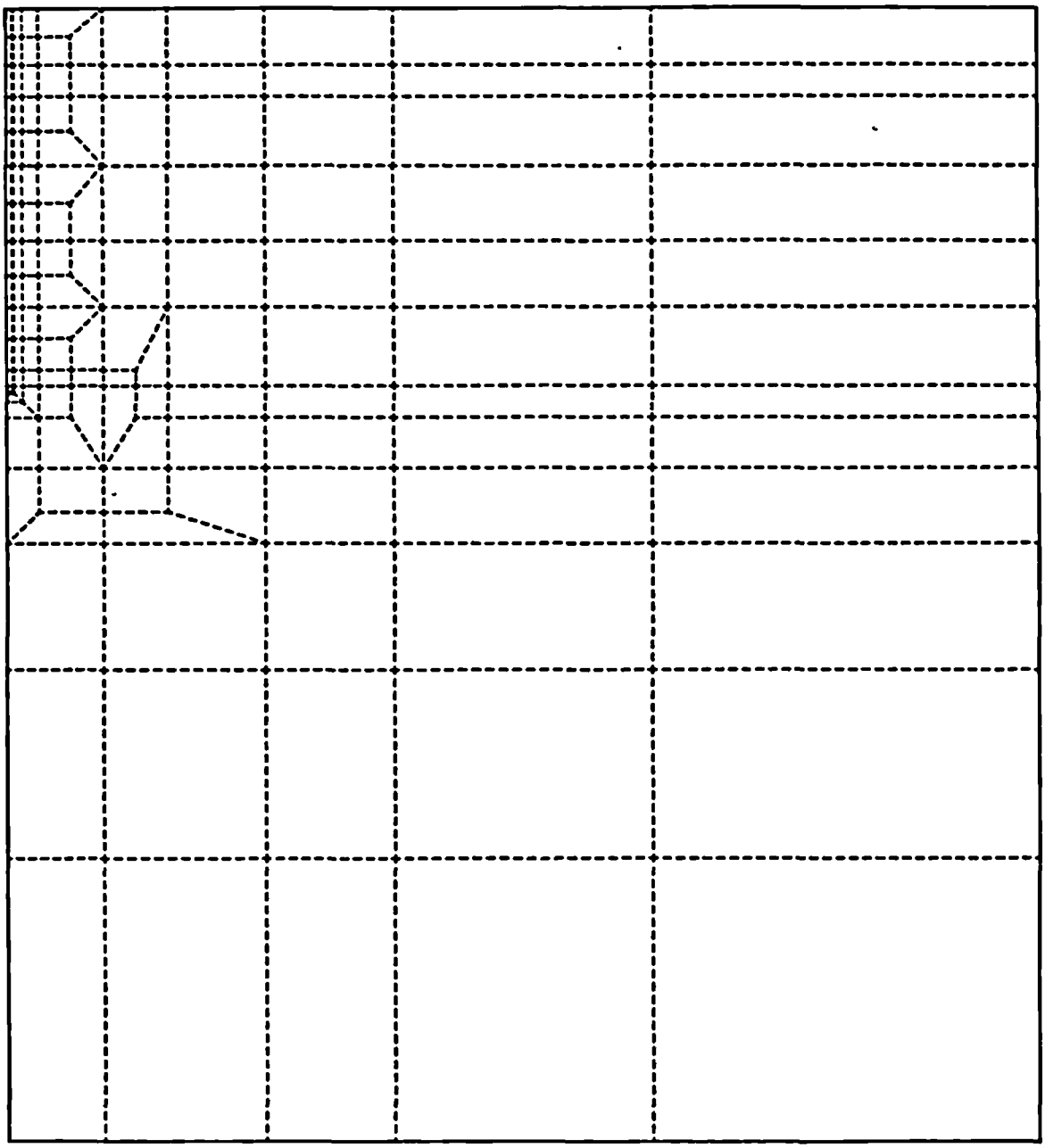


Figure 11.10. Comparisons between Hutton and Magnus profiles.



ΓON - MESH GENERATION FOR SINGLE PILE

Figure 11.11.

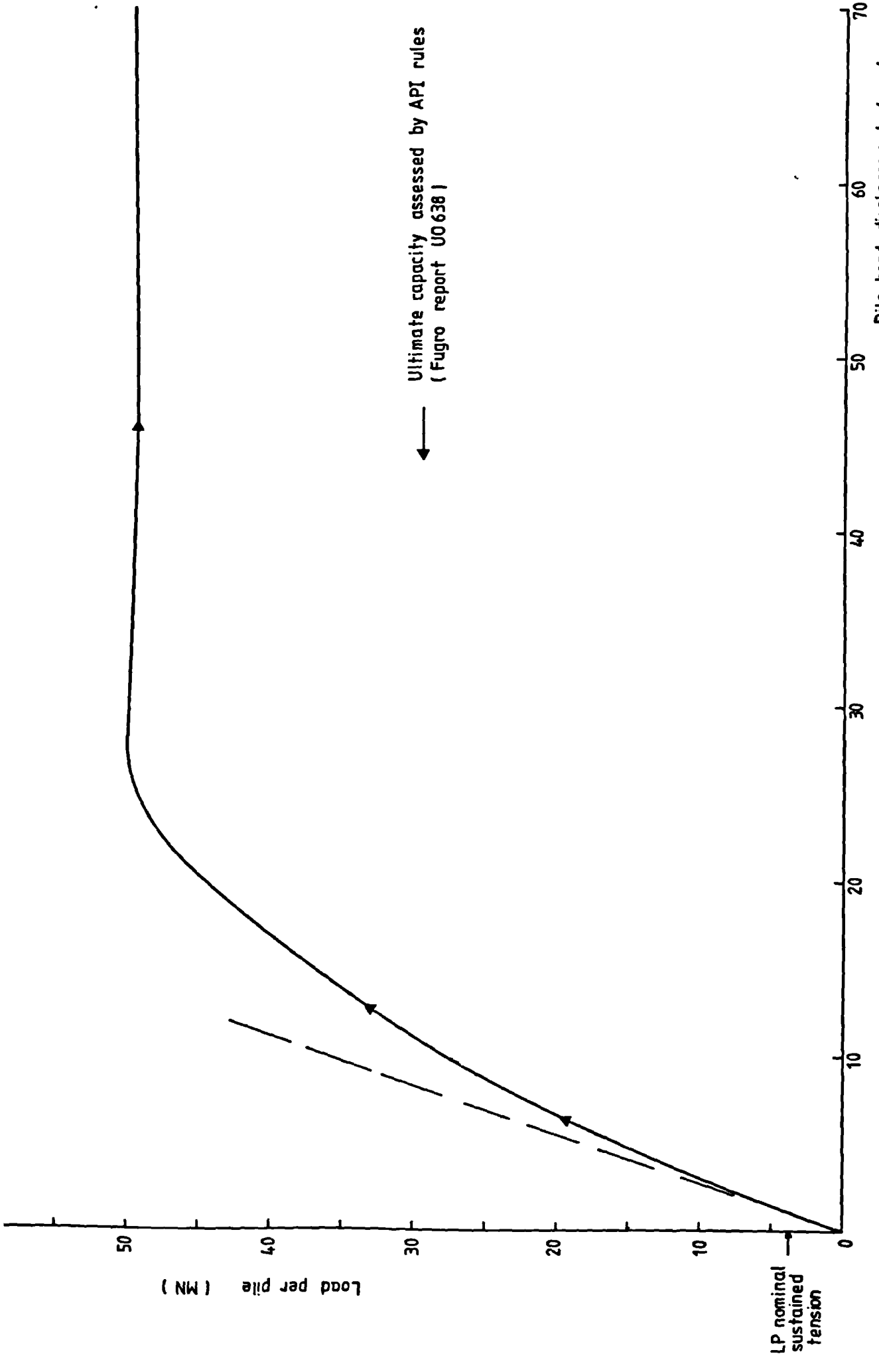


Figure 11.12. Predicted load-displacement curve for a single pile (displacement is upward).

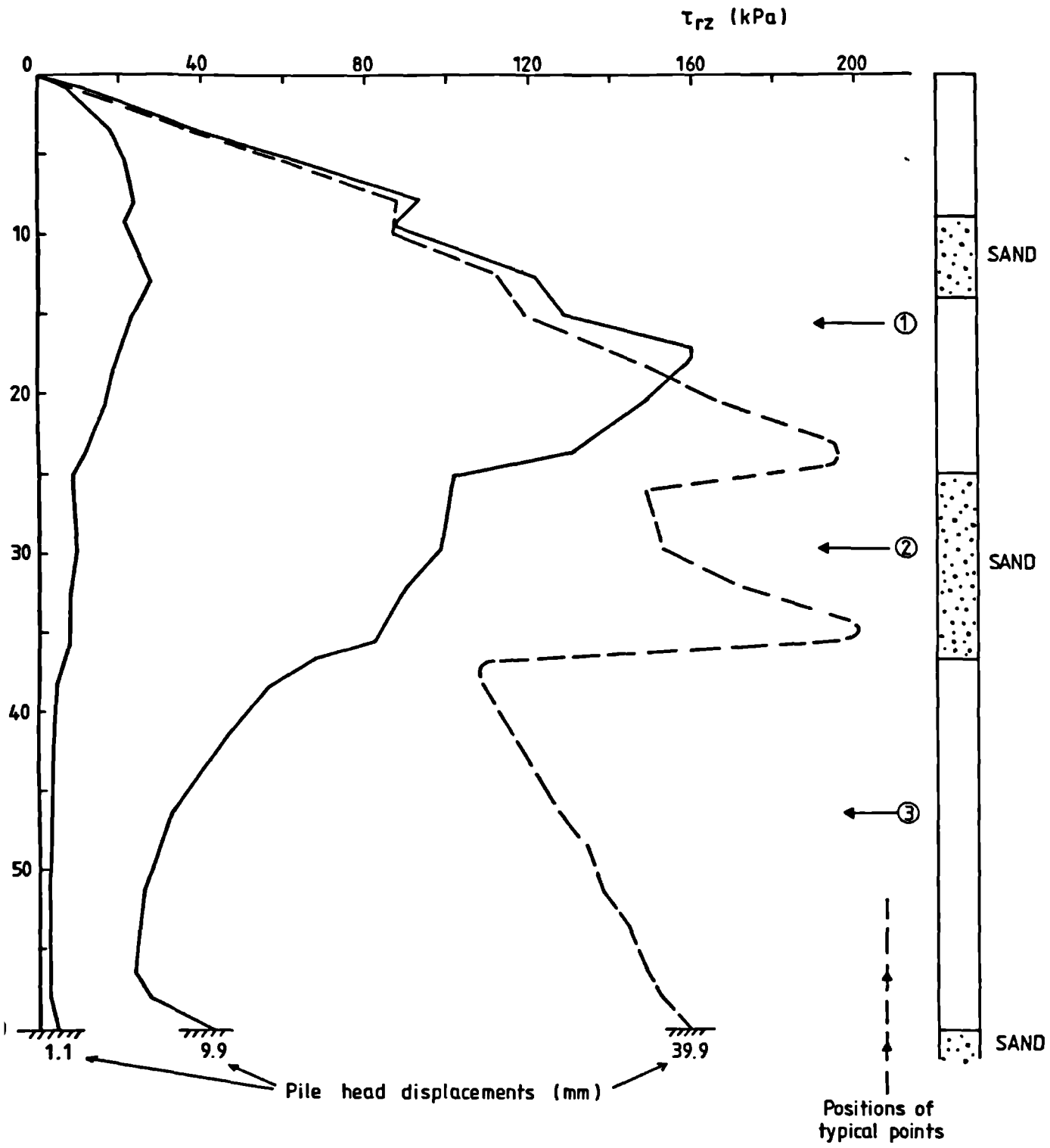


Figure 11.13. Profiles of skin friction for three displacements.

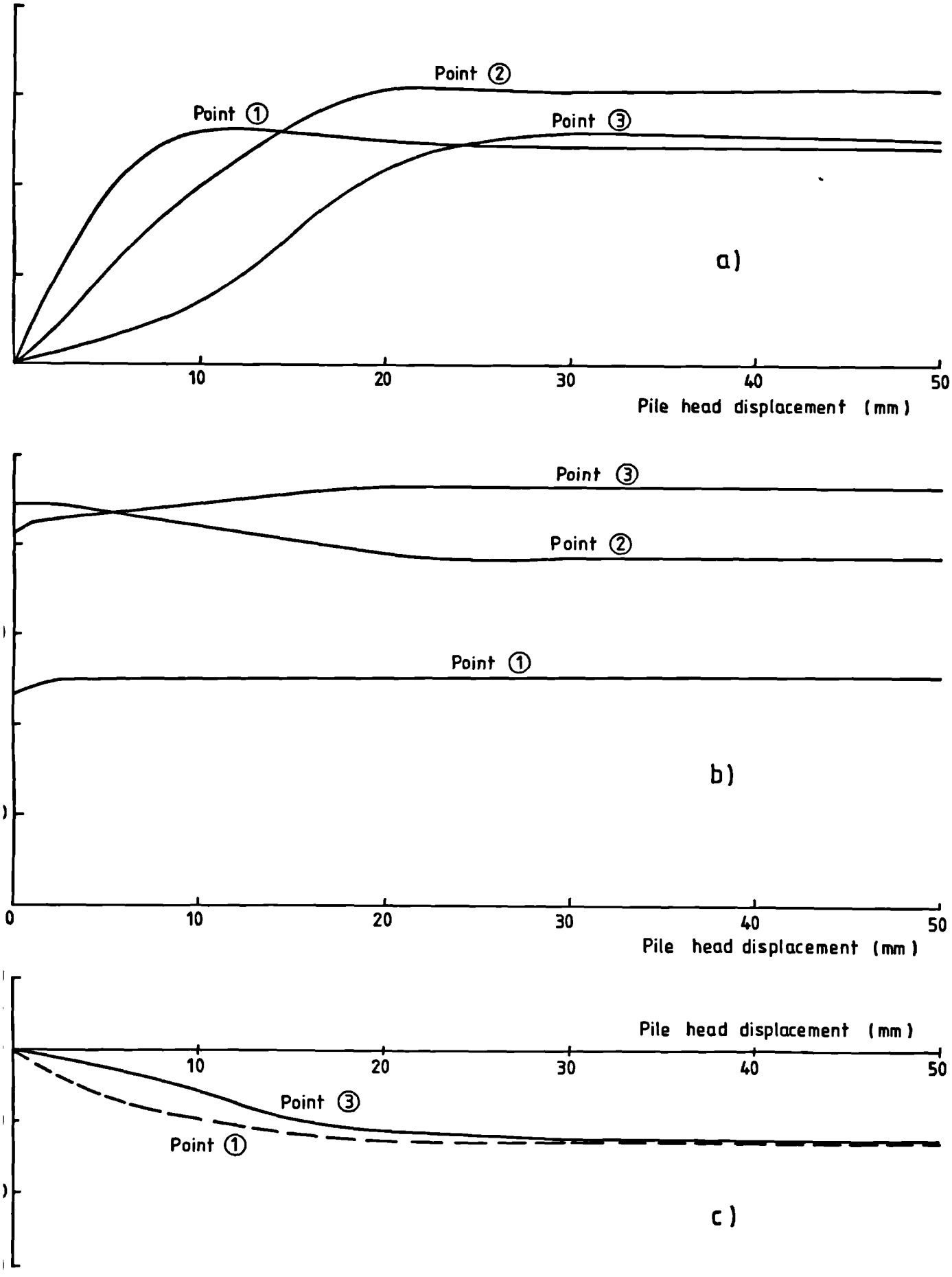


Figure 11.14. Variations of τ_{rz}, σ'_r and pore water pressure with displacement for three typical points on the pile shaft.

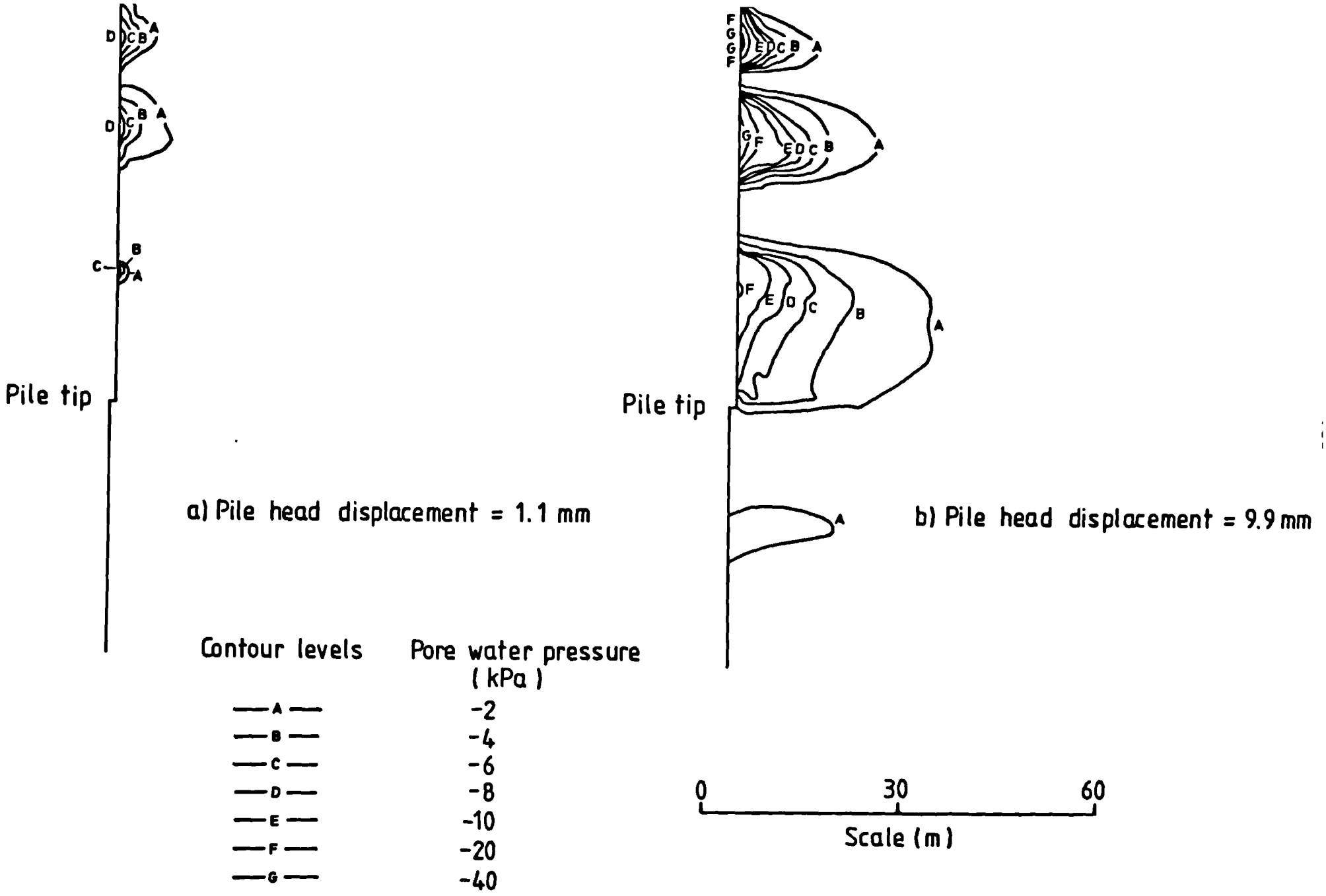


Figure 11.15. Contours of pore water pressure change for two displacements.

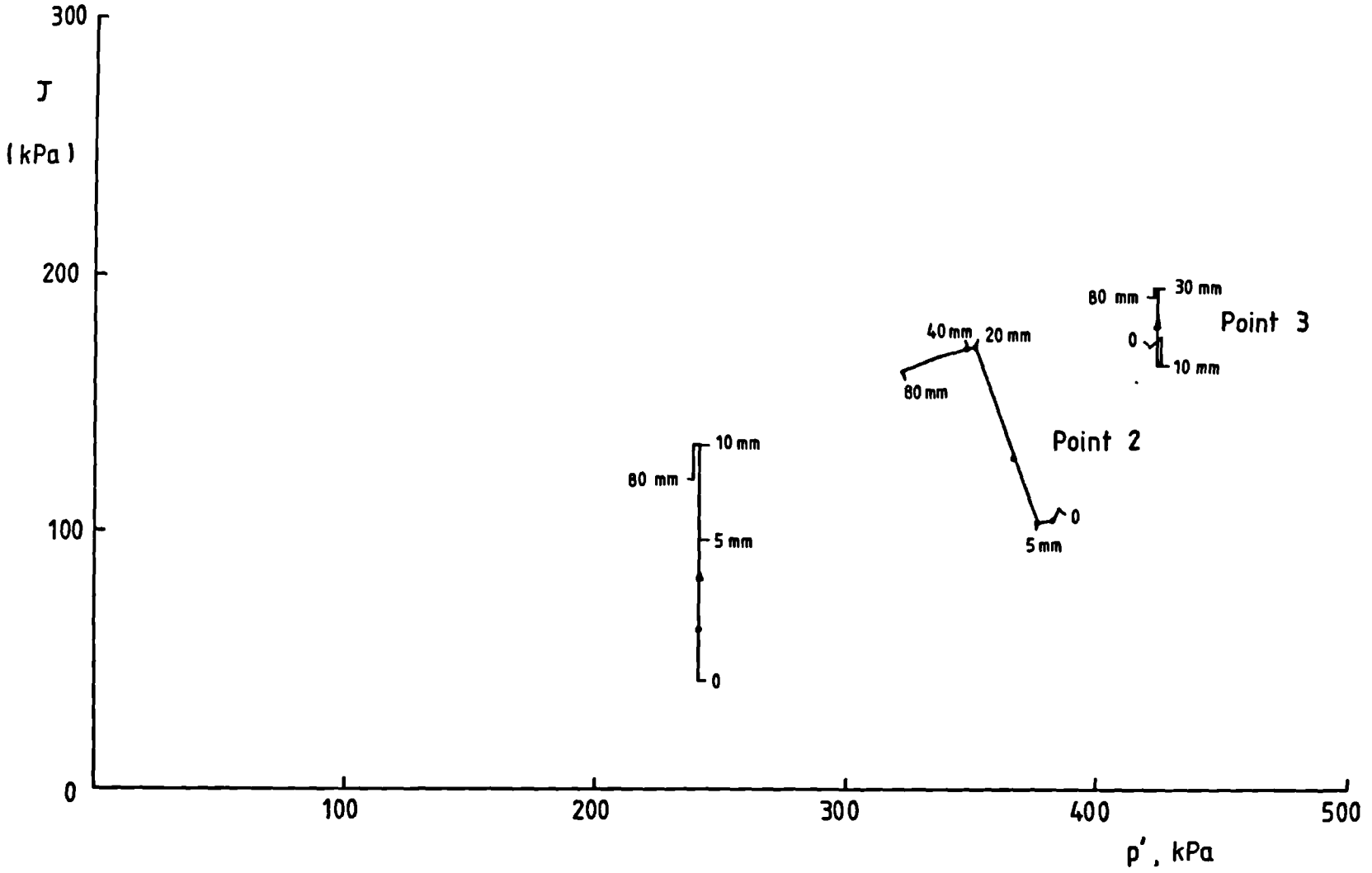


Figure 11.16. Effective stress paths followed by three typical points on pile shaft.

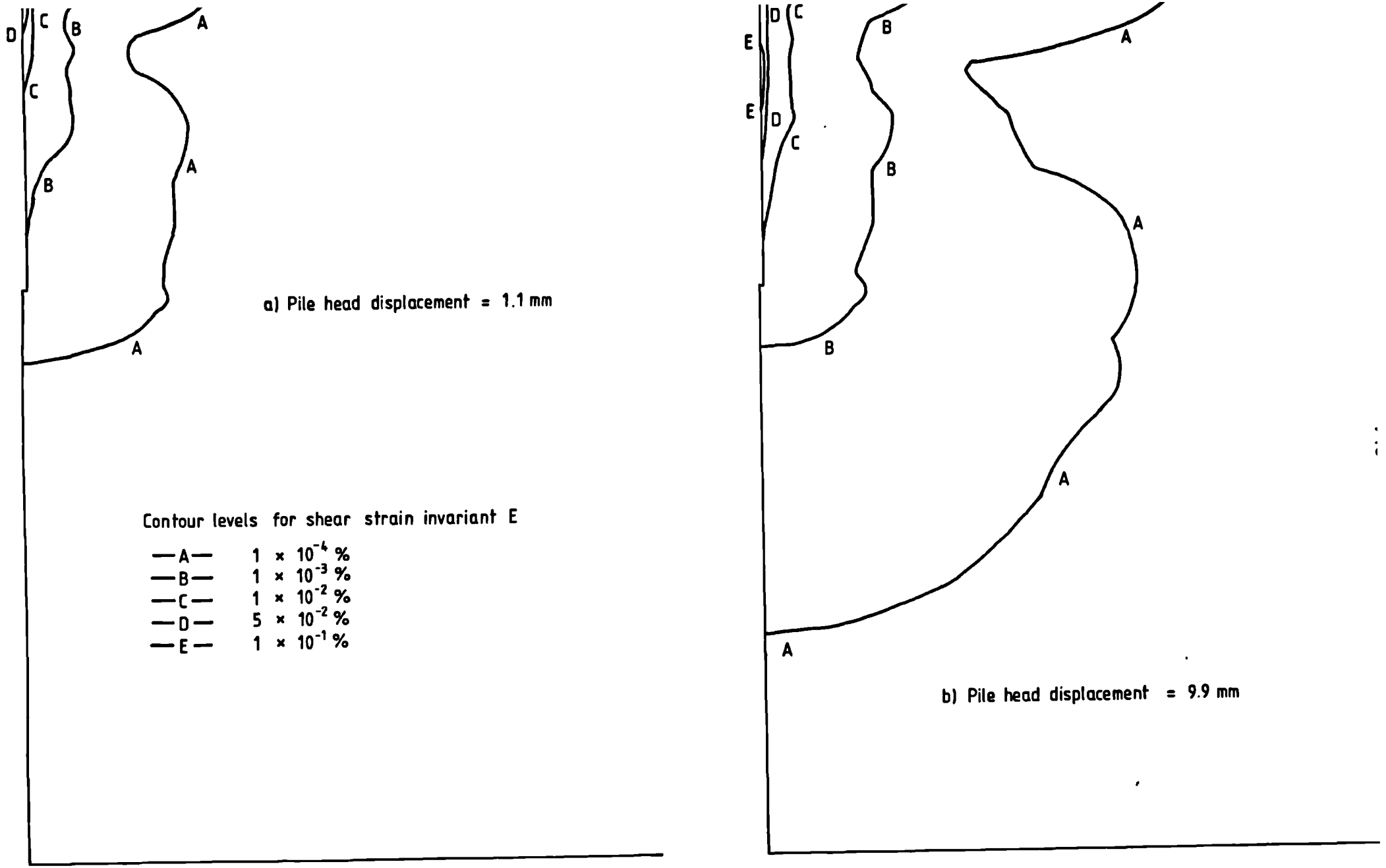


Figure 11.17. Contours of shear strain invariant E for two displacements, (noting $E = \sqrt{3}\ \varepsilon_a$ for an undrained triaxial test).

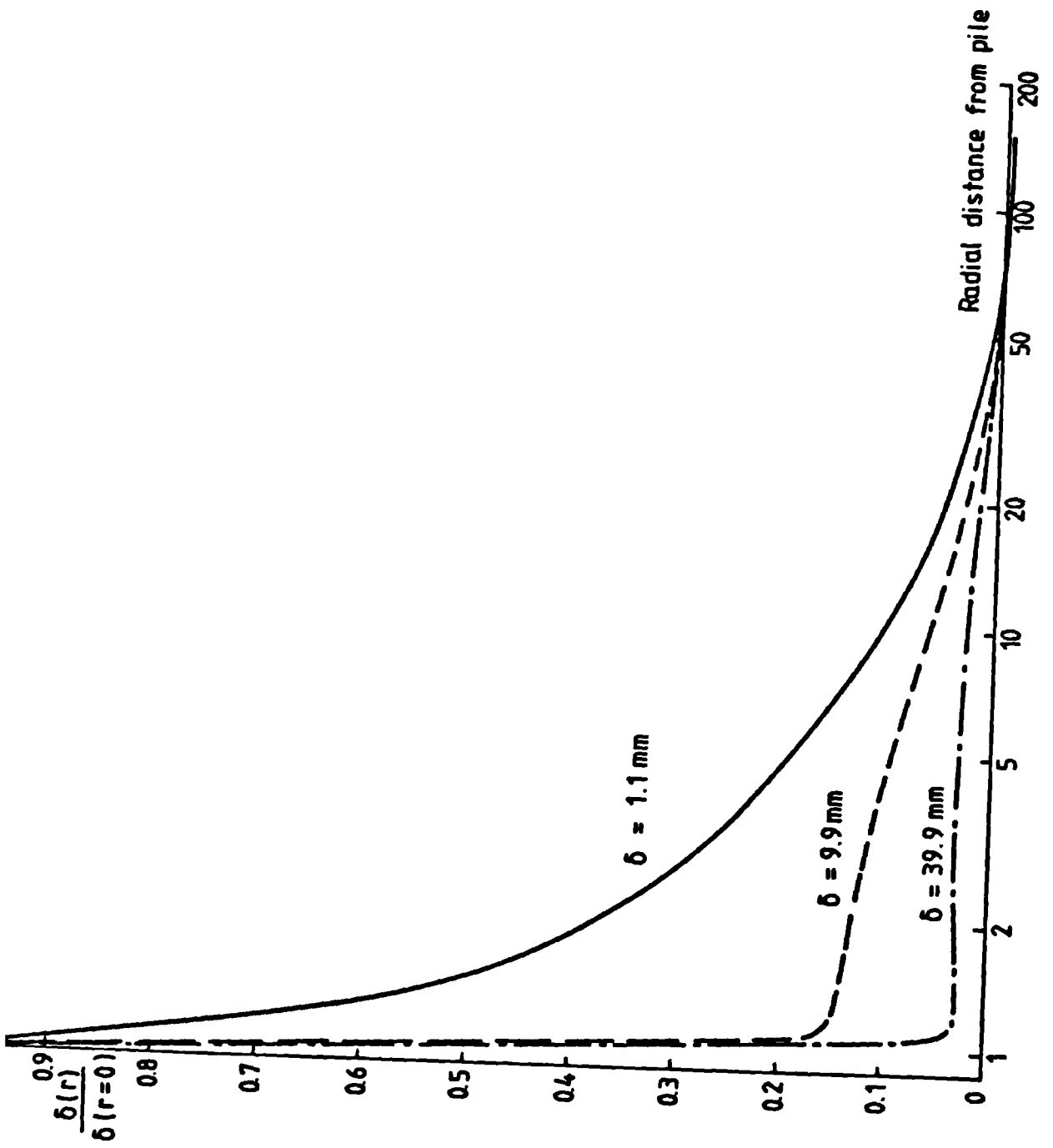


Figure 11.18. Ground surface profiles for two values of upward displacement.

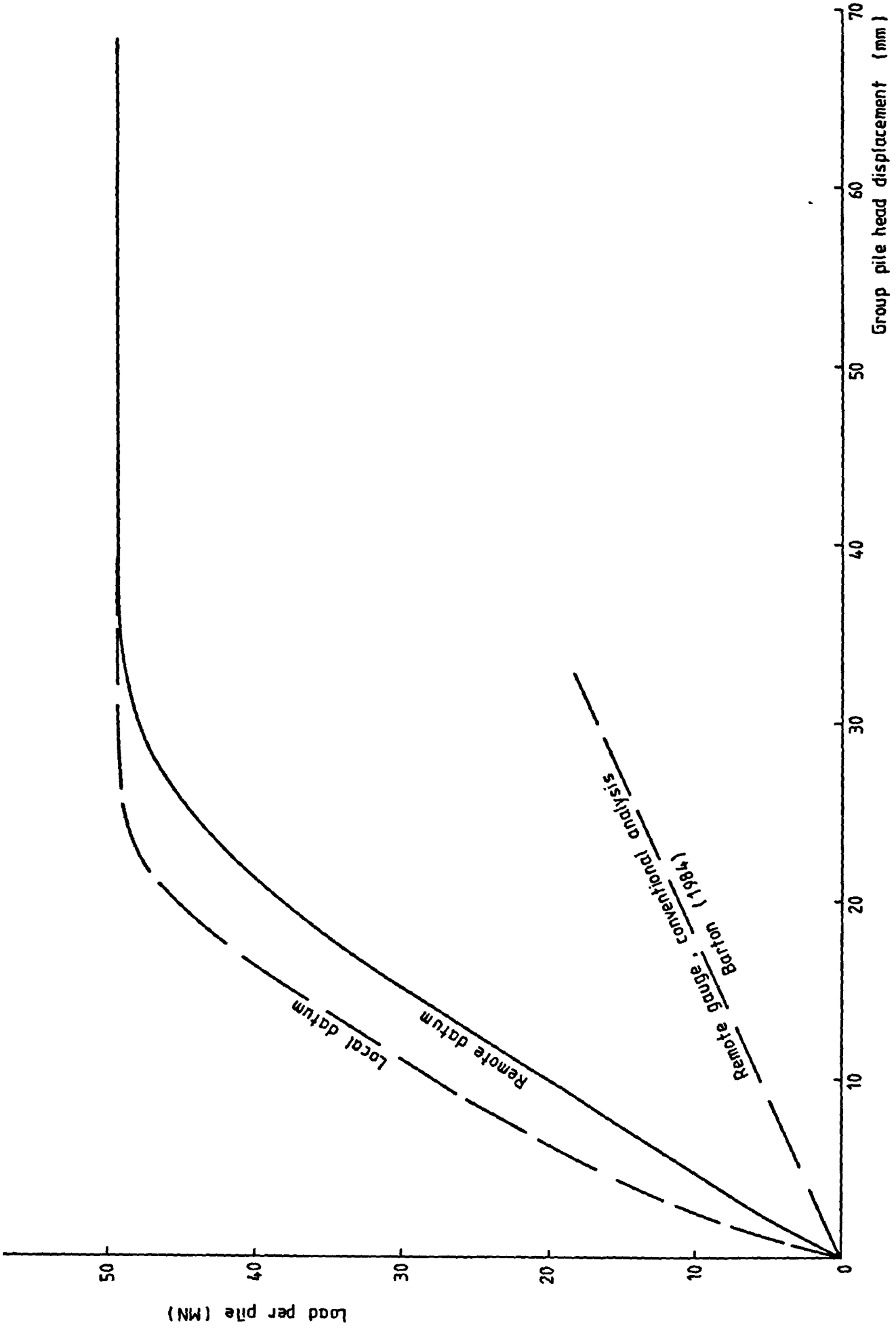
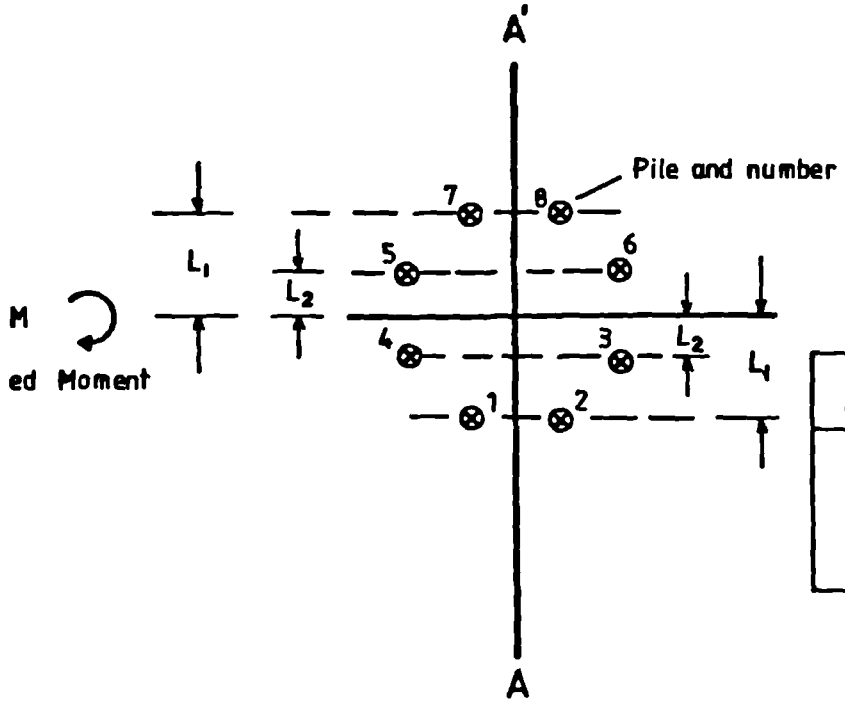
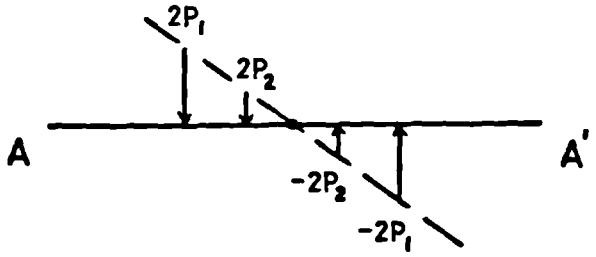


Figure 11.19. Group load-displacement curves, (displacement is upward).



Symmetrical Group Geometry

Pile no.	INCREMENTAL	
	Pile force	Pile disp.
1, 2	P_1	δ_1
3, 4	P_2	δ_2
5, 6	$-P_2$	$-\delta_1$
7, 8	$-P_1$	$-\delta_2$



Force increments for piles section through A-A'

$$\left(\text{Assume } \frac{P_1}{P_2} = \frac{L_1}{L_2}\right)$$

$$M = 4\,(P_1 . L_1 + P_2 . L_2)$$

Displacement increments for piles section through A-A'

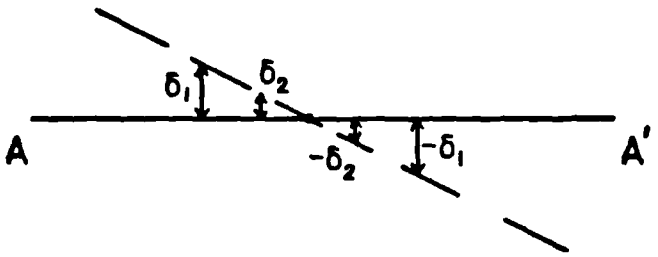


Figure 11.20. System of forces and displacements used as first assumption in the analysis of group moment-rotation analysis (assumes pin joints at pile heads).

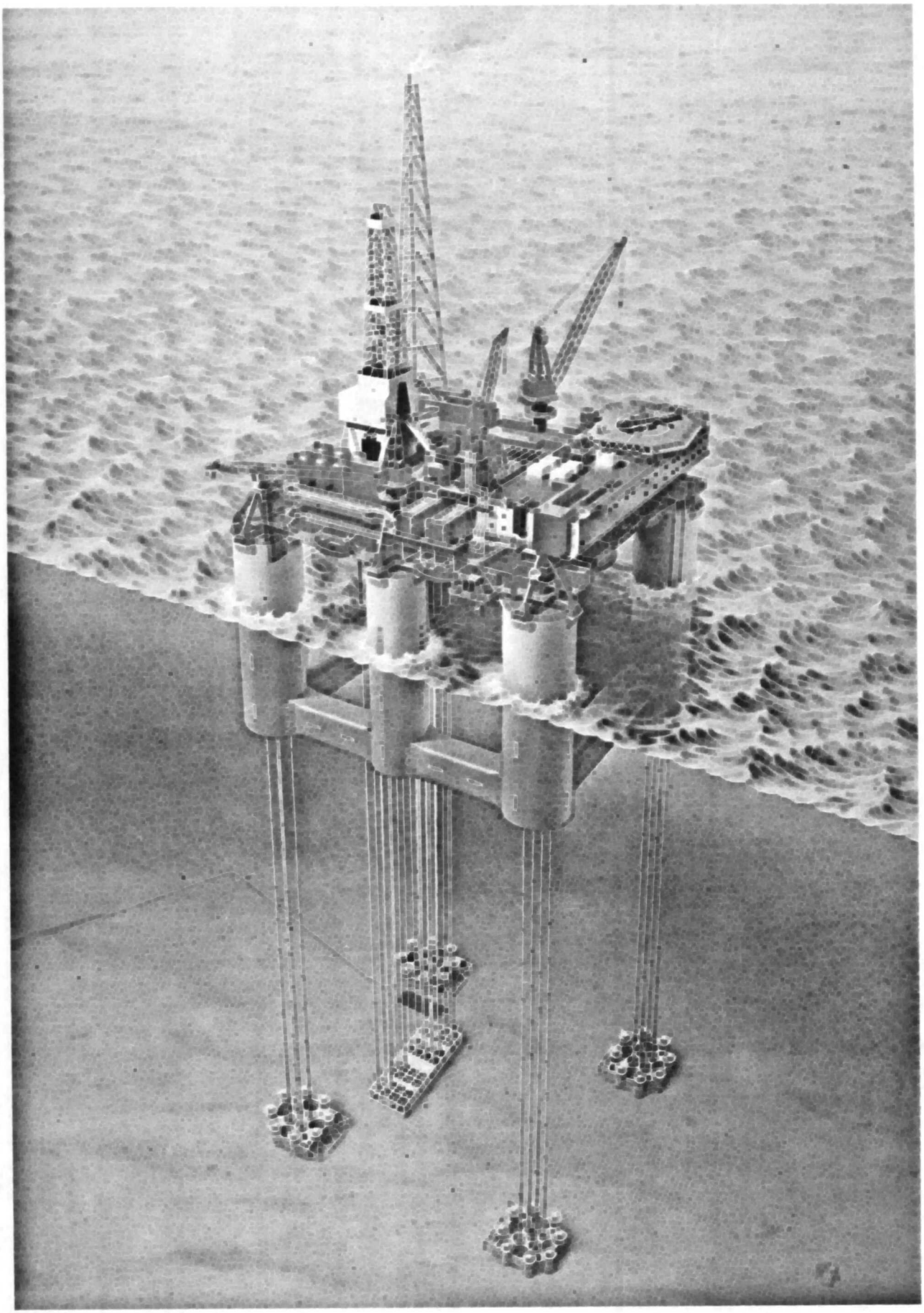
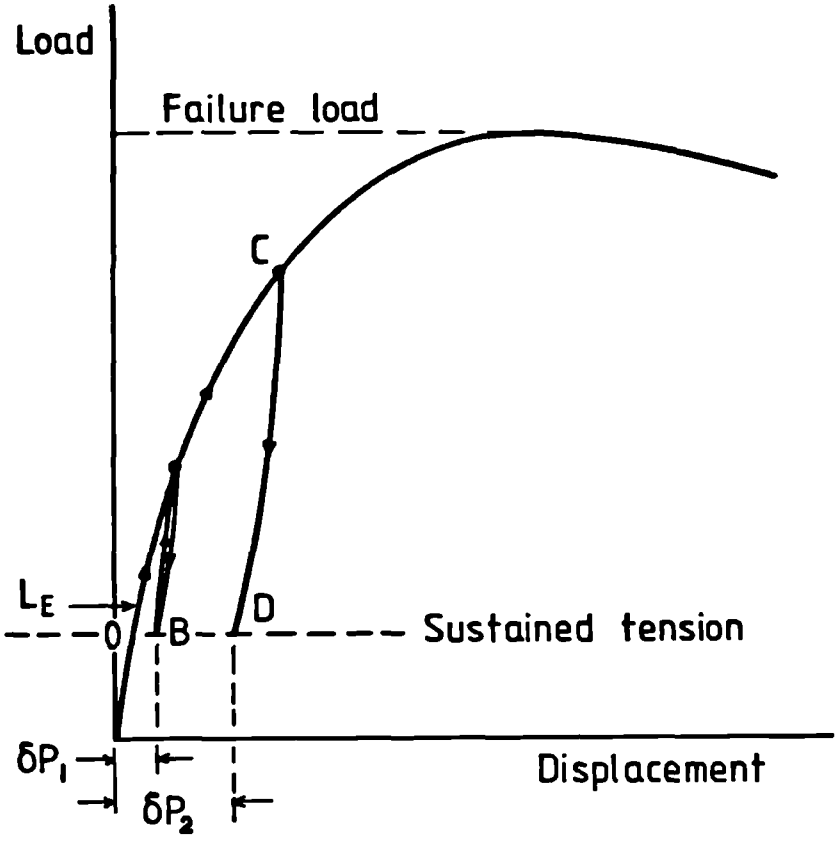


Figure 11.21. Artist's impression of Hutton TLP, showing foundations.



δP_1 permanent displacement after loading to A
δP_2 " " " " " C

Figure 11.22. Definitions employed for load-unload analysis of Hutton pile groups.

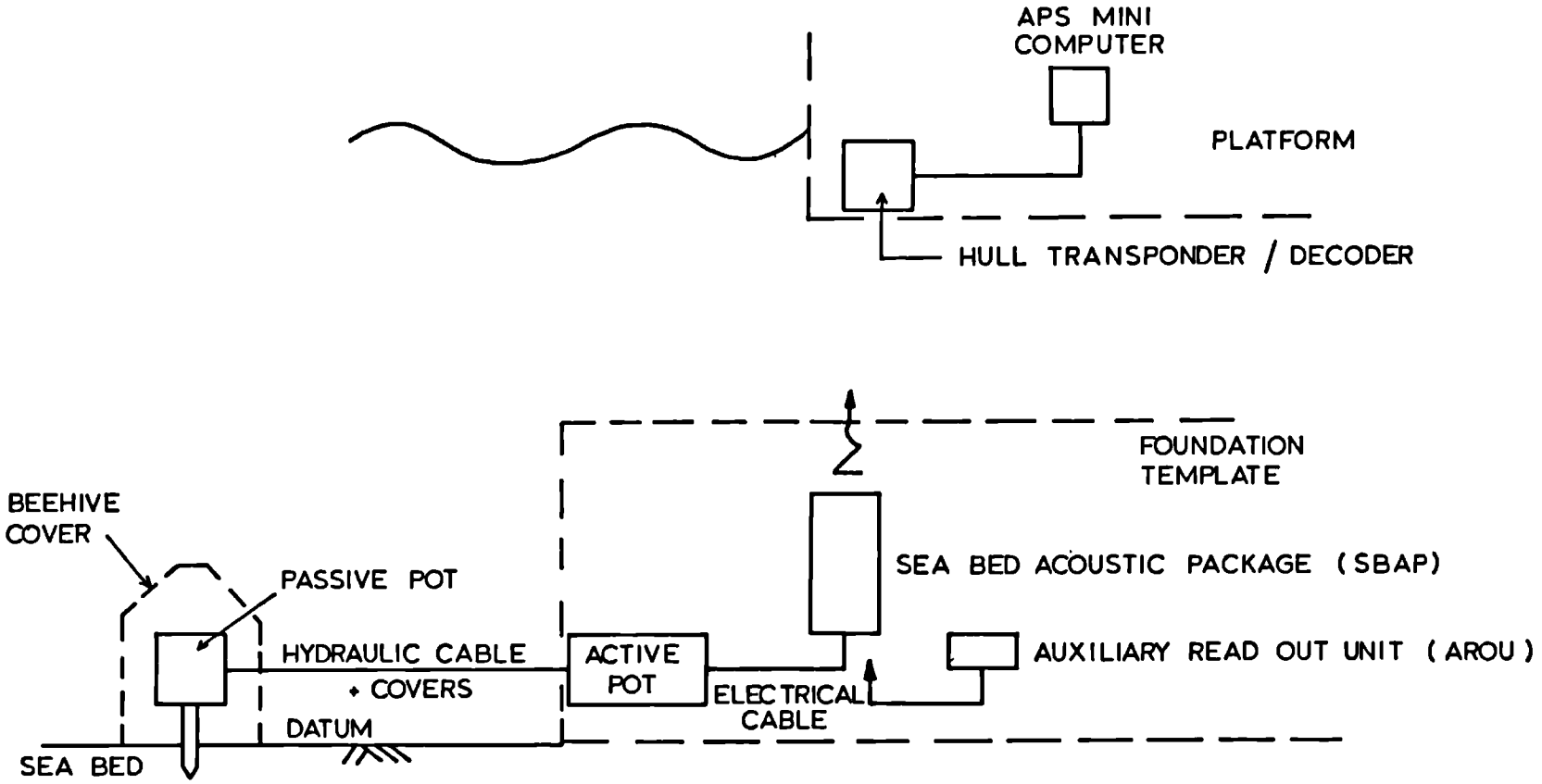


Figure 11.23. COMPONENTS OF SYSTEM

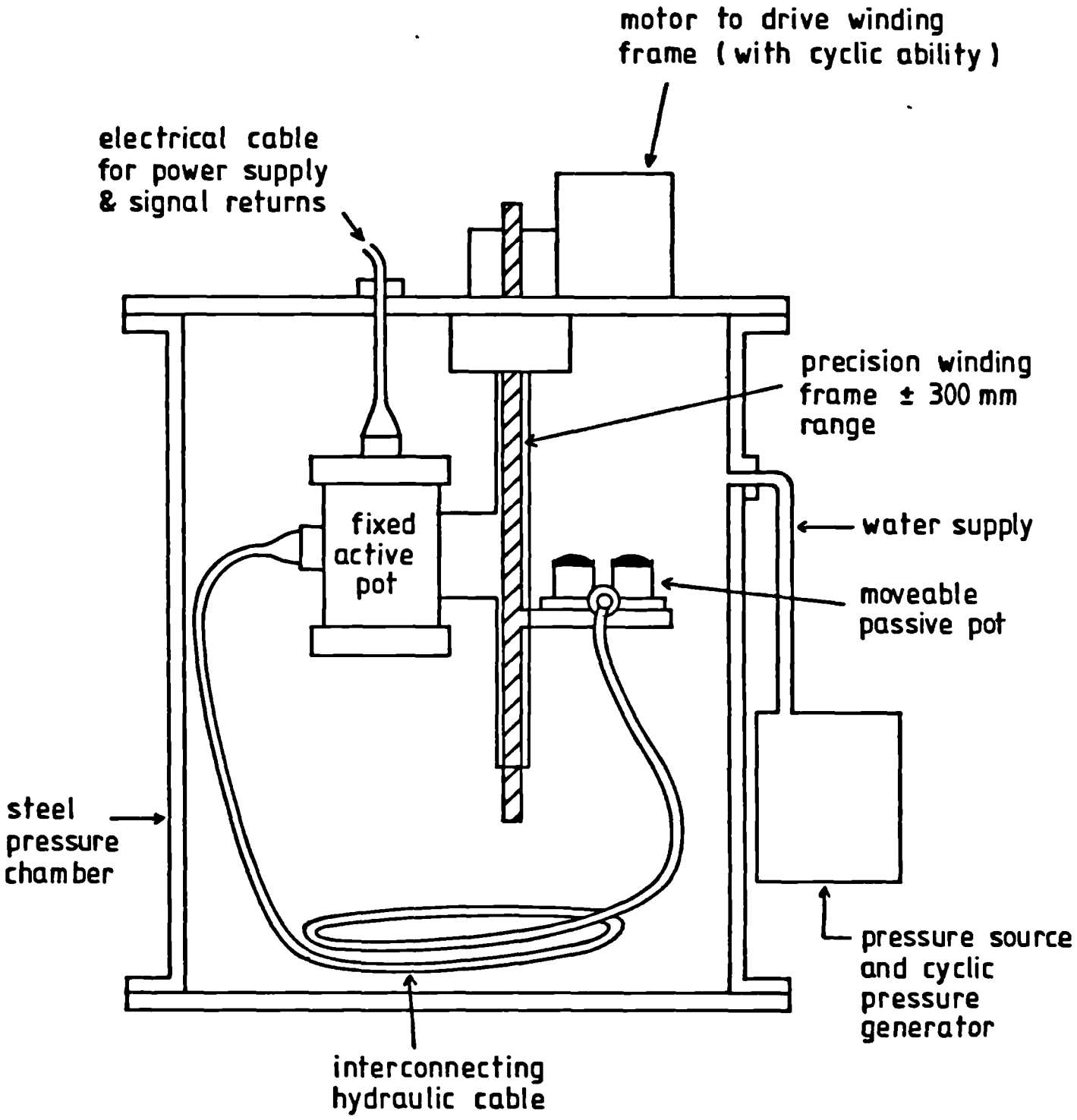


Figure 11.24. Hyperbaric calibration system for settlement gauges.

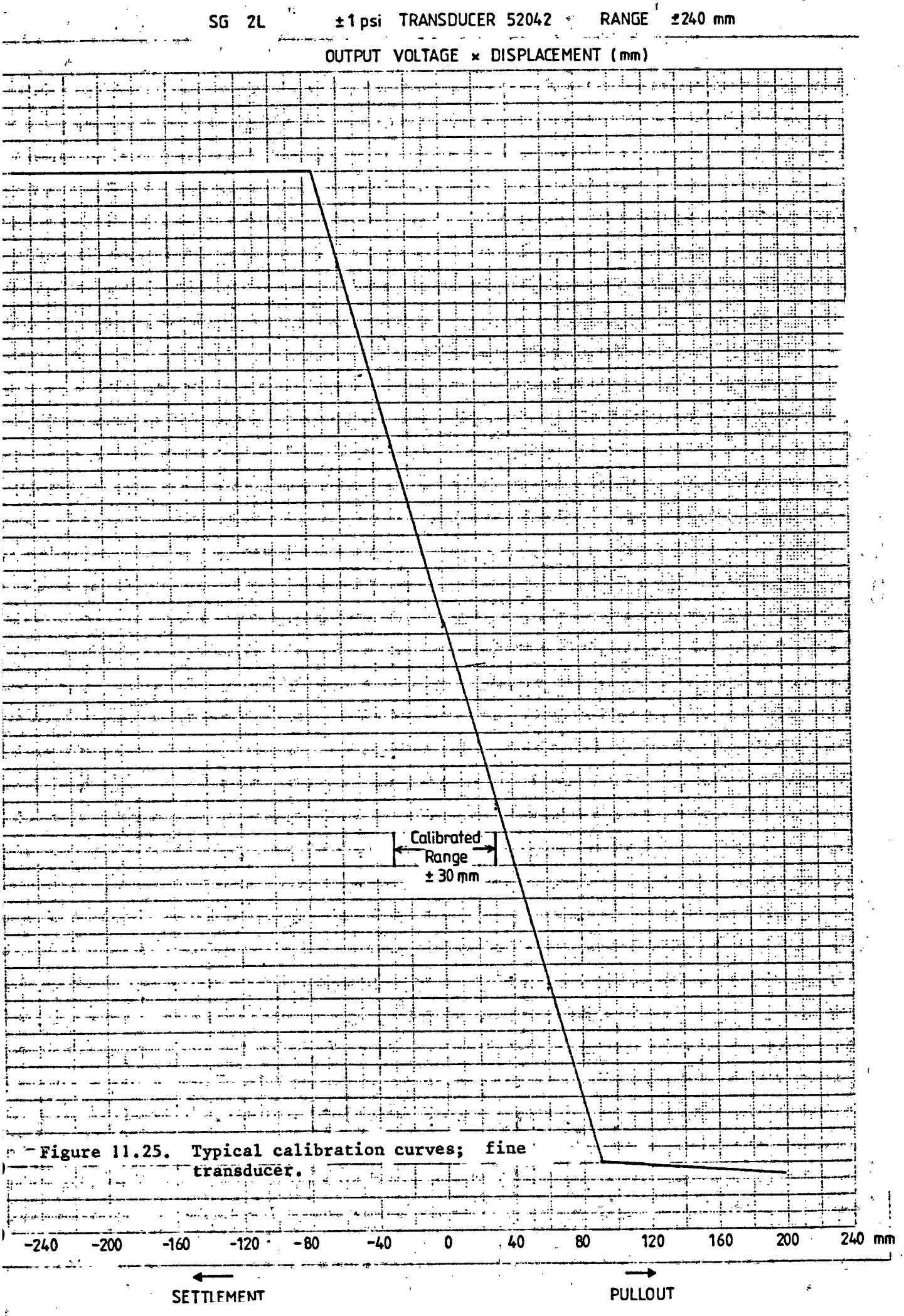


Figure 11.25. Typical calibration curves; fine transducer.

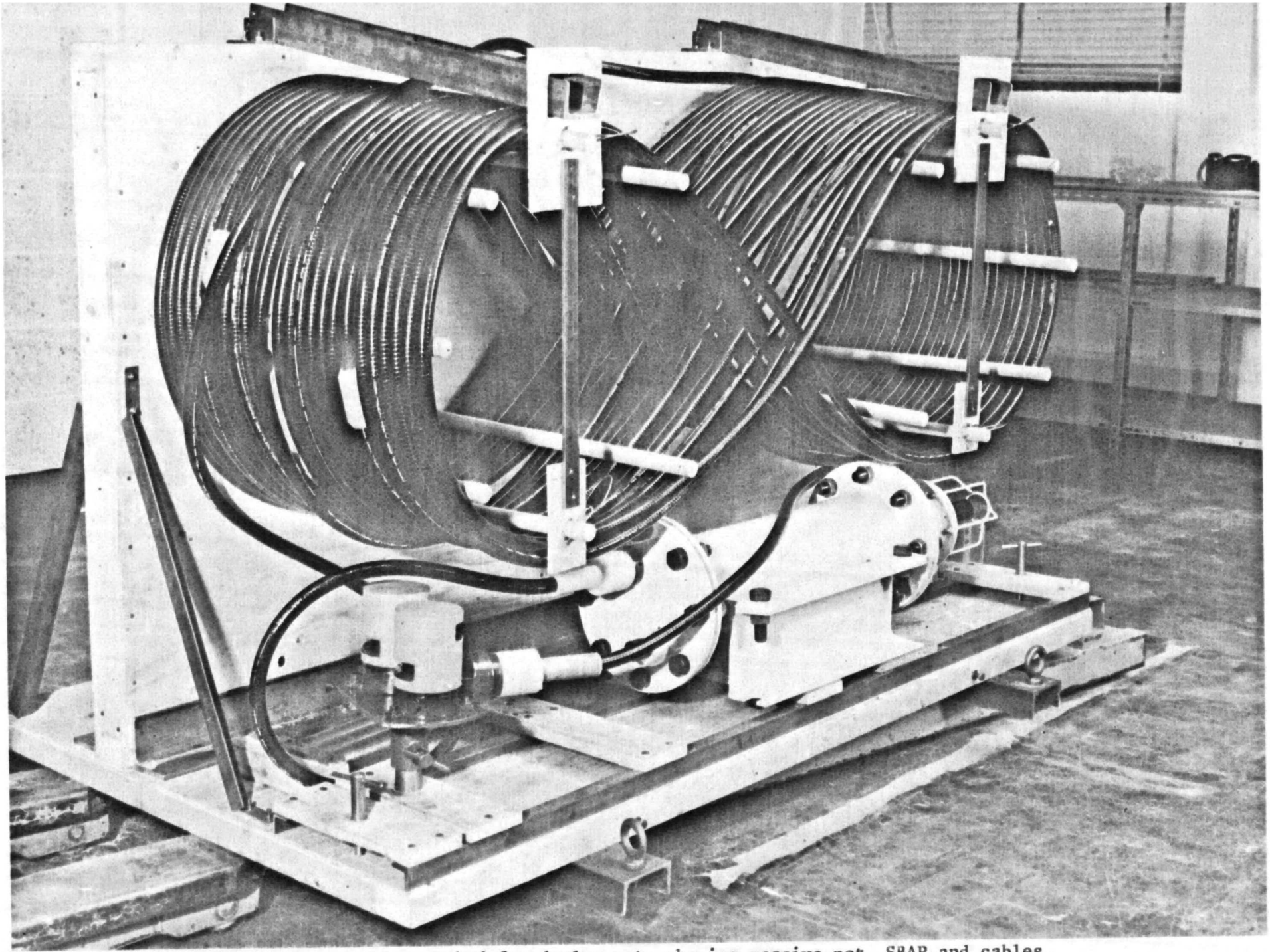


Figure 11.26. Settlement gauge system packed for deployment; showing passive pot, SBAP and cables.



Figure 11.27. FOUNDATION TEMPLATE



Active pot mounted on Template

(photo taken by divers working at 148 M depth).

Figure 11.28.

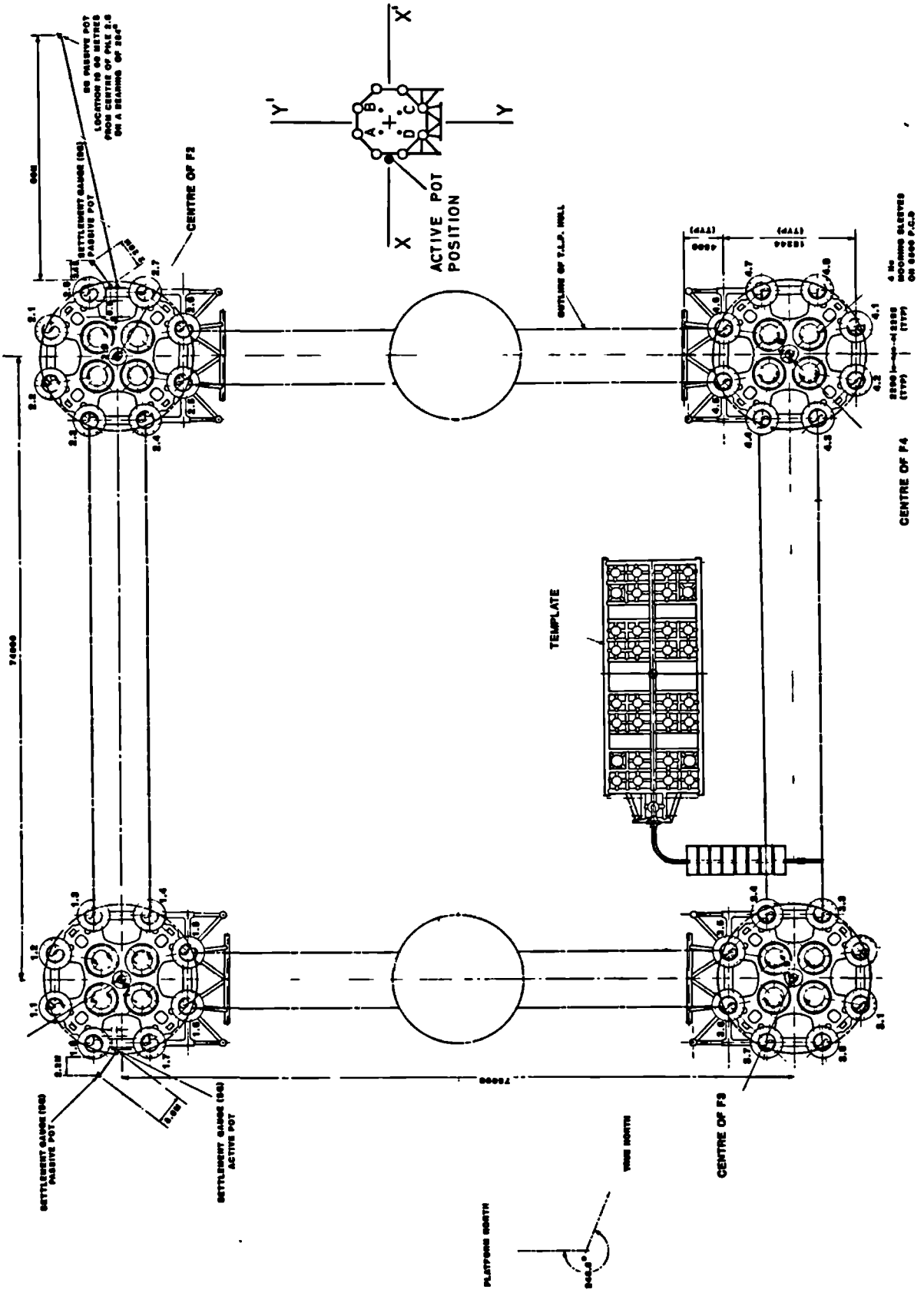
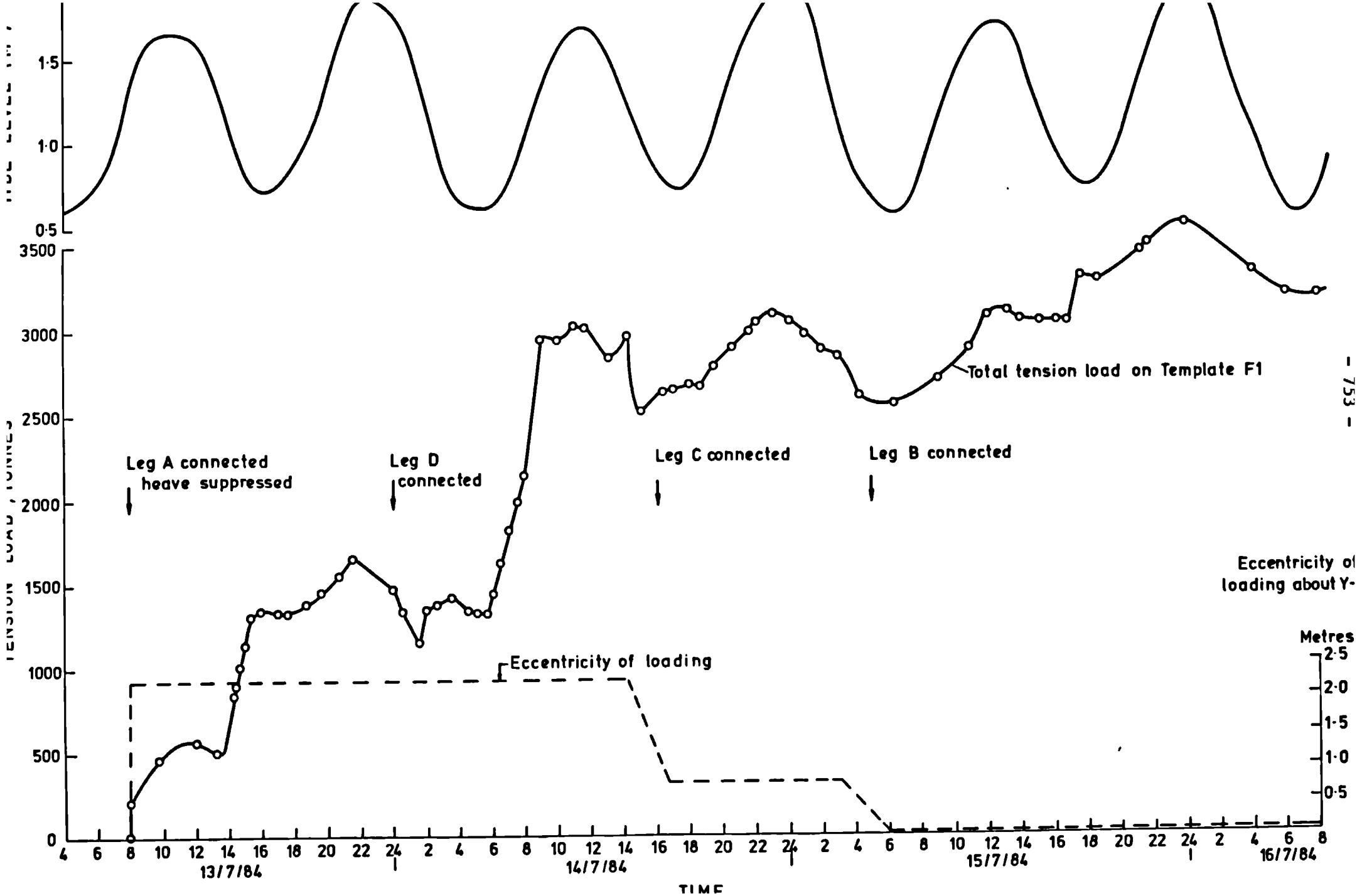


Figure 11.29. Plan view of TLP hull and foundation templates.


1·5
1·0
0·5
3500
3000
2500
2000
1500
1000
500
0
Total tension load on Template F1
Leg A connected
heave suppressed
Leg D
connected
Leg C connected
Leg B connected
Eccentricity of loading
Eccentricity of
loading about Y-
Metres
2·5
2·0
1·5
1·0
0·5
4 6 8 10 12 14 16 18 20 22 24 2 4 6 8 10 12 14 16 18 20 22 24 2 4 6 8 10 12 14 16 18 20 22 24 2 4 6 8
13/7/84
14/7/84
15/7/84
16/7/84
TIME

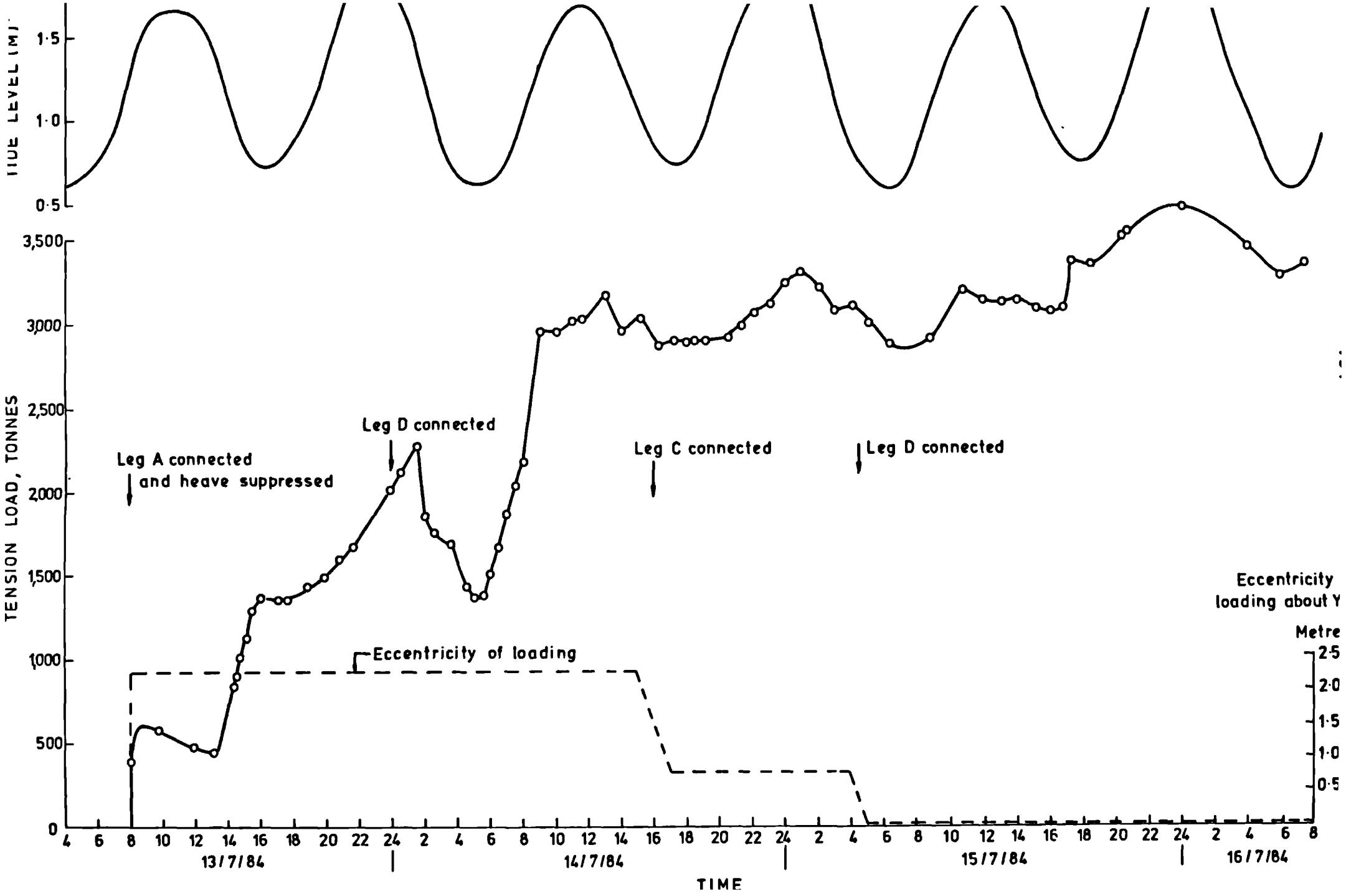

TIDE LEVEL (M)
1·5
1·0
0·5
3,500
3,000
2,500
2,000
1,500
1,000
500
0
TENSION LOAD, TONNES
Leg A connected
and heave suppressed
Leg D connected
Leg C connected
Leg D connected
Eccentricity of loading
Eccentricity
loading about Y
Metre
2·5
2·0
1·5
1·0
0·5
4 6 8 10 12 14 16 18 20 22 24 2 4 6 8 10 12 14 16 18 20 22 24 2 4 6 8 10 12 14 16 18 20 22 24 2 4 6 8
13/7/84
14/7/84
15/7/84
16/7/84
TIME

Figure 11.32. TEMPLATE F1, SG 2L

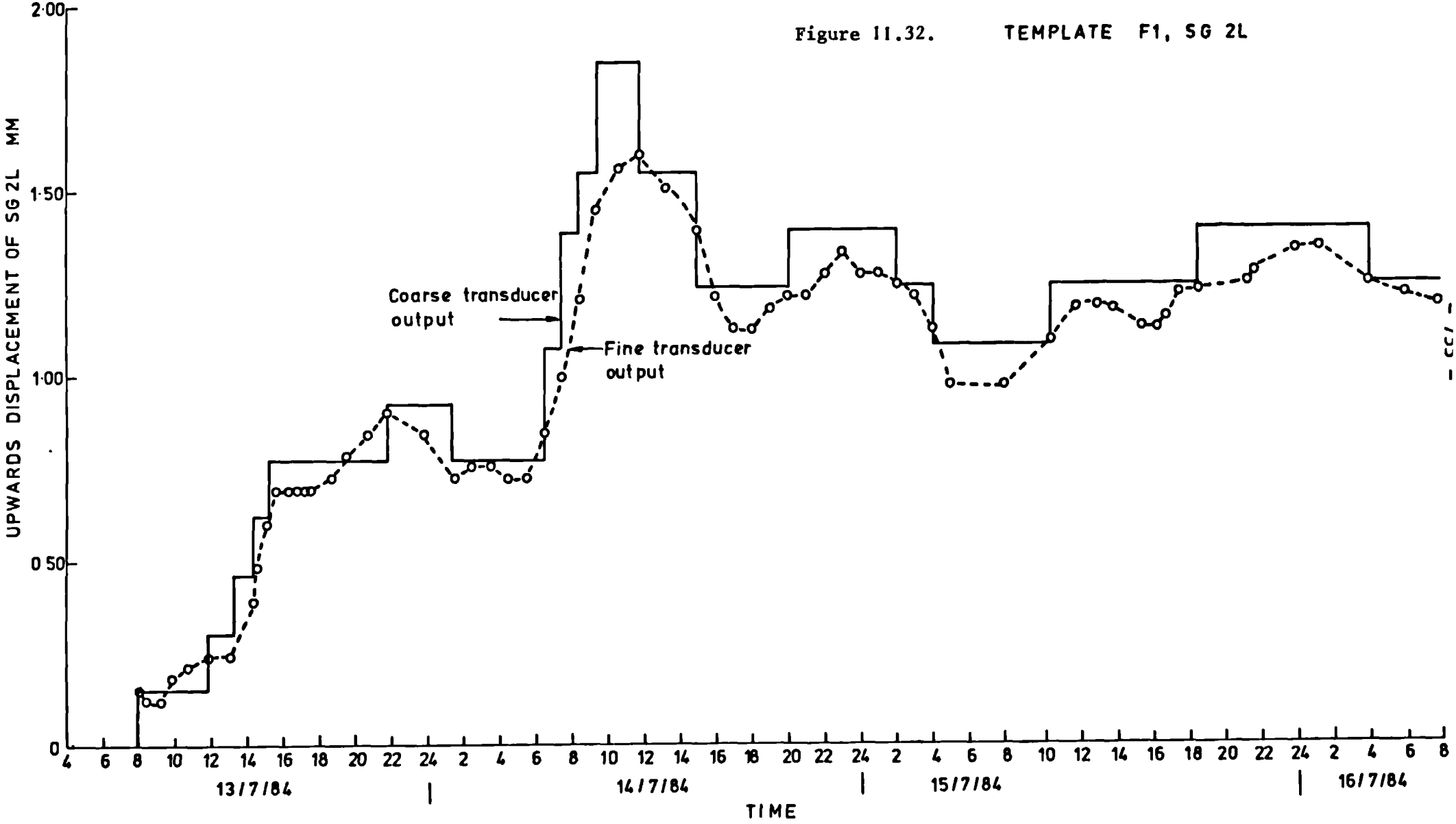


Figure 11.33. TEMPLATE F2, SG 4L

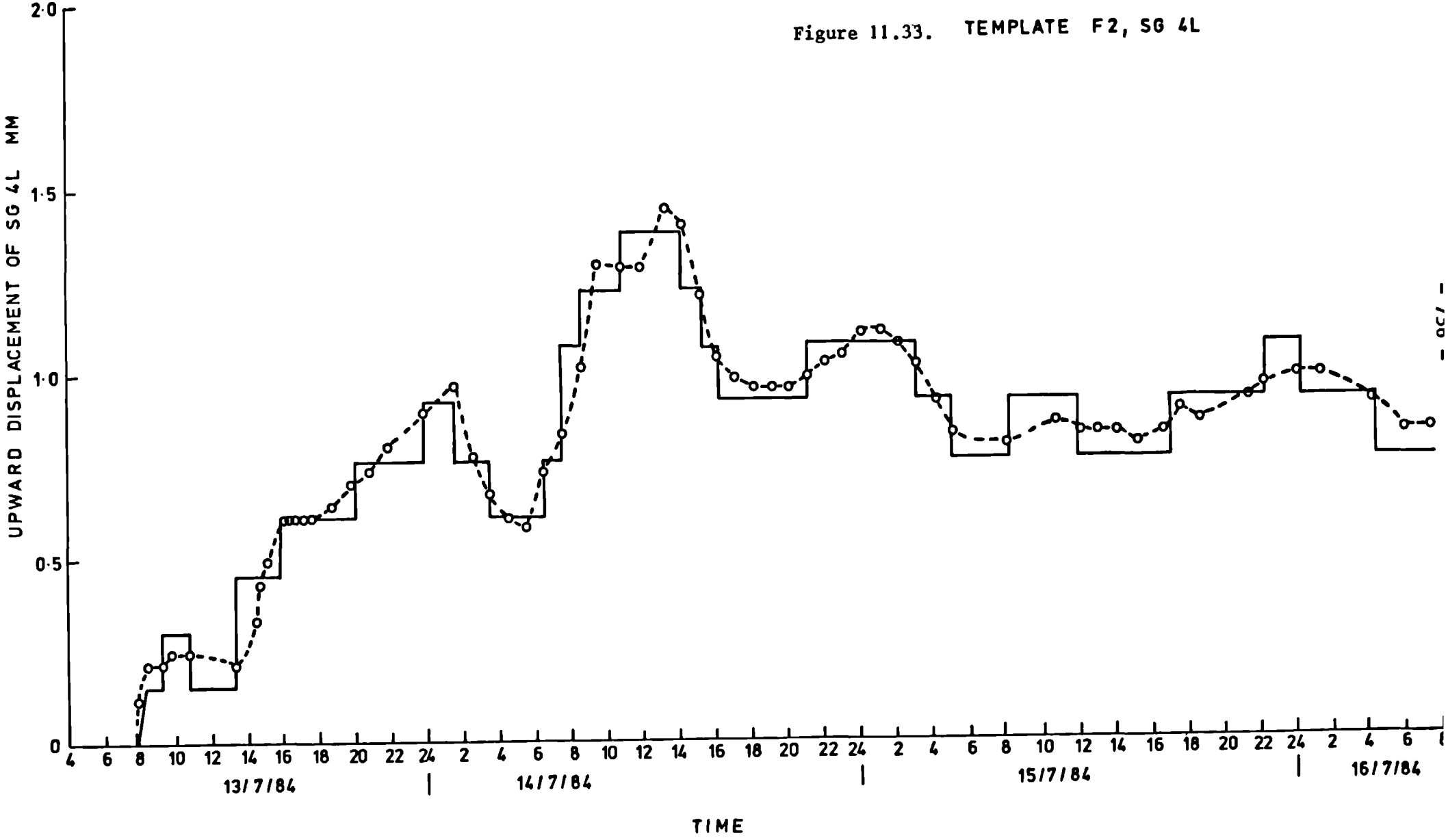
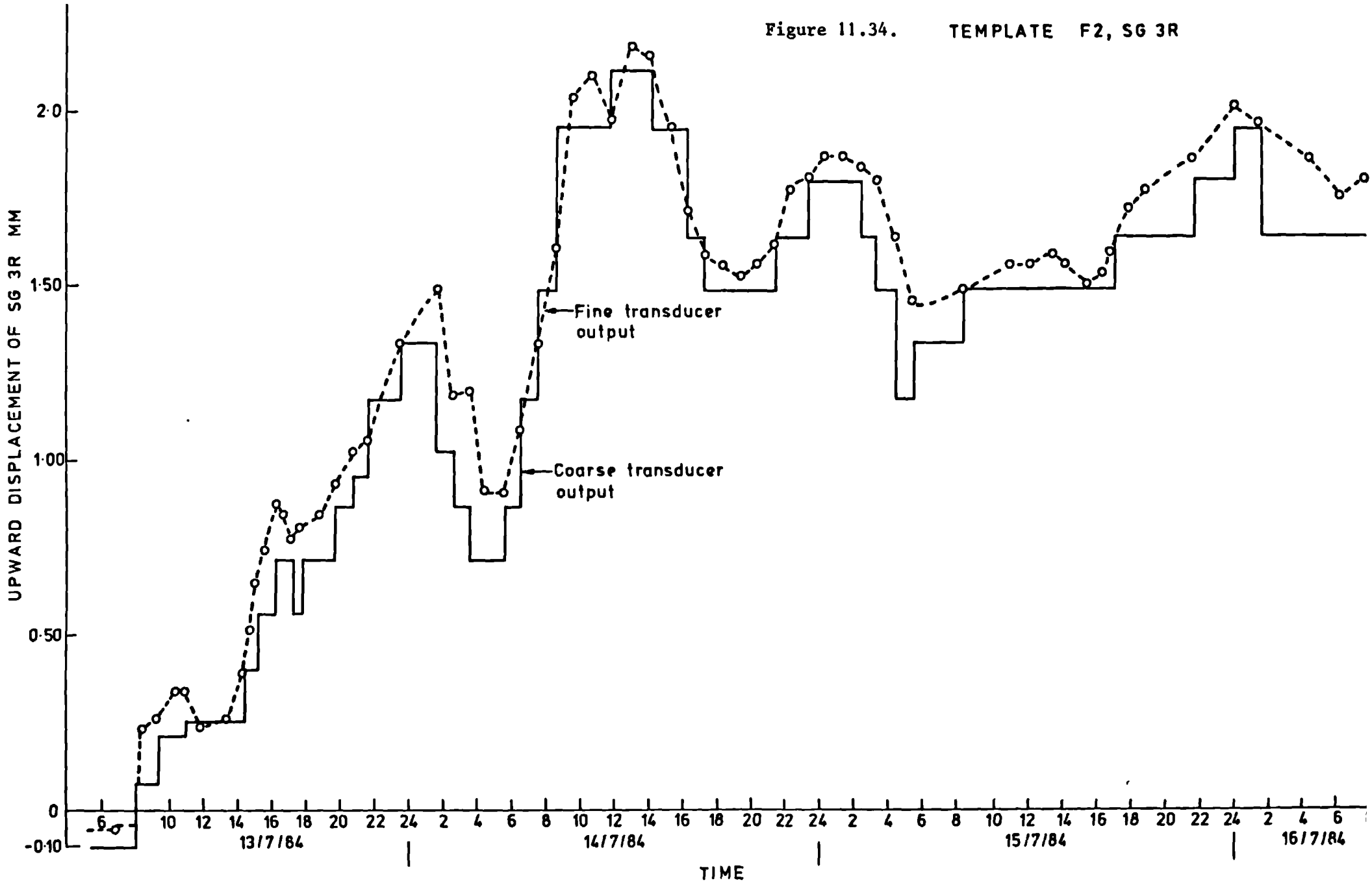


Figure 11.34. TEMPLATE F2, SG 3R



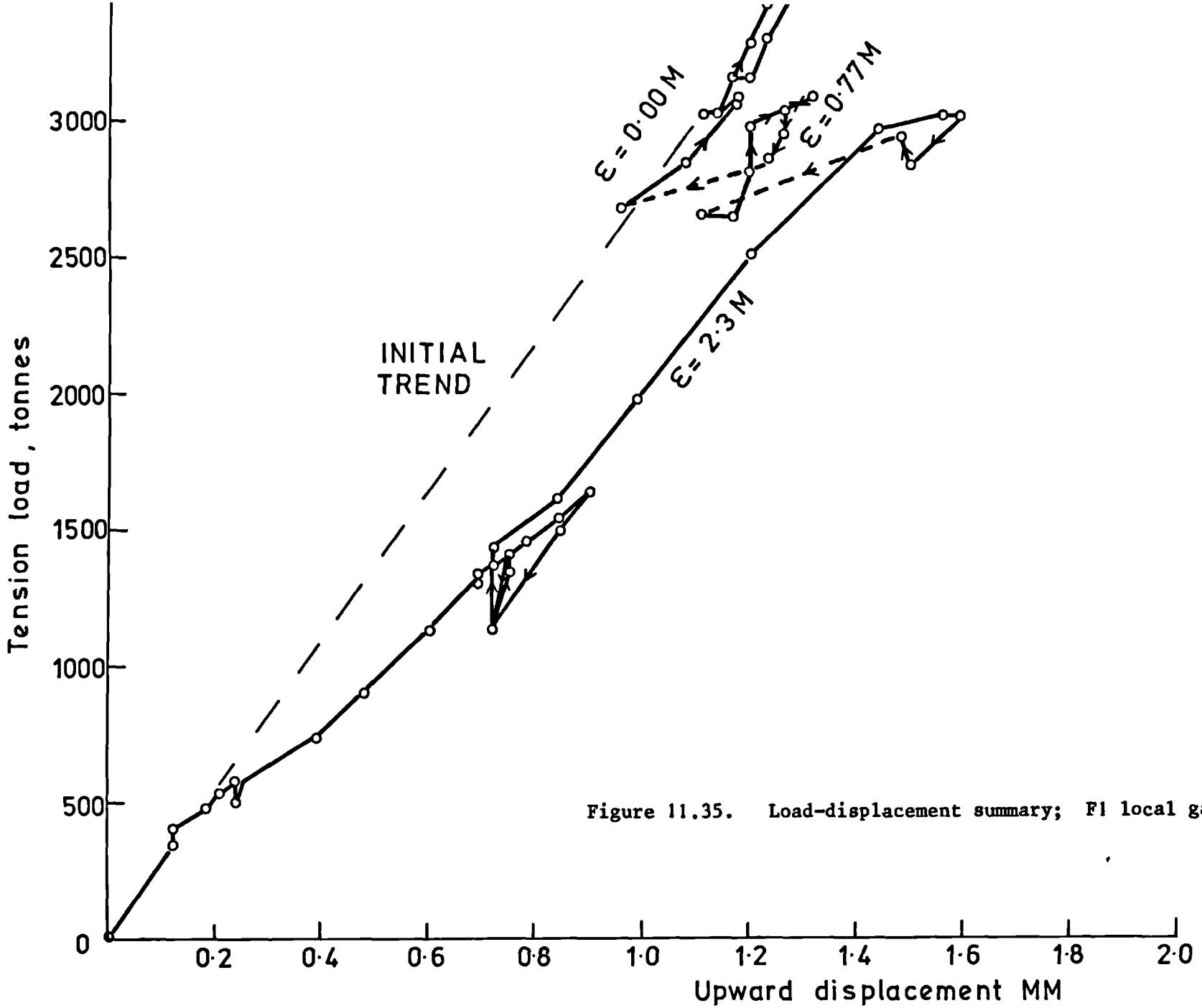


Figure 11.35. Load-displacement summary; F1 local gauge (SG2L).

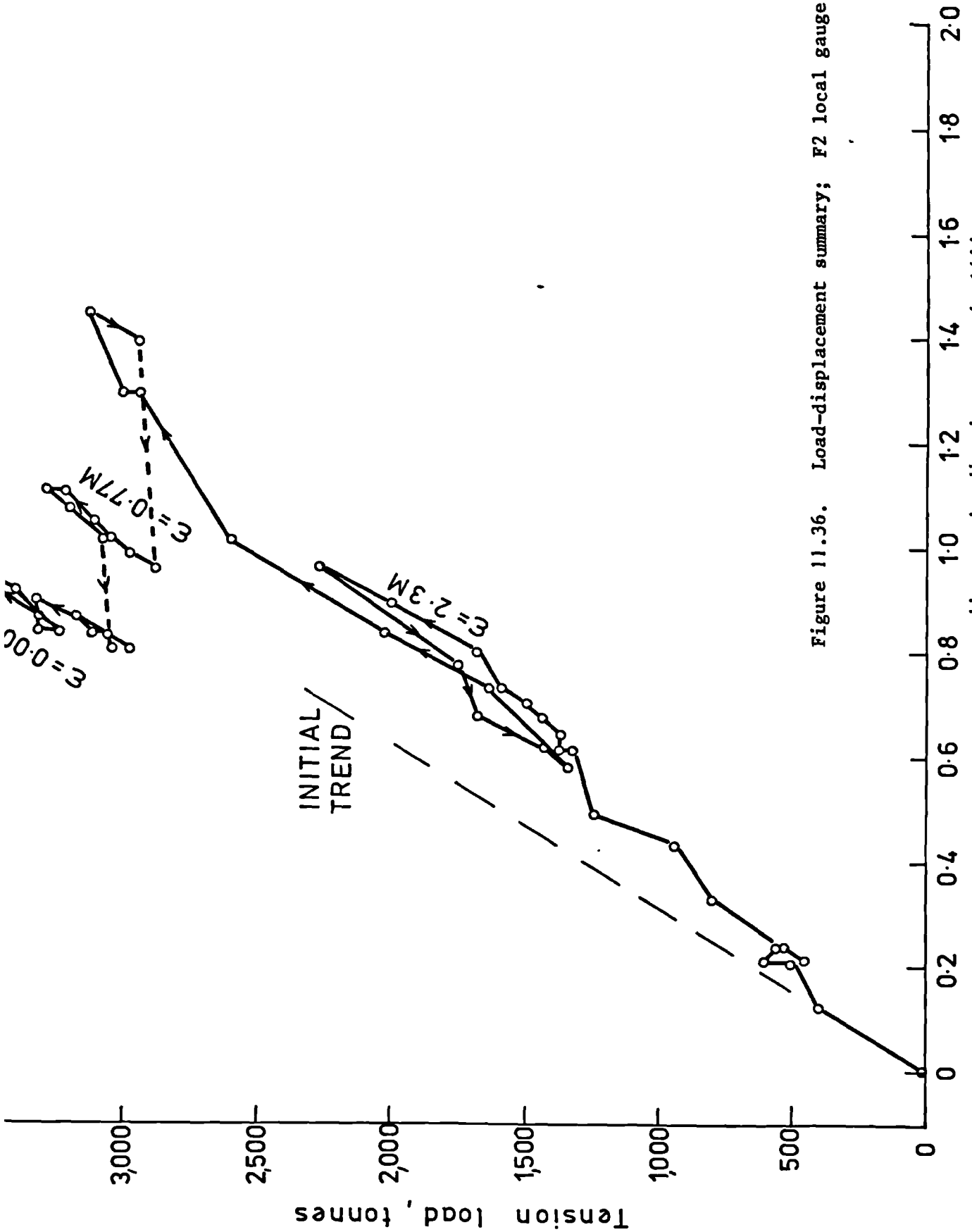


Figure 11.36. Load-displacement summary; F2 local gauge (SG4L).

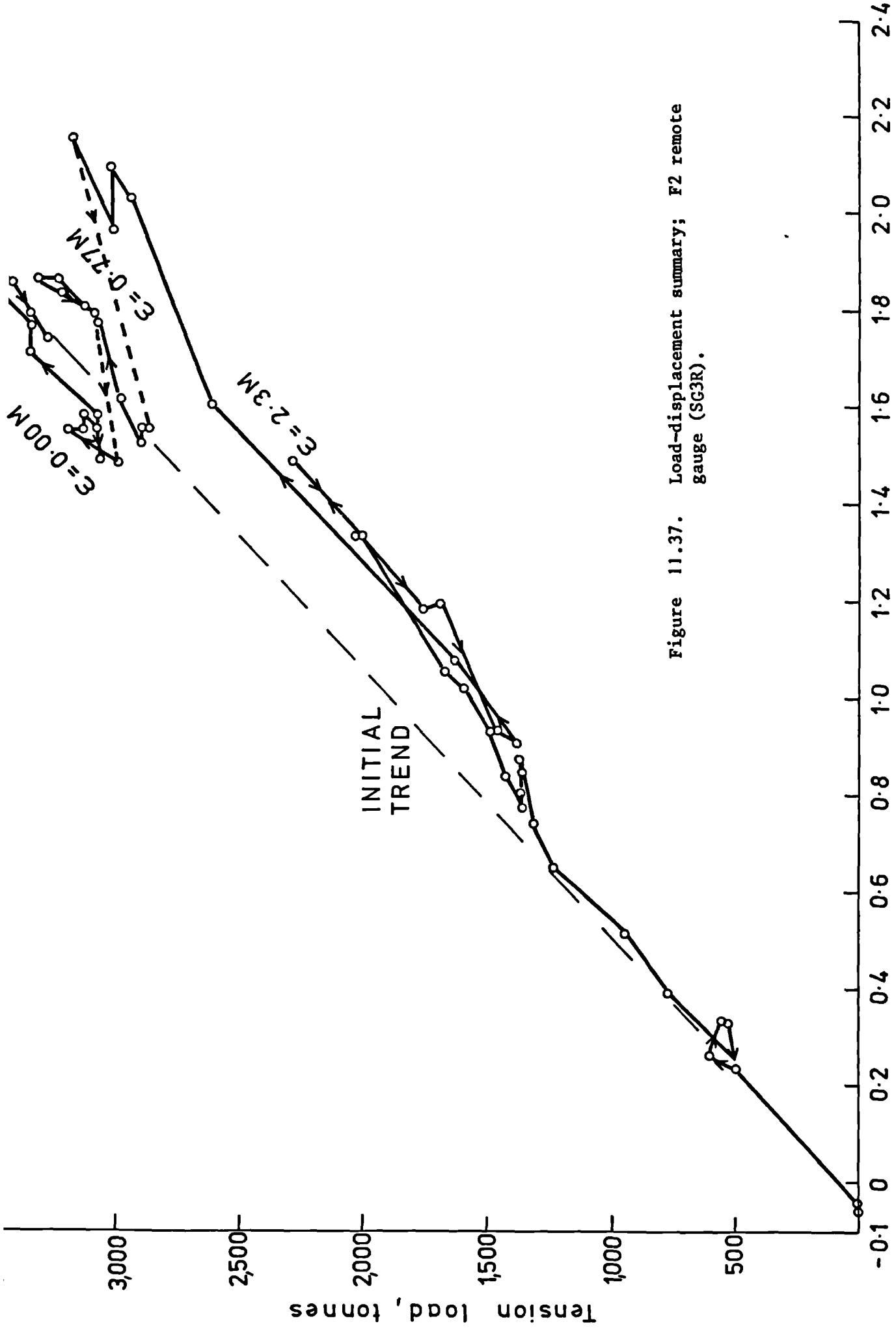


Figure 11.37. Load-displacement summary; F2 remote gauge (SG3R).

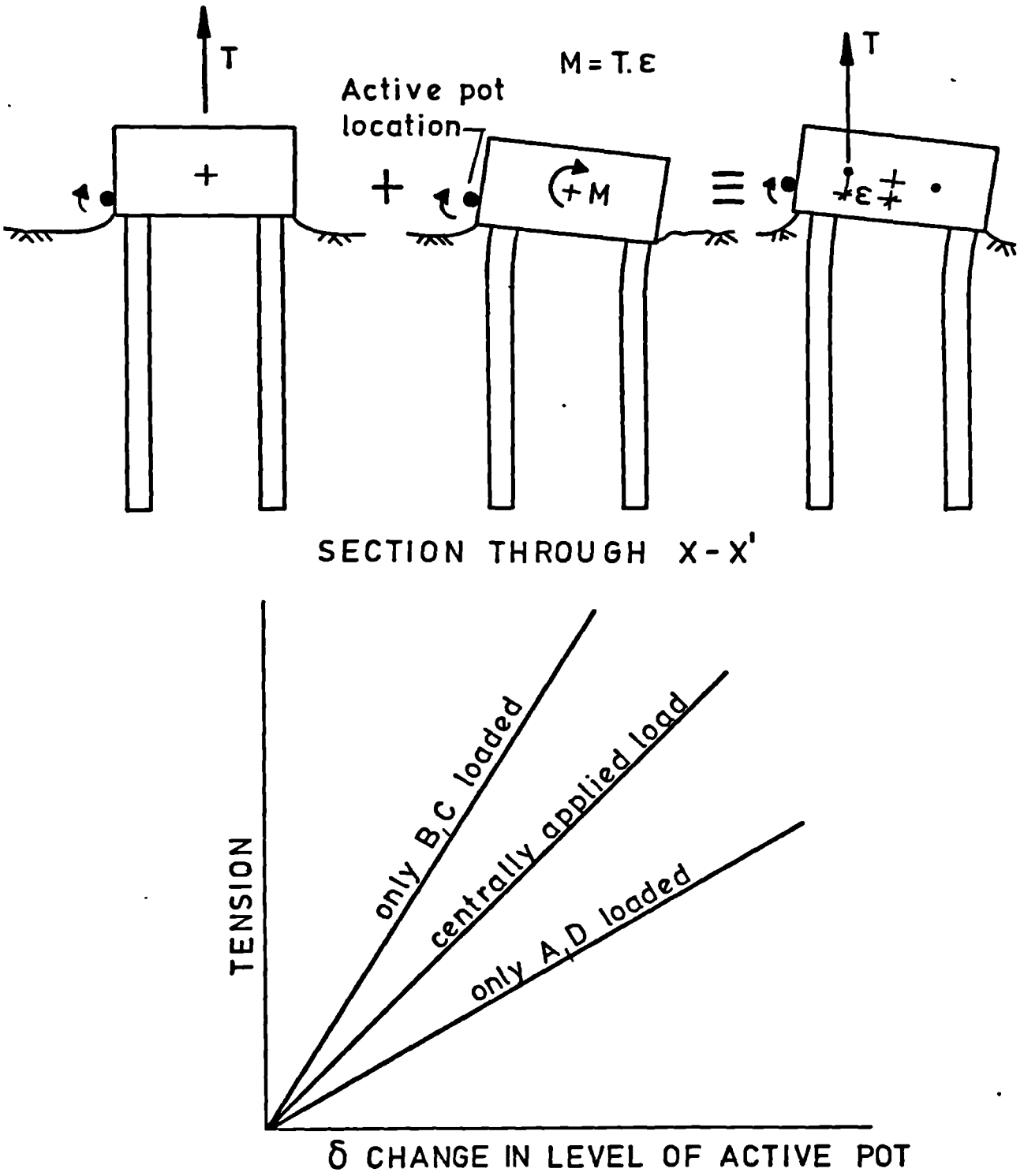


Figure 11.38. Effects of eccentric loading on settlement gauge data; above schematic, below characteristics of a linear system.

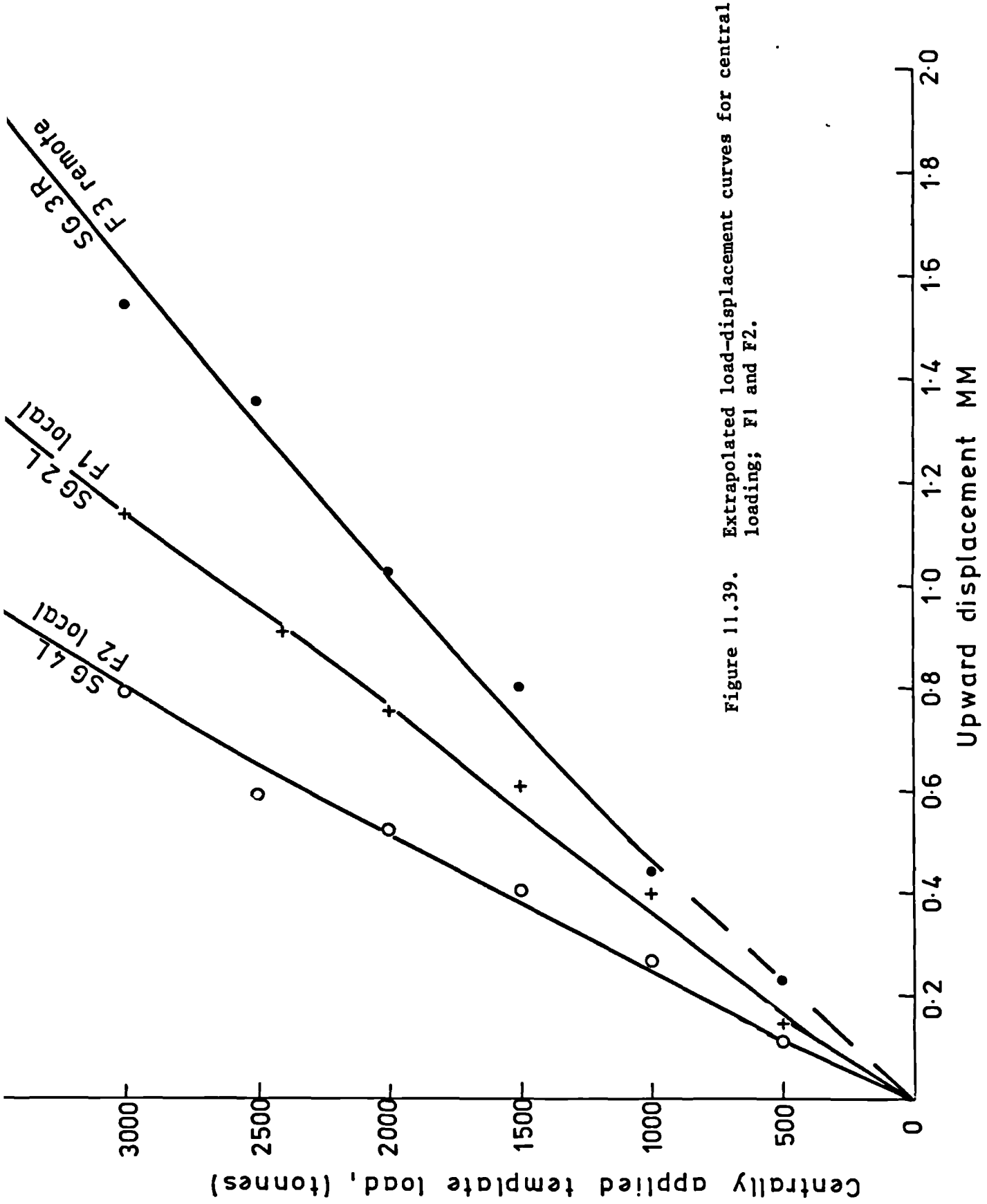


Figure 11.39. Extrapolated load-displacement curves for central loading; F1 and F2.

APPENDICES

Tables and Figures

Section in Thesis	Description of Analysis		Assumptions Made				
			gy(θ)	gp(θ)	Hvorslev surface	Shear Modulus	Drained Bulk Modulus
Chapter 3 3.6, 3.10 and 3.11	Cavity Expansion analyses by Randolph et al. (1979), Wroth et al. (1979) and Carter et al. (1979)		Constant M (Surface of Revolution)	Associated	Not Employed	Finite, varying with OCR	Derived from swelling line
3.8	Cavity Expansion analyses by Fathallah (1978)		"	"	"	"	"
3.13	Pile loading analysis by Potts and Martins (1982)	Model A	"	"	"	"	"
		Model B	Constant ϕ' (Mohr-Coulomb)	Non-associated; X, Y Z chosen to give realistic b value in plane strain	"	"	"
Chapter 4 4.2	Study of model pile apparatus	Model B	"	"	Inclination to horizontal taken as $\phi'/2$	"	"
4.4 to 4.6	Study of Hutton TLP foundations		"	Associated	"	"	"
Chapter 10	Study of Magnus platform foundations		"	"	Inclination to horizontal taken as $3\phi'/4$	Specified as a function of shear strain invariant	Specified as a function of volume strain
Chapter 11	Study of Hutton TLP foundations		"	"	"	"	"

Table A2.1

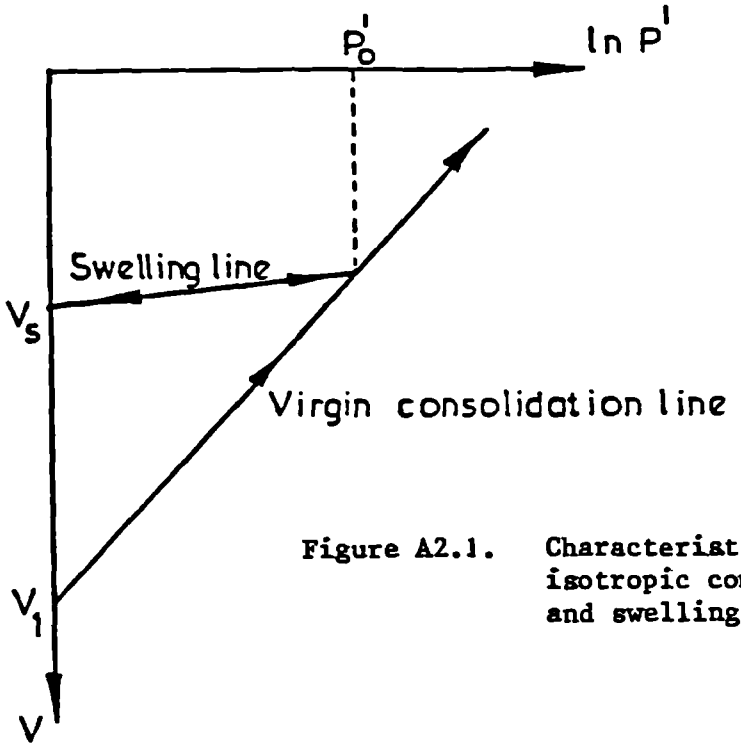


Figure A2.1. Characteristics in isotropic compression and swelling.

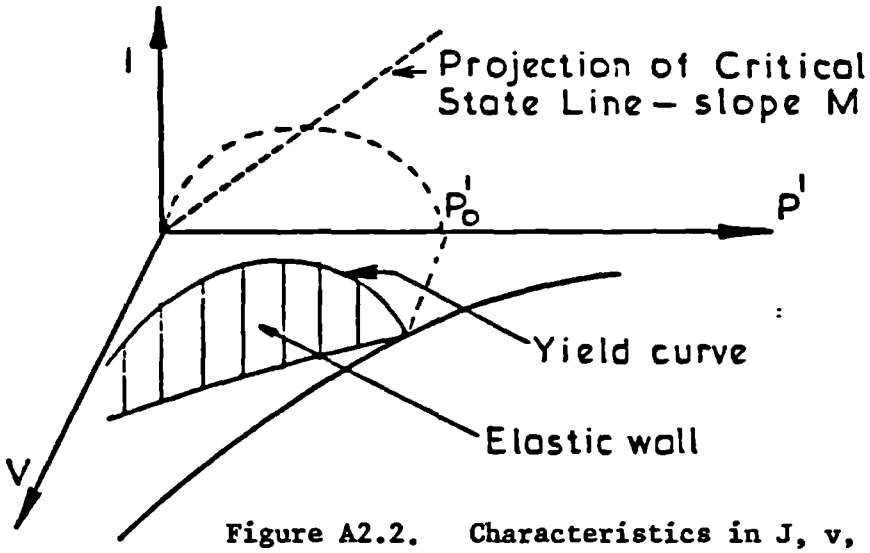


Figure A2.2. Characteristics in J, v, p' space.

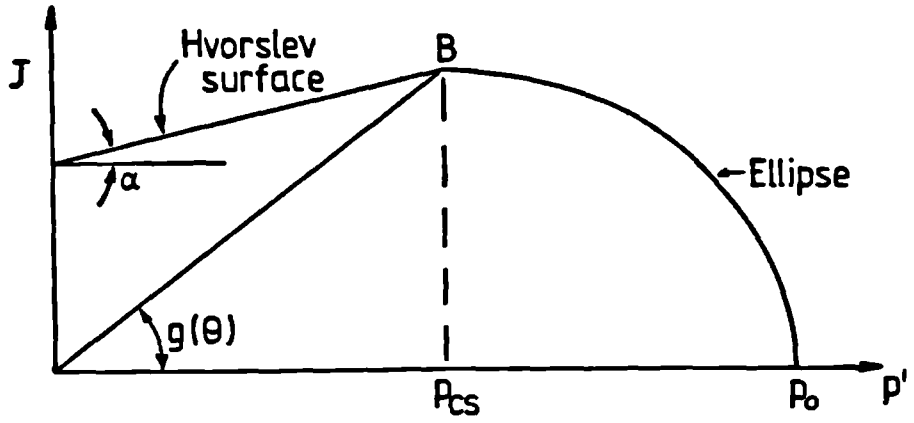
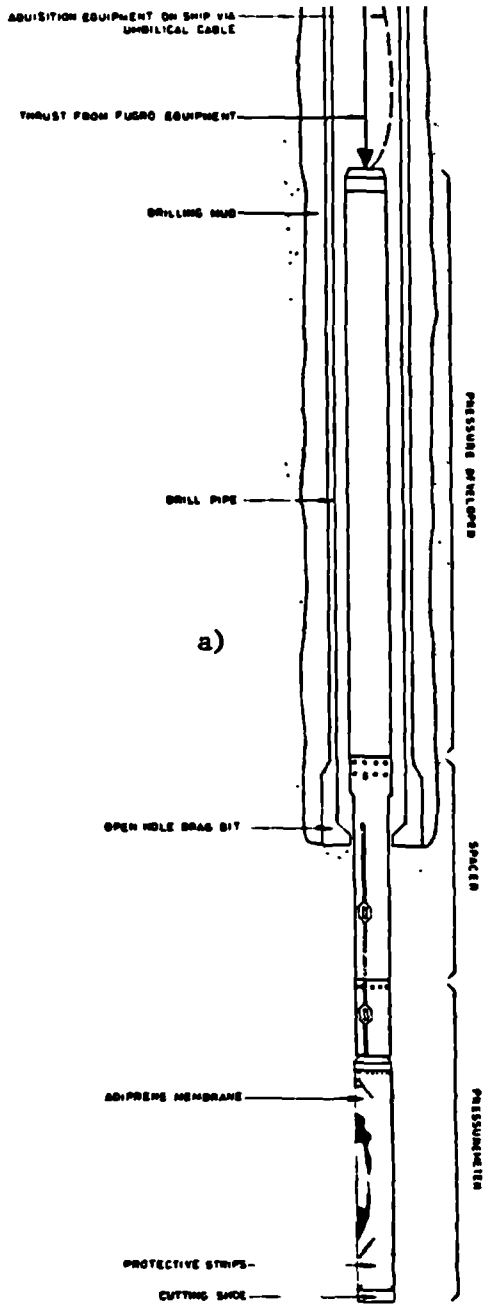


Figure A2.3. Modified Cam-Clay with Hvorslev surface in J, p' space.



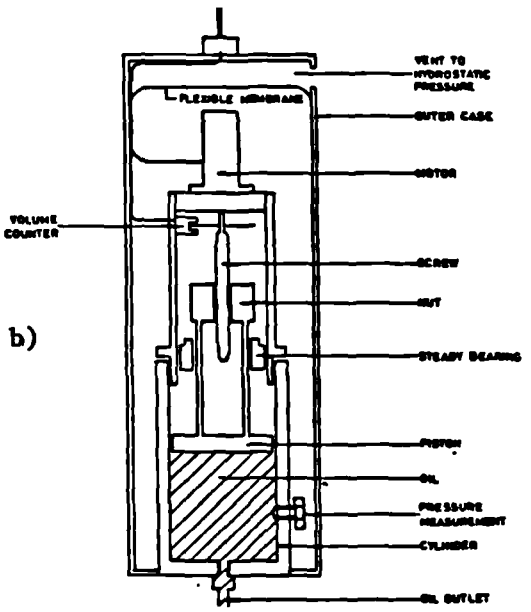


DIAGRAM OF PUMP

Figure A3.1, a), b), c)
Push in Pressuremeter Details.

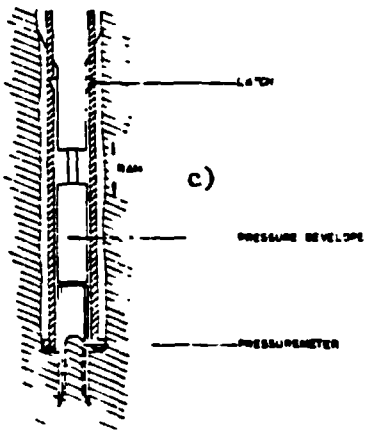


DIAGRAM OF FUGRO INSERT SYSTEM

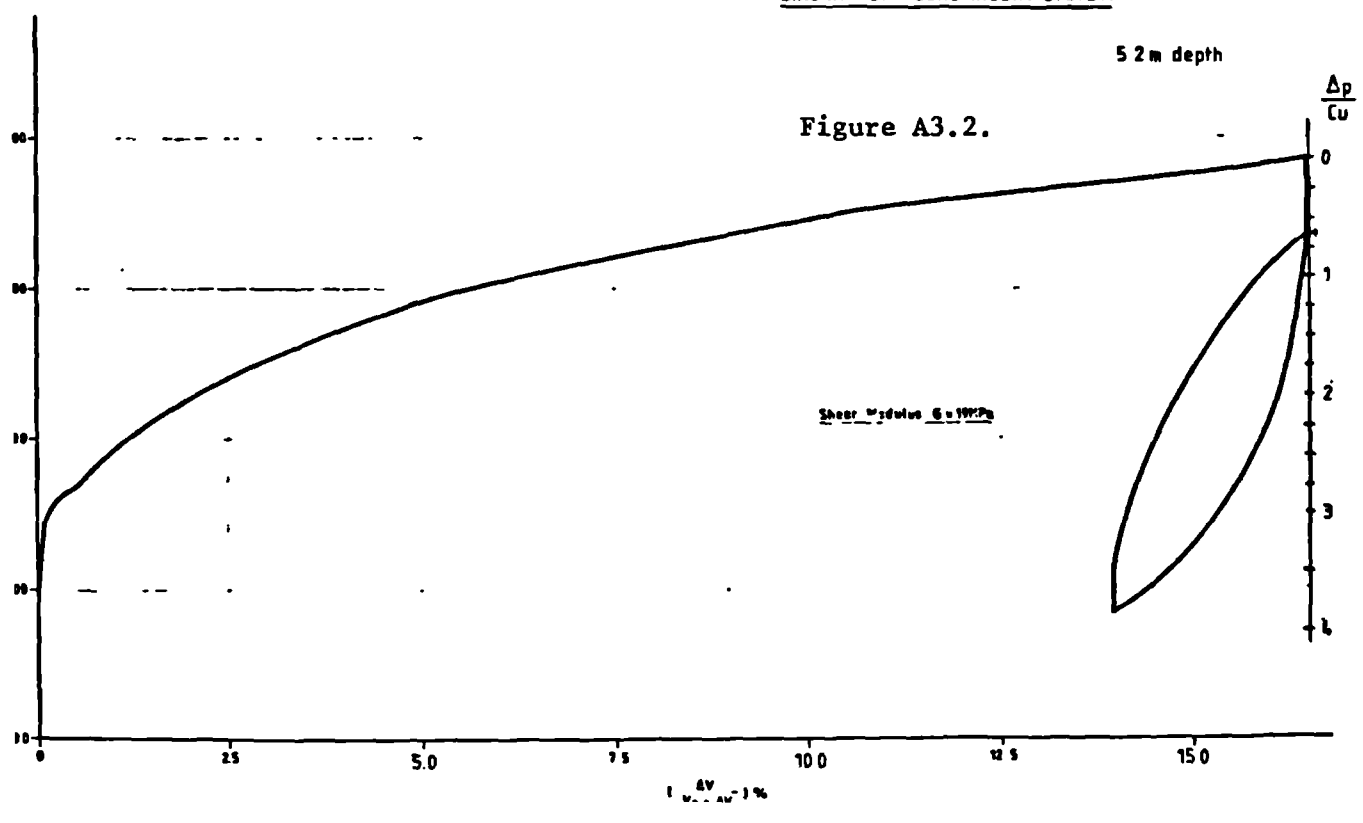


Figure A3.2.

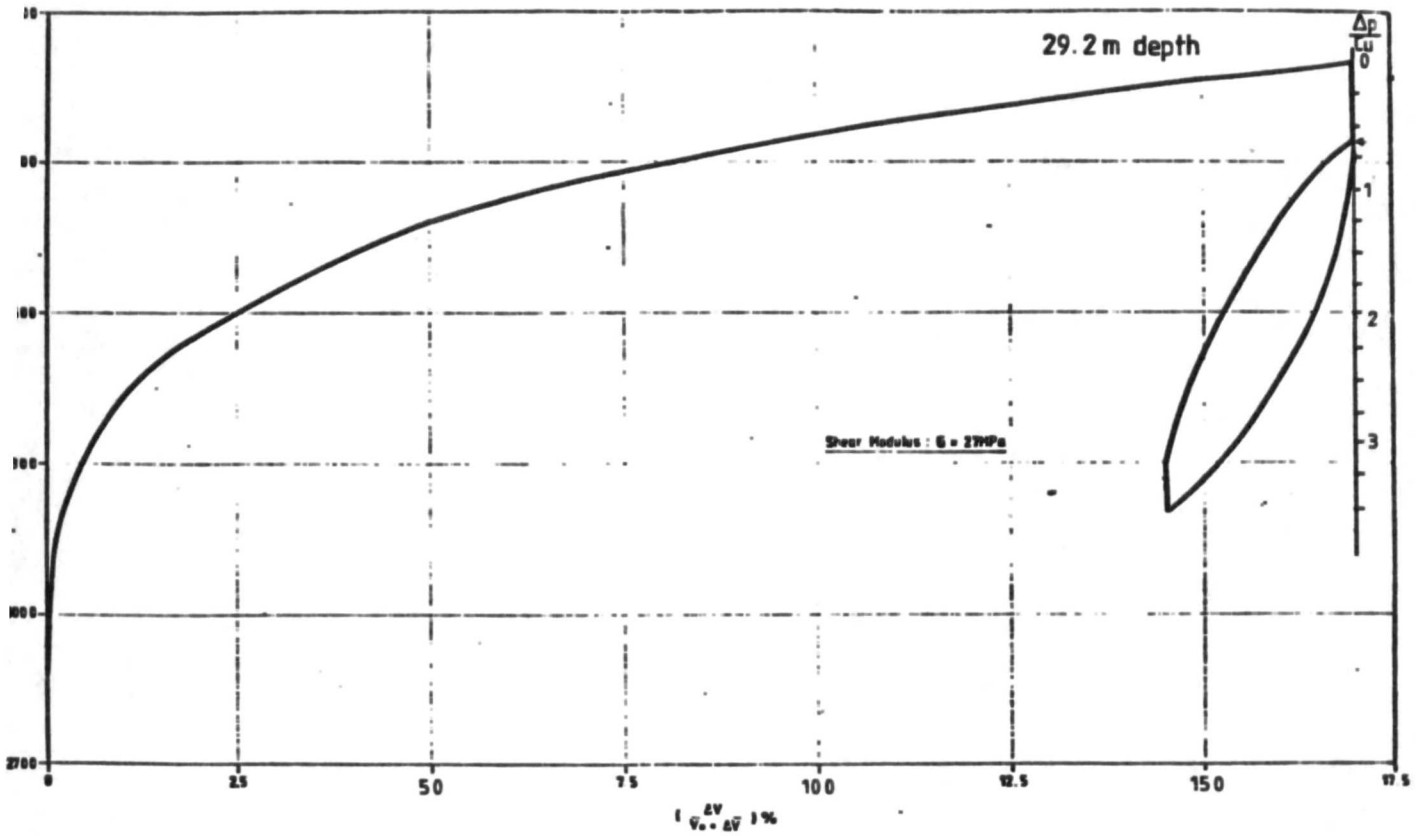


Figure A3.3.

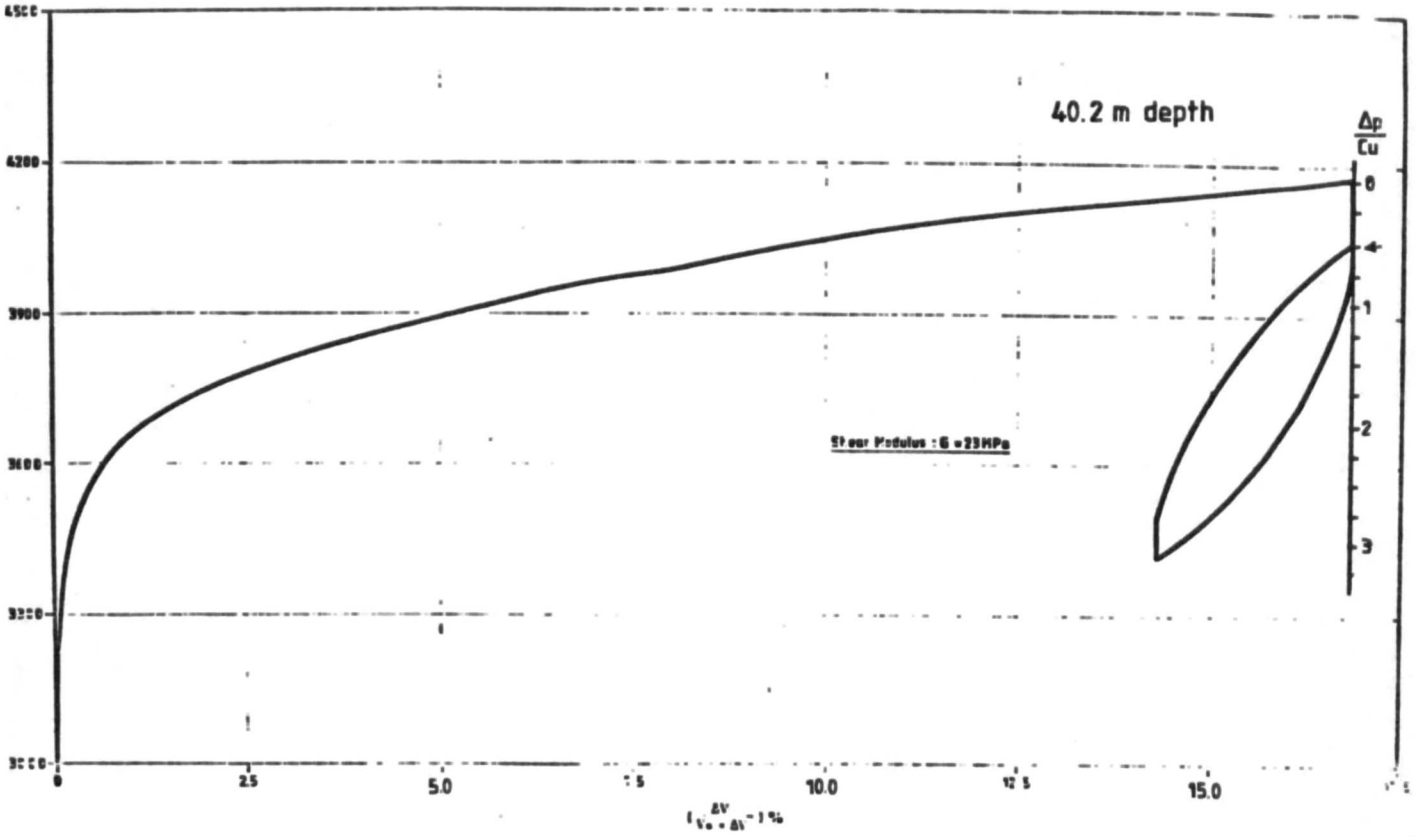


Figure A3.4.

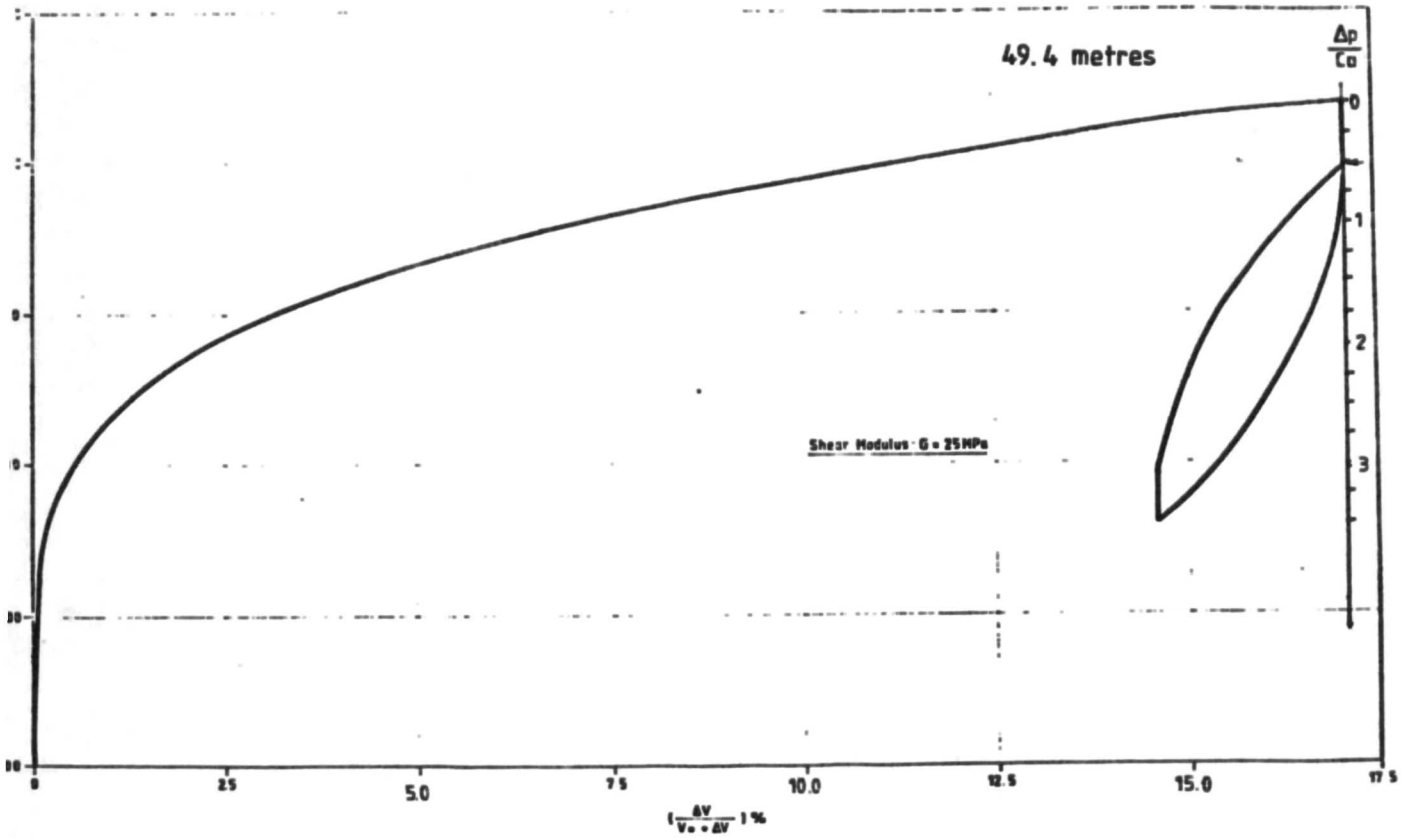


Figure A3.5.

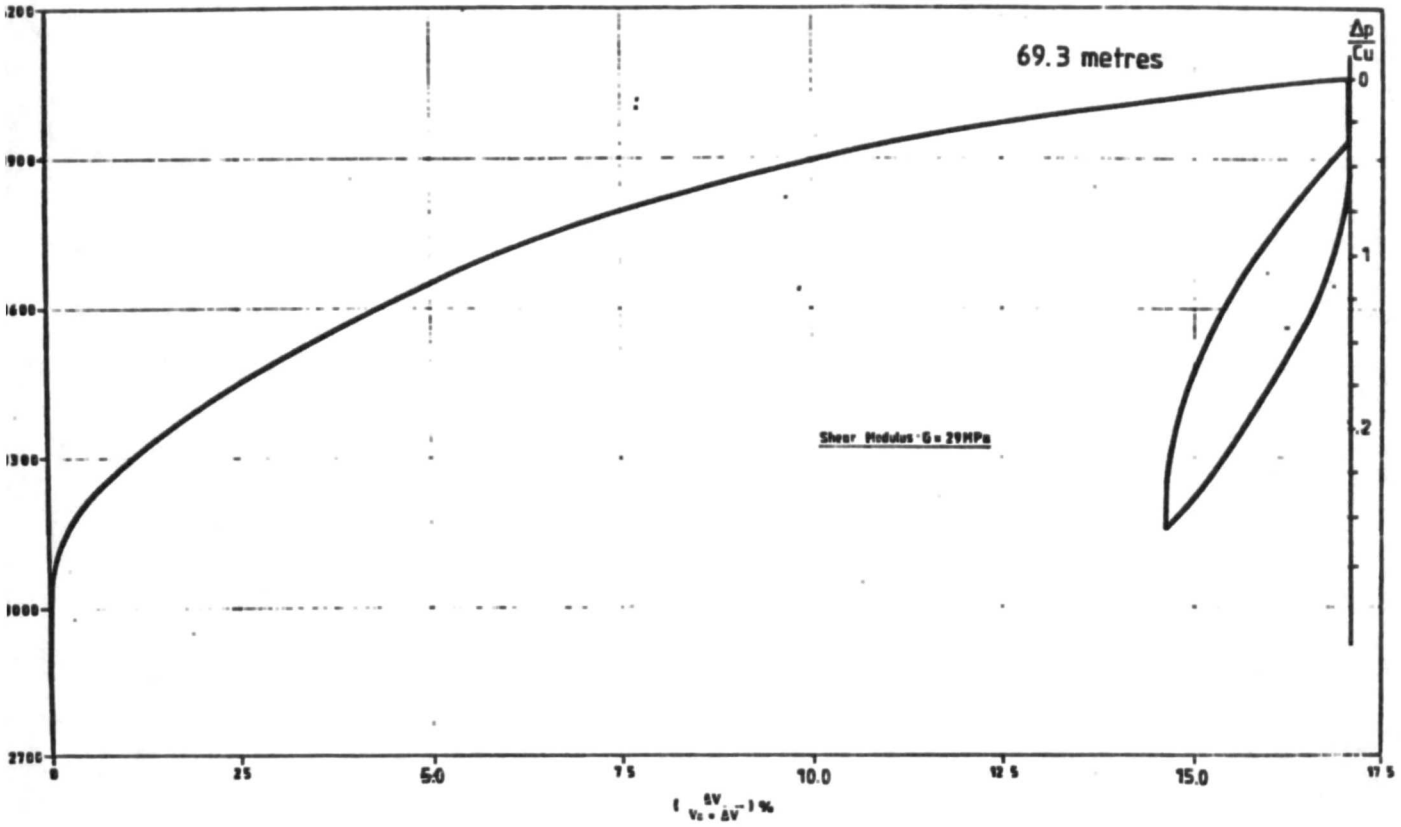
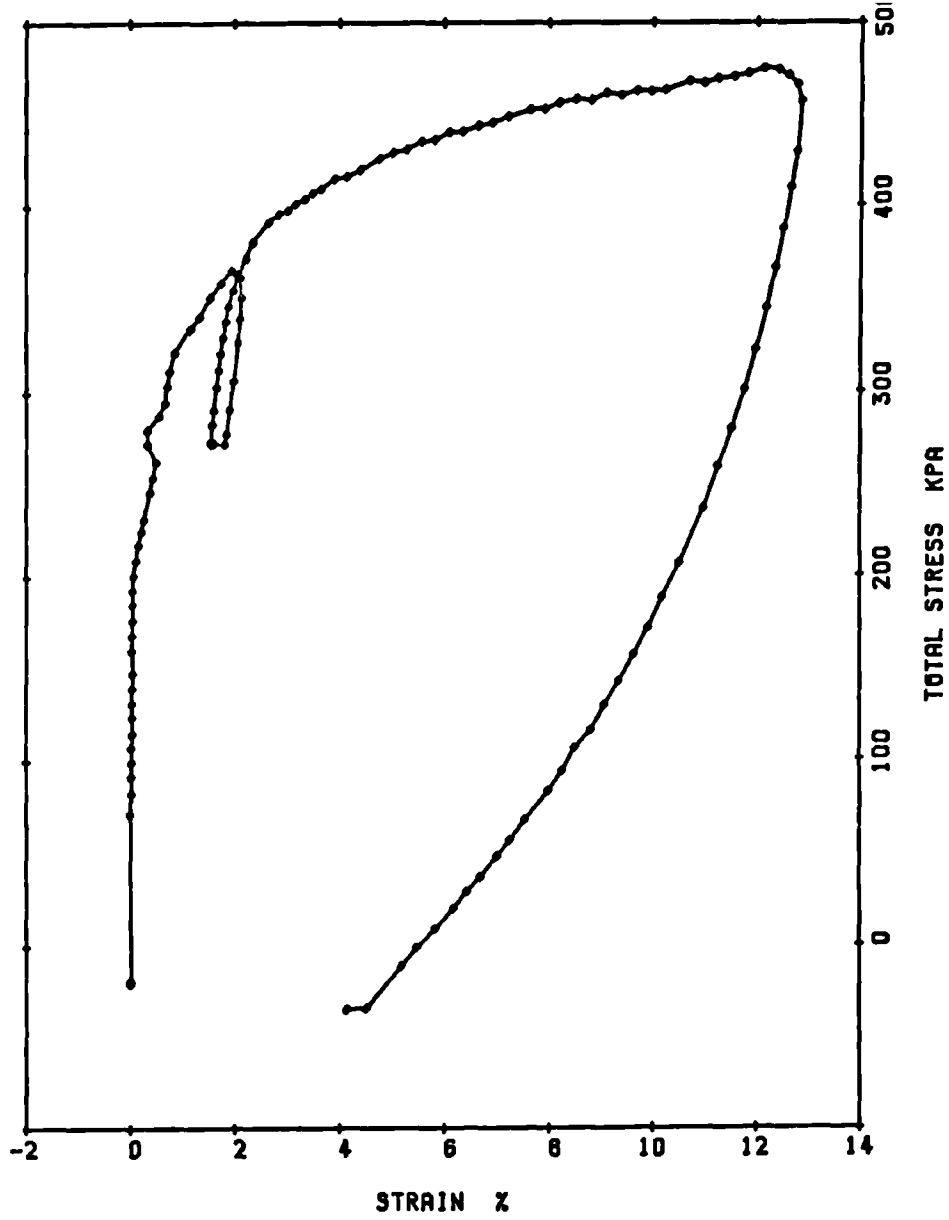


Figure A3.6.

TOTAL STRESS KPA
-20
0
20
40
60
80
100
-2
0
2
4
6
8
10
12
14
STRAIN %
Insitu Techniques
CANNONS PARK
BH SBP1 TEST 1 DEPTH 0.85
FIG.A4.1

TOTAL STRESS KPA
-20
0
20
40
60
80
100
-2
0
2
4
6
8
10
12
14
STRAIN %
Insitu Techniques
CANNONS PARK
BH SBP2 TEST 1 DEPTH 1.8
FIG.A4.2

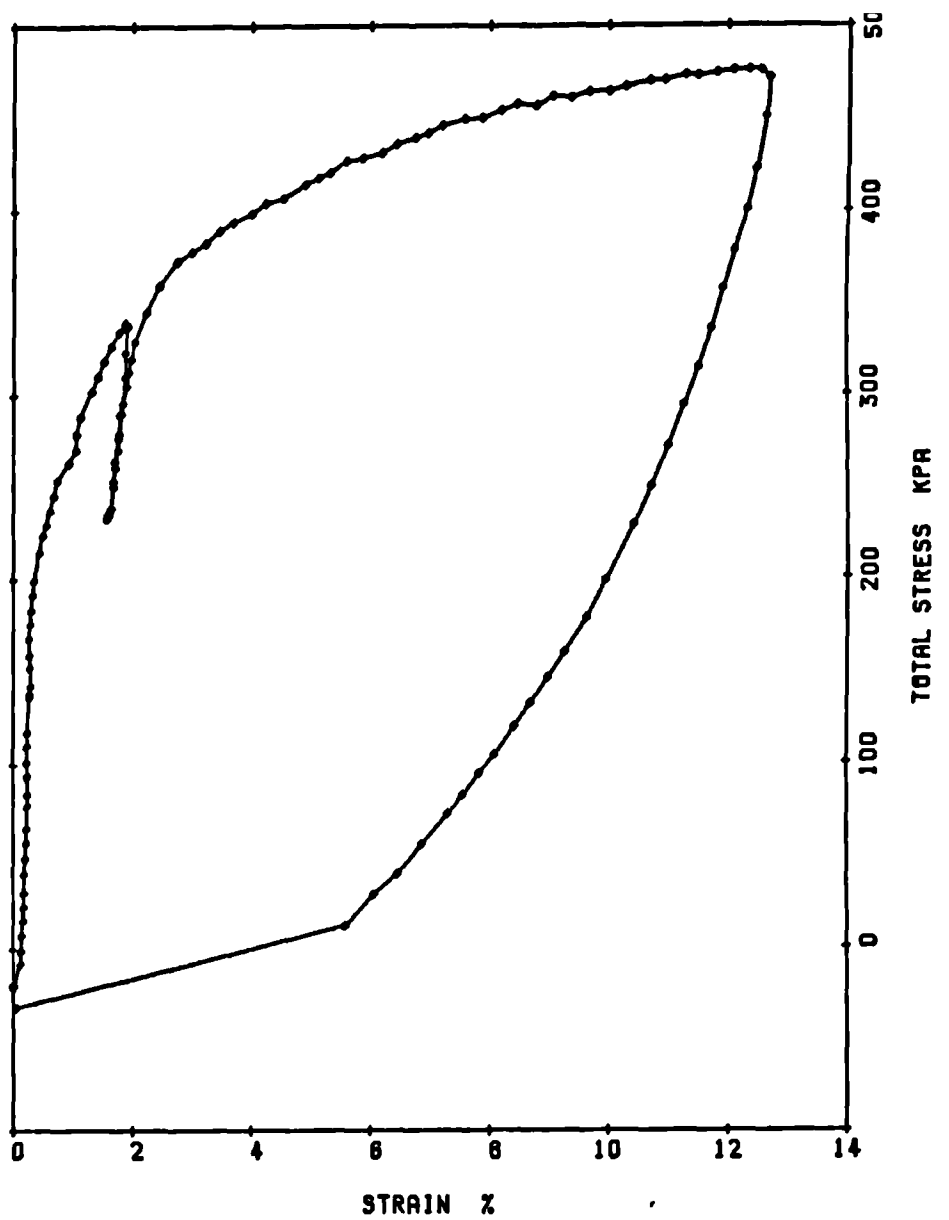


Insitu Techniques

CANNONS PARK

BH SBP1 TEST 2 DEPTH 3.25

FIG.A4.3

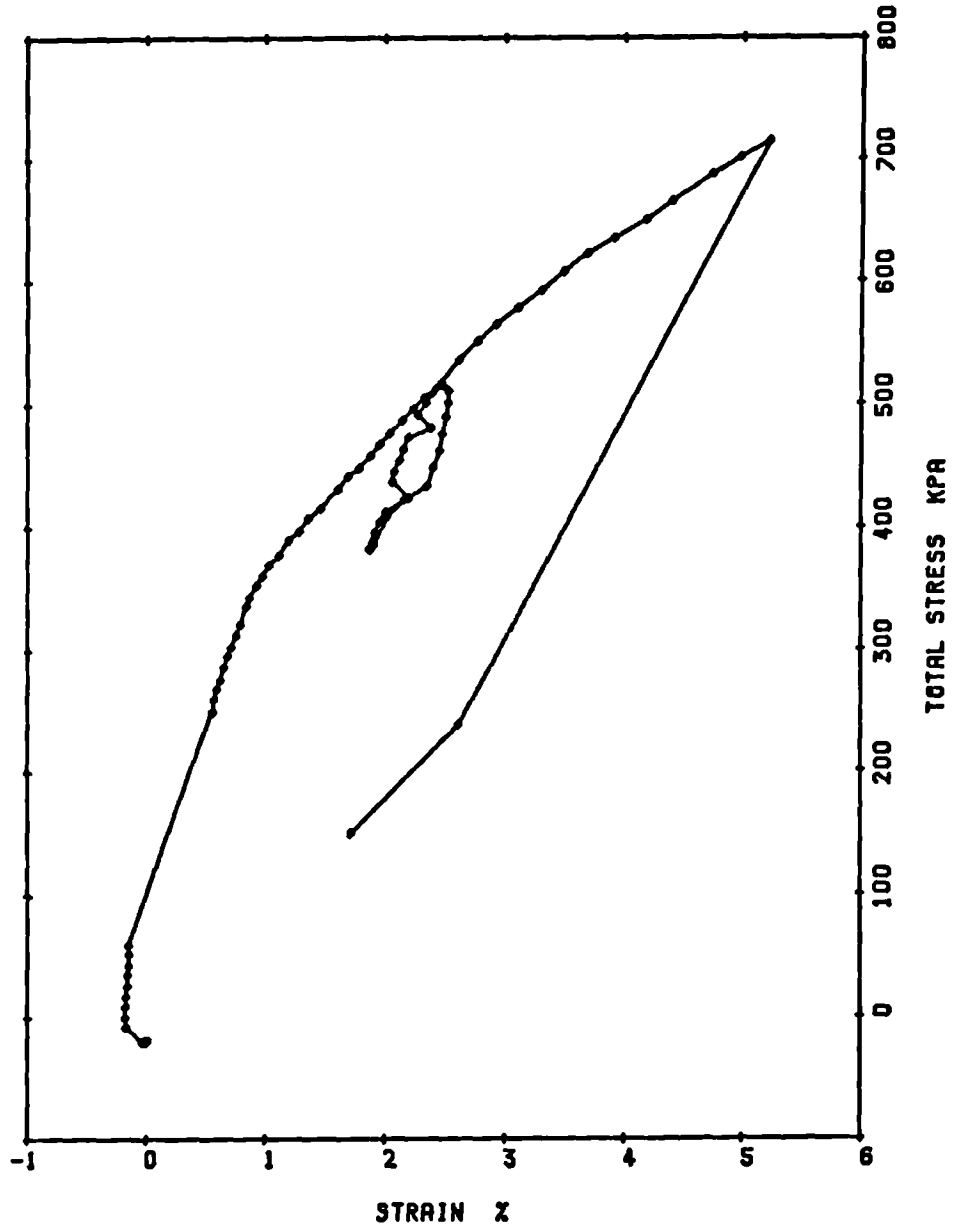


Insitu Techniques

CANNONS PARK

BH SBP1 TEST 3 DEPTH 4.2

FIG.A4.4

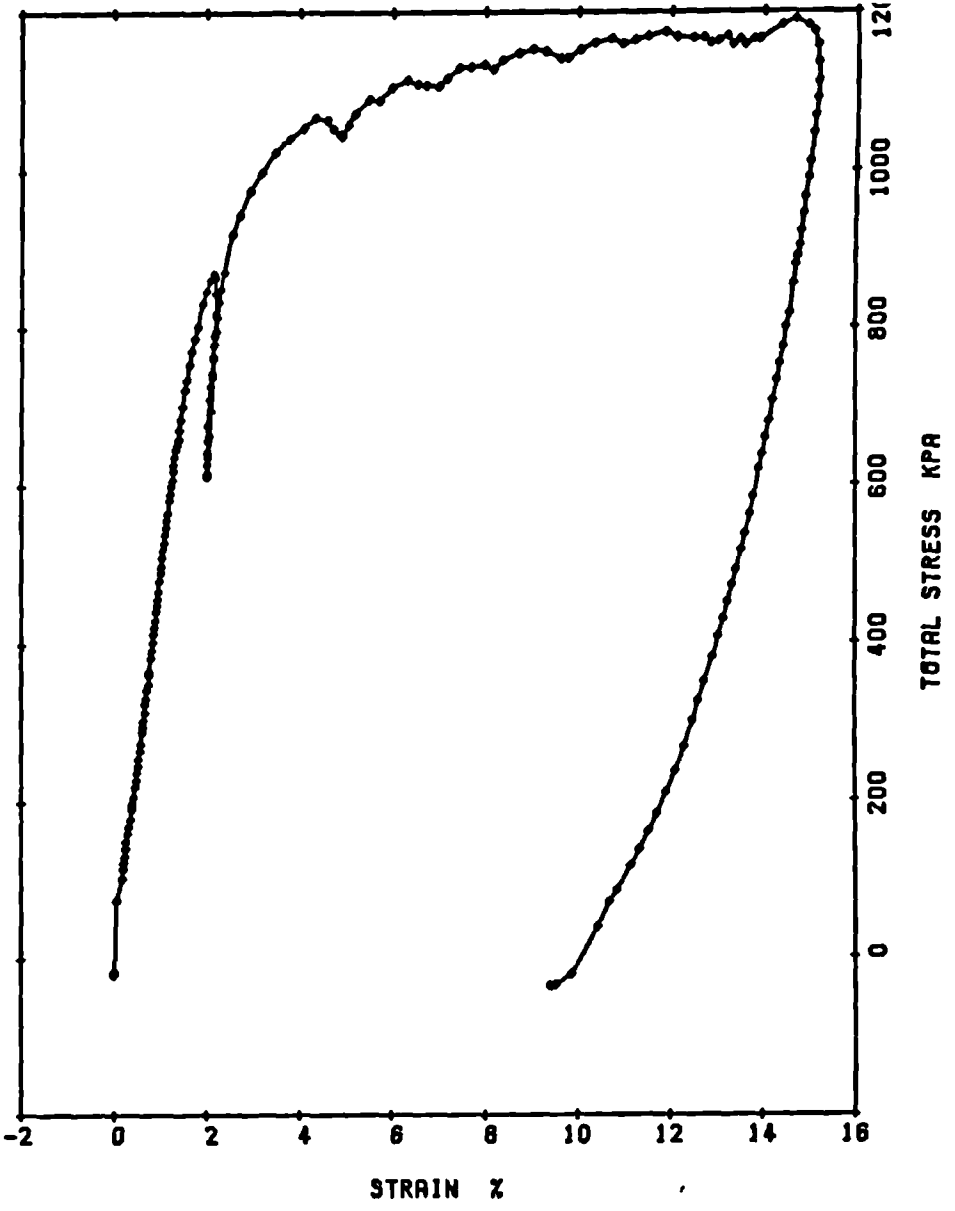


Insitu Techniques

CANNONS PARK

BH SBP1 TEST 4 DEPTH 4.0

FIG.A4.5



Insitu Techniques

CANNONS PARK

BH SBP1 TEST 5 DEPTH 8.3

FIG.A4.6

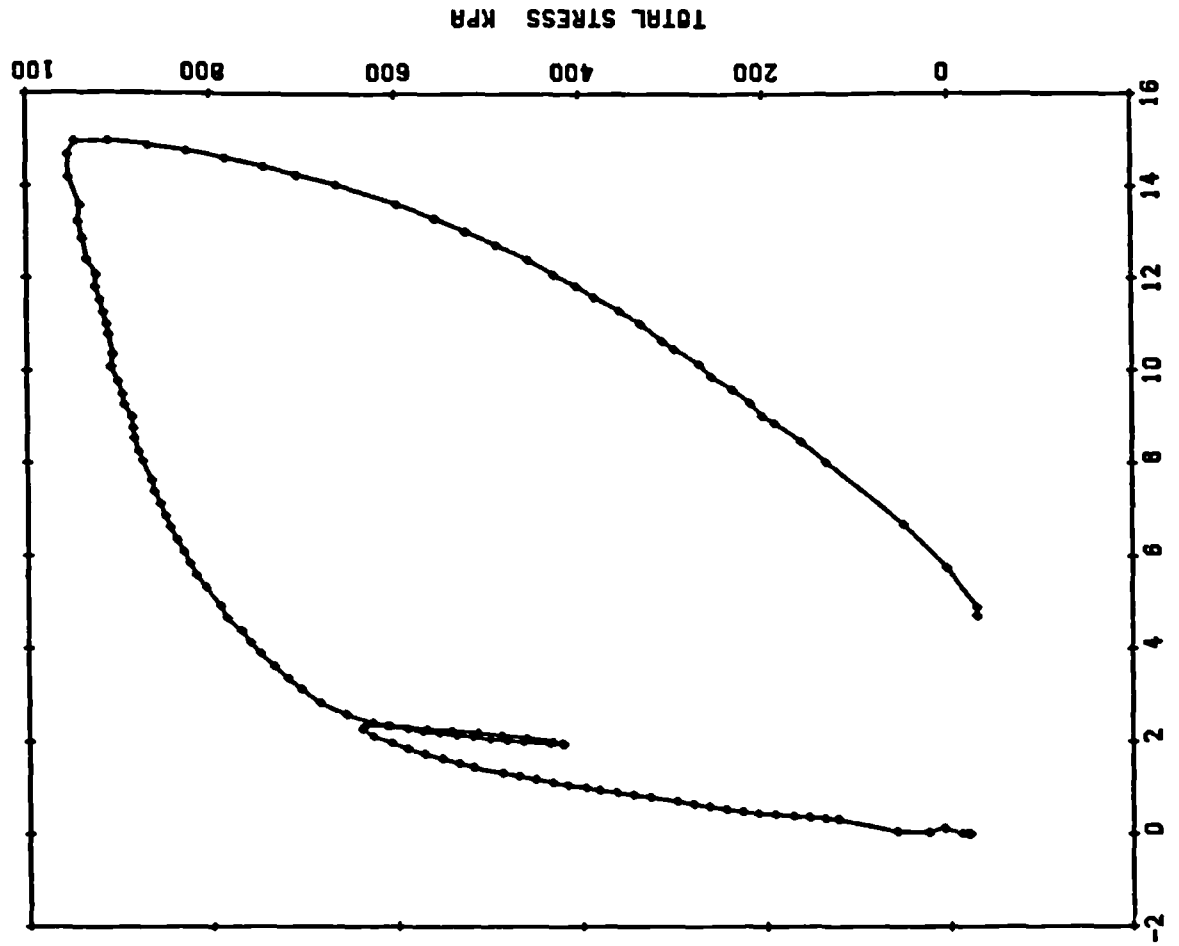
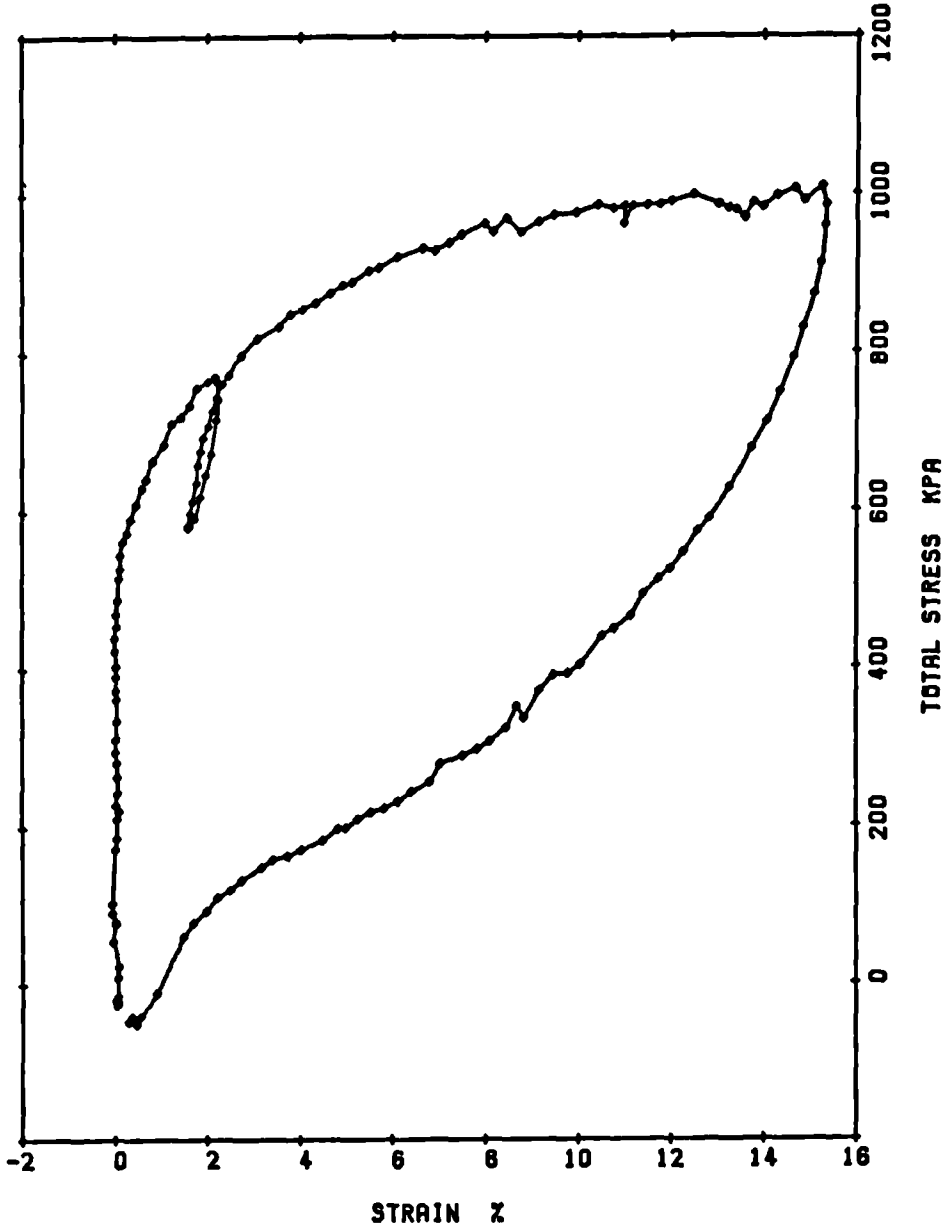


FIG.A4.7

FIG.A4.8

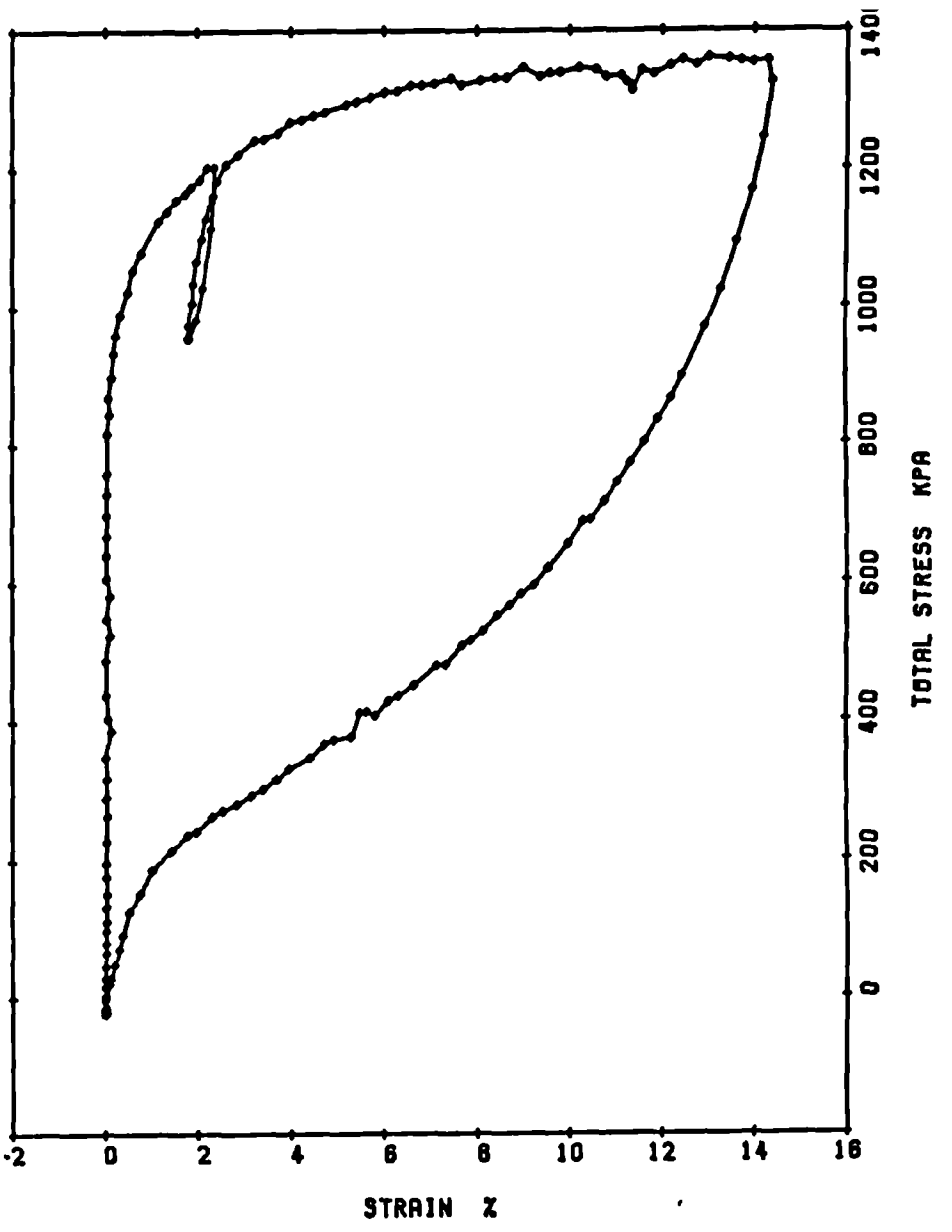


Insitu Techniques

CANNONS PARK

BH 98P1 TEST 8 DEPTH 9.3

FIG.A4.9



Insitu Techniques

CANNONS PARK

BH 98P1 TEST 8 DEPTH 10.3

FIG.A4.10

Case No.	System Employed	Time for 95% Equalisation, t_{qs}	Amplitude Factor T_ω = 20s	Amplitude Factor T_ω = 10s	Phase Shift (seconds) T_ω = 20s	Phase Shift (seconds) T_ω =10s
1	Bonded strain gauge transducer, $^3/_{16}$" tubing, 65 m long no air	20.7 s	0.42	0.22	3.6 s	2.1 s
2	As 1 with 1 cc of trapped air	22.4 s	0.31	0.16	4.0 s	2.2 s
3	As 1, 32.5 m long tubing	10.3 s	0.69	0.43	2.6 s	1.8 s
4	As 1 increasing tube diameter by 30%.	7.2 s	0.80	0.55	2.2 s	1.6 s
5	As 1, but with semi-conductor transducer.	0.0012 s	1.00	0	1.0	0

Table A6.1. Parametric studies of dynamic characteristics of an offshore settlement gauge.

Parameter	Period	Depth (metres)					
	(Seconds) T_ω	50	100	150	200	300	400
Wave length, L_ω (M)		100	100	100	100	100	100
depth factor, K	8	8.6×10^{-2}	3.7×10^{-3}	1.6×10^{-4}	7×10^{-6}	1×10^{-8}	2.4×10^{-11}
L_ω (M)		204.5	225	225	225	225	225
K	12	4.1×10^{-1}	1.2×10^{-1}	3.0×10^{-2}	7.5×10^{-3}	4.6×10^{-4}	2.8×10^{-5}
L_ω (M)		308	373	400	400	400	400
K	16	6.4×10^{-1}	3.6×10^{-1}	1.9×10^{-1}	8.6×10^{-2}	1.8×10^{-2}	3.7×10^{-3}
L_ω (M)		390	523	577	605	624	624
K	20	7.5×10^{-1}	5.5×10^{-1}	3.8×10^{-1}	2.4×10^{-1}	9.7×10^{-2}	3.6×10^{-2}

Table A6.2. Sea bed pressure variations, dependence of response factor K on wave period and bottom depth.

Approx. Storm return period Years	Typical T_ω Seconds	Surf. wave Amplitude Metres	Depth Factor K	Gauge error factor $\Delta P^*/\Delta P_{max}$	Amplitude of settlement ripple mm
				(δt = 0.1 second)	
50	16	15	1.1×10^{-1}	0.039	5.0
10	14.5	13.3	5.7×10^{-2}	0.043	2.6
1	13.5	11	3.3×10^{-3}	0.047	0.1

Table A6.3. Effect of periodic waves on an offshore settlement gauge.

Transducer	Manufacturers' Details					Components
	Weight	Combined	Line Pressure,	Compliance	Electrical Principal	(based on previous experience in I.C. Laboratories)
Bell and Howell	1.8 kg +fittings	±0.5% F.R.O.	350 bar, max. line +3.5 bar, −0.7 bar diff.		unbonded foil strain gauge	Good long-term stability
Sensotec	3.8 kg +fittings	±0.25%F.R.O. and ±0.1% F.R.O.	106 bar, max. line ±106 bar differential	±0.16 cc/ F.S.O.	bonded foil strain gauge	Can give drift problems
Druck	0.3 kg +fittings	±0.1% F.R.O.	35 bar max. line + 2.1 bar, −1.4 bar diff.	$\pm 1.2 \times 10^{-5}$ cc/ F.S.O.	semiconductor strain gauge	Can give drift problems and are temperature sensitive.

Table A6.4. Manufacturs' specifications for differential pressure transducers.

Channel	Test Series	mm settlement/ Volt output	Mean error from B.S.L. (mm)
Gauge 1, Sensotec	Hyperbaric C.	62.0	0.25
" 1, "	Laboratory*	62.0	0.60
" 1, Druck	Hyperbaric C.	83.8	0.25
" 1, "	Laboratory*	83.8	0.60
Gauge 2, Sensotec	Laboratory*	69.9	0.60
" 2, Druck	Laboratory*	84.5	0.80

Table A6.5. Summary of calibrations for prototype settlement gauges.

* Tests carried out at 700 Kpa line pressure.

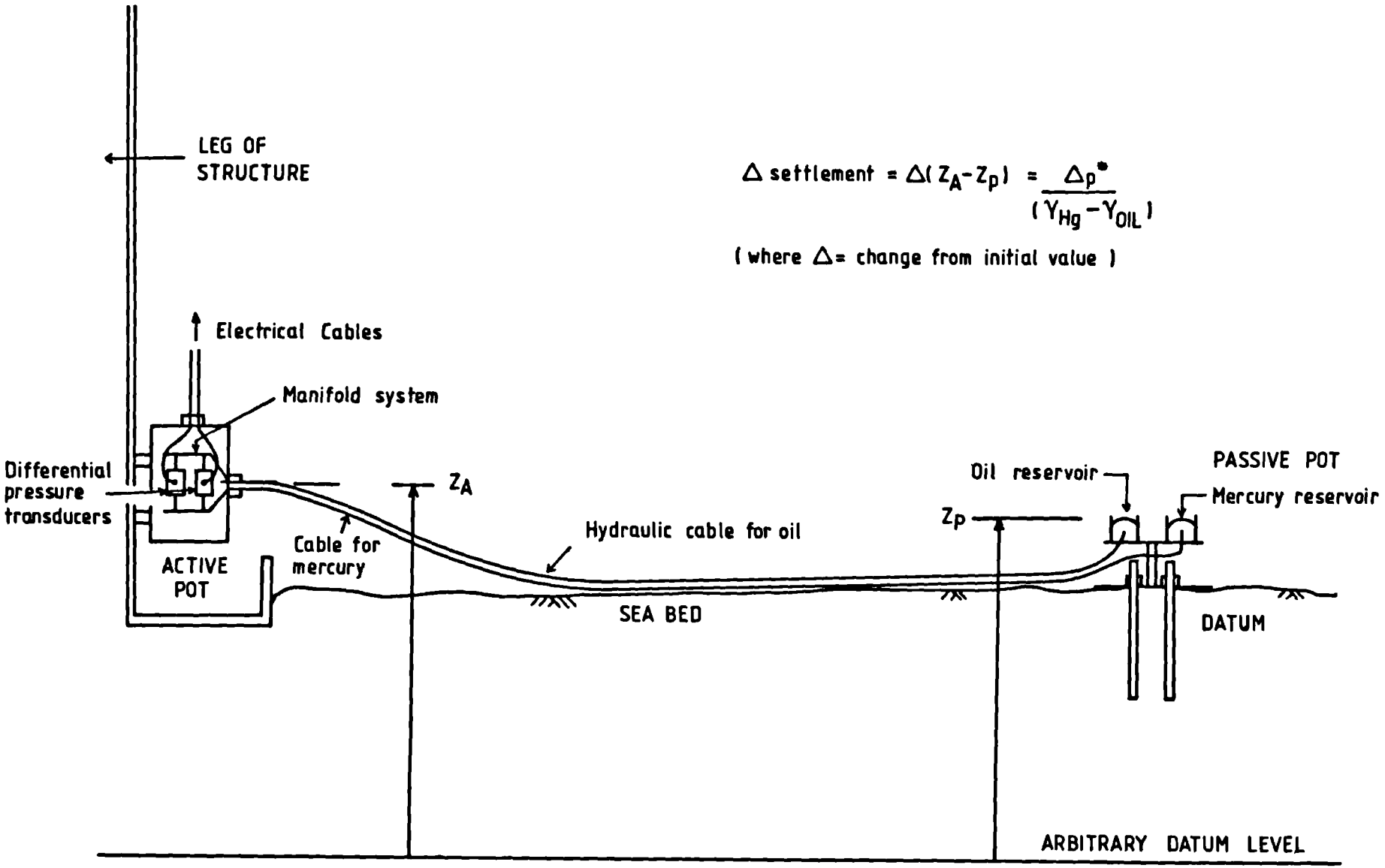


Figure A6.1. General principle of settlement gauge.

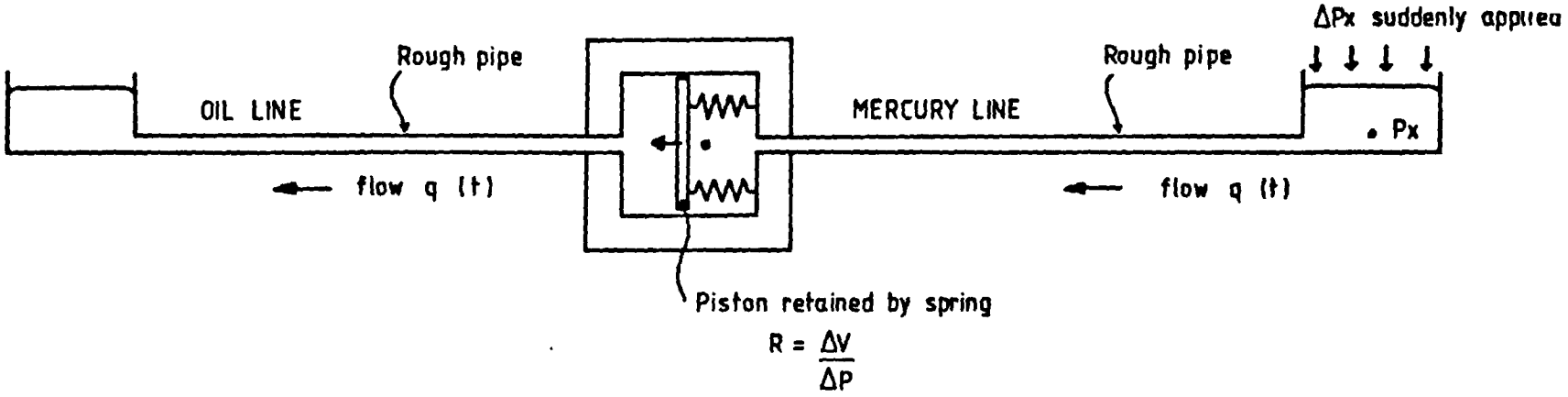


Figure A6.2. Schematic of equilibration following a sudden change in relative level.

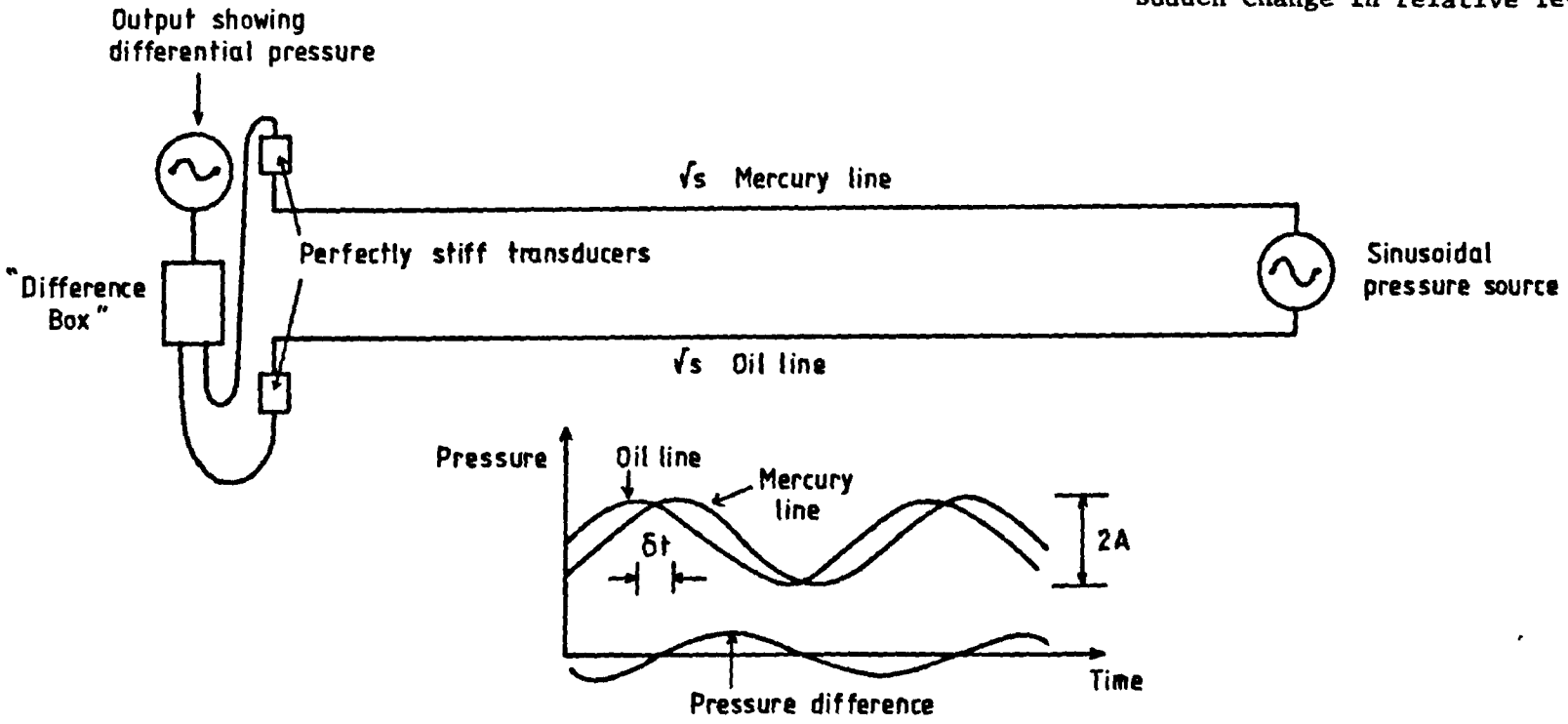
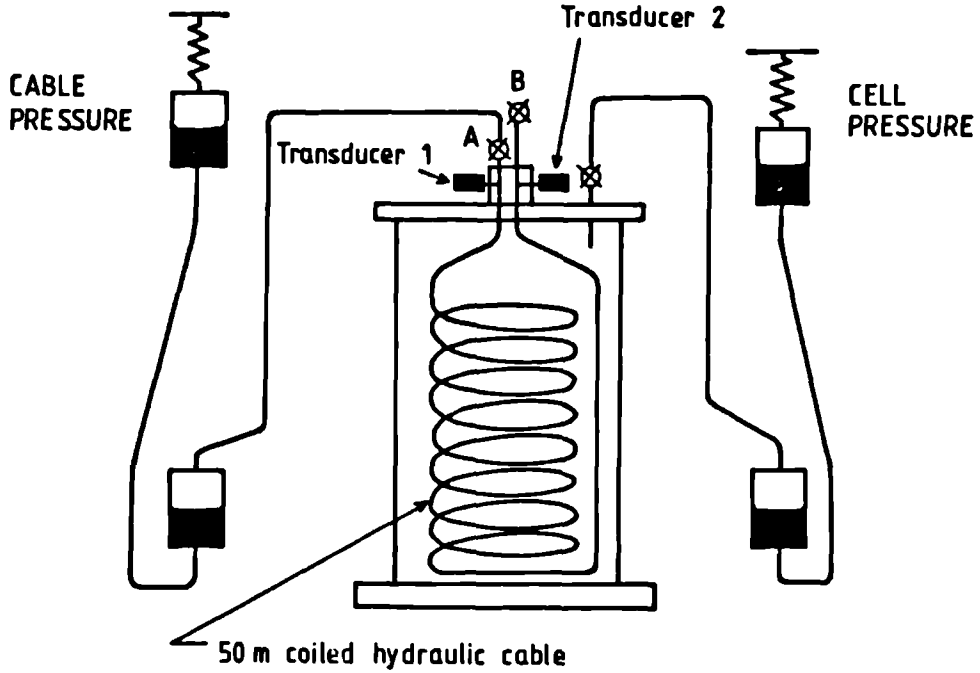


Figure A6.3. Schematic for effects of sea bed pressure fluctuations.



Procedure

(i) Cell pressure set at 90 psi
(ii) Inner cable pressure set at 90 psi (Valve B closed)
(iii) Valve A closed
(iv) Cable pressure supply set at 110 psi
(v) Valve A opened quickly to generate pressure wave. Wave arrival recorded by transducers 1 and 2 at either end of cable. Traces monitored on Dual Beam Storage Oscilloscope

Figure A6.4. Experiments to monitor time lags for mercury and oil filled tubing.

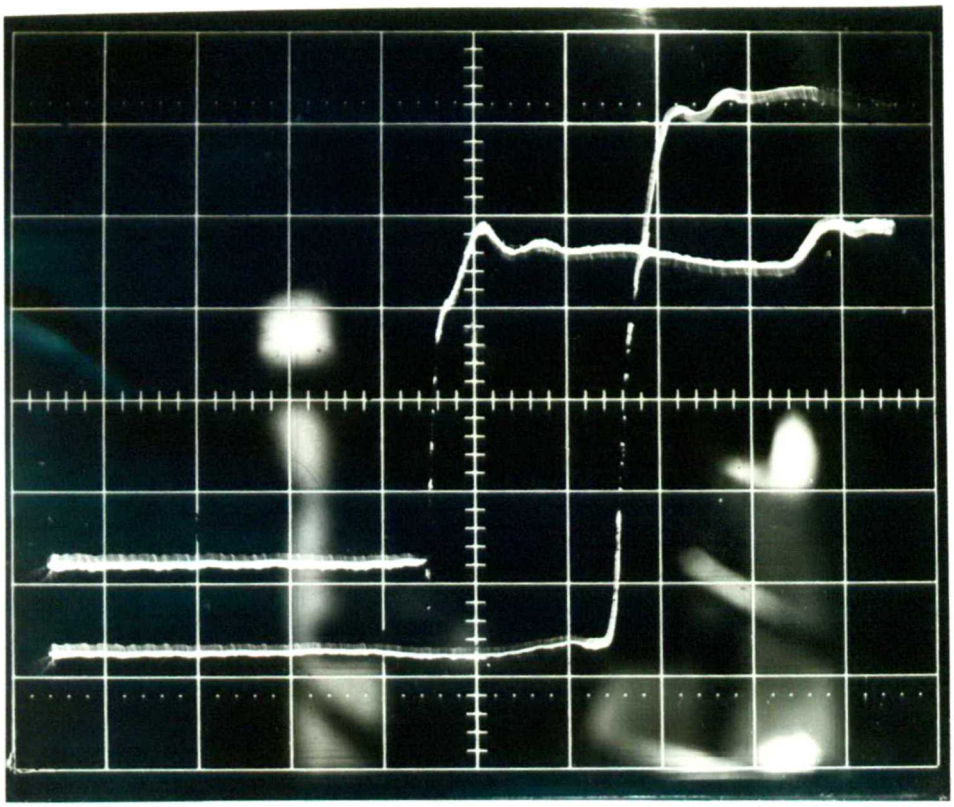
OPPOSITE

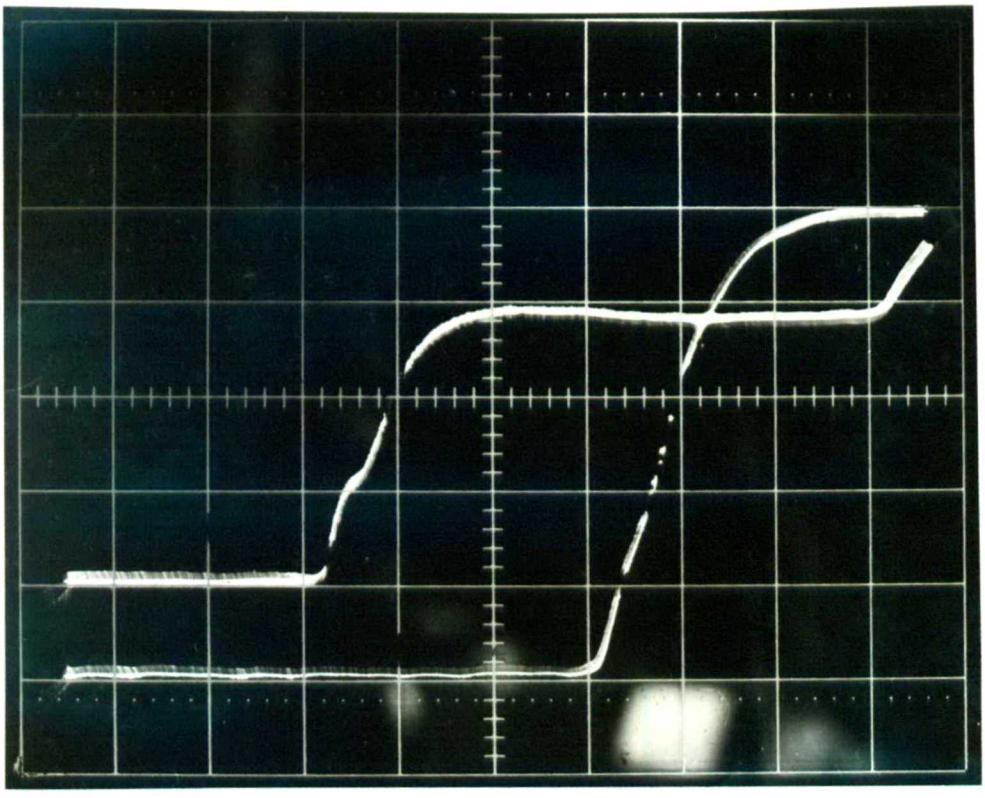
Above

Figure A6.5. Oscilloscope traces for mercury filled tube, one time division is equivalent to 50 ms.

Below

Figure A6.6. Oscilloscope traces for water filled tube, one time division is equivalent to 10 ms.





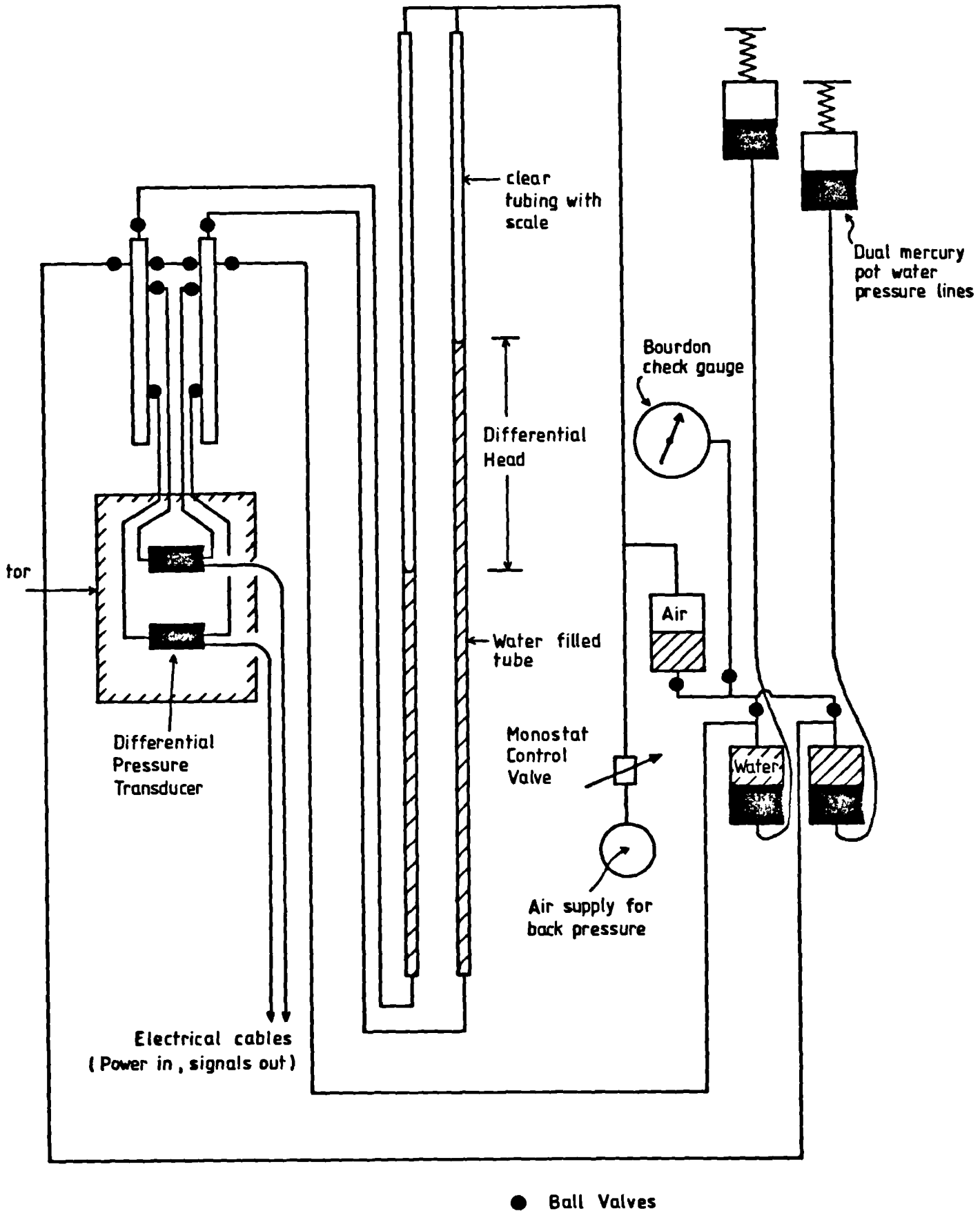


Figure A6.7. Apparatus for the calibration of differential pressure transducers.

OPPOSITE

Top

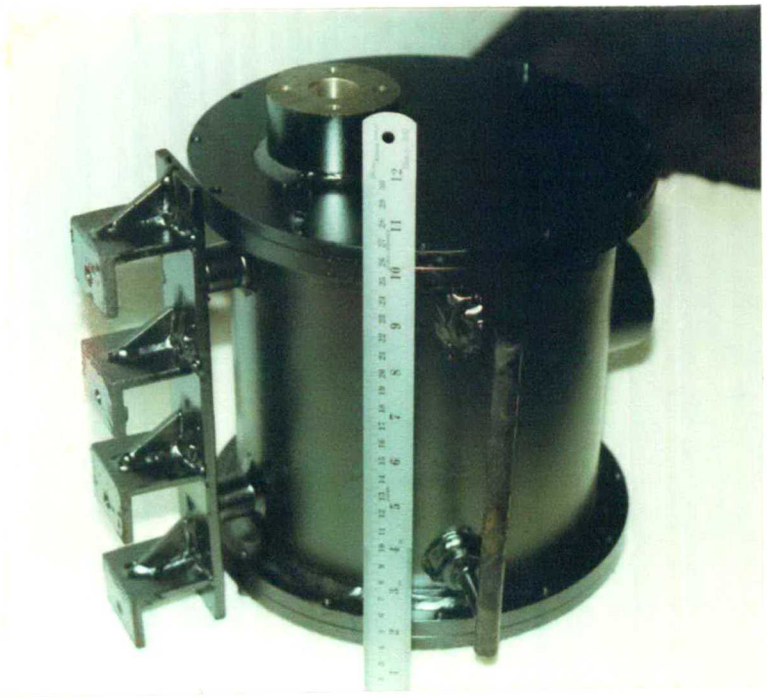
Figure A6.8. Active pot, painted in Epoxy Coal Tar.

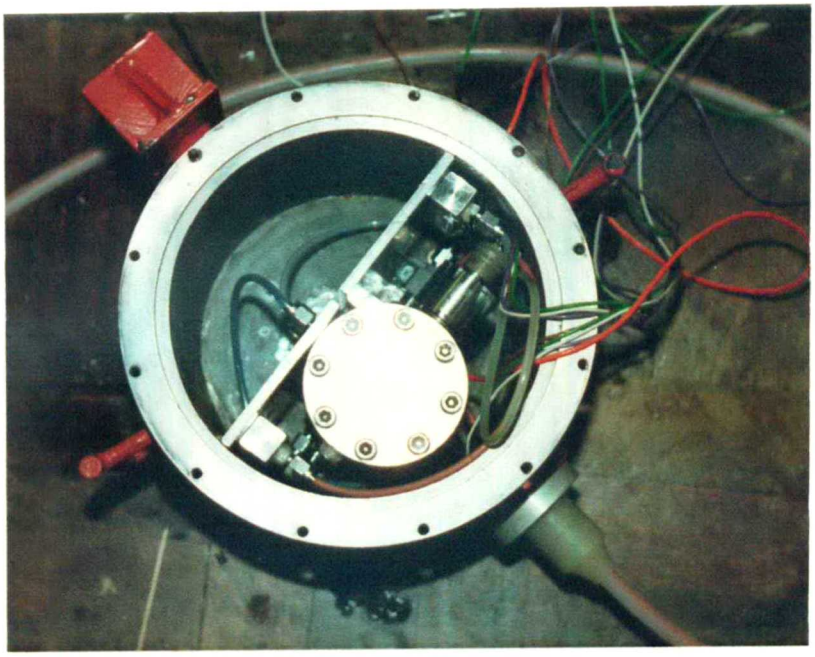
Middle

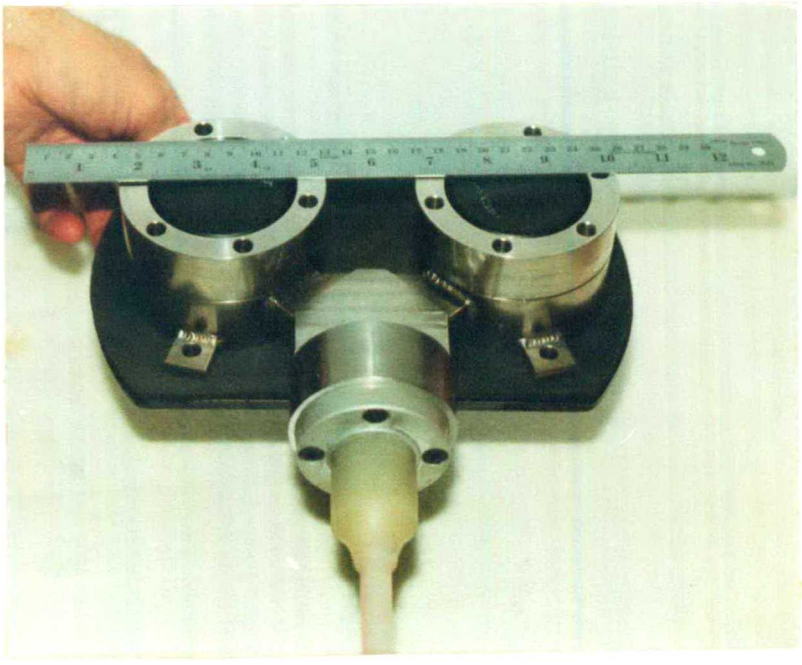
Figure A6.9. Active pot, top view showing transducers and space for signal conditioning.

Bottom

Figure A6.10. Passive pot, general view.







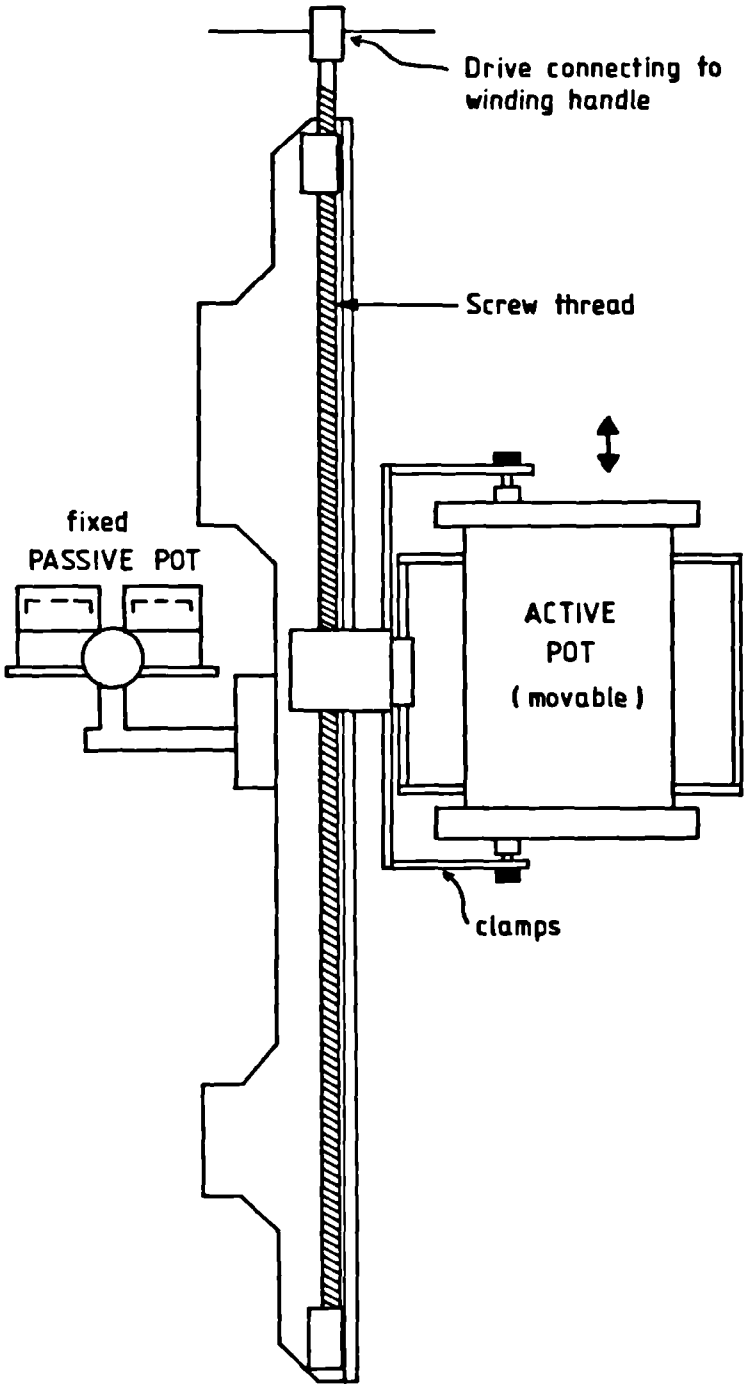
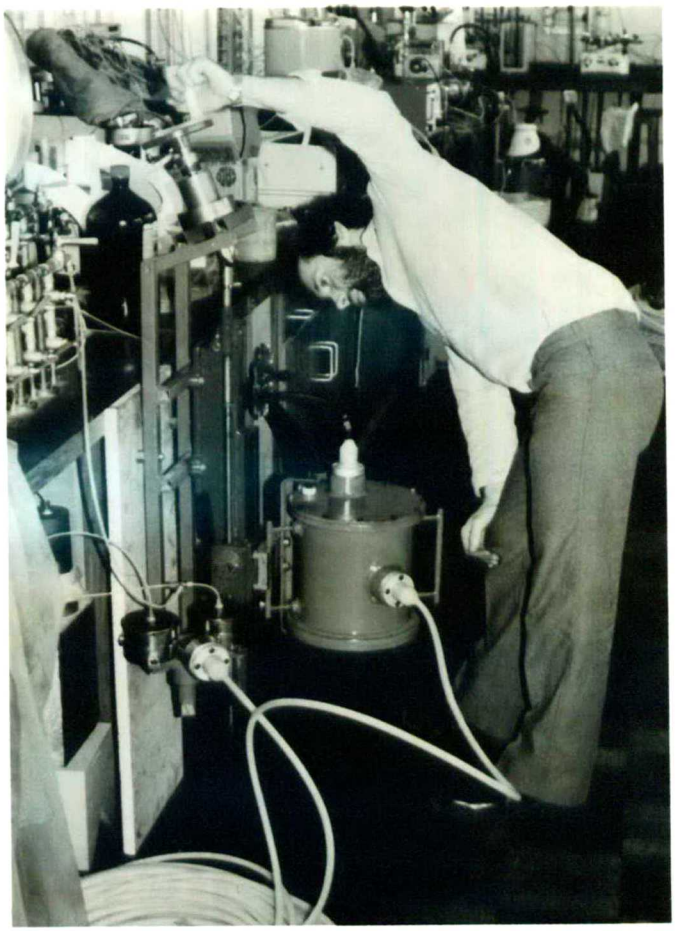


Figure A6.11. Apparatus for the calibration of settlement gauge.

Figure A6.12. (on following page). Photograph of gauge undergoing laboratory calibration.



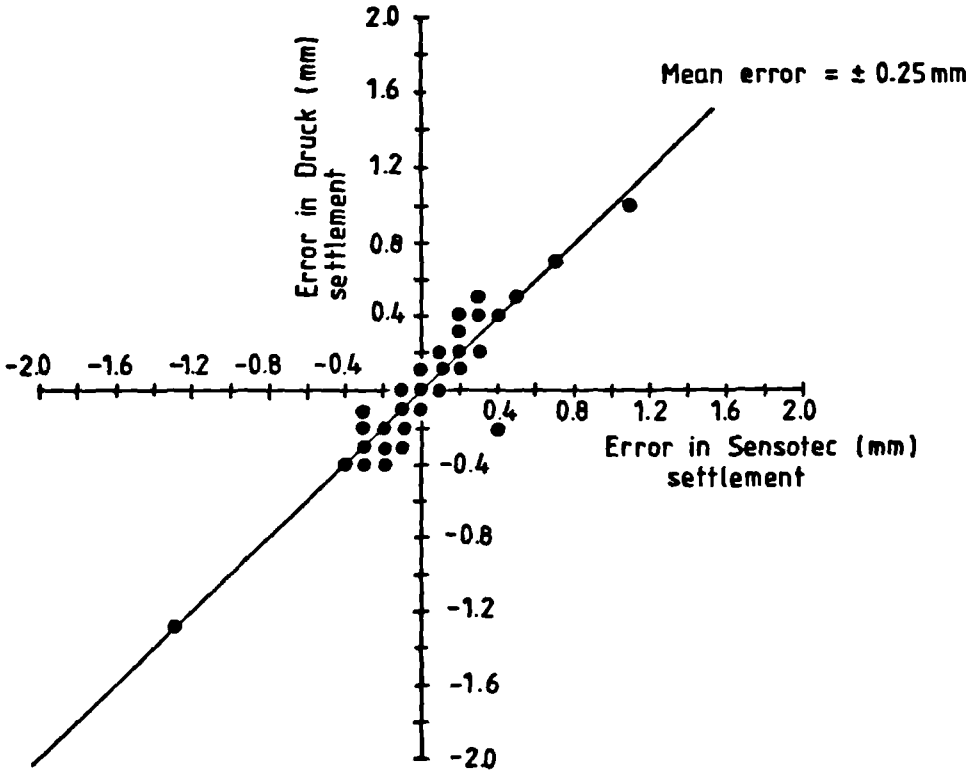


Figure A6.13. Scatter plot for settlement gauge errors from a best fit line.

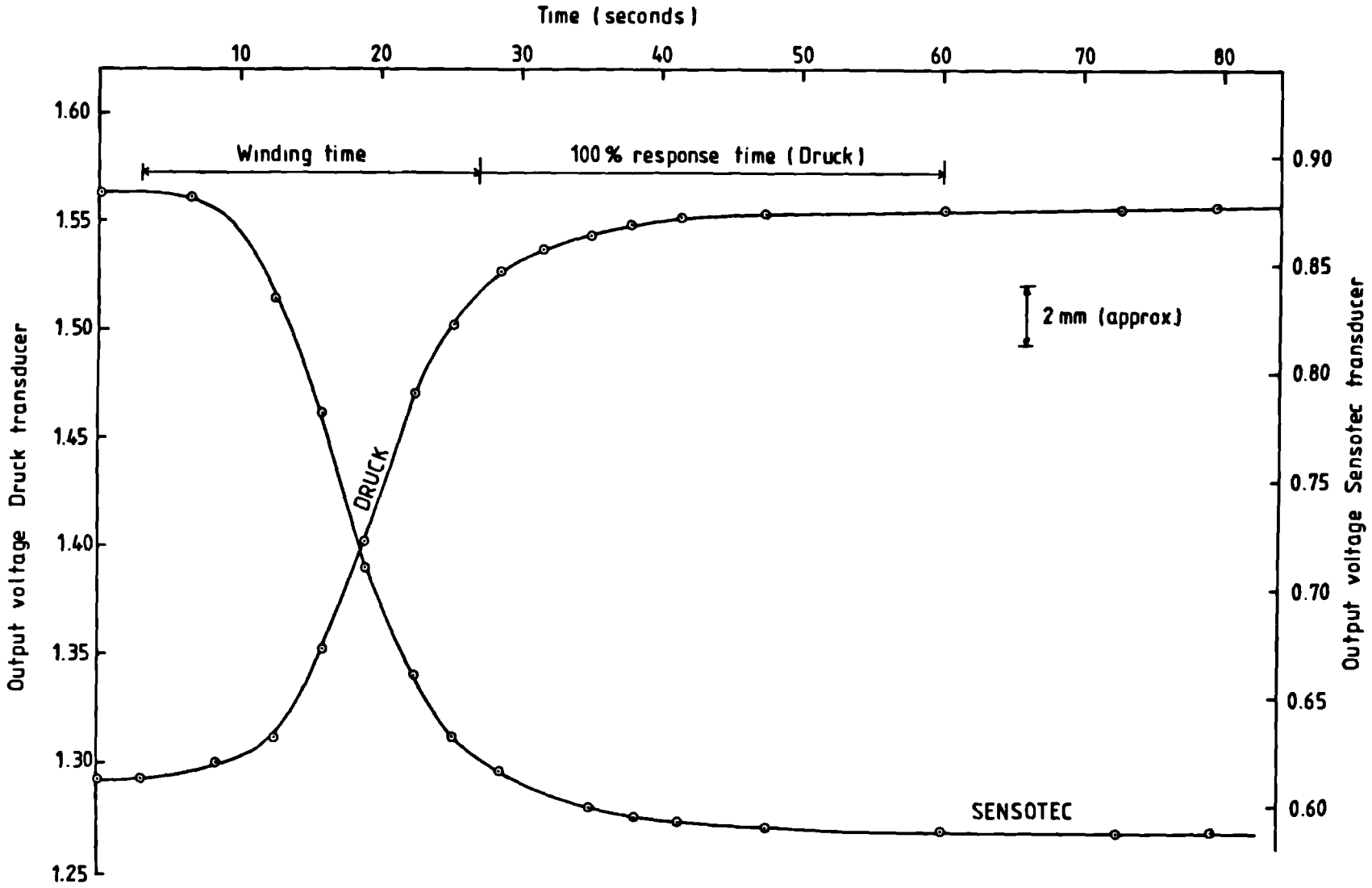


Figure A6.14. Settlement gauge response to a rapid change in relative level.

OPPOSITE

Above

Figure A6.15. Packaged equipment being lowered into position on Leg A4 at Nigg Bay construction yard.

Below

Figure A6.16. General view of Leg A4 at Nigg Bay, note man in blue overalls standing at settlement gauge location, near to left hand top of pile guide cluster.




22
21
20
19
18
17